Les granites pegmatitiques enrichis en éléments de terres rares légères marqueurs des processus de croissance et de différenciation crustale : exemple de la Province Protérozoïque de Grenville, Québec

François Turlin

Ecole Doctorale RP2E « Ressources, Procédés, Produits, Environnement »
Collegium Sciences et Technologies
Université de Lorraine – LabEx Ressources 21
UMR 7359 GeoRessources

THÈSE

Présentée pour l'obtention du grade de

Docteur de l'Université de Lorraine
Spécialité Géosciences

Par
François Turlin

Les granites pegmatitiques enrichis en éléments de terres rares légères marqueurs des processus de croissance et de différenciation crustale : Exemple de la Province Protérozoïque de Grenville, Québec

Light rare-earth elements enriched pegmatitic granite as tracers of crustal growth and differentiation processes: example of the Proterozoic Grenville Province, Quebec

Soutenance publique le 15 Décembre 2017

Membres du jury :

Rapporteurs :	
Mme Kathryn Goodenough	Géologue senior, Directrice adjointe, British Geological Survey, Edinburgh
M. Philippe Boulvais	Maître de conférences, Université de Rennes 1
Examinateurs :	
Mme Marieke Van Lichtervelde	Chercheur, IRD, Toulouse
M. Philippe Muchez	Professeur, Université de Leuven, Belgique
M. Toby Rivers	Professeur, Memorial University (NL), Canada
M. Jean-Marc Montel	Professeur, Université de Lorraine
Directeurs de thèse :	
Mme Anne-Sylvie André-Mayer	Professeur, Université de Lorraine
M. Olivier Vanderhaeghe	Professeur, Université Toulouse III
Invités :	
M. Félix Gervais	Professeur adjoint, Polytechnique Montréal (QC), Canada
M. Abdelali Moukhsil	Géologue expert, Ministère de l'Énergie et des Ressources naturelles (QC), Canada
M. Aurélien Eglinger	Maître de conférences, Université de Lorraine

Résumé : Les éléments de terres rares (ÉTR) sont des métaux de grand intérêt économique et des traceurs géologiques de premier ordre mais leur cycle métallogénique reste encore méconnu. La Province de Grenville expose sa racine orogénique et présente une grande concentration d'occurrences d'ÉTR, notamment associées à des granites pegmatitiques (« PGD ») dans le Grenville central. Deux mécanismes peuvent être à l'origine de ces PGD, (i) la fusion partielle d'une croûte continentale archéenne et/ou paléoprotérozoïque de la racine orogénique, ou (ii) l'extrême différenciation de magmas mantelliques produits en contexte d'extension post-orogénique. Une approche multi-méthodes (terrain, pétrogéochimie, géochronologie et isotopie) permet de caractériser ces PGD à ÉTR et de discuter leur pétrogénèse dans le cadre de l'évolution géodynamique de la province. Ils ont intrudé à ~1005-1000 Ma (U-Pb monazite et zircon) des métaplutons (minéralisation en allanite) ou des séries métasédimentaires (minéralisation en monazite) du segment de moyenne pression de la ceinture Allochtone. La datation U-Pb sur monazite et apatite d'un leucosome de ces paragneiss migmatitiques met en évidence un pic de métamorphisme au faciès granulite à 1080-1050 Ma suivi d'un refroidissement lent à un taux de 2 à 6°C/Ma, d'abord dans les conditions suprasolidus jusqu'à l'intrusion des PGD dans des conditions proches du solidus hydraté, puis dans des conditions subsolidus jusqu'à l'isotherme 450-500°C enregistré à 970-950 Ma. L'intrusion des PGD est synchrone de l'initiation dès ~1005 Ma de la fusion partielle prolongée (> 20 Ma) des métasédiments parautochtones sous-jacents. Le caractère peralumineux des PGD, l'étude de zircons néoformés des PGD (isotopes U-Pb-Hf-O et éléments traces), et l'étude pétrogéochimique des PGD et des métapélites paléoprotérozoïques à archéennes de la ceinture Parautochtone, issues de l'érosion de la marge de Laurentia, traduisent la formation des PGD par leur fusion partielle. Au contraire, un PGD issu de la remobilisation de plutons allochtones est peu minéralisé en ÉTR, confirmant que l'extraction des ÉTR de ces occurrences du Grenville central est associée à des roches d'affinité crustale du Craton du Supérieur.

Abstract: The Rare Earth Elements (REE) are of great economic interest and first order geological tracers. However, their metallogenic cycle remains poorly defined. The Grenville Province exposes its orogenic root and shows numerous REE occurrences that are especially associated with pegmatitic granite dykes ("PGD") in the central Grenville. Two hypotheses can account for the genesis of these PGD, whether (i) the partial melting of the orogenic root composed of reworked Archean and/or Proterozoic pre-existing continental crust, or (ii) the extreme differentiation of mantle melts produced during post-orogenic extension. A multi-method approach (field geology, petrogeochemistry, geochronology and isotopy) allow to characterize the PGD and discuss their petrogenesis during the geodynamic evolution of the province. They intruded at ca. 1005-1000 Ma (U-Pb on monazite and zircon) metaplutons (mineralization hosted in allanite) or metasedimentary sequences (mineralization hosted in monazite) from the mid-pressure allochthonous crustal segment. U-Pb dating on monazite and apatite from a single leucosome of these migmatitic paragneisses evidence for a peak of metamorphism at ca. 1080-1050 Ma that was followed by a slow cooling at a rate of 2 to 6°C/Ma, first under suprasolidus conditions until the close to wet-solidus intrusion of PGD, and then under subsolidus conditions down to the 450-500°C isotherm dated at ca. 970-950 Ma. The intrusion of the PGD is coeval with the initiation as early as ca. 1005 Ma of the protracted (> 20 Ma) partial melting of underlying parautochthonous paragneisses. The peraluminous character of the PGD, the investigation of pristine magmatic zircon of the PGD (U-Pb-Hf-O isotopes and trace elements), and the petrogeochemical investigations of parautochthonous Paleoproterozoic-Archean metapelites that derive from the Laurentian margin's erosion, points to the derivation of the PGD from their partial melting. To the contrary, one PGD derived from the reworking of allochthonous plutonic units is poorly mineralized in REE, and confirms that REE from the central Grenville occurrences are issued from crustal rocks of the Superior Craton.

Cette thèse a été financée par la région Lorraine (Grand-Est) et le Laboratoire d'Excellence Ressources 21 à travers le programme national des « Investissements d'avenir » et s'intègre dans l'axe Terres Rares Canada. Je tiens donc à remercier l'ensemble des personnes et partenaires impliqués dans la genèse de ce projet.

Cette thèse a également bénéficié du soutien du réseau DIVEX auquel notre réflexion a été intégrée. Merci à toutes les personnes et partenaires impliqués dans ce réseau.

Merci aux membres du jury d'avoir évalué ce travail : Madame Kathryn Goodenough et Monsieur Philippe Boulvais pour votre intérêt pour mon travail et vos commentaires constructifs, et à Madame Marieke Van Lichtervelde, et Messieurs Philippe Muchez, Toby Rivers et Jean-Marc Montel pour vos apports sur vos spécialités respectives.

Un très grand merci à mes deux directeurs de thèse, Anne-Sylvie André-Mayer et Olivier Vanderhaeghe (le duo de choc !), qui m'ont fait confiance depuis le Master en me confiant un projet sur les minéralisations cuprifères du gisement de Lumwana en Zambie, connexe à la thèse d'Aurélien Eglinger. Merci à tous les deux d'avoir souhaité poursuivre, après ces deux années, l'aventure en thèse en me proposant ce sujet passionnant et de m'avoir intégré à la réflexion dès le montage du projet ! Vous avez pris en compte mes attentes et avez fait en sorte que ce projet me ressemble (6 critères sur 7 Anne-Sylvie, c'était au top !), merci à vous ! Votre encadrement au quotidien, votre soutien sans faille, vos conseils et votre expérience m'ont énormément apporté depuis 5 ans maintenant ! Merci pour votre professionnalisme, d'avoir toujours cru en moi, de m'avoir laissé prendre des directions parfois métallogéniques parfois géodynamiques et de m'avoir donné autant d'autonomie au quotidien ! Anne-Sylvie, merci d'avoir toujours pris le temps d'échanger même pendant le rush du congrès SGA de Nancy et même depuis l'étranger pendant tes divers déplacements ! Merci pour ces souvenirs mémorables de terrain, je pense notamment à Lebel-sur-Quévillon avec Laure (« Anne-Sylvie, c'est le centre-ville, il y a la SAQ… »), pour ton optimisme quotidien, ta bienveillance, de m'avoir intégré à d'autres projets de recherche, de m'avoir confié des enseignements, bref de m'avoir autant fait confiance ! Cela a été « excellent ! » de travailler à tes côtés, j'espère que ça continuera ! Olivier, même depuis Toulouse tu as toujours été présent (tu commentes des coupes à minuit et demi !) par mail, téléphone, Skype… bref tous les moyens étaient bons pour échanger sur l'échelle lithosphérique et la tectonique du camembert ! Merci pour ta vision grande échelle, ton esprit critique, ta créativité, d'avoir sans cesse été un agitateur d'idées (même si des fois il faut que ça se repose un peu !) et de m'avoir forcé à faire des coupes ! J'espère que nous nous retrouverons sur d'autres projets à l'avenir !

Félix, merci d'avoir accepté d'intégrer ce projet après notre rencontre à Québec Mines 2014, d'avoir apporté une telle rigueur, ton expérience sur la zone d'étude et tes conseils sur la rédaction d'articles scientifiques. Cela a été très enrichissant de travailler avec toi et cela m'a forcé à argumenter mes idées. Merci à toi.

Ce projet n'aurait pu être développé sans le soutien d'Abdelali Moukhsil du Ministère de l'Énergie des Ressources naturelles du Québec qui m'a fait confiance dès le début et a été d'une grande aide dans la définition des objets d'étude, dans la préparation et la logistique du terrain, et dans la compréhension de cette géologie complexe. Merci pour ton expertise et pour tout ce que tu m'as apporté, j'espère que nous continuerons à travailler ensemble ! J'en profite pour remercier également Patrice Roy pour avoir soutenu le projet et Fabien Solgadi, pour toute ton expérience, les discussions enrichissantes que nous avons eues et les parties de tarot sur le camp après manger ! Merci à tous pour votre accueil à Val d'Or !

Merci également à toute l'équipe du Ministère de l'Énergie des Ressources naturelles du Québec de Val d'Or (Mehdi, Hugo, Pénélope…), de Rouyn-Noranda (Jean) et de Québec (Jonathan et tes collègues de l'entrepôt) pour votre accueil et votre aide dans la préparation des campagnes de terrain, vous retrouver à Québec Mines était un réel plaisir qui me manquera ! Merci à toutes les équipes Grenville avec lesquelles j'ai eu la chance de travailler : Aziz, Saïd, Louise, Audrey, Lisa, Félix et Gabriel ; Guillaume et Carl pour votre accueil à Manic et le prêt de la scie à roches ; et Wellie et Robert pour l'échantillonnage !, ainsi que tous les autres croisés sur le terrain ou à la table à roches !

La première campagne de terrain a été réalisée à la suite de l'école de terrain en Abitibi. Je tiens à remercier toutes les personnes impliquées dans ce programme et qui permettent depuis tant d'années à des étudiants d'avoir une telle expérience au Québec : Alain Cheilletz, Robert Marquis, Denis Bois, Louise Labbé, Li Zhen Cheng, ainsi que tous les intervenants que j'ai eu sur le terrain : Jean Goutier, François Leclerc, Hugo Dubé-Loubert, Ali Moukhsil, Fabien Solgadi, et bien sûr Anne-Sylvie ! Merci à mes collègues de cette école Laurène, Rocio, Antoine, Landry, Simo et Pierre.

Cette thèse n'aurait pu se faire sans les collaborations de Marc Poujol et d'Armin Zeh sur la géochronologie/isotopie monazite, apatite et zircon. Merci à tous les deux pour le partage de votre expérience et pour les discussions que nous avons eu ! Merci à Etienne Deloule et Nordine Bouden pour l'acquisition, les conseils et l'aide au traitement des analyses isotopiques sur la SIMS au CRPG. Merci également à Marieke Van Lichtervelde pour toutes les discussions

passionnées sur les pegmatites que ce soit au Cap de Creus (merci encore pour l'invitation !), à Toulouse ou Nancy. Tu m'as apporté ton expérience sur ces objets, même si celles-ci continuent de t'intriguer ! À bientôt pour la suite ! Merci également à Michel Cuney, Arnaud Villaros pour votre expérience sur les granites à métaux rares, et à Niels Hulsbosch et Philippe Muchez pour les discussions passionnantes sur ces « granites pegmatitiques » si « bizarres ! » !

Merci également aux personnes impliquées dans le projet Terres Rares Canada sur la partie écotoxicologie avec qui la rencontre a été plus qu'enrichissante et a amené à un choc des cultures sur le terrain ! Je pense à Ana et en particulier à Laure avec qui la mission de terrain à Lebel-sur-Quévillon a été une sacrée expérience ! Merci pour toutes les discussions que nous avons eu pendant ces trois ans et pour nous avoir fait découvrir avec Anne-Sylvie votre activité de recherche.

Ces trois ans ont également été riches de rencontres diverses avec des étudiants et des chercheurs et enseignants chercheurs, à Nancy comme ailleurs. Je pense notamment à Periclex (merci pour m'intégrer à la valorisation de ton passage si dépaysant à Nancy), François-Xavier Masson, Flavien Choulet… Merci à toutes les personnes rencontrées dans les divers laboratoires visités au cours de ces trois ans : Christophe Ballouard, Anthony Pochon (merci encore pour les apatites !) à Rennes ; Stéphanie Duchêne, Michel Grégoire, Michel de Saint-Blanquat, Stefano Salvi, Didier Béziat, Julien Serrano, Baptiste Lemire et Guillaume Estrade pour votre accueil à Toulouse et les échanges associés ; et à Sophie Jannin (merci pour les échanges sur cette zone que tu connais si bien !), Pierre-Henri Trapy et Alex Brodeur-Grenier (merci pour ce terrain sur la 117 !) pour votre accueil dans votre bureau de Poly !

Merci à tous les autres comme Arnaud Fontaine, Frédéric Massei, Benjamin Roméo et Marco (et la poutine du chef !) pour vos accueils si appréciés au Québec.

Merci aux étudiants du Student Chapter SGA qui ont repris le flambeau et qui ont continué à faire vivre cette association de la meilleure des manières !

Ce travail a également bénéficié de l'implication de plusieurs étudiants de l'École Nationale Supérieure de Géologie et de la Faculté des Sciences et Technologies que j'ai eu la chance d'encadrer au cours de leur stage et sans qui la concrétisation de ce manuscrit n'aurait pas été possible : Matthias Jauvin et Solène Mieral, mais également Alexandre Crépon (merci encore pour ton aide précieuse sur cet échantillonnage intense de l'été 2016) et Clara Deruy (merci pour tout le travail fourni et ton adaptation aux évolutions du sujet, j'espère que nous retravaillerons ensemble sur d'autres projets). Enfin, merci également à Marion Grosjean (« la

schkoumoune ») qui m'a fait garder un pied en Zambie au cours de l'encadrement de son stage de Master/ENSG et qui m'a forcé à jongler entre acquisitions de données pour ma thèse et isotopie du cuivre ! Bon courage pour ta thèse à Genève !

Merci à toute l'équipe de GeoRessources, notamment les personnels administratifs pour tout le travail que l'on ne voit pas mais sans lequel rien n'est possible. Merci de vous être adaptés à mes contraintes de missions de terrains parfois prévues peu de temps à l'avance, je pense notamment à Marie-Odile, Aurélie et Mélanie. Merci également aux techniciens, ingénieurs, chercheurs, enseignants-chercheurs pour votre intégration et les échanges pendant toute cette période. Merci en particulier à Chantal pour les analyses LA-ICP-MS, à Olivier pour la microsonde, Sandrine, Lise et Andreï pour le MEB, à Robert, Frédéric, Jean-Marie et Christophe pour la séparation des zircons, et à Zira pour ta bienveillance et ta bonne humeur. Merci beaucoup à Patrick pour toute ton aide, tes conseils toujours avisés, ton adaptation à mes coups de bourre et d'avoir toujours été là pour les problèmes rencontrés.

Ce travail de thèse a été le fruit d'un renouvellement de collaboration avec Aurélien (Monsieur) Eglinger sur les aspects qui lui sont chers : métamorphisme, géodynamique, minéralisations et les monazites ! Nous avons commencé à travailler ensemble au cours de mon Master, merci pour tout ce que tu m'as appris à cette période sur le travail de fond que demande une activité de recherche, sur l'organisation, la rigueur, l'exigence de rédaction (j'essaie d'être moins littéraire promis !) et sur les figures (« en noir et blanc chef ! »). C'est ton encadrement quotidien au cours de ce stage qui m'a donné les bases nécessaires pour faire cette thèse, merci pour cela. Je suis content de t'avoir accroché sur mon projet et de t'avoir amené sur le Grenville, la collaboration semble avoir été fructueuse via l'encadrement du stage de Clara ! Merci pour ton apport d'expérience sur ces thématiques, pour les discussions dans ton fauteuil « biblio », les x coupes faites sur un coin de table, d'avoir toujours eu la porte ouverte quand j'avais besoin de toi malgré ton planning chargé en enseignements et de m'avoir rassuré dans les moments de doute. Merci pour tout et j'espère que nous continuerons à travailler ensemble sur de futurs projets !

Merci à tous les rouennais si peu vus pendant ces trois ans (promis maintenant ce sera plus simple !), mais pourtant si importants : Thomas (sans qui je ne serai pas à Nancy aujourd'hui), Seg, No, Mathieu ; mais aussi les choucroutes : Julian, Alban, Charly et Louis, sans oublier bien sûr Romain (Maître Karl, bientôt on se refait une session Kerguerec !), soutien sans faille depuis tant d'années. Merci à vous tous !

Bien sûr je tiens à remercier tout particulièrement Pierre-Arthur Groulier, P.A., sans qui je n'en serais pas là !! Tous les deux nous nous suivons depuis bientôt 7 ans maintenant, deux nouveaux arrivants à Nancy, toi en M1, moi en L3, ayant découvert ensemble la fac et la vie nocturne nancéienne via quelques rencontres et lieux pour le moins… insolites… comme les 2P avec Lolotte et Marie, le gala de l'école des mines de Nancy, le p'tit T et j'en passe. Ton stage de Master avec Anne-Sylvie a ouvert la voie à mon sujet de thèse, merci de me faire collaborer sur la valorisation de ce beau projet ! Cette rencontre à la fac n'était qu'un début, poursuivi par ma participation à l'école de terrain en Abitibi et par notre mission de terrain mémorable de 3 mois dans cette mer de gneiss inhospitalière qu'est le Grenville ! C'est en effet avec toi que j'ai connu les premières attaques de mouches et autres « bibites » si typiques du Québec au cours de notre première nuit dans ce chalet centenaire de Petit-Saguenay encaissé dans ces falaises monumentales. Ce premier matin avec 25 piqures sur chaque bras annonçait la couleur du reste de l'été ! Merci de m'avoir emmené dans cette ZEC pleine d'ours (je suis sûr que c'était un ours derrière nous pendant cette traverse !) et d'orignaux, de m'avoir fait découvrir les joies du calfeutrage de cheminée au chalet de Petit-Saguenay et les Escoumins où nous partagions notre temps entre logs de séquences volcanosédimentaires, discussion sur les basaltes Grenvilliens (oui OK P.A. je te l'accorde il y a des basaltes en coussins…), et apéros au Pharillon de Claudette face au Saint Laurent où ces quelques verres de vin étaient ponctués de baleines à bosses et autres cétacés qui nous donnaient rendez-vous vers 17h ! Tant de souvenirs qu'il serait trop long de les citer tous mais une mention spéciale aux brunchs du dimanche chez « le belge », les parties de pêche qui suivaient, la découverte du Motel de l'Énergie au kilomètre 211 de la 389 (on a survécu à la 389 !), les diverses rencontres hivernales à Québec Mines et à Montréal, etc. Merci d'avoir partagé ton expérience avec moi, de m'avoir aidé sur le terrain, et pour tous les échanges Grenvilliens ou non que nous avons eu depuis ! À l'époque de nos sorties nancéiennes, il aurait été difficile de nous imaginer tous les deux en doctorat, courage pour la finalisation du tien !

La thèse est un travail de longue haleine qui pour ma part n'aurait pu se faire sans mes exceptionnels collègues de la communauté « Doc GeoRessources » regroupant les thésards, post-docs et divers étudiants de master avec qui j'ai pu partager ces trois années. Merci à Matthieu (l'escroc, et ton iPhone Serge) et Roland (père Castor et ses histoires si riches en détails !) et leur fameux BDC et FCM !, à Julien (merci pour avoir toujours veillé à ce que nous ayons notre dose de café quotidienne en gérant les commandes de gros toujours plus récurrentes de Malongo !), Max (doc d'argent !), à Tof (je te donne les dates auxquelles je quitte Nancy

pour que tu puisses prévoir un barbecue sereinement ?), à Raph notre dandy végétarien, à Benoît, Héloïse, Jérémy, Justine, Maïa (tu aurais pu la faire cette BD dans le programme SGA2015, j'en suis sûr !), Nora (A4 !), Yoram, mais aussi à Alexy, Andrea, Audrey, Jessica, Roman, Zeying, sans oublier les jeunes thésards Rodrigue, Hoan, et bien sûr Hilaire et Vincent qui forment avec Monsieur Perret (merci encore pour toute ton aide, plus qu'à maitriser le dosage à 10 cuillères rases et tu seras fin prêt !) la « golden team » de Doc GeoRessources ! Sans vous tous rien n'aurait été possible ! J'ajoute quelques mentions spéciales, tout d'abord à Joséphine (la Gig'), ma collègue du bureau 604 (le bureau des gentils comme tu l'appelles !) qui a dû supporter Chaton et moi en rédaction de thèse ! Il fallait bien quelqu'un de positif comme toi pour supporter nos changements d'humeurs toujours plus brusques, nos énervements plus que réguliers, nos craquages et notre humour parfois… incisif ! Merci pour la sérénité que tu as apporté dans cet environnement ! Bon courage pour la suite de ton projet ! Enfin, nous sommes quatre thésards à avoir soutenus fin 2017, les quatre à avoir fait leur stage de M2 dans le bureau 617: Guillaume (Guigui, le roi de la TSR) qui a eu la lourde de tâche d'être le premier d'entre nous à soutenir et en avance ! Et bien sûr mes deux compagnons de rédaction, ainsi devenus de véritables amis, avec qui je passais mes journées, mes soirées (nuits ??) et mes weekends au labo pendant 3 mois : Hélène (on est docteurs, elle est choucarde celle-là ou pas ??) et Pierre (Chaton), mon collègue de bureau. Je n'ose compter les litres de café et les délicieux mets du Super U du Vélodrome consommés pendant cette période ! Pierre, merci de m'avoir fait découvrir tant de pépites culturelles, en particulier (les autres n'ayant pas vraiment leur place ici…) le chant diphonique mongol dont Hélène (mais je t'assure que ça détend) a subit les effets vers 22-23h ! Sans votre appui quotidien pendant ces trois années et en particulier ces trois longs mois je n'aurai pas pu tenir la cadence et je n'en serai pas là aujourd'hui, merci beaucoup !

Pour finir j'adresserai quelques mots à mes proches et à ma famille, merci de votre soutien depuis trois ans, de votre compréhension sur mes absences et mes indisponibilités en particulier pendant cet été de rédaction. Merci d'avoir crus en moi. Merci également à Hélène et Sreekanth, je vous ai plus vu depuis que vous êtes retournés au Québec que quand vous viviez à Amsterdam ! Merci pour votre accueil systématique (et les nombreuses capsules Nespresso) à chacune de mes missions au Québec (il y en a eu quelques-unes !!), et pour m'avoir fait partager de si bons moments avec Matthew ! J'espère pouvoir revenir vous voir tous les trois très bientôt ! Merci également à Papa et Maman, si fiers d'avoir un fils géologue et docteur, vous qui m'avez soutenu depuis si longtemps, depuis mes années où je vivotais dans mes études

à Rouen, d'abord au Lycée puis à l'IUT, jusqu'au changement radical de rythme à Nancy et mon investissement total dans ce projet. Désolé pour les absences dans les moments difficiles. Merci de votre compréhension, d'avoir cru en moi, pour tout ce que vous avez fait pour moi et pour votre soutien inébranlable.

Enfin je terminerai par toi Géraldine. Merci pour ton soutien sans faille dès notre Master, d'avoir supporté mes absences prolongées, notamment avec l'école de terrain en Abitibi, d'avoir toujours été là et à l'écoute dans les bons comme dans les mauvais moments. Merci de m'avoir épaulé, d'avoir été aussi présente malgré la distance et de m'avoir supporté quand j'étais stressé ou en rush. C'est grâce à toi que j'en suis là aujourd'hui.

TABLE DES MATIÈRES

INTRODUCTION

1. Contexte général de la thèse et problématique

Cette thèse s'intègre dans le projet scientifique du Laboratoire d'Excellence (LabEx) Ressources 21 « Métaux stratégiques du 21ème siècle » dont le but est tracer le cycle des métaux stratégiques depuis leur extraction mantellique jusqu'aux processus de surface et leurs impacts environementaux. Plus spécifiquement cette étude s'intègre dans l'axe « Terres Rares » du LabEx et se focalise sur l'étude d'occurrences de terres rares magmatiques associées à des dykes de granite pegmatitique de la Province de Grenville central.

1.1. Importance économique des terres rares

Les terres rares correspondent à quinze éléments chimiques du groupe des lanthanides, du Lanthane au Lutétium (La-Lu) de la classification périodique. Elles ont de nombreuses applications et sont disséminées dans les objets de la vie courante, dans chaque ordinateur, écran de télévision, téléphone portable, etc. (par exemple Chakhmouradian et Wall, 2012 ; Hatch, 2012 ; Massari et Ruberti, 2013). Ces métaux sont également utilisés dans les « énergies vertes » avec près de 25% du marché des terres rares dédiés à la fabrication d'aimants à NdFeB pour les éoliennes ou encore les véhicules hybrides, électriques et les batteries (par exemple Rapport du BGS, 2011 ; Chakhmouradian et Wall, 2012 ; Hatch, 2012 ; Massari et Ruberti, 2013). Les prédictions récentes de la demande des terres rares suggèrent qu'elle sera dominée par ces utilisations ainsi que par la demande en fibre optique à Erbium (Goodenough et al., 2017).

Bien que de nombreuses occurrences de terres rares soient recensées en Europe, suffisamment pour que l'Union Européenne assure sa propre demande dans un futur relativement proche, leur valorisation reste à développer pour garantir une exploitation viable (Goodenough et al., 2016). Ainsi, à l'heure actuelle l'Union Européenne est totalement dépendante de l'importation de terres rares étrangères (Commission Européenne, 2017; Guyonnet et al., 2015). En plus de la quasi-absence de recyclage (8% pour les légères, 3% pour les lourdes) et la difficulté de les substituer, la Commission Européenne a défini les terres rares comme « matières premières critiques » sur la base d'un risque de pénurie d'approvisionnement et de leur impact sur l'économie (Fig. 0-1) (Commission Européenne, 2014, 2017). En effet, la Chine est à l'heure actuelle le principal producteur mondial et représente 95% de la production avec le gisement de Bayan Obo (Kynicky et al., 2012). C'est le fournisseur le plus important de l'Union Européenne (40%), suivi de près par les États-Unis (34%) et la Russie (25%) (Commission Européenne, 2017).

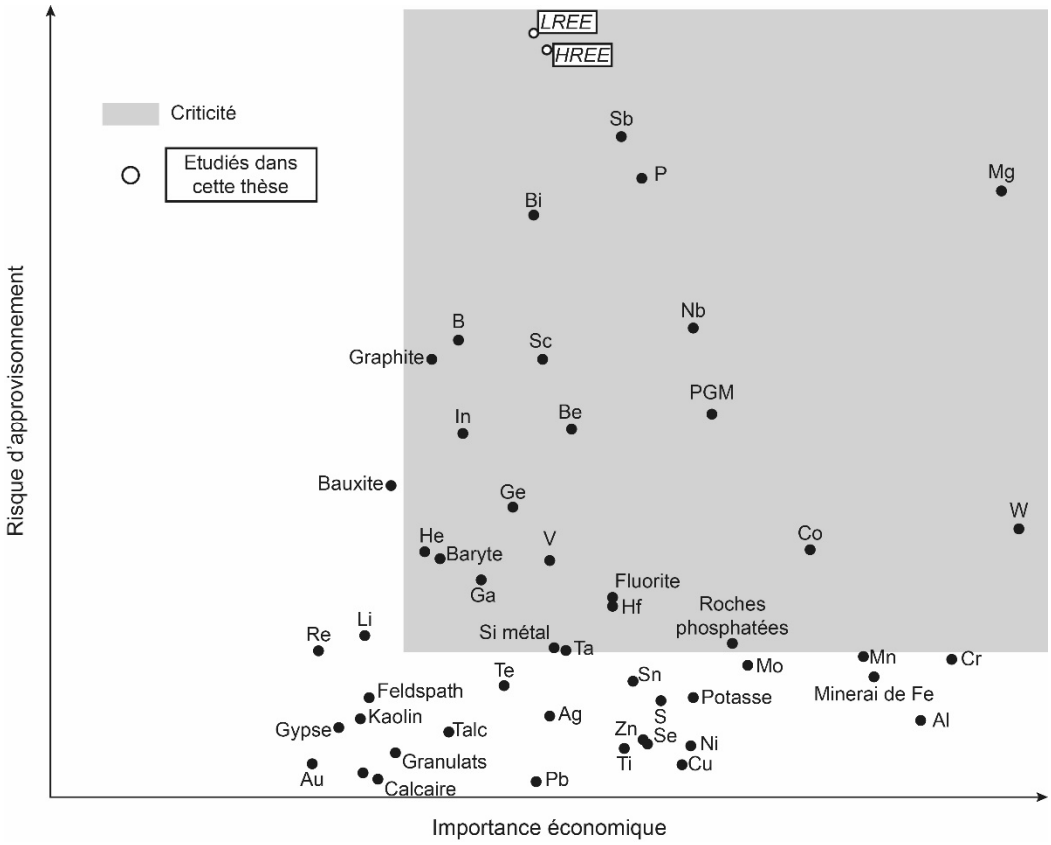

Figure 0-1 : Matrice de criticité publiée par la Commission Européenne (2014), mise à jour en 2017.

1.2. Propriétés physico-chimiques des terres rares

Le rapport entre la charge d'un élément (*Z*) et son rayon ionique (*r*) sont définis comme le potentiel ionique (*Z/r*) (Cartledge, 1928 ; Goldschmidt, 1937). Celui-ci contrôle le comportement géochimique des éléments et permet en particulier la distinction de deux groupes que sont les LILEs (large-ion lithophile elements) et les HFSEs (high-field strength elements) (Goldschmidt, 1937 ; Rollinson, 1993). Les LILEs comprennent entre autres Cs^{+}, Rb^{+}, K^{+}, Pb^{2+}, Sr^{2+}, et Eu^{2+}, et les HFSEs Ln^{3+} (La^{3+} à Lu^{3+}), Y^{3+}, Sc^{3+}, U^{4+}, U^{6+}, Th^{4+}, Hf^{4+}, Zr^{4+}, Ta^{5+} et Nb^{5+}. Ces deux groupes d'éléments étant incompatibles (concentrés dans les phases liquides au cours de la cristallisation fractionnée) dans les processus magmatiques mafiques, ils sont essentiellement concentrés dans la croûte où leur comportement diffère essentiellement dans les processus magmatiques plus différenciés. Les LILEs sont compatibles dans les phases silicatées telles que les feldspaths ou les micas, contrairement aux HFSEs qui, en raison de leur charge élevée, ne peuvent se substituer dans ces minéraux. Ainsi, au cours de la cristallisation fractionnée de magmas évolués, la concentration des LILEs dans le liquide a tendance à diminuer (compatibles) alors que celle des HFSEs a tendance à augmenter, ces derniers se concentrant donc en général dans les magmas les plus évolués.

Les terres rares sont composées des quinze éléments chimiques constituant les lanthanides, du La au Lu (numéro atomique 57 à 71), auxquelles sont généralement ajoutés le Sc et l'Y (par exemple Chakhmouradian et Wall, 2012 ; Goodenough et al., 2017). Leur abondance décroit avec leur numéro atomique dans la croûte terrestre, suivant l'effet « Oddo-Harkins », lequel décrit une abondance des éléments chimiques de numéro atomique pair supérieure à celle des éléments de numéro impair. Les terres rares appartiennent toutes au groupe des HFSEs, à l'exception de l'Eu dans son état d'oxydation 2+, appartenant aux LILEs (Rollinson, 1993). Elles ont donc des propriétés et des comportements géochimiques proches avec en particulier un état d'oxydation de 3+ (parfois de 2+ (Eu) ou de 4+ (Ce)). Cependant, la réduction du rayon ionique, ou « contraction des lanthanides », induit une augmentation de la compatibilité du La au Lu à l'origine des spectres de terres rares normalisés au manteau primitif miroirs entre un manteau appauvri et une croûte continentale (par exemple Chakhmouradian et Wall, 2012). Avec cette normalisation, le manteau primitif présente une pente positive dans les terres rares légères et la croûte continentale une pente négative. Ces différences physico-chimiques (rayons ioniques et d'état d'oxydation, principalement) sont à l'origine du fractionnement des terres rares dans les environnements géologiques, ce qui en fait des traceurs des processus géologiques de premier ordre.

1.3. Problématique de la thèse

Les premières exploitations de terres rares se sont concentrées sur les placers à monazite, des gisements faciles d'accès et à faible coût d'exploitation (Chakhmouradian et Wall, 2012). Depuis les années 1950s, les exploitations de terres rares associées à des complexes ignés ont fourni les principales ressources avec l'exploitation de la carbonatite de Mountains Pass (Californie, États-Unis), du complexe alcalin de Lovozero (Russie) et du gisement Fe-terres rares-Nb de Bayan Obo fournissant à lui seul près de la moitié des terres rares chinoises (Castor et Hedrick, 2006 ; Chakhmouradian et Wall, 2012 ; Kynicky et al., 2012). Depuis cet intérêt porté aux gisements de terres rares associées à des roches ignées (±hydrothermales), une grande partie de la recherche sur la métallogénie des terres rares a été focalisée sur ces cas très spécifiques (Castor, 2008 ; Kynicky et al., 2012 ; Mariano et Mariano, 2012) ou sur des synthèses géographiques par exemple en Amérique du Nord (Mariano et Mariano, 2012) et en Chine (Kynicky et al., 2012). Ainsi, la synthèse de Chakhmouradian et Wall (2012) propose une coupe géologique des environnements tectoniques des principaux gisements de terres rares, dans laquelle un environnement correspond globalement à un gisement et inversement (Fig. 0-2).

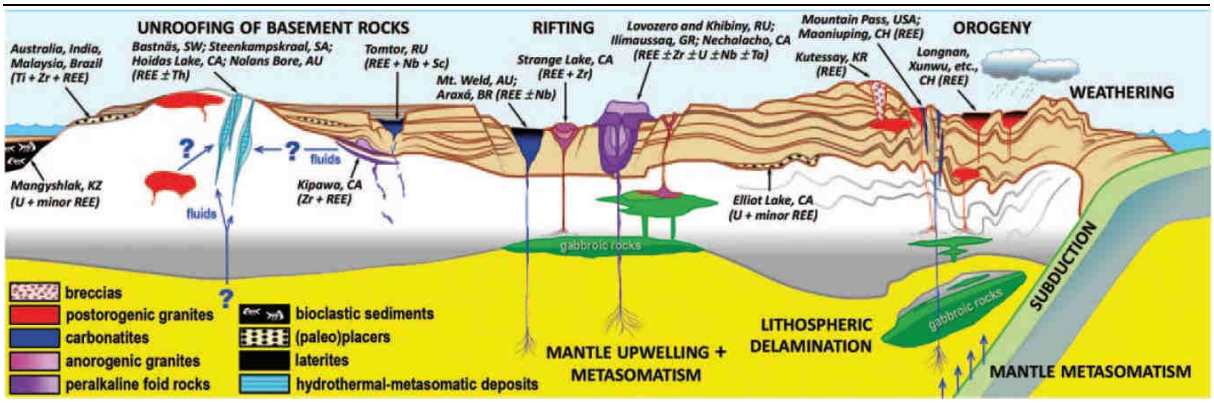

Figure 0-2 : Principaux gisements de terres rares dans leur contexte géodynamique (d'après Chakhmouradian et Wall, 2012). Abréviations : AU = Australie ; CA = Canada ; CH = Chine ; KR = Kyrgyzstan ; KZ = Kazakhstan ; RU = Russie ; SA = Afrique du Sud ; SW = Suède ; USA = États-Unis.

Ainsi, aucune étude scientifique ne s'est attachée à la caractérisation du cycle métallogénique des terres rares à l'échelle d'une province orogénique en intégrant l'évolution spatio-temporelle d'occurrences de terres rares dans un cadre géodynamique.

L'intégration des gisements dans leur contexte géodynamique à grande échelle temporelle a été proposée par de nombreux auteurs (par exemple Barley and Groves, 1992 ; Bierlein et al., 2002 ; Cawood et Hawkesworth, 2015 ; Groves et Bierlein, 2007 ; Kerrich et al., 2000, 2005 ; Meyer, 1981, 1988). Peu d'études zooment cependant à l'échelle d'un cycle orogénique (Eglinger, 2013 ; Eglinger et al., 2016 ; Toé, 2012 ; Turlin et al., 2016). Ce travail de thèse se propose donc d'utiliser des occurrences de terres rares magmatiques comme traceurs de processus de croissance et différenciation de la croûte.

1.4. Choix de la cible géologique

La Province de Grenville est la partie affleurant essentiellement au Québec et en Ontario (Canada) d'une ceinture orogénique s'étendant du Texas au bouclier Svécofennien (par exemple Rivers et al., 2012). Elle s'est formée à la suite d'une longue histoire d'accrétion tectono-magmatique d'arcs à la marge Sud-Est de Laurentia, suivie par une collision continentale entre Laurentia et Amazonia entre 1090 et 980 Ma (par exemple Li et al., 2008 ; Rivers et al., 2012 ; Tohver et al., 2006). Cette ceinture orogénique, décrite comme le climax orogénique de la Terre (Van Kranendonk and Kirkland, 2013), est un équivalent protérozoïque de la ceinture Himalaya-Tibet actuelle (par exemple Rivers, 2008). Particulièrement riche en occurrences de terres rares associées à un large spectre de roches magmatiques (Fig. 0-3), elle expose sa racine orogénique composée de roches de haut-grade métamorphique et permet donc l'étude de processus magmatiques profonds (Rivers, 2008 ; Rivers et al., 2012). Cette cible représente ainsi un laboratoire naturel idéal pour l'intégration de ces occurrences dans un cycle orogénique.

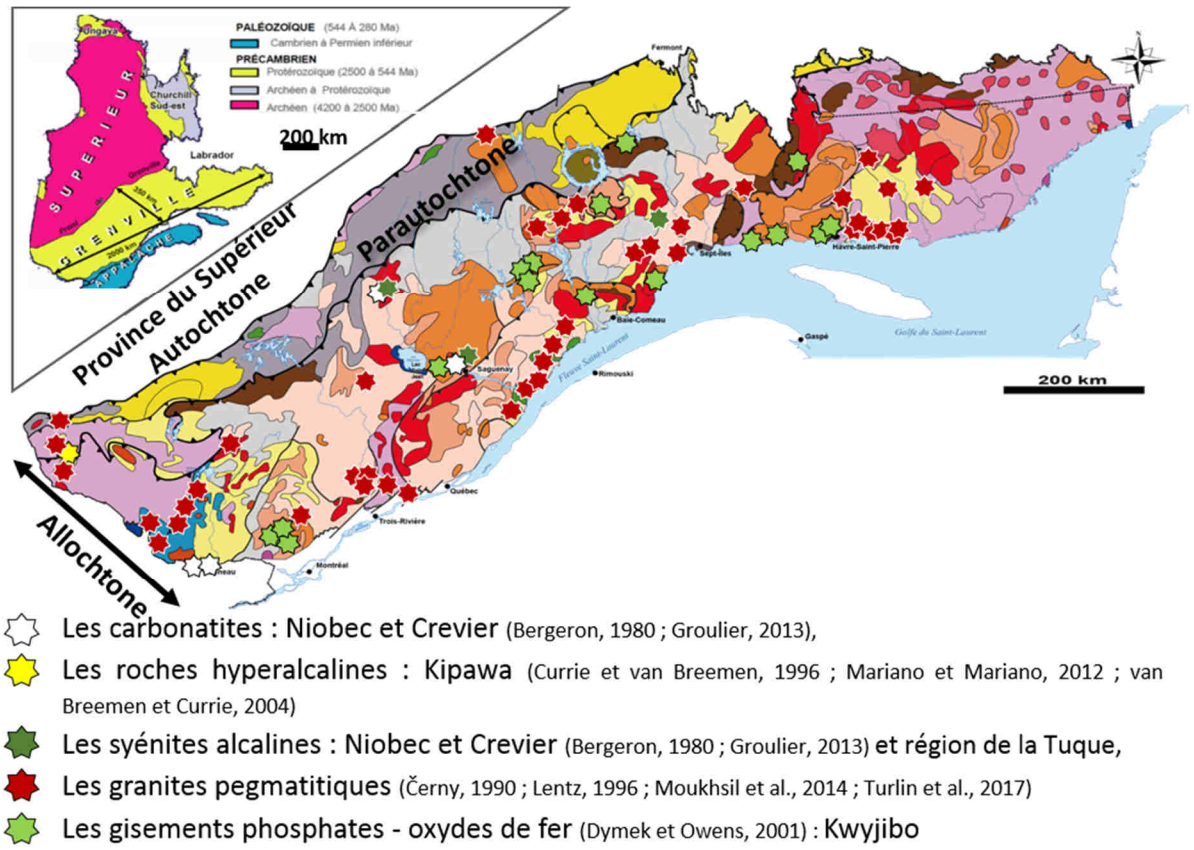

Figure 0-3 : Carte géologique simplifiée de la Province de Grenville au Québec et au Sud du Labrador (Canada) sur laquelle sont repositionnées une partie des occurrences de terres rares recensées dans cette province et associées à un large spectre de composition magmatique (compilé d'après Bergeron, 1980 ; Černý, 1990 ; Corriveau et al., 2007 ; Currie et Breemen, 1996 ; Dymek et Owens, 2001 ; Groulier, 2013 ; Hébert, 1995 ; Lentz, 1996 ; Moukhsil et al., 2014 ; Moukhsil et Solgadi, 2013 ; Nantel, 2008 ; Sangster et al., 1992 ; Turlin et al., 2017 ; van Breemen et Currie, 2004) (modifiée d'après Moukhsil et Solgadi, 2013).

Parmi les occurrences de terres rares magmatiques de la Province de Grenville, les granites pegmatitiques sont particulièrement représentés (Fig. 0-3) et les moins étudiés. Suite à des travaux de cartographie dans le Grenville central, à proximité de l'impact météoritique de Manicouagan, Moukhsil et al. (2014) ont identifié sept occurrences de terres rares associées des granites pegmatitiques. Ce travail de thèse porte sur ces occurrences de terres rares avec pour objectifs de répondre aux questions suivantes :

- Quelles sont les caractéristiques minéralogiques et géochimiques de ces granites pegmatitiques, et notamment quels sont les porteurs des terres rares ?
- Quelle est la source de ces magmas ? Ces magmas sont-ils issus de la fusion partielle d'un manteau dont la nature est à déterminer ? Ou bien ces magmas proviennent-ils de la remobilisation d'une croûte préexistante dont l'héritage archéen à mésoprotérozoique sont à identifier ?

- Quel est le contexte géodynamique favorable à la pétrogénèse et à la mise en place de ces magmas en référence à l'évolution orogénique grenvillienne ? Les magmas sont-ils plutôt générés lors de la période d'accrétion tectonique-magmatique le long d'une marge active marquée par une subduction, ou bien lors de la collision, ou encore en lien avec l'évolution tardi- à post-orogénique ?

2. Méthodologie

Plusieurs études ont été réalisées dans cette thèse afin de répondre aux questions énoncées précédemment. La caractérisation de la nature des occurrences magmatiques de terres rares associées à des granites pegmatitiques sur lesquelles se focalisent ce projet (***premier objectif***) est réalisée par différentes approches, de l'échelle de l'affleurement à celle du minéral porteur des terres rares. Des cartographies de détail et mesures structurales permettent de contraindre les relations des granites pegmatitiques avec leurs encaissants respectifs. Les données pétrographiques et de géochimie roche totale permettent de caractériser la signature en éléments majeurs et traces de ces objets et les porteurs de la minéralisation et ainsi de comparer ces occurrences de terres rares aux classifications de pegmatites communément utilisées dans la littérature.

Afin de replacer ces granites pegmatitiques dans le contexte géodynamique et d'évolution crustale de l'orogenèse Grenvillienne (***deuxième objectif***), une étude géochronologique des zircons et monazites de ces dykes, et des monazites et apatites des encaissants métasédimentaires permettent de retracer l'évolution thermique de la croûte et la phase du cycle orogénique favorable à la genèse et la formation de ces occurrences.

Le traçage de la source de ces magmas et la contrainte des contributions respectives du manteau et d'une croûte préexistante archéenne à mésoprotérozoique (***troisième objectif***) se base sur une approche multi-méthodes. Les signatures isotopiques (Hf-O) et éléments traces des zircons des dykes de granite pegmatitique apportent des informations sur la source du magma à l'origine de ces occurrences, relatives à (i) son caractère juvénile ou mature, (ii) son âge, et (iii) sa nature. Après identification de ces critères, les caractéristiques pétrogéochimiques d'une source potentielle sont comparées à celles des dykes de granite pegmatitique, permettant ainsi l'identification des processus magmatiques (fusion partielle d'un protolithe fertile ou cristallisation fractionnée) responsables de la formation des granites pegmatitiques à terres rares.

L'approche pluri-disciplinaire de ce travail implique la collaboration de plusieurs équipes de recherche des laboratoires GeoRessources (Nancy), CRPG (Nancy), Géosciences Environnement Toulouse, Polytechnique Montréal, Géosciences Rennes, Institut für Geowissenschaften (Frankfurt), KIT-Karlsruhe Institute of Technology (Karlsruhe), Memorial University (St John's), ainsi que les géologues du Ministère de l'Énergie et des Ressources naturelles du Québec.

3. Organisation du manuscrit

La réponse à ces objectifs scientifiques fait l'objet de ce manuscrit, organisé en trois parties comprenant un total de 5 chapitres.

La ***première partie*** du manuscrit (***partie I***) fait l'objet de la caractérisation des dykes de granite pegmatitique à terres rares sur lesquels se porte ce travail. Suite à un bref rappel de la classification des pegmatites, un premier chapitre (***chapitre 1***), publié dans *Ore Geology Reviews*, a pour objectif la caractérisation (i) des relations de terrain de ces dykes via des cartographies de détail, (ii) de leur texture, (iii) de leur composition en éléments majeurs et traces en particulier en terres rares, (iv) l'identification des phases porteuses de terres rares, et (v) les premières contraintes géochronologiques d'intrusion de ces dykes. Au-delà de la caractérisation d'occurrences de terres rares inhabituelles de par leurs associations géochimiques en éléments majeurs et traces, cette partie permet de soulever les grandes interrogations relatives au contexte géodynamique de leur mise en place, à leur source, et aux processus pétrogénétiques ayant conduits à la genèse de ces occurrences. Ce sont ces points qui font l'objet des autres parties du manuscrit.

La ***deuxième partie*** du manuscrit (***partie II***) traite du contexte géodynamique de mise en place des dykes de granites pegmatitiques à terres rares du Grenville central. Un premier chapitre (***chapitre 2***) discute de l'évolution thermique du segment de croûte de moyenne et basse pression de la ceinture Allochtone intrudé par les dykes de granites pegmatitiques à terres rares. Cette réflexion fait l'objet d'un article soumis à *Terra Nova*. Un second chapitre (***chapitre 3***) présente des données originales isotopiques (U-Pb-Hf-O) et d'éléments traces sur les zircons néoformés de trois dykes de granite pegmatitique. Ces données permettent de contraindre la nature et l'âge de la source de ces dykes, et de discuter du contexte géodynamique de leur intrusion. Ce chapitre fait l'objet d'un article à soumettre à *Precambrian Research*.

La ***troisième partie*** du manuscrit (***partie III***) discute les processus pétrogénétiques responsables de la genèse de ces occurrences de terres rares magmatiques. Suite à la

caractérisation de la nature et de l'âge de la source dans le chapitre 3, un premier chapitre (***chapitre 4***) compare les caractéristiques pétro-géochimiques des métapélites du Groupe du Knob Lake (Terrane de Gagnon, ceinture Parautochtone) à celles d'un dyke de granite pegmatitique à monazite mis en place dans la ceinture Allochtone. Ces données permettent de contraindre le rôle respectif des processus magmatiques de fusion partielle et de cristallisation fractionnée dans la genèse de ces occurrences de terres rares associées à des magmas peralumineux. Cette réflexion fait l'objet d'un article en préparation pour *Journal of Petrology*. Un second chapitre (***chapitre 5***) présente les caractéristiques pétrogéochimiques et isotopiques sur zircons d'un dyke de granite pegmatitique dont la minéralisation en terres rares se concentre exclusivement aux épontes. Ces données mettent en évidence une source différente des dykes fortement minéralisés et permettent de discuter des implications sur (i) la source et (ii) les conditions favorables à la genèse de dykes de granite pegmatitique à terres rares dans la Province de Grenville central. Cette étude fait l'objet d'un article en préparation pour *Canadian Journal of Earth Sciences*. Enfin, une étude préliminaire des facteurs contrôlant l'expression de la minéralisation sous la forme de monazite ou d'allanite dans les dykes de granite pegmatitiques par leurs encaissants respectifs (complexes métasédimentaires ou métaplutoniques) conclue cette partie. Elle se base sur des données de géochimie roche totale obtenues sur les différents faciès des dykes et de leurs encaissants respectifs, échantillonnés à différentes distances du contact.

Ce manuscrit se conclut par une **discussion** reprenant l'ensemble des résultats obtenus au cours de cette thèse. Elle fait l'objet d'une réflexion globale sur l'évolution crustale de la croûte orogénique au cours de l'orogenèse Grenvillienne et considère le cycle des terres rares dans un modèle géodynamique. Cette discussion se conclue sur les perspectives qu'offre ce travail de thèse.

Références

Barley, M.E., Groves, D.I., 1992. Supercontinent cycles and the distribution of metal deposits through time. Geology 20, 291–294. doi:10.1130/0091-7613(1992)020<0291:SCATDO>2.3.CO;2

Bergeron, A., 1980. Pétrographie et géochimie du complexe igné alcalin de Crevier et de son encaissant métasomatisé (Unpublished MSc thesis). Université du Québec à Chicoutimi, Chicoutimi.

BGS, 2011. Rare-Earth Elements (Profile report). British Geological Survey - Natural Environment Research Council.

Bierlein, F.P., Gray, D.R., Foster, D.A., 2002. Metallogenic relationships to tectonic evolution – the Lachlan Orogen, Australia. Earth and Planetary Science Letters 202, 1–13. doi:10.1016/S0012-821X(02)00757-4

Cartledge, G.H., 1928. Studies on the periodic system. I. The ionic potential as a periodic function. J. Am. Chem. Soc. 50, 2855–2863. doi:10.1021/ja01398a001

Castor, S.B., 2008. Rare Earth Deposits of North America. Resource Geology 58, 337–347. doi:10.1111/j.1751-3928.2008.00068.x

Castor, S.B., Hedrick, J.B., 2006. Rare earth elements, in: Kogel JE, Trivedi NC, Barker JM (Eds) Industrial Minerals and Rocks, Society for Mining, Metallurgy and Exploration. Kogel JE, Trivedi NC, Barker JM, pp. 769–792.

Cawood, P.A., Hawkesworth, C.J., 2015. Temporal relations between mineral deposits and global tectonic cycles. Geological Society, London, Special Publications 393, 9–21. doi:10.1144/SP393.1

Černý, P., 1990. Distribution, affiliation and derivation of rare-element granitic pegmatites in the Canadian Shield. Geol. Rundsch. 79, 183–226. doi:10.1007/BF01830621

Chakhmouradian, A.R., Wall, F., 2012. Rare Earth Elements: Minerals, Mines, Magnets (and More). Elements 8, 333–340. doi:10.2113/gselements.8.5.333

Commission Européenne, 2017. Communication de la Commission au Parlement Européen, au Conseil, au Comité économique et social Européen et au comité des Régions relative à la liste 2017 des matières premières critiques pour l'UE (Rapport technique). Commission Européenne, Bruxelles, Belgique.

Commission Européenne, 2014. Report on Critical Raw Materials for the EU (Rapport technique). Commission Européenne (entreprises et industrie), Bruxelles, Belgique.

Corriveau, L., Perreault, S., Davidson, A., 2007. Prospective metallogenic settings of the Grenville Province. Special Publication - Geological Association of Canada. Mineral Deposits Division 5, 819–848.

Currie, K.L., van Breemen, O., 1996. The origin of rare minerals in the Kipawa syenite complex, western Quebec. Can. Mineral. 34, 435–451.

Dymek, R.F., Owens, B.E., 2001. Petrogenesis of apatite-rich rocks (nelsonite and oxide-apatite gabronorites) associated with massif anorthosite. Economic Geology 96, 797–815.

Eglinger, A., 2013. Cycle de l'uranium et évolution tectonométamorphique de la ceinture orogénique Pan-Africaine du Lufilien (Zambie) (Unpublished PhD. Dissertation). Université de Lorraine, France.

Eglinger, A., Vanderhaeghe, O., André-Mayer, A.-S., Goncalves, P., Zeh, A., Durand, C., Deloule, E., 2016. Tectono-metamorphic evolution of the internal zone of the Pan-African Lufilian orogenic belt (Zambia): Implications for crustal reworking and syn-orogenic uranium mineralizations. Lithos 240–243, 167–188. doi:10.1016/j.lithos.2015.10.021

Goldschmidt, V.M., 1937. The principles of distribution of chemical elements in minerals and rocks. The seventh Hugo Müller Lecture, delivered before the Chemical Society on March 17th, 1937. J. Chem. Soc. 655–673. doi:10.1039/JR9370000655

Goodenough, K.M., Schilling, J., Jonsson, E., Kalvig, P., Charles, N., Tuduri, J., Deady, E.A., Sadeghi, M., Schiellerup, H., Müller, A., Bertrand, G., Arvanitidis, N., Eliopoulos, D.G., Shaw, R.A., Thrane, K., Keulen, N., 2016. Europe's rare earth element resource potential: An overview of REE metallogenetic provinces and their geodynamic setting. Ore Geology Reviews 72, Part 1, 838–856. doi:10.1016/j.oregeorev.2015.09.019

Goodenough, K.M., Wall, F., Merriman, D., 2017. The Rare Earth Elements: Demand, Global Resources, and Challenges for Resourcing Future Generations. Nat Resour Res 1–16. doi:10.1007/s11053-017-9336-5

Groulier, P.-A., 2013. Étude des minéralisations en Nb-Ta du complexe igné alcalin de Crevier (Québec) (Rapport de Master). Université de Lorraine.

Groves, D.I., Bierlein, F.P., 2007. Geodynamic settings of mineral deposit systems. Journal of the Geological Society 164, 19–30. doi:10.1144/0016-76492006-065

Guyonnet, D., Planchon, M., Rollat, A., Escalon, V., Tuduri, J., Charles, N., Vaxelaire, S., Dubois, D., Fargier, H., 2015. Material flow analysis applied to rare earth elements in

Europe. Journal of Cleaner Production 107, 215–228. doi:10.1016/j.jclepro.2015.04.123

Hatch, G.P., 2012. Dynamics in the Global Market for Rare Earths. Elements 8, 341–346. doi:10.2113/gselements.8.5.341

Hébert, Y., 1995. Les gîtes de terres rares et éléments associés dans les districts miniers de Montréal-Laurentides, Estrie-Laurentide et Côte-Nord - Nouveau Québec. Gouvernement du Québec, Ministère des Ressources Naturelles, Secteur des Mines, MB 94-17, 140 p.

Kerrich, R., Goldfarb, R., Groves, D.I., Garwin, S., 2000. The geodynamics of world-class gold deposits ; characteristics, space-time distribution, and origins. In: Hagemann, S.G. & Brown, E.L. (eds) Gold in 2000. Reviews in Economic Geology 13, 501–551.

Kerrich, R., Goldfarb, R., Richards, J.P., 2005. Metallogenic provinces in an evolving geodynamic framework. Economic Geology 100th Anniversary Volume, 1097–1136.

Kynicky, J., Smith, M.P., Xu, C., 2012. Diversity of rare earth deposits: the key example of China. Elements 8, 361–367. doi:10.2113/gselements.8.5.361

Lentz, D., 1996. U, Mo, and REE mineralization in late-tectonic granitic pegmatites, southwestern Grenville Province, Canada. Ore Geology Reviews 11, 197–227. doi:10.1016/0169-1368(95)00034-8

Li, Z.X., Bogdanova, S.V., Collins, A.S., Davidson, A., De Waele, B., Ernst, R.E., Fitzsimons, I.C.W., Fuck, R.A., Gladkochub, D.P., Jacobs, J., Karlstrom, K.E., Lu, S., Natapov, L.M., Pease, V., Pisarevsky, S.A., Thrane, K., Vernikovsky, V., 2008. Assembly, configuration, and break-up history of Rodinia: A synthesis. Precambrian Research, Testing the Rodinia hypothesis: Records in its building blocks 160, 179–210. doi:10.1016/j.precamres.2007.04.021

Mariano, A.N., Mariano, A., 2012. Rare earth mining and exploration in North America. Elements 8, 369–376. doi:10.2113/gselements.8.5.369

Massari, S., Ruberti, M., 2013. Rare earth elements as critical raw materials: Focus on international markets and future strategies. Resources Policy 38, 36–43. doi:10.1016/j.resourpol.2012.07.001

Meyer, C., 1988. Ore deposits as guides to geologic history of the Earth. Annual Review of Earth and Planetary Sciences 16, 147–171. doi:10.1146/annurev.ea.16.050188.001051

Meyer, C., 1981. Ore-forming processes in geologic history. Economic Geology 75th Anniversary Volume, 6–41.

Moukhsil, A., Solgadi, F., 2013. Explorer la province de Grenville : un ABC de sa géologie, ses gîtes et son potentiel. Québec Mines 2013, Quebec, november 2013.

Moukhsil, A., Solgadi, F., Belkacim, S., Elbasbas, A., Augland, L.E., 2014. Géologie de la région du lac Okaopéo, Côte-Nord. Ministère de l'Energie et des Ressources Naturelles, Québec, RG 2014-03, 34 p.

Nantel, S., 2008. Géologie et aperçu de la géochronologie et des indices métalliques entre 1996 et 2007 dans la partie nord de la Ceinture centrale de métasédiments, Province de Grenville, région de Mont-Laurier. Ministère des Ressources Naturelles et de la Faune, Québec DV 2008-04, 17 p.

Rivers, T., 2008. Assembly and preservation of lower, mid, and upper orogenic crust in the Grenville Province—Implications for the evolution of large hot long-duration orogens. Precambrian Research 167, 237–259. doi:10.1016/j.precamres.2008.08.005

Rivers, T., Culshaw, N., Hynes, A., Indares, A., Jamieson, R., Martignole, J., 2012. The Grenville Orogen - A Post-LITHOPROBE Perspective, in: J.A. Percival, F.A. Cook, and R.M. Clowes (eds) Tectonic Styles in Canada: The LITHOPROBE Perspective, Geological Association of Canada. Special Paper 49, pp. 97–236.

Rollinson, H.R., 1993. Using Geochemical Data: Evaluation, Presentation, Interpretation. Routledge.

Sangster, A.L., Gauthier, M., Gower, C.F., 1992. Metallogeny of structural zones, Grenville Province, northeastern North America. Precambrian Research, Precambrian Metallogeny Related to Plate Tectonics 58, 401–426. doi:10.1016/0301-9268(92)90127-A

Toé, W., 2012. Minéralisations uranifères de la ceinture orogénique Pan-Africaine du Damara (Namibie): Implications de la fusion partielle, de la migration et de la mise en place des magmas sur le remaniement de la croûte continentale (Unpublished PhD. Dissertation). Université de Lorraine, France.

Tohver, E., Teixeira, W., Pluijm, B. van der, Geraldes, M.C., Bettencourt, J.S., Rizzotto, G., 2006. Restored transect across the exhumed Grenville orogen of Laurentia and Amazonia, with implications for crustal architecture. Geology 34, 669–672. doi:10.1130/G22534.1

Turlin, F., André-Mayer, A.-S., Moukhsil, A., Vanderhaeghe, O., Gervais, F., Solgadi, F., Groulier, P.-A., Poujol, M., 2017. Unusual LREE-rich, peraluminous, monazite- or allanite-bearing pegmatitic granite in the central Grenville Province, Québec. Ore Geology Reviews 89, 627–667. doi:10.1016/j.oregeorev.2017.04.019

Turlin, F., Eglinger, A., Vanderhaeghe, O., André-Mayer, A.-S., Poujol, M., Mercadier, J., Bartlett, R., 2016. Synmetamorphic Cu remobilization during the Pan-African orogeny: Microstructural, petrological and geochronological data on the kyanite-micaschists hosting the Cu(–U) Lumwana deposit in the Western Zambian Copperbelt of the Lufilian belt. Ore Geology Reviews 75, 52–75. doi:10.1016/j.oregeorev.2015.11.022

van Breemen, O., Currie, K. l., 2004. Geology and U–Pb geochronology of the Kipawa Syenite Complex — a thrust related alkaline pluton — and adjacent rocks in the Grenville Province of western Quebec. Can. J. Earth Sci. 41, 431–455.

Van Kranendonk, M.J.V., Kirkland, C.L., 2013. Orogenic climax of Earth: The 1.2–1.1 Ga Grenvillian superevent. Geology 41, 735–738. doi:10.1130/G34243.1

PARTIE I : GRANITES PEGMATITIQUES À REE DU GRENVILLE CENTRAL

1. Préambule

Depuis quelques années, la région du Grenville central a fait l'objet de nombreux travaux de recherches conduits sur un transect de Baie-Comeau au Front de Grenville, essentiellement menés par l'équipe d'A. Indares et de G. Dunning de Memorial University (St John's, NL, Canada). En parallèle, plusieurs campagnes de cartographie ont été conduites dans la Province de Grenville central (Fig. 0-4) par A. Moukhsil pour le compte du Ministère de l'Énergie et des Ressources naturelles du Québec du Sud-Ouest au Sud-Est de l'impact de Manicouagan dans les ceintures Allochtone et Parautochtone (Moukhsil et al., 2012, 2013a, 2013b, 2014). Elles complètent les travaux de cartographie de Gobeil et al. (2002) ainsi que le travail de synthèse de Moukhsil et al. (2009) réalisé sur la région de Baie-Comeau plus au Sud.

Outre le raffinement de la carte géologique détaillée de cette région (Fig. 0-4), ces campagnes de cartographie ont également permis l'identification de nombreuses occurrences métallogéniques, et en particulier en terres rares (Moukhsil et al., 2014). C'est au cours de la campagne menée en 2013 sur la région du Lac Okaopéo qu'ont été identifiées sept nouvelles occurrences de terres rares magmatiques dans le segment crustal de moyenne à basse pression de la ceinture Allochtone, toutes associées à des dykes de granites pegmatitiques. Ce sont ces occurrences sur lesquelles se focalise ce travail de thèse.

Après un bref rappel de la classification des pegmatites largement utilisé dans la littérature, le premier chapitre de ce manuscrit (***chapitre 1***) a pour objectif de caractériser ces granites pegmatitiques en détaillant : (i) leurs relations avec les encaissants via des cartographies de détail des affleurements ; (ii) leur texture ; (iii) leur composition en éléments majeurs et traces, notamment les teneurs en terres rares des faciès les plus minéralisés ; (iv) d'identifier les porteurs de la minéralisation ; et (v) d'apporter les premières contraintes géochronologiques sur leur mise en place.

L'ensemble de ces résultats permet la définition d'un type de granites pegmatitiques inhabituel par son caractère peralumineux, ses fortes teneurs en terres rares jusqu'à plus de 9000 ppm (essentiellement légères) et de soulever les questions auxquelles nous apportons des contraintes dans cette thèse relatives (i) à leur contexte géodynamique de mise en place, (ii) à leur source, et (iii) aux processus pétrogénétiques ayant permis de telles concentrations dans des magmas peralumineux.

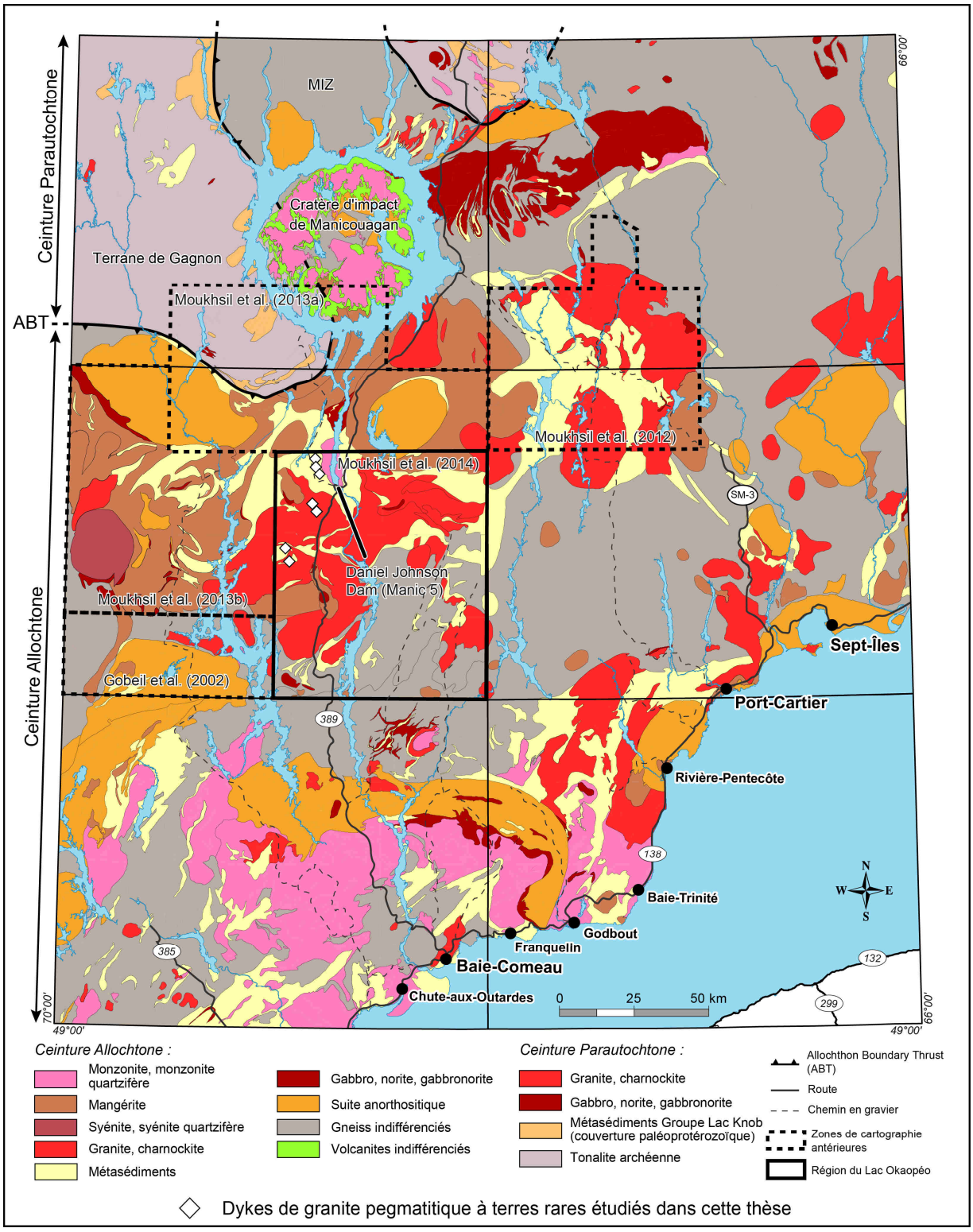

Figure 0-4 : Carte géologique de la Province de Grenville central repositionnant les zones cartographiées au cours de ces dernières années et la position des dykes de granite pegmatitique à terres rares étudiés au cours de cette thèse (modifiée d'après Moukhsil et al., 2014). Abréviation : MIZ = Zone Imbriquée de Manicouagan.

2. The classification scheme of granitic pegmatites

Over the last few decades classifications of mineralized granitic pegmatites have been progressively refined (e.g. Černý, 1991a, 1991b, 1990; Černý and Ercit, 2005; Ercit, 2005; Ginsburg et al., 1979), the last of which (summarized in Černý et al., 2012b) being widely used (Fig. 0-2). It subdivides the mineralized granitic pegmatites based on two criteria that are (i) the metamorphic environment of their host rocks, and (ii) their petrologic-geochemical signature leading to a petrogenetic model.

Class	Subclass	Type	Subtype	Family
Abyssal	HREE			NYF
	LREE			
	U			NYF
	BBe			LCT
Muscovite				
Muscovite-rare element	REE			NYF
	Li			LCT
Rare element	REE	allanite-monazite euxenite gadolinite		NYF
	Li	beryl	beryl-columbite beryl-columbite-phosphate	LCT
		complex	spodumene petalite lepidolite elbaite amblygonite	
		albite-spodumene albite		
Miarolitic	REE	topaz-beryl gadolinite-fergusonite		NYF
	Li	beryl-topaz spodumene petalite lepidolite		LCT

Figure 0-5 : Pegmatite classification scheme as defined by Černý and Ercit (2005) (redrawn from Černý et al., 2012b). Dark grey areas refer to NYF family and light grey areas to LCT family. Abbreviations: LCT = Li-Cs-Ta family; LREE = light rare-earth elements; HREE = heavy rare-earth elements; NYF = Nb-Y-F family.

On the one hand, five classes of granitic pegmatites are distinguished based on their metamorphic environment, namely abyssal, muscovite, muscovite-rare element, rare-element and miarolitic (Fig. 0-2) (Černý, 1990, 1991a, 1991b; Černý et al., 2012b; Černý and Ercit, 2005; Ercit, 2005; London, 2005, 2008). Granitic pegmatites that were emplaced at upper amphibolite facies to low- to high-pressure (P) granulite facies are grouped into the abyssal

class; those in high-P, Barrovian amphibolite facies to the muscovite class (Černý, 1991a). The other classes correspond to granitic pegmatites emplaced in lower grade metamorphic environments, from lower amphibolite facies ((muscovite-)rare-element), to shallow to sub-volcanic environment for the muscovite-rare element, rare-element and miarolitic classes respectively (Černý, 1991a). The abyssal class is further subdivided into four subclasses, namely HREE-Y, LREE, U-Th, B-Be as a function of their trace element content.

On the other hand, three families of mineralized granitic pegmatites are distinguished as a function of their petrologic and geochemical signatures (Fig. 0-2). The LCT family groups granitic pegmatites enriched in Li-Cs-Ta, with complementary substantial enrichment in Rb, Ga, Sn, Hf, P, F (Černý, 1991a). They have compositional affinities with S-type granite formed in subduction contexts, and parent melts that can be formed either (i) by partial melting of undepleted upper- to middle-crust metasedimentary and metavolcanic protoliths or (ii) by low-percentage partial melting of (meta-)igneous rocks of the basement (Černý et al., 2012b; Černý and Ercit, 2005, and references therein; Chappell and White, 2001; Martin and De Vito, 2005). Granitic pegmatites from the LCT family are characterized by the predominance of Li-minerals, such as spodumene, Cs-minerals, such as beryl and micas (mostly muscovite), Ta-rich oxides, such as columbite, and by the presence of tourmaline (e.g. Černý et al., 2012b). The NYF family encompasses granitic pegmatites enriched in Nb-Y-F, with high HREE, Ti, U, Th, Y, Zr, Be, and F content, and complementary substantial enrichment in Nb compared to Ta (Černý, 1991a). It is characterized by the predominance of Nb-Ta-Y-REE minerals, such as euxenite/aeschynite, samarskite/fergusonite, gadolinite and allanite(-Y) (Černý et al., 2012b). They have compositional affinities with A-type granite with parent melts that can be formed by a wide range of processes including: (i) partial melting of a middle- to lower-crust and/or undepleted juvenile igneous rocks; (ii) partial melting of an acidic crust pre-enriched in NYF elements; or (iii) direct differentiation of mantle-derived fluids from mantle-derived basaltic magmas (Černý et al., 2012b; Eby, 1990; Ercit, 2005; Isseini et al., 2012; London, 2008; Martin and De Vito, 2005).

Unequivocal evidence for the derivation of granitic pegmatites from a plutonic body were provided by: (i) field relationships showing highly fractionated pegmatitic bodies that can be traced back to their granitic source (Černý et al., 2012a; London, 2005) as for the Gatumba field (central Rwanda, e.g. Hulsbosch et al., 2014); (ii) strong contrasts in isotopic signatures between the granitic pegmatites and their host rock precluding any petrogenetic links between the two (e.g. Sr isotopic signature, London, 2005 and references therein); and (iii) experimental

studies that failed to produce beryl-saturated granitic pegmatites by partial melting (e.g. Evensen and London, 2002; London, 2005). Alternatively, an origin by partial melting for granitic pegmatites is invoked owing to (i) the common difficulty to link the composition of highly evolved pegmatitic bodies to potential plutonic sources; (ii) the common lack of coeval plutonic bodies in the vicinity of the granitic pegmatites fields; and (iii) chemical evidence for interactions between the granitic pegmatites and the intruded rocks (London, 2005, and references therein). One of the few crustal-scale sections that allows the identification of the structural links between migmatites, granitic plutons and granitic pegmatites, is the hinterland of the Damara Belt in Namibia, where a continuous section is exposed from migmatites derived from partial melting of paragneisses and orthogneisses with minor amphibolites to leucogranitic plutons emplaced higher in the crust but rooted to the migmatites via a network of granitic dykes and sills, and structurally linked to pegmatitic bodies including the so-called U-bearing alaskites (Toé et al., 2013).

References

Černý, P., 1991a. Rare-element Granitic Pegmatites. Part I: Anatomy and Internal Evolution of Pegmatitic Deposits. Geoscience Canada 18, 49–67.

Černý, P., 1991b. Rare-element Granitic Pegmatites. Part II: Regional to Global Environments and Petrogenesis. Geoscience Canada 18, 68–81.

Černý, P., 1990. Distribution, affiliation and derivation of rare-element granitic pegmatites in the Canadian Shield. Geol. Rundsch. 79, 183–226. doi:10.1007/BF01830621

Černý, P., Ercit, T.S., 2005. The classification of granitic pegmatites revisited. Can. Mineral. 43, Part 6, 2005–2026.

Černý, P., Halden, N.M., Ferreira, K., Meintzer, R.E., Brisbin, W.C., Chackowsky, L.E., Corkery, M.T., Longstaffe, F.J., Trueman, D.L., 2012a. Extreme Fractionation and Deformation of the Leucogranite – Pegmatite Suite at Red Cross Lake, Manitoba, Canada. Ii. Petrology of the Leucogranites and Pegmatites. Can. Mineral. 50, 1807–1822. doi:10.3749/canmin.50.6.1807

Černý, P., London, D., Novák, M., 2012b. Granitic Pegmatites as Reflections of Their Sources. Elements 8, 289–294. doi:10.2113/gselements.8.4.289

Chappell, B.W., White, A.J.R., 2001. Two contrasting granite types: 25 years later. Australian Journal of Earth Sciences 48.

Eby, G.N., 1990. Alkaline Igneous Rocks and CarbonatitesThe A-type granitoids: A review of their occurrence and chemical characteristics and speculations on their petrogenesis. Lithos 26, 115–134. doi:10.1016/0024-4937(90)90043-Z

Ercit, T.S., 2005. REE-enriched granitic pegmatites. Short Course Notes - Geological Association of Canada 17, 175–199.

Evensen, J.M., London, D., 2002. Experimental silicate mineral/melt partition coefficients for beryllium and the crustal Be cycle from migmatite to pegmatite. Geochimica et Cosmochimica Acta 66, 2239–2265. doi:10.1016/S0016-7037(02)00889-X

Ginsburg, A.I., Timofeyev, I.N., Feldman, L.G., 1979. Principles of Geology of the Granitic Pegmatites. Nedra, Moscow.

Gobeil, A., Hébert, C., Clark, T., Beaumier, M., Perreault, S., 2002. Géologie de la région du lac De la Blache (22K/03 et 22K/04). Ministère des Ressources Naturelles, Québec, RG 2002-01, 53 p.

Hulsbosch, N., Hertogen, J., Dewaele, S., André, L., Muchez, P., 2014. Alkali metal and rare earth element evolution of rock-forming minerals from the Gatumba area pegmatites (Rwanda): Quantitative assessment of crystal-melt fractionation in the regional zonation of pegmatite groups. Geochimica et Cosmochimica Acta 132, 349–374. doi:10.1016/j.gca.2014.02.006

Isseini, M., André-Mayer, A.-S., Vanderhaeghe, O., Barbey, P., Deloule, E., 2012. A-type granites from the Pan-African orogenic belt in south-western Chad constrained using geochemistry, Sr–Nd isotopes and U–Pb geochronology. Lithos, Seventh Hutton Symposium on Granites and Related Rocks 153, 39–52. doi:10.1016/j.lithos.2012.07.014

London, D., 2008. Pegmatites, Mineralogical Association of Canada.

London, D., 2005. Granitic pegmatites: an assessment of current concepts and directions for the future. Lithos, Granitic systems Ilmari Haapala Volume Symposium “Granitic Systems –State of the Art and Future Avenues” 80, 281–303. doi:10.1016/j.lithos.2004.02.009

Martin, R.F., De Vito, C., 2005. The patterns of enrichment in felsic pegmatites ultimately depend on tectonic setting. Can. Mineral. 43, 2027–2048. doi:10.2113/gscanmin.43.6.2027

Moukhsil, A., Lacoste, P., Gobeil, A., David, J., 2009. Synthèse géologique de la région de Baie-Comeau. Ministère des Ressources naturelles et de la Faune, Québec, RG 2009-03, 30 p.

Moukhsil, A., Solgadi, F., Belkacim, S., Elbasbas, A., Augland, L.E., 2014. Géologie de la région du lac Okaopéo, Côte-Nord. Ministère de l'Energie et des Ressources Naturelles, Québec, RG 2014-03, 34 p.

Moukhsil, A., Solgadi, F., Clark, T., Blouin, S., Indares, A., Davis, D.W., 2013a. Géologie du nord-ouest de la région du barrage Daniel-Johnson (Manic 5), Côte-Nord. Ministère des Ressources Naturelles, Québec, RG 2013-01, 46 p.

Moukhsil, A., Solgadi, F., Indares, A., Belkacim, S., 2013b. Géologie de la région septentrionale du réservoir aux Outardes 4, Côte-Nord. Ministère des Ressources Naturelles, Québec, RG 2013-03, 33 p.

Moukhsil, A., Solgadi, F., Lacoste, P., Gagnon, M., David, J., 2012. Géologie de la région du lac du Milieu (SNRC 22O03, 22O04, 22O06, 22J13 et 22J14). Ministère des Ressources Naturelles et de la Faune, Québec, RG 2012-01, 33 p.

Toé, W., Vanderhaeghe, O., André-Mayer, A.-S., Feybesse, J.-L., Milési, J.-P., 2013. From migmatites to granites in the Pan-African Damara orogenic belt, Namibia. Journal of African Earth Sciences 85, 62–74. doi:10.1016/j.jafrearsci.2013.04.009

Chapitre 1 : Unusual LREE-rich, peraluminous, monazite- or allanite-bearing pegmatitic granite in the central Grenville Province, Québec

François Turlin[a,*], Anne-Sylvie André-Mayer[a], Abdelali Moukhsil[b], Olivier Vanderhaeghe[c], Félix Gervais[d], Fabien Solgadi[e], Pierre-Arthur Groulier[f], Marc Poujol[g]

Article publié en 2017 dans *Ore Geology Reviews* 89, 627-667.

[a] *GeoRessources lab., UMR 7359, Université de Lorraine, CNRS, CREGU, Faculté des Sciences et Technologies, Vandœuvre-lès-Nancy, F-54506, France*

[b] *Ministère de l'Énergie et des Ressources naturelles, Direction du Bureau de la connaissance géoscientifique du Québec, 5700, 4e Avenue Ouest, Québec (Québec), G1H 6R1*

[c] *Géosciences Environnement Toulouse, GET, Université de Toulouse, CNRS, IRD, UPS, CNES (Toulouse), France*

[d] *Département des génies civil, géologiques et des mines, Ecole Polytechnique de Montréal, Canada*

[e] *Ministère de l'Énergie et des Ressources naturelles, Direction du Bureau de la connaissance géoscientifique du Québec, 400, boulevard Lamaque, Val-d'Or (Québec), J9P 3L4*

[f] *Earth Sciences Department, Memorial University, St. John's, NL A1B 3X5, Canada*

[g] *Géosciences Rennes, UMR 6118, OSUR, Université de Rennes 1, 35042 Rennes Cedex, France*

Abstract

This contribution presents an original study combining detailed mapping, petrography, whole-rock geochemistry and geochronological constraints on the recently identified LREE (Light Rare Earth Elements) occurrences associated with pegmatitic granite dykes (PGD) from the central Grenville (Lac Okaopéo region). These PGD intrude paragneisses or meta-igneous complexes with a REE mineralization hosted either in monazite-(Ce) or in allanite-(Ce) respectively. The investigated samples display peraluminous signatures and are dominated by a quartz + K-feldspar + plagioclase + biotite + monazite/allanite assemblage. Field relationships and the magmatic textures of the dykes combined with U-Pb dating of magmatic monazite grains at 1005.4±4.4 Ma and 996.7±5.3 Ma (concordant igneous ages) imply that the LREE-rich PGD were emplaced in a post-tectonic setting. Allanite-(Ce)- and monazite-(Ce)-bearing PGD have ΣREE contents up to 9242 ppm and 7048 ppm, respectively. The allanite-rich assemblage is consistent with the petrographic assemblage of LREE-enriched PGD identified in the southwestern Grenville Province and elsewhere in the world, but this study constitutes the first evidence for a sole presence of monazite as LREE-bearing phase in strongly peraluminous PGD from the Grenville Province.

Keywords: Grenville Province; Peraluminous; Pegmatitic Granite; LREE; Whole-rock geochemistry; Allanite/Monazite

1. Introduction

Granitic pegmatites host numerous metallic occurrences, mostly rare-metals such as U-Th, Nb-Ta, Y, Rare Earth Elements (REE), Ti, Zr, Be, Li, Cs, Mo, Rb, B, P, Pb, F. Due to their small sizes, REE-rich granitic pegmatites are generally not considered as good economic target when compared to their plutonic counterparts, and have thus not received the same attention (e.g. Ercit, 2005; Goodenough et al., 2016; London, 2016). However, the worldwide overwhelming occurrences of REE-bearing granitic pegmatites may potentially represent important sources of REE and are to be included in the further global investigations of the REE metallogenic system. The lack of detailed field descriptions, whole-rock and mineralogical compositions, as well as structural data for the pegmatitic bodies and their host and country rocks prevent a good understanding of the source, the formation and the concentration of REE-bearing pegmatites (Dill, 2015; Ercit, 2005). Classification schemes, such as the NYF (Nb-Y-F) classes of Černý et al. (2012) or the "chessboard" scheme of Dill (2010), generally depict REE-rich granitic pegmatites as being derived from an alkaline melt fractionation (Dill, 2010, 2015). However, in some cases (e.g. in the Grenville Province) where the lack of coeval granitic pluton is not necessarily due to a lack of outcrops, a derivation of REE-rich granitic pegmatites from partial melting of a crustal/sub-crustal component is generally inferred, but not clearly demonstrated (Ercit, 2005 and references therein).

With this in mind, the Proterozoic Grenville Province, mainly exposed in Quebec and Ontario (Canada, Fig. 1-1), offers the possibility to study numerous magmatic REE occurrences, mainly late- to post-Grenvillian in age, and associated with a large spectrum of magmatic environments including nepheline-syenite (e.g. Saint-Honoré, Crevier, Bergeron, 1980; Gauthier and Chartrand, 2005; Groulier, 2013; Sangster et al., 1992), carbonatite (e.g. Niobec, Crevier, Bergeron, 1980; Groulier, 2013), as well as numerous granitic pegmatites (e.g. Ayres and Černý, 1982; Černý, 1990; Ercit, 2005; Ford, 1982; Lentz, 1996; Masson and Gordon, 1981; Moukhsil et al., 2014). Other "non-magmatic" REE occurrences are described in this province such as the metasomatic mineralization of Kipawa or the Kwyjibo IOCG-type deposit, with a REE mineralization dated at ca. 1030 Ma (Saucier et al., 2013; van Breemen and Currie, 2004) and ca. 985-970 Ma (Gauthier et al., 2004; Perreault and Lafrance, 2015 and references therein), respectively.

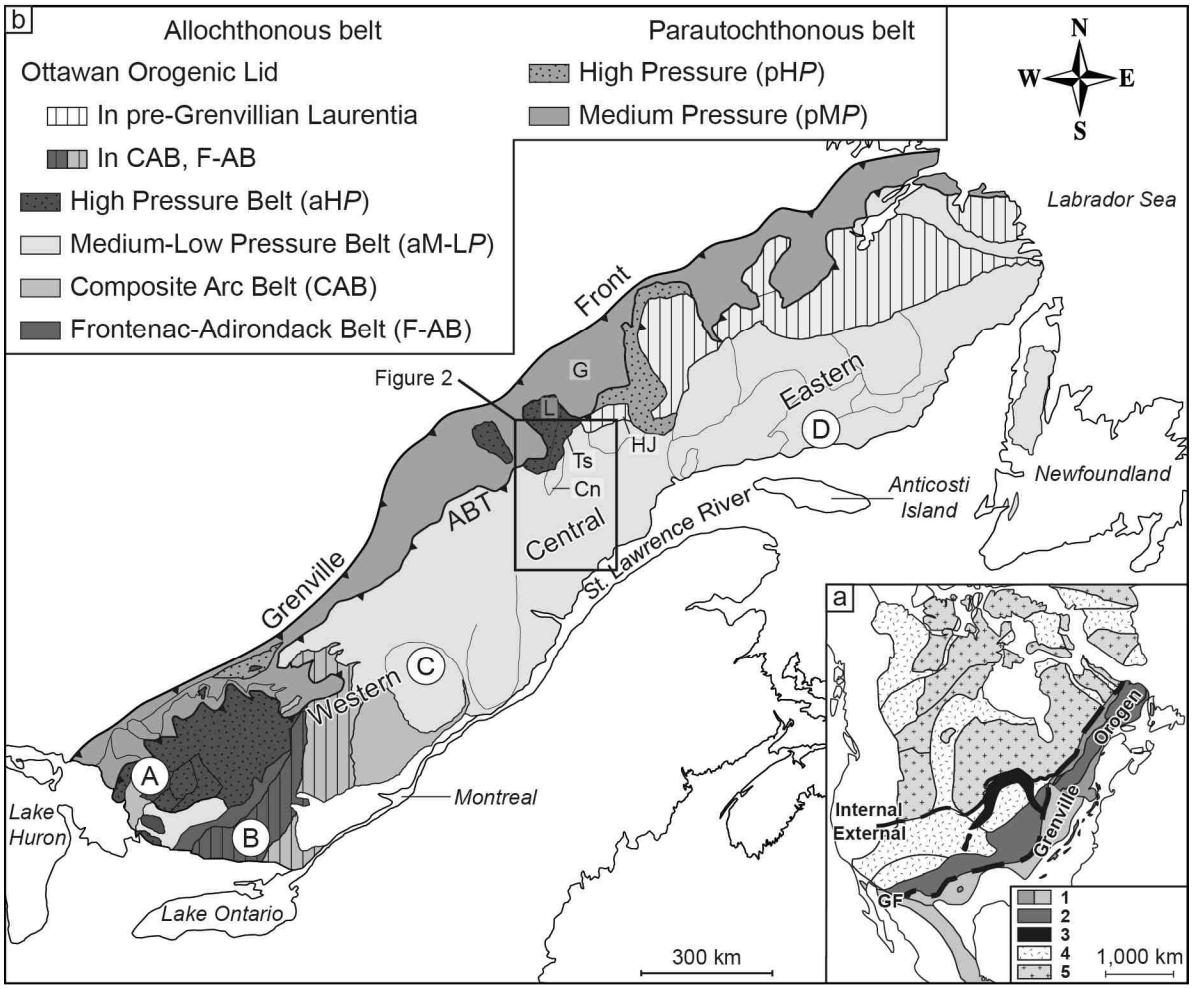

Figure 1-1: a: Position of the Grenville orogen in Laurentia. Paleozoic and younger cover omitted (modified from Hoffman, 1989; Rivers, 2008; Rivers et al., 2012). The northern dashed line represents the boundary between Internal and External Paleoproterozoic Laurentia and the southern dashed line represents the Grenville Front (GF). Abbreviations: 1 = exposed Grenville Province, light grey represents the inferred extension of subsurface allochthonous Grenville Province; 2 = Granite-Rhyolite Igneous Province, ca. 1.50-1.34 Ga and reworked equivalents in the Grenville Province; 3 = Mid-Continental Rift system; 4 = Paleoproterozoic orogens, ca. 1.9-1.8 Ga, ca. 1.65 Ga and reworked equivalents in the Grenville Province; 5 = Archean cratons; GF = Grenville Front. b: Simplified tectonic map of the Grenville Province (modified after Rivers, 2008; Rivers et al., 2012). Letters in circle represent the localization of the main Grenvillian granitic pegmatites field as reviewed in Ayres and Černý (1982) and Černý (1990): A = Central Gneiss Belt; B = Central Metasedimentary Belt; C = Central Granulite Terrain; D = eastern part of the Grenville Province. Abbreviations: ABT = Allochthon Boundary Thrust; Cn = Canyon domain; G = Gagnon Terrane; HJ = Hart-Jaune terrane; L = Lelukuau terrane; Ts = Tshenukutish terrane.

During the past few decades, several studies investigated the distribution, mineralogy and petrogenesis of granitic pegmatites from the Grenville Province (Ayres and Černý, 1982; Černý, 1990; Fowler and Doig, 1983; Lentz, 1996, 1991; Masson and Gordon, 1981). They typically comprise U-Th, Nb-Ta, Y, Ti, Zr, REE, Be, Mo, P, Pb, F (Ayres and Černý, 1982; Černý, 1990; Fowler and Doig, 1983; Gauthier and Chartrand, 2005; Lentz, 1996; Masson and Gordon, 1981). They are generally interpreted as representing a silicate melt extracted from partially molten rocks between ca. 1.1 to 0.9 Ga during the late stages of major intrusive events coeval with the end of Grenvillian high-grade metamorphism based on (i) the lack of coeval

granitic pluton, (ii) their magmatic and undeformed texture, and (iii) their discordant and intrusive nature in brittle zones within competent units (Ayres and Černý, 1982; Ercit, 2005; Lentz, 1991; Lumbers, 1964; Masson and Gordon, 1981). Accordingly, the presence of REE-enriched pegmatitic granite dykes *(further designated as 'PGD')* in the Grenville Province raises the question of (i) the source of these magmas and (ii) the geodynamic context that prevailed during their emplacement. Were these granitic magmas produced by partial melting of the thermally relaxed orogenic root composed of reworked Archean and/or Proterozoic pre-existing continental crust, or do they correspond to extremely differentiated mantle melts produced by decompression owing to post-orogenic extension?

The previous studies mentioned above have been mainly focused on the western parts of the Grenville Province and, to our knowledge, no REE-rich PGD have been described in the central part of the Grenville Province (Fig. 1-1). A recent campaign of cartography in the Lac Okaopéo region conducted by Moukhsil et al. (2014) (Figs. 1-2, 1-3) has led to the identification of seven REE magmatic occurrences associated with discordant PGD intrusive either in migmatitic paragneisses or in metaplutonic complexes (Fig. 1-3, Table 1-1, Moukhsil et al., 2014). These PGD have ΣREE contents ranging from 1418 to 9242 ppm (this study, Table 1-2) and represent new REE occurrences in the Grenville Province. The present paper is dedicated (i) to describe the field relationships between the various PGD and their host rocks to constrain their structural framework; (ii) to characterize their petrography and whole-rock geochemistry, allowing to discuss potential sources and processes responsible for their emplacement and concentration; and (iii) to constrain the timing of REE mineralization by LA-ICP-MS U-Pb dating on monazite in order to replace these PGD in the tectonic-metamorphic framework of the Grenvillian Orogeny. Finally, these results will be compared to other LREE-enriched granitic pegmatites reported elsewhere.

2. Geological framework

2.1. The Grenville Orogenic Belt

The study area is located in the central Grenville Province (Fig. 1-1b), which mainly crops out along the southeastern Canadian Shield (Fig. 1-1a). It results from a long history of tectonic-magmatic accretion through the Mesoproterozoic and subsequent continent-continent collision designated as the Grenvillian Orogeny *sensu stricto* (e.g. Carr et al., 2000; Dunning and Indares, 2010; Gower and Krogh, 2002; Rivers et al., 2012; Tucker and Gower, 1994).

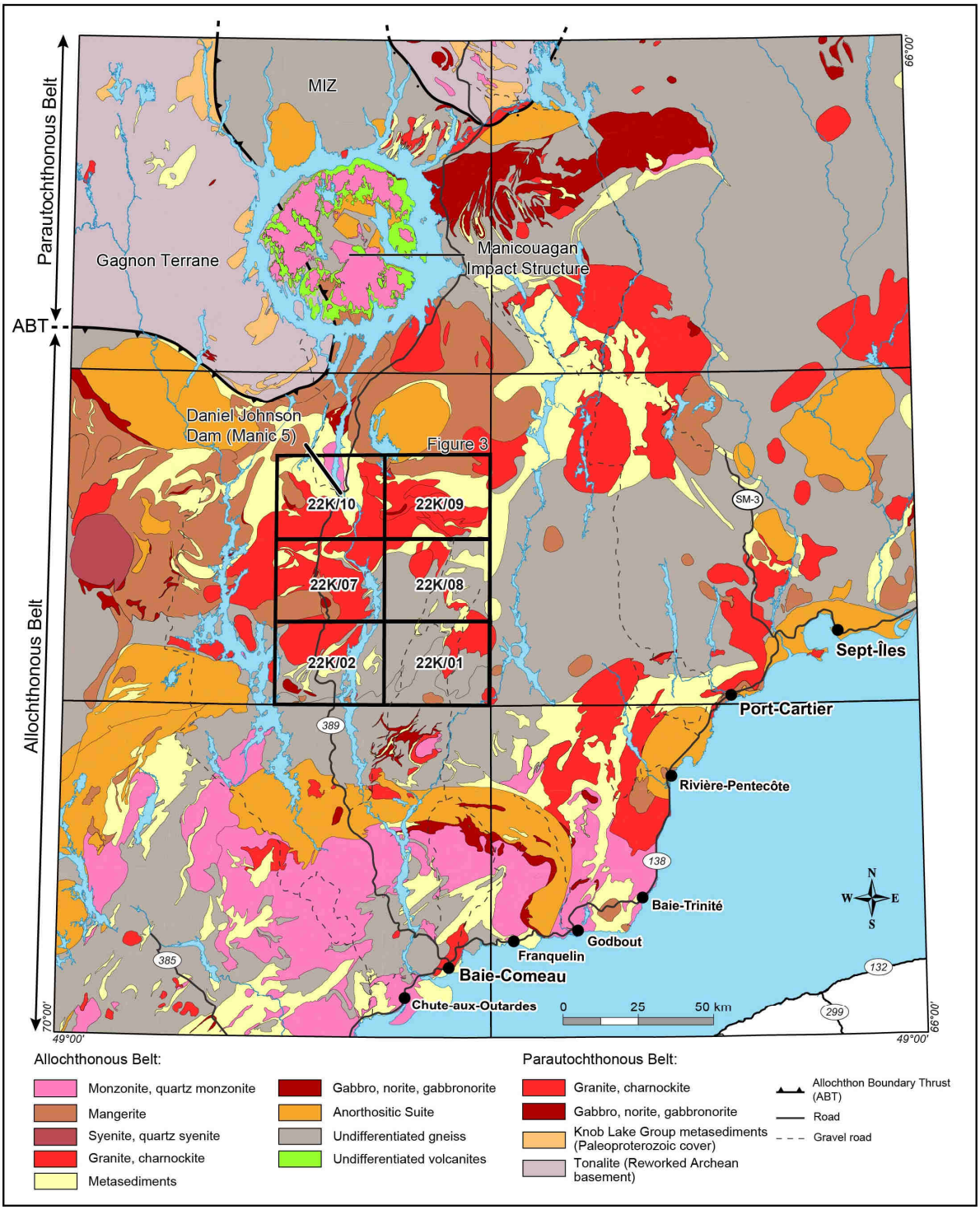

Figure 1-2: Geological map of the central Grenville (Quebec) showing the position of the studied Lac Okaopéo region (NTS sheets 22K/01, 22K/02, 22K/07, 22K/08, 22K/09, 22K/10, modified after Moukhsil et al., 2014). Abbreviations: ABT = Allochthon Boundary Thrust; MIZ = Manicouagan Imbricate Zone.

The two main tectonometamorphic domains of the Grenville Province, namely the Allochthonous and the Parautochthonous belts recorded the Grenvillian Orogeny as two distinct phases. The Allochthonous Belt (Fig. 1-1b) is made of terranes that originated outboard of, and were accreted to Laurentia during the Mesoproterozoic (Rivers et al., 2012). The underlying

Parautochthonous Belt (Fig. 1-1b) corresponds to rocks of the Superior Province and its cover sequence or to previously accreted arc that were reworked during the Grenvillian Orogeny (Rivers et al., 1989, 2012). The Allochthonous and the Parautochthonous belts are separated by the southeast-dipping and orogen-scale high-grade shear zone designated as the Allochthon Boundary Thrust (ABT, Figs. 1-1b, 1-2). The "Ottawan" crustal thickening phase is the first of the Grenvillian Orogeny, and was characterized by the development of a hot ductile crust underneath an orogenic plateau ("Orogenic Lid", Fig. 1-1b) with a lower limit inferred to be the ABT, between ca. 1090 and 1020 Ma in the Allochthonous Belt (e.g. Carr et al., 2000; Dunning and Indares, 2010; Indares et al., 2000; Rivers, 2008, 1997; Rivers et al., 2012). This plateau is inferred to have collapsed on itself after the Ottawan phase resulting in the formation of several normal-sense shear zones commonly associated with the emplacement of PGD, and assisted by the intrusion of AMCG suites that resulted in weakening and lubricating of the shear zones (Ketchum et al., 1998; Rivers, 2012; Rivers and Schwerdtner, 2015; Soucy La Roche et al., 2015). Renewed convergence during the relatively short-lived Rigolet phase (1005-960 Ma, Rivers, 2009) resulted in foreland-ward propagation of Grenvillian thrusting and high-grade metamorphism, the northwest limit of which is the Grenville Front (Fig. 1-1), an orogen-scale, southeast-dipping shear zone that was active during the Rigolet orogenic phase (Krogh, 1994; Rivers et al., 1989; Rivers, 2008, 2009). Synkinematic PGD and sills were intruded at upper and lower structural levels of the Parautochthonous and Allochthonous belts, respectively, between 993 and 961 Ma during this later phase on the south shore of the Manicouagan Reservoir (Fig. 1-2, Jannin et al., In press).

North of Manicouagan Reservoir, the Ottawan tectonic phase reached a metamorphic peak at ca. 1450 MPa and 860-900ºC between ca. 1080-1040 Ma (Indares et al., 1998; Indares and Dunning, 2001; Lasalle et al., 2013; Lasalle and Indares, 2014; Rivers et al., 2002) in kyanite-bearing rocks from the Manicouagan Imbricate Zone (MIZ, central Grenville, Fig. 1-2), a high-grade nappe of Paleoproterozoic and Mesoproterozoic rocks of the Allochthonous H*P* Belt (aH*P*, Fig. 1-1b). It was followed by the exhumation of the MIZ over a crustal-scale ramp structurally above the Parautochthonous Belt at ca. 1100 MPa and 870ºC between ca. 1040-1030 Ma (Indares et al., 1998; Indares and Dunning, 2001; Lasalle et al., 2013; Lasalle and Indares, 2014; Rivers et al., 2002), and by the subsequent pervasive intrusion of mantle-derived magmas in the thickened orogenic crust (e.g. Dunning and Indares, 2010; Hynes et al., 2000; Indares et al., 2000; Indares and Dunning, 2004). South of the Manicouagan reservoir (just north of our study area, Fig. 1-2), however, peak metamorphic conditions at sillimanite-

grade conditions reached ca. 950 MPa and 850°C between ca. 1080 and 1040 Ma (Dunning and Indares, 2010; Lasalle et al., 2014; Lasalle and Indares, 2014). In the Parautochthonous Belt south of the reservoir, granulite-facies peak metamorphic conditions of ca. 1500 MPa and 850°C were reached between ca. 1005 and 980 Ma (Hynes et al., 2000; Jordan et al., 2006; Rivers, 2009; Rivers et al., 2012; van Gool et al., 2008) in metapelites from the Knob Lake Group Paleoproterozoic sequence of the Gagnon Terrane that unconformably overlie the Laurentian Archean basement (Parautochthonous Belt, Fig. 1-2, Dunning and Indares, 2010; Hynes et al., 2000; Rivers, 1980; Rivers et al., 1989). A recent study indicated that high-grade deformation continued until at least ca. 986 Ma (but could be as young ca. 961 Ma) as rocks of the upper and lower parts of the Parautochthonous and the Allochthonous belts, respectively, were likely flowing as an orogenic channel (Jannin et al., In press).

2.2. The Lac Okaopéo lithotectonic units and structures

The Lac Okaopéo region is located south of the MIZ and of the Daniel-Johnson dam (Manic-5, Fig. 1-2). The various lithotectonic units identified in this region (Gobeil et al., 2002; Moukhsil et al., 2014, 2013a, 2013b, 2012, 2009, 2007) belong to the Allochthonous M*P* Belt of the Grenville Province, structurally above the Allochthon Boundary Thrust (ABT, Fig. 1-2).

2.2.1. PGD host rocks

The PGD investigated in this study are hosted either in paragneisses or in two distinct metaplutonic suites, designated as the Bardoux and the Castoréum. The paragneisses from the Plus-Value Complex mainly crop out in the northwestern part of the region (Fig. 1-3) and are the oldest protolith in the region with a deposition age between 1765 and 1497 Ma (Augland et al., 2015; Lasalle et al., 2013; Moukhsil et al., 2014, 2013b).

The Bardoux plutonic suite (Fig. 1-3) is a greyish metagranite dominated by a metaluminous I-type to minor peraluminous S-type signature with millimetric garnet and biotite completed with phenocrysts (up to 5 cm) of K-feldspar (microcline) showing locally rapakivi texture, and containing some enclaves of diorite, monzonite and monzodiorite, that represent continental-arc granitoids emplaced into the Laurentian margin (Augland et al., 2015; Moukhsil et al., 2014, 2012). It has been dated at 1487.6±6.8 Ma in the Lac du Milieu region (U-Pb on zircon, Moukhsil et al., 2012), and at 1497±5 Ma in the Lac Okaopéo region (U-Pb on zircon, Augland et al., 2015). The Castoréum Plutonic Suite, which is intrusive in the Plus-Value Complex and in the Bardoux Plutonic Suite (Fig. 1-3), is dominated by a facies of homogeneous porphyric to porphyroclastic metagranite with a metamorphic fabric delineated by the preferred

orientation of biotite, hornblende and recrystallized or fractured feldspar phenocrysts (Moukhsil et al., 2014, 2013b). It is associated with minor charnockite, mangerite, granitic gneisses, and metatonalite (Moukhsil et al., 2014, 2013b). It has been dated at 1393±8 Ma (U-Pb on zircon) and emplaced in an arc-setting (Augland et al., 2015).

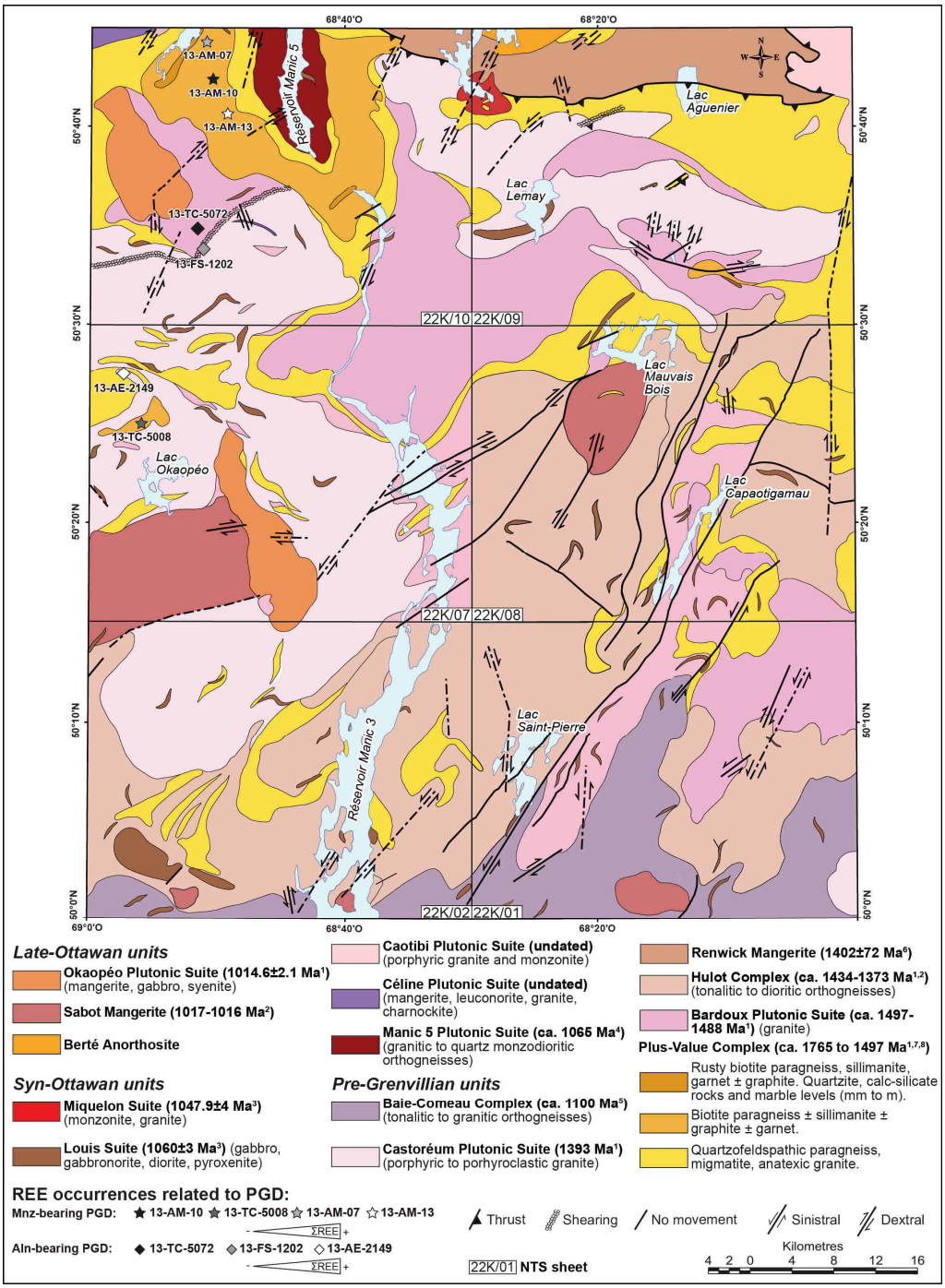

Figure 1-3: Simplified geological map of the studied Lac Okaopéo region (modified after Moukhsil et al., 2014) showing the geology of the environment of the REE occurrences identified in 2013 by Moukhsil et al. (2014). Stars and diamonds represent monazite-bearing and allanite-bearing pegmatitic granite outcrops respectively. Coordinates of the REE occurrences are proposed in Table 1-1. [1]: Augland et al. (2015); [2]: Gobeil et al. (2002); [3]: David (2006); [4]: Dunning and Indares (2010); [5]: David et al. (2009); [6]: Moukhsil et al. (2013a); [7]: Moukhsil et al. (2012); [8]: Lasalle et al. (2013). Abbreviation: PGD = pegmatitic granite dyke.

2.2.2. Other lithotectonic units exposed in the Lac Okaopéo region

The Lac Okaopéo region displays other lithotectonic units besides the ones intruded by the PGD (Fig. 1-3). All are younger than the Plus-Value Complex paragneisses and the Bardoux Plutonic Suite but their emplacement ages spread over the pre-Grenvillian and Grenvillian history. Pre-Grenvillian units include granitic to dioritic orthogneisses, metamangerite and metagranite. As they were emplaced between 1450 Ma and 1100 Ma (Augland et al., 2015; David et al., 2009; Gobeil et al., 2002; Moukhsil et al., 2007, 2012, 2013a, 2013b, 2014), their emplacement, encompasses most of the Mesoproterozoic evolution of the Province from the late-Pinwarian (ca. 1470-1450 Ma, Ketchum et al., 1994; Tucker and Gower, 1994) to the post-Elzevirian (ca. 1245-1225 Ma, Rivers et al., 2012). Several Grenvillian units are coeval with the Ottawan peak of high-grade metamorphism and include granitic to quartz monzodioritic orthogneisses, monzonitic to granitic slightly deformed plutons, and undeformed mafic rocks (David, 2006; Dunning and Indares, 2010; Moukhsil et al., 2007, 2009, 2013b, 2014). Late-Ottawan units include the Berté anorthosite intrusive in the Renwick Mangerite; the weakly deformed metaluminous mangerite and charnockite±leuconorite±granite from the Céline Plutonic Suite (undated), ascribed to the volcanic arc granite domain; the Sabot Mangerite (ca. 1016-1017 Ma); and the high-alkalic mangerite±gabbro±syenite from the Okaopéo Plutonic Suite (1014.6±2.1 Ma) (Gobeil et al., 2002; Moukhsil et al., 2014, 2013b, 2013a, 2009, 2007).

3. Sampling and analytical methods

3.1. Sampling

The seven PGD sampled for this study are accessible by gravel roads branching from the 389 highway, from Baie-Comeau to the Daniel Johnson dam (Manic-5, Figs. 1-2, 1-3). They are located in the northwestern part of the studied region (NTS sheets 22K/07 and 22K/10, Figs. 2-3, Table 1-1), and are aligned along a north to south trend (Fig. 1-3, Moukhsil et al., 2014). The studied PGD are mainly composed of quartz + K-feldspar + plagioclase + biotite ± monazite/allanite (Figs. 1-4, 1-6, 1-7, Appendices A-B). Their color and mineralogy are correlated to the nature of the intruded lithologies. Dykes hosted in paragneisses of the Plus-Value Complex are whitish and contain monazite [$(Ce,La,Nd,Th)PO_4$] as the LREE-bearing phase (outcrops 13-AM-07, -10, -13 and 13-TC-5008, Figs. 1-6, 1-8 to 1-10), while those hosted in metaplutonic complexes of the Bardoux and Castoréum Plutonic Suites are pinkish (fresh color) and contain allanite [$(Ce,Ca)_2(Al,Fe^{3+})_3(SiO_4)_3(OH)$] (outcrops 13-TC-5072, 13-FS-1202 and 13-AE-2149, Figs. 1-7, 1-11, 1-12).

3.2. Whole rock geochemistry

Whole-rock geochemistry of the most REE enriched facies of the PGD identified on each outcrop was performed by Actlabs (Ancaster, Ontario). Samples were chosen according to the abundance of REE phases, i.e. monazite and allanite, and using a RS125 scintillometer allowing for the identification of LREE-rich and LREE-poor facies as they are hosted in U-Th-bearing phases. Powdered samples were prepared by Li-metaborate or -tetraborate. Major elements were analysed by inductively coupled plasma - atomic emission spectroscopy (ICP‑AES), and trace elements by inductively coupled plasma - mass spectrometry (ICP‑MS). Results are reported in Table 1-2. In the present contribution, we report original geochemical data and we include an analysis from Moukhsil et al. (2014) for sample 13-AE-2149 (Tables 1-1, 1-2).

3.3. Electron microprobe (EMP)

Element composition and chemical maps were obtained by the Electron Microprobe (EMP) method using a Cameca computer-controlled SX-100 (GeoRessources, Nancy) equipped with a wavelength dispersive spectrometer (WDS).

For quantitative analyses and chemical mapping of monazite from the 13-AM-13 and the 13-TC-5008 PGD, major and trace elements (Si, P, Ca, Y, La, Ce, Pr, Nd, Sm, Gd, Pb, Th, U) were measured using an accelerating voltage of 20 kV and a beam current of 100 nA. Peak counting time was set to 120 s for Pb, 100 s for U and 20 s for the others elements. Results are reported in Table 1-3. Chemical mapping were realized at 15 kV and 100 nA, using a stage scanning mode. Dwell time per pixel was adjusted to 30 ms and pixel step range from 0.3 to 0.9 µm. The chosen X-ray lines were: Ce*L*α and Th*M*α. Maps are reported in Fig. 1-9.

For quantitative analyses of allanite from the 13-TC-5072 and the 13-FS-1202 PGD, major and trace elements (F, Mg, Al, Si, P, K, Ca, Ti, Mn, Fe, Sr, Y, La, Ce, Pr, Nd, Sm, Gd, Pb, Th, U) were measured using an accelerating voltage of 20 kV and a beam current of 100 nA. Peak counting time was set to 120 s for Pb, 100 s for U and 20 s for the others elements. Results are reported in Table 1-4.

3.4. U-Pb dating on monazite using Laser Ablation-Inductively Coupled Plasma-Mass Spectrometry (LA-ICP-MS)

U-Pb geochronology of monazite grains from two PGD (13-AM-13 and 13-TC-5008) was conducted directly on thin sections at Géosciences Rennes (France) by in-situ laser ablation inductively coupled plasma mass spectrometry (LA-ICP-MS) using an ESI NWR193UC Excimer laser coupled to a quadripole Agilent 7700x ICP-MS.

The signals of ^{204}(Pb + Hg), ^{206}Pb, ^{207}Pb, ^{208}Pb and ^{238}U masses have been acquired during the course of the analyses. The ^{235}U signal is calculated from ^{238}U on the basis of the ratio $^{238}U/^{235}U = 137.88$. Single analyses consisted of 20 s of background integration followed by 60 s integration with the laser firing followed by a 10 s delay to wash out the previous sample. Spot diameters of 10 µm associated with repetition rates of 2 Hz and a laser fluency of 6.5 J.cm^{-2} were used during the present study. For more information on the settings of the instrument, see Ballouard et al. (2015) and the Appendix D for details and operating conditions of the LA-ICP-MS measurements. Data reduction was carried out with the GLITTER® software package developed by the Macquarie Research Ltd (Van Achterbergh et al., 2001). Raw data were corrected for Pb/U laser-induced elemental fractionation and for instrumental mass discrimination by standard bracketing with repeated measurements of the Moacir monazite standard (Gasquet et al., 2010). To control the reproducibility and accuracy of the corrections, repeated analyses of the Manangoutry monazite standard (554.8±4.2 Ma; MSWD = 0.94, n = 8 for the 13-AM-13 sample; 554.4±3.4 Ma; MSWD = 0.94, n = 8 for the 13-TC-5008 sample; TIMS age 555±2 Ma; Paquette and Tiepolo, 2007) were treated as unknown. No common Pb correction was applied. Concordia diagrams were generated using Isoplot/Ex (Ludwig, 2001). All errors given in Table 1-5 are listed at 1 sigma.

4. Outcrop description and detailed mapping

4.1. Monazite-bearing PGD (paragneisses-hosted)

Four of the REE occurrences associated with PGD identified by Moukhsil et al. (2014) intrude migmatitic paragneisses of the Plus-Value Complex (Fig. 1-3). An example of detailed mapping of a monazite-bearing PGD (13-AM-13 outcrop) is provided in Fig. 1-4, and detailed description and mapping for each of the monazite-bearing outcrops are provided in Appendix A. Structural measurements of the dykes' walls and of the foliation of the host rocks are indicated for each outcrop in Appendix C.

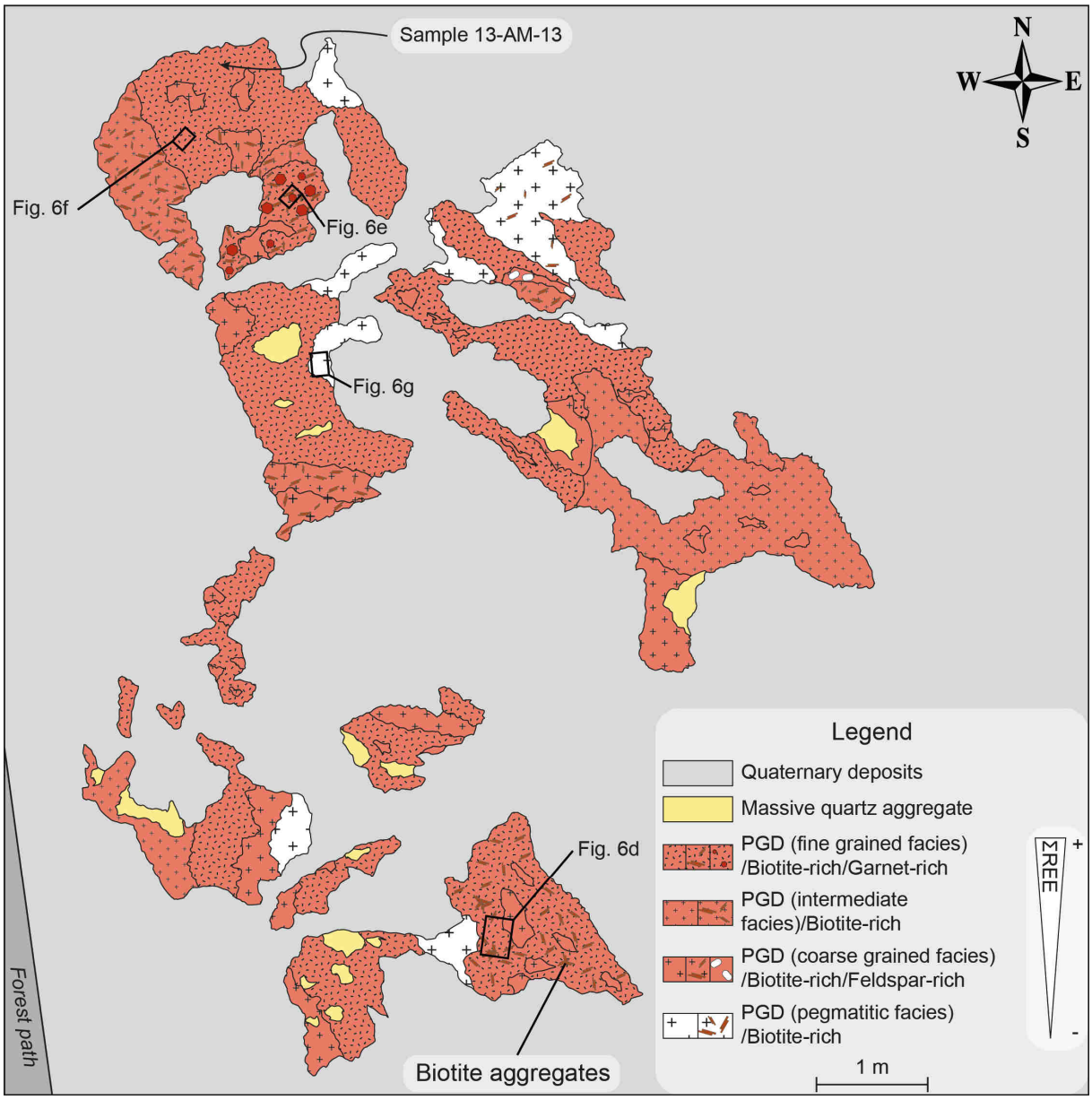

Figure 1-4: Example of detailed map for the 13-AM-13 monazite-bearing pegmatitic granite outcrop from the Lac Okaopéo region showing the relationships between the different identified facies of the pegmatitic granite and the sampling areas. The detailed map for the six other outcrops are proposed in appendices A and B. Abbreviation: PGD = pegmatitic granite dyke.

To the north of the studied area, PGD are exposed within small (a few square meters in surface) and flat lying outcrops (Fig. 1-6a) or steep-dipping outcrop along a gravel road. They are made of decimeter- to decameter-sized single dyke bodies with steeply dipping to subvertical walls trending N/S to locally NW/SE or NE/SW that dominantly plunge towards south, and are strongly (Fig. 1-6b) to slightly (Fig. 1-6c) discordant to the foliation of their host (Fig. 1-5a). Stockscheider-like textures delineate the contact between the 13-AM-07 PGD and the intruded paragneisses (Fig. 1-6b). All contacts are slightly (over a few millimeters, Fig. 1-6b) to locally diffuse (outcrop 13-TC-5008, Fig. 1-6c) and do not correspond to fractures

crosscutting the host-rock minerals (Fig. 1-6c). These PGD display various facies that are (i) fine grained (1 mm to over 1 cm, Fig. 1-6b and d) with garnet and sub-euhedral monazite (Fig. 1-6e, f), (ii) intermediate, (iii) coarse-grained (sometimes over 3 cm, Fig. 1-6d) dominated by quartz and feldspar with minor biotite, and (iv) pegmatitic dominated by quartz + feldspar ± biotite (Fig. 1-6g) with very few accessory phases, no garnet and only few monazite crystals. The transition between the fine- and coarse-grained facies is diffuse but is locally underlined by biotite aggregates (Fig. 1-6d). Locally, skeletal biotite (up to 15 cm crystals) are arranged as an arborescent texture (Fig. 1-6h). Up to ca. 20 cm centimeters wide quartz aggregates are expressed with no identifiable link with any of the previous facies (Fig. 1-4).

These PGD with monazite as the REE-hosting mineral, will further be referred as *'monazite-bearing'* (or *'Mnz-bearing'*) *PGD.*

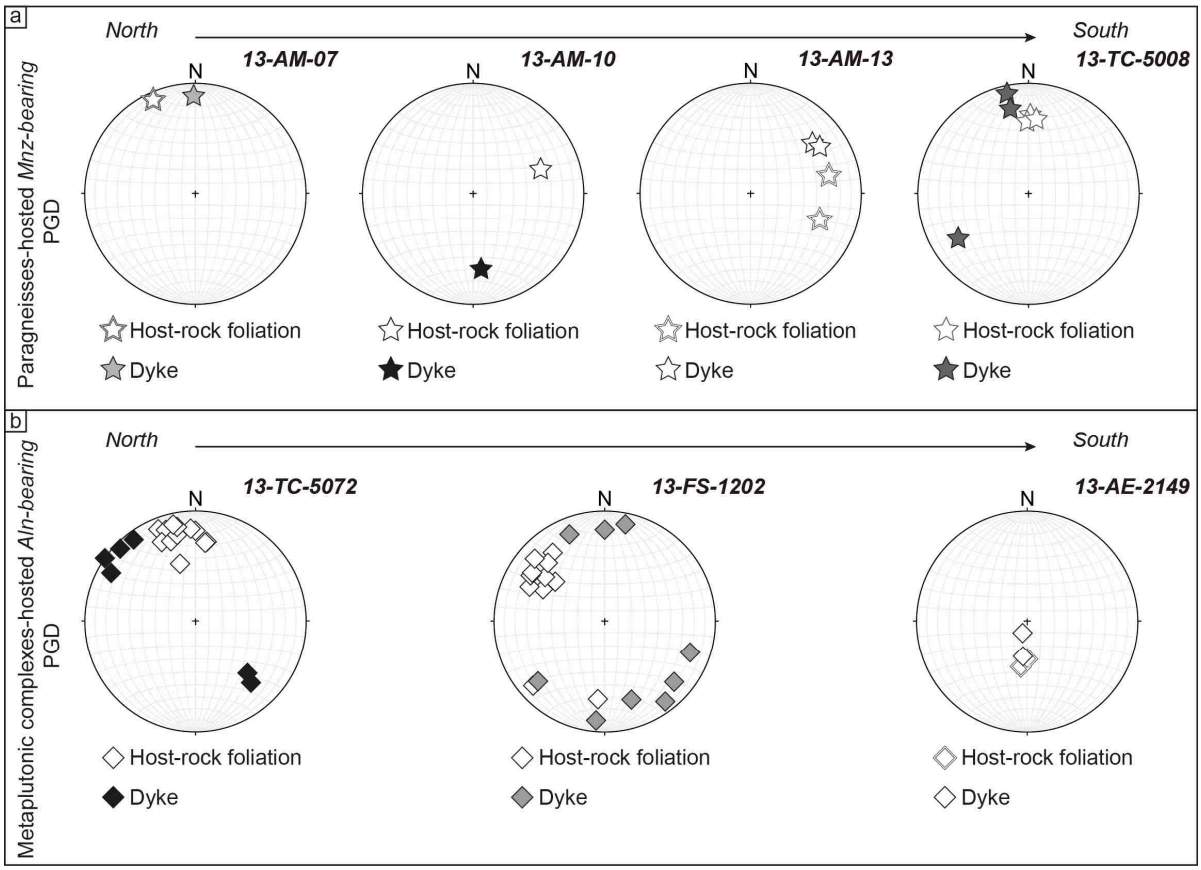

Figure 1-5: Structural measurements of the investigated pegmatitic granite dykes from the Lac Okaopéo region and of the foliation of their host rocks. a: structural measurements from the outcrops of paragneisses-hosted monazite-bearing pegmatitic granite dykes; b: structural measurements from the outcrops of metaplutonic complexes-hosted allanite-bearing pegmatitic granite dykes. Stars and diamonds represent monazite-bearing and allanite-bearing pegmatitic granite outcrops respectively. Note that a larger number of measurements are reported for outcrops of metaplutonic complexes-hosted pegmatitic granite dykes on which allanite-bearing dykes are expressed as dyke swarms. In addition, the concordant/discordant veins connected to the main dyke of the 13-AE-2149 outcrop form a network of undulating veins that do not allow clear 3D observations. Therefore, these veins have not been measured. Abbreviations: Aln-bearing PGD = allanite-bearing pegmatitic granite dyke; Mnz-bearing PGD = monazite-bearing pegmatitic granite dyke.

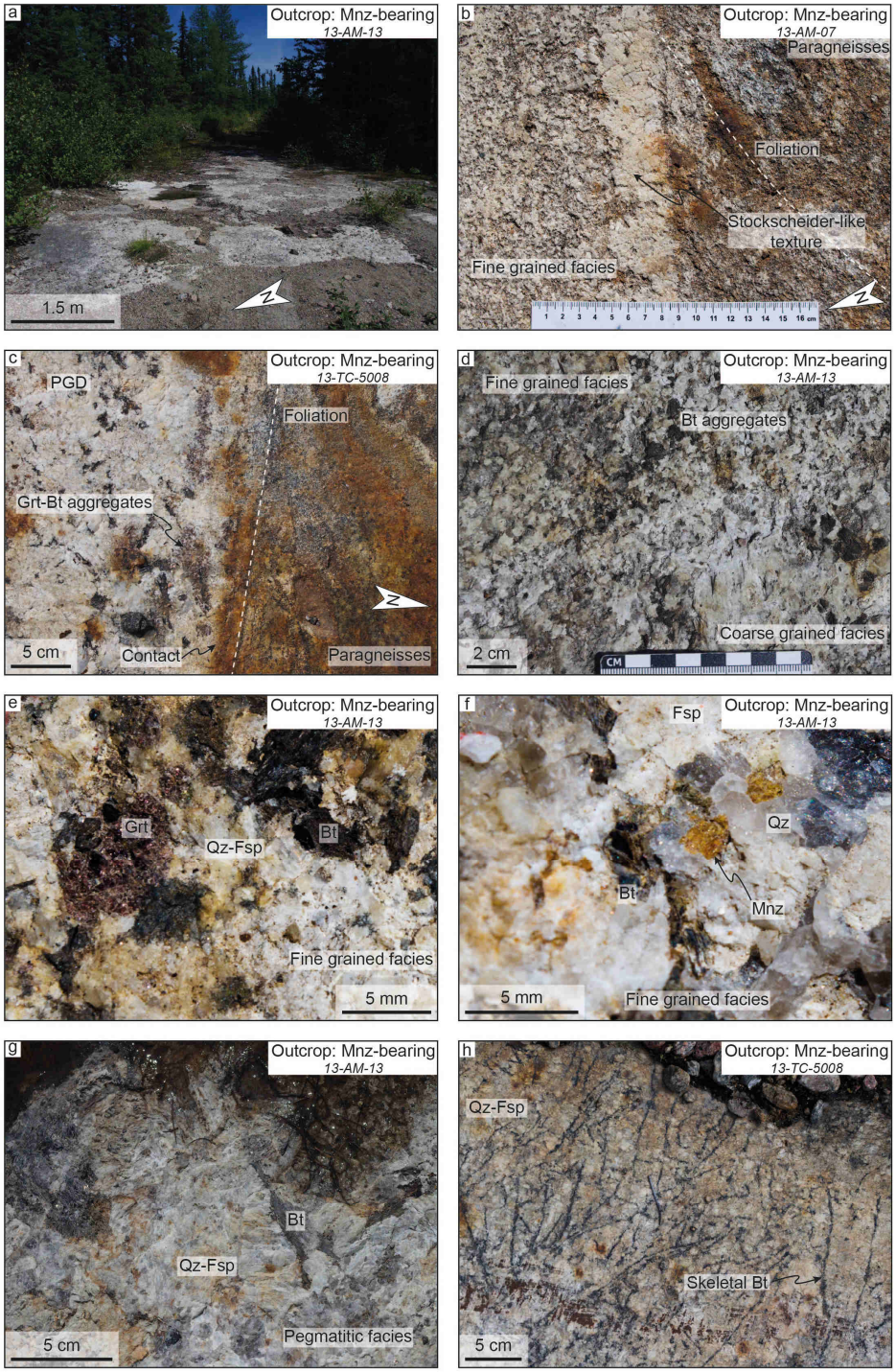

Figure 1-6: Representative photographs of the monazite-bearing pegmatitic granite outcrops from the Lac Okaopéo region (from the outcrops 13-AM-07, -13 and 13-TC-5008). a: general view of the 13-AM-13 outcrop composed of a pegmatitic granite intruding paragneisses from the Plus-Value Complex; b: detailed view of Stockscheider-like contact between the 13-AM-07 pegmatitic granite dyke and the intruded paragneisses marked by the crystallization of feldspar from the dyke perpendicular to the contact; c: locally diffuse contact between the 13-TC-5008 pegmatitic granite dyke and the intruded paragneisses delineated by garnet-biotite aggregates; d: typical transition between the fine and coarse grained facies of the 13-AM-13 pegmatitic granite dyke underlined by biotite aggregates. Note that the abundance of biotite in the fine grained facies on this photograph is related to the vicinity of the coarse grained facies; e: detailed view of a garnet phenocryst in the fine grained facies; f: monazite crystals from the fine grained facies; g: typical pegmatitic facies essentially composed of a quartz + feldspar + biotite assemblage in which feldspar and biotite crystals can reach over 5 cm; h: arborescent textures made by skeletal crystals of biotite reaching up to 15 cm long in the 13-TC-5008 pegmatitic granite dyke. Abbreviations: Bt = biotite; Grt = garnet; Fsp = feldspar; Mnz = monazite; Mnz-bearing = monazite-bearing pegmatitic granite; PGD = pegmatitic granite dyke; Qz = quartz.

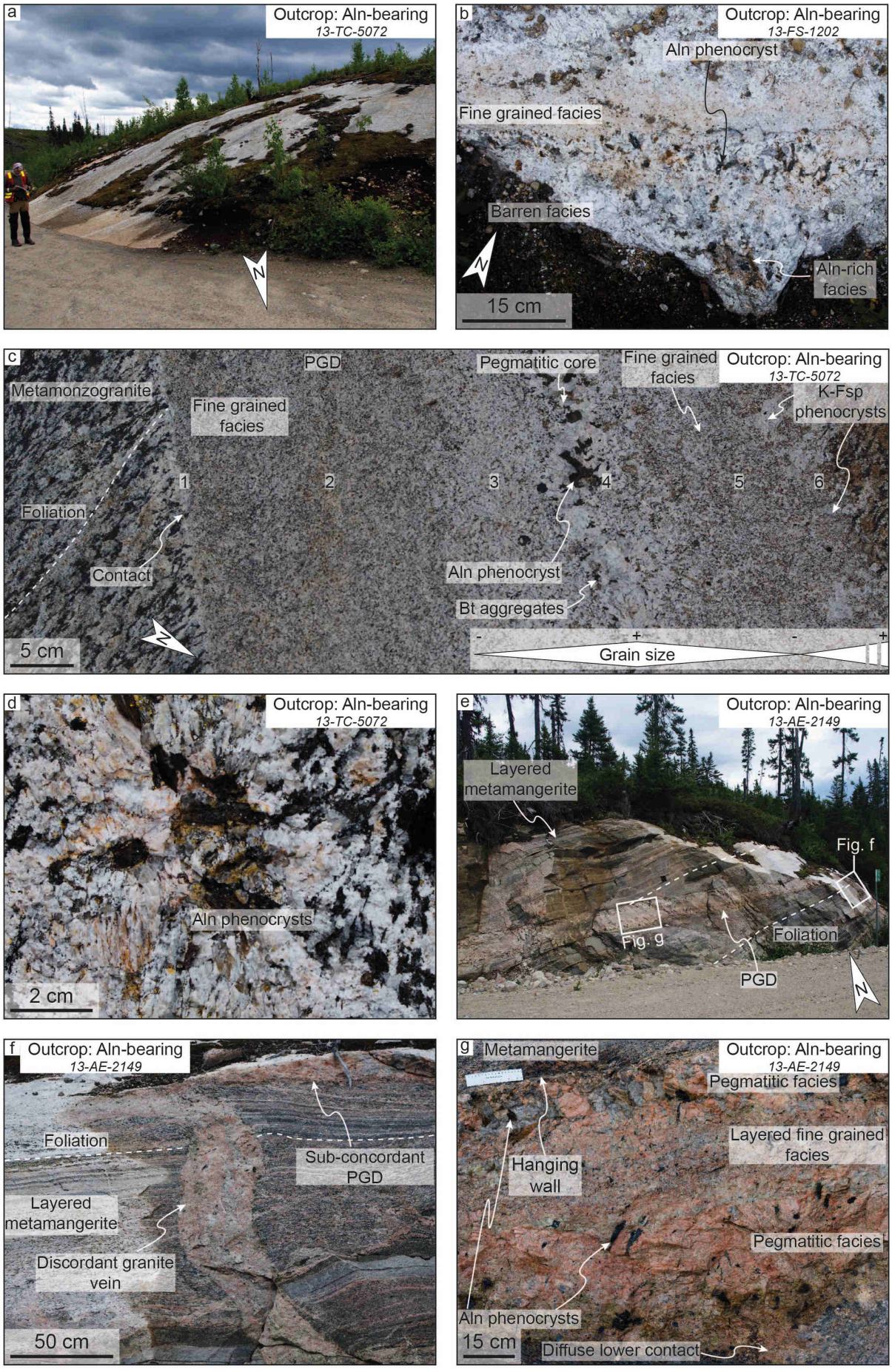
a
Outcrop: Aln-bearing
13-TC-5072
N
b
Outcrop: Aln-bearing
13-FS-1202
Aln phenocryst
Fine grained facies
Barren facies
Aln-rich facies
N
15 cm
c
PGD
Pegmatitic core
Fine grained facies
Outcrop: Aln-bearing
13-TC-5072
K-Fsp phenocrysts
Metamonzogranite
Fine grained facies
1
2
3
4
5
6
Foliation
Contact
Aln phenocryst
Bt aggregates
5 cm
N
- + - +
Grain size
d
Outcrop: Aln-bearing
13-TC-5072
Aln phenocrysts
2 cm
e
Outcrop: Aln-bearing
13-AE-2149
Layered metamangerite
Fig. f
Fig. g
Foliation
PGD
N
f
Outcrop: Aln-bearing
13-AE-2149
Foliation
Sub-concordant PGD
Layered metamangerite
Discordant granite vein
50 cm
g
Metamangerite
Outcrop: Aln-bearing
13-AE-2149
Pegmatitic facies
Layered fine grained facies
Hanging wall
Pegmatitic facies
Aln phenocrysts
15 cm
Diffuse lower contact

4.2. Allanite-bearing PGD (metaplutonic complexes-hosted)

Three of the REE occurrences associated with PGD identified by Moukhsil et al. (2014) intrude the metaplutonic complexes of the Bardoux or the Castoréum Plutonic Suite (Fig. 1-3). Detailed mapping and description for each of the allanite-bearing outcrops are provided in Appendix B and structural measurements of the dykes' walls and of the foliation of the host rocks are indicated for each outcrop in Appendix C.

Outcrops 13-TC-5072, 13-FS-1202 and 13-AE-2149 are either dome shaped (Fig. 1-7a), flat lying or large steep-dipping (Fig. 1-7e). Two of these outcrops (13-TC-5072 and 13-FS-1202) are made of decimeter- to meter-sized dyke swarms with steeply dipping to subvertical walls trending NW/SE to locally N/S or NE/SW that plunge variably towards north and south, and are slightly to strongly discordant to the foliation of their host metamonzogranite and quartz metamonzodiorite (Fig. 1-5b), respectively. The contacts of these two dykes with their host is slightly diffuse (over a few millimeters, Fig. 1-7c). One outcrop (13-AE-2149), is made of a main shallow dipping dyke oriented NE/SW that plunges towards the north, in textural continuity to granitic veins concordant/discordant to the foliation of the host metamangerite (Figs. 1-5b, 1-7e and f). This dyke is slightly discordant to locally sub-concordant to the foliation of its host rock (Fig. 1-5b) and locally show a very diffuse contact with its host rock at its lower contact (Fig. 1-7g). None of the contacts of the allanite-bearing PGD correspond to fractures crosscutting the host-rock minerals (Figs. 1-7c and g).

Figure 1-7: Representative photographs of the allanite-bearing pegmatitic granite outcrops from the Lac Okaopéo region (from the outcrops 13-TC-5072, 13-FS-1202 and 13-AE-2149). a: general view of the dome-shaped 13-TC-5072 outcrop composed of a pegmatitic granite intruding as a dyke swarm a metamonzogranite from the Bardoux Plutonic Suite; b: detailed view of the typical zoning observed in the 13-FS-1202 pegmatitic granite. Note that the allanite phenocrysts are associated with a coarse grained facies; c: typical dyke zonation of the 13-TC-5072 pegmatitic dykes, with a southeastern boundary (1) marked by a thin zone of reaction with the host rock developed over a few millimeters with almost no biotite, followed by a fine grained facies with increasing grain size and proportions of biotite (2, 3) up to a pegmatitic core (4). This core is followed by a progressive fine grained facies with a decreasing grain size zone (5). The northern contact (6) is marked by the development of K-feldspar phenocrysts perpendicular to the contact. Note that these phenocrysts are locally disconnected to the contact that contrast with a Stockscheider-like texture as represented in Fig. 1-6b, and that dyke is discordant to the foliation of the intruded metamonzogranite; d: typical allanite phenocrysts in pegmatitic granite dykes intruding the metamonzogranite; e: general view of the 13-AE-2149 outcrop composed of a pegmatitic granite dyke intruding a layered metamangerite from the Castoréum Plutonic Suite; f: detailed view of one of the pegmatitic granite vein from the 13-AE-2149 outcrop discordant to the foliation of its host rock and its connection with the main pegmatitic granite dyke expressed on this outcrop, here with a sub-concordant contact with the layered metamangerite; g: detailed view of the whole 13-AE-2149 shallow-dipping dyke zonation from its upper to its lower contact, both marked by a pegmatitic facies with large allanite crystals, through a layered fine grained facies making the core of the dyke. Abbreviations: Aln = allanite; Aln-bearing = allanite-bearing pegmatitic granite; Bt = biotite; K-Fsp = K-feldspar; PGD = pegmatitic granite dyke.

The metamonzogranite-hosted PGD (13-TC-5072) typically display a fine-grained quartz + feldspar ± biotite facies at the contact, with northern boundaries usually marked by K-feldspar phenocrysts (Fig. 1-7c), and an increasing grain size towards the allanite-rich pegmatitic core that are delineated by biotite aggregates (southern boundary for the dyke represented in Fig. 1-7c). Allanite from this outcrop may reach several centimeters (Figs. 1-7c-d). When zoned, the quartz metamonzodiorite-hosted PGD (13-FS-1202) display an internal layering marked by coarse (over 3 cm) allanite-rich and barren facies alternating with fine-grained (0.1-3 cm) allanite-rich facies (Fig. 1-7b). The metamangerite-hosted PGD (13-AE-2149) is a ca. 1 m wide dyke (Fig. 1-7e), which displays diffuse contacts with its host rock, the lower being more diffuse than the upper (Fig. 1-7g). Upper and lower contacts are marked by ca. 20 cm and ca. 45 cm wide pegmatitic facies (some grains being over 10 cm in size), respectively, composed of quartz + feldspar ± disseminated allanite phenocrysts. The latter are oriented with their long axis perpendicular to the contact (Fig. 1-7g). The core of the dyke is a layered fine-grained facies with ca. 30 cm long quartz + K-feldspar-rich lenses that alternate with quartz + plagioclase-rich lenses (Fig. 1-7g).

These PGD with allanite as the REE-hosting mineral, will further be referred as *'allanite-bearing'* (or *'Aln-bearing'*) *PGD*.

5. Detailed petrography of the monazite- and allanite-bearing PGD

5.1. Petrography of the monazite-bearing PGD (paragneisses-hosted)

All monazite-bearing PGD are dominated by a quartz + K-feldspar + plagioclase ± biotite assemblage (Fig. 1-8a), with a grain size spreading from millimeter to several centimeters (up to 5 cm in some facies). It is completed with minor garnet, zircon and monazite that are more abundant in the finest grained facies, and accessory rare pyrite and Ti-oxides. All facies show a magmatic texture and lack evidence for solid-state deformation (Fig. 1-8a).

The monazite crystals from paragneisses-hosted PGD have been investigated in two PGD (the 13-AM-13 and the 13-TC-5008, Figs. 1-8a-c, 1-9). In both cases, monazite is expressed as pristine sub-millimetric to several millimeters wide crystals that do not show any signs of corrosion/dissolution. A main difference between monazite crystals from these two samples lies in their inner textures and composition (Figs. 1-9, 1-10, Table 1-3).

Monazite grains from the 13-AM-13 PGD show oscillatory zoning with a *LREE(Ce)-rich* core surrounded by several overgrowths with a composition grading toward a *Th-Si-rich*

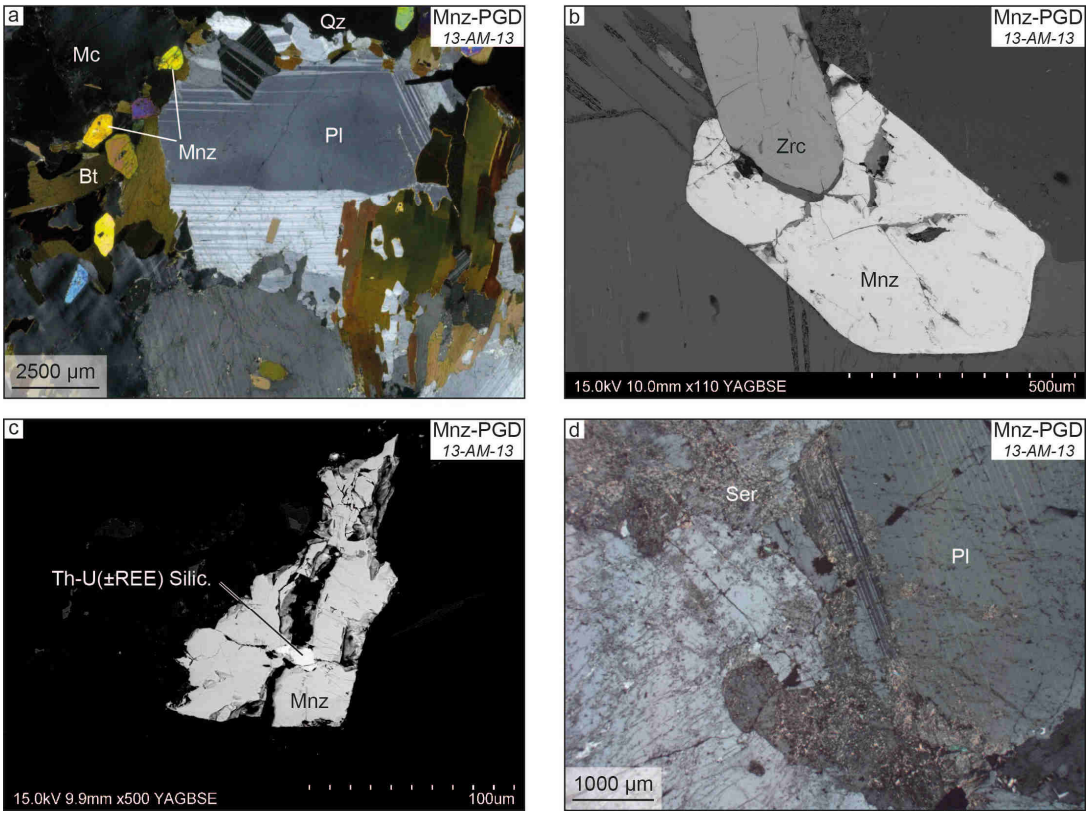

Figure 1-8: Typical petrography of monazite-bearing pegmatitic granite dykes from the Lac Okaopéo region. a: major phases composing the monazite-bearing granite (polarized and analysed light); b: syn- to late-zircon growth monazite crystal (SEM); c: late-magmatic crystallization of Th-U±REE silicates filling fractures of monazite crystals (SEM); d: late-sericite affecting plagioclase (polarized and analysed light). Abbreviations: Bt = biotite; Mc = microcline; Mnz = monazite; Mnz-PGD = monazite-bearing pegmatitic granite dyke; Pl = plagioclase; Qz = quartz; Ser = sericite; Silic. = silicates; Zrc = zircon.

pole (Figs. 1-9a-c). These zones display monazite-(Ce) compositions that shift towards monazite-(La) compositions with increasing proportion of Th and Si (Fig. 1-10a) that is consistent with the concurrent increase in huttonite end-member (from 3.78 % to 12.27 %, Fig. 1-10b, Table 1-3), where Th or U + Si = REE + P (Spear and Pyle, 2002). The proportion of brabantite (from 8.66 % to 9.62 %) remains quite stable (Fig. 1-10b, Table 1-3).

Monazite grains from the 13-TC-5008 PGD are rather homogeneous or weakly zoned as expressed in SEM and X-ray maps. Chemical zoning consists of three zones that grade from a *LREE(Ce)-rich* to a *Th-Si-rich* composition toward the grain boundaries as identified in X-ray maps (Figs. 1-9d-f, Table 1-3). The compositions of all the grains are clustered into the monazite-(Ce) field (Fig. 1-10c) as marked by the quite stable P_2O_5, and REE oxides contents (Table 1-3) from *LREE(Ce)-rich* zones to *Th-Si-rich* overgrowths. A slight increase in SiO_2 and ThO_2 is consistent with the increase in huttonite end-member (from 4.02 % to 5.39 %, Fig. 1-10d). The proportion of brabantite (from 2.77 % to 3.37 %) remains quite stable (Fig. 1-10d, Table 1-3). Plotted in a Th + U + Si vs REE + Y + P diagram, the three investigated zones cluster and spread along a narrow range of the huttonite substitution curve (Fig. 1-10d).

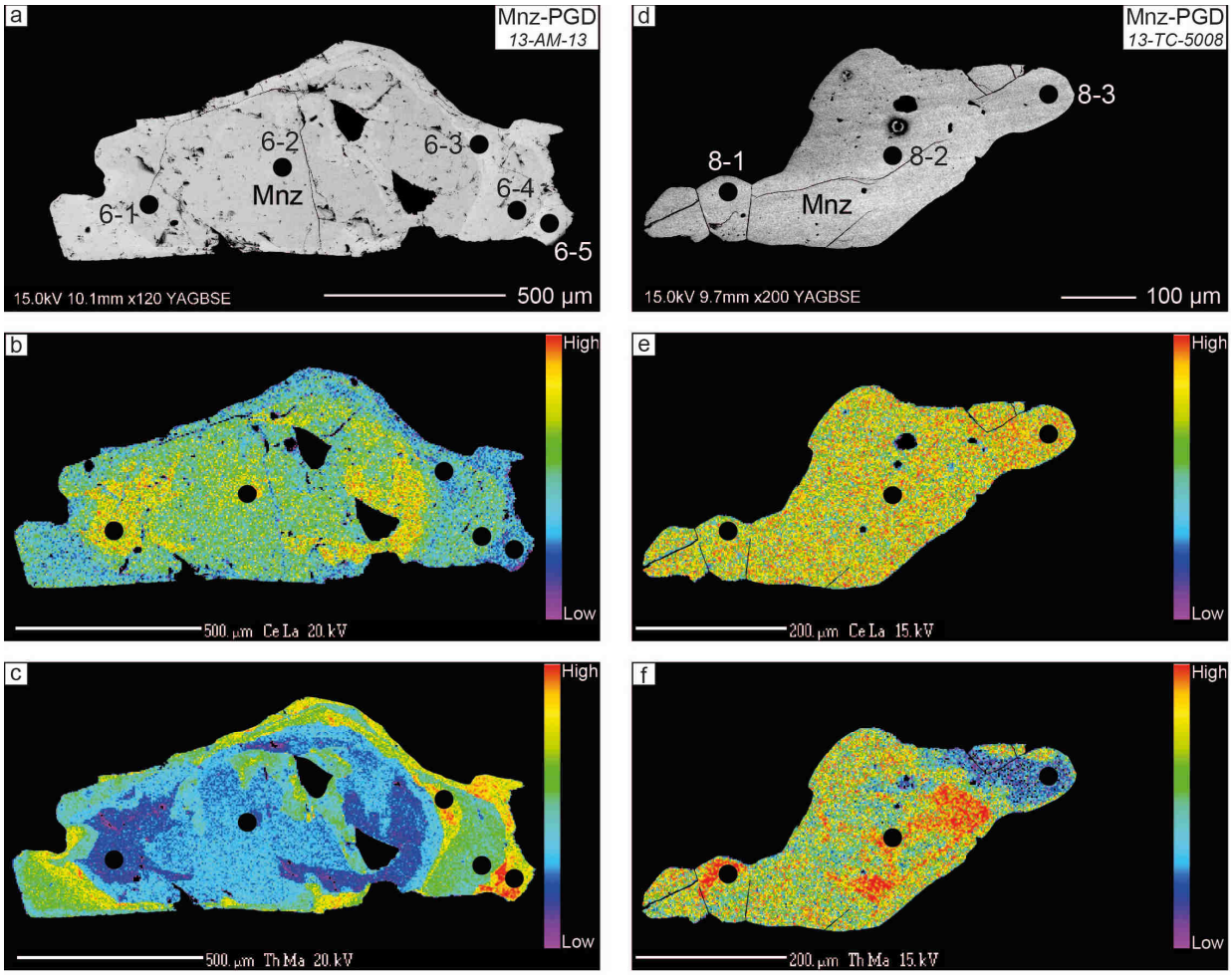

Figure 1-9: Chemical mapping of monazite grains from the 13-AM-13 and 13-TC-5008 monazite-bearing pegmatitic granite dykes from the Lac Okaopéo region. Numbers in figures a and d refer to the U-Pb dating analyses conducted using LA-ICP-MS, and reported in Table 1-5. a to c: BSE image with spot positions of LA-ICP-MS U-Pb dating and Ce and Th X-ray maps of a representative oscillatory zoned monazite grain from the 13-AM-13 monazite-bearing pegmatitic granite; d to f: BSE image with spot positions of LA-ICP-MS U-Pb dating and Ce and Th X-ray maps of a representative rather homogeneous and weakly zoned monazite grain from the 13-TC-5008 monazite-bearing pegmatitic granite. Abbreviations: Mnz = monazite Mnz-PGD = monazite-bearing pegmatitic granite dyke.

Monazite-bearing PGD also comprise sub-euhedral zircon grains (up to 1-1.5 mm, Fig. 1-8b) that may represent up to ca. 1% of the whole assemblage, mainly in fine grained to intermediate facies. Late-magmatic Th-U(±REE) silicates (Fig. 1-8c) are present as interstitial few micrometers wide bands in the vicinity of or as filling fractures of monazite crystals. Finally, sericite is expressed as an alteration product of feldspar (K-feldspar and plagioclase, Fig. 1-8d).

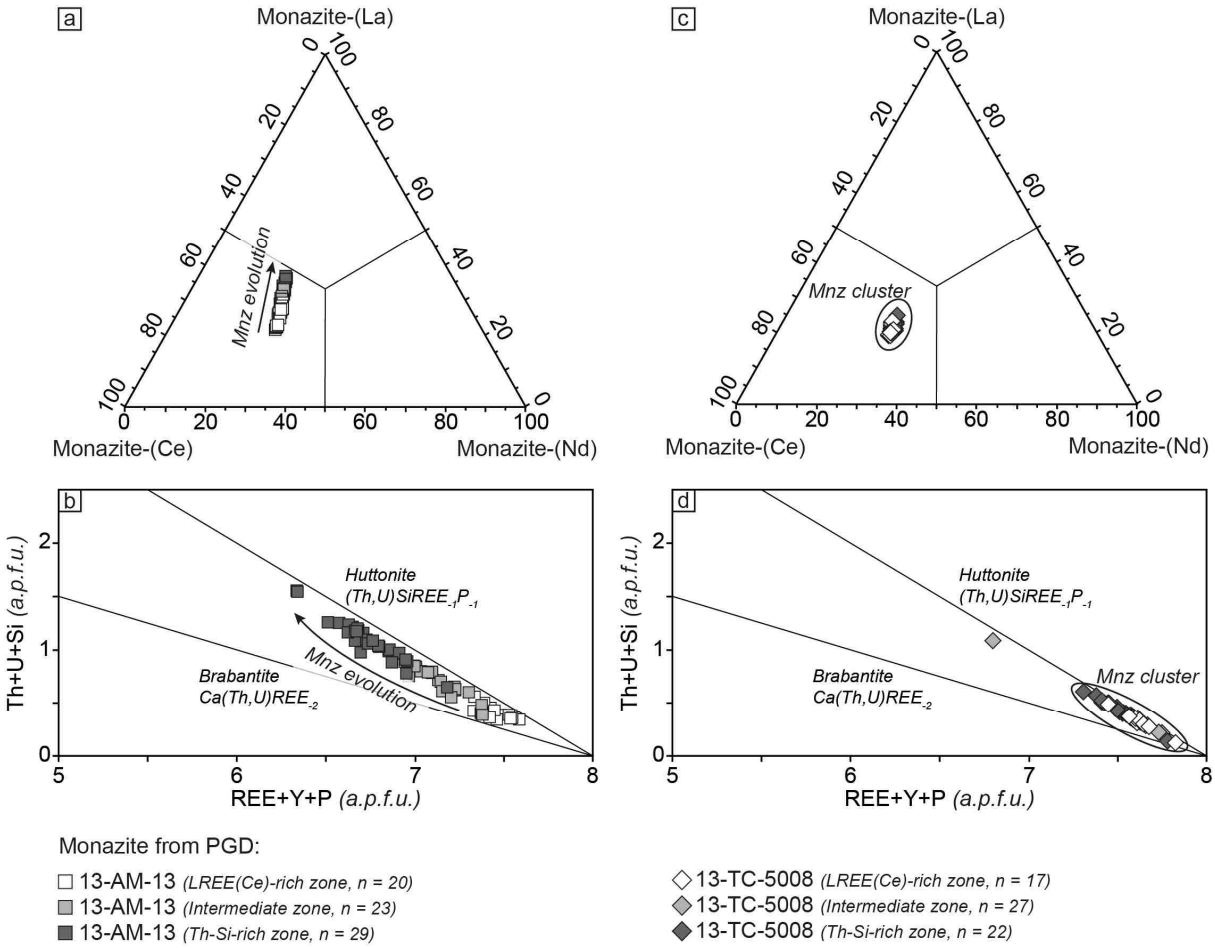

Figure 1-10: Chemical compositions of the different zones identified in monazite grains from the 13-AM-13 and 13-TC-5008 pegmatitic granite samples from the Lac Okaopéo region. a: ternary plot of the monazite compositions from the 13-AM-13 monazite-bearing pegmatitic granite. For the three identified zones, the monazite grains are dominated by monazite-(Ce) compositions, but evolve towards monazite-(La) compositions with increasing Th and Si proportion over LREE and P; b: Th + U + Si vs REE + Y + P diagram with compositional trends of huttonite and brabantite end-members for monazite grains from the 13-AM-13 pegmatitic granite. The huttonite substitution tends to be dominant with increasing Th and Si proportion over LREE and P; c: ternary plot of the monazite compositions from the 13-TC-5008 monazite-bearing pegmatitic granite. For the three identified zones, the monazite grains are clustered into the monazite-(Ce) composition field with no significant changes with increasing Th and Si proportion over LREE and P; d: Th + U + Si vs REE + Y + P diagram with compositional trends of huttonite and brabantite end-members for monazite grains from the 13-TC-5008 pegmatitic granite. Note these grains are mainly characterized by the huttonite end-member with no significant changes with increasing Th and Si proportion over LREE and P. Abbreviations: Mnz = monazite; PGD = pegmatitic granite dyke.

5.2. Petrography of the allanite-bearing PGD (metaplutonic complexes-hosted)

All allanite-bearing PGD are dominated by a quartz + K-feldspar + plagioclase ± biotite (Figs. 1-11a-c) assemblage with a grain size ranging from millimeter to several centimeters (over 10 cm in some pegmatitic facies, outcrop 13-AE-2149). This assemblage is completed with zircon and allanite, and rare apatite (some grains are present in the pegmatitic facies of the 13-AE-2149 outcrop). The abundance of accessory minerals is not correlated with the grain size. All facies display a magmatic texture and lack evidence for solid-state deformation (Figs. 1-11a-c).

The textural characteristics of allanite from metaplutonic complexes-hosted PGD depend on the host pegmatitic granite. Allanite crystals were investigated in the 13-TC-5072 and the 13-FS-1202 samples and in both cases are sub-euhedral and sub-millimetric to several millimeters wide (Figs. 1-6b-d, g, 1-11b-c).

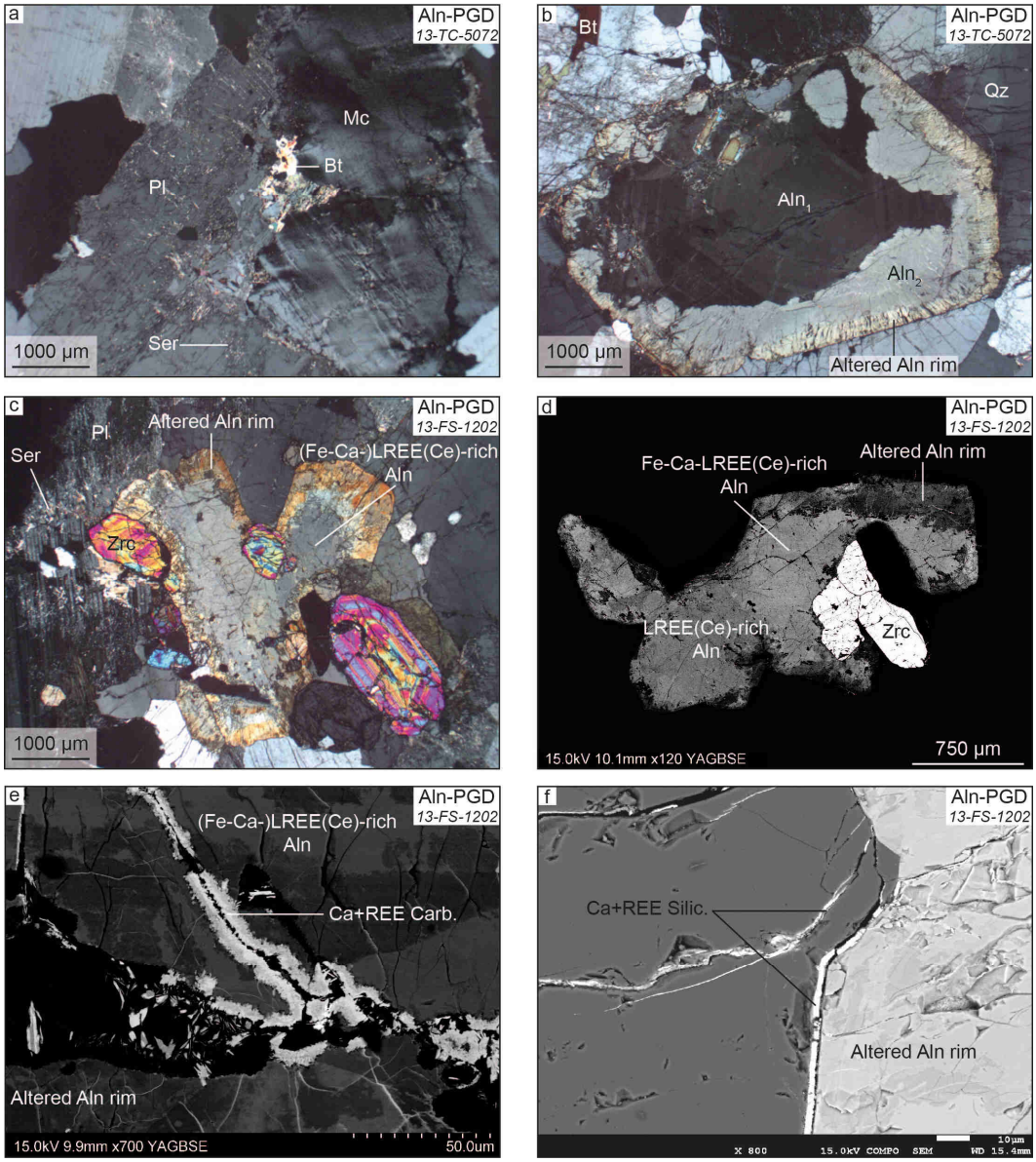

Figure 1-11: Typical petrography of allanite-bearing pegmatitic granite dykes from the Lac Okaopéo region. a: major phases composing the allanite-bearing granite dykes (polarized and analysed light); b: allanite crystal displaying an Aln_1 oscillatory zoned core corroded by an Aln_2 overgrowth of similar composition (Table 1-4) and altered by a rim associated with fluids circulation probably related to the magmatic-hydrothermal transition (polarized and analysed light); c: allanite grains display rims probably associated with the late-sericitization of feldspar. Note the syn- to late-zircon growth crystallization of the allanite phenocrysts (polarized and analysed light); d: typical millimetric allanite phenocryst from the 13-FS-1202 pegmatitic granite showing LREE-rich and Fe-Ca-LREE(Ce)-rich zones (Table 1-4) surrounded by an alteration rim probably associated with fluids circulation probably related to the magmatic-hydrothermal transition; e: veinlets of Ca + REE carbonates on the boundary or filling fractures of allanite crystals most probably associated with fluids circulation at the magmatic-hydrothermal transition (SEM); f: veinlets of Ca + REE silicates on the boundary or filling fractures of allanite crystals most probably associated with fluids circulation at the magmatic-hydrothermal transition (SEM). Abbreviations: Aln = allanite; Aln-PGD = allanite-bearing pegmatitic granite dyke; Bt = biotite; Carb. = carbonates; Mc = microcline; Pl = plagioclase; Qz = quartz; Ser = sericite; Silic. = silicates; Zrc = zircon.

Allanite grains from the 13-TC-5072 PGD show an oscillatory zoned core, further designated as '*Aln$_1$*', corroded and crosscut by an overgrowth of a second generation of intermediate composition allanite, further designated as '*Aln$_2$*' (Fig. 1-11b), that forms the sub-euhedral shape of allanite phenocrysts. It is surrounded by an alteration rim (Fig. 1-11b). These three zones cluster as typical allanite compositions plotted in the REE vs Al diagram (Fig. 1-12a) of Petrík et al. (1995) and display quite similar compositions, except for the decrease in FeO (from 11.11 to 9.76 wt.%) content from the *Aln$_1$* cores to the alteration rims (Table 1-4).

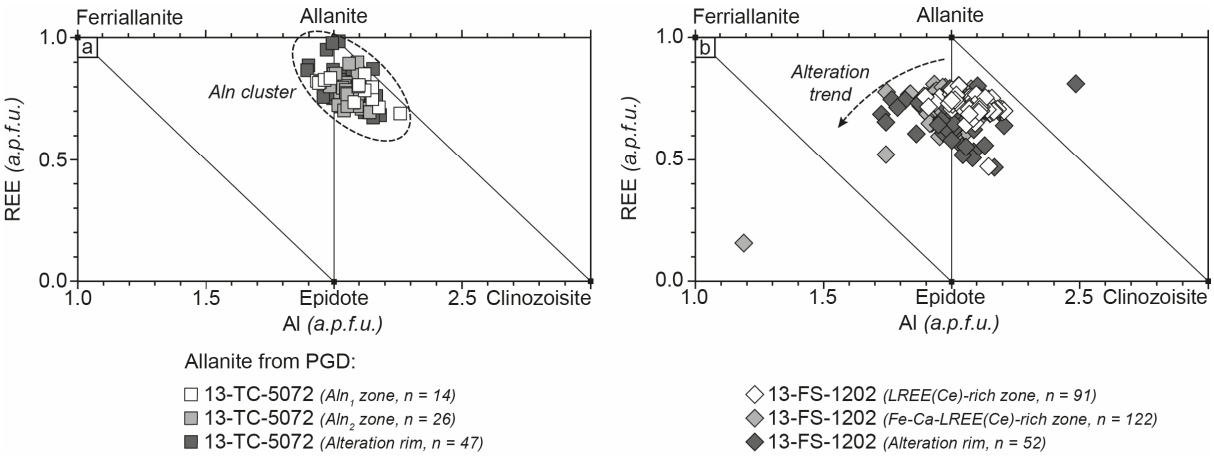

Figure 1-12: Chemical compositions of the different zones identified in allanite grains from the 13-TC-5072 and 13-FS-1202 pegmatitic granite samples from the Lac Okaopéo region. a: REE vs Al composition of allanite grains from the 13-TC-5072 allanite-bearing pegmatitic granite obtained using EMP (Petrík et al., 1995). Note the clustering of compositions of the different zones close to the allanite pole; b: REE vs Al composition of allanite grains from the 13-FS-1202 allanite-bearing pegmatitic granite obtained using EMP (Petrík et al., 1995). Note the alteration trend that lead to more 'epidote like' compositions. Abbreviations: Aln = allanite; PGD = pegmatitic granite dyke.

Allanite grains from the 13-FS-1202 PGD display internal patchy zoning between '*LREE(Ce)-rich*' and '*Fe-Ca-LREE(Ce)-rich*' zones (Fig. 1-11d). They are surrounded by an alteration rim (Figs. 1-11c-f). The three zones plot between the epidote and allanite composition in the REE vs Al diagram (Fig. 1-12b) of Petrík et al. (1995). The *Fe-Ca-LREE(Ce)-rich* zone displays the most allanite-like composition, whereas the alteration rim is marked by a shift towards the epidote composition (Fig. 1-12b) associated with an increase in SiO_2 and a decrease in LREE (Table 1-4).

Allanite-bearing PGD also contain sub-euhedral zircon grains (up to 1-1.5 mm, Figs. 1-11c and d) that may represent up to ca. 1% of the whole assemblage, mainly in fine to coarse grained facies. Late-magmatic Ca±REE carbonates or silicates are present as interstitial thin bands (a few micrometers wide) in the vicinity of or in fracture of allanite crystals (Figs. 1-11e-f). Finally, sericite is expressed as an alteration product of feldspar (K-feldspar and plagioclase, Figs. 1-11a and c).

6. Whole-rock geochemistry of the monazite- and allanite-bearing PGD

6.1. Geochemistry of the monazite-bearing PGD (paragneisses-hosted)

Three of the four monazite-bearing PGD (samples 13-AM-07, 13-AM-10 and 13-TC-5008) display typical granitic composition with a SiO_2 content of 71.03 wt.%, 70.80 wt.% and 70.79 wt.% respectively (Table 1-2), and a strong peraluminous character (Fig. 1-13a) as marked by their (i) ASI (Aluminum Saturation Index, ASI = Al/(Ca – 1.67 x P + Na + K) Frost et al., 2001; Shand, 1943), (ii) A/CNK (A/CNK = Al/(Na + K + Ca/2), Shand, 1943), and (iii) A/NK (A/NK = Al/(Na + K), Shand, 1943) above 1.19, 1.27 and 1.55 respectively (Table 1-2). In contrast, one monazite-bearing PGD (13-AM-13) does not display a typical granitic composition as its SiO_2 content is down to 60.24 wt.% (Table 1-2). This low content is associated with the highest Al_2O_3, CaO and Na_2O contents of 18.58 wt.%, 3.10 wt.% and 4.02 wt.% respectively, and a low K_2O content of 4.36 wt.% leading to the highest ASI ratio of the monazite-bearing serie at 1.36 (Table 1-2) that corresponds to a strongly peraluminous signature (Fig. 1-13a).

All the monazite-bearing samples display high ΣREE content ranging from 1418 to 7048 ppm (Table 1-2). Their REE patterns are strongly fractionated in LREE over HREE (Fig. 1-13b), as evidenced by the La_N/Yb_N ratios ranging from 784 to 938 (Table 1-2), and more or less developed Eu negative anomaly (Fig. 1-13b), which intensity increases with the ΣREE content, as marked by decreasing Eu/Eu* from 0.72 down to 0.14 (Table 1-2). The ΣREE content is also associated with (i) increasing U and Th contents (up to 19.10 and 1300 ppm respectively, Fig. 1-13c, Table 1-2) and Nb/Ta ratio (up to 56 with Nb ranging from 5.60 to 21 ppm and Ta ranging from 0.10 to 0.40 ppm, Fig. 1-13e, Table 1-2), (ii) increasing Na_2O, CaO and P_2O_5 contents (up to 4.02, 3.10, 0.40 wt.% respectively, Figs. 1-13d and f, Table 1-2), and (iii) decreasing K_2O content (down to 4.36 wt.%, Fig. 1-13d, Table 1-2). The ΣREE content of monazite-bearing PGD is not linked to the $Fe_2O_{3\,(total)}$ nor MgO contents (Fig. 1-13g, Table 1-2). The Zr/Hf ratios are quite stable (ranging from 36 to 44, Fig. 1-13e, Table 1-2) with Zr ranging from 195 to 1480 ppm and Hf ranging from 4.40 to 41.50 ppm (Table 1-2).

6.2. Geochemistry of the allanite-bearing PGD (metaplutonic complexes-hosted)

Two of the three allanite-bearing PGD (samples 13-TC-5072 and 13-FS-1202) have typical granitic composition with a SiO_2 content of 70.27 wt.% and 70.85 wt.% respectively (Table 1-2), and a strong peraluminous character (Fig. 1-13a) as marked by their ASI, A/CNK,

and A/NK over 1.18, 1.24 and 1.64 respectively (Table 1-2). In contrast, one of the PGD (sample 13-AE-2149) does not display a typical granitic composition as its SiO_2 content is down to 55.84 wt.% (Table 1-2). This low content is associated with the highest Al_2O_3, CaO, Na_2O contents of 15.05 wt.%, 5.54 wt.%, 4.28 wt.% respectively, and a low K_2O content of 1.93 wt.%, leading to the lowest ASI and A/CNK ratio of the allanite-bearing serie at 1.08 and 0.87 (Table 1-2) that corresponds to a weakly peraluminous signature (Fig. 1-13a).

All the allanite-bearing samples display high ΣREE content ranging from 2393 to 9242 ppm (Table 1-2). The REE patterns of the 13-TC-5072 and 13-FS-1202 samples are strongly fractionated in LREE over HREE (Fig. 1-13b), as evidenced by the La_N/Yb_N ratios ranging from 261 to 619 (Table 1-2). The REE pattern of the low-SiO_2 PGD (13-AE-2149 sample) is more enriched in HREE and displays a less fractionated pattern, as marked by its lower La_N/Yb_N ratio of 28 (Table 1-2). The intensity of the negative Eu anomaly increases with the ΣREE content as shown by decreasing Eu/Eu* from 0.36 down to 0.12 (Table 1-2). The ΣREE content is also associated with (i) increasing U and Th contents (up to 30.30 and 766 ppm respectively, Fig. 1-13c, Table 1-2), (ii) increasing Na_2O, CaO, $Fe_2O_{3\ (total)}$ and MgO contents (up to 4.28, 5.54, 12.42 and 0.85 wt.% respectively, Figs. 1-13d and g, Table 1-2), and (iii) decreasing K_2O content (down to 1.33 wt.%, Fig. 1-13d, Table 1-2) and Nb/Ta ratio (down to 41 with Nb ranging from 7.50 to 132 ppm and Ta ranging 0.11 to 3.20 ppm, Fig. 1-13e, Table 1-2). The ΣREE content of allanite-bearing granite dykes is not linked to the P_2O_5 content (Fig. 1-13f, Table 1-2), nor to the Zr/Hf ratios that remain quite stable (ranging from 35 to 39, Fig. 1-13e, Table 1-2) with Zr ranging from 290 to 6340 ppm and Hf ranging from 7.40 to 171 ppm (Fig. 1-13e, Table 1-2).

7. U-Pb dating of magmatic monazite

Monazite grains from the paragneiss-hosted 13-AM-13 PGD have been investigated through 25 analyses performed directly on thin sections on 7 different grains. Plotted on a concordia diagram, data define a discordia yielding an upper intercept of 1003.9±4.7 Ma (MSWD = 0.43) if the lower intercept is anchored to 0±0 Ma (Fig. 1-14a, Table 1-5). Eleven of these 25 analyses are concordant and define a concordia age (as of Ludwig, 1998) of 996.7±5.3 Ma (MSWD = 0.98, Fig. 1-14b). Even though the monazite grains from this sample are zoned (Figs. 1-9a-c, 1-10a-b), these data do not show any signs of inherited cores with distinctly older ages nor isotopic heterogeneity within a grain as all the data spread on the same discordia and point to a single upper intercept date (Fig. 1-14a).

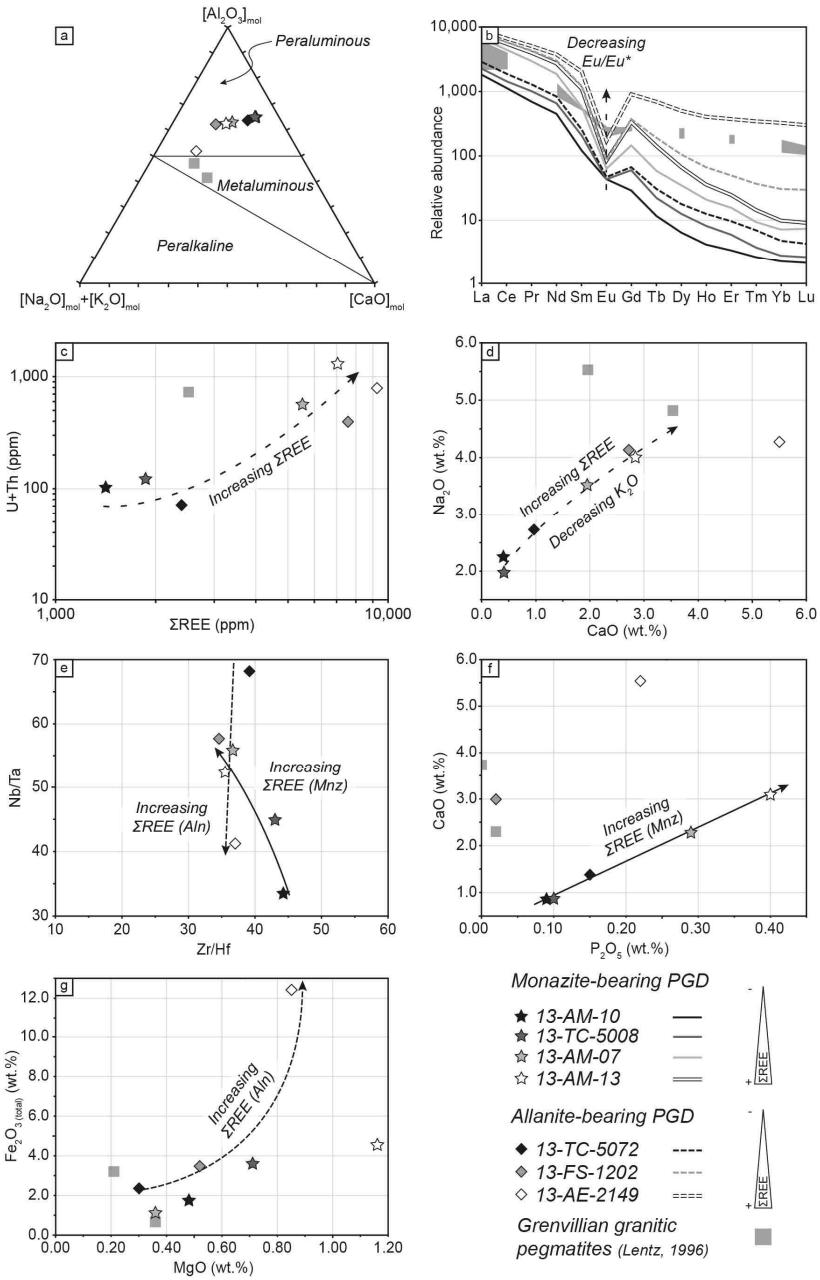

Figure 1-13: Whole rock geochemistry of the REE-richest facies of the investigated pegmatitic granite dykes from the Lac Okaopéo region, compared to data of REE-rich granitic pegmatites samples from Lentz (1996). a: peraluminous, metaluminous and peralkaline fields showing the peraluminous character of the pegmatitic granite samples; b: chondrite normalized REE patterns of the pegmatitic granite samples. Note that six of them display a similar tendency of strong fractionation of LREE over HREE that contrast with the lower fractionation of the 13-AE-2149 dyke. The ΣREE increases with decreasing Eu/Eu* (normalization after McDonough and Sun, 1995); c: U + Th (ppm) vs ΣREE (ppm) diagram showing the close relationship between an increase in REE and an increase in U and Th for all the investigated pegmatitic granite samples; d: Na2O (wt.%) vs CaO (wt.%) diagram that evidence a coeval increase of Na2O, CaO and the REE associated with a decrease in K2O for all the investigated pegmatitic granite samples; e: Nb/Ta vs Zr/Hf diagram showing a contradictory behavior of Nb and Ta between the monazite-bearing and the allanite-bearing samples, as Nb/Ta increases with the ΣREE in the former and decreases with the ΣREE in the latter. Note that the Zr/Hf ratio remain quite stable for both series; f: CaO (wt.%) vs P2O5 (wt.%) diagram showing that the formation of monazite (Mnz-bearing pegmatitic granite samples) is associated with increasing CaO and P2O5 contents. Note that the Aln-bearing pegmatitic granite samples do not display a similar trend; g: Fe2O3 (total) (wt.%) vs MgO (wt.%) diagram showing that the formation of allanite (Aln-bearing pegmatitic granite samples) is associated with increasing Fe2O3 and MgO contents. Note that the Mnz-bearing pegmatitic granite samples do not display a similar trend. Abbreviations: Aln = allanite; Mnz = monazite; PGD = pegmatitic granite dyke.

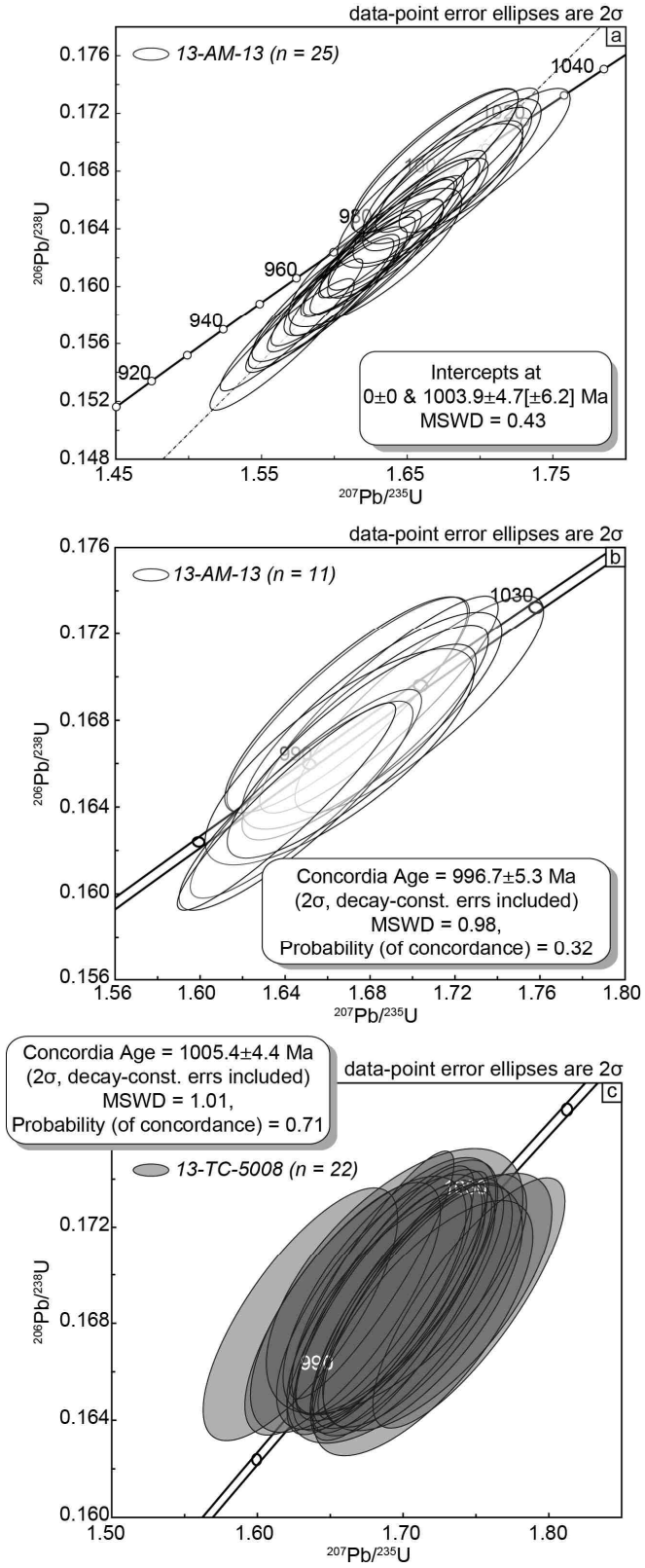

Figure 1-14: U-Pb ages of monazite grains from the 13-AM-13 and 13-TC-5008 pegmatitic granite dykes from the Lac Okaopéo region. a: Concordia plots for the monazite grains from the 13-AM-13 pegmatitic granite (n = 25, data-point error ellipses are 2σ); b: Concordia plots for the over 98% of concordance analyses from the 13-AM-13 pegmatitic granite (n = 11, data-point error ellipses are 2σ); c: Concordia plots for the monazite grains from the 13-TC-5008 granite (n = 22, data-point error ellipses are 2σ).

The monazite grains from the paragneisses-hosted 13-TC-5008 PGD have been investigated through 22 analyses performed on 9 different grains. Plotted on a concordia diagram, data plot on the concordia curve, and yield a concordia age of 1005.4±4.4 Ma (MSWD = 1.01; Fig. 1-14c, Table 1-5). As for the 13-AM-13 PGD, these data do not point to the presence of inherited cores with an older age nor heterogeneity within a grain as all the data plot on the concordia curve (Fig. 1-14c). This is consistent with the lack of chemical zoning on the studied monazite grains (Figs. 1-9d-f, 1-10c-d).

8. Discussion

8.1. LREE-rich PGD from the Lac Okapéo region in the frame of the Grenvillian Orogeny

The Grenville Province hosts numerous granitic pegmatites (e.g. Ayres and Černý, 1982; Černý, 1990; Ercit, 2005; Ford, 1982; Fowler and Doig, 1983; Lentz, 1996, 1991; Lumbers, 1979; Masson and Gordon, 1981), mainly in the Central Gneiss Belt, in the Central Metasedimentary Belt, in the Central Granulite Terrain and in the Eastern Grenville (Fig. 1-1b). They are discordant and intrusive in brittle zones within competent units, show magmatic and undeformed texture, and geochronological constraints evidence for their late-Grenvillian Orogeny timing of emplacement (Ford, 1982; Fowler and Doig, 1983; Lentz, 1996, 1991, Lumbers, 1979, 1964). These granitic pegmatites are assumed to be either derived (i) from partial melting of paragneiss and/or orthogneiss, consistent with the presence of migmatites and the lack of coeval intrusive granitic plutons (e.g. Ayres and Černý, 1982; Lentz, 1996, 1991; Lumbers, 1964; Masson and Gordon, 1981), or (ii) from the differentiation of a melt segregated from a granite at the end of fractional crystallization (Ayres and Černý, 1982; Masson and Gordon, 1981).

The main features of the LREE-rich PGD from the Lac Okaopéo region obtained in this study have been summarized in Table 1-6. They are discordant to the foliation of their host rocks and present magmatic textures with no macroscopic nor microscopic evidence for solid-state deformation (Figs. 1-5 to 1-7, 1-8a, d, 1-11a-c). All of these PGD, to the noticeable exception of one (13-AE-2149 PGD), are steep-dipping dykes with limited diffuse contacts and no interconnection with leucosome (Figs. 1-5 to 1-7) suggesting they are intrusive into the Paleoproterozoic to Mesoproterozoic Plus-Value paragneisses and Bardoux and Castoréum metaplutonic suites, in a late- to post-tectonic regime, as other REE-rich Grenvillian granitic pegmatites (Ercit, 2005; Lentz, 1996, 1991).

The 13-AE-2149 PGD is a shallow-dipping dyke connected to a network of concordant/discordant veins to the foliation of its host layered mangerite (Figs. 1-5b, 1-7e-f) suggesting a distinct and shallower source, and/or a different stress regime. The diffuse contact at its lower contact (Fig. 1-7g) emphasizes a different petrogenetic process which might have involved syn-crystallization fluid expulsion.

Formation of an orogenic plateau between ca. 1080 and 1050 Ma has been proposed to be related to ductile lateral flow of the orogenic root beneath the ABT at the base of the Orogenic Lid (Fig. 1-1b, Rivers, 2008). Late-Ottawan gravitational collapse is inferred to have started in the central Grenville Province by ca. 1065 Ma (Rivers and Schwerdtner, 2015; Soucy La Roche et al., 2015) and to have been completed by ca. 1020 Ma in the western part of the Grenville Province, as evidenced by the reworking of the ABT as an extensional shear zone (Ketchum et al., 1998; Rivers, 2008; Rivers et al., 2012). In the central Grenville, normal shear-sense indicators in a 1015 Ma granite (Indares et al., 2000) in the MIZ and the intrusion of mafic to intermediate magmatic rocks, such as the ca. 1015 Ma Okaopéo Plutonic Suite (Fig. 1-3) that crosscuts the Ottawan metamorphic fabrics, have been attributed to a phase of crustal extension compatible with this model (e.g. Augland et al., 2015; Indares et al., 2000). Following the poor tectonic record from ca. 1020 to 1005-1000 Ma, the Rigolet orogenic phase at ca. 1005-980 Ma, marked by the deformation and metamorphism of the Parautochthonous Belt structurally below the ABT, is interpreted to represent a short-lived crustal thickening event (e.g. Dunning and Indares, 2010; Jordan et al., 2006; Lasalle et al., 2013). U-Pb dating on magmatic monazite grains from two PGD of the Lac Okaopéo region yield dates of 996.7±5.3 Ma (13-AM-13 PGD, Figs. 1-14a-b, Table 1-5) and 1005.4±4.4 Ma (13-TC-5008 PGD, Fig. 1-14c, Table 1-5) (see section 7 for details) that are comparable within uncertainty. According to the lack of corrosion of the monazite grains, their oscillatory zoning with no recrystallized domains or their unzoned character, these ca. 1005-1000 Ma concordant dates are interpreted as reflecting their igneous crystallization ages (Crowley et al., 2008) and are therefore attributed to post-Ottawan peak of metamorphism corresponding to the initiation of the Rigolet orogenic phase. These emplacement ages are consistent (i) with the discordant contacts of the dykes to the foliation of their hosts (Figs. 1-5, 1-6b, 1-7c, e-f) and (ii) with the magmatic textures with no evidence for a solid-state deformation nor interconnection with leucosomes (Figs. 1-6, 1-7, 1-8a, d, 1-11a-c). These features suggest a post-tectonic and metamorphic intrusion of the PGD relative to the paragneisses and the metaplutonic complexes of the Allochthonous Belt they intrude and which were affected by the Ottawan orogenic phase (Augland et al., 2015; Moukhsil et al., 2014). This

timing of emplacement is similar to the late- to post-Grenvillian Orogeny age of pegmatitic bodies in the western Grenville Province (Fowler and Doig, 1983; Lentz, 1996, 1991, Lumbers, 1979, 1964).

8.2. Potential sources of the LREE-rich PGD from the Lac Okaopéo region

In granitic pegmatite fields reported in the literature, e.g. in Cap de Creus (northeastern Spain, Alfonso and Melgarejo, 2008; Druguet et al., 2014; Van Lichtervelde et al., 2016) or in Gatumba (central Rwanda, Hulsbosch et al., 2014; Melcher et al., 2015), the closest bodies from the sources (usually a granite) (i) are the least evolved, and (ii) contain biotite but no muscovite nor rare-element minerals (i.e. Li, B, Be, Rb, Sn, Nb-Ta… e.g. Hulsbosch et al., 2014; London, 2016, 2008) or REE mineralization (e.g. Ercit, 2005). In the case of the PGD from the Lac Okaopéo region, the ubiquitous presence of biotite in all the investigated dykes with no muscovite nor other rare elements minerals than monazite or allanite and zircon suggests that they do not represent the last melts that differentiated from the source.

The intrusive contacts of the PGD (Figs. 1-5, 1-6b, 1-7c) and the lack of textural continuity between the PGD and the leucosomes of the host rocks (except for the 13-AE-2149 dyke), are pointing to an origin from a deeper-seated source. This interpretation is corroborated by their emplacement age during the early Rigolet orogenic phase (ca. 1.0 Ga) in host rocks that have recorded deformation and metamorphism during the Ottawan orogenic phase. Furthermore, their pronounced peraluminous signatures (Fig. 1-13a) are not compatible with a magma derived from the fractionation of the late-Ottawan mafic to intermediate Plutonic Suites of the Lac Okaopéo region, nor of the undated metaluminous volcanic arc granite Céline Plutonic Suite (Augland et al., 2015; Moukhsil et al., 2014, 2013a, 2009).

Jannin et al. (in press) documented that partial melting at a lower structural level than our study area was initiated at least from ca. 1002 Ma at high-pressure in the presence of garnet with pegmatite emplacement taking place between 993 down to possibly 961 Ma. These results confirm that the Parautochthonous Belt experienced the Rigolet crustal thickening phase under granulite facies metamorphism (up to ca. 15 kbar and 850°C between ca. 1005 and 980 Ma, Jordan et al., 2006), i.e. conditions that are favorable for the partial melting of the Parautochthonous Belt and coeval with the emplacement of the PGD. Nb/Ta ratios of the PGD from the Lac Okaopéo region are very high (ranging from 34 to 68, Fig. 1-13e, Table 1-2) and are associated with low (except for the 13-AE-2149 dyke) Nb and Ta contents (up to 21 and 0.40 respectively, Table 1-2). Such low values are consistent with the lack of Nb-Ta-bearing

minerals in the PGD, and associated with high Nb/Ta are consistent with high-temperature partial melting resulting in a total consumption of biotite from the protolith and the formation of Ti-oxides in the residue that are preferential hosts for Nb and Ta and preferentially fractionate the latter (Stepanov et al., 2014). Phase equilibria modeling of metapelite such as those of the Knob Lake Group indicates that a common partial-melting reaction in high-pressure granulite is Bt + Pl ± Ky = Liq + Grt + Kfs + Qtz + Rt (Gervais and Crowley, 2017). In addition to producing leucosome with zircon depleted in HREE because of their sequestration in garnet, such as those in leucosome of the Parautochthonous Belt (Jannin et al., In press), the growth of peritectic rutile associated with this reaction should produce melt with the Nb-Ta features observed in the investigated PGD.

The strongly peraluminous character of these PGD (Fig. 1-13a, Table 1-2) contrasts with the metaluminous signature of the western Grenvillian REE-rich granitic pegmatites reported by Lentz (1996) (Fig. 1-13a, Table 1-2) and is compatible with their derivation by partial melting of a metasedimentary unit (e.g. Chappell and White, 2001; Cuney, 2014; White and Chappell, 1977). The high La_N/Yb_N ranging from 784 to 938 (monazite-bearing PGD) and from 261 to 619 (13-TC-5072 and 13-FS-1202 allanite-bearing PGD) suggest that these dykes represent melts segregated from a molten crustal component enriched in a HREE-bearing phase, most probably garnet as it is very common in paragneisses especially in those from the Knob Lake Group of the Gagnon Terrane (Bea, 1996; Hönig et al., 2014; Jordan et al., 2006). These features are consistent with the lack of evidence for coeval kilometric scale granitic intrusive body at this stage of the Grenvillian Orogeny and with the results of the great majority of studies dealing with Grenvillian REE-rich granitic pegmatites (e.g. Ercit, 2005; Lentz, 1996, 1991). In addition, it brings evidence that REE-rich granitic pegmatites do not necessarily derive from the fractionation of a granitic intrusive body and that they may be metamorphic in origin as it is proposed by default, especially in the Grenville Province, because of the lack of an exposed coeval granitic intrusive body (Ercit, 2005). Even though the timing of emplacement and field relationships of the dykes are in favor of a source belonging to the Parautochthonous Belt, whether the molten paragneisses that led to the formation of these dykes belong to the deep Allochthonous (Plus-Value Complex, Figs. 1-2, 1-3, Moukhsil et al., 2014, 2012) or to the Parautochthonous Belt (Knob Lake Group of the Gagnon Terrane, Fig. 1-2, e.g. Rivers, 2008) remains an open question.

The 13-AE-2149 allanite-bearing PGD displays quite different features when compared to other PGD such as (i) a shallow-dipping and diffuse contact (Figs. 1-5b, 1-7g), (ii) higher Nb

and Ta contents of 132 and 3.20 ppm respectively (Table 1-2), (iii) a weakly peraluminous character (ASI of 1.08, Fig. 1-13a, Table 1-2), and (iv) a much lower La_N/Yb_N of 28 (Fig. 1-13b, Table 1-2). These features suggest its possible derivation by differentiation of a late-Ottawan garnet/rutile-poor source (Bea, 1996; Hönig et al., 2014; Stepanov et al., 2014) such as the ca. 1015 Ma Okaopéo Plutonic Suite (high-alkalic mangerite±gabbro±syenite) and Sabot Mangerite (Augland et al., 2015; Moukhsil et al., 2014), combined with late-crystallization fluid release and/or an interaction with its pre-Grenvillian host metamangerite during its intrusion.

8.3. Unusual petrogeochemical characteristics of the LREE-rich PGD from the Lac Okapéo region

Previous studies have shown that Grenvillian granitic pegmatites are dominated by quartz + K-feldspar + plagioclase ± a ferromagnesian phase, completed with a variety of other major and minor phases (e.g. pyroxene, amphibole, biotite, titanite, magnetite, sulfides, allanite, zircon, garnet, monazite, pyrochlore-group minerals and U-Th phases, Ercit, 2005; Fowler and Doig, 1983). Grenvillian granitic pegmatites commonly host REE together with other metals such as U-Th, Nb-Ta, Y, Ti, Zr, Be, Mo, P, Pb, F, with no REE-only mineralization described in these occurrences. The mineralogical assemblage of the PGD from the Lac Okaopéo region is dominated by quartz + K-feldspar + plagioclase + biotite, as proposed by Ercit (2005), Ford (1982) and Lentz (1996, 1991), and is completed with zircon and monazite or allanite (Figs. 1-8 to 1-12, Tables 1-3 and 1-4). No complementary rare-element minerals have been recognized in the PGD of the Lac Okaopéo region, except for the late but micrometric Th-U(±REE) silicates (Fig. 1-8c) and the Ca±REE silicates or carbonates (Fig. 1-11e-f) identified in the monazite- and allanite-bearing PGD, respectively, and that represent a negligible part of the whole rock. The accessory phases assemblages, even if not uncommon in worldwide abyssal class pegmatitic bodies (Ercit, 2005), is less diverse than for the rest of the LREE-enriched Grenvillian PGD (Ford, 1982; Lentz, 1996, 1991). Accordingly, the PGD from the Lac Okaopéo region represent the first evidence of magmatic REE-only mineralization in this region.

Monazite and allanite crystals from the PGD investigated in this study are monazite-(Ce) and allanite-(Ce) and generally display a core to rim zoning (Figs. 1-9, 1-10a, c, 1-11b, d, Tables 1-3 and 1-4). Monazite crystals from the two investigated PGD present a dominant substitution expressed by the huttonite end-member that is consistent with the concurrent evolution of Th and ΣREE contents (13-AM-13 and 13-TC-5008, Figs. 1-10b and d, 1-13c, e.g.

Spear and Pyle, 2002). Monazite from the 13-TC-5008 PGD are rather homogeneous (Figs. 1-9d-f, 1-10c-d) whereas oscillatory zoned monazite from the 13-AM-13 PGD are characterized by a gradient trending towards monazite-(La) from LREE(Ce)-rich cores to Th-Si-rich rims (Figs. 1-9a-c, 1-10a-b, Table 1-3). This suggests an evolution of the melt composition during crystallization from LREE-rich towards Th-Si-rich most probably related to the crystallization of zircon, the only LREE-poor/Th-Si-bearing phase present in the dykes (e.g. Bea, 1996; Hanchar et al., 2001). Its crystallization would generate a LREE-rich/Th-Si-poor residual melt, allowing the preferential incorporation of LREE into the monazite lattice and a relatively LREE-impoverished/Th-Si-enriched residual melt after zircon growth is completed. In contrast, allanite crystals from the 13-TC-5072 and the 13-FS-1202 PGD display distinct textures. Those from the former show oscillatory zoned cores (Aln_1) corroded by overgrowths (Aln_2, Fig. 1-11b) with stable compositions (Fig. 1-12a, Table 1-4). This is most probably related to a new magmatic pulse and not to a significant change in the melt composition. Allanite phenocrysts from the latter however show inner patchy and not oscillatory zoning suggesting a random organization between LREE(Ce)-rich and Fe-Ca-LREE(Ce)-rich zones (Fig. 1-11d, Table 1-4). This points to more complex petrogenetic processes than successive growths associated with distinct magmatic pulses. However, a compositional change is recorded in the Fe-poor and in the Si-rich/LREE-poor alteration rims that are expressed on every allanite phenocrysts from the 13-TC-5072 (Fig. 1-11b) and the 13-FS-1202 (Figs. 1-11d-e) PGD, respectively (Table 1-4). According to the lack of corrosion of previous zones associated with no changes in the euhedral shape of the grains, its association with the late-sericitization of feldspar (Fig. 1-11a, c) and formation of late-Ca±REE carbonates or silicates veinlets (Fig. 1-11e-f), this alteration is most likely related to magmatic-hydrothermal transition processes. In summary, monazite crystals would record the fractionation of zircon during the course of melt crystallization of paragneisses-hosted PGD marked by syn-zircon growth LREE-rich/Th-Si-poor monazite cores and post-zircon growth LREE-poor/Th-Si-rich zones. In contrast, allanite phenocrysts do not allow to discuss magmatic fractionation but offer insights on the magmatic-hydrothermal transition associated with the formation of allanite alteration rims coeval with late veinlets of carbonates or silicates and most probably with feldspar sericitization.

The empirical relation of monazite in paragneisses-hosted PGD and allanite in metaplutonic-hosted PGD might reflect either (i) an initial geochemical difference between the two granitic series, and/or (ii) interactions of the melt with different rocks during ascent and/or at emplacement level. On the one hand, the former hypothesis is strengthened by (i) the positive

correlation between the P_2O_5, CaO and the ΣREE contents (Fig. 1-13f) in monazite-bearing PGD, unlike in allanite-bearing, and (ii) the positive correlation between the $Fe_2O_{3\ (total)}$, MgO and the ΣREE contents in allanite-bearing PGD (Fig. 1-13g). On the other hand, the hypothesis of an interaction between melts and surrounding rocks is supported by the empirical relationship (i) between monazite-bearing PGD and wide outcropping areas of metasediments (3 over 4 PGD hosted in the Plus-Value Complex), and (ii) between allanite-bearing PGD and metaplutonic complexes (2 over 3 PGD hosted in the Bardoux and Castoréum Plutonic Suites) (Figs. 1-3, 1-6, 1-7). These suggest that the crystallization of monazite and allanite could be related to interactions of the granitic melt (i) with the more sodic metasedimentary host of the Plus-Value complex for the former, and conversely (ii) with the more calcic igneous rocks of the Bardoux and Castoréum suites for the latter. This hypothesis is consistent with the locally diffuse contact of the 13-TC-5008 monazite-bearing PGD (Fig. 1-6c) and the very diffuse contact at the lower contact of the 13-AE-2149 allanite-bearing PGD (Fig. 1-7g). Such a model has been proposed for granitic pegmatites from the southwestern Grenville Province and is designated as "hybridization" by Lentz (1996, 1991), who evidenced bi-metasomatic exchange processes leading to Ca, Fe, Mg±Ti enrichment in the melts and to the crystallization of titanite and allanite. However, (i) the lack of macroscopic mineralogical reaction zone at the contact of most of the dykes with their host rocks, and (ii) the close geographical association of the 13-TC-5008 monazite-bearing and the 13-AE-2149 allanite-bearing PGD (Fig. 1-3), make the hypotheses of a control of the mineralization by deep interaction between the magma and rocks of distinct chemical composition unlikely. In addition, both monazite- and allanite-bearing samples display a similar positive correlation between the Na_2O, the CaO and the ΣREE contents (Fig. 1-13d) suggesting that the hypothesis of an initial geochemical difference between the two granitic series is most likely. Therefore we propose that the control of the mineralization either as monazite or allanite observed in the PGD from the Lac Okaopéo may not only be correlated with the activities of Na and Ca as proposed in the models of Berger et al. (2009) and Budzyń et al. (2011) but by the initial CaO and P_2O_5 contents, and the $Fe_2O_{3\ (total)}$ and MgO, respectively. Exception is the 13-AE-2149 dyke emplaced in an intermediate host metamangerite with a diffuse lower contact, and that displays a weakly peraluminous character (ASI of 1.08, Fig. 1-13a, Table 1-2) that is intermediate between the other PGD investigated in this study and those reported by Lentz (1996). This lower peraluminous signature may reflect an interaction of the dyke with its host during its emplacement, as proposed by Lentz (1996) for western Grenvillian granitic pegmatites.

The weak to strong peraluminous character associated with P_2O_5 contents of 0.02-0.40 wt.% (Fig. 1-13f, Table 1-2) of the PGD from the Lac Okaopéo region correspond to the peraluminous intermediate phosphorous serie defined by Linnen and Cuney (2005). It contrasts with the metaluminous Grenvillian LREE-enriched granitic pegmatites of Lentz (1996) (Fig. 1-13a) and with REE-enriched granitic pegmatites reported elsewhere that are ascribed to alkaline intrusive (Dill, 2015, 2010; Ercit, 2005; London, 2016). Allanite is a major LREE carrier in granitoids with ASI below 1.2 (Bea, 1996) and in LREE-enriched granitic pegmatites from the abyssal class, usually ascribed to metaluminous to subaluminous compositions (Ercit, 2005; Ford, 1982; Lentz, 1996, 1991), i.e. not in strongly peraluminous melt. In the PGD from the Lac Okaopéo region, allanite is hosted in three metaplutonic hosted PGD, two of them displaying ASI ranging from 1.18 to 1.35 (13-TC-5072 and 13-FS-1202 PGD respectively, Table 1-2) that are not compatible with the formation of allanite. In contrast, the presence of monazite in paragneisses-hosted PGD with ASI ranging from 1.19 to 1.36 (Table 1-2) is consistent with its expression as a major and widespread LREE-carrier in a variety of granitoids especially in peraluminous granite and abyssal granitic pegmatites (Bea, 1996; Ercit, 2005; Linnen and Cuney, 2005; Montel, 1993; Rapp and Watson, 1986), but its sole presence as LREE-bearing phase in PGD is shown for the first time in the Grenville Province.

The monazite- and allanite-bearing PGD from the Lac Okaopéo region are generally more concentrated in REE and more fractionated in LREE over HREE than those of the most enriched samples of Lentz (1996), with ΣREE between 1418 to 7048 ppm (monazite-bearing PGD) and between 2393 to 9242 ppm (allanite-bearing PGD), associated with La_N/Yb_N up to 938 (Fig. 1-13b, Table 1-2). The ΣREE content of PGD from the Lac Okaopéo region increases with (i) decreasing Eu/Eu* from 0.72 down to 0.12 (Fig. 1-13b, Table 1-2), and (ii) with increasing U and Th contents (Fig. 1-13c), Th being much more concentrated than U (Th/U ratio between 25 and 74, Table 1-2). Both features are consistent with the increasing proportion of REE-bearing phases relative to major minerals that represent sinks for Eu (e.g. Bea, 1996; London, 2008). The U and Th contents increase more rapidly with ΣREE in monazite-bearing than in allanite-bearing dykes (Fig. 1-13c) as marked by the formation of ThO_2-rich monazite relative to allanite (Tables 1-3 and 1-4).

The monazite- and allanite-bearing PGD present unusual and some distinct geochemical trends (Fig. 1-13). The high Zr/Hf ratio (Fig. 1-13e) associated with high contents of Zr and Hf (up to 6340 and 171 ppm respectively, Table 1-2) and the very low contents of Nb and Ta of the PGD (Table 1-2) is characteristic of alkaline melts (Linnen and Cuney, 2005; Linnen and

Keppler, 2002; Zaraisky et al., 2009). The quite stable Zr/Hf with increasing ΣREE is also a characteristic feature of alkaline melts in which the high zircon solubility prevents the fractionation of Zr over Hf associated with zircon growth (Ellison and Hess, 1986; Linnen, 1998; Linnen and Cuney, 2005; Linnen and Keppler, 2002; Zaraisky et al., 2009). The contrasting behavior of the Nb/Ta ratio in monazite- and allanite-bearing PGD, with increasing Nb/Ta ratio and ΣREE content in monazite-bearing and decreasing Nb/Ta ratio with increasing ΣREE content in allanite-bearing PGD (Fig. 1-13e), suggest either distinct (i) magmatic processes, or (ii) fractionation of Nb over Ta associated with distinct sources or (iii) with the crystallization of monazite over allanite. The former hypothesis is unlikely according to the lack of Nb and Ta minerals in the dykes. Accordingly, the whole-rock geochemistry of the REE-rich PGD from the Lac Okaopéo region display contrasting signatures with (i) major elements characteristics of intermediate phosphorous peraluminous granites (e.g. Linnen and Cuney, 2005), and (ii) trace elements (Zr-Hf-Nb-Ta and the REE) enrichment and fractionation more akin to a peralkaline signature of the melts (e.g. Ellison and Hess, 1986; Linnen, 1998; Linnen and Cuney, 2005; Linnen and Keppler, 2002; Zaraisky et al., 2009).

8.4. LREE-rich PGD from the Lac Okapéo region in the granitic pegmatite classification scheme

The PGD from the Lac Okaopéo region display peraluminous signatures (Fig. 1-13a, Table 1-2), are LREE enriched (Fig. 1-13b) and are composed of a quartz + K-feldspar + plagioclase + biotite (for major minerals, Figs. 1-8a, d, 1-11a-c) with either monazite or allanite and ubiquitous zircon (Figs. 1-8a-c, 1-11b-f). Mineralized granitic pegmatites displaying a peraluminous signature usually belong to the LCT family (Černý et al., 2012; Černý and Ercit, 2005; Ercit, 2005; London, 2008, 2005; Martin and De Vito, 2005). Even though the seven PGD described in this paper are peraluminous, they do not share any other characteristic of this family since none of them contain any muscovite, nor Li-, Cs- or Ta-minerals, nor tourmaline or beryl and are not enriched in Rb, Ga or Sn. In addition, their trace elements geochemistry is more akin to alkaline melts (e.g. Linnen and Cuney, 2005; Linnen and Keppler, 2002). In the classical classification scheme, the NYF family contains pegmatitic bodies derived from alkaline intrusive bodies and are enriched in Nb, Y, F, Be, Ti, Sc, Zr with LREE concentrations up to 100 to 800 times chondritic and little depletion in HREE (Černý et al., 2012; Černý and Ercit, 2005; Ercit, 2005; London, 2005, 2008). PGD investigated from the Lac Okaopéo region do not contain any minerals hosting the usual rare-metals of the NYF family, show a LREE enrichment from over 1,000 to almost 10,000 times the chondritic value (Fig. 1-13b), a strong

depletion of HREE and, for six of them (exception is the 13-AE-2149 PGD) are most probably derived by partial melting of a deeper-seated metasedimentary source. Therefore, they are not characteristic of the NYF family neither. Ercit (2005) reviewed the general characteristics of world-wide REE-enriched granitic pegmatites. These are mainly observed in Colorado, Virginia and Northern Carolina (USA), Kola-Karelia and Pribaikal regions, and Aldan Shield (Russia), southern Japan, Antsirabé-Kitsamby and Ankazobe districts (Madagascar), and finally in the SW Grenville Province, that represents one of the major districts of such REE occurrences (e.g. Ford, 1982; Lentz, 1996, 1991). Ercit (2005) emphasized that REE-enriched granitic pegmatites do not always fall in fields of the previously described granitic pegmatites families (either LCT or NYF) of Černý (1991). However, in the abyssal class, two main types of REE-enriched granitic pegmatites are common: (i) the LREE-enriched that typically host REE as an allanite-monazite and/or uraninite assemblage, and (ii) the (Y,HREE)-enriched that typically host REE assemblage as more complex rare-element assemblages than the previous one (Ercit, 2005). The PGD from the Lac Okaopéo region display ΣLREE contents between 1407 and 8757 ppm hosted in either monazite or allanite (Figs. 1-6f, 1-7b-d, g, 1-8a-c, 1-9 to 1-12 and 1-13b) and ΣHREE contents between 11 and 485 ppm (Fig. 1-13b, Table 1-2) and can therefore be ascribed to the LREE-enriched type of Ercit (2005).

According to previous sections of the discussion, the zoned PGD from the Lac Okaopéo region intruded metamorphosed sedimentary units and metaplutonic complexes in a post-tectonic setting relative to the structure and metamorphism of their host rocks with no link, for six of them (except for the 13-AE-2149 PGD), to a plutonic body (see sections 8.1. and 8.2.) and therefore correspond to the class of 'pseudopegmatites' proposed by Dill (2016) in its CMS (Chemical composition - Mineral assemblage - Structural geology) classification scheme. The 13-AE-2149 PGD however could derive by differentiation of a late-Ottawan plutonic suite and would therefore correspond to the 'pegmatite' class of Dill (2016). In addition, according to the same scheme the monazite-bearing PGD are paragneisses-hosted zoned meter-sized (Zr)-LREE quartz-feldspar-biotite pseudopegmatite (monazite), whereas the 13-TC-5072 and the 13-FS-1202 allanite-bearing PGD are metamonzogranite-hosted zoned decimeter- to meter-sized (Zr)-LREE quartz-feldspar-biotite pseudopegmatite (allanite) and quartz metamonzodiorite-hosted zoned decimeter- to meter-sized (Zr)-LREE quartz-feldspar-biotite pseudopegmatite (allanite), respectively. In the same way and according to its possible derivation from a plutonic source, the 13-AE-2149 allanite-bearing PGD is a metamangerite-hosted zoned centimeter- to meter-sized (Zr)-LREE quartz-feldspar-biotite (pseudo)pegmatite (allanite) according to Dill (2016).

Conclusions

The seven pegmatitic granite dykes (PGD) from the Lac Okaopéo region described in this paper represent new LREE-only occurrences in the central Grenville Province. They intrude paragneisses from the Plus-Value Complex or felsic to intermediate metaplutonic complexes from the Bardoux and Castoréum Plutonic Suites that are part of the Allochthonous Belt of the Grenville Province. These LREE occurrences are undeformed dykes discordant to the foliation of their host rocks with no evidence for interconnection with leucosomes and are thus considered as post-tectonic relative to the structure and metamorphism of their host rocks that recorded the Ottawan orogenic phase. Their peraluminous signature, high Nb/Ta ratio and high fractionation of LREE over HREE suggest their derivation by partial melting of metasedimentary units, either belonging to the base of the Allochthonous or to the Parautochthonous Belt. U-Pb dating of magmatic monazite from two of the LREE occurrences yield concordant igneous ages at 996.7±5.3 Ma and 1005.4±4.4 Ma that correspond to an emplacement at the initiation of the Rigolet orogenic phase considered to represent a short-lived phase of renewed crustal thickening as recorded by deformation and metamorphism of the Parautochthonous Belt between ca. 1005 and 980 Ma. Further isotopic and geochronological investigations are needed to constrain their derivation either from the Allochthonous or the Parautochthonous Belt. Field relationships show that monazite host the LREE-mineralization for PGD hosted by paragneisses of the Plus-Value Complex, and that allanite host the LREE-mineralization for PGD hosted by metagranitoids of the Bardoux and Castoréum Plutonic Suites, in both cases without complementary rare-metals minerals. The geochemistry and rare-metals assemblage do not allow to ascribe these PGD to the classical LCT and NYF family. In addition, even if a peraluminous character is marked by the major elements whole-rock geochemistry, the Zr/Hf ratio associated with high Zr and Hf contents, the very low contents in Nb and Ta and the very high contents in LREE are more akin to a peralkaline series.

The peraluminous signature of the mineralized PGD contrasts with the typical metaluminous to subaluminous signature of REE-enriched granitic pegmatites reported elsewhere. This peraluminous composition is consistent with the crystallization of monazite-(Ce) but is at odd with the presence of allanite-(Ce). This contribution constitutes the first evidence in the Grenville Province of such a monazite-only mineralization hosted in PGD. Further investigations are required to identify the factors controlling the crystallization of allanite in some of these PGD.

Acknowledgements

The authors would like to thank the Ministère de l'Energie et des Ressources naturelles (Québec, Canada) for providing technical and financial support for the field work and analyses. This contribution constitutes a Ministère de l'Energie et des Ressources naturelles du Québec (Canada) publication n°8449-2016-2017-04. The authors are grateful to Sandrine Mathieu (SEM), Lise Salsi (SEM) and Olivier Rouer (EMP) (GeoRessources, Nancy) for technical support in providing analytical data on SEM and EMP, to Alexandre Crépon (GeoRessources, Nancy) for his help during field work and to Aurélien Eglinger (GeoRessources, Nancy) for his help in handling geochronological data. The authors also thank Harald G. Dill and an anonymous reviewer for their detailed review that helped to improve the paper, and Franco Pirajno for editorial handling. This work was funded by the Labex Ressources 21 (supported by the French National Research Agency – France) through the national program "Investissements d'avenir", reference ANR-10-LABX-21–LABEX RESSOURCES 21 and the Région Grand-Est. It benefited from the framework of the DIVEX "Rare earth element" research program.

Table 1-1: Location, present coordinates and results presented in this study of the REE occurrences from the Lac Okaopéo region, first ordered by type of occurrence then from north to south. Abbreviations: Aln-bearing = allanite-bearing pegmatitic granite dyke; Mnz-bearing = monazite-bearing pegmatitic granite dyke; NTS = National Topographic System; UTM = Universal Transverse Mercator.

Type of REE occurrence	Outcrop n°	NTS sheet	UTM zone[1]	Easting[1]	Northing[1]	Localization (see Fig. 1-3)	Results presented in this study				
							Detailed map	Structural measures[2]	Whole-rock geochemistry[3]	Accessory mineral composition	Dating (U-Pb monazite)
Mnz-bearing	**13-AM-07**	22K10	U19	510199	5620952	North of the 22K/10 NTS sheet	Fig. A-1	Fig. 1-5a	Table 1-2	-	-
	13-AM-10	22K10	U19	511236	5618292	North of the 22K/10 NTS sheet	Fig. A-3	Fig. 1-5a	Table 1-2	-	-
	13-AM-13	22K10	U19	512052	5614036	North of the 22K/10 NTS sheet	Figs. 4, A-5	Fig. 1-5a	Table 1-2	Table 1-3 – Figs. 1-10a, b	Table 1-5 – Figs. 1-14a-b
	13-TC-5008	22K07	U19	504614	5585041	North of the 22K/07 NTS sheet	Fig. A-7	Fig. 1-5a	Table 1-2	Table 1-3 - Figs. 1-10c, d	Table 1-5 – Fig. 1-14c
Aln-bearing	**13-TC-5072**	22K10	U19	510668	5603384	South of the 22K/10 NTS sheet	Fig. B-1	Fig. 1-5b	Table 1-2	Table 1-4 - Figs. 1-12a	-
	13-FS-1202	22K10	U19	510162	5601234	South of the 22K/10 NTS sheet	Fig. B-3	Fig. 1-5b	Table 1-2	Table 1-4 - Figs. 1-12b	-
	13-AE-2149	22K07	U19	503389	5589641	North of the 22K/07 NTS sheet	Fig. B-5	Fig. 1-5b	Moukhsil et al. (2014)	-	-

[1] Coordinates are reported as Universal Transverse Mercator (UTM).
[2] All the structural measurements (foliation of the host rocks and dykes) are available in Appendix C.
[3] Geochemical data are represented in Fig. 1-13.

Table 1-2: Whole rock geochemistry of the REE-richest facies of the pegmatitic granite dykes from the Lac Okaopéo region, first ordered by type of occurrence then from north to south. Data for the 13-AE-2149 pegmatitic granite is from (Moukhsil et al., 2014). Abbreviations: A/CNK = Al/ (Na + K + Ca/2) (Shand, 1943); Allanite-bearing = allanite-bearing pegmatitic granite dyke; A/NK = Al/(Na + K) (Shand, 1943); ASI = Aluminum Saturation Index given by the expression ASI = Al/(Ca – 1.67 x P + Na + K) (Frost et al., 2001; Shand, 1943); Monazite-bearing = monazite-bearing pegmatitic granite dyke.

Type of REE occurrence	*Monazite-bearing*			*Allanite-bearing*			
Sample	**13-AM-07**	**13-AM-10**	**13-AM-13**	**13-TC-5008**	**13-TC-5072**	**13-FS-1202**	**13-AE-2149**
SiO_2 *(wt.%)*	71.03	70.80	60.24	70.79	70.27	70.85	55.84
TiO_2	0.24	0.50	0.89	0.69	0.34	0.43	0.63
Al_2O_3	15.93	13.85	18.58	12.90	14.18	14.83	15.05
$Fe_2O_{3\,(total)}$	1.23	1.80	4.60	3.67	2.38	3.48	12.42
MnO	0.01	0.01	0.03	0.02	0.02	0.05	0.22
MgO	0.36	0.48	1.16	0.71	0.30	0.52	0.85
CaO	2.29	0.87	3.10	0.88	1.38	2.99	5.54
Na_2O	3.53	2.26	4.02	1.99	2.74	4.14	4.28
K_2O	4.32	6.68	4.36	6.25	5.90	1.33	1.93
P_2O_5	0.29	0.09	0.40	0.10	0.15	0.02	0.22
Cr_2O_3	< 0.01	< 0.01	< 0.01	< 0.01	< 0.01	< 0.01	< 0.01
LOI	0.63	0.92	0.82	0.60	0.73	1.01	0.83
Total	**99.87**	**98.26**	**98.19**	**98.58**	**98.39**	**99.64**	**97.80**
ASI	1.30	1.19	1.36	1.20	1.18	1.35	1.08
A/CNK	1.28	1.30	1.27	1.29	1.24	1.30	0.87
A/NK	2.03	1.55	2.22	1.57	1.64	2.71	2.42
Sr *(ppm)*	448.00	342.00	550.00	213.00	164.00	275.00	147.00
Ba	1191.00	2424.00	899.00	1662.00	661.00	147.00	181.00
Nb	5.60	8.40	21.00	15.70	7.50	17.30	132.00
V	16.00	23.00	27.00	27.00	7.00	15.00	38.00
Co	2.00	2.00	6.00	5.00	2.00	3.00	6.00
Ga	39.00	22.00	60.00	26.00	29.00	53.00	79.00
Ge	4.70	2.10	6.90	2.40	2.90	7.40	9.70
In	< 0.1	< 0.1	< 0.1	< 0.1	< 0.1	< 0.1	0.20
Sn	< 1	< 1	< 1	< 1	< 1	2.00	4.00
Cs	0.50	0.70	1.50	0.70	0.30	1.00	0.70
Pb	35.00	29.00	34.00	22.00	31.00	17.00	41.00
Be	2.00	< 1	3.00	< 1	< 1	4.00	9.00
Hf	23.40	4.40	41.50	9.00	7.40	50.80	171.00
Ta	0.10	0.25	0.40	0.35	0.11	0.30	3.20
W	0.90	0.80	1.10	0.80	1.40	0.80	3.00
Tl	0.97	1.08	1.40	1.10	0.97	0.75	0.34
Bi	< 0.1	< 0.1	< 0.1	< 0.1	< 0.1	< 0.1	< 0.1
Th	561.00	102.00	1300.00	123.00	70.50	392.00	766.00
U	11.00	2.02	19.10	1.66	1.11	6.88	30.30
Rb	98.00	141.00	214.00	172.00	122.00	58.00	42.00
Y	29.50	5.90	52.90	10.00	15.80	83.50	544.00
Zr	860.00	195.00	1480.00	388.00	290.00	1760.00	6340.00
Nb/Ta	56	34	53	45	68	58	41
Zr/Hf	37	44	36	43	39	35	37
Th/U	51	50	68	74	64	57	25
La	1560.00	433.00	1800.00	538.00	674.00	1870.00	2150.00
Ce	2720.00	690.00	3370.00	884.00	1160.00	3580.00	4130.00
Pr	271.00	64.10	370.00	92.20	120.00	406.00	470.00
Nd	843.00	202.00	1250.00	300.00	377.00	1400.00	1710.00
Sm	84.60	17.50	159.00	30.40	37.70	179.00	297.00
Eu	3.47	2.37	4.74	2.40	2.62	4.71	9.39
Gd	28.60	5.70	65.20	11.80	13.00	73.30	180.00
Tb	2.07	0.41	5.03	0.78	1.09	6.81	24.90
Dy	8.41	1.55	16.30	2.99	4.33	25.70	123.00
Ho	1.12	0.22	1.93	0.43	0.67	3.58	21.80
Er	2.42	0.52	3.81	0.91	1.51	7.73	59.00
Tm	0.23	0.06	0.35	0.09	0.17	0.90	8.34
Yb	1.13	0.35	1.56	0.43	0.74	4.87	51.80
Lu	0.17	0.05	0.22	0.06	0.10	0.72	7.22
ΣLREE	5479	1407	6949	1845	2369	7435	8757
ΣHREE	47	11	99	19	24	128	485
ΣREE	**5526**	**1418**	**7048**	**1864**	**2393**	**7563**	**9242**
La_N/Yb_N[1]	938	840	784	850	619	261	28
Eu/Eu*[1]	0.22	0.72	0.14	0.39	0.36	0.13	0.12
Cd	< 0.5	< 0.5	< 0.5	< 0.5	< 0.5	< 0.5	< 0.5

Cu	5.00	3.00	20.00	2.00	2.00	6.00	16.00
Ag	< 0.3	< 0.3	< 0.3	< 0.3	< 0.3	3.60	-
Ni	< 1	< 1	3.00	2.00	< 1	< 1	3.00
Mo	2.00	< 1	4.00	1.00	5.00	< 1	6.00
Zn	27.00	32.00	110.00	103.00	46.00	56.00	288.00
S	300.00	300.00	1100.00	100.00	< 100	300.00	600.00
Au	< 2	< 2	< 2	< 2	< 2	< 2	< 2
As	< 0.5	< 0.5	< 0.5	< 0.5	3.30	< 0.5	< 0.5
Br	< 0.5	< 0.5	< 0.5	< 0.5	< 0.5	< 0.5	< 0.5
Cr	58.00	47.00	70.00	49.00	59.00	75.00	48.00
Ir	< 5	< 5	< 5	< 5	< 5	< 5	< 5
Sc	1.10	1.70	3.50	1.70	2.60	6.70	31.90
Sb	< 0.1	< 0.1	< 0.1	< 0.1	< 0.1	< 0.1	< 0.1
Se	< 3	< 3	< 3	< 3	< 3	< 3	< 3

[1] Normalization after McDonough and Sun (1995).

Table 1-3: Analyses of monazite grains from the 13-AM-13 and the 13-TC-5008 pegmatitic granite dykes from the Lac Okaopéo region. Data were obtained using EMP and were performed on LREE-rich, intermediate and Th-Si-rich zones of monazite grains. They are reported with confidence interval of 95% in brackets (n = number of analyses). Abbreviations: Brab. = brabantite; Hutt. = huttonite; Mnz. = monazite; Xen. = xenotime.

Sample		***13-AM-13***			***13-TC-5008***		
Zonation type		**LREE(Ce)-rich**	**Intermediate**	**Th-Si-rich**	**LREE(Ce)-rich**	**Intermediate**	**Th-Si-rich**
Oxides/wt.%	P_2O_5	29.07	27.59	25.63	28.99	28.87	28.43
		(0.22)	(0.33)	(0.40)	(0.17)	(0.10)	(0.20)
	SiO_2	0.99	1.92	3.14	1.03	1.09	1.38
		(0.12)	(0.19)	(0.24)	(0.11)	(0.05)	(0.14)
	CaO	0.89	0.93	0.89	0.31	0.31	0.37
		(0.15)	(0.11)	(0.12)	(0.03)	(0.02)	(0.03)
	Y_2O_3	0.26	0.17	0.10	0.09	0.07	0.08
		(0.06)	(0.03)	(0.02)	(0.04)	(0.02)	(0.05)
	La_2O_3	15.59	14.48	14.04	17.98	18.07	17.91
		(0.38)	(0.16)	(0.17)	(0.18)	(0.12)	(0.25)
	Ce_2O_3	30.44	28.57	26.69	31.88	31.77	31.07
		(0.50)	(0.32)	(0.34)	(0.25)	(0.15)	(0.29)
	Pr_2O_3	3.47	3.30	3.04	3.39	3.37	3.30
		(0.04)	(0.04)	(0.05)	(0.05)	(0.04)	(0.05)
	Nd_2O_3	10.83	10.52	9.43	10.62	10.53	10.28
		(0.09)	(0.16)	(0.17)	(0.16)	(0.11)	(0.22)
	Sm_2O_3	1.40	1.34	1.07	1.10	1.09	1.05
		(0.08)	(0.06)	(0.05)	(0.05)	(0.03)	(0.06)
	Gd_2O_3	0.67	0.63	0.47	0.44	0.45	0.43
		(0.06)	(0.03)	(0.03)	(0.04)	(0.02)	(0.05)
	PbO	0.57	0.44	0.95	0.02	0.01	0.07
		(0.22)	(0.18)	(0.20)	(0.03)	(0.02)	(0.13)
	ThO_2	7.06	11.07	15.93	4.57	4.85	6.19
		(0.46)	(0.68)	(0.80)	(0.48)	(0.24)	(0.52)
	UO_2	0.10	0.11	0.10	0.05	0.05	0.07
		(0.01)	(0.01)	(0.01)	(0.01)	(0.01)	(0.02)
	Total	101.34	101.07	101.49	100.48	100.52	100.63
		(0.24)	(0.24)	(0.20)	(0.17)	(0.12)	(0.15)
Oxygens		4	4	4	4	4	4
Cations	P	0.963	0.927	0.876	0.965	0.962	0.950
		(0.005)	(0.008)	(0.010)	(0.004)	(0.002)	(0.005)
	Si	0.039	0.076	0.127	0.041	0.043	0.055
		(0.005)	(0.008)	(0.010)	(0.004)	(0.002)	(0.005)
	ΣT-site	1.002	1.004	1.003	1.006	1.005	1.005
		(0.001)	(0.001)	(0.001)	(0.001)	(0.001)	(0.001)
	Ca	0.037	0.039	0.039	0.013	0.013	0.016
		(0.006)	(0.005)	(0.005)	(0.001)	(0.001)	(0.001)
	Y	0.005	0.004	0.002	0.002	0.001	0.002
		(0.001)	(0.001)	(0.000)	(0.001)	(0.000)	(0.001)
	La	0.225	0.212	0.209	0.261	0.262	0.261
		(0.006)	(0.002)	(0.002)	(0.003)	(0.002)	(0.004)
	Ce	0.436	0.415	0.395	0.459	0.458	0.449
		(0.008)	(0.004)	(0.004)	(0.003)	(0.002)	(0.004)
	Pr	0.049	0.048	0.045	0.049	0.048	0.047
		(0.001)	(0.001)	(0.001)	(0.001)	(0.001)	(0.001)
	Nd	0.151	0.149	0.136	0.149	0.148	0.145
		(0.001)	(0.002)	(0.002)	(0.002)	(0.002)	(0.003)
	Sm	0.019	0.018	0.015	0.015	0.015	0.014
		(0.001)	(0.001)	(0.001)	(0.001)	(0.000)	(0.001)
	Gd	0.009	0.008	0.006	0.006	0.006	0.006
		(0.001)	(0.000)	(0.000)	(0.001)	(0.000)	(0.001)
	Pb	0.006	0.005	0.010	0.000	0.000	0.001
		(0.002)	(0.002)	(0.002)	(0.000)	(0.000)	(0.001)
	Th	0.063	0.100	0.147	0.041	0.043	0.056
		(0.004)	(0.006)	(0.008)	(0.004)	(0.002)	(0.005)
	U	0.001	0.001	0.001	0.000	0.000	0.001
		(0.000)	(0.000)	(0.000)	(0.000)	(0.000)	(0.000)
	Σa-site	1.003	1.000	1.004	0.995	0.996	0.997
		(0.002)	(0.002)	(0.003)	(0.002)	(0.002)	(0.002)
	% Hutt.	3.78	7.47	12.27	4.02	4.27	5.39
		(0.46)	(0.76)	(0.98)	(0.45)	(0.22)	(0.54)
	% Brab.	8.66	8.85	9.62	2.77	2.68	3.37
		(1.20)	(0.81)	(0.95)	(0.27)	(0.20)	(0.27)
	% Mnz.	87.56	83.68	78.11	93.21	93.05	91.24
	+ Xen.	(0.92)	(0.85)	(0.96)	(0.48)	(0.27)	(0.53)
	n	20	23	29	17	27	22

Table 1-4: Analyses of allanite grains from the 13-TC-5072 and 13-FS-1202 pegmatitic granite dykes from the Lac Okaopéo region. Data were obtained using EMP and were performed on LREE(Ce)-rich zones, intermediate zones and alteration rims of allanite grains from the 13-TC-5072 pegmatitic granite, and on LREE(Ce)-rich zones, Fe-Ca-LREE(Ce)-rich zones and alteration rims of allanite grains from the 13-FS-1202 pegmatitic granite. They are reported with confidence interval of 95% in brackets (n = number of analyses). Abbreviation: Aln = allanite.

Sample		***13-TC-5072***			***13-FS-1202***		
Zonation type		**Intermediate (Aln_1)**	**LREE(Ce)-rich (Aln_2)**	**Alteration rims**	**LREE(Ce)-rich**	**Fe-Ca-LREE(Ce)-rich**	**Alteration rims**
Oxides/wt.%	SiO_2	31.97	31.82	32.30	33.52	32.81	35.77
		(0.25)	(0.54)	(0.44)	(0.28)	(0.37)	(0.81)
	P_2O_5	0.22	0.21	0.25	0.23	0.24	0.22
		(0.01)	(0.01)	(0.02)	(0.02)	(0.00)	(0.02)
	CaO	9.88	10.02	9.75	10.73	11.27	9.55
		(0.12)	(0.23)	(0.20)	(0.25)	(0.19)	(0.47)
	Y_2O_3	0.00	0.00	0.00	0.00	0.00	0.00
		(0.00)	(0.00)	(0.00)	(0.00)	(0.00)	(0.00)
	La_2O_3	6.20	6.41	6.17	5.35	5.34	4.79
		(0.25)	(0.31)	(0.15)	(0.05)	(0.09)	(0.13)
	Ce_2O_3	11.69	11.83	11.55	10.49	10.53	9.97
		(0.32)	(0.48)	(0.25)	(0.19)	(0.17)	(0.31)
	Pr_2O_3	1.35	1.32	1.30	1.29	1.29	1.25
		(0.05)	(0.05)	(0.03)	(0.01)	(0.02)	(0.03)
	Nd_2O_3	3.73	3.79	3.71	3.95	3.90	3.85
		(0.13)	(0.17)	(0.10)	(0.03)	(0.06)	(0.11)
	Sm_2O_3	0.33	0.35	0.34	0.48	0.48	0.50
		(0.02)	(0.02)	(0.01)	(0.01)	(0.01)	(0.02)
	Gd_2O_3	0.00	0.00	0.00	0.00	0.00	0.00
		(0.00)	(0.00)	(0.00)	(0.00)	(0.00)	(0.00)
	ΣREE_2O_3	23.30	23.70	23.07	21.57	21.54	20.36
		(0.73)	(1.01)	(0.52)	(0.24)	(0.34)	(0.55)
	FeO	11.11	10.54	9.76	8.41	9.73	7.97
		(0.94)	(0.36)	(0.31)	(0.21)	(0.28)	(0.47)
	K_2O	0.01	0.02	0.03	0.01	0.02	0.03
		(0.01)	(0.00)	(0.01)	(0.00)	(0.01)	(0.01)
	MgO	0.43	0.34	0.33	0.31	0.41	0.35
		(0.12)	(0.03)	(0.03)	(0.04)	(0.05)	(0.07)
	Al_2O_3	18.94	18.63	18.92	18.88	18.44	18.93
		(0.53)	(0.22)	(0.25)	(0.17)	(0.19)	(0.36)
	TiO_2	0.95	0.92	1.05	0.85	0.81	0.95
		(0.06)	(0.04)	(0.07)	(0.03)	(0.04)	(0.07)
	MnO	0.27	0.29	0.30	0.34	0.30	0.33
		(0.07)	(0.03)	(0.02)	(0.02)	(0.01)	(0.02)
	SrO	0.09	0.13	0.14	0.26	0.23	0.25
		(0.04)	(0.02)	(0.02)	(0.01)	(0.01)	(0.03)
	PbO	0.04	0.04	0.04	0.03	0.04	0.04
		(0.00)	(0.00)	(0.01)	(0.00)	(0.00)	(0.00)
	ThO_2	0.69	0.62	0.73	1.12	1.00	1.19
		(0.06)	(0.04)	(0.04)	(0.04)	(0.07)	(0.08)
	UO_2	0.01	0.01	0.01	0.01	0.01	0.01
		(0.01)	(0.00)	(0.00)	(0.00)	(0.00)	(0.00)
	F	0.46	0.70	0.63	0.52	0.55	0.44
		(0.11)	(0.21)	(0.09)	(0.02)	(0.02)	(0.03)
	Total	98.37	97.98	97.31	96.79	97.38	96.39
		(0.88)	(0.35)	(0.45)	(0.28)	(0.27)	(0.85)
Oxygens		12.5	12.5	12.5	12.5	12.5	12.5
Cations	Si	2.968	2.961	2.999	3.090	3.033	3.240
		(0.021)	(0.038)	(0.024)	(0.020)	(0.022)	(0.051)
	P	0.017	0.017	0.019	0.018	0.019	0.017
		(0.001)	(0.000)	(0.002)	(0.001)	(0.000)	(0.001)
	Ca	0.983	0.999	0.971	1.061	1.119	0.929
		(0.016)	(0.020)	(0.022)	(0.025)	(0.022)	(0.047)
	Y	0.000	0.000	0.000	0.000	0.000	0.000
		(0.000)	(0.000)	(0.000)	(0.000)	(0.000)	(0.000)
	La	0.212	0.220	0.212	0.182	0.182	0.161
		(0.009)	(0.012)	(0.006)	(0.002)	(0.003)	(0.005)
	Ce	0.397	0.404	0.393	0.354	0.357	0.332
		(0.011)	(0.019)	(0.010)	(0.007)	(0.006)	(0.012)
	Pr	0.046	0.045	0.044	0.043	0.044	0.041
		(0.002)	(0.002)	(0.001)	(0.001)	(0.001)	(0.001)
	Nd	0.124	0.126	0.123	0.130	0.129	0.125
		(0.004)	(0.006)	(0.004)	(0.001)	(0.002)	(0.004)
	Sm	0.010	0.011	0.011	0.015	0.015	0.015

	(0.001)	(0.001)	(0.000)	(0.000)	(0.000)	(0.001)
Gd	0.000	0.000	0.000	0.000	0.000	0.000
	(0.000)	(0.000)	(0.000)	(0.000)	(0.000)	(0.000)
ΣREE	0.789	0.806	0.783	0.725	0.727	0.675
	(0.025)	(0.039)	(0.020)	(0.009)	(0.012)	(0.021)
Fe	0.862	0.820	0.759	0.649	0.754	0.605
	(0.073)	(0.026)	(0.025)	(0.017)	(0.023)	(0.036)
K	0.002	0.002	0.004	0.002	0.002	0.004
	(0.001)	(0.001)	(0.001)	(0.000)	(0.001)	(0.001)
Mg	0.059	0.048	0.046	0.042	0.056	0.047
	(0.017)	(0.005)	(0.004)	(0.006)	(0.007)	(0.009)
Al	2.072	2.044	2.071	2.050	2.010	2.024
	(0.053)	(0.018)	(0.018)	(0.015)	(0.018)	(0.035)
Ti	0.066	0.065	0.073	0.059	0.056	0.065
	(0.004)	(0.003)	(0.005)	(0.002)	(0.003)	(0.005)
Mn	0.021	0.023	0.024	0.027	0.023	0.025
	(0.005)	(0.003)	(0.002)	(0.002)	(0.001)	(0.002)
Sr	0.005	0.007	0.008	0.014	0.012	0.013
	(0.002)	(0.001)	(0.001)	(0.001)	(0.001)	(0.002)
Pb	0.001	0.001	0.001	0.001	0.001	0.001
	(0.000)	(0.000)	(0.000)	(0.000)	(0.000)	(0.000)
Th	0.015	0.013	0.015	0.024	0.021	0.025
	(0.001)	(0.001)	(0.001)	(0.001)	(0.002)	(0.002)
U	0.000	0.000	0.000	0.000	0.000	0.000
	(0.000)	(0.000)	(0.000)	(0.000)	(0.000)	(0.000)
F	0.135	0.207	0.185	0.153	0.160	0.127
	(0.032)	(0.063)	(0.028)	(0.006)	(0.006)	(0.009)
Total	7.996	8.012	7.958	7.913	7.994	7.994
	(0.027)	(0.022)	(0.023)	(0.019)	(0.018)	(0.018)
n	14	26	47	91	122	52

Table 1-5: U-Pb monazite dating using LA-ICP-MS from the 13-AM-13 and 13-TC-5008 monazite-bearing pegmatitic granite dykes from the Lac Okaopéo region. Abbreviation: Conc. (%) = degree of concordance.

Sample	Analysis no.	Isotopic ratios				Ages / Ma						
		$^{206}Pb/^{238}U$	1σ	$^{207}Pb/^{235}U$	1σ	$^{207}Pb/^{206}Pb$	1σ	$^{206}Pb/^{238}U$	1σ	$^{207}Pb/^{235}U$	1σ	Conc. (%)
13-AM-13	**1-1**	0.1641	0.0020	1.645	0.022	1006.2	24.62	979.3	10.9	987.6	8.6	98.2
	1-2	0.1589	0.0019	1.593	0.021	1005.2	23.84	950.9	10.6	967.4	8.3	96.2
	1-3	0.1646	0.0020	1.650	0.022	1005.5	24.12	982.3	11.0	989.5	8.5	98.4
	1-4	0.1620	0.0020	1.628	0.024	1010.8	27.58	967.8	10.9	981.1	9.4	97.1
	1-5	0.1560	0.0019	1.564	0.020	1006.6	22.97	934.4	10.4	956.1	8.0	95.0
	2-1	0.1640	0.0020	1.641	0.021	1001.1	22.54	979.1	10.9	985.9	8.1	98.5
	2-2	0.1573	0.0019	1.571	0.020	997.4	22.48	941.9	10.5	958.7	7.9	96.1
	2-3	0.1626	0.0020	1.630	0.022	1004.8	23.59	971.5	10.8	981.7	8.3	97.7
	2-4	0.1666	0.0020	1.671	0.024	1007.5	26.05	993.1	11.2	997.6	9.1	99.0
	2-5	0.1595	0.0019	1.597	0.022	1003.7	24.57	953.7	10.7	968.9	8.5	96.5
	3-1	0.1687	0.0020	1.703	0.024	1019.6	25.59	1005.2	11.3	1009.7	9.0	99.0
	3-2	0.1601	0.0019	1.605	0.021	1005.2	22.89	957.5	10.7	972.1	8.1	96.7
	4-1	0.1587	0.0019	1.590	0.021	1005.0	23.19	949.4	10.6	966.3	8.1	96.1
	4-2	0.1606	0.0019	1.608	0.021	1004.1	23.31	959.9	10.7	973.4	8.2	96.9
	5-1	0.1629	0.0020	1.636	0.022	1009.7	23.46	972.8	10.9	984.2	8.3	97.5
	5-2	0.1628	0.0020	1.631	0.022	1005.0	23.50	972.3	10.9	982.4	8.3	97.8
	5-4	0.1613	0.0019	1.622	0.022	1012.2	23.69	964.0	10.8	978.8	8.3	96.7
	6-1	0.1680	0.0021	1.681	0.025	1001.9	27.45	1001.0	11.3	1001.3	9.5	99.9
	6-2	0.1641	0.0020	1.650	0.023	1013.1	24.51	979.2	11.0	989.7	8.6	97.7
	6-3	0.1688	0.0020	1.684	0.023	996.8	24.40	1005.3	11.2	1002.6	8.6	100.6
	6-4	0.1687	0.0020	1.669	0.023	978.4	25.58	1005.2	11.3	996.8	8.9	101.9
	6-5	0.1687	0.0020	1.669	0.023	979.7	25.20	1004.9	11.3	997.0	8.8	101.8
	7-1	0.1613	0.0020	1.620	0.022	1009.7	24.92	964.1	10.8	978.1	8.7	96.9
	7-2	0.1663	0.0020	1.666	0.026	1004.2	29.03	991.7	11.3	995.6	9.9	99.1
	7-3	0.1675	0.0020	1.677	0.024	1004.3	25.66	998.1	11.2	1000.0	9.0	99.6
13-TC-5008	**1-1**	0.1700	0.0021	1.678	0.023	974.6	24.7	1012.3	11.6	1000.4	8.8	102.6
	1-2	0.1689	0.0021	1.703	0.027	1018.8	29.2	1005.8	11.7	1009.8	10.1	99.1
	2-1	0.1689	0.0021	1.745	0.027	1067.5	28.3	1005.9	11.7	1025.4	10.0	96.1
	2-2	0.1692	0.0021	1.692	0.027	1001.0	29.7	1007.6	11.8	1005.5	10.2	100.4
	3-1	0.1689	0.0022	1.724	0.032	1041.7	35.6	1006.1	12.0	1017.3	12.0	97.7
	3-2	0.1692	0.0021	1.700	0.024	1010.8	25.3	1007.7	11.6	1008.6	9.0	99.8
	4-2	0.1683	0.0021	1.700	0.026	1020.8	27.9	1003.0	11.6	1008.5	9.7	98.8
	5-1	0.1694	0.0021	1.688	0.025	993.4	27.0	1008.8	11.7	1003.9	9.4	101.1
	5-2	0.1688	0.0021	1.690	0.027	1003.3	29.2	1005.3	11.7	1004.6	10.0	100.1
	5-3	0.1686	0.0021	1.659	0.027	967.2	31.2	1004.6	11.8	992.8	10.5	102.6
	5-4	0.1686	0.0021	1.699	0.025	1015.5	27.5	1004.6	11.6	1008.0	9.6	99.3
	6-1	0.1686	0.0021	1.684	0.026	998.4	28.5	1004.4	11.7	1002.4	9.8	100.4
	7-1	0.1686	0.0021	1.706	0.028	1024.6	30.8	1004.4	11.8	1010.7	10.6	98.6
	7-2	0.1695	0.0022	1.694	0.029	1000.0	32.2	1009.4	11.9	1006.4	10.9	100.6
	8-1	0.1684	0.0021	1.630	0.027	933.9	31.8	1003.3	11.8	981.7	10.5	105.1
	8-2	0.1688	0.0022	1.669	0.030	978.2	34.7	1005.5	12.0	996.9	11.5	101.9
	8-3	0.1696	0.0022	1.691	0.030	994.7	33.5	1009.9	12.0	1005.0	11.3	101.0
	9-1	0.1678	0.0022	1.714	0.031	1043.3	34.0	1000.2	11.9	1013.7	11.5	97.2
	9-2	0.1690	0.0021	1.715	0.029	1031.4	31.1	1006.4	11.8	1014.2	10.7	98.3
	9-3	0.1689	0.0022	1.685	0.029	995.9	32.9	1006.1	11.9	1002.8	11.1	100.7
	9-4	0.1698	0.0023	1.694	0.036	996.9	41.4	1010.8	12.4	1006.3	13.6	100.9
	9-5	0.1684	0.0022	1.701	0.033	1021.3	37.0	1003.4	12.1	1008.9	12.4	98.8

Table 1-6: Summary of the main characteristics of the REE-rich pegmatitic granite dykes from the Lac Okaopéo region, first ordered by type of occurrence then from north to south. Abbreviations: Aln-bearing = allanite-bearing pegmatitic granite dyke; ASI = Aluminum Saturation Index given by the expression ASI = Al/(Ca – 1.67 x P + Na + K) (Frost et al., 2001; Shand, 1943); Mnz-bearing = monazite-bearing pegmatitic granite dyke.

Type of REE occurrence	Outcrop n°	Field expression	Dip	Contact	Texture (from contact towards core)	Accessory minerals[1]		Geochemical features	Geochronology (U-Pb on monazite)
						Type	REE-bearing phase composition		
Mnz-bearing	**13-AM-07**	Single dyke	Steep-dipping		Stockscheider contact – fine-grained – pegmatitic	Zircon-monazite	-		-
	13-AM-10	Single dyke	Steep-dipping	Slightly diffuse – Discordant	Homogeneous	Zircon-monazite	-	*High:* ASI, ΣLREE, La_N/Yb_N, Th, Zr/Hf, Zr and Hf, Nb/Ta	-
	13-AM-13	Single dyke	Steep-dipping		Patchy zoning (fined grained to pegmatitic)	Zircon-monazite-(Ce)(-minor garnet and Ti-oxides)	LREE-rich cores/Th-Si-rich overgrowths	*Low:* ΣHREE, Eu/Eu*, Nb and Ta *Positive correlation:* P_2O_5 and CaO with ΣREE	996.7±5.3 Ma
	13-TC-5008	Single dyke	Steep-dipping	Locally diffuse – Discordant	Patchy zoning (coarse-grained to skeletal Bt-rich)	Zircon-monazite-(Ce)(-minor garnet)	Rather homogeneous		1005.4±4.4 Ma
Aln-bearing	**13-TC-5072**	Dyke swarm	Steep-dipping	Slightly diffuse – Discordant to sub-concordant	Fine-grained – pegmatitic	Zircon-allanite-(Ce)	Homogeneous cores – Fe-rich rims	*High:* ASI, ΣLREE, La_N/Yb_N, Th, Zr/Hf, Zr and Hf, Nb/Ta *Low:* ΣHREE, Eu/Eu*, Nb and Ta *Positive correlation:* $Fe_2O_{3\ (total)}$ and MgO with ΣREE	-
	13-FS-1202	Dyke swarm	Steep-dipping	Slightly diffuse – Discordant	Patchy to layered zoning (fined grained to pegmatitic)	Zircon-allanite-(Ce)	LREE-rich/ Fe-Ca-LREE-rich cores – Si-rich/LREE-poor rims		-
	13-AE-2149	Single dyke connected to concordant/ discordant veins	Shallow-dipping	Very diffuse – Discordant to sub-concordant	Pegmatitic contacts – fine-grained core	Zircon-allanite(-rare apatite)	-	*Lower[2]:* ASI, La_N/Yb_N, Nb/Ta, Eu/Eu* *Higher[2]:* ΣLREE, ΣHREE, Zr and Hf, Nb and Ta *Intermediate[2]:* Th, Zr/Hf	-

[1] All samples are dominated by a quartz+K-feldspar+plagioclase±biotite assemblage.
[2] In comparison with the other dykes investigated in this study.

Appendix A: Detailed mapping of the monazite-bearing pegmatitic granite outcrops

A.1. 13-AM-07 monazite-bearing PGD

The 13-AM-07 monazite-bearing pegmatitic granite dyke (PGD) and REE occurrence is located in the north of the 22K/10 NTS sheet (Fig. 1-3) and is exposed as a small (a few square meters in surface) and flat lying outcrop (Fig. A-2a). The detailed map of this outcrop is available in the Fig. A-1.

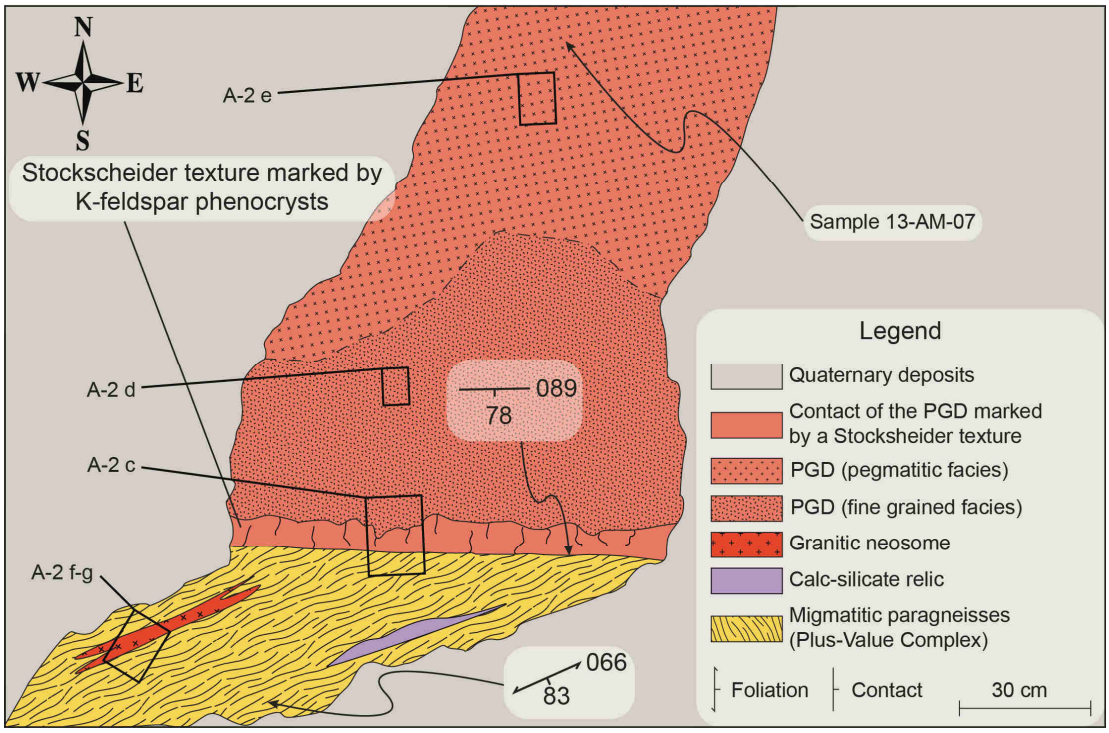

Figure A-1: Detailed map of the 13-AM-07 outcrop made of migmatitic paragneisses from the Plus-Value Complex intruded by a discordant REE-rich pegmatitic granite dyke. Abbreviation: PGD = pegmatitic granite dyke.

The PGD is steep-dipping and discordant to the foliation of the Plus-Value Complex migmatitic paragneisses (Figs. A-2b-c, 1-5a). The dyke is whitish (Figs. A-2b-e) and is layered parallel to the contact. The discordant contact with the paragneisses is marked by the development of a Stockscheider texture visible in the development of K-feldspar phenocrysts reaching a length of up to 5 cm (Fig. A-2c). From the contact and towards the core of the dyke, these phenocrysts are in contact with a 20 to 50 cm wide fine-grained facies (Figs. A-2b and d) grading onto a pegmatitic facies (Figs. A-2b and e) with crystals reaching up to ca. 3 cm in the center of the dyke.

The host paragneisses from the Plus-Value Complex are migmatitic with granitic±garnet-biotite leucosomes that can reach several tens of centimeters in width (Figs. A-2b, f-g).

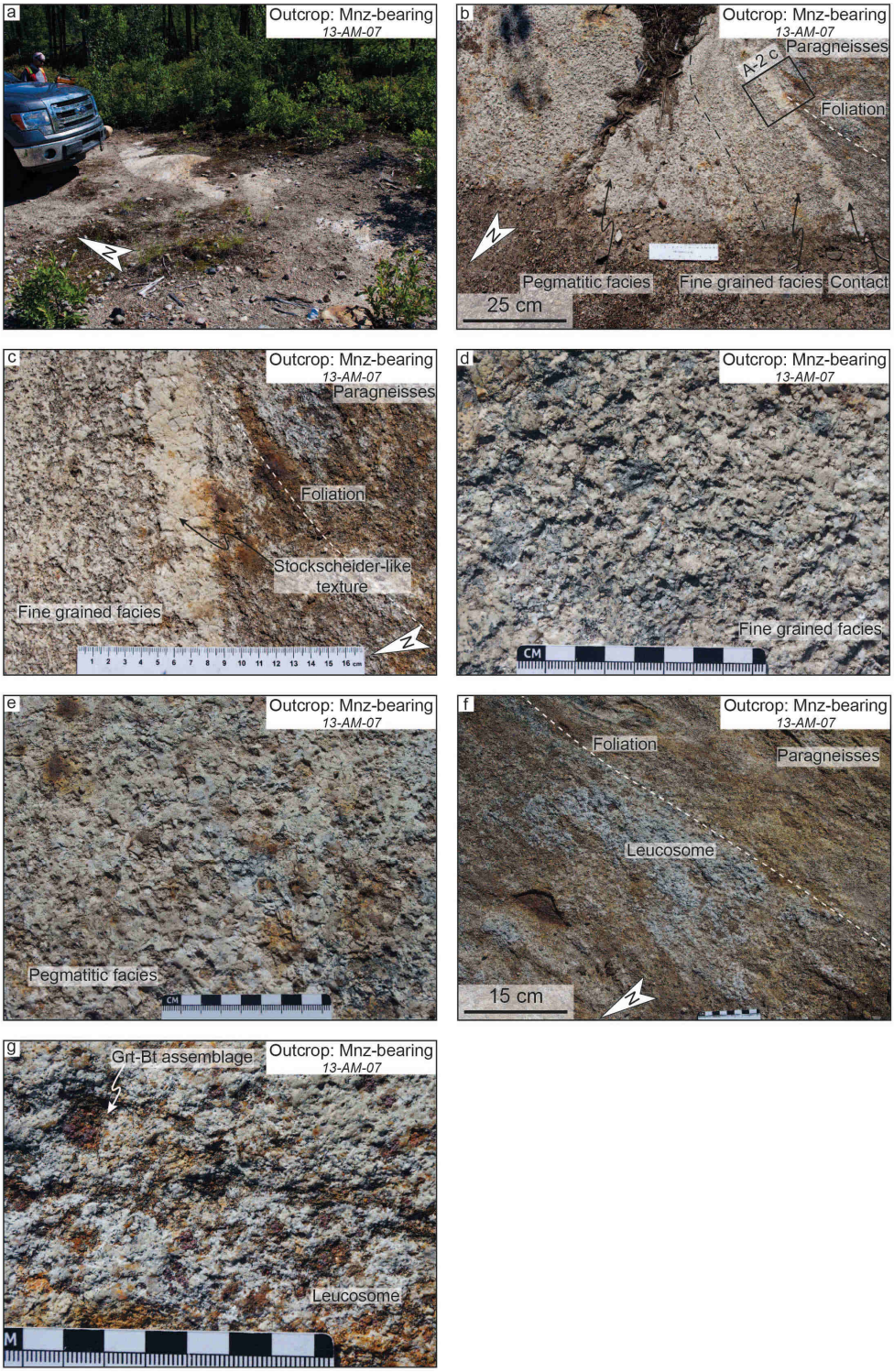

Figure A-2: Photographs of the 13-AM-07 outcrop from the Lac Okaopéo region. a: general view of the 13-AM-07 outcrop composed of a pegmatitic granite dyke intruding paragneisses from the Plus-Value Complex; b: large view of the relationships between the dyke and the paragneisses. Note the discordant contact as evidenced by the crosscut foliation of the paragneisses by the dyke; c: detailed view of Stockscheider-like contact between the pegmatitic granite dyke and the intruded paragneisses marked by the crystallization of feldspar from the dyke perpendicular to the contact; d: detailed view of the fine grained facies dominated by feldspar and quartz; e: detailed view of the pegmatitic facies dominated by feldspar and quartz; f: typical facies of the Plus-Value Complex paragneisses showing the importance of leucosomes in this facies; g: mineralogy of the leucosomes from the migmatitic Plus-Value Complex paragneisses. Note the domination of quartz-feldspar in this granitic leucosome, the abundance of the garnet-biotite assemblage expressed as several millimeters crystals and the lack of deformation in these leucosomes. Abbreviations: Bt = biotite; Grt = garnet; Mnz-bearing = monazite-bearing pegmatitic granite dyke.

A.2. 13-AM-10 monazite-bearing PGD

The 13-AM-10 monazite-bearing PGD and REE occurrence is located at the south of the 13-AM-07 outcrop, in the north of the 22K/10 NTS sheet (Fig. 1-3), and is exposed as a steep-dipping outcrop along a gravel road (Fig. A-4a). The detailed map of this outcrop is available in Fig. A-3.

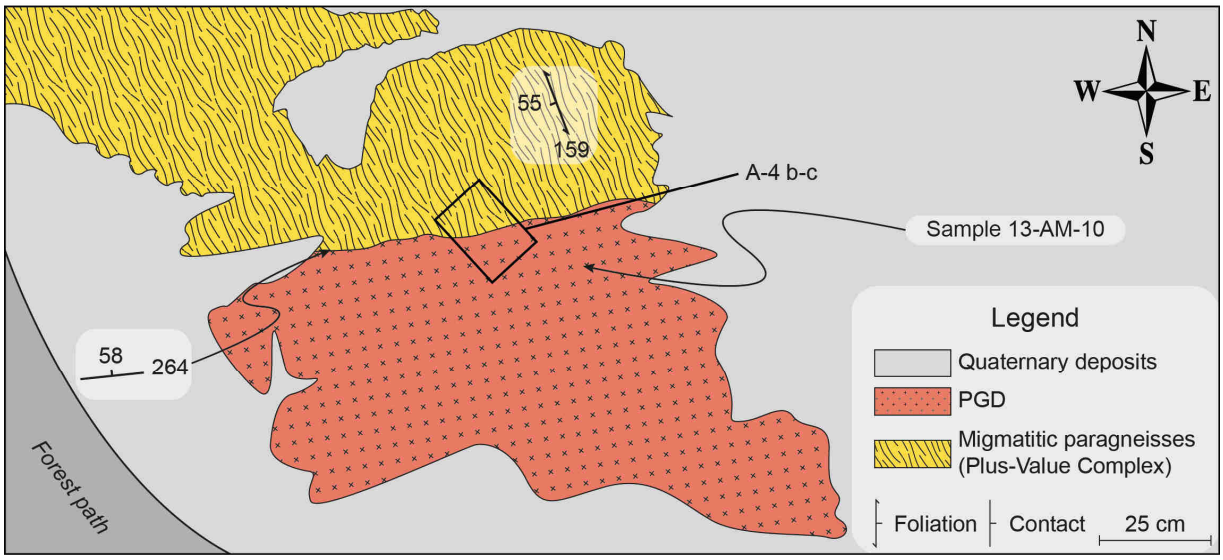

Figure A-3: Detailed map of the 13-AM-10 outcrop made of migmatitic paragneisses from the Plus-Value Complex intruded by a discordant REE-rich pegmatitic granite dyke. Abbreviation: PGD = pegmatitic granite dyke.

The PGD is steep-dipping and discordant to the rusty Plus-Value Complex migmatitic paragneisses (Figs. A-4b-c, 1-5a). The contact between the dyke and the host paragneiss is straight but is slightly diffuse (over a few millimeters, Fig. A-4b) and the dyke do not display noticeable facies variations.

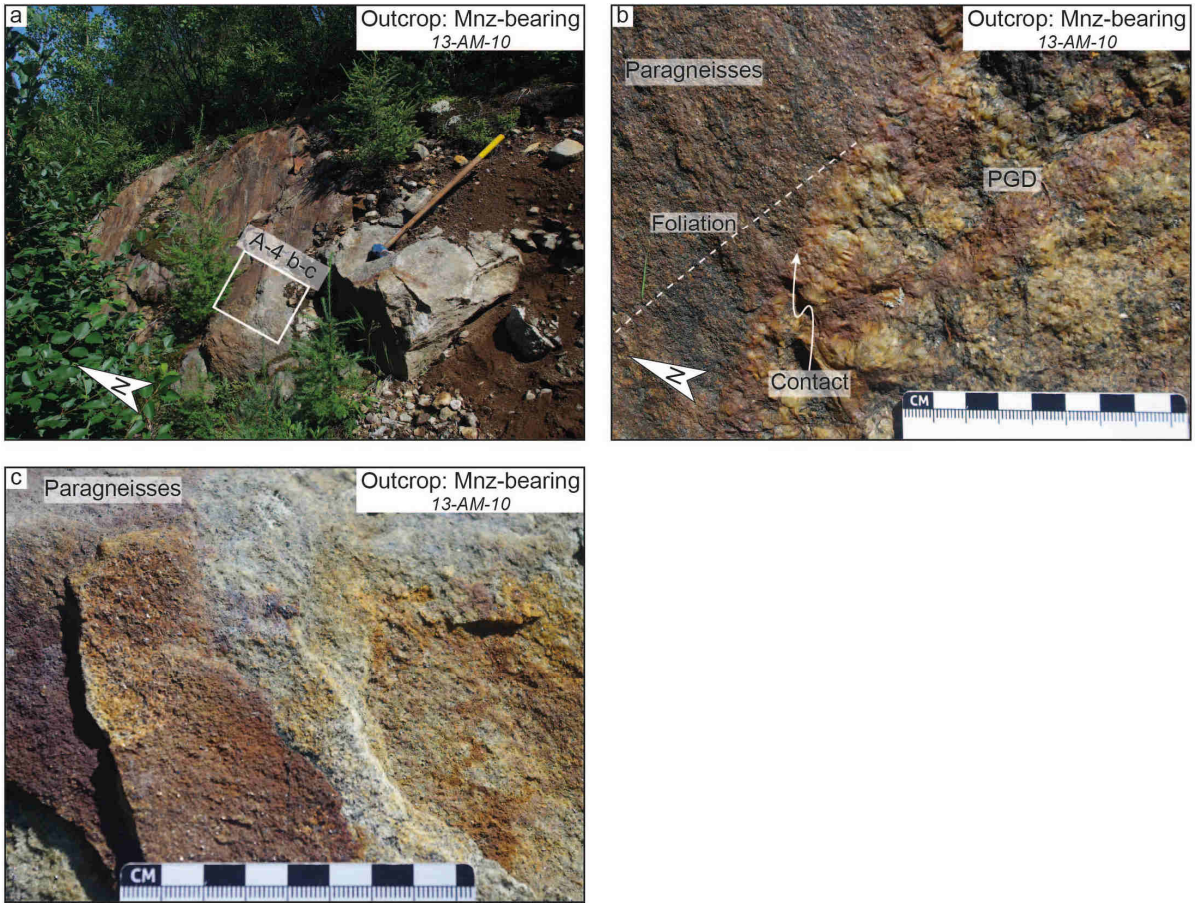

Figure A-4: Photographs of the 13-AM-10 outcrop from the Lac Okaopéo region. a: general view of the 13-AM-10 outcrop composed of a pegmatitic granite dyke intruding paragneisses from the Plus-Value Complex. The hammer is ca. 1.2 m long; b: detailed view of the relationships between the dyke and the paragneisses. The foliation is not noticeable on this photograph but its general orientation is represented; c: detailed view of the intruded paragneisses. Abbreviations: Mnz-bearing = monazite-bearing pegmatitic granite dyke; PGD = pegmatitic granite dyke.

A.3. 13-AM-13 monazite-bearing PGD

The whitish 10 to 20 meters wide 13-AM-13 monazite-bearing PGD and REE occurrence is located at the south of the 13-AM-10 outcrop, in the north of the 22K/10 NTS sheet (Fig. 1-3), and is exposed as a large flat lying outcrop (Fig. A-6a). The Fig. A-5 proposes the detailed mapping of this outcrop with localization of the samples and of the photographs presented in Fig. A-6.

The PGD is steep-dipping and discordant to the foliation of the paragneisses from the Plus-Value Complex (Fig. 1-5a). The contact between the PGD and the host paragneisses is poorly exposed but the distribution of outcrops suggests that the contact is not straight over several meters.

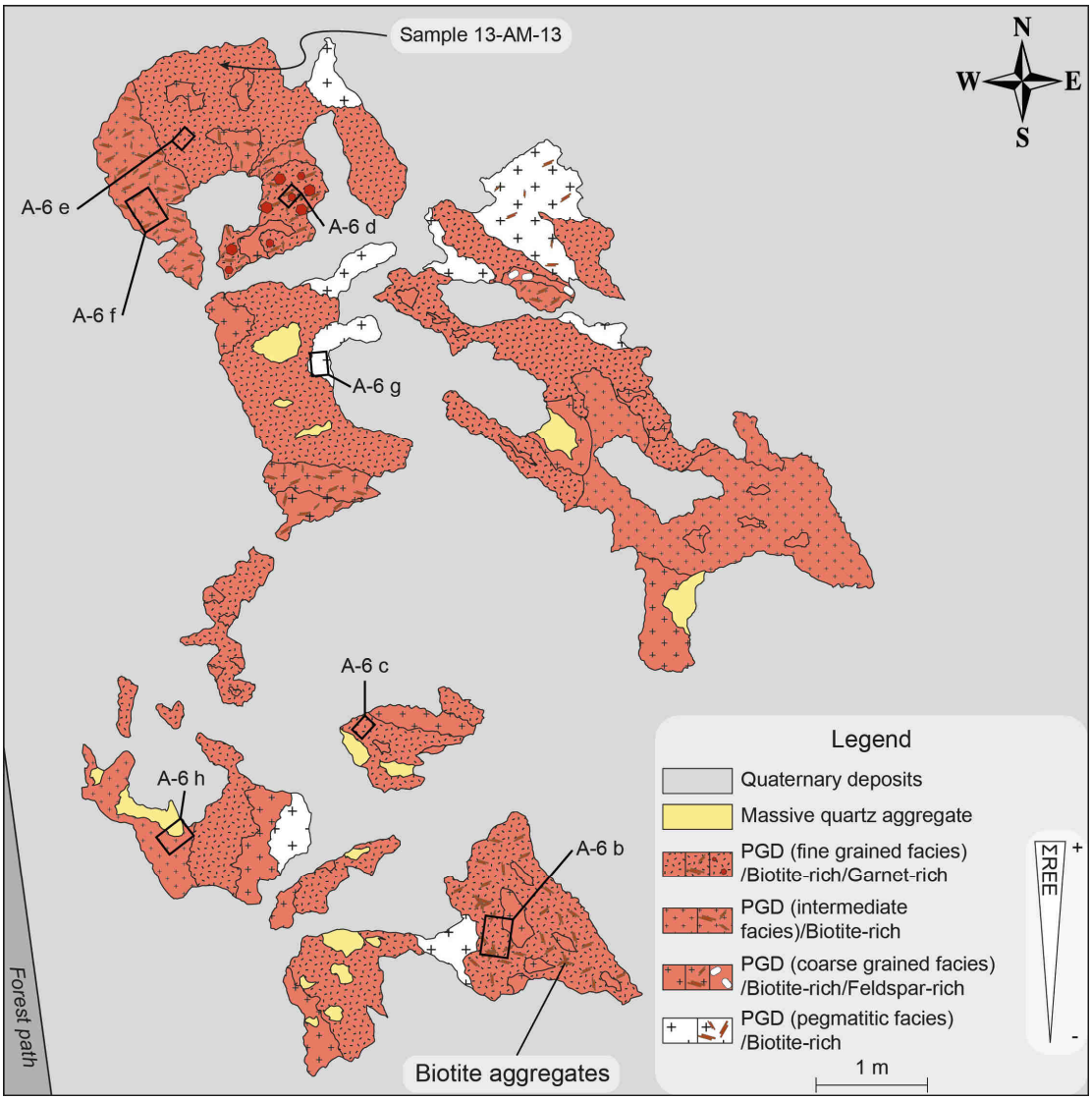

Figure A-5: Detailed map of the 13-AM-13 outcrop made of migmatitic paragneisses from the Plus-Value Complex intruded by a discordant REE-rich pegmatitic granite dyke. Abbreviation: PGD = pegmatitic granite dyke.

The PGD is dominated by a fine-grained (1 mm to sometimes over 1 cm) quartz and feldspar-rich facies with minor biotite and garnet (Figs. A-5 and 6b-e). This facies is the main host for the mineralization expressed as sub-euhedral monazite grains (Fig. A-6e). The PGD comprises randomly distributed tens of centimeters to 1 m large patchy zones characterized by (i) an intermediate quartz and feldspar-rich±biotite facies (Figs. A-5, A-6f), (ii) a coarse-grained quartz and feldspar-rich facies with more or less abundant biotite and phenocrysts of feldspar (Fig. A-6b), and (iii) a pegmatitic quartz and feldspar-rich±biotite facies (some grains over 5 cm, Fig. A-6g). Locally, up to ca. 20 cm centimeters wide quartz aggregates are also noticeable but do not seem associated with any of the previous facies (Figs. A-5 and 6h). The transition between two facies is mostly diffuse and difficult to delineate, but it may also be underlined by biotite aggregates (Fig. A-6b).

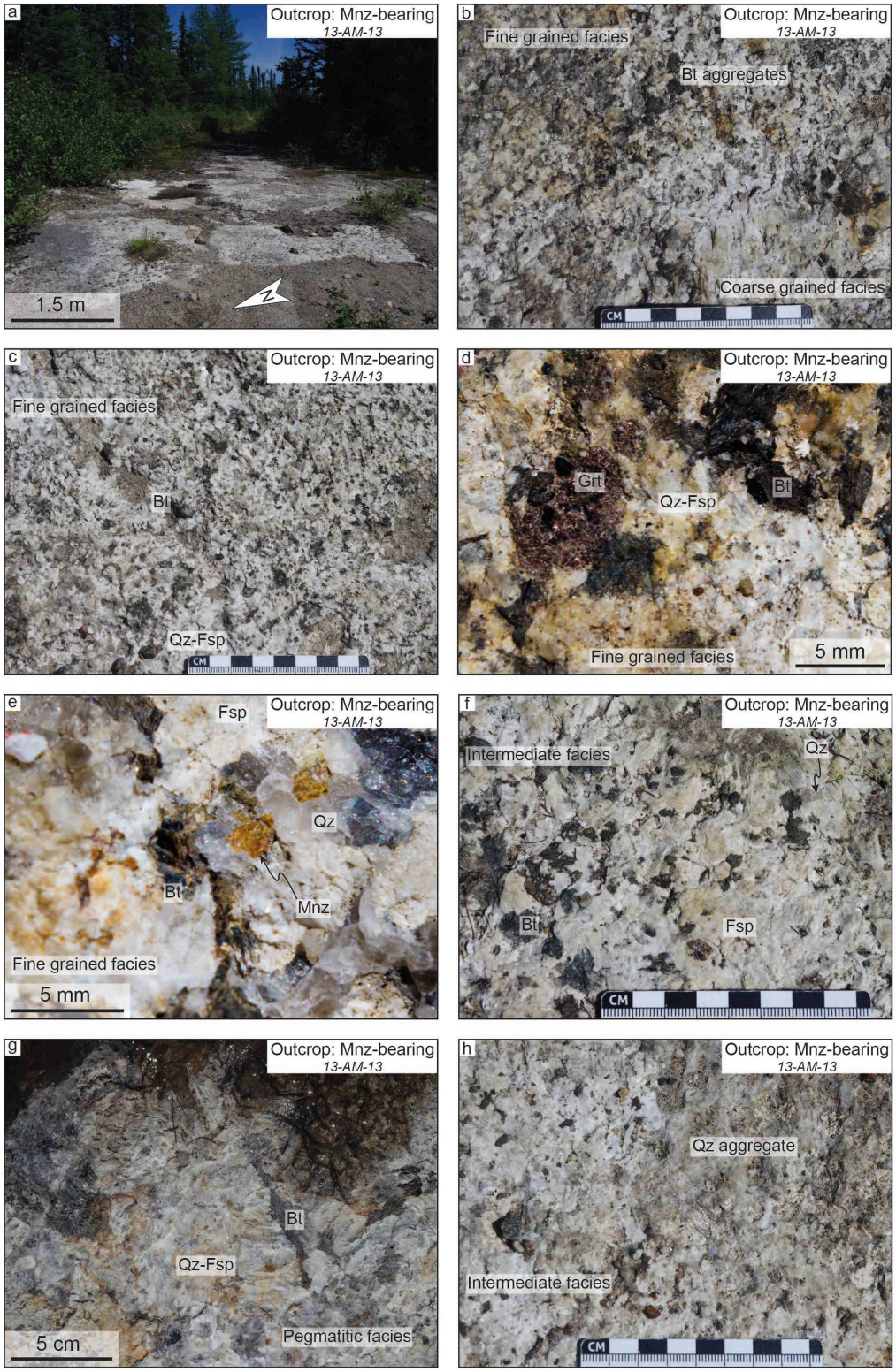

Figure A-6: Photographs of the 13-AM-13 outcrop from the Lac Okaopéo region. a: general view of the 13-AM-13 outcrop composed of a pegmatitic granite intruding paragneisses from the Plus-Value Complex; b: typical transition between the fine and coarse grained facies underlined by biotite aggregates. Note that the abundance of biotite in the fine grained facies on this photograph is related to the vicinity of the coarse grained facies; c: typical fine grained facies dominated by a quartz+feldspar±biotite assemblage; d: detailed view of a garnet phenocryst in the fine grained facies; e: monazite crystals from the fine grained facies; f: typical intermediate facies composed of a quartz-feldspar-biotite assemblage; g: typical pegmatitic facies essentially composed of a quartz-feldspar-biotite assemblage in which feldspar and biotite crystals can reach over 5 cm; h: quartz aggregates in the intermediate facies. Abbreviations: Bt = biotite; Fsp = feldspar; Grt = garnet; Mnz = monazite; Mnz-bearing = monazite-bearing pegmatitic granite dyke; Qz = quartz.

A.4. 13-TC-5008 monazite-bearing PGD

The 13-TC-5008 monazite-bearing PGD and REE occurrence is located in the north of the 22K/07 NTS sheet (Fig. 1-3) and is exposed as a large flat lying outcrop (Fig. A-8a). The Fig. A-7 proposes the detailed mapping of this outcrop with localization of the samples and of the photographs presented in Fig. A-8.

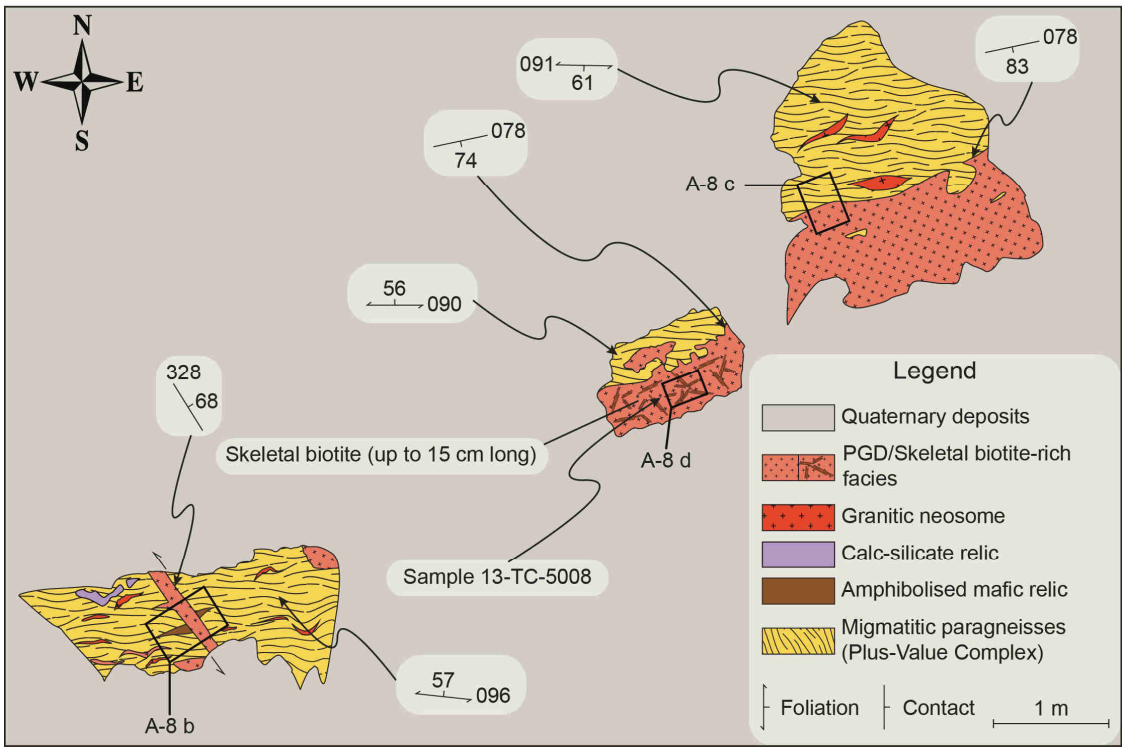

Figure A-7: Detailed map of the 13-TC-5008 outcrop made of migmatitic paragneisses from the Plus-Value Complex intruded by a discordant REE-rich pegmatitic granite dyke. Abbreviation: PGD = pegmatitic granite dyke.

The 13-TC-5008 outcrop displays several showings of a few square meters large area (Figs. A-7, A-8a) made of large or thin (ca. 10 cm wide, Fig. A-8b) steep-dipping PGD discordant to the foliation of the migmatitic paragneisses of the Plus-Value Complex (Figs. A-8b, 1-5a). The contact is locally diffuse (over a few millimeters) and is either straight or wavy (Figs. A-8b-c). It seems to represent a zone of reactions between the granitic melt and the intruded metasediments as it may be underlined in the PGD by garnet-biotite aggregates (Fig. A-8c).

The few square meters PGD showings and the thin whitish PGD do not display any zoning from the contact to their core. However, some patchy zoning made of facies enriched in skeletal biotite (cluster as arborescent arrangements of up to 15 cm biotite crystals, Fig. A-8d) are noticeable and are about a few tens of centimeters wide. The transition between these patches and the dominant facies is diffuse.

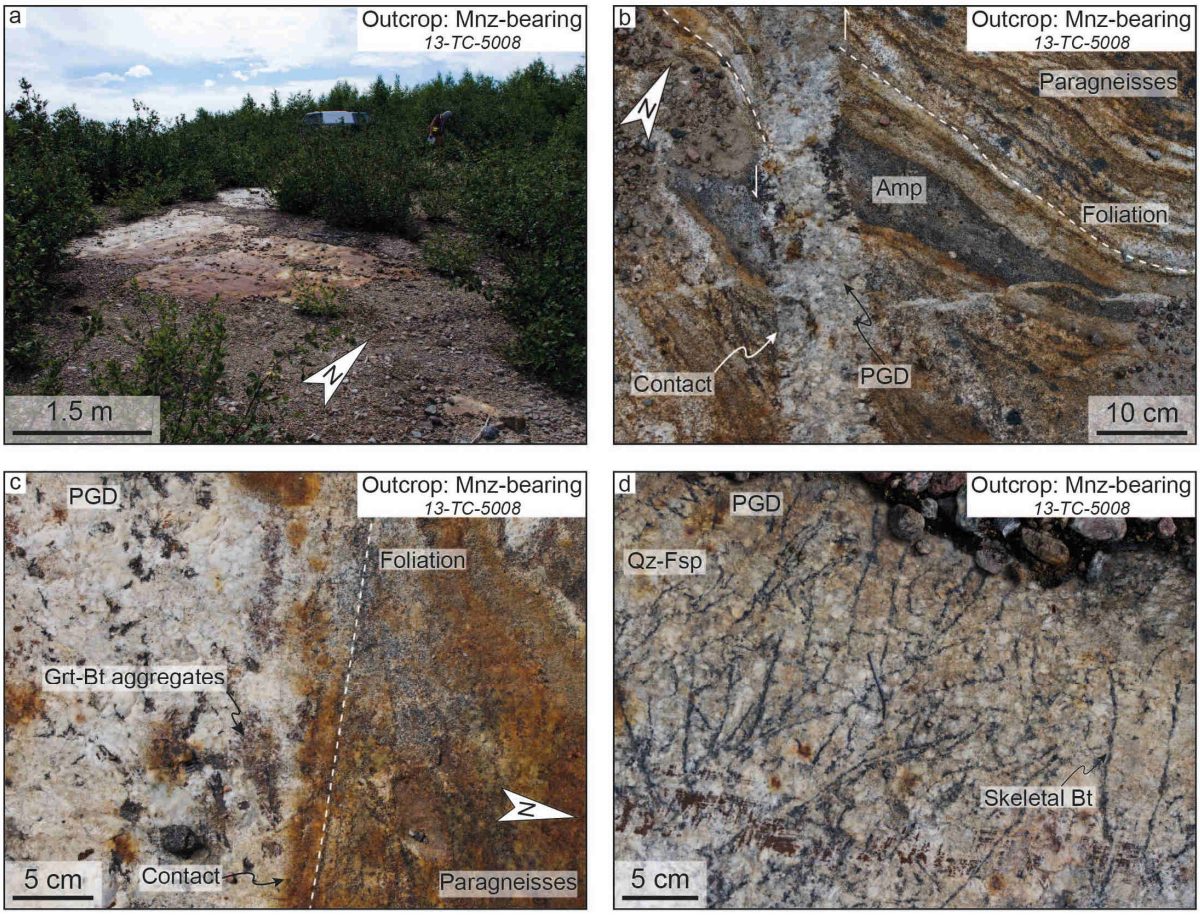

Figure A-8: Photographs of the 13-TC-5008 outcrop from the Lac Okaopéo region. a: general view of the 13-TC-5008 outcrop composed of a pegmatitic granite intruding paragneisses from the Plus-Value Complex; b: intrusion of a pegmatitic granitic dyke favored by a sinistral shearing that affect both the migmatitic paragneisses from the Plus-Value Complex and the amphibolized mafic relic it contains. The resulting contact is discordant as evidenced by the crosscut foliation of the intruded paragneisses by the dyke; c: locally diffuse contact between the dyke and the intruded paragneisses delineated by garnet-biotite aggregates; d: arborescent textures made by skeletal crystals of biotite reaching up to 15 cm long. Abbreviations: Amp = amphibolized mafic relic; Bt = biotite; Fsp = feldspar; Grt = garnet; Mnz-bearing = monazite-bearing pegmatitic granite dyke; PGD = pegmatitic granite dyke; Qz = quartz.

Appendix B: Detailed mapping of the allanite-bearing pegmatitic granite outcrops

B.1. 13-TC-5072 allanite-bearing PGD

The 13-TC-5072 allanite-bearing pegmatitic granite dyke (PGD) and REE occurrence is located in the south of the 22K/10 NTS sheet (Fig. 1-3) and is exposed as a large and dome shaped outcrop (Fig. B-2a). The detailed map of this outcrop is available in the Fig. B-1. It consists in numerous straight pinkish (fresh color) PGD (up to 4 m wide, Figs. B-1 and B-2b-f) intruding a metamonzogranite from the Bardoux Plutonic Suite.

The dykes are steep-dipping and mostly discordant to the fabric of the host metamonzogranite but are locally sub-concordant (Figs. B-2b, c and e, 1-5b). Several of these dykes may present internal zoning which typically consists in (i) a thin contact (few millimeter to a centimeter wide, zone 1, Figs. B-2b-c), followed by (ii) a ca. 20 to 30 cm wide fine grained facies (ca. < 1 mm and 2 mm, zone 2, Figs. B-2b-c), and (iii) by a coarser grain size zone (ca. 1 to 5 mm, zone 3, Figs. B-2b and d). The (iv) core of the dykes (zone 4, Figs. B-2b and d) may vary from a few centimeters to tens of centimeters wide and displays a pegmatitic texture. It is followed by (v) another fine grained facies (zone 5, Figs. B-2b, B-2d-e), which transition is quite diffuse from the later one, that ends at the boundary of the dyke by (vi) the growth of K-feldspar phenocrysts perpendicular to the contact (zone 6, Figs. B-2b and e). The whole contact is not marked by these phenocrysts that also developed in the fine grained facies with no relations with the dyke boundary (Fig. B-2e), suggesting that it does not correspond to Stockscheider textures. This kind of internal zoning in the dykes of this outcrop is quite representative as most of them display either this sequence or its repetition, probably related to several magmatic pulses. A few intrusive bodies, mostly wider than the dykes, do not display any evident zoning. Allanite grains (Fig. B-2f) are present in both zoned and unzoned intrusive bodies, and seems mostly associated with fine to medium grained facies.

The intruded metamonzogranite from the Bardoux Plutonic Suite displays various textures related to the degree of deformation it underwent, from a foliated facies with rounded rapakivi K-feldspar porphyroclasts to a mylonitic texture with elongated K-feldspar porphyroclasts (Fig. B-2g).

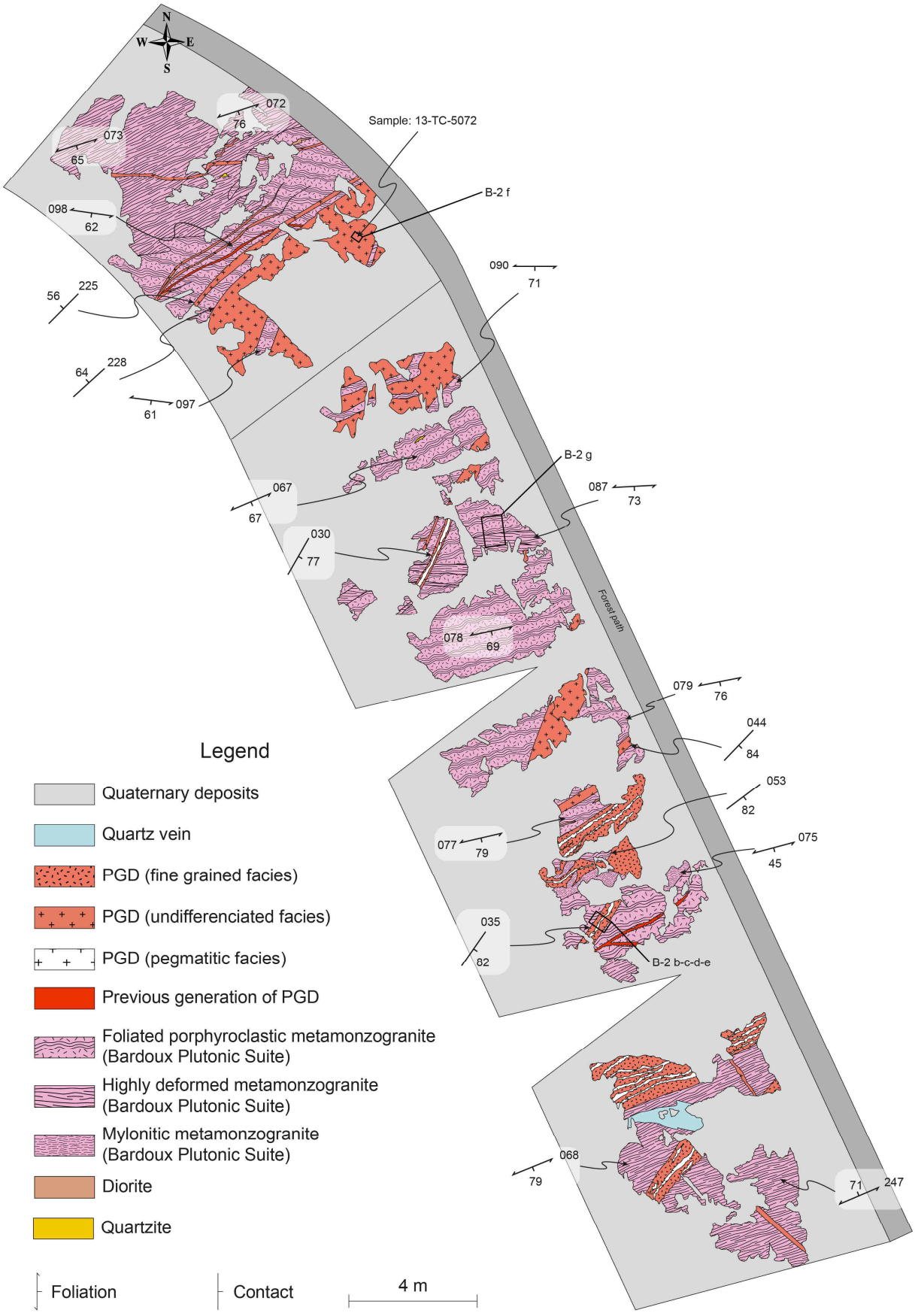

Figure B-1: Detailed map of the 13-TC-5072 outcrop made of a metamonzogranite from the Bardoux Plutonic Suite intruded by discordant REE-rich pegmatitic granite dykes. Abbreviation: PGD = pegmatitic granite dyke.

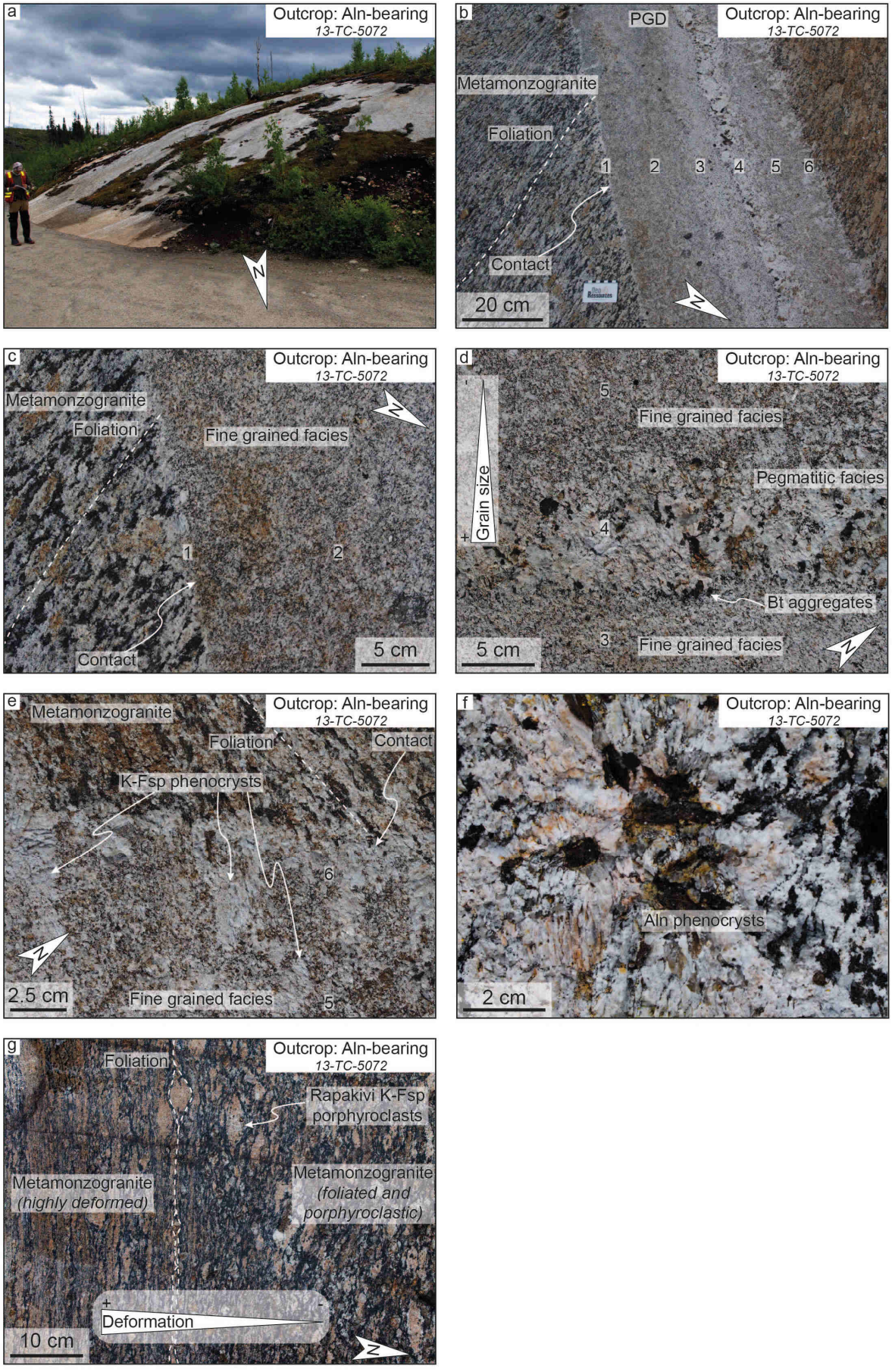
a
Outcrop: Aln-bearing
13-TC-5072
N
b
PGD
Outcrop: Aln-bearing
13-TC-5072
Metamonzogranite
Foliation
1
2
3
4
5
6
Contact
20 cm
N
c
Outcrop: Aln-bearing
13-TC-5072
Metamonzogranite
Foliation
Fine grained facies
N
1
2
Contact
5 cm
d
Outcrop: Aln-bearing
13-TC-5072
5
Fine grained facies
Pegmatitic facies
Grain size
+
4
Bt aggregates
5 cm
3
Fine grained facies
N
e
Metamonzogranite
Outcrop: Aln-bearing
13-TC-5072
Foliation
Contact
K-Fsp phenocrysts
6
N
2.5 cm
Fine grained facies
5
f
Outcrop: Aln-bearing
13-TC-5072
Aln phenocrysts
2 cm
g
Foliation
Outcrop: Aln-bearing
13-TC-5072
Rapakivi K-Fsp
porphyroclasts
Metamonzogranite
(highly deformed)
Metamonzogranite
(foliated and
porphyroclastic)
+
-
Deformation
10 cm
N

B.2. 13-FS-1202 allanite-bearing PGD

The 13-FS-1202 allanite-bearing PGD and REE occurrence is located at the south of the 13-TC-5072 PGD, in the south of the 22K/10 NTS sheet (Fig. 1-3), and is exposed as a large (several tens square meters in surface) and flat lying outcrop (Fig. B-4a). The detailed map of this outcrop is available in the Fig. B-3. It consists in numerous straight pinkish (fresh color) PGD (2-5 m wide, Figs. B-3 and B-4b) intruding a quartz metamonzodiorite from the Castoréum Plutonic Suite.

The dykes are steep-dipping and slightly to strongly discordant to the fabric of the host quartz metamonzodiorite (Fig. 1-5b). The contacts of the PGD with their hosts are straight or irregular, and are slightly diffuse (over a few millimeters). This dyke is mainly composed of quartz, feldspar and biotite and contains large allanite phenocrysts (>1 cm, Fig. B-4b). The most mineralized zone, i.e. containing the most allanite grains that may reach over 1 cm, corresponds to an intermediate facies which is layered with a pegmatitic (over 3 cm) barren facies at the contact and a finer-grained (0.1-3 cm) allanite-rich facies in the center (Fig. B-4b). The rest of the PGD does not display any sign of organization with random patches ranging from a medium grained allanite-rich facies to a coarse grained barren facies. Coarse grained to pegmatitic facies may locally present allanite aggregates.

Figure B-2: Photographs of the 13-TC-5072 outcrop from the Lac Okaopéo region. a: general view of the 13-TC-5072 outcrop composed of a pegmatitic granite intruding as a dyke swarm a metamonzogranite from the Bardoux Plutonic Suite; b: typical dyke zonation of the 13-TC-5072 pegmatitic dykes, with a southeastern boundary (1) marked by a thin zone of reaction with the host rock developed over a few millimeters with almost no biotite, followed by a fine grained facies with increasing grain size and proportions of biotite (2, 3) up to a pegmatitic core (4). This core is followed by a progressive fine grained facies with decreasing grain size zone (5). The northern contact (6) is marked by the development of K-feldspar phenocrysts perpendicular to the contact. Note that the dyke is discordant to the foliation of the intruded metamonzogranite; c: detailed view of the southern contact presented in figure b. Numbers refer to the zones identified in figure b; d: detailed view of the pegmatitic core of the dyke presented in figure b. Note the pegmatitic facies is underlined on its southern boundary by biotite aggregates whereas the northern one is opened to a fine grained facies which transition is undulating along the core. Numbers refer to the zones identified in figure b; e: detailed view of the northern contact presented in figure b. Note the diffuse boundary and the crystallization of K-feldspar phenocrysts perpendicular to the contact. Numbers refer to the zones identified in figure b; f: typical allanite phenocrysts in pegmatitic granite dykes intruding the metamonzogranite; g: typical metamonzogranite facies variations from a foliated and porphyroclastic facies where porphyroclasts of rapakivi K-feldspar are wrapped by the foliation (north) to transposed in a highly deformed facies (south). Abbreviations: Aln = allanite; Aln-bearing = allanite-bearing pegmatitic granite dyke; Bt = biotite; K-Fsp = K-feldspar; PGD = pegmatitic granite dyke.

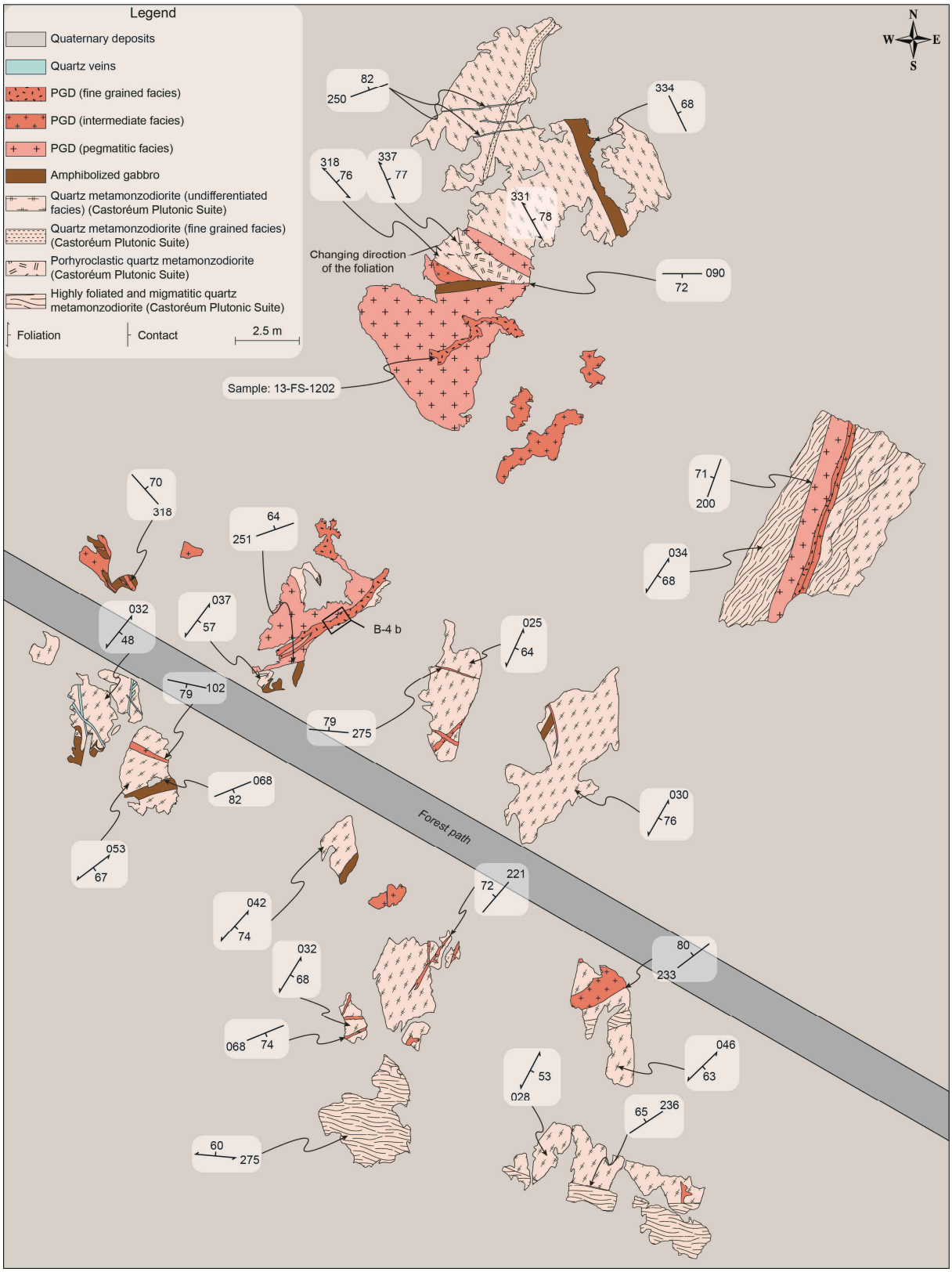

Figure B-3: Detailed map of the 13-FS-1202 outcrop made of a quartz metamonzodiorite from the Castoréum Plutonic Suite intruded by discordant REE-rich pegmatitic granite dykes. Abbreviation: PGD = pegmatitic granite dyke.

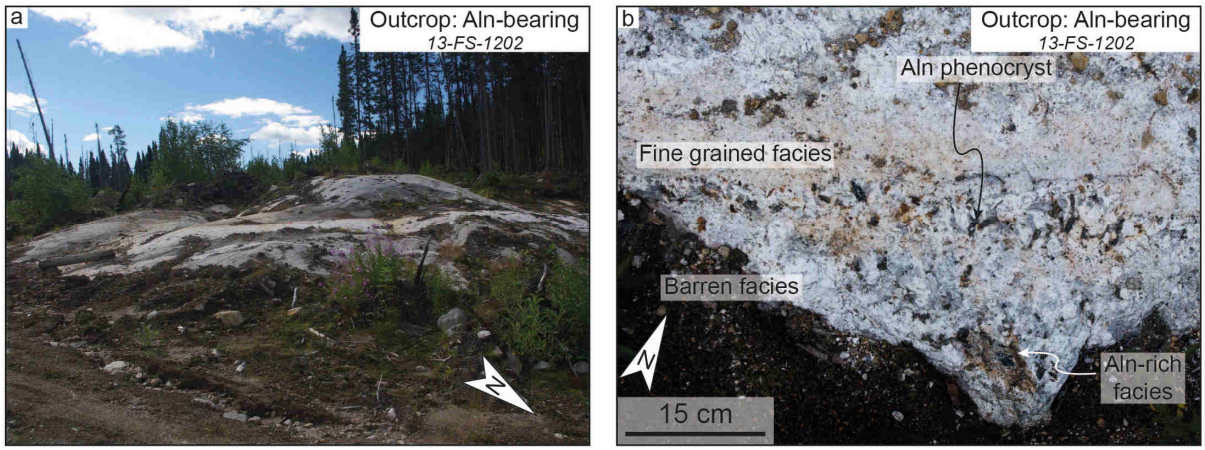

Figure B-4: Photographs of the 13-FS-1202 outcrop from the Lac Okaopéo region. a: general view of the 13-FS-1202 outcrop composed of a pegmatitic granite intruding as a dyke swarm a quartz metamonzodiorite from the Castoréum Plutonic Suite; b: detailed view of the typical zoning observed in the pegmatitic granite. Note that the allanite phenocrysts are associated with an intermediate size grained facies. Abbreviations: Aln = allanite; Aln-bearing = allanite-bearing pegmatitic granite dyke.

B.3. 13-AE-2149 allanite-bearing PGD

The 13-AE-2149 allanite-bearing PGD and REE occurrence is located in the north of the 22K/07 NTS sheet (Fig. 1-3) and is exposed as a large and steep-dipping outcrop. The detailed map of this outcrop is available in the Fig. B-5. It consists in a main straight pinkish PGD (up to ca. 1 m wide, Figs. B-5 and B-6a) intruding a layered metamangerite from the Castoréum Plutonic Suite.

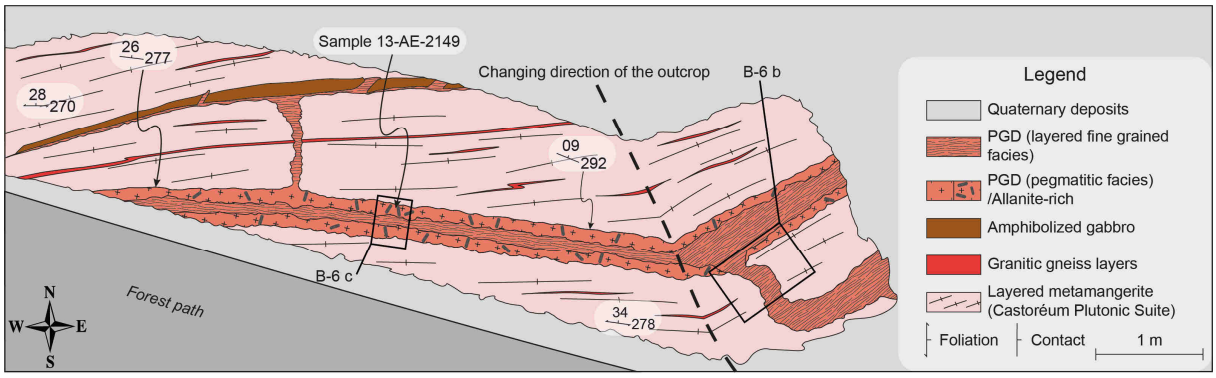

Figure B-5: Detailed map of the 13-AE-2149 outcrop made of a layered metamangerite from the Castoréum Plutonic Suite intruded by a discordant REE-rich pegmatitic granite dyke. Abbreviation: PGD = pegmatitic granite dyke.

This PGD is connected to a network of texturally continuous veins concordant and discordant to the foliation of the host layered metamangerite from the Castoréum Plutonic Suite (Fig. B-6b). The main dyke is shallow-dipping (Fig. 1-5b) and the contact between the PGD and the metamangerite is slightly discordant to locally sub-concordant and may be very diffuse (Figs. B-6c, 1-5b).

The upper contact of the dyke is marked by a ca. 20 cm wide pegmatitic facies with a grain size over 10 cm. A few large allanite phenocrysts are disseminated across this contact, and may reach over 10 cm (Fig. B-6c). The core of the dyke is composed of a layered fine grained facies composed of alternating (i) quartz-K-feldspar-rich lenses, and (ii) quartz-plagioclase-rich lenses that are generally not longer than 30 cm (Fig. B-6c). The lower contact of the dyke is similarly marked by a pegmatitic facies up to ca. 45 cm in width (Fig. B-6c). Allanite phenocrysts are up to ca. 10 cm, with a long axis mainly perpendicular to the walls of the dyke. The lower contact of the dyke with the layered metamangerite is more diffuse than at the upper contact and might reflect melt/crystal segregation (Fig. B-6c).

A few meters away from the contacts with granitic veins, the host layered metamangerite displays a homogeneous texture and structure while close to the contacts, the metamangerite grades into a migmatitic gneiss dominated by K-feldspar and clinopyroxene.

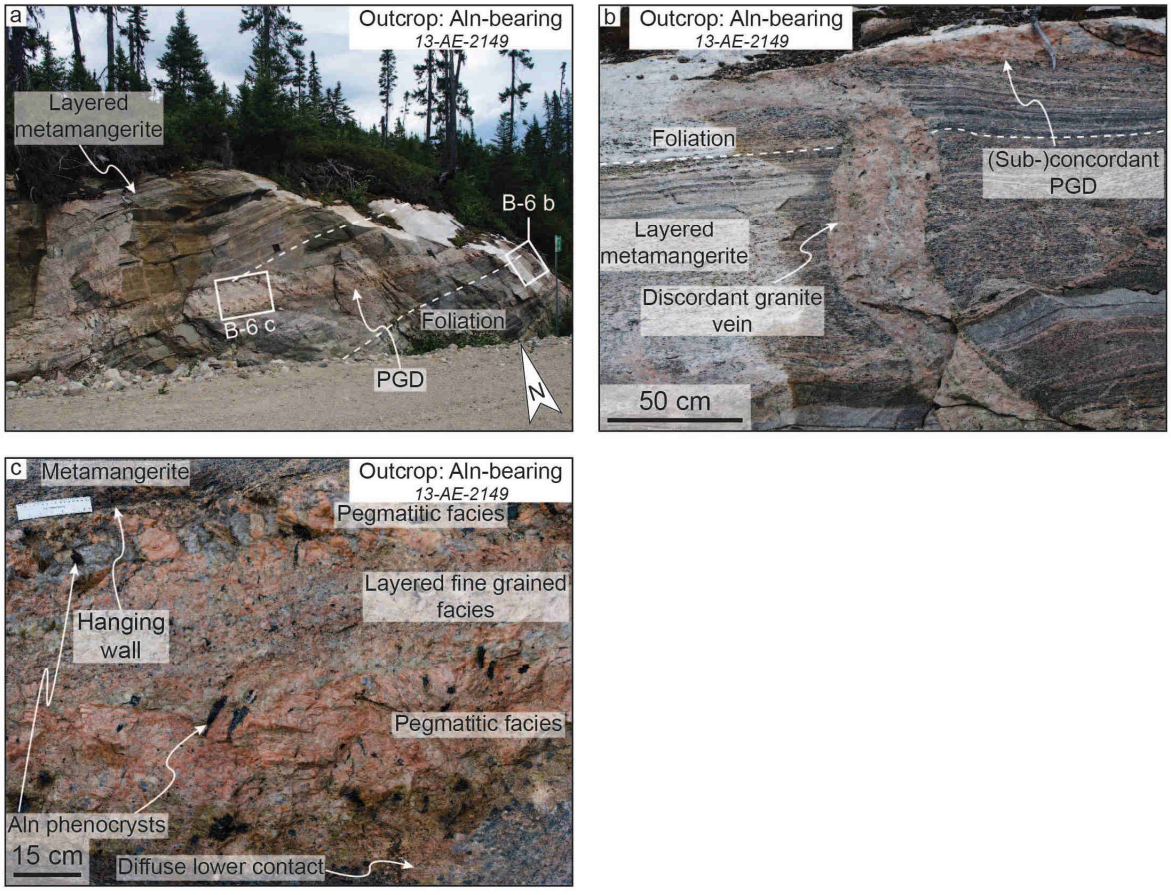

Figure B-6: Photographs of the 13-AE-2149 outcrop from the Lac Okaopéo region. a: general view of the 13-AE-2149 outcrop composed of a pegmatitic granite dyke intruding a layered metamangerite from the Castoréum Plutonic Suite; b: detailed view of one of the pegmatitic granite vein discordant to the foliation of its host rock and its connection with the main pegmatitic granite dyke expressed on this outcrop, here with a sub-concordant contact with the layered metamangerite; c: detailed view of the whole dyke zonation from its upper to its lower contact, both marked by a pegmatitic facies with large allanite phenocrysts, through a layered fine grained facies. Abbreviations: Aln = allanite; Aln-bearing = allanite-bearing pegmatitic granite dyke; PGD = pegmatitic granite dyke.

Appendix C: Planar fabrics measured on the pegmatitic granite dykes from the Lac Okaopéo region, first ordered by type of occurrence then from north to south. Planar structures are plotted in stereograms in Fig. 1-5 and are represented on detailed mapping of each outcrop from Appendices A and B.

Type of REE occurrence	***Monazite-bearing***		***Monazite-bearing***		***Monazite-bearing***		***Monazite-bearing***		***Allanite-bearing***		***Allanite-bearing***		***Allanite-bearing***	
	13-AM-07		**13-AM-10**		**13-AM-13**		**13-TC-5008**		**13-TC-5072**		**13-FS-1202**		**13-AE-2149**	
Intruded unit	**Plus-Value Complex**		**Plus-Value Complex**		**Plus-Value Complex**		**Plus-Value Complex**		**Bardoux Plutonic Suite**		**Castoréum Plutonic Suite**		**Castoréum Plutonic Suite**	
Planar structures	**Foliation[1]**	**Dyke[2]**	**Foliation[1]**	**Dyke[2]**	**Foliation[1]**	**Dyke[2]**	**Foliation[1]**	**Dyke[2]**	**Foliation[1]**	**Dyke[2]**	**Foliation[1]**	**Dyke[2]**	**Foliation[1]**	**Dyke[2]**
	Strike/Dip	**Strike/Dip**	**Strike/Dip**	**Strike/Dip**	**Strike/Dip**	**Strike/Dip**	**Strike/Dip**	**Strike/Dip**	**Strike/Dip**	**Strike/Dip**	**Strike/Dip**	**Strike/Dip**	**Strike/Dip**	**Strike/Dip**
	066/83	089/78	159/55	264/58	200/56	140/62	091/61	078/83	072/76	-	037/57	251/64	278/34	292/09
	-	-	-	-	166/62	145/65	090/56	078/74	073/65	228/64	039/48	318/70	270/28	277/26
	-	-	-	-	-	-	096/57	328/64	098/62	225/56	053/67	102/79	-	-
	-	-	-	-	-	-	-	-	097/61	-	318/76	090/72	-	-
	-	-	-	-	-	-	-	-	090/71	-	337/77	-	-	-
	-	-	-	-	-	-	-	-	067/67	-	331/78	-	-	-
	-	-	-	-	-	-	-	-	087/73	030/77	025/64	275/79	-	-
	-	-	-	-	-	-	-	-	078/69	044/84	030/76	-	-	-
	-	-	-	-	-	-	-	-	079/76	053/82	042/74	-	-	-
	-	-	-	-	-	-	-	-	077/79	035/82	032/68	221/72	-	-
	-	-	-	-	-	-	-	-	075/45	-		068/74	-	-
	-	-	-	-	-	-	-	-	068/79	-	275/60	-	-	-
	-	-	-	-	-	-	-	-	247/71	-	046/63	233/80	-	-
	-	-	-	-	-	-	-	-	-	-	028/53	-	-	-
	-	-	-	-	-	-	-	-	-	-	034/68	200/71	-	-

[1] Measures of the foliations of the intruded lithologies

[2] Measures of the contacts between the REE-rich pegmatitic granite dykes and their host rocks

Appendix D: Operating conditions for the LA-ICP-MS equipment.

	U-Pb monazite analyses
Laboratory & Sample Preparation	
Laboratory name	Géosciences Rennes, UMR CNRS 6118, Université Rennes 1, Rennes, France
Sample type/mineral	Magmatic monazite
Sample preparation	Thin-sections
Imaging	Hitachi S-4800 SEM, GeoRessources, UMR 7359, Université de Lorraine, Vandœuvre-lès-Nancy, France
Laser ablation system	
Make, Model & type	ESI NWR193UC, Excimer
Ablation cell	ESI NWR TwoVol2
Laser wavelength	193 nm
Pulse width	< 5 ns
Fluence	6.5 J/cm^{-2}
Repetition rate	2 Hz
Spot size	10 µm (round spot)
Sampling mode / pattern	Single spot
Carrier gas	100% He, Ar make-up gas and N_2 (3 ml/mn) combined using in-house smoothing device
Background collection	20 seconds
Ablation duration	60 seconds
Wash-out delay	10 seconds
Cell carrier gas flow (He)	0.75 l/min
ICP-MS Instrument	
Make, Model & type	Agilent 7700x, Q-ICP-MS
Sample introduction	Via conventional tubing
RF power	1350W
Sampler, skimmer cones	Ni
Extraction lenses	X type
Make-up gas flow (Ar)	0.87 l/min
Detection system	Single collector secondary electron multiplier
Data acquisition protocol	Time-resolved analysis
Scanning mode	Peak hopping, one point per peak
Detector mode	Pulse counting, dead time correction applied, and analog mode when signal intensity > ~ 10^6 cps
Masses measured	^{204}(Hg + Pb), ^{206}Pb, ^{207}Pb, ^{208}Pb, ^{238}U
Sensitivity / Efficiency	25000 cps/ppm Pb (50µm, 10Hz)
Dwell time per isotope	10-30 ms depending on the masses
Data Processing	
Gas blank	20 seconds on-peak
Calibration strategy	Moacir Monazite used as primary reference material, Manangoutry Monazite used as secondary reference material (quality control)
Reference Material info	Moacir (Gasquet et al., 2010) Manangoutry (Paquette and Tiepolo, 2007)
Data processing package	Glitter (Van Achterbergh et al., 2001)
Quality control / Validation	Manangoutry: 554.8 ± 4.2 Ma (MSWD=0.94; n=8) (sample 13-AM-13); 554.4 ± 3.4 Ma (MSWD=0.94; n=8) (sample 13-TC-5008)

References

Alfonso, P., Melgarejo, J.C., 2008. Fluid Evolution in the Zoned Rare-Element Pegmatite Field at Cap De Creus, Catalonia, Spain. Can. Mineral. 46, 597–617. doi:10.3749/canmin.46.3.597

Augland, L.E., Moukhsil, A., Solgadi, F., Indares, A., McFarlane, C., 2015. Pinwarian to Grenvillian magmatic evolution in the central Grenville Province: new constraints from ID-TIMS U-Pb ages and coupled Lu-Hf S-MC-ICP-MS data. Can. J. Earth Sci. 52, 701–721. doi:10.1139/cjes-2014-0232

Ayres, L.D., Černý, P., 1982. Metallogeny of granitoid rocks in the Canadian Shield. Can. Mineral. 20, 439–536.

Ballouard, C., Boulvais, P., Poujol, M., Gapais, D., Yamato, P., Tartèse, R., Cuney, M., 2015. Tectonic record, magmatic history and hydrothermal alteration in the Hercynian Guérande leucogranite, Armorican Massif, France. Lithos 220–223, 1–22. doi:10.1016/j.lithos.2015.01.027

Bea, F., 1996. Residence of REE, Y, Th and U in Granites and Crustal Protoliths; Implications for the Chemistry of Crustal Melts. J. Petrol. 37, 521–552. doi:10.1093/petrology/37.3.521

Berger, A., Rosenberg, C., Schaltegger, U., 2009. Stability and isotopic dating of monazite and allanite in partially molten rocks: examples from the Central Alps. Swiss J. Geosci. 102, 15–29. doi:10.1007/s00015-009-1310-8

Bergeron, A., 1980. Petrographie et geochimie du complexe igne alcalin de crevier et de son encaissant metasomatise (Unpublished MSc thesis). Université du Québec à Chicoutimi, Chicoutimi.

Budzyń, B., Harlov, D.E., Williams, M.L., Jercinovic, M.J., 2011. Experimental determination of stability relations between monazite, fluorapatite, allanite, and REE-epidote as a function of pressure, temperature, and fluid composition. Am. Mineral. 96, 1547–1567. doi:10.2138/am.2011.3741

Carr, S.D., Easton, R.M., Jamieson, R.A., Culshaw, N.G., 2000. Geologic transect across the Grenville orogen of Ontario and New York. Can. J. Earth Sci. 37, 193–216. doi:10.1139/e99-074

Černý, P., 1991. Rare-element Granitic Pegmatites. Part I: Anatomy and Internal Evolution of Pegmatitic Deposits. Geosci. Can. 18, 49–67.

Černý, P., 1990. Distribution, affiliation and derivation of rare-element granitic pegmatites in the Canadian Shield. Geol. Rundsch. 79, 183–226. doi:10.1007/BF01830621

Černý, P., Ercit, T.S., 2005. The classification of granitic pegmatites revisited. Can. Mineral. 43, Part 6, 2005–2026.

Černý, P., London, D., Novák, M., 2012. Granitic Pegmatites as Reflections of Their Sources. Elements 8, 289–294. doi:10.2113/gselements.8.4.289

Chappell, B.W., White, A.J.R., 2001. Two contrasting granite types: 25 years later. Aust. J. Earth Sci. 48.

Crowley, J.L., Brown, R.L., Gervais, F., Gibson, H.D., 2008. Assessing Inheritance of Zircon and Monazite in Granitic Rocks from the Monashee Complex, Canadian Cordillera. J. Petrol. 49, 1915–1929. doi:10.1093/petrology/egn047

Cuney, M., 2014. Felsic magmatism and uranium deposits. B. Soc. Geol. Fr. 185, 75–92. doi:10.2113/gssgfbull.185.2.75

David, J., 2006. Géochronologie d'échantillons provenant de Géologie Québec, année 2005-2006 - Rapport final. Ministère de l'Energie et des Ressources Naturelles, Québec GM 63236, 12 p.

David, J., Moukhsil, A., Clark, T., Hébert, C., Nantel, S., Dion, C., Sappin, A.-A., 2009. Datations U-Pb effectuées dans les provinces de Grenville et de Churchill en 2006-2007. Ministère des Ressources naturelles et de la Faune, Québec, RP2009-03, 32 p.

Dill, H.G., 2016. The CMS classification scheme (Chemical composition-Mineral assemblage-Structural geology) - linking geology to mineralogy of pegmatitic and aplitic rocks. N. Jb. Miner. Abh. (J. Min. Geochem.) 193, 231–263.

Dill, H.G., 2015. Pegmatites and aplites: Their genetic and applied ore geology. Ore Geol. Rev. 69, 417–561. doi:10.1016/j.oregeorev.2015.02.022

Dill, H.G., 2010. The "chessboard" classification scheme of mineral deposits: Mineralogy and geology from aluminum to zirconium. Earth Sci. Rev. 100, 1–420. doi:10.1016/j.earscirev.2009.10.011

Druguet, E., Castro, A., Chichorro, M., Pereira, M.F., Fernández, C., 2014. Zircon geochronology of intrusive rocks from Cap de Creus, Eastern Pyrenees. Geol. Mag. 151, 1095–1114. doi:10.1017/S0016756814000041

Dunning, G., Indares, A., 2010. New insights on the 1.7–1.0 Ga crustal evolution of the central Grenville Province from the Manicouagan – Baie Comeau transect. Precambrian Res. 180, 204–226. doi:10.1016/j.precamres.2010.04.005

Ellison, A.J., Hess, P.C., 1986. Solution behavior of +4 cations in high silica melts: petrologic and geochemical implications. Contr. Mineral. Petrol. 94, 343–351. doi:10.1007/BF00371443

Ercit, T.S., 2005. REE-enriched granitic pegmatites. Short Course Notes - Geological Association of Canada 17, 175–199.

Ford, K.L., 1982. Uraniferous pegmatites of the Sharbot Lake area, Ontario, Uranium in Granites. Geological Survey Canada, Paper 81-23.

Fowler, A.D., Doig, R., 1983. The significance of europium anomalies in the REE spectra of granites and pegmatites, Mont Laurier, Quebec. Geochim. Cosmochim. Ac. 47, 1131–1137. doi:10.1016/0016-7037(83)90243-0

Frost, B.R., Barnes, C.G., Collins, W.J., Arculus, R.J., Ellis, D.J., Frost, C.D., 2001. A geochemical classification for granitic rocks. J. Petrol. 42, 2033–2048.

Gasquet, D., Bertrand, J.-M., Paquette, J.-L., Lehmann, J., Ratzov, G., Guedes, R.D.A., Tiepolo, M., Boullier, A.-M., Scaillet, S., Nomade, S., 2010. Miocene to Messinian deformation and hydrothermal activity in a pre-Alpine basement massif of the French western Alps: new U-Th-Pb and argon ages from the Lauzière massif. B. Soc. Geol. Fr. 181, 227–241. doi:10.2113/gssgfbull.181.3.227

Gauthier, M., Chartrand, F., 2005. Metallogeny of the Grenville Province revisited. Can. J. Earth Sci. 42, 1719–1734. doi:10.1139/E05-051

Gauthier, M., Chartrand, F., Cayer, A., David, J., 2004. The Kwyjibo Cu-REE-U-Au-Mo-F Property, Quebec: A Mesoproterozoic Polymetallic Iron Oxide Deposit in the Northeastern Grenville Province. Econ. Geol. 99, 1177–1196. doi:10.2113/gsecongeo.99.6.1177

Gervais, F., Crowley, J.L., 2017. Prograde and near-peak zircon growth in a migmatitic pelitic schist of the southeastern Canadian Cordillera. Lithos 282–283, 65–81. doi:10.1016/j.lithos.2017.02.016

Gobeil, A., Hébert, C., Clark, T., Beaumier, M., Perreault, S., 2002. Géologie de la région du lac De la Blache (22K/03 et 22K/04). Ministère des Ressources Naturelles, Québec, RG 2002-01, 53 p.

Goodenough, K.M., Schilling, J., Jonsson, E., Kalvig, P., Charles, N., Tuduri, J., Deady, E.A., Sadeghi, M., Schiellerup, H., Müller, A., Bertrand, G., Arvanitidis, N., Eliopoulos, D.G., Shaw, R.A., Thrane, K., Keulen, N., 2016. Europe's rare earth element resource potential: An overview of REE metallogenetic provinces and their geodynamic setting. Ore Geol. Rev. 72, Part 1, 838–856. doi:10.1016/j.oregeorev.2015.09.019

Gower, C.F., Krogh, T.E., 2002. A U–Pb geochronological review of the Proterozoic history of the eastern Grenville Province. Can. J. Earth Sci. 39, 795–829. doi: 10.1139/E01-090

Groulier, P.-A., 2013. Étude des minéralisations en Nb-Ta du complexe igné alcalin de Crevier (Québec) (Rapport de Master), Université de Lorraine, 77 p.

Hanchar, J.M., Finch, R.J., Hoskin, P.W.O., Watson, E.B., Cherniak, D.J., Mariano, A.N., 2001. Rare earth elements in synthetic zircon: Part 1. Synthesis, and rare earth element and phosphorus doping. Am. Mineral. 86, 667–680. doi:10.2138/am-2001-5-607

Hoffman, P.F., 1989. Precambrian geology and tectonic history of North America The geology of North America. Geol. Soc. Am. : Boulder, CO, United States, United States, pp. 447–512.

Hönig, S., Čopjaková, R., Škoda, R., Novák, M., Dolejš, D., Leichmann, J., Galiová, M.V., 2014. Garnet as a major carrier of the Y and REE in the granitic rocks: An example from the layered anorogenic granite in the Brno Batholith, Czech Republic. Am. Mineral. 99, 1922–1941. doi:10.2138/am-2014-4728

Hulsbosch, N., Hertogen, J., Dewaele, S., André, L., Muchez, P., 2014. Alkali metal and rare earth element evolution of rock-forming minerals from the Gatumba area pegmatites (Rwanda): Quantitative assessment of crystal-melt fractionation in the regional zonation of pegmatite groups. Geochim. Cosmochim. Ac. 132, 349–374. doi:10.1016/j.gca.2014.02.006

Hynes, A., Indares, A., Rivers, T., Gobeil, A., 2000. Lithoprobe line 55: integration of out-of-plane seismic results with surface structure, metamorphism, and geochronology, and the tectonic evolution of the eastern Grenville Province. Can. J. Earth Sci. 37, 341–358. doi:10.1139/e99-076

Indares, A., Dunning, G., 2004. Crustal architecture above the high-pressure belt of the Grenville Province in the Manicouagan area: new structural, petrologic and U–Pb age constraints. Precambrian Res. 130, 199–228. doi:10.1016/j.precamres.2003.11.005

Indares, A., Dunning, G., 2001. Partial Melting of High-P–T Metapelites from the Tshenukutish Terrane (Grenville Province): Petrography and U–Pb Geochronology. J. Petrol. 42, 1547–1565. doi:10.1093/petrology/42.8.1547

Indares, A., Dunning, G., Cox, R., 2000. Tectono-thermal evolution of deep crust in a Mesoproterozoic continental collision setting: the Manicouagan example. Can. J. Earth Sci. 37, 325–340. doi:10.1139/e99-069

Indares, A., Dunning, G., Cox, R., Gale, D., Connelly, J., 1998. High-pressure, high-temperature rocks from the base of thick continental crust: Geology and age constraints from the Manicouagan Imbricate Zone, eastern Grenville Province. Tectonics 17, 426–440. doi:10.1029/98TC00373

Jannin, S., Gervais, F., Moukhsil, A., Crowley, J.L., Augland, L.E., In press. Datation U/Pb des déformations inverses et normales dans la Province de Grenville central (Manicouagan, Québec): évidence d'un chenal orogénique dans le Parautochtone, in: Géologie et Ressources Minérales de La Partie Centrale de La Province de Grenville; Abdelali Moukhsil Coordonnateur, Ministère de l'Énergie et Des Ressources Naturelles, Québec.

Jordan, S.L., Indares, A., Dunning, G., 2006. Partial melting of metapelites in the Gagnon terrane below the high-pressure belt in the Manicouagan area (Grenville Province): pressure–temperature (P–T) and U–Pb age constraints and implications. Can. J. Earth Sci. 43, 1309–1329. doi:10.1139/E06-038

Ketchum, J.W.F., Heaman, L.M., Krogh, T.E., Culshaw, N.G., Jamieson, R.A., 1998. Timing and thermal influence of late orogenic extension in the lower crust: a U-Pb geochronological study from the southwest Grenville orogen, Canada. Precambrian Res. 89, 25–45. doi:10.1016/S0301-9268(97)00079-X

Ketchum, J.W.F., Jamieson, R.A., Heaman, L.M., Culshaw, N.G., Krogh, T.E., 1994. 1.45 Ga granulites in the southwestern Grenville province: Geologic setting, P-T conditions, and U-Pb geochronology. Geology 22, 215–218. doi:10.1130/0091-7613(1994)022<0215:GGITSG>2.3.CO;2

Krogh, T.E., 1994. Precise U-Pb ages for Grenvillian and pre-Grenvillian thrusting of Proterozoic and Archean metamorphic assemblages in the Grenville Front tectonic zone, Canada. Tectonics 13, 963–982. doi:10.1029/94TC00801

Lasalle, S., Dunning, G., Indares, A., 2014. In situ LA–ICP–MS dating of monazite from aluminous gneisses: insights on the tectono-metamorphic history of a granulite-facies domain in the central Grenville Province. Can. J. Earth Sci. 51, 558–572. doi:10.1139/cjes-2013-0170

Lasalle, S., Fisher, C.M., Indares, A., Dunning, G., 2013. Contrasting types of Grenvillian granulite facies aluminous gneisses: Insights on protoliths and metamorphic events from zircon morphologies and ages. Precambrian Res. 228, 117–130. doi:10.1016/j.precamres.2013.01.014

Lasalle, S., Indares, A., 2014. Anatectic record and contrasting P-T paths of aluminous gneisses from the central Grenville Province. J. Metamorph. Geol. 32, 627–646. doi:10.1111/jmg.12083

Lentz, D., 1996. U, Mo, and REE mineralization in late-tectonic granitic pegmatites, southwestern Grenville Province, Canada. Ore Geol. Rev. 11, 197–227. doi:10.1016/0169-1368(95)00034-8

Lentz, D.R., 1991. Petrogenesis of uranium-, thorium-, molybdenum-, and rare earth element-bearing pegmatites, skarns, and veins in the central metasedimentary belt of the Grenville Province, Ontario and Quebec. (Unpublished Ph.D. thesis). University of Ottawa (Canada), 491 p.

Linnen, R.L., 1998. The solubility of Nb-Ta-Zr-Hf-W in granitic melts with Li and Li + F; constraints for mineralization in rare metal granites and pegmatites. Econ. Geol. 93, 1013–1025. doi:10.2113/gsecongeo.93.7.1013

Linnen, R.L., Cuney, M., 2005. Granite-related rare-element deposits and experimental constraints on Ta-Nb-W-Sn-Zr-Hf mineralization. Short Course Notes - Geological Association of Canada 17, 45–68.

Linnen, R.L., Keppler, H., 2002. Melt composition control of Zr/Hf fractionation in magmatic processes. Geochim. Cosmochim. Ac. 66, 3293–3301. doi:10.1016/S0016-7037(02)00924-9

London, D., 2016. Rare-Element Granitic Pegmatites. Rev. Econ. Geol. 18, 165–193.

London, D., 2008. Pegmatites, Can. Mineral. Spec. Publ. 10, 368 p.

London, D., 2005. Granitic pegmatites: an assessment of current concepts and directions for the future. Lithos 80, 281–303. doi:10.1016/j.lithos.2004.02.009

Ludwig, K.R., 2001. Isoplot/Ex Version 2.49. A Geochronological Toolkit for Microsoft Excel. Berkeley Geochronology Center, Special Publication vol. 1a, pp. 1–55.

Ludwig, K.R., 1998. On the Treatment of Concordant Uranium-Lead Ages. Geochim. Cosmochim. Ac. 62, 665–676. doi:10.1016/S0016-7037(98)00059-3

Lumbers, S.B., 1979. The Grenville Province of Ontario, in: 5th Ann. Meeting Int. Union Geol. Sci, Subcomm. Precamb. Stratigraphy. pp. 1–35.

Lumbers, S.B., 1964. Preliminary report on the relationship of mineral deposits to intrusive rocks and metamorphism in part of the Grenville Province of southeastern Ontario. Ont. Dep. Mines Rep. No. PR1964-4.

Martin, R.F., De Vito, C., 2005. The Patterns of Enrichment in Felsic Pegmatites Ultimately Depend on Tectonic Setting. Can. Mineral. 43, 2027–2048. doi:10.2113/gscanmin.43.6.2027

Masson, S.L., Gordon, J.B., 1981. Radioactive mineral deposits of the Pembroke-Renfrew area. Ont. Geol. Surv. Mineral Deposits Circ., No. 23.

McDonough, W.F., Sun, S. -s., 1995. The composition of the Earth. Chem. Geol. 120, 223–253. doi:10.1016/0009-2541(94)00140-4

Melcher, F., Graupner, T., Gäbler, H.-E., Sitnikova, M., Henjes-Kunst, F., Oberthür, T., Gerdes, A., Dewaele, S., 2015. Tantalum–(niobium–tin) mineralisation in African pegmatites and rare metal granites: Constraints from Ta–Nb oxide mineralogy, geochemistry and U–Pb geochronology. Ore Geol. Rev. 64, 667–719. doi:10.1016/j.oregeorev.2013.09.003

Montel, J.-M., 1993. A model for monazite/melt equilibrium and application to the generation of granitic magmas. Chem. Geol. 110, 127–146. doi:10.1016/0009-2541(93)90250-M

Moukhsil, A., Lacoste, P., Gobeil, A., David, J., 2009. Synthèse géologique de la région de Baie-Comeau. Ministère des Ressources naturelles et de la Faune, Québec, RG 2009-03, 30 p.

Moukhsil, A., Lacoste, P., Simard, M., Perreault, S., 2007. Géologie de la région septentrionale de Baie-Comeau (22F07, 22F08, 22F09, 22F15 et 22F16). Ministère des Ressources naturelles et de la Faune, Québec, RP 2007-04, 16 p.

Moukhsil, A., Solgadi, F., Belkacim, S., Elbasbas, A., Augland, L.E., 2014. Géologie de la région du lac Okaopéo, Côte-Nord. Ministère de l'Energie et des Ressources Naturelles, Québec, RG 2014-03, 34 p.

Moukhsil, A., Solgadi, F., Clark, T., Blouin, S., Indares, A., Davis, D.W., 2013a. Géologie du nord-ouest de la région du barrage Daniel-Johnson (Manic 5), Côte-Nord. Ministère des Ressources Naturelles, Québec, RG 2013-01, 46 p.

Moukhsil, A., Solgadi, F., Indares, A., Belkacim, S., 2013b. Géologie de la région septentrionale du réservoir aux Outardes 4, Côte-Nord. Ministère des Ressources Naturelles, Québec, RG 2013-03, 33 p.

Moukhsil, A., Solgadi, F., Lacoste, P., Gagnon, M., David, J., 2012. Géologie de la région du lac du Milieu (SNRC 22O03, 22O04, 22O06, 22J13 et 22J14). Ministère des Ressources Naturelles et de la Faune, Québec, RG 2012-01, 33 p.

Paquette, J.L., Tiepolo, M., 2007. High resolution (5 μm) U–Th–Pb isotope dating of monazite with excimer laser ablation (ELA)-ICPMS. Chem. Geol. 240, 222–237. doi:10.1016/j.chemgeo.2007.02.014

Perreault, S., Lafrance, B., 2015. Kwyjibo, a REE-enriched iron oxides-copper-gold (IOCG) deposit, Grenville Province, Québec. Symposium on critical and strategic materials. British Columbia Geological Survey Paper 3, 139–145.

Petrík, I., Broska, I., Lipka, J., Siman, P., 1995. Granitoid Allanite-(Ce) Substitution Relations, Redox Conditions and REE Distributions (on an Example of I-Type Granitoids, Western Carpathians, Slovakia). Geol. Carpath. 46, 79–94.

Rapp, R.P., Watson, E.B., 1986. Monazite solubility and dissolution kinetics: implications for the thorium and light rare earth chemistry of felsic magmas. Contr. Mineral. Petrol. 94, 304–316. doi:10.1007/BF00371439

Rivers, T., 2012. Upper-crustal orogenic lid and mid-crustal core complexes: signature of a collapsed orogenic plateau in the hinterland of the Grenville Province. Can. J. Earth Sci. 49, 1–42. doi:10.1139/e11-014

Rivers, T., 2009. The Grenville Province as a large hot long-duration collisional orogen – insights from the spatial and thermal evolution of its orogenic fronts. Geol. Soc., Lond., Spec. Publ. 327, 405–444. doi:10.1144/SP327.17

Rivers, T., 2008. Assembly and preservation of lower, mid, and upper orogenic crust in the Grenville Province—Implications for the evolution of large hot long-duration orogens. Precambrian Res. 167, 237–259. doi:10.1016/j.precamres.2008.08.005

Rivers, T., 1997. Lithotectonic elements of the Grenville Province: review and tectonic implications. Precambrian Res. 86, 117–154. doi:10.1016/S0301-9268(97)00038-7

Rivers, T., 1980. Revised stratigraphic nomenclature for Aphebian and other rock units, southern Labrador Trough, Grenville Province. Can. J. Earth Sci. 17, 668–670. doi:10.1139/e80-062

Rivers, T., Culshaw, N., Hynes, A., Indares, A., Jamieson, R., Martignole, J., 2012. The Grenville Orogen - A Post-LITHOPROBE Perspective, in: Tectonic Styles in Canada: The LITHOPROBE Perspective, Geological Association of Canada, Special Paper 49. J.A. Percival, F.A. Cook, and R.M. Clowes, pp. 97–236.

Rivers, T., Ketchum, J., Indares, A., Hynes, A., 2002. The High Pressure belt in the Grenville Province: architecture, timing, and exhumation. Can. J. Earth Sci. 39, 867–893. doi: 10.1139/E02-025.

Rivers, T., Martignole, J., Gower, C.F., Davidson, A., 1989. New tectonic divisions of the Grenville Province, Southeast Canadian Shield. Tectonics 8, 63–84. doi:10.1029/TC008i001p00063

Rivers, T., Schwerdtner, W., 2015. Post-peak Evolution of the Muskoka Domain, Western Grenville Province: Ductile Detachment Zone in a Crustal-scale Metamorphic Core Complex. Geosci. Can. 42, 403–436. doi:10.12789/geocanj.2015.42.080

Sangster, A.L., Gauthier, M., Gower, C.F., 1992. Metallogeny of structural zones, Grenville Province, northeastern North America. Precambrian Res. 58, 401–426. doi:10.1016/0301-9268(92)90127-A

Saucier, G., Noreau, C., Casgrain, P., Côté, P., Larochelle, E., Bilodeau, M., Hayden, A., Poirier, E., Garon, M., Bertrand, V., Kissiova, M., Malloux, M., Rouger, M., Camus, Y., Gagnon, G., 2013. NI-43-101 report-feasibility study for the Kipawa project Temiscamingue area, Québec, Canada. Matamec Explorations Inc., Montréal.

Shand, S.J., 1943. The Eruptive Rocks, 2nd edition. ed. New York: John Wiley, 444 p.

Soucy La Roche, R., Gervais, F., Tremblay, A., Crowley, J.L., Ruffet, G., 2015. Tectono-metamorphic history of the eastern Taureau shear zone, Mauricie area, Québec: Implications for the exhumation of the mid-crust in the Grenville Province. Precambrian Res. 257, 22–46. doi:10.1016/j.precamres.2014.11.012

Spear, F.S., Pyle, J.M., 2002. Apatite, Monazite, and Xenotime in Metamorphic Rocks. Rev. Mineral. Geochem. 48, 293–335. doi:10.2138/rmg.2002.48.7

Stepanov, A., Mavrogenes, J.A., Meffre, S., Davidson, P., 2014. The key role of mica during igneous concentration of tantalum. Contrib. Mineral. Petrol. 167, 1009–1016. doi:10.1007/s00410-014-1009-3

Tucker, R.D., Gower, C.F., 1994. A U-Pb geochronological framework for the Pinware Terrane, Grenville Province, Southeast Labrador. J. Geol. 102, 67–78.

Van Achterbergh, E., Ryan, C.G., Jackson, S.E., Griffin, W.L., 2001. Data reduction software for LA-ICP-MS: appendix. Laser-Ablation-ICPMS in the earth sciences—principles and applications. Mineralogical Association of Canada (short course series) 29, 239–243.

van Breemen, O., Currie, K. l., 2004. Geology and U–Pb geochronology of the Kipawa Syenite Complex — a thrust related alkaline pluton — and adjacent rocks in the Grenville Province of western Quebec. Can. J. Earth Sci. 41, 431–455.

van Gool, J.A.M., Rivers, T., Calon, T., 2008. Grenville Front zone, Gagnon terrane, southwestern Labrador: Configuration of a midcrustal foreland fold-thrust belt. Tectonics 27, TC1004. doi:10.1029/2006TC002095

Van Lichtervelde, M., Grand'Homme, A., Saint-Blanquat, M. de, Olivier, P., Gerdes, A., Paquette, J.-L., Melgarejo, J.C., Druguet, E., Alfonso, P., 2016. U-Pb geochronology on zircon and columbite-group minerals of the Cap de Creus pegmatites, NE Spain. Miner. Petrol., 1–21. doi:10.1007/s00710-016-0455-1

White, A.J.R., Chappell, B.W., 1977. Ultrametamorphism and granitoid genesis. Tectonophysics 43, 7–22. doi:10.1016/0040-1951(77)90003-8

Zaraisky, G.P., Aksyuk, A.M., Devyatova, V.N., Udoratina, O.V., Chevychelov, V.Y., 2009. The Zr/Hf ratio as a fractionation indicator of rare-metal granites. Petrol. 17, 25. doi:10.1134/S0869591109010020

PARTIE II : CONTEXTE GÉODYNAMIQUE ET TRAÇAGE DE LA SOURCE

Préambule

Turlin et al. (2017) ont décrit sept dykes de granite pegmatitique (« PGD ») à terres rares intrudant des complexes métasédimentaires (PGD à monazite) ou métaplutoniques (PGD à allanite). Parmi ces PGD, l'un d'eux (13-AE-2149) présente des caractéristiques structurales, texturales et géochimiques distinctes des six autres et ne sera pas discuté dans cette partie.

1. Évolution thermique du segment crustal moyenne-basse pression de la ceinture Allochtone intrudé par les PGD

Les six autres PGD présentés par Turlin et al. (2017) ont des contacts principalement discordants et fortement pentés, présentent des textures magmatiques sans déformation à l'état solide, compatibles avec leur caractère intrusif dans les séries métasédimentaires et les métaplutons hôtes (Turlin et al., 2017). L'un de ces dykes (13-TC-5008) présente un contact lobé avec son encaissant métasédimentaire sans évidence de métamorphisme de contact ni d'échange thermique. Les âges à ~1005-1000 Ma sur monazites de deux de ces PGD, et en particulier du PGD 13-TC-5008, ont été interprétés par Turlin et al. (2017) comme représentant l'âge de cristallisation des PGD. Celui-ci est postérieur au pic de métamorphisme Ottawan (~1070-1050 Ma) affectant ce segment moyenne-basse pression de la ceinture Allochthone (aM-L*P*) hôte des PGD (Lasalle et al., 2014). L'âge du pic de métamorphisme a été contraint par la datation U-Pb de monazites prograde en inclusions dans des grenats péritectiques des paragneiss migmatitiques du Complexe de la Plus-Value, hôtes de plusieurs PGD. Les mêmes monazites présentent des couronnes datées à ~1010-990 Ma, interprétées comme datant des circulations fluides au faciès schistes verts au cours du trajet *P-T* rétrograde, c'est-à-dire dans des conditions subsolidus (Lasalle et al., 2014). Ces résultats sont en contradiction avec les relations de terrain observées pour le PGD 13-TC-5008 dont le contact avec son encaissant métasédimentaire suggère une intrusion dans des conditions proches du solidus hydraté. Cette contradiction soulève la question suivante : ce segment de croûte allochtone a-t-il enregistré un pic de métamorphisme dans des conditions suprasolidus entre ~1070 et 1050 Ma suivi d'un refroidissement rapide jusque dans des conditions subsolidus dès ~1010 Ma, ou ce trajet rétrograde est-il associé à des taux de refroidissements plus lents préservant des conditions suprasolidus jusqu'à l'intrusion des PGD à ~1005 Ma ?

Le premier chapitre de cette partie (***chapitre 2***) se focalise sur l'étude des paragneiss migmatitiques du Complexe de la Plus-Value de l'affleurement 13-TC-5008. Les (i) relations de terrain entre les paragneiss et le PGD sont couplées (ii) aux informations pétrographiques,

(iii) texturales et (iv) géochronologiques (U-Pb sur monazite et apatite) des leucosomes des paragneiss, et (v) aux contraintes géochronologiques du métamorphisme présentées dans la littérature sur les gneiss alumineux de ce même segment crustal. L'ensemble de ces données est réintégrée dans un modèle temps vs température permettant de proposer une nouvelle interprétation de l'évolution thermique de ce segment crustal.

2. Traçage de la source des PGD

Les âges sur monazite de deux PGD à ~1005-1000 Ma présentés par Turlin et al. (2017) sont synchrones de l'initiation de l'épaississement crustal Rigolet associé à un métamorphisme de haut grade jusque dans les conditions de la fusion partielle dans la ceinture Parautochtone sous-jacente (~1005-960 Ma) (Jannin et al., sous presse ; Rivers et al., 2012). Le caractère fortement peralumineux de ces PGD et les rapports Nb/Ta élevés associés à de faibles concentrations de Nb et de Ta ont été interprété par Turlin et al. (2017) comme le résultat de la fusion partielle d'une source métasédimentaire dont l'âge et l'appartenance (ceinture Allochtone ou Parautochtone) restent à déterminer.

Le couplage des données isotopiques U-Pb-Hf-O aux éléments traces des zircons a prouvé son efficacité dans le traçage de l'âge et de la nature de la source des zircons considérés (par exemple Belousova et al., 2010 ; Cawood et al., 2013 ; Dhuime et al., 2012 ; Eglinger et al., 2017 ; Hawkesworth et al., 2009, 2010 ; Hawkesworth et Kemp, 2006 ; Ibanez-Mejia et al., 2015 ; Spencer et al., 2015 ; Zeh et al., 2014).

Le deuxième chapitre de cette partie (***chapitre 3***) présente des données isotopiques U-Pb-Hf-O et d'éléments traces de zircons d'un PGD à monazite (13-AM-13) et de deux PGD à allanite (13-TC-5072 et 13-FS-1202). Couplées à la texture des grains analysés, ces données permettent (i) de démontrer l'absence d'héritage chimique et isotopique des zircons et ainsi de discuter (ii) l'âge de cristallisation de ces PGD en le comparant aux âges sur monazite présentés par Turlin et al. (2017), et (iii) la nature et l'âge de la source. Cette étude permet de réintégrer les PGD dans l'évolution géodynamique du Grenville central.

Références

Belousova, E.A., Kostitsyn, Y.A., Griffin, W.L., Begg, G.C., O'Reilly, S.Y., Pearson, N.J., 2010. The growth of the continental crust: Constraints from zircon Hf-isotope data. Lithos 119, 457–466. doi:10.1016/j.lithos.2010.07.024

Cawood, P.A., Hawkesworth, C.J., Dhuime, B., 2013. The continental record and the generation of continental crust. GSA Bulletin 125, 14–32. doi:10.1130/B30722.1

Dhuime, B., Hawkesworth, C.J., Cawood, P.A., Storey, C.D., 2012. A Change in the Geodynamics of Continental Growth 3 Billion Years Ago. Science 335, 1334–1336. doi:10.1126/science.1216066

Eglinger, A., Thébaud, N., Zeh, A., Davis, J., Miller, J., Parra-Avila, L.A., Loucks, R., McCuaig, C., Belousova, E., 2017. New insights into the crustal growth of the Paleoproterozoic margin of the Archean Kéména-Man domain, West African craton (Guinea): Implications for gold mineral system. Precambrian Research 292, 258–289. doi:10.1016/j.precamres.2016.11.012

Hawkesworth, C., Cawood, P., Kemp, T., Storey, C., Dhuime, B., 2009. A Matter of Preservation. Science 323, 49–50. doi:10.1126/science.1168549

Hawkesworth, C.J., Dhuime, B., Pietranik, A.B., Cawood, P.A., Kemp, A.I.S., Storey, C.D., 2010. The generation and evolution of the continental crust. Journal of the Geological Society 167, 229–248. doi:10.1144/0016-76492009-072

Hawkesworth, C.J., Kemp, A.I.S., 2006. Using hafnium and oxygen isotopes in zircons to unravel the record of crustal evolution. Chemical Geology, Special Issue in Honour of R.K. O'Nions 226, 144–162. doi:10.1016/j.chemgeo.2005.09.018

Ibanez-Mejia, M., Pullen, A., Arenstein, J., Gehrels, G.E., Valley, J., Ducea, M.N., Mora, A.R., Pecha, M., Ruiz, J., 2015. Unraveling crustal growth and reworking processes in complex zircons from orogenic lower-crust: The Proterozoic Putumayo Orogen of Amazonia. Precambrian Research 267, 285–310. doi:10.1016/j.precamres.2015.06.014

Jannin, S., Gervais, F., Moukhsil, A., Crowley, J.L., Augland, L.E., in press. Datation U/Pb des déformations inverses et normales dans la Province de Grenville central (Manicouagan, Québec): évidence d'un chenal orogénique dans le Parautochtone, in: Géologie et Ressources Minérales de La Partie Centrale de La Province de Grenville; Abdelali Moukhsil Coordonnateur, Ministère de l'Énergie et Des Ressources Naturelles, Québec.

Lasalle, S., Dunning, G., Indares, A., 2014. In situ LA–ICP–MS dating of monazite from aluminous gneisses: insights on the tectono-metamorphic history of a granulite-facies domain in the central Grenville Province. Can. J. Earth Sci. 51, 558–572. doi:10.1139/cjes-2013-0170

Rivers, T., Culshaw, N., Hynes, A., Indares, A., Jamieson, R., Martignole, J., 2012. The Grenville Orogen - A Post-LITHOPROBE Perspective, in: Tectonic Styles in Canada: The LITHOPROBE Perspective, Geological Association of Canada, Special Paper 49. J.A. Percival, F.A. Cook, and R.M. Clowes, pp. 97–236.

Spencer, C.J., Cawood, P.A., Hawkesworth, C.J., Prave, A.R., Roberts, N.M.W., Horstwood, M.S.A., Whitehouse, M.J., 2015. Focus paper: Generation and preservation of continental crust in the Grenville Orogeny. Geoscience Frontiers 6, 357–372. doi:10.1016/j.gsf.2014.12.001

Turlin, F., André-Mayer, A.-S., Moukhsil, A., Vanderhaeghe, O., Gervais, F., Solgadi, F., Groulier, P.-A., Poujol, M., 2017. Unusual LREE-rich, peraluminous, monazite- or allanite-bearing pegmatitic granite in the central Grenville Province, Québec. Ore Geology Reviews 89, 627–667. doi:10.1016/j.oregeorev.2017.04.019

Zeh, A., Stern, R.A., Gerdes, A., 2014. The oldest zircons of Africa—Their U–Pb–Hf–O isotope and trace element systematics, and implications for Hadean to Archean crust–mantle evolution. Precambrian Research 241, 203–230. doi:10.1016/j.precamres.2013.11.006

Chapitre 2 : A record of 70 Ma suprasolidus conditions in the Grenville large, hot and long-duration orogen

François Turlin[1], Clara Deruy[1], Aurélien Eglinger[1], Olivier Vanderhaeghe[2], Anne-Sylvie André-Mayer[1], Marc Poujol[3], Abdelali Moukhsil[4], Fabien Solgadi[4]

Article soumis à *Terra Nova*

[1] GeoRessources lab., UMR 7359, Université de Lorraine, CNRS, CREGU, Faculté des Sciences et Technologies, Vandœuvre-lès-Nancy, F-54506, France

[2] Géosciences Environnement Toulouse, GET, Université de Toulouse, CNRS, IRD, UPS, CNES (Toulouse), France

[3] Géosciences Rennes, UMR 6118, OSUR, Université de Rennes 1, 35042 Rennes Cedex, France

[4] Ministère de l'Énergie et des Ressources naturelles, Direction du Bureau de la connaissance géoscientifique du Québec (Canada)

Abstract

In this paper, we use petrochronology of magmatic monazite and apatite from a single paragneiss leucosome to document the thermal evolution of the Allochthonous Belt of the central Grenville Province. Monazite records suprasolidus metamorphism from ca. 1080 to 1020 Ma under high temperature up to 850°C. Apatite from the same leucosome dated at ca. 960 Ma is consistent with constant cooling of this crustal segment down to subsolidus conditions of ca. 450°C. A pegmatitic granite dyke, with lobate contacts, dated at ca. 1005 Ma is interpreted to intrude the paragneisses at a temperature of ca. 650°C close to the wet-solidus. These data document slow cooling at a rate of 2 to 6°C/Ma for the middle crust of the Grenville orogenic belt marked by protracted suprasolidus conditions for at least 70 Ma. We propose to define this type of orogenic belts as a large, hot and long-duration orogen.

Keywords: Large hot and long duration orogens; Suprasolidus conditions; Petrochronology; Monazite/Apatite; Grenville Province

1. Introduction

Petrochronology term was recently defined to describe the consideration of the texture of dated minerals in order to decrypt geological processes (Engi et al., 2017). Using petrochronological data coupled with thermo-mechanical models provides new clues to decipher the evolution of crustal orogenic belts (e.g. Vanderhaeghe, 2012; Brown, 2014). The timing and duration of metamorphic processes in a variety of tectonothermal environments are still debated, especially for continental collisions marked by high temperature metamorphism (e.g. Kohn, 2008; Johnson *et al.*, 2015). The main question is how long the rocks remained at suprasolidus temperatures in the middle-lower crust during the history of large, hot and long-duration orogens controlled by flow of a partially molten root such as the Tibetan orogenic plateau (Nelson et al., 1996; Vanderhaeghe, 2009).

The exhumed orogenic root of the Proterozoic Grenville Province exposes high-grade metamorphic rocks mainly in Québec and Ontario (Canada) that offer a unique opportunity to investigate the deep crustal processes occurring during a long-lived continental collision. These highly deformed and metamorphosed rocks underwent protracted granulite-facies conditions under an orogenic plateau similar to the present Tibetan plateau (e.g. Indares and Dunning, 2004; Rivers, 2008; Rivers *et al.*, 2012). Suprasolidus growth of monazite has been documented in aluminous gneisses from the mid- to low-pressure segment of the Allochthonous Belt (aM-L*P*) from the central Grenville during a ca. 1070-1020 Ma moderate clockwise *P-T-t* path (Lasalle et al., 2014; Lasalle and Indares, 2014). However, the actual duration of suprasolidus conditions in this aM-L*P* segment remains unconstrained. Original LA-ICP-MS U-Th-Pb dating of monazite and apatite from a single leucosome sampled in migmatitic paragneisses of the Allochthonous Belt of the central Grenville Province (Plus-Value Complex, Fig. 2-1) will be compared to data from anatectic aluminous gneisses from the same aM-L*P* segment of the same area to explore the petrochronology of both monazite and apatite in this high-grade terrane under protracted suprasolidus conditions.

2. Monazite-apatite crystallization and cooling in anatectic aluminous gneisses

2.1. *P-T-t* record of the central Grenville

The Grenvillian Orogeny has been described as a two-stage late-Mesoproterozoic to early-Neoproterozoic continental collision involving the Laurentian and Amazonian cratons (Rivers, 2008; Rivers et al., 2012). The oldest Ottawan tectonic phase with ages spreading from ca. 1090 to 1020 Ma is interpreted as a long-lived period of crustal thickening associated with

the formation of hot ductile mid-crust layer above the Allochthon Boundary Thrust (ABT), inferred to have played the role of a shallow-dipping crustal scale ramp during syn-Ottawan crustal lateral extrusion (Rivers, 2008; Rivers et al., 2012). In the aM-L*P* segment south of the Manicouagan Reservoir, the Ottawan high-grade peak of metamorphism is recorded as a moderate-gradient *P-T* path, up to sillimanite-grade conditions, of ca. 950 MPa and 850°C, corresponding to the thermal peak (Lasalle and Indares, 2014; Rivers et al., 2012). Several studies investigated the timing of the Ottawan phase using monazite U-Pb dating from anatectic gneisses (metapelites and aluminous gneisses, Fig. 2-1, Dunning and Indares, 2010; Lasalle *et al.*, 2014). A group of ages at ca. 1080-1020 Ma is dominated by a cluster at ca. 1070-1050 Ma (maximum temperature), and with ages spreading down to ca. 1025 Ma (LA-ICP-MS, Lasalle et al., 2014) and 1020±2 Ma (ID-TIMS, Dunning and Indares, 2010). These ages are recorded by (i) prograde monazite grains shielded in peritectic garnet ($^{207}Pb/^{206}Pb$ ages as old as 1098±38 Ma, Lasalle et al., 2014, and by (ii) monazite grains from the matrix. The complex dissolution/precipitation textures of monazite from the matrix and the large range of ages was interpreted as the consequence of distinct monazite growth events in response to several melt crystallization pulses. In contrast, in the western Grenville, a similar spread of zircon U-Pb ages between ca. 1090 and 1040 Ma was interpreted as reflecting a 20 to 30 Ma long partial melting event at mid-crust level (Slagstad et al., 2004).

In aluminous gneisses from the central Grenville, a younger group of ages at ca. 1010-990 Ma is restricted to rims of monazite from the matrix and has been attributed to fluid circulations under greenschist-facies *P-T* conditions on the basis of chlorite filling garnet cracks and pseudomorphs of sillimanite by aggregates of what is considered to be sericite (Lasalle *et al.*, 2014). However, no relationships with the dated monazite is reported and no geochronological evidence supports the coeval formation of chlorite and monazite rims. Slightly younger ages reported in this area range from 995±3 to 987±11 Ma and were obtained on titanite from pre-Grenvillian metatuffs and metagranite (protolith ages of ca. 1410 Ma, Dunning and Indares, 2010, and ca. 1200 Ma, Indares and Dunning, 2004), and from a syn-Ottawan metagranite (protolith age of ca. 1065 Ma, Dunning and Indares, 2010). These ages are interpreted as a late-Grenvillian magmatic/metamorphic/deformation event occurring under semi-brittle conditions, consistent with the subsolidus closure temperature of titanite at ca. 550-650°C (Schoene and Bowring, 2007; Yakymchuk et al., 2017). These younger ages are coeval with the Rigolet tectonic phase attributed to crustal thickening at ca. 1005-960 Ma (Jannin et al., accepted; Rivers, 2008; Rivers et al., 2012) recorded in the underlying Parautochthonous

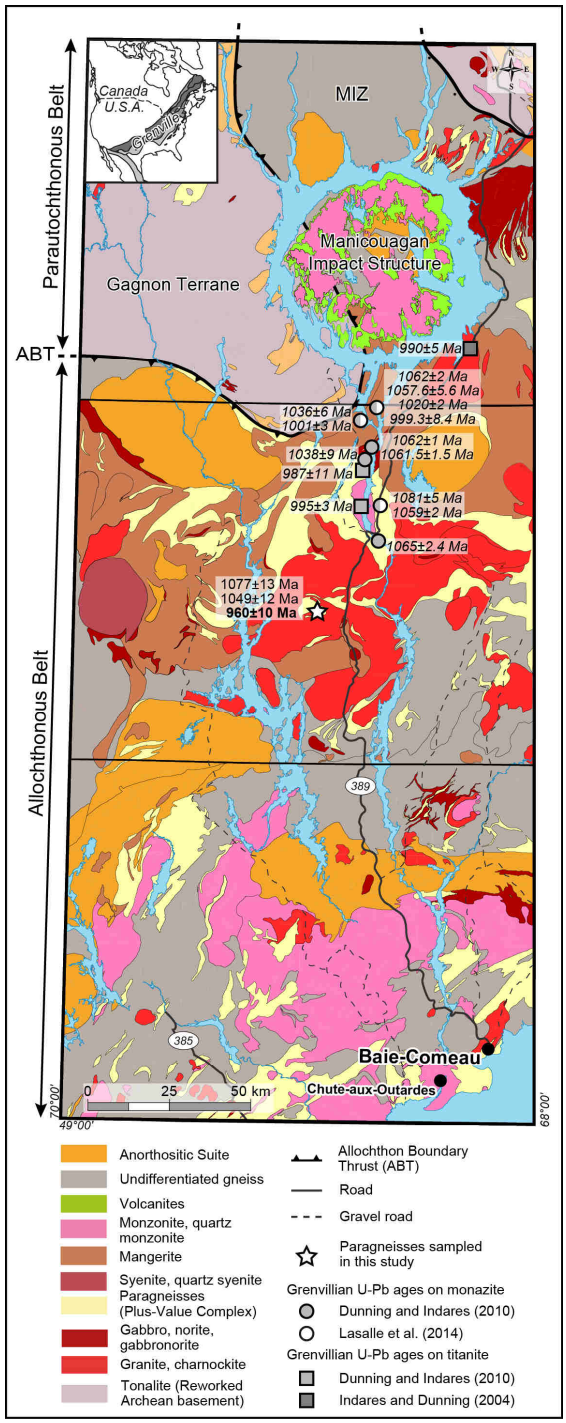

Figure 2-1: Geological map of the central Grenville Province (Quebec) showing the position of the investigated paragneisses (star) and of data from literature discussed in this study (circles and squares) (modified after Turlin *et al.*, 2017). U-Th-Pb ages on monazite and apatite from this study are reported in regular and bold text, respectively. Abbreviations: ABT = Allochthon Boundary Thrust; MIZ = Manicouagan Imbricate Zone.

Belt with a high-grade peak of metamorphism up to 1250-1500 MPa and 815-850°C (Jordan *et al.*, 2006). The 10 to 20 Ma geochronological hiatus marked in the Grenville Province is interpreted as corresponding to the transition from post-Ottawan orogenic gravitational collapse to renewed crustal thickening owing to the Rigolet tectonic phase (Rivers, 2008).

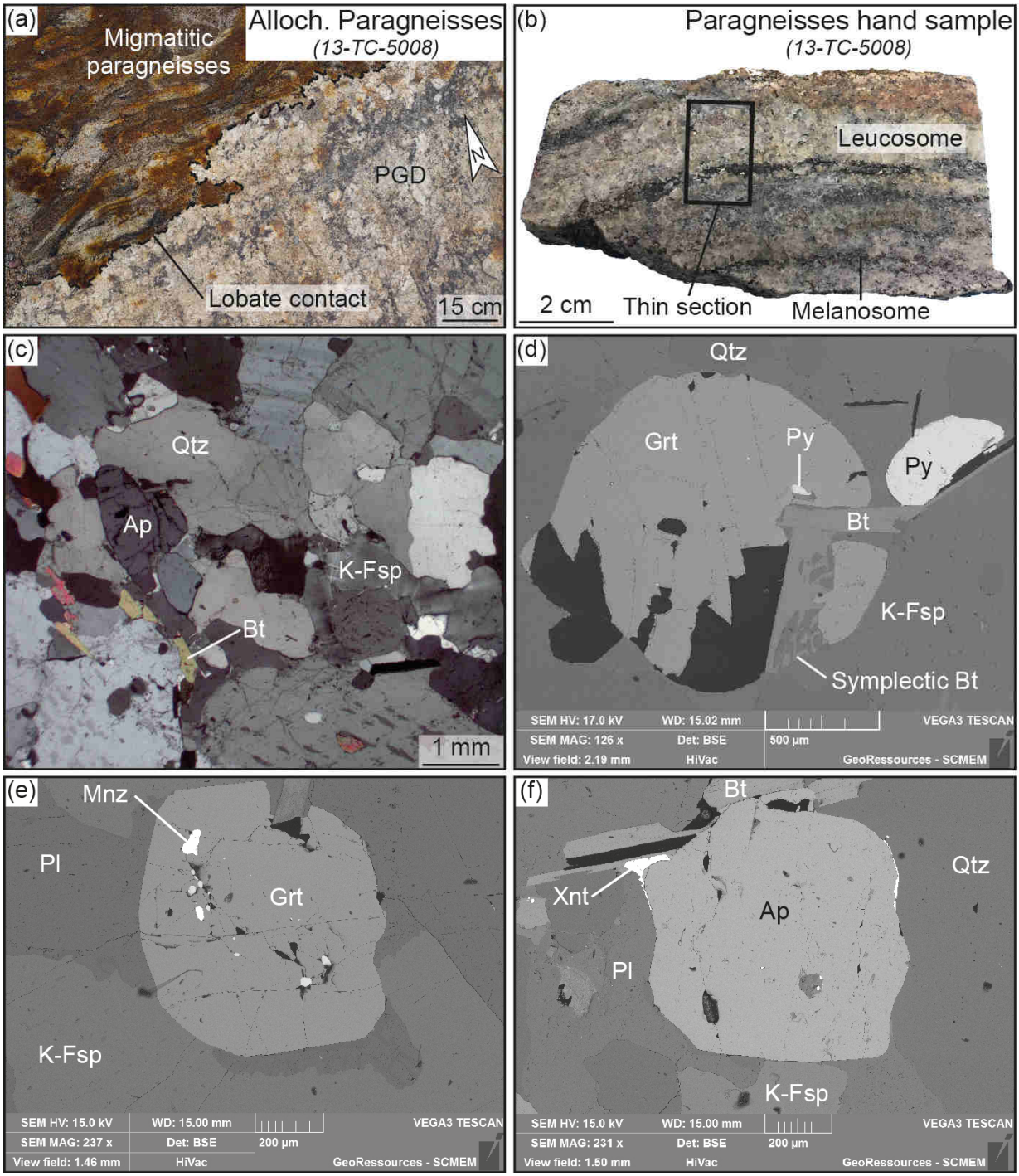

Figure 2-2: Sampled migmatitic paragneisses and phase relationships of the leucosome. (a): lobate contact between the migmatitic paragneisses and the intrusive 1005±4.4 Ma pegmatitic granite dyke (Turlin *et al.*, 2017) with no evidence for contact metamorphism nor thermal exchange between the dyke and the host paragneisses that collectively support a close to wet-solidus temperature of the host at ca. 1005 Ma; (b): Hand sample of the investigated paragneisses. Note the magmatic texture of the leucosomes with no mineral orientation; (c): microstructural position of apatite in the leucosome. Note the magmatic texture of the apatite and the lack of corrosion and dissolution/precipitation textures; (d): biotite and K-feldspar intergrowths form a symplectic texture around inclusion-rich garnet phenocrysts. This texture provides evidences for the incomplete biotite dehydration reaction at the *P-T* peak of metamorphism (maximum temperature); (e): prograde monazite shielded in a peritectic porphyroblast of garnet (SEM); (f): magmatic spherical apatite in the Qtz+Pl+K-Fsp+Bt matrix. Abbreviations: Alloch. = allochthonous; Ap = apatite; Bt = biotite; Grt = garnet; K-Fsp = K-feldspar; Mnz = monazite; PGD = pegmatitic granite dyke; Pl = plagioclase; Py = pyrite; Qtz = quartz; Xnt = xenotime.

2.2. Petrochronology of monazite and apatite from migmatitic paragneisses

Migmatitic paragneisses from the Plus-Value Complex of the central Grenville sampled for this study (Fig. 2-1) have deposition ages comprised between ca. 1.6 and 1.5 Ga (U-Pb on detrital zircon cores and on zircon from the intrusive Bardoux Plutonic Suite, (Augland et al., 2015; Lasalle et al., 2013; Moukhsil et al., 2014). They are composed of centimetric leucosomes and melanosomes underlining the syn-migmatitic foliation (Fig. 2-2a-b). They are intruded by a 1005±4.4 Ma (U-Pb dating on magmatic monazite, Turlin *et al.*, 2017) pegmatitic granite dyke (PGD) (Fig. 2-2a). The walls of the dyke do not correspond to fractures cutting across minerals of the paragneiss but are rather lobate suggesting intrusion in a ductile rock. Moreover, the paragneisses do not show evidence for contact metamorphism (Fig. 2-2a). These features indicate a close to wet-solidus temperature of the latter at that time (Vanderhaeghe, 2001), i.e. above ca. 650-700°C in such metapelites (e.g. Yakymchuk and Brown, 2014). Investigated monazite and apatite grains were sampled from a single leucosome of this migmatitic paragneisses.

Leucosomes show a magmatic texture (Fig. 2-2b-c) and are made of a coarse grained (1-5 mm) assemblage of sub-euhedral to xenomorph and undeformed quartz, plagioclase completed by peritectic K-feldspar and garnet (45:35:15:5, Figs. 2-2c-d). In addition, some biotite and K-feldspar intergrowths form a symplectic texture (Fig. 2-2d). As identified by (Lasalle et al., 2014), sub-euhedral, uncorroded and inheritance-free monazite grains (100-300 µm) are found (i) as inclusions in peritectic garnet (Fig. 2-2e) and K-feldspar, and (ii) in the matrix. These monazite grains have homogeneous compositions with a significant part of brabantite and xenotime end-members (Table S2-1), consistent with the observations of Lasalle et al. (2014). Plotted on a Concordia diagram, U-Th-Pb isotopic data spread along the Concordia curve with $^{208}Pb/^{232}Th$ ages ranging between 1077±26 and 1049±25 Ma (2σ, Fig. 2-3a, Table 2-1). No inherited ages were identified in the isotopic ratios, consistent with the homogeneous and unzoned character of the grains.

Apatite grains (300-600 µm) occur as sub-euhedral spherical grains in the leucosome matrix (Fig. 2-2c, f). Along with their sub-euhedral shape, the lack of inherited cores/domains or dissolution/precipitation textures, and their homogeneous compositions (Table S2-2 and 2-2) provide evidence for the crystallization of apatite grains in equilibrium with the residual melt (Fig. 2-2c, f). According to the generally low radiogenic-Pb/common-Pb ratio in apatite (Pochon et al., 2016), data were plotted in a Tera-Wasserburg diagram (Tera and Wasserburg,

1972), in which the variable $^{206}Pb/^{207}Pb$ ratios define a discordia line with a lower intercept of 960±10 Ma (MSWD=1.11, Fig. 2-3b, Table 2-2) and an initial $^{206}Pb/^{207}Pb$ ratio of 0.90 consistent with the model evolution of Stacey and Kramers (1975). The closure temperatures of these crystals were calculated between 526±24 and 459±22°C, using the equation of Dodson (1973) and data from (Cherniak et al., 1991) (Table 2-3).

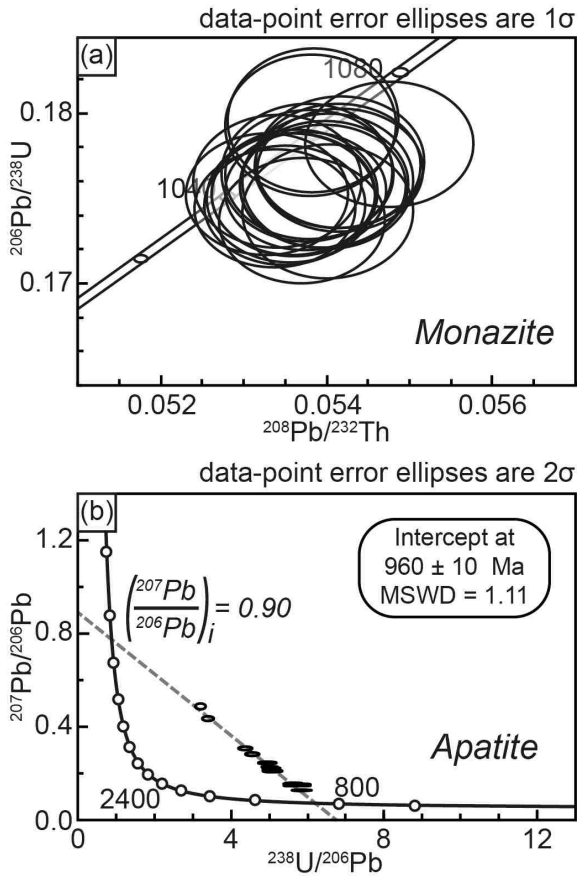

Figure 2-3: U-Th-Pb dating of the leucosome of migmatitic paragneisses from the Allochthonous Belt of the central Grenville. (a): Concordia plots for the monazite analyses (n=21); (b): Tera-Wasserburg concordia diagram for apatite analyses (n=23).

3. Discussion and summary

3.1. Protracted suprasolidus conditions

Monazite grains investigated in this study share (i) microstructural positions and (ii) a range of U-Th-Pb ages similar to the ca. 1080-1020 Ma monazite grains from aluminous gneisses of this aM-L*P* segment reported by (Dunning and Indares, 2010; Lasalle et al., 2014). Accordingly, the investigated migmatitic paragneiss records similar *P-T-t* conditions of ca. 950 MPa and 850°C between ca. 1070-1050 Ma (Fig. 2-4).

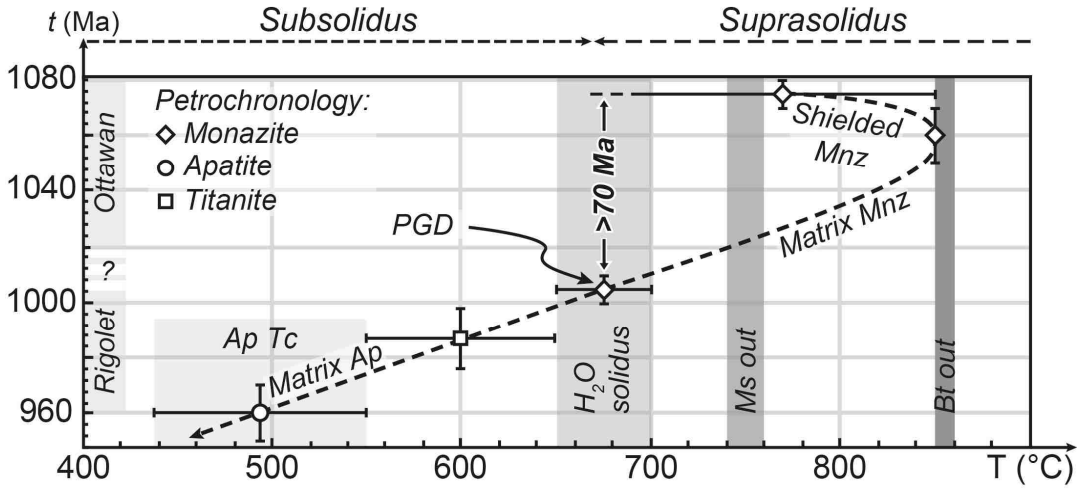

Figure 2-4: Time vs temperature diagram of aluminous gneisses from mid-pressure crustal segment of the central Grenville considered in this study. It was constructed using the geochronological data and thermometric constraints from this study and those reported by Dunning and Indares (2010), Indares and Dunning (2004), Lasalle and Indares (2014) and Lasalle et al. (2014). Temperatures of partial melting reactions are from Lasalle and Indares (2014). The suprasolidus prograde *T-t* path is recorded by shielded monazite in peritectic garnet and K-feldspar up to a temperature of ca. 850°C characterized by the biotite breakdown and indicated by the biotite-K-feldspar symplectite. The suprasolidus retrograde *T-t* path is recorded by monazite from the matrix and down to ca. 1005 Ma as indicated by the intrusion of a pegmatitic granite dyke into paragneisses which lobate contact with no evidence of contact metamorphism nor thermal exchange with the host provide evidence for the close to wet-solidus temperature of the host. The retrograde *T-t* path is recorded by titanite from the same segment and dated between ca. 1000 and 975 Ma, and by apatite from the matrix of the investigated leucosome dated at ca. 960±10 Ma with isotopic closure temperatures of ca. 440-550°C. Abbreviations: Ap = apatite; Bt = biotite; Mnz = monazite; Ms = muscovite; PGD = pegmatitic granite dyke; Tc = isotopic closure temperature.

Reaction sequences for the clockwise *P-T* path published by Lasalle and Indares (2014) involve three main partial melting reactions for these paragneisses: (i) the consumption of free aqueous fluid, (ii) the muscovite and (iii) biotite dehydration-melting. Monazite grains shielded within peritectic K-feldspar and garnet (Fig. 2-2e) formed, respectively, by the incongruent breakdown of muscovite at ca. 700-750°C and the partial breakdown of biotite at ca. 800-850°C, consistent with biotite-feldspar symplectite. As argued by Lasalle et al. (2014), these grains grew during prograde heating and partial melting between ca. 700 and 850°C (Kelsey et al., 2008; Yakymchuk and Brown, 2014) and thus correspond to prograde suprasolidus monazite (Yakymchuk, 2017).

Accordingly, data obtained on monazite from this study along with data reported by Dunning and Indares (2010) and Lasalle et al. (2014) point to the crystallization of monazite (i) during the prograde *P-T* path as early as ca. 1080 Ma under temperatures of at least 700-750°C, with (ii) a maximum temperature of 850°C between ca. 1070 and 1050 Ma, and (iii) down to ca. 1020 Ma, during the retrograde *P-T* path (Fig. 2-4). The assumption that younger monazite ages between ca. 1010-990 Ma (Lasalle et al., 2014) are coeval with greenschist-facies conditions is reappraised on the basis of the textural relationships between the investigated paragneisses and the intrusive PGD at ca. 1005 Ma (Fig. 2-2a, Turlin *et al.*, 2017). The lobate

contact of the PGD with its host paragneisses in this aM-L*P* segment provide evidence for limited, if any, thermal exchange and thus a close to wet-solidus (ca. 650-700°C) temperature of the host rock at the time of intrusion (Figs. 2-2a, 2-4, Turlin *et al.*, 2017).

These features are consistent with a mid-crust residence of this aM-L*P* segment under suprasolidus conditions between ca. 1080 and 1005 Ma in the central Grenville Province, i.e. suprasolidus conditions lasted for at least 70 Ma (Figs. 2-4, 2-5a-b). A key point to explain such a long residence at *HT* may be found in the syn-Ottawan extrusion of ductile mid- to low-crust over the ABT associated with some form of channel flow (Rivers, 2008) that was however inferred to be terminated by ca. 1050 Ma. In contrast, data presented here are suggestive of persistence of a melt fraction in the Ottawan channel for at least ca. 70 Ma (Fig. 2-5a-b).

3.2. Subsolidus thermal history

Youngest Grenvillian metamorphic ages reported in this aM-L*P* range from 987±11 to 995±3 Ma and were obtained on titanite from (i) pre-Grenvillian metatuffs and metagranite (protolith ages of ca. 1410 Ma, Dunning and Indares, 2010, and ca. 1200 Ma, Indares and Dunning, 2004), and from (ii) a syn-Ottawan metagranite (protolith age of ca. 1065 Ma, Dunning and Indares, 2010). They are interpreted as a late-Grenvillian magmatic/metamorphic/deformation event under semi-brittle conditions, consistent with the subsolidus closure temperature of titanite at ca. 550-650°C (Fig. 2-4, Dunning and Indares, 2010; Indares and Dunning, 2004; Schoene and Bowring, 2007; Yakymchuk et al., 2017). Apatite grains from the leucosome investigated in this paper crystallized in equilibrium with the residual melt as indicated by their textural position, their homogeneous composition and the lack of inherited cores/domains or dissolution/precipitation textures (Fig. 2-2c, f, Table 2-2, S2-2). Their crystallization ages at 960±10 Ma (Fig. 2-3b) along with their estimated closure temperatures between 526±24 and 459±22°C (Table 2-3) allow to determine the residence of this aM-L*P* crustal segment at temperature above 450-500°C for at least ca. 110 Ma (Figs. 2-4, 2-5c).

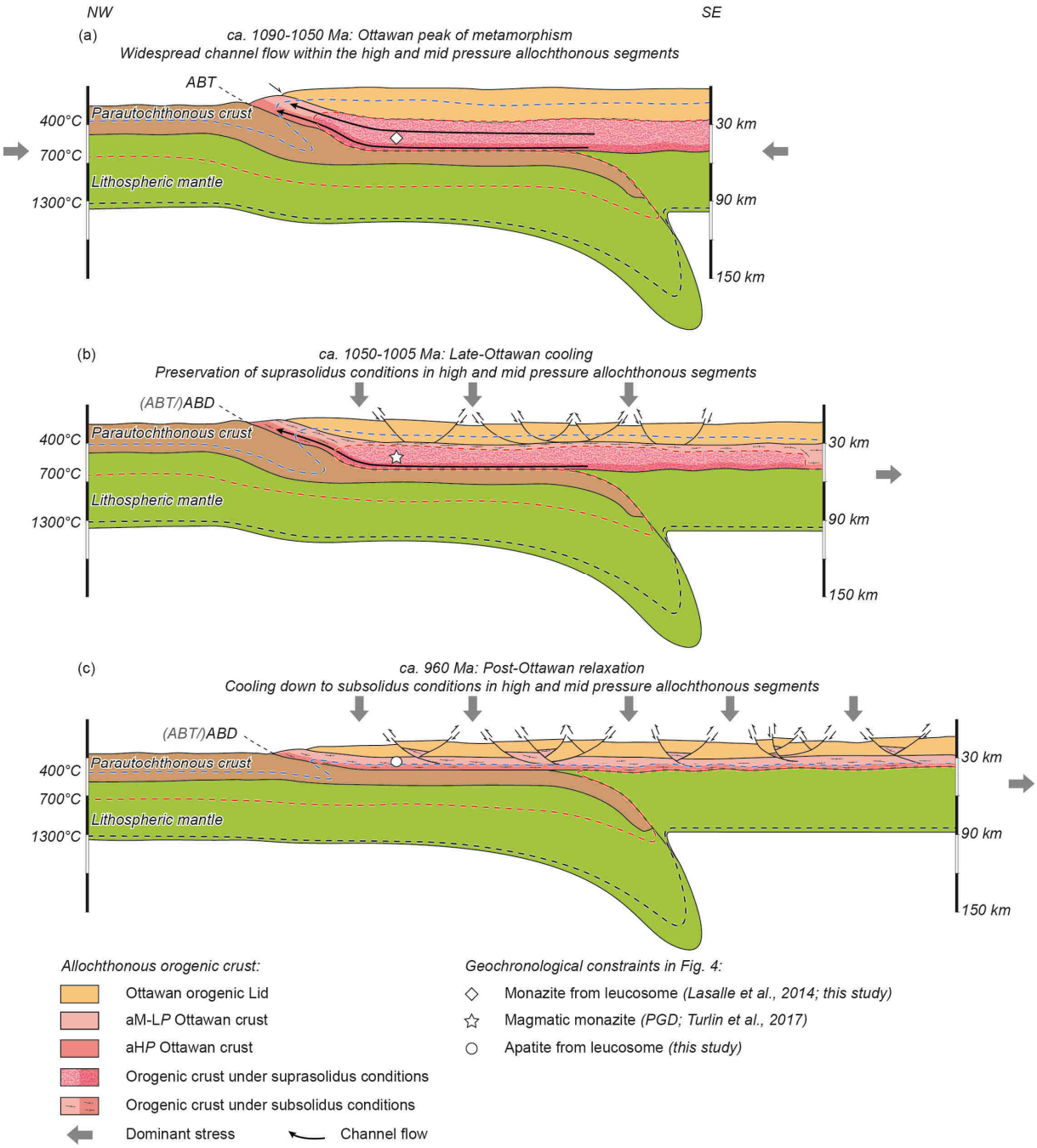

Figure 2-5: Schematic cross sections illustrating the thermal evolution of the high and mid pressure crustal segments of the Allochthonous Belt of the central Grenville Province (after Rivers, 2008). (a): Ottawan prograde *P-T* path (ca. 1090-1080 Ma) and peak of metamorphism (ca. 1070-1050 Ma) marked by the development of a channel flow in the high and mid pressure crustal segments of the Allochthonous Belt; (b) suprasolidus conditions are preserved within high and mid pressure crustal segments of the Allochthonous Belt from ca. 1050 Ma down to ca. 1005 Ma corresponding to the timing of intrusion of the 13-TC-5008 pegmatitic granite dyke (Turlin *et al.*, 2017); (c): cooling down to subsolidus conditions of the mid pressure crustal segments of the Allochthonous Belt at ca. 960 Ma. Abbreviations: ABT/ABD = Allochthonous Boundary Thrust/Detachment; aH*P* = allochthonous high pressure Ottawan crust; aM-L*P* = allochthonous mid-low pressure Ottawan crust; PGD = pegmatitic granite dyke.

Data from this study coupled with results of Dunning and Indares (2010), Indares and Dunning (2004), Lasalle et al. (2014), Lasalle and Indares (2014) in the Allochthonous Belt of the central Grenville allowed the estimations of cooling rates from the early-Ottawan initiation of suprasolidus conditions to the post-Ottawan cooling down to subsolidus conditions (Table 2-4). They provide evidence for (i) a syn-Ottawan cooling rate of 2.3 to 4.4°C/Ma, and (ii) a post-Ottawan cooling rate of 1.8 to 7.5°C/Ma (Table 2-4), dominated by the range 2.7 to 6.1°C/Ma. Post-Ottawan rates are similar to those reported for aM-L*P* segments of the southwestern Grenville Province determined from $^{40}Ar/^{39}Ar$ of hornblende, muscovite, biotite and K-feldspar (see Rivers et al., 2012 and references therein) and more generally for ca. 1 Ga old orogens (Dunlap, 2000). These data indicate that the central Grenville represents a large, hot and long-duration orogeny that recorded protracted *HT* metamorphism in the presence of melt for at least ca. 70 Ma followed by a slow cooling history (Figs. 2-4, 2-5).

Acknowledgments

This work was funded by the Labex Ressources 21 (supported by the French National Research Agency) through the national program “Investissements d’avenir”, reference ANR-10-LABX-21–LABEX RESSOURCES 21 and the Région Grand-Est, and benefited from the framework of the DIVEX “Rare earth element” research program. Authors are grateful to the Ministère de l’Énergie et des Ressources naturelles (Québec) for technical and financial support for field work and analyses, to Alexandre Crépon, Frédéric Diot (GeoRessources, Nancy), Emmanuel Davy (CRPG, Nancy), Andreï Lecomte and Jean Cauzid (GeoRessources, Nancy) for their help in field work, sample preparation and SEM imaging, respectively, to Anthony Pochon (Géosciences Rennes) for his help in handling closure temperatures of apatite, to Flavien Choulet for his constructive comments on a previous version of the manuscript, and to Félix Gervais for our discussions on the geodynamic context of the Grenvillian Orogeny. This contribution is the Ministère de l’Energie et des Ressources naturelles du Québec (Canada) publication n° 8449-2017-2018-03.

Table 2-1: U-Th-Pb dating of monazite from a leucosome of migmatitic allochthonous paragneisses from the central Grenville Province.

Analysis no.	Concentrations			Isotopic ratios				Ages/Ma			
	Pb (ppm)	U (ppm)	Th (ppm)	$^{206}Pb/^{238}U$	2σ	$^{208}Pb/^{232}Th$	2σ	$^{206}Pb/^{238}U$	2σ	$^{208}Pb/^{232}Th$	2σ
Mnz-03	2568	5657	35563	0.1754	0.0046	0.0538	0.0013	1042	25	1058	25
Mnz-04	2874	10542	28447	0.1744	0.0046	0.0534	0.0013	1036	25	1051	25
Mnz-06	2365	7613	26481	0.1746	0.0046	0.0535	0.0013	1038	25	1054	25
Mnz-07	2748	6731	37166	0.1753	0.0047	0.0533	0.0013	1041	26	1049	25
Mnz-08	3577	17411	23848	0.1752	0.0047	0.0536	0.0013	1041	26	1055	25
Mnz-09	2586	5887	35691	0.1767	0.0048	0.0542	0.0013	1049	26	1066	25
Mnz-10	2583	5744	36107	0.1769	0.0048	0.0541	0.0013	1050	26	1066	25
Mnz-11	2878	6435	40465	0.1757	0.0048	0.0540	0.0013	1044	26	1062	25
Mnz-12	2495	6866	30822	0.1781	0.0049	0.0548	0.0013	1057	27	1077	26
Mnz-13	2584	6776	34297	0.1737	0.0048	0.0537	0.0013	1032	27	1057	25
Mnz-14	3187	6099	48278	0.1758	0.0049	0.0540	0.0013	1044	27	1062	26
Mnz-15	2378	6356	31272	0.1753	0.0049	0.0536	0.0013	1041	27	1056	25
Mnz-16	2384	6332	31314	0.1764	0.0050	0.0538	0.0013	1047	27	1059	26
Mnz-17	3078	9311	37637	0.1750	0.0050	0.0536	0.0013	1040	27	1055	26
Mnz-18	2465	6522	32261	0.1771	0.0051	0.0542	0.0013	1051	28	1066	26
Mnz-19	2650	7494	34203	0.1760	0.0052	0.0534	0.0013	1045	28	1051	26
Mnz-20	3080	10383	34931	0.1742	0.0052	0.0540	0.0014	1035	28	1063	26
Mnz-21	3043	7898	40976	0.1760	0.0053	0.0540	0.0014	1045	29	1063	26
Mnz-22	4040	17441	34861	0.1765	0.0053	0.0538	0.0014	1048	29	1058	26
Mnz-23	2946	8983	35659	0.1793	0.0055	0.0538	0.0014	1063	30	1059	26
Mnz-24	2416	5590	34395	0.1796	0.0055	0.0538	0.0014	1065	30	1060	26

Table 2-2: U-Pb dating of apatite from a leucosome of migmatitic allochthonous paragneisses from the central Grenville Province.

Analysis no.	Concentrations		Isotopic ratios			
	Pb (ppm)	U (ppm)	$^{238}U/^{206}Pb$	2σ	$^{207}Pb/^{206}Pb$	2σ
Ap-1	3.5	18	4.77	0.16	0.2487	0.0031
Ap-2	3.3	20	5.02	0.17	0.2281	0.0028
Ap-3	2.5	35	5.61	0.19	0.1476	0.0019
Ap-4	3.0	57	5.82	0.19	0.1290	0.0014
Ap-5	3.0	58	5.86	0.20	0.1295	0.0018
Ap-6	3.8	54	5.68	0.19	0.1470	0.0018
Ap-7	27	179	5.14	0.17	0.2106	0.0028
Ap-8	17	90	4.98	0.17	0.2458	0.0033
Ap-9	25	318	5.64	0.19	0.1469	0.0017
Ap-10	50	149	4.37	0.15	0.3082	0.0050
Ap-11	71	419	4.68	0.16	0.2776	0.0041
Ap-12	14	102	5.03	0.17	0.2109	0.0033
Ap-13	3.2	5.8	3.41	0.13	0.4336	0.0085
Ap-14	3.5	5.4	3.21	0.11	0.4878	0.0098
Ap-15	4.8	33	5.04	0.17	0.2119	0.0028
Ap-16	5.7	38	5.08	0.18	0.2227	0.0036
Ap-17	6.4	44	5.04	0.18	0.2213	0.0039
Ap-18	9.1	40	4.56	0.16	0.2833	0.0049
Ap-19	7.3	94	5.83	0.20	0.1534	0.0028
Ap-20	7.8	93	5.63	0.19	0.1568	0.0019
Ap-21	7.4	88	5.59	0.19	0.1554	0.0016
Ap-22	7.2	100	5.83	0.19	0.1465	0.0017
Ap-23	5.9	30	4.89	0.17	0.2461	0.0030

Table 2-3: Closure temperature of investigated apatite calculated on the basis of their spherical shape, crystal diameters of 300 and 600 µm, and a range of typical late- to post-Grenvillian and ca. 1 Ga orogen cooling rates of 1°C/Ma, 3°C/Ma, 5°C/Ma and 7°C/Ma (e.g. Dunlap, 2000; Rivers et al., 2012).

Crystal diameter (µm)	Cooling rate (°C/Ma)	Closure temperatures[1] (°C)	± (°C)
300	1	459	22
600	1	485	23
300	3	479	23
600	3	507	24
300	5	489	23
600	5	518	24
300	7	497	24
600	7	526	24

[1]: Calculated using the Dodson (1973)'s equation with data from Cherniak et al. (1991)

Table 2-4: Grenvillian cooling rates calculated using data from the literature coupled with the data presented in this study on a single leucosome from migmatitic paragneisses of the central Grenville Province. Note the similar cooling rates obtained for both Ottawan and post-Ottawan orogenic phases suggesting a continuum of cooling from the former to the latter.

Grenvillian orogenic phase	Age (Ma)	Temperature (°C)	Cooling rate (°C/Ma)
Ottawan	1070-1050[1] 1005[2]	850[1] 650-700[2]	2.3-4.4
Post-Ottawan	960±10[3]	437[4] 550[5]	3.9-7.5[6] 1.8[6]-4.3

[1]: Temperature and timing of the peak metamorphism from Lasalle and Indares (2014)
[2]: Close to wet-solidus temperature of the migmatitic paragneisses at the time of intrusion of the pegmatitic granite dyke (Turlin et al., 2017)
[3]: Subsolidus timing of apatite isotopic closure (this study)
[4]: Minimum closure temperature of investigated apatite grains (this study)
[5]: Maximum closure temperature of investigated apatite grains (this study)
[6]: Extreme values. Cooling rates are predominantly in the range 2.7 to 6.1°C/Ma

Supplementary material

S1. Sampling

Paragneisses from the Plus-Value Complex (Lac Okaopéo region, Allochthonous Belt, Fig. 2-1) have been sampled in 2016 on the flat lying 13-TC-5008 outcrop (Figs. 2-1 and 2-2a-b, Turlin et al., 2017). This outcrop is accessible from the 389 highway from Baie-Comeau towards the Daniel Johnson Dam (Manic-5, Quebec, Canada) and is located at the present coordinates 50°25'03.08" N, 68°56'05.86" W.

S2. Analytical methods: Electron microprobe (EMP)

Major and trace element analyses were carried out on EMP using a Cameca computer-controlled SX-100 at GeoRessources (Nancy, France) equipped with the wavelength spectrometer (WDS).

Quantitative analyses of monazite from the leucosome of paragneisses sampled in the Allochthonous Belt were performed using an accelerating voltage of 20 kV, a beam current of 100 nA and a peak counting time of 120 s for Pb, 100 s for U and 20 s for Si, P, Ca, Y, La, Ce, Pr, Nd, Sm, Gd, and Th. Results are reported in Table S2-1.

Quantitative analyses of apatite from the leucosome of paragneisses sampled in the Allochthonous Belt were performed using an accelerating voltage of 15 kV, a beam current of 12 nA and a peak counting time 10s/per element for major and trace elements analyses (F, Na, P, Si, Mg, Ca, Cl, Mn, Fe, Sr, Y, Pb, S, La, Ce, Th, U). Results are reported in Table S2-2.

Table S2-1: Monazite compositions from the paragneisses leucosomes obtained using EMP. They are reported with confidence interval of 95% in brackets (n = number of analyses). Abbreviations: Brab. = brabantite; Hutt. = huttonite; Mnz. = monazite; Xen. = xenotime.

Mineral		Monazite
Oxides (wt.%)	**P_2O_5**	30.23
		(1.03)
	SiO_2	0.22
		(0.09)
	CaO	0.83
		(0.16)
	Y_2O_3	2.22
		(0.67)
	La_2O_3	13.67
		(0.37)
	Ce_2O_3	27.76
		(0.69)
	Pr_2O_3	3.67
		(0.32)
	Nd_2O_3	12.04
		(0.68)
	Sm_2O_3	1.72
		(0.40)
	Gd_2O_3	1.58
		(0.34)
	PbO	0.00
		(0.00)
	ThO_2	3.81
		(0.88)
	UO_2	0.60
		(0.34)
	Total	98.36
		(0.67)
	Oxygens	4
Cations	**P**	1.003
		(0.017)
	Si	0.009
		(0.003)
	ΣT-site	1.012
		(0.017)
	Ca	0.035
		(0.007)
	Y	0.046
		(0.014)
	La	0.198
		(0.007)
	Ce	0.399
		(0.014)
	Pr	0.052
		(0.005)
	Nd	0.169
		(0.010)
	Sm	0.023
		(0.005)
	Gd	0.021
		(0.004)
	Pb	0.000
		(0.000)
	Th	0.034
		(0.008)
	U	0.005
		(0.003)
	Σa-site	0.982
		(0.029)
	% Hutt.	0.88
		(0.35)
	% Brab.	8.04
		(1.40)
	% Mnz.	84.36
		(1.96)
	% Xen.	6.71
		(1.50)
	n	33

Table S2-2: Apatite compositions from the paragneisses leucosomes obtained using EMP. They are reported with confidence interval of 95% in brackets (n = number of analyses).

Mineral		Apatite
Oxides (wt.%)	**F**	3.42
		(0.40)
	Na_2O	0.13
		(0.06)
	P_2O_5	43.50
		(0.52)
	SiO_2	0.06
		(0.09)
	MgO	0.02
		(0.02)
	CaO	54.28
		(0.77)
	Cl	0.38
		(0.14)
	MnO	0.19
		(0.10)
	FeO	0.14
		(0.10)
	SrO	0.07
		(0.04)
	Y_2O_3	0.16
		(0.08)
	PbO	0.01
		(0.03)
	SO_2	0.01
		(0.01)
	La_2O_3	0.08
		(0.11)
	Ce_2O_3	0.11
		(0.13)
	ThO_2	0.01
		(0.03)
	UO_2	0.02
		(0.03)
	Total	103.06
		(1.21)
Oxygens		13.5
Cations	**F**	0.993
		(0.117)
	Na	0.023
		(0.011)
	P	3.379
		(0.041)
	Si	0.005
		(0.008)
	Mg	0.002
		(0.003)
	Ca	5.336
		(0.076)
	Cl	0.059
		(0.022)
	Mn	0.015
		(0.007)
	Fe	0.010
		(0.008)
	Sr	0.003
		(0.002)
	Y	0.008
		(0.004)
	Pb	0.000
		(0.001)
	S	0.001
		(0.001)
	La	0.003
		(0.004)
	Ce	0.004
		(0.004)
	Th	0.000
		(0.001)
	U	0.000
		(0.001)
n		368

S3. Analytical methods: U-Th-Pb dating using Laser Ablation – Inductively Coupled Plasma – Mass Spectrometry (LA-ICP-MS)

Leucosomes of the Plus-Value Complex paragneisses were carefully separated from the mesosomes and melanosomes. Monazite and apatite from the leucosome were separated using classical separation techniques (crushing, heavy liquids and magnetic separation, handpicking under binocular microscope) in GeoRessources and CRPG (Nancy, France) and mounted in epoxy mounts. LA-ICP-MS U-Th-Pb dating of monazite and apatite grains were carried out in June 2017 in Géosciences Rennes (France), following the procedures detailed in Ballouard et al. (2015) for monazite and in Pochon et al. (2016) for apatite. Detailed operating conditions of LA-ICP-MS measurements of monazite and apatite are reported in Tables S2-3 and S2-4, respectively, and results of U-Th-Pb dating in Tables 2-1 and 2-2, respectively.

Monazite and apatite crystals analyzed for this study range between ca. 100 and 300 µm for the former, and between ca. 300 and 600 µm for the latter (Fig. S2-1). In both cases, SEM imaging did not reveal any inner zonation, nor inherited cores/domains or overgrowths/rims, which is consistent with the homogeneous chemical compositions of both monazite and apatite crystals. Twenty-two U-Th-Pb dating analyses were carried out on five monazite grains and twenty-four U-Pb analyses were carried out on fourteen apatite grains.

Table S2-3: Operating conditions for the monazite U-Th-Pb dating LA-ICP-MS analyses.

	U-Th-Pb monazite analyses
Laboratory & Sample Preparation	
Laboratory name	Géosciences Rennes, UMR CNRS 6118, Université Rennes 1, Rennes, France
Sample type/mineral	Magmatic monazite
Sample preparation	Conventional mineral separation, 1 inch resin mount, 1µm polish to finish
Imaging	VEGA3-TESCAN SEM, GeoRessources, UMR 7359, Université de Lorraine, Vandœuvre-lès-Nancy, France
Laser ablation system	
Make, Model & type	ESI NWR193UC, Excimer
Ablation cell	ESI NWR TwoVol2
Laser wavelength	193 nm
Pulse width	< 5 ns
Fluence	6.6 J/cm-2
Repetition rate	3 Hz
Spot size	10 µm (round spot)
Sampling mode / pattern	Single spot
Carrier gas	100% He, Ar make-up gas and N_2 (3 ml/mn) combined using in-house smoothing device
Background collection	20 seconds
Ablation duration	60 seconds
Wash-out delay	10 seconds
Cell carrier gas flow (He)	0.75 l/min
ICP-MS Instrument	
Make, Model & type	Agilent 7700x, Q-ICP-MS
Sample introduction	Via conventional tubing
RF power	1350W
Sampler, skimmer cones	Ni
Extraction lenses	X type
Make-up gas flow (Ar)	0.87 l/min
Detection system	Single collector secondary electron multiplier
Data acquisition protocol	Time-resolved analysis
Scanning mode	Peak hopping, one point per peak
Detector mode	Pulse counting, dead time correction applied, and analog mode when signal intensity > ~ 10^6 cps
Masses measured	^{204}(Hg + Pb), ^{206}Pb, ^{207}Pb, ^{208}Pb, ^{232}Th and ^{238}U
Sensitivity / Efficiency	25000 cps/ppm Pb (50µm, 10Hz)
Dwell time per isotope	10-30 ms depending on the masses
Data Processing	
Gas blank	20 seconds on-peak
Calibration strategy	Moacir Monazite used as primary reference material, Manangoutry Monazite used as secondary reference material (quality control)
Reference Material info	Moacir (Gasquet et al., 2010) Manangoutry (Paquette and Tiepolo, 2007)
Data processing package	Glitter (Van Achterbergh et al., 2001)
Quality control / Validation	Manangoutry: 558 ± 4.6 Ma (MSWD=0.54; n=4)

Table S2-4: Operating conditions for the apatite U-Pb dating LA-ICP-MS analyses.

	U-Pb apatite analyses
Laboratory & Sample Preparation	
Laboratory name	Géosciences Rennes, UMR CNRS 6118, Université Rennes 1, Rennes, France
Sample type/mineral	Magmatic apatite
Sample preparation	Conventional mineral separation, 1 inch resin mount, 1µm polish to finish
Imaging	VEGA3-TESCAN SEM, GeoRessources, UMR 7359, Université de Lorraine, Vandœuvre-lès-Nancy, France
Laser ablation system	
Make, Model & type	ESI NWR193UC, Excimer
Ablation cell	ESI NWR TwoVol2
Laser wavelength	193 nm
Pulse width	< 5 ns
Fluence	6 J/cm-2
Repetition rate	5 Hz
Spot size	40 µm (round spot)
Sampling mode / pattern	Single spot
Carrier gas	100% He, Ar make-up gas and N_2 (3 ml/mn) combined using in-house smoothing device
Background collection	20 seconds
Ablation duration	60 seconds
Wash-out delay	10 seconds
Cell carrier gas flow (He)	0.75 l/min
ICP-MS Instrument	
Make, Model & type	Agilent 7700x, Q-ICP-MS
Sample introduction	Via conventional tubing
RF power	1350W
Sampler, skimmer cones	Ni
Extraction lenses	X type
Make-up gas flow (Ar)	0.87 l/min
Detection system	Single collector secondary electron multiplier
Data acquisition protocol	Time-resolved analysis
Scanning mode	Peak hopping, one point per peak
Detector mode	Pulse counting, dead time correction applied, and analog mode when signal intensity > ~ 10^6 cps
Masses measured	^{43}Ca, ^{204}(Hg + Pb), ^{206}Pb, ^{207}Pb, ^{208}Pb, ^{232}Th and ^{238}U
Sensitivity / Efficiency	25000 cps/ppm Pb (50µm, 10Hz)
Dwell time per isotope	10-30 ms depending on the masses
Data Processing	
Gas blank	20 seconds on-peak
Calibration strategy	Madagascar Apatite used as primary reference material, Durango and McClure apatite standards used as secondary reference material (quality control)
Reference Material info	Madagascar (Thomson et al., 2012) Durango (McDowell et al., 2005) McClure (Schoene and Bowring, 2006)
Data processing package	Iolite (Paton et al., 2010), VizualAge UcomPbine (Chew et al., 2014)
Quality control / Validation	Durango: 32.9 ± 2.9 Ma (MSWD=1.9; n=5) McClure: 526 ± 14 Ma (MSWD=0.32; n=4)

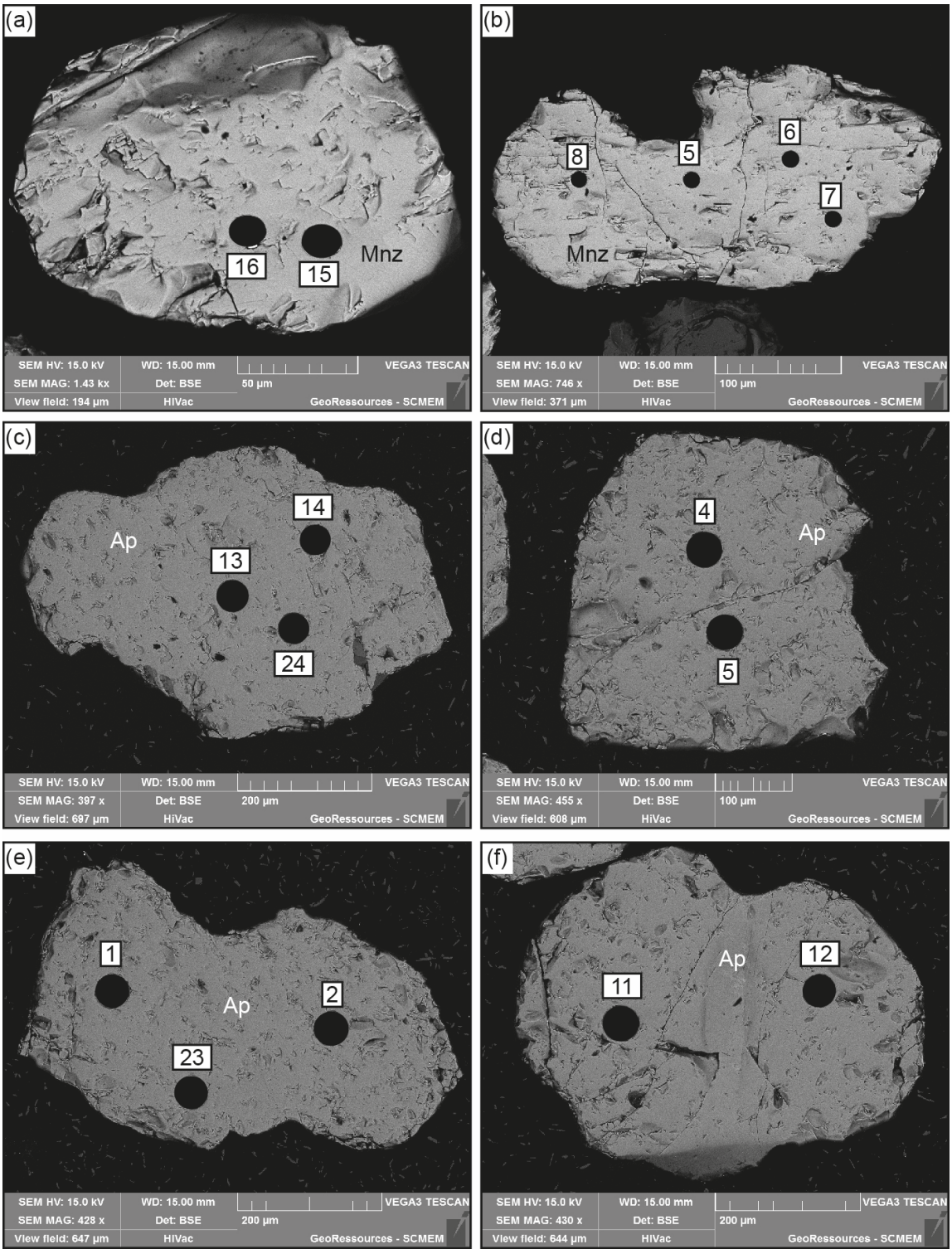

Figure S2-1. Representative SEM images of monazite (a and b) and apatite (c to f) crystals investigated for LA-ICP-MS U-(Th-)Pb dating. Numbers in white squares refer to U-(Th-)Pb dating analyses reported in Table 2-1 for monazite and in Table 2-2 for apatite grains. Note the unzoned character of both monazite and apatite crystals, consistent with their homogeneous chemical compositions. Abbreviations: Ap = apatite; Mnz = monazite.

References

Augland, L.E., Moukhsil, A., Solgadi, F., Indares, A. and McFarlane, C., 2015. Pinwarian to Grenvillian magmatic evolution in the central Grenville Province: new constraints from ID-TIMS U-Pb ages and coupled Lu-Hf S-MC-ICP-MS data: *Canadian Journal of Earth Sciences*, **52**, p. 701–721, doi: 10.1139/cjes-2014-0232.

Ballouard, C., Boulvais, P., Poujol, M., Gapais, D., Yamato, P., Tartèse, R. and Cuney, M., 2015. Tectonic record, magmatic history and hydrothermal alteration in the Hercynian Guérande leucogranite, Armorican Massif, France: *Lithos*, **220–223**, p. 1–22, doi: 10.1016/j.lithos.2015.01.027.

Brown, M., 2014. The contribution of metamorphic petrology to understanding lithosphere evolution and geodynamics: *Geoscience Frontiers*, **5**, p. 553–569, doi: 10.1016/j.gsf.2014.02.005.

Cherniak, D.J., Lanford, W.A. and Ryerson, F.J., 1991. Lead diffusion in apatite and zircon using ion implantation and Rutherford Backscattering techniques: *Geochimica et Cosmochimica Acta*, **55**, p. 1663–1673, doi: 10.1016/0016-7037(91)90137-T.

Chew, D.M., Petrus, J.A. and Kamber, B.S., 2014. U–Pb LA–ICPMS dating using accessory mineral standards with variable common Pb: *Chemical Geology*, **363**, p. 185–199, doi: 10.1016/j.chemgeo.2013.11.006.

Dodson, M., 1973. Closure temperature in cooling geochronological and petrological systems: *Contributions to Mineralogy & Petrology*, **40**, p. 259.

Dunlap, W.J., 2000. Nature's diffusion experiment: The cooling-rate cooling-age correlation: *Geology*, **28**, p. 139–142, doi: 10.1130/0091-7613(2000)28<139:NDETCC>2.0.CO;2.

Dunning, G. and Indares, A., 2010. New insights on the 1.7–1.0 Ga crustal evolution of the central Grenville Province from the Manicouagan – Baie Comeau transect: *Precambrian Research*, **180**, p. 204–226, doi: 10.1016/j.precamres.2010.04.005.

Engi, M., Lanari, P. and Kohn, M.J., 2017. Significant ages - An introduction to petrochronology: *Reviews in Mineralogy & Geochemistry*, **83**, p. 1–12, doi: 10.2138/rmg.2017.83.1.

Gasquet, D., Bertrand, J.-M., Paquette, J.-L., Lehmann, J., Ratzov, G., Guedes, R.D.A., Tiepolo, M., Boullier, A.-M., Scaillet, S. and Nomade, S., 2010. Miocene to Messinian

deformation and hydrothermal activity in a pre-Alpine basement massif of the French western Alps: new U-Th-Pb and argon ages from the Lauzière massif: *Bulletin de la Societe Geologique de France*, **181**, p. 227–241, doi: 10.2113/gssgfbull.181.3.227.

Indares, A. and Dunning, G., 2004. Crustal architecture above the high-pressure belt of the Grenville Province in the Manicouagan area: new structural, petrologic and U–Pb age constraints: *Precambrian Research*, **130**, p. 199–228, doi: 10.1016/j.precamres.2003.11.005.

Jannin, S., Gervais, F., Moukhsil, A., Augland, L.E. and Crowley, J.L., accepted. Déformations tardi-grenvilliennes dans la Ceinture parautochtone (Province de Grenville centrale) : contraintes géochronologiques par couplage de méthodes U/Pb de haute résolution spatiale et de haute précision: *Canadian Journal of Earth Sciences*,.

Johnson, T.E., Clark, C., Taylor, R.J.M., Santosh, M. and Collins, A.S., 2015. Prograde and retrograde growth of monazite in migmatites: An example from the Nagercoil Block, southern India: *Geoscience Frontiers*, **6**, p. 373–387, doi: 10.1016/j.gsf.2014.12.003.

Jordan, S.L., Indares, A. and Dunning, G., 2006. Partial melting of metapelites in the Gagnon terrane below the high-pressure belt in the Manicouagan area (Grenville Province): pressure–temperature (P–T) and U–Pb age constraints and implications: *Canadian Journal of Earth Sciences*, **43**, p. 1309–1329, doi: 10.1139/E06-038.

Kelsey, D.E., Clark, C. and Hand, M., 2008. Thermobarometric modelling of zircon and monazite growth in melt-bearing systems: examples using model metapelitic and metapsammitic granulites: *Journal of Metamorphic Geology*, **26**, p. 199–212, doi: 10.1111/j.1525-1314.2007.00757.x.

Kohn, M.J., 2008. P-T-t data from central Nepal support critical taper and repudiate large-scale channel flow of the Greater Himalayan Sequence: *GSA Bulletin*, **120**, p. 259–273, doi: 10.1130/B26252.1.

Lasalle, S., Dunning, G. and Indares, A., 2014. In situ LA–ICP–MS dating of monazite from aluminous gneisses: insights on the tectono-metamorphic history of a granulite-facies domain in the central Grenville Province: *Canadian Journal of Earth Sciences*, **51**, p. 558–572, doi: 10.1139/cjes-2013-0170.

Lasalle, S., Fisher, C.M., Indares, A. and Dunning, G., 2013. Contrasting types of Grenvillian granulite facies aluminous gneisses: Insights on protoliths and metamorphic events from

zircon morphologies and ages: *Precambrian Research*, **228**, p. 117–130, doi: 10.1016/j.precamres.2013.01.014.

Lasalle, S. and Indares, A., 2014. Anatectic record and contrasting P-T paths of aluminous gneisses from the central Grenville Province: *Journal of Metamorphic Geology*, **32**, p. 627–646, doi: 10.1111/jmg.12083.

McDowell, F.W., McIntosh, W.C. and Farley, K.A., 2005. A precise 40Ar–39Ar reference age for the Durango apatite (U–Th)/He and fission-track dating standard: *Chemical Geology*, **214**, p. 249–263, doi: 10.1016/j.chemgeo.2004.10.002.

Moukhsil, A., Solgadi, F., Belkacim, S., Elbasbas, A. and Augland, L.E., 2014. Géologie de la région du lac Okaopéo, Côte-Nord: *Ministère de l'Energie et des Ressources Naturelles, Québec,* **RG 2014-03**, p. 34 p.

Nelson, K.D., Zhao, W., Brown, L.D., Kuo, J., Che, J., Liu, X., Klemperer, S.L., Makovsky, Y., Meissner, R., Mechie, J., Kind, R., Wenzel, F., Ni, J., Nabelek, J., Leshou, C., Tan, H., Wei, W., Jones, A.G., Booker, J., Unsworth, M., Kidd, W.S.F., Hauck, M., Alsdorf, D., Ross, A., Cogan, M., Wu, C., Sandvol, E. and Edwards, M., 1996. Partially Molten Middle Crust Beneath Southern Tibet: Synthesis of Project INDEPTH Results: *Science*, **274**, p. 1684–1688, doi: 10.2307/2890941.

Paquette, J.L. and Tiepolo, M., 2007. High resolution (5 μm) U–Th–Pb isotope dating of monazite with excimer laser ablation (ELA)-ICPMS: *Chemical Geology*, **240**, p. 222–237, doi: 10.1016/j.chemgeo.2007.02.014.

Paton, C., Woodhead, J.D., Hellstrom, J.C., Hergt, J.M., Greig, A. and Maas, R., 2010. Improved laser ablation U-Pb zircon geochronology through robust downhole fractionation correction: *Geochemistry, Geophysics, Geosystems*, **11**, p. Q0AA06, doi: 10.1029/2009GC002618.

Pochon, A., Poujol, M., Gloaguen, E., Branquet, Y., Cagnard, F., Gumiaux, C. and Gapais, D., 2016. U-Pb LA-ICP-MS dating of apatite in mafic rocks: Evidence for a major magmatic event at the Devonian-Carboniferous boundary in the Armorican Massif (France): *American Mineralogist*, **101**, p. 2430–2442, doi: 10.2138/am-2016-5736.

Rivers, T., 2008. Assembly and preservation of lower, mid, and upper orogenic crust in the Grenville Province—Implications for the evolution of large hot long-duration orogens: *Precambrian Research*, **167**, p. 237–259, doi: 10.1016/j.precamres.2008.08.005.

Rivers, T., Culshaw, N., Hynes, A., Indares, A., Jamieson, R. and Martignole, J., 2012. The Grenville Orogen - A Post-LITHOPROBE Perspective. In: J.A. Percival, F.A. Cook, and R.M. Clowes (eds) *Tectonic Styles in Canada: The LITHOPROBE Perspective*, *Geological Association of Canada, Special Paper 49,* p. 97–236.

Schoene, B. and Bowring, S.A., 2007. Determining accurate temperature–time paths from U–Pb thermochronology: An example from the Kaapvaal craton, southern Africa: *Geochimica et Cosmochimica Acta*, **71**, p. 165–185, doi: 10.1016/j.gca.2006.08.029.

Schoene, B. and Bowring, S.A., 2006. U–Pb systematics of the McClure Mountain syenite: thermochronological constraints on the age of the 40Ar/39Ar standard MMhb: *Contributions to Mineralogy and Petrology*, **151**, p. 615, doi: 10.1007/s00410-006-0077-4.

Slagstad, T., Hamilton, M.A., Jamieson, R.A. and Culshaw, N.G., 2004. Timing and duration of melting in the mid orogenic crust: Constraints from U-Pb (SHRIMP) data, Muskoka and Shawanaga domains, Grenville Province, Ontario: *Canadian Journal of Earth Sciences*, **41**, p. 1339–1365, doi: 10.1139/e04-068.

Stacey, J.S. and Kramers, J.D., 1975. Approximation of terrestrial lead isotope evolution by a two-stage model: *Earth and Planetary Science Letters*, **26**, p. 207–221, doi: 10.1016/0012-821X(75)90088-6.

Tera, F. and Wasserburg, G.J., 1972. U-Th-Pb systematics in lunar highland samples from the Luna 20 and Apollo 16 missions: *Earth and Planetary Science Letters*, **17**, p. 36–51, doi: 10.1016/0012-821X(72)90257-9.

Thomson, S.N., Gehrels, G.E., Ruiz, J. and Buchwaldt, R., 2012. Routine low-damage apatite U-Pb dating using laser ablation–multicollector–ICPMS: *Geochemistry, Geophysics, Geosystems*, **13**, p. Q0AA21, doi: 10.1029/2011GC003928.

Turlin, F., André-Mayer, A.-S., Moukhsil, A., Vanderhaeghe, O., Gervais, F., Solgadi, F., Groulier, P.-A. and Poujol, M., 2017. Unusual LREE-rich, peraluminous, monazite- or allanite-bearing pegmatitic granite in the central Grenville Province, Québec: *Ore Geology Reviews*, **89**, p. 627–667, doi: 10.1016/j.oregeorev.2017.04.019.

Van Achterbergh, E., Ryan, C.G., Jackson, S.E. and Griffin, W.L., 2001. Data reduction software for LA-ICP-MS: appendix: *Laser-Ablation-ICPMS in the earth sciences—principles and applications. Miner Assoc Can (short course series)*, **29**, p. 239–243.

Vanderhaeghe, O., 2001. Melt segragation, pervasive melt migration and magma mobility in the continental crust: the structural record from pores to orogens: *Physics and Chemistry of the Earth, Part A: Solid Earth and Geodesy*, **26**, p. 213–223, doi: 10.1016/S1464-1895(01)00048-5.

Vanderhaeghe, O., 2009. Migmatites, granites and orogeny: Flow modes of partially-molten rocks and magmas associated with melt/solid segregation in orogenic belts: *Tectonophysics*, **477**, p. 119–134, doi: 10.1016/j.tecto.2009.06.021.

Vanderhaeghe, O., 2012. The thermal–mechanical evolution of crustal orogenic belts at convergent plate boundaries: A reappraisal of the orogenic cycle: *Journal of Geodynamics*, **56**–**57**, p. 124–145, doi: 10.1016/j.jog.2011.10.004.

Yakymchuk, C., 2017. Behaviour of apatite during partial melting of metapelites and consequences for prograde suprasolidus monazite growth: *Lithos*, **274**–**275**, p. 412–426, doi: 10.1016/j.lithos.2017.01.009.

Yakymchuk, C. and Brown, M., 2014. Behaviour of zircon and monazite during crustal melting: *Journal of the Geological Society*, **171**, p. 465–479, doi: 10.1144/jgs2013-115.

Yakymchuk, C., Clark, C. and White, R.W., 2017. Phase Relations, Reaction Sequences and Petrochronology: *Reviews in Mineralogy & Geochemistry*, **83**, p. 13–53, doi: 10.2138/rmg.2017.83.2.

Chapitre 3 : Pegmatitic granite dykes in the central Grenville Belt a result of partial melting of Paleoproterozoic-Archean metasedimentary rocks: evidence from zircon U-Pb-Hf-O isotope and trace element analyses

François Turlin[a], Olivier Vanderhaeghe[b], Félix Gervais[c], Anne-Sylvie André-Mayer[a], Abdelali Moukhsil[d], Armin Zeh[e,f], Fabien Solgadi[g], I.P.T.N.[h]

Article à soumettre à *Precambrian Research*

[a] *GeoRessources lab., Université de Lorraine, CNRS, CREGU, Campus Aiguillettes, Faculté des Sciences et Technologies, rue Jacques Callot, Vandœuvre-lès-Nancy, F-54506, France*

[b] *Géosciences Environnement Toulouse, UMR 5563, Université de Toulouse, France*

[c] *Département des génies civil, géologiques et des mines, Polytechnique Montréal, Canada*

[d] *Ministère de l'Énergie et des Ressources naturelle, Direction du Bureau de la connaissance géoscientifique du Québec, 5700, 4e Avenue Ouest, Québec (Québec)*

[e] *Institut für Geowissenschaften, Frankfurt, Germany*

[f] *Now at KIT-Karlsruhe Institute of Technology, Campus South, Institute for Applied Geosciences, Mineralogy and Petrology*

[g] *Ministère de l'Énergie et des Ressources naturelles, Direction du Bureau de la connaissance géoscientifique du Québec, 400, boulevard Lamaque, Val-d'Or (Québec)*

[h] *Ion Probe Team Nancy, CRPG, UMR 7358, CNRS, Université de Lorraine, Vandœuvre-lès-Nancy, F-54501, France*

Abstract

The Allochthonous Belt of the central Grenville Province hosts LREE-rich pegmatitic granite dykes (PGD) intrusive into orthogneisses and migmatitic paragneisses. Shapes, internal zoning, trace elements and isotopic data of zircon grains from a monazite-bearing PGD and two allanite-bearing PGD of the Lac Okaopéo region were investigated. Results of U-Pb dating yield Concordia ages of 1004.2±2.1 Ma, 1001.9±3.9 Ma and 1004.2±2.3 Ma, respectively, and indicate that emplacement of all three dykes occurred during the early-Rigolet orogenic phase, the same period when rocks of the adjacent Parautochthonous Belt were affected by high-grade metamorphism up to granulite facies conditions. Trace elements contents (U, Yb, Y), subchondritic $\varepsilon Hf_{(1003\ Ma)}$ values of zircon grains from -4.7 to -11.8, Hf model ages from 2.05 to 2.44 Ga, and predominately supra-mantellic dominated mode of distribution of $\delta^{18}O_{V\text{-}SMOW}$ values (>5.3‰) of zircons suggest that the dykes were formed by high-temperature partial melting of Paleoproterozoic-Archean metasedimentary units at depth belonging either to the Allochthonous (Plus-Value Complex paragneisses) and/or Parautochthonous Belt (Knob Lake Group paragneisses). High temperature partial melting is also suggested by the lack of any inherited zircon xenocrysts in the dykes.

These results point to the partially molten character of Paleoproterozoic-Archean metasedimentary units underneath a thickened Allochthonous Belt before ca. 1005 Ma in the central Grenville. This study therefore contributes to the integration of the petrogenesis of LREE pegmatitic granite dykes into the geodynamic context of the Grenville Province at the transition between the Ottawan and Rigolet orogenic phases.

Keywords: Zircon; U-Pb dating; Hf-O isotopes; Trace elements; Grenville Province; Pegmatitic granite

1. Introduction

Tracing the source of igneous rocks and their petrogenesis in the frame of the tectonic-metamorphic evolution of the crust is a recurrent theme in geology, especially for granitic magmas for which most of the debate focuses on the relative importance of mantellic vs crustal input during collision- vs subduction-related magmatism (e.g. Barbarin, 1999; Chappell and White, 2001; Healy et al., 2004; Moyen et al., 2017; Smithies et al., 2011; Toé et al., 2013). When considering their pegmatitic end-members, studies have essentially focused on proving their derivation by extreme fractionation of their igneous parents, as shown by the commonly used classifications of Černý et al. (2012) and Černý and Ercit (2005) that distinguish their igneous parents on the basis of their orogenic (crustal shortening, subduction and collision: LCT pegmatites) or anorogenic settings (crustal thinning and rifting: NYF pegmatites) (Martin and De Vito, 2005, and references therein). However, several contributions concluded to a probable derivation of such intrusives by partial melting of a crustal/sub-crustal component (e.g. Černý et al., 2012; Ercit, 2005; Lentz, 1991; London, 2016; Martin and De Vito, 2005). Pegmatitic granites are particularly abundant in the Grenville Belt (e.g. Ayres and Černý, 1982; Ercit, 2005; Fowler and Doig, 1983; Masson and Gordon, 1981; Turlin et al., 2017) and thus represent a potential target to test these hypotheses.

The Grenvillian Orogeny results from a continent-continent collision (Hynes and Rivers, 2010), most likely between Laurentia and Amazonia (e.g. Hoffman, 1991; Li et al., 2008; Tohver et al., 2006), which occurred between ca. 1090 and 960 Ma. It is characterized by two diachronous and spatially disconnected phases of crustal thickening, namely the (i) Ottawan phase (ca. 1090-1020 Ma) in the Allochthonous Belt and the (ii) Rigolet phase (ca. 1005-960 Ma) in the Parautochthonous Belt. The Allochthonous Belt consists of terranes that originated outboard of and were accreted to the Laurentia margin, and the Parautochthonous Belt comprises ancient rocks from the Superior Province, its cover sequences, or previously accreted arcs which all were reworked during the Grenvillian Orogeny (Fig. 3-1b) (e.g. Carr et al., 2000; Dunning and Indares, 2010; Gower and Krogh, 2002; Jannin et al., accepted; Rivers, 2008; Rivers et al., 2012; Tucker and Gower, 1994). In the Allochthonous Belt, the Ottawan phase is characterized by the formation of an orogenic plateau overlying a ductile mid-crustal allochthonous crust above the Allochthon Boundary Thrust (ABT) (Rivers, 2008; Rivers et al., 2012). The ABT corresponds to an orogenic-scale southeast shallow-dipping high-grade shear zone that separates the Allochthonous from the Parautochthonous Belt (Rivers et al., 1989; Rivers, 2008; Rivers et al., 2012). In the Parautochthonous Belt, up to granulite-facies peak of

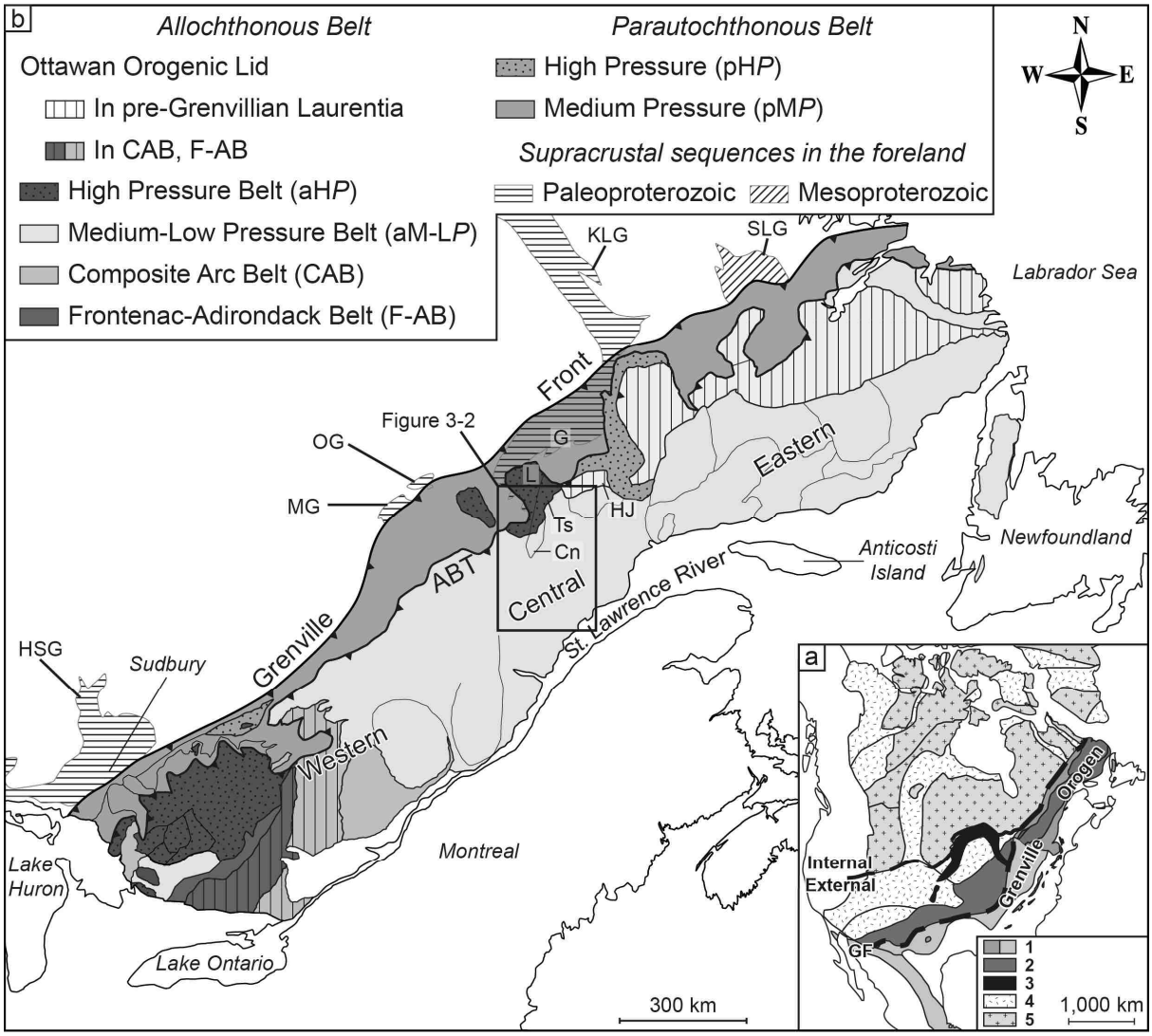

Figure 3-1: a: Map of Proterozoic Laurentia showing the different north-American orogens with Paleozoic and younger cover omitted (modified from Hoffman, 1989; Rivers et al., 2012). The northern dashed line represents the boundary between Internal and External Paleoproterozoic Laurentia and the southern dashed line represents the Grenville Front (GF); b: Simplified geological map of the Grenville Province. Extension of supracrustal sequences in the foreland after Rivers (2008). Abbreviations: 1 = exposed Grenville Province, light grey represents the inferred extension of subsurface allochthonous Grenville Province; 2 = Granite-Rhyolite Igneous Province, ca. 1.50-1.34 Ga and reworked equivalents in the Grenville Province; 3 = Mid-Continental Rift system; 4 = Paleoproterozoic orogens, ca. 1.9-1.8 Ga, ca. 1.65 Ga and reworked equivalents in the Grenville Province; 5 = cratons; Cn = Canyon domain; G = Gagnon Terrane; GF = Grenville Front; HJ = Hart-Jaune terrane; HSG = Huron Supergroup; KLG = Knob Lake Group; L = Lelukuau terrane; MG = Mistassini Group; OG = Otish Group; SLG = Seal Lake Group; Ts = Tshenukutish terrane.

metamorphism represents the foreland-ward propagation of Grenvillian thrusting and metamorphism (Fig. 3-1b, Hynes et al., 2000; Jannin et al., accepted; Jordan et al., 2006; Rivers, 2009; Rivers et al., 2012; van Gool et al., 2008). The two phases are separated by a hiatus in magmatic and metamorphic activity of ca. 10-20 Ma. It is suggested to reflect the redevelopment of a steady-state state geotherm following the cooling of mid crustal levels provoked by their juxtaposition to cooler upper crustal levels in response to late-Ottawan orogenic collapse (Rivers, 2008, 2009).

Turlin et al. (2017) reported the occurrence of LREE-rich (monazite-bearing or allanite-bearing) peraluminous pegmatitic granite dykes *(further designated as 'PGD')* in the Lac Okaopéo region, which is part of the Allochthonous Belt of the central Grenville Province (Figs. 3-2 and 3-3). In this region, structures and metamorphic assemblages have been attributed to the Ottawan orogenic phase (Augland et al., 2015; Dunning and Indares, 2010; Lasalle et al., 2013, 2014; Lasalle and Indares, 2014). The discordant position of the PGD relative to their country rocks, their magmatic textures, and their U/Pb ages on monazite from monazite-bearing PGD of ca. 1005-1000 Ma led Turlin et al. (2017) to propose a post-tectonic emplacement of these PGD. Moreover, on the basis of their peraluminous character they suggested an origin of the PGD by partial melting of metapelites but the source(s) of these PGD remains unconstrained. They can belong to the base of the Allochthonous or to the Parautochthonous Belt. Even though allanite-bearing PGD were interpreted to be coeval with monazite-bearing PGD during the Rigolet orogenic phase (Turlin et al., 2017), no geochronological data support this statement. One of the best attempts of integration of pegmatitic granite in a tectonic-metamorphic setting in the Grenville Province lies in the model of Lentz (1991) who proposed a model of mid-crustal melting associated with crustal thickening and late-tectonic gravitational uplift during the late-stages of the Grenvillian Orogeny for REE-enriched pegmatitic granite. However, in this province, the derivation of pegmatitic granite by partial melting of a preexisting crust is only inferred based on the lack of coeval granitic plutons (Ercit, 2005; Lentz, 1991). The latter is commonly inferred in the Grenville Province according to the lack of coeval granitic plutons (Ercit, 2005; Lentz, 1991).

Over the last few decades, zircon has proved to be one of the most reliable tools to investigate both the timing of magmatic crystallization and the crust-mantle evolution by combining petrography, geochemistry, U-Pb dating and Lu-Hf-O isotope analyses (e.g. Belousova et al., 2010; Cawood et al., 2013; Dhuime et al., 2012; Hawkesworth et al., 2009; Spencer et al., 2015; Zeh et al., 2014). In this study, we present new trace element and U-Pb-Hf-O isotopic data of well characterized zircon grains from a monazite-bearing PGD and two allanite-bearing PGD from the Lac Okaopéo region (central Grenville, Figs. 3-2 and 3-3). These data place new constraints on the nature of the PGD sources within the crust and mantle, and the timing of their emplacement. Furthermore, they provide new information about the deep-crustal processes which occurred at the transition between the Ottawan and the Rigolet orogenic phases of the Grenvillian Orogeny.

2. Geological framework

2.1. Geodynamic evolution of the central Grenville

The Grenville Province results from a protracted accretion along the southeastern margin of Laurentia from the late-Paleoproterozoic to the late-Mesoproterozoic. This accretion process is reflected by several orogenies, comprising the Labradorian (ca. 1.71-1.60 Ga), Pinwarian (ca. 1.47-1.45 Ga), Elzevirian (ca. 1.25-1.23 Ma) and Shawinigan (ca. 1.19-1.14 Ga) orogenies. Tectono-metamorphic overprints related to the two latter orogenies are restricted to the western Grenville Province (Ketchum et al., 1994; Rivers, 1997; Rivers et al., 2012; Tucker and Gower, 1994). The Grenvillian Orogeny *sensu stricto* was caused by a continent-continent collision in the late-Mesoproterozoic to the early-Neoproterozoic (e.g. Carr et al., 2000; Dunning and Indares, 2010; Gower and Krogh, 2002; Rivers et al., 2012; Tucker and Gower, 1994).

The central Grenville Province is divided into two major tectono-metamorphic-magmatic domains, the Allochthonous Belt and the Parautochthonous Belt, which are of different origin and were affected by a different style of metamorphic overprint (e.g. Rivers et al., 2012). The Allochthonous Belt was formed during the Ottawan crustal thickening at ca. 1070-1050 Ma. The Allochthonous Belt is subdivided further into a medium to low pressure Allochthonous Belt (aM-L*P*, Fig. 3-1b), and a high pressure Allochthonous Belt (aH*P*, Fig. 3-1b). The aM-L*P* belt south of the Manicouagan reservoir hosts the PGD investigated in this study and is characterized by sillimanite-bearing gneisses which reached peak metamorphic *P-T* conditions of ca. 950 MPa at 850 °C (Dunning and Indares, 2010; Lasalle et al., 2014; Lasalle and Indares, 2014). The aH*P* belt is structurally below the aM-L*P* belt hosting the PGD and comprises Paleoproterozoic and Mesoproterozoic rocks of the Manicouagan Imbricate Zone (MIZ, Fig. 3-2). These mostly contain kyanite and reached peak metamorphic *P-T* conditions of ca. 1450-1600 MPa and 860-900 °C (Indares et al., 1998; Indares and Dunning, 2001; Lasalle and Indares, 2014; Rivers et al., 2002). Both styles of metamorphic overprint have been attributed to syn-Ottawan channel flow of the ductile aH*P* and aM-L*P* crustal segments underneath a thickened orogenic plateau, which is inferred to stop at ca. 1050 Ma (e.g. Rivers, 2008).

Subsequently, this thickened orogenic plateau collapsed during the late- to post-Ottawan phase (ca. 1050-1020 Ma). It resulted in mid-crust thinning accommodated by simple and pure shear mechanisms (Rivers, 2012) and in the reworking of the northwest-directed ABT as a top-

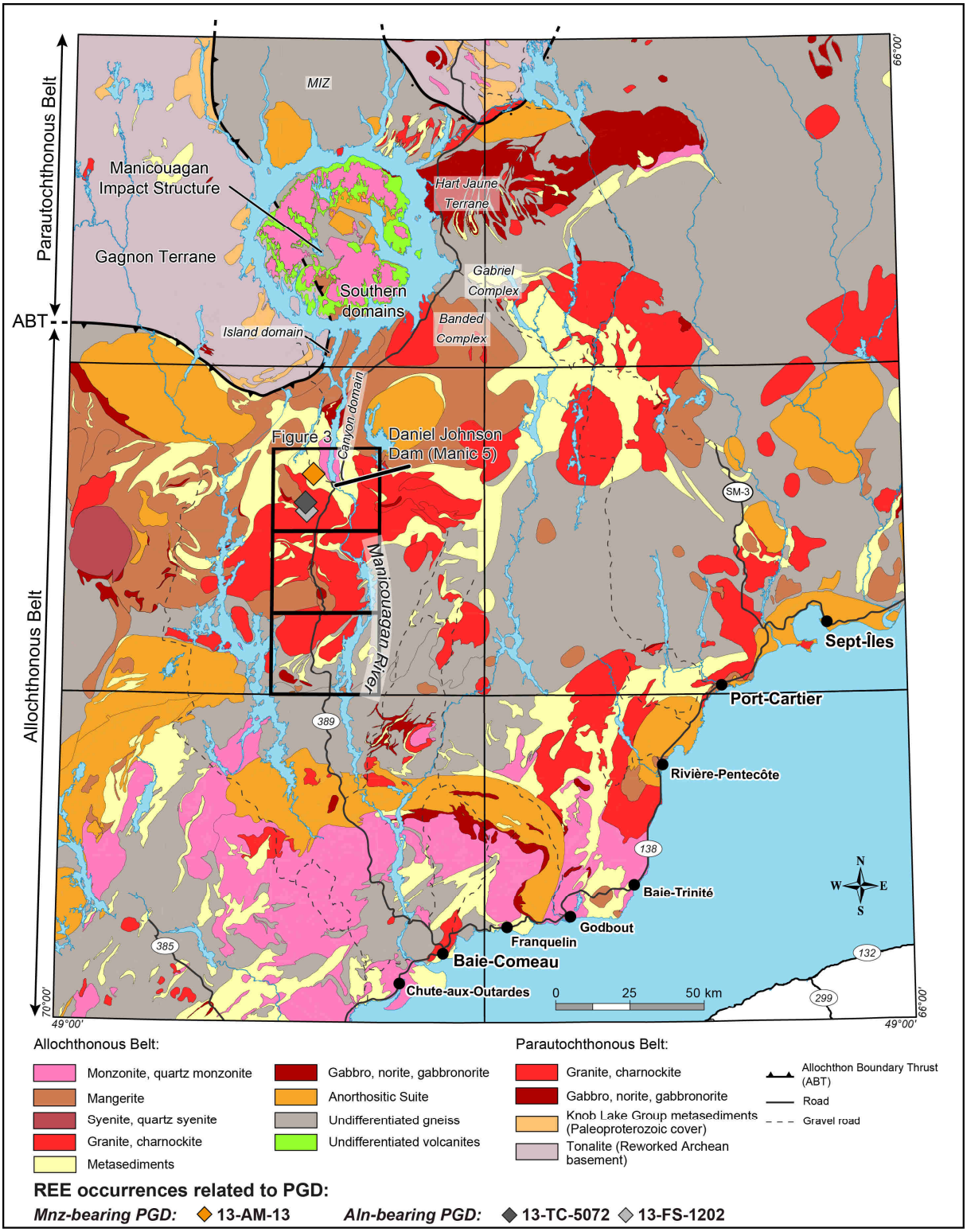

Figure 3-2: Geological map of the central Grenville (Quebec) showing the position of the investigated monazite- and allanite-bearing pegmatitic granite dykes (modified after Moukhsil et al., 2014; Turlin et al., 2017). Abbreviations: ABT = Allochthon Boundary Thrust; Aln-bearing PGD = allanite-bearing pegmatitic granite dyke; MIZ = Manicouagan Imbricate Zone; Mnz-bearing PGD = monazite-bearing pegmatitic granite dyke.

to-the-southeast normal-sense shear zone (Allochthonous Boundary Detachment, ABD). Evidence for material extrusion in response to orogenic collapse in the central Grenville Province (Tshenukutish Terrane, a*HP* belt, Fig. 3-1) consist in the activation of the

Tshenukutish shear zone until ca. 1020 Ma (Hynes et al., 2000; Indares et al., 2000; Rivers et al., 2002). This extensional setting resulted in the formation of a crustal-scale horsts (aM-L*P* segments) and grabens (Orogenic Lid) architecture, and by subhorizontal normal-sense flow of mid-crustal levels (Culshaw et al., 1994; Ketchum et al., 1998; Rivers, 2008, 2012).

Following a ca. 10-20 Ma metamorphic and magmatic hiatus, the subsequent Rigolet orogenic phase (1005-960 Ma) is recorded in a medium pressure segment of the Parautochthonous Belt (pM*P*, Fig. 3-1b) of the central Grenville by a granulite-facies peak of metamorphism between ca. 1005 and 980 Ma, at *P-T* conditions of ca. 1250-1500 MPa and ca. 815-850 °C (Hynes et al., 2000; Jannin et al., accepted; Jordan et al., 2006; Rivers, 2009; Rivers et al., 2012; van Gool et al., 2008). These conditions were reached in the Knob Lake Group Paleoproterozoic metapelites (south of the reservoir) that unconformably overlie the Laurentian basement (Fig. 3-2, Gagnon Terrane, Dunning and Indares, 2010; Hynes et al., 2000; Rivers, 1980; Rivers et al., 1989). The high-grade metamorphism was associated with the dehydration melting of muscovite (Ms + Qtz + Pl → Kfs + Al_2SiO_5 + Liq.), and the subsequent dehydration melting of biotite (Bt + Al_2SiO_5 + Qtz → Kfs + Grt + Liq.), both in the kyanite stability field (Jannin et al., accepted). The U-Pb dating as early as ca. 1002 Ma of metamorphic rims of zircon grains which exhibit HREE-depletion and absence of negative Eu anomalies, indicating their growth in presence of peritectic garnet with no plagioclase are evidence for the partial melting of these metasediments (Jannin et al., accepted). The retrograde *P-T* path occurred in the sillimanite stability field (Jannin et al., accepted; Jordan et al., 2006) and most probably lasted until ca. 961 Ma, as shown by synkinematic intrusion of dykes and sills of pegmatite on the southern shore of the Manicouagan Reservoir at upper and lower structural levels of the Parautochthonous and Allochthonous belts, respectively (Fig. 3-2, Jannin et al., accepted). The Rigolet orogenic phase is interpreted as the foreland-ward propagation of Grenvillian high-grade metamorphism and thrusting towards the Grenville Front (Fig. 3-1) that represents a syn-Rigolet orogen-scale southeast-dipping shear zone (Krogh, 1994; Rivers et al., 1989; Rivers, 2008, 2009).

2.2. Isotopic signatures of the Allochthonous Belt

The study area is located south of the Manicouagan Impact Structure (Fig. 3-2) in the Allochthonous Belt of central Grenville and is composed of various pre-Grenvillian units. The oldest rocks are paragneisses of the Plus-Value Complex (Fig. 3-2), showing deposition ages ranging between 1765 (U-Pb ages on detrital zircon from a quartzite) and 1497 Ma (U-Pb on

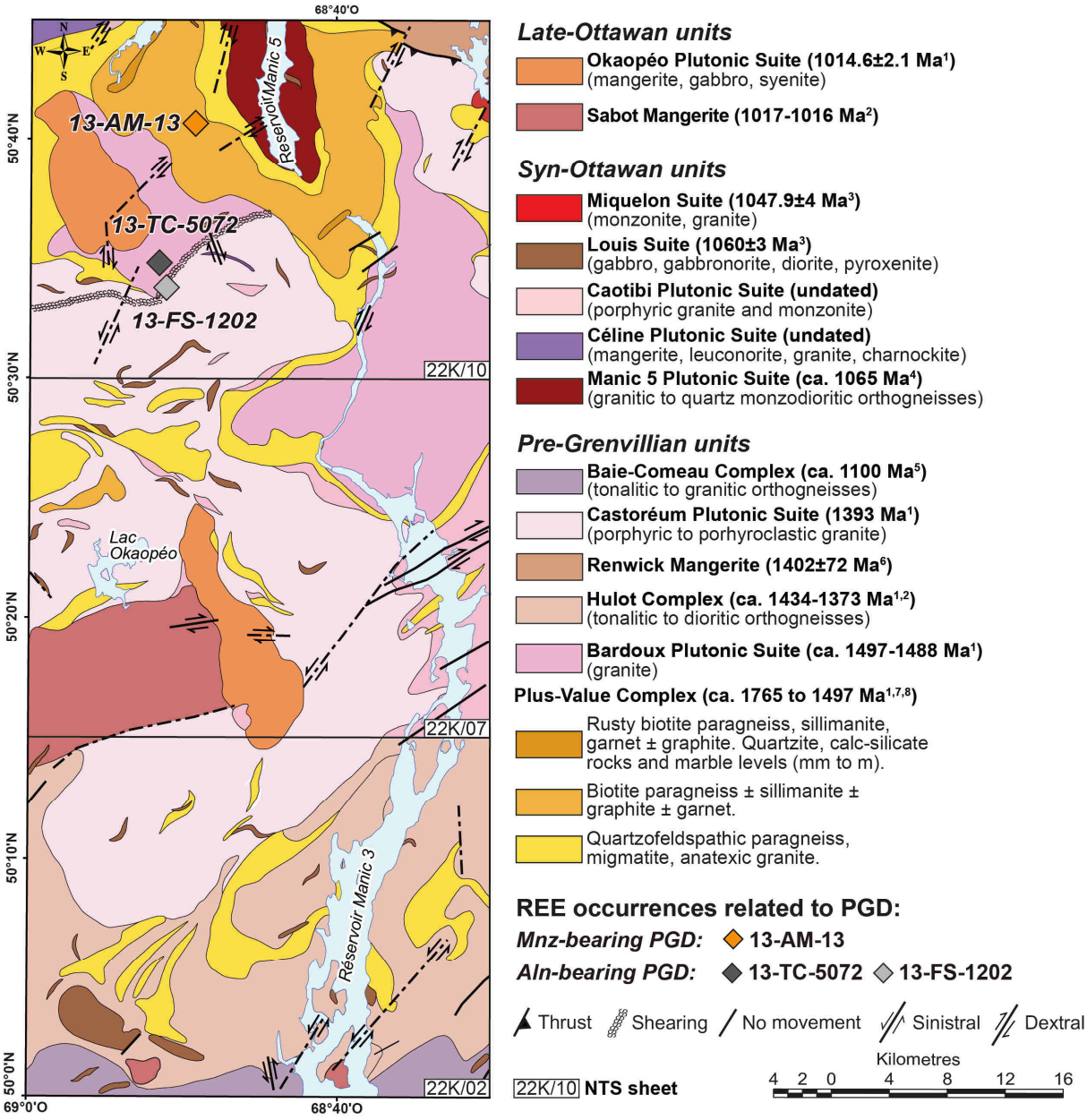

Figure 3-3: Simplified geological map of the environment of the investigated REE-rich pegmatitic granite dykes in the Lac Okaopéo region (modified after Moukhsil et al., 2014; Turlin et al., 2017). Star and diamonds represent monazite-bearing and allanite-bearing pegmatitic granite outcrops respectively. [1]: Augland et al. (2015); [2]: Gobeil et al. (2002); [3]: David (2006); [4]: Dunning and Indares (2010); [5]: David et al. (2009); [6]: Moukhsil et al. (2013a); [7]: Moukhsil et al. (2012); [8]: Lasalle et al. (2013). Abbreviation: PGD = pegmatitic granite dyke.

zircon from the intrusive Bardoux Plutonic Suite) (Augland et al., 2015; Lasalle et al., 2013; Moukhsil et al., 2013b, 2014). Detrital zircon grains in these paragneisses yield U-Pb ages between 2.70 and 1.50 Ga, but most grains gave ages between 1.90 and 1.50 Ga. The zircon detritus reflects (i) their provenance from the Laurentian margin and (ii) their correlation with other units such as the Archean basement and the Paleoproterozoic sequences of the Gagnon Terrane (Parautochthonous Belt) (Jordan et al., 2006; Lasalle et al., 2013; van Gool et al., 2008). Younger units are represented by the numerous Mesoproterozoic plutonic suites emplaced between ca. 1450 Ma and 1100 Ma, i.e. from the late-Pinwarian (ca. 1470-1450 Ma) to the post-

Elzevirian (ca. 1245-1225 Ma) orogenies. They include granitic, tonalitic to dioritic orthogneisses, metamangerite, metagranite and gabbronorite dykes (Augland et al., 2015; David et al., 2009; Gobeil et al., 2002; Moukhsil et al., 2007, 2012, 2013a, 2013b, 2014). The supra-chondritic $\varepsilon Hf_{1434\text{-}1383.4\ Ma}$ signatures for late-Pinwarian tonalitic orthogneisses and gabbronorite provide evidence for their mixed crustal and mantle sources (Augland et al., 2015). Among these are the Bardoux and Castoréum Plutonic Suites. The Bardoux Plutonic Suite corresponds to a metaluminous continental-arc I-type to minor peraluminous S-type metagranite emplaced into the Laurentian margin between ca. 1497 and 1488 Ma (U-Pb on zircon) with similar supra-chondritic $\varepsilon Hf_{1497\ Ma}$ signatures between +2.3 and +4.70 (Fig. 3-9, Augland et al., 2015; Moukhsil et al., 2014, 2012). The Castoréum Plutonic Suite corresponds to metagranite associated with minor charnockite, mangerite, granitic gneisses and metatonalite emplaced at 1393±8 Ma (U-Pb on zircon) in an arc-setting (Augland et al., 2015; Moukhsil et al., 2013b, 2014). Syn-Ottawan peak of high-grade metamorphism units include granitic to quartz-monzodioritic orthogneisses, slightly deformed monzonitic to granitic plutonic bodies and undeformed mafic rocks (David, 2006; Dunning and Indares, 2010; Moukhsil et al., 2007, 2009, 2013b, 2014). The subsequent late-Ottawan units include anorthosite, mangerite and charnockite±leuconorite±granite. The latest units are represented by the Sabot Mangerite (ca. 1016-1017 Ma) and the high-alkalic mangerite±gabbro±syenite from the Okaopéo Plutonic Suite (1014.6±2.1 Ma) with a near-chondritic $\varepsilon Hf_{1015\ Ma}$ signature between -1.73 and -1.01 (Augland et al., 2015; Gobeil et al., 2002; Moukhsil et al., 2007, 2009, 2013a, 2013b, 2014).

2.3. The pegmatitic granite dykes (PGD) intruding the Allochthonous Belt

Turlin et al. (2017) described REE-enriched PGD in the Allochthonous Belt of the central Grenville Province that intrude either paragneisses from the Plus-Value Complex (Figs. 3-3, 3-4a) or metaplutons from the Bardoux (Fig. 3-3, 3-4d) or from the Castoréum Plutonic Suites (Fig. 3-3, 3-4g). Rare-earth elements are hosted in monazite in paragneisses-hosted PGD and in allanite in metaplutons-hosted PGD (Turlin et al., 2017). All PGD considered in this contribution show steep-dipping walls discordant to the foliation of their hosts with no textural continuity with leucosomes and display magmatic textures with no evidence for solid-state deformation (Figs. 3-4a-i) and are thus considered as post-tectonic relative to their hosts (Turlin et al., 2017). In these PGD, textural relationships between zircon and monazite and the Th-Si-depleted/LREE-enriched cores of the latter provide evidence for the formation of zircon grains pre- to syn-LREE-bearing phases crystallization (Fig. 3-4 c, f and i, Turlin et al., 2017).

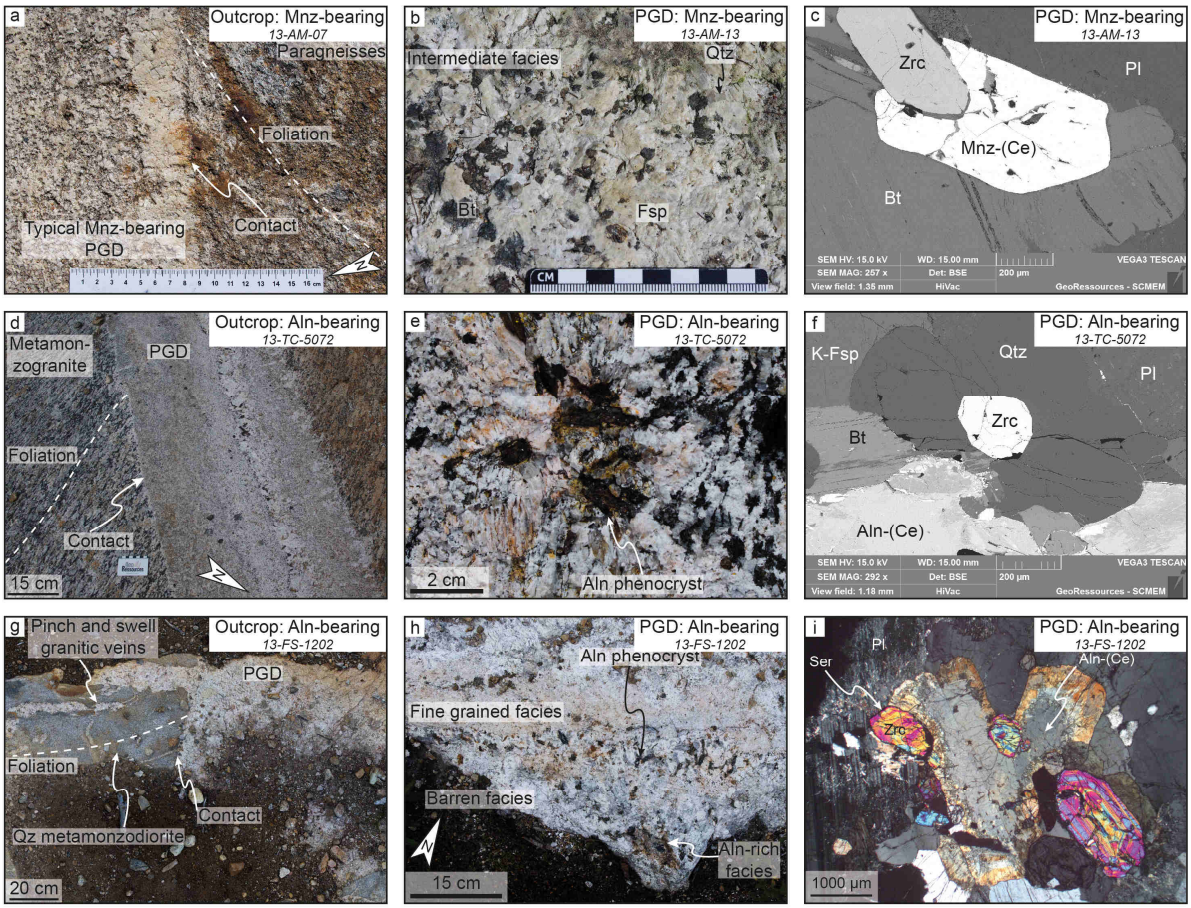

Figure 3-4: Representative photographs of outcrops, facies and petrography of monazite- and allanite-bearing pegmatitic granite dykes from the central Grenville investigated in this study. a: photograph of a discordant contact of a monazite-bearing dyke intruding paragneisses from the Plus-Value Complex. Note the Stockscheider texture underlining the contact in the dyke; b: typical quartz+feldspar+biotite dominated intermediate facies of the 13-AM-13 monazite-bearing PGD as defined by Turlin et al. (2017) sampled for this study; c: early- to syn-monazite crystallization zircon crystal (SEM) from the 13-AM-13 monazite-bearing dyke; d: photograph of a typical allanite-bearing pegmatitic granite dyke from the 13-TC-5072 outcrop showing discordant contacts with its host (metamonzogranite from the Bardoux Plutonic Suite); e: typical quartz+feldspar+biotite assemblage completed with phenocrysts of allanite from the 13-TC-5072 allanite-bearing pegmatitic granite dyke; f: sub-euhedral zircon grains and its relationships with the quartz+plagioclase+K-feldspar+biotite±allanite assemblage; g: photograph of a discordant contact of an allanite-bearing dyke with its host from the 13-FS-1202 outcrop (quartz-metamonzodiorite from the Castoréum Plutonic Suite). Note the textural continuity between the PGD and 'pinch and swell' granitic veins transposed in the foliation of the host; h: typical facies observed in the 13-FS-1202 pegmatitic granite; i: prismatic zircon grains and their relationships with the quartz+plagioclase+K-feldspar+biotite±allanite assemblage. Abbreviations: Aln = allanite; Aln-bearing = allanite-bearing pegmatitic granite dyke; Bt = biotite; Fsp = feldspar; K-Fsp = K-feldspar; Mnz = monazite; Mnz-bearing = monazite-bearing pegmatitic granite dyke; PGD = pegmatitic granite dyke; Pl = plagioclase; Qtz = quartz; Ser = sericite; Zrc = zircon.

3. Sampling and analytical methods

3.1. Sampling and preparation

One monazite- (13-AM-13, Fig. 3-4a-c) and two allanite-bearing (13-TC-5072, Fig. 3-4d-f, and 13-FS-1202, Fig. 3-4g-i) PGD described by Turlin et al. (2017) have been sampled for this study. These dykes display a variety of facies marked in particular by the heterogeneous

distribution of accessory minerals including zircon. We chose to sample the intermediate facies of these three PGD as defined by Turlin et al. (2017).

Classical separation techniques were performed at GeoRessources (Nancy, France) on the PGD to allow the liberation of the zircon grains investigated in this study. Hand-samples were crushed using a jaw and a roll crusher. The heavy fractions were then separated by classical density techniques (bromoform: density = 2.87 g/cm^3) and zircon grains of various shapes and sizes (100-2,500 µm) were handpicked under binocular microscope. The most representative crystals were mounted on an epoxy mount and characterized by means of back scattered electron (BSE) imaging performed at Goethe University Frankfurt (Germany). Inherited cores have nowhere been observed and porous domains have been avoided during analyses.

3.2. U-Pb dating and Lu-Hf isotope analyses of zircon

In-situ U-Pb and Lu-Hf isotopes analyses of nineteen zircon grains from the monazite-bearing PGD, fourteen zircon grains from the 13-TC-5072, and twenty-five zircon grains from the 13-FS-1202 allanite-bearing PGD were carried out by laser ablation-inductively coupled plasma-sector field-mass spectrometry (LA-ICP-SF-MS) at Goethe University Frankfurt (Germany), using similar methods and instruments as described by Gerdes and Zeh (2006, 2009), with modifications explained in Zeh and Gerdes (2012). Laser spots of Lu-Hf analyses (round spots with a size of 64-100 µm) were placed on-top of U-Pb laser spots (round spots with a size of 20-42 µm). Detailed analytical methods of U-Pb dating and Lu-Hf isotopes analyses and results are provided in Supplementary material and in Tables S3-1 and S3-2, respectively.

3.3. Trace elements analyses of zircon

Among zircon analyzed for U-Pb dating and Lu-Hf isotopes analyses, eleven zircon grains from the monazite-bearing PGD, thirteen zircon grains from the 13-TC-5072 and fifteen zircon grains from 13-FS-1202 allanite-bearing PGD were selected for trace elements analyses.

In-situ trace elements analyses were carried out by using LA-SF-ICP-MS at Goethe University Frankfurt (Germany). Laser spots (round spots with a size of 42 µm) were placed on representative domains of the investigated grains, when possible as close as possible of U-Pb and Lu-Hf laser spots. For this study, the following isotopes have been analyzed: ^{44}Ca, ^{49}Ti, ^{57}Fe, ^{89}Y, ^{139}La, ^{140}Ce, ^{141}Pr, ^{146}Nd, ^{147}Sm, ^{151}Eu, ^{158}Gd, ^{159}Tb, ^{161}Dy, ^{165}Ho, ^{167}Er, ^{169}Tm, ^{172}Yb,

^{175}Lu, ^{232}Th, and ^{238}U. Detailed analytical methods of trace elements analyses and results are provided in Supplementary material and in Table S3-3, respectively.

3.4. O isotopes analyses of zircon

Among zircon analyzed for U-Pb dating and Lu-Hf isotopes analyses, fourteen zircon grains from the monazite-bearing PGD, all zircon grains from the 13-TC-5072 and seventeen zircon grains from the 13-FS-1202 allanite-bearing PGD were selected for O isotopes analyses.

In-situ ion probe oxygen isotopes analyses were performed with the Cameca IMS 1280 HR2 ion microprobe, following Martin et al. (2008). The Cs^+ primary ion beam of 5 to7 nA was focused on a 20 µm diameter area and the electron gun used for the charge compensation. The negative secondary ions were measured with a mass resolution of 3000 (M/ΔM) with an energy slit of 35 eV. Before each measurement, the sample was pre-sputtered for 60 s with a beam rastering on 10 µm to clean up the sample surface, then the secondary beam was automatically centered in the field aperture and contrast aperture. The measurements were made on FC in multicollection mode with counting time of 120 s. The instrumental mass fractionation was determined on the reference zircon 91500. The results are shown in Table S3-4.

4. Zircon texture and pristine character

4.1. Zircon texture

4.1.1. Monazite-bearing PGD (sample 13-AM-13)

Zircon grains from the monazite-bearing PGD (sample 13-AM-13) can be subdivided into two groups. The predominant zircon population have length between 400 and 2200 µm and elongated sub- moderate aspect ratio of mostly 1:2 (Fig. 3-5a). These grains display prismatic shapes with dominant {100} crystal faces and subrounded terminations. SEM images mostly reveal an oscillatory zoning, which was locally affected by dissolution, prior to new overgrowth.

The minor zircon population is characterized by a complex, non-systematic zoning (Fig. 3-5a). It is characterized by smaller grains with length ranging from 350 to 850 µm. Aspect ratio of most grains are at 1:2, but are at 1:1 ratio for minor grains.

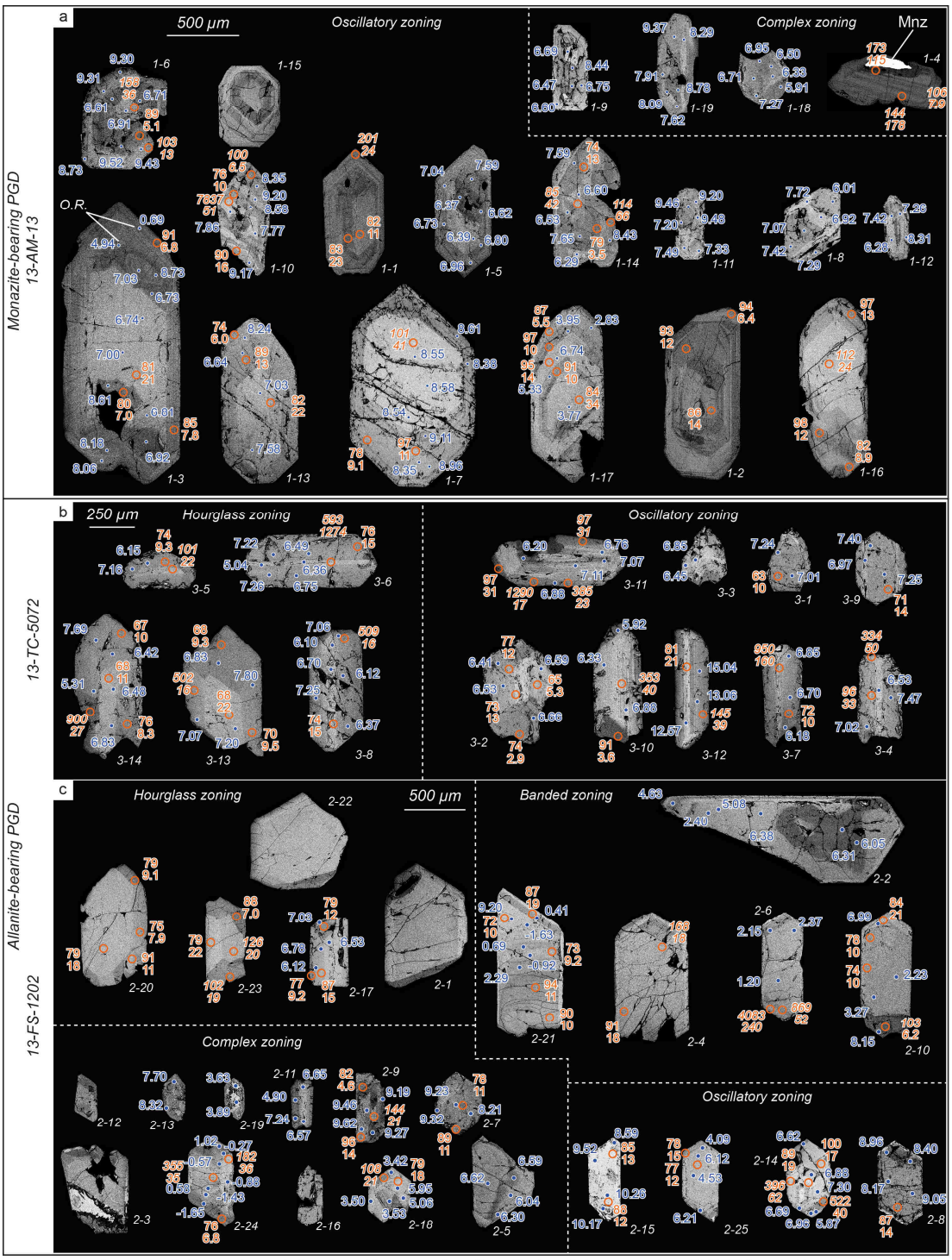

Figure 3-5: Back scattered electron (BSE) images of zircon grains from the 13-AM-13 monazite-bearing and the 13-TC-5072 and 13-FS-1202 allanite-bearing pegmatitic granite dykes of the central Grenville. The circles mark the position of the laser ablation analyses for trace elements (orange), U-Pb dating (red) and Lu-Hf isotopes (green), and of the SIMS spots for $\delta^{18}O$ analyses (blue), with associated Ca+Fe and ΣLREE content, $\delta^{18}O_{V\text{-}SMOW}$ signatures, $^{207}Pb/^{206}Pb$ ages and $\varepsilon Hf_{(1003\ Ma)}$ signatures. Italic trace elements values identify the LREE-Ca-Fe-rich domains (see text for details). a: zircon grains from the monazite-bearing dyke (sample 13-AM-13); b and c: zircon grains from the allanite-bearing dykes (samples 13-TC-5072 and 13-FS-1202). Abbreviations: Aln-bearing = allanite-bearing pegmatitic granite dyke; Mnz = monazite; Mnz-bearing = monazite-bearing pegmatitic granite dyke; O.R. = outer rims discussed in the text; PGD = pegmatitic granite dyke.

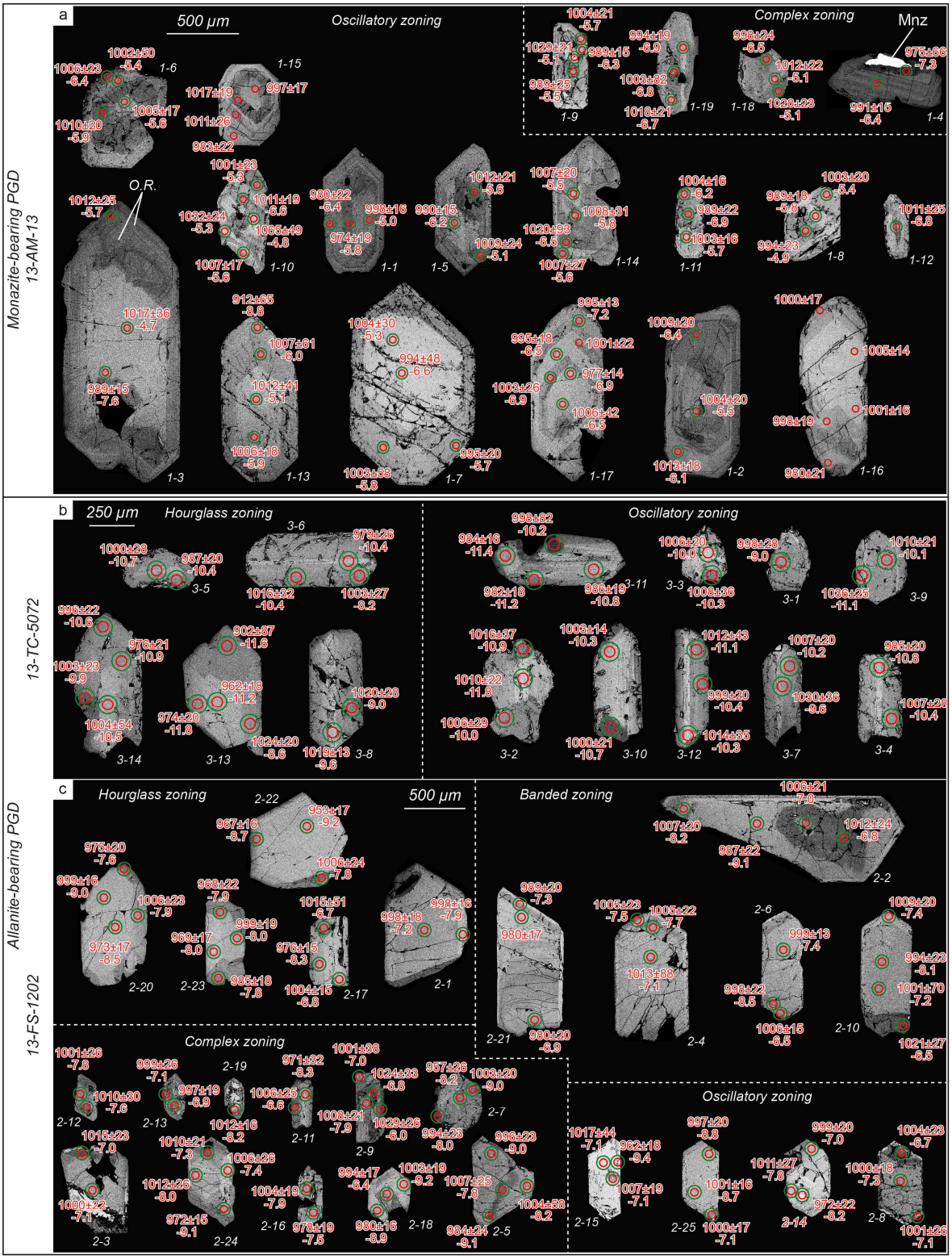

Legend: ○ U-Pb analysis ○ Lu-Hf isotopes analysis

Upper number: $^{206}Pb/^{207}Pb$ age and 2σ error (Ma); lower number: $\varepsilon Hf_{(1003\ Ma)}$

4.1.2. Allanite-bearing PGD (sample 13-TC-5072)

Zircon grains from the 13-TC-5072 allanite-bearing PGD can also be divided into two groups. The dominant population is characterized by an oscillatory zoning locally interrupted by dissolution textures (Fig. 3-5b). The grains show elongations between 250 and 700 µm, moderate aspect ratio between 1:1 and 1:3, and prismatic shapes with predominantly {100} crystal faces and subrounded terminations.

The second population reveals a typical sector (hourglass) zoning, Fig. 3-5b). Elongations of these grains range between 350 and 750 µm, and their aspect ratios between 1:2 and 1:3.

4.1.3. Allanite-bearing PGD (sample 13-FS-1202)

Zircon grains from the 13-FS-1202 allanite-bearing PGD can be subdivided into four populations. The first population shows a typical sector (hourglass) zoning in BSE images (Fig. 3-5c), is composed of elongated sub-euhedral grains with moderate aspect ratio ranging from 1:2 to 1:3 and a length comprised between ca. 550 and 2500 µm. SEM images reveal an internal hourglass zoning.

A second group (Banded zoning, Fig. 3-5c) is composed of elongated sub-euhedral grains with moderate aspect ratio ranging from 1:2 to 1:3 and a length comprised between ca. 900 and 2100 µm. SEM images reveal an internal banded zoning.

A third group (Complex zoning, Fig. 3-5c) is composed of rounded to elongated sub-euhedral grains with moderate aspect ratio ranging from 1:1 to 1:3 and a length comprised between ca. 300 and 850 µm. SEM images reveal an internal complex and randomly organized zoning.

A fourth group (Oscillatory zoning, Fig. 3-5c) is composed of rounded to elongated sub-euhedral grains with moderate aspect ratio ranging from 1:1 to 1:3 and a length comprised between ca. 600 and 700 µm. SEM images reveal a poorly developed to fine oscillatory zoning.

4.2. Definition of zircon pristine character

Zircon alteration is commonly expressed by enrichments in large ionic radii/low ionic charge trace elements that do not fit in the zircon lattice such as Ca, Fe and LREE (mainly La) occurring as nanoscale pores fillings or micrometric inclusions in fractures or porous or metamict domains (e.g. Geisler et al., 2001, 2007; Hanchar et al., 2001; Hoskin and Schaltegger,

2003; Zeh et al., 2014). Zircon domains impacted by such enrichments may show U-Pb discordance and elevated common Pb contents (e.g. Geisler et al., 2007; Pidgeon, 1992; Rayner et al., 2005). Following these authors, we used chemical criteria to distinguish pristine and non-pristine domains in the zircon grains relative to their magmatic growth. Some trace elements analyses reported Fe content below the detection limit (Table S3-1). Pristine domains are defined on the basis of ΣLREE and Ca+Fe contents below 30 ppm and 100 ppm, respectively (Fig. 3-6a, Table 3-1). If these criteria are not met, zircon domains are defined as non-pristine and are designated as *'LREE-Ca-Fe-rich'*.

5. Results

5.1. Trace elements

5.1.1. Monazite-bearing PGD (sample 13-AM-13)

Analyses mostly report a pristine character (n = 26) with low ΣLREE below 23 ppm, Ca below 94 ppm and Fe below 11 ppm contents (Fig. 3-6a, Table 3-1). Th/U ratios and ΣHREE contents of these domains range from 0.16 to 0.60 and from 197 to 825 ppm (Fig. 3-6b, Table 3-1), respectively. They are associated with rather homogeneous chondrite normalized REE patterns marked by (i) a strong fractionation of the HREE over the LREE (Yb_N/Sm_N ranging from 34 to 64), (ii) positive Ce (Ce/Ce* from 3.39 to 37.49) and Sm (Sm/Sm* from 5.20 to 9.73) anomalies, (iii) negative Pr (Pr/Pr* from 0.08 to 0.56) and Eu (Eu/Eu* from 0.04 to 0.08) anomalies, and (iv) a progressive increase in the HREE (Yb_N/Gd_N from 9.4 to 15) (Fig. 3-6e, Table 3-1). Steep LREE slopes in the chondrite normalized patterns are marked by high Sm_N/La_N ratios generally ranging from 163 to 2268 (Fig. 3-6e, Table 3-1; exception is reported for the grain 1-10, zone 2 with a ratio of 59, analysis 42, Tables 3-1 and S3-3). The Th, U, Y and Yb contents of these domains range from 40 to 311 ppm, from 246 to 756 ppm, from 285 to 1324 ppm and from 81 to 302 ppm (Table 3-1), respectively.

On the one hand, compared to pristine domains, trace elements analyses of non-pristine LREE-Ca-Fe-rich domains of zircon grains from the monazite-bearing PGD (n = 13) show LREE, Ca and Fe enrichments up to 115 ppm, 7816 ppm and 96 ppm (Table 3-1), respectively, that are associated with a slight reduction of the Eu negative anomaly (Eu/Eu* up to 0.17), an increase of Th content (up to 820 ppm) and, to a lesser degree, of U content (up to 1374 ppm), leading to an increase of the Th/U ratio (up to 1.43) (Figs. 3-6b and d, Table 3-1). On the other hand, these domains show a general flattening of the LREE in the chondrite normalized patterns

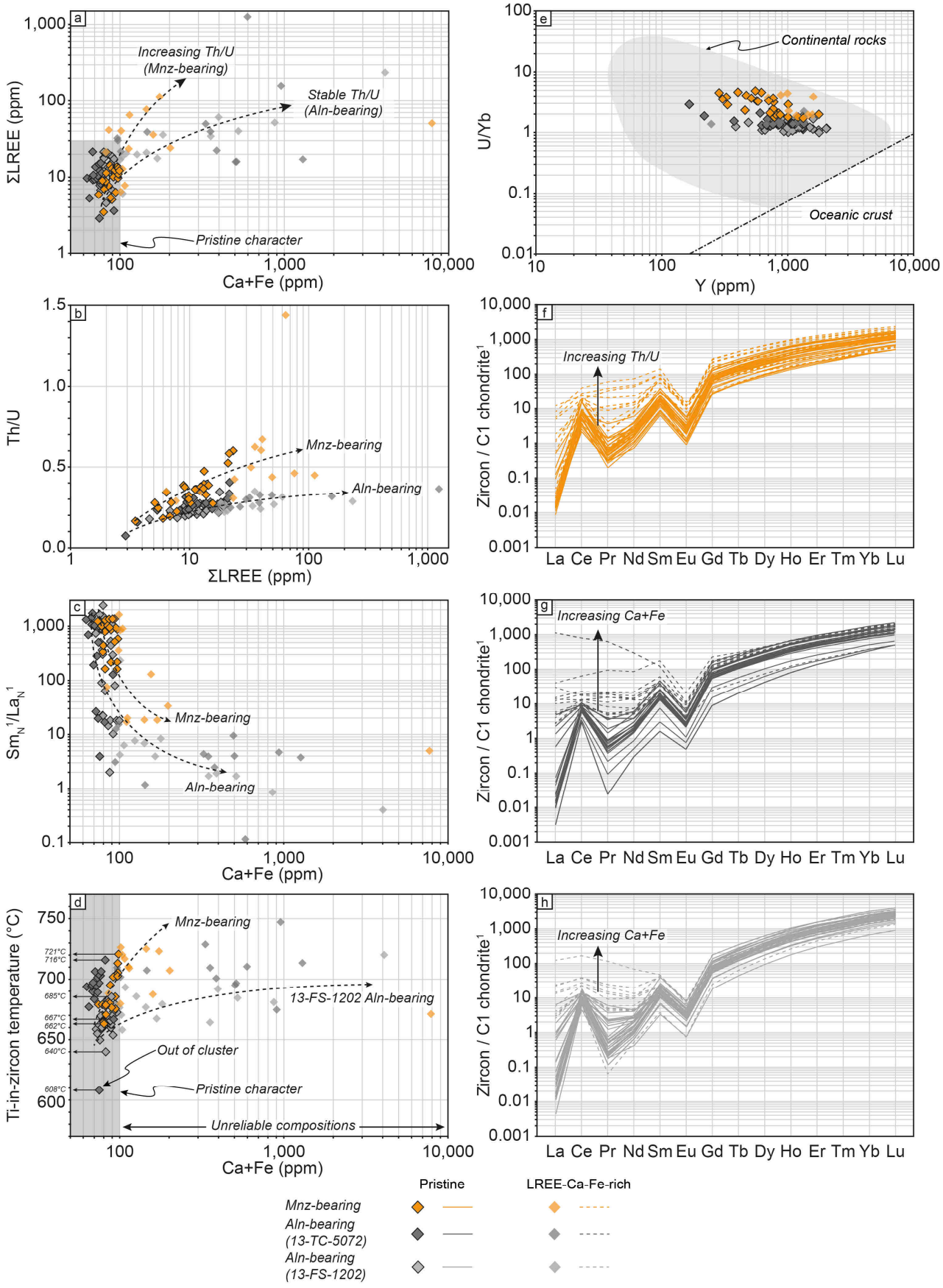
a
ΣLREE (ppm)
Ca+Fe (ppm)
Increasing Th/U
(Mnz-bearing)
Stable Th/U
(Aln-bearing)
Pristine character
b
Th/U
ΣLREE (ppm)
Mnz-bearing
Aln-bearing
c
Sm_N/La_N
Ca+Fe (ppm)
Mnz-bearing
Aln-bearing
d
Ti-in-zircon temperature (°C)
Ca+Fe (ppm)
Mnz-bearing
13-FS-1202 Aln-bearing
Out of cluster
Pristine character
Unreliable compositions
721°C
716°C
685°C
667°C
662°C
640°C
608°C
e
U/Yb
Y (ppm)
Continental rocks
Oceanic crust
f
Zircon / C1 chondrite
Increasing Th/U
La Ce Pr Nd Sm Eu Gd Tb Dy Ho Er Tm Yb Lu
g
Zircon / C1 chondrite
Increasing Ca+Fe
La Ce Pr Nd Sm Eu Gd Tb Dy Ho Er Tm Yb Lu
h
Zircon / C1 chondrite
Increasing Ca+Fe
La Ce Pr Nd Sm Eu Gd Tb Dy Ho Er Tm Yb Lu
Pristine
LREE-Ca-Fe-rich
Mnz-bearing
Aln-bearing
(13-TC-5072)
Aln-bearing
(13-FS-1202)

with decreasing Sm_N/La_N ratio down to 4.7. Non-pristine domains are also characterized by a reduction of the Ce, Pr and Sm anomalies illustrated by decreasing (i) Ce/Ce* down to 0.98, (ii) Pr/Pr* down to 0.11 and (iii) Sm/Sm* down to 2.72 (Fig. 3-6e, Table 3-1). The (i) ΣHREE content (from 238 to 1194 ppm), (ii) their fractionation over the LREE (Yb_N/Sm_N from 4.6 to 54) (Fig. 3-6e), (iii) Y (from 325 to 1767 ppm) and (iv) Yb (from 94 to 414 ppm) contents (Table 3-1) are similar to pristine domains.

The chemical variations between pristine and non-pristine zircon domains could not be attributed to specific zircon groups or zones represented in Fig. 3-5a. Plotted in the U/Yb vs Y (ppm) (Fig. 3-6e) diagrams of Grimes et al. (2007), data from both pristine and LREE-Ca-Fe-rich domains plot in the continental rocks domains.

5.1.2. Allanite-bearing PGD (sample 13-TC-5072)

Analyses mostly indicate a pristine character (n = 19) with low ΣLREE below 22 ppm, Ca below 83 ppm and Fe below 11 ppm (Fig. 3-6a, Tables 3-1 and S3-1). Th/U ratios and ΣHREE contents of these pristine domains range from 0.07 to 0.40 and from 146 to 906 ppm (Fig. 3-6b, Table 3-1), respectively, and are associated with similarly shaped chondrite normalized REE patterns marked by (i) a strong fractionation of the HREE over the LREE (Yb_N/Sm_N ranging from 29 to 206), (ii) positive Ce (Ce/Ce* from 2.20 to 214.88) and Sm (Sm/Sm* from 4.12 to 8.24) anomalies, (iii) negative Pr (Pr/Pr* from 0.01 to 0.58) and Eu (Eu/Eu* from 0.06 to 0.09) anomalies, and (iv) a progressive increase in the HREE (Yb_N/Gd_N from 8 to 38) (Fig. 3-6f, Table 3-1). LREE slopes in the chondrite normalized patterns are more or less steep as marked by the variable Sm_N/La_N ratios ranging from 4 to 1728 (Fig. 3-6f, Table

Figure 3-6: Trace elements characteristics of zircon grains from the monazite- and the 13-TC-5072 and 13-FS-1202 allanite-bearing pegmatitic granite dykes investigated in this study. The grey shaded area represent the pristine domain defined on the basis on the LREE, Ca and Fe contents (see text for details). a: ΣLREE (ppm) vs Ca+Fe (ppm) diagram. Note that a majority of zircon analyses are restricted to the pristine domain and that the analyses from the monazite- and the allanite-bearing dykes display distinct trends of enrichments, the former being more sensible to a LREE increase and associated with a increase of the Th/U ratio; b: Th/U vs ΣLREE (ppm) diagram. Note the distinct trends of increasing LREE content, associated with an increase of the Th/U ratio for zircon from the monazite-bearing pegmatitic granite dyke and with rather stable Th/U ratio for the others; c: Sm_N/La_N vs Ca+Fe (ppm) diagram of zircon grains showing the correlation between the increase in the Ca and Fe contents and the flattening of the LREE slope; d: Ti-in-zircon temperature vs Ca+Fe (ppm) diagram. Temperature calculations are based on the thermometer defined by Ferry and Watson (2007). The computed temperatures of zircon from the monazite- and the 13-FS-1202 allanite-bearing dykes are correlated with an increase in the Ca and Fe contents. Therefore, only temperatures computed on zircon with a pristine character are considered as reliable; e: U/Yb vs Y (ppm) diagrams of Grimes et al. (2007). Note that all analyses from both pristine and LREE-Ca-Fe-rich domains plot in the continental field; f to h: chondrite normalized REE patterns of zircon grains. The pristine zircon domains are associated with typical granitic zircon (see text for details). To the contrary, LREE-Ca-Fe-rich domains yield flat LREE patterns as shown by the loss of the Ce anomaly. The HREE patterns remain rather stable for both types. [1]: chondrite normalization after McDonough and Sun (1995). Abbreviations: Aln-bearing = allanite-bearing pegmatitic granite dyke; Mnz-bearing = monazite-bearing pegmatitic granite dyke.

3-1). The variable importance of the anomalies and of the fractionation of the REE is associated with variable amounts of both LREE and HREE (Fig. 3-6f, Table 3-1), respectively. The Th, U, Y and Yb contents of these domains range from 15 to 162 ppm, from 148 to 502 ppm, from 165 to 1347 ppm and from 71 to 363 ppm (Table S3-1), respectively.

On the one hand, compared to pristine domains, trace elements analyses of non-pristine LREE-Ca-Fe-rich domains of zircon grains from the 13-TC-5072 allanite-bearing PGD (n = 13) show LREE, Ca and Fe enrichments up to 1274 ppm, 474 ppm and 1215 ppm (Table 3-1), respectively, that are associated with (i) an increase of the Th and U contents (up to 236 ppm and 741 ppm respectively), (ii) an increase of the Pr anomaly in the chondrite normalized pattern (up to 1.30), and (iii) a slight reduction of the Eu negative anomaly (Eu/Eu* up to 0.16) (Figs. 3-6b and f, Table 3-1). On the other hand, these domains show a general flattening of the REE in the chondrite normalized patterns with decreasing fractionation of the HREE over the LREE as marked by Yb_N/Sm_N down to 9 and Sm_N/La_N down to 0.1 (Table 3-1). The latter is associated with a reduction of the Ce and Sm anomalies marked by decreasing (i) Ce/Ce* (down to 0.76) and (ii) Sm/Sm* (down to 0.80) (Fig. 3-6f, Table 3-1). The (i) Th/U ratio (from 0.24 to 0.36), (ii) the ΣHREE content (from 185 to 892 ppm, Fig. 3-6f), (iii) Y (from 252 to 1385 ppm) and (iv) Yb (from 80 to 349 ppm) contents (Table 3-1) are similar to pristine domains.

The chemical variations between pristine and non-pristine zircon domains could not be attributed to specific zircon groups or zones represented in Fig. 3-5b. Plotted in the U/Yb vs Y (ppm) (Fig. 3-6e) diagrams of Grimes et al. (2007), data from both pristine and LREE-Ca-Fe-rich domains plot in the continental rocks domains.

5.1.3. Allanite-bearing PGD (sample 13-FS-1202)

Analyses mostly report a pristine character (n = 31) with low ΣLREE (below 22 ppm), Ca (below 89 ppm) and Fe (below 22 ppm) contents (Fig. 3-6a, Tables 3-1 and S3-1). Th/U ratios and ΣHREE contents of these domains range from 0.18 to 0.34 and from 299 to 1492 ppm (Fig. 3-6b, Table 3-1), respectively, and are associated with rather homogeneous HREE but variable LREE chondrite normalized REE patterns characterized by (i) a strong fractionation of the HREE over the LREE (Yb_N/Sm_N ranging from 71 to 200), (ii) a variable positive Ce (Ce/Ce* from 2.28 to 103.46) anomaly, (iii) a positive Sm (Sm/Sm* from 3.72 to 7.20) anomaly, (iv) negative Pr (Pr/Pr* from 0.03 to 0.65) and Eu (Eu/Eu* from 0.06 to 0.08) anomalies, and (iv) a progressive increase in the HREE (Yb_N/Gd_N from 16 to 36) (Fig. 3-6g, Table 3-1). LREE slopes in the chondrite normalized patterns are irregular marked by variable

Sm_N/La_N ratios ranging from 2 to 2410 (Fig. 3- 6g, Table 3-1). The Th, U, Y and Yb contents of these non-pristine domains range from 31 to 244 ppm, from 176 to 897 ppm, from 386 to 2037 ppm and from 141 to 672 ppm (Table S3-1), respectively.

On the one hand, compared to pristine domains, trace elements analyses of non-pristine LREE-Ca-Fe-rich domains of zircon grains from the 13-FS-1202 allanite-bearing PGD (n = 12) show LREE, Ca and Fe enrichments up to 240 ppm, 186 ppm and 3897 ppm (Table 3-1), respectively, that are associated with a slight reduction of the Pr and Eu negative anomaly (Pr/Pr* up to 0.98 and Eu/Eu* up to 0.13) and an increasing fractionation of the HREE over the LREE (Yb_N/Sm_N from 37 to 256) (Fig. 3-6g, Table 3-1). On the other hand, these non-pristine domains show a general flattening of the LREE in the chondrite normalized patterns with decreasing Sm_N/La_N ratio (down to 0.4), and a reduction of the Ce and Sm anomalies marked by decreasing (i) Ce/Ce* (down to 1.41, except for the analysis 69 from grain 2-10, zone 4 with a Ce/Ce* value of 154.79, Table 3-1) and (ii) Sm/Sm* (down to 1.26) (Fig. 3-6g, Table 3-1). The (i) Th/U ratio (from 0.18 to 0.34), (ii) ΣHREE content (from 438 to 1424 ppm, Table 3-1), (iii) Y (from 487 to 2020 ppm) and (v) Yb (from 207 to 585 ppm) contents (Table 3-1) are similar to pristine domains.

The chemical variations between pristine and non-pristine zircon domains could not be attributed to specific zircon groups or zones represented in Fig. 3-5c. Plotted in the U/Yb vs Y (ppm) (Fig. 3-6e) diagrams of Grimes et al. (2007), data from both pristine and LREE-Ca-Fe-rich domains plot in the continental rocks domains.

5.2. Ti-in-zircon temperatures

The pristine zircon domains of the monazite-bearing and of the 13-TC-5072 and 13-FS-1202 allanite-bearing PGD have Ti contents ranging from 3.8 to 7.6 ppm, from 1.1 to 4.3 ppm, and 1.7 to 3.0 ppm (Table 3-1), respectively. These analyses allow the calculations of zircon crystallization temperatures based on the Ti-in-zircon thermometer defined by Ferry and Watson (2007). Data used in this study are: $a(SiO_2) = a(TiO_2) = 1$ for the monazite-bearing PGD, and $a(SiO_2) = 1$ and $a(TiO_2) = 0.6$ for both allanite-bearing PGD according to the presence or the lack of Ti-oxides in the peraluminous dykes, respectively (Hayden and Watson, 2007; Turlin et al., 2017).

Calculated temperatures from pristine domains (Fig. 3-6d) range from 662 to 721 °C for zircon from the monazite-bearing PGD, from 667 to 716 °C for the 13-TC-5072 and from 640 to 685 °C for the 13-FS-1202 allanite-bearing PGD (Table 3-1). A lower Ti content obtained

on a pristine zircon domain from the 13-TC-5072 allanite-bearing PGD yields a lower temperature of 608 °C that is out of the range of the main cluster. These temperatures are not correlated to the Ca and Fe content of the zircon grains.

5.3. Oxygen isotopes

Ninety-one O isotopes analyses were carried out on fifteen zircon grains from the 13-AM-13 monazite-bearing PGD (Table 3-1). Eighty-five analyses yield supra-mantellic (>5.3 ‰ as defined by Valley et al., 2005) $\delta^{18}O_{V\text{-}SMOW}$ values ranging between +5.91 and +9.52 ‰ (2σ error below 0.18 ‰) with a mean $\delta^{18}O_{V\text{-}SMOW}$ value of +7.65 ‰ (Table 3-1). Zircon grains from the 'Complex zoning' group (Fig. 3-5a) all have supra-mantellic $\delta^{18}O_{V\text{-}SMOW}$ signatures rather homogeneous within a grain. Zircon grains from the 'Oscillatory zoning' group are dominated by supra-mantellic $\delta^{18}O_{V\text{-}SMOW}$ signatures (Table 3-1). These supra-mantellic values are generally rather homogeneous within a grain (e.g. grains 1-5, 1-8, 1-10, Fig. 3-5a, Table 3-1) but up to ca. 3 ‰ variations can be recorded a in grain 1-6 (Fig. 3-5a, Table 3-1). In this group, six analyses yield mantellic to sub-mantellic $\delta^{18}O_{V\text{-}SMOW}$ values between +0.69 and +5.33 ‰ (2σ error below 0.28 ‰) with a mean $\delta^{18}O_{V\text{-}SMOW}$ value of +3.58 ‰ (Table 3-1). They are exclusively recorded in grain 1-3, where they are mostly associated with outer rims external overgrowths, and in grain 1-17 where they are recorded from the core to outer rims (Fig. 3-5a, Table 3-1). To these exceptions, $\delta^{18}O_{V\text{-}SMOW}$ signatures are rather homogeneous within single zircon grains (Table 3-1).

Fifty-one O isotopes analyses were carried out on fourteen zircon grains from the 13-TC-5072 allanite-bearing PGD (Table 3-1). Among these, forty-nine analyses yield supra-mantellic $\delta^{18}O_{V\text{-}SMOW}$ values, dominated by the range +5.92 to +7.80 ‰ (2σ error below 0.19 ‰) with a mean $\delta^{18}O_{V\text{-}SMOW}$ value of +6.79 ‰ (n = 46, Table 3-1). Three high $\delta^{18}O_{V\text{-}SMOW}$ values are recorded within a single grain from the 'Oscillatory zoning' group (grain 3-12, Fig. 3-5b) and range from +12.57 to +15.04 ‰ (2σ error below 0.19 ‰) with a mean $\delta^{18}O_{V\text{-}SMOW}$ value of +13.55 ‰ (Table 3-1). Two mantellic $\delta^{18}O_{V\text{-}SMOW}$ values of +5.04 and +5.31 ‰ (2σ error below 0.16 ‰) are recorded in grains 3-6 and 3-14 from the 'Hourglass zoning' group but are not correlated to specific zones (Fig. 3-5b, Table 3-1). The $\delta^{18}O_{V\text{-}SMOW}$ values are very homogeneous within single zircon grains (Table 3-1).

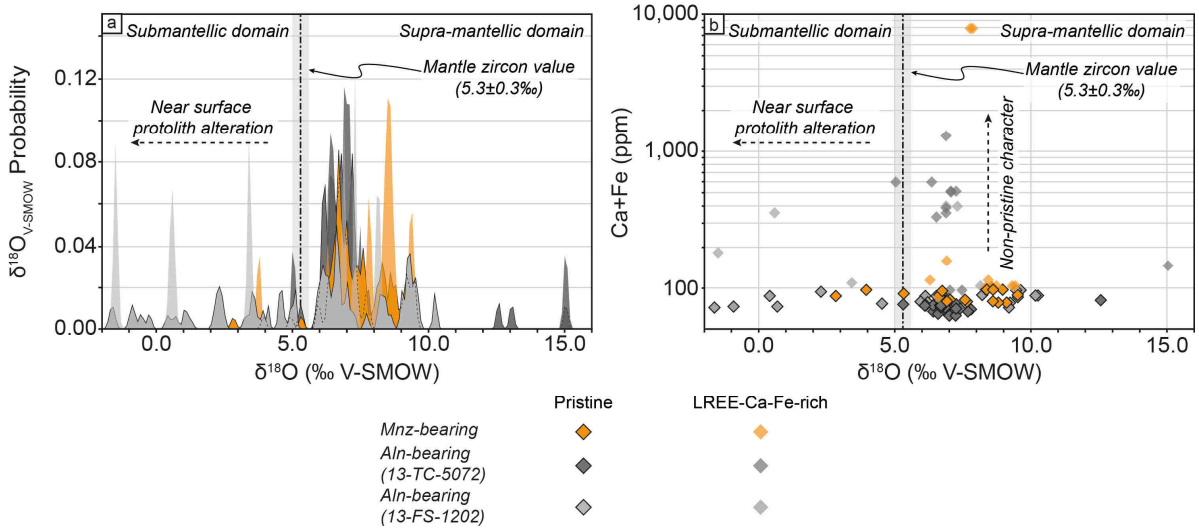

Figure 3-7: $\delta^{18}O_{V\text{-}SMOW}$ signatures of zircon grains from the monazite- and the 13-TC-5072 and 13-FS-1202 allanite-bearing pegmatitic granite dykes investigated in this study. a: probability density plot of $\delta^{18}O_{V\text{-}SMOW}$ signatures of zircon grains. Note the multimodal distribution of analyses from the 13-FS-1202 allanite-bearing PGD and the supra-mantellic dominated distribution of other samples; b: Ca+Fe (ppm) vs $\delta^{18}O_{V\text{-}SMOW}$ signatures showing no correlation between the Ca and Fe enrichments and the associated $\delta^{18}O_{V\text{-}SMOW}$ values. Abbreviations: Aln-bearing = allanite-bearing pegmatitic granite dyke; Mnz-bearing = monazite-bearing pegmatitic granite dyke.

Seventy-four O isotopes analyses were carried out on seventeen zircon grains from the 13-FS-1202 allanite-bearing PGD (Table 3-1). Data from this sample are very variable (Fig. 3-7, Table 3-1). Forty-four analyses yield supra-mantellic $\delta^{18}O_{V\text{-}SMOW}$ values ranging between +5.87 and +10.26 ‰ (2σ error below 0.37 ‰) with a mean $\delta^{18}O_{V\text{-}SMOW}$ value of +7.58 ‰ (Table 3-1). Two analyses yielded mantellic $\delta^{18}O_{V\text{-}SMOW}$ values of +5.06 and +5.08 ‰ (2σ error below 0.13 ‰, Table 3-1). Twenty-eight analyses yield sub-mantellic $\delta^{18}O_{V\text{-}SMOW}$ values between -1.65 and +4.90 ‰ (2σ error below 0.42 ‰) with a mean $\delta^{18}O_{V\text{-}SMOW}$ value of +1.77 ‰ (Table 3-1). These $\delta^{18}O_{V\text{-}SMOW}$ values are either highly variable or rather homogeneous within single zircon grains. The former is best shown in grain 2-21 that may comprise supra- to sub-mantellic $\delta^{18}O_{V\text{-}SMOW}$ values from -1.63 to +9.20 ‰ (2σ error below 0.24 ‰, Fig. 3-5c, Table 3-1). The homogenous signatures are shown in grains 2-7, 2-8, 2-9 and 2-15 that only have high supra-mantellic $\delta^{18}O_{V\text{-}SMOW}$ values comprised between +8.21 and +10.26 ‰ (2σ error below 0.17 ‰, Fig. 3-5c, Table 3-1), and in grain 2-24 that show strongly sub-mantellic $\delta^{18}O_{V\text{-}SMOW}$ values ranging from -1.65 to +1.02 (2σ error below 0.21 ‰, Fig. 3-5c, Table 3-1). The observed variations in the $\delta^{18}O_{V\text{-}SMOW}$ signatures cannot be attributed to a specific zircon group.

Variations of $\delta^{18}O_{V\text{-}SMOW}$ values are not correlated to Ca and Fe contents (Fig. 3-7a) and therefore cannot be attributed to the pristine or non-pristine character of the zircon domains.

5.4. U-Pb dating

Sixty-seven U-Pb isotopes analyses on nineteen zircon grains from the monazite-bearing PGD, thirty-six on fourteen grains from the 13-TC-5072 allanite-bearing PGD and seventy-four on twenty-five grains from the 13-FS-1202 allanite-bearing PGD were carried out on both pristine and non-pristine LREE-Ca-Fe-rich domains (Fig. 3-5, Table 3-1). Plotted on a Concordia diagram, concordant analyses define Concordia ages of 1004.2±2.1 Ma (n = 47, Fig. 3-8a), 1001.9±3.9 Ma (n = 14, Fig. 3-8b) and 1004.2±2.3 Ma (n = 42, Fig. 3-8c), respectively. The degree of concordance of U-Pb dating analyses is not correlated to the LREE, Ca and Fe content, i.e. is not dependent of the pristine character of the zircon grains (Figs. 3-8d and e).

5.5. Lu-Hf isotopes

Lu-Hf isotopes ablation spots have been performed directly 'on-top' of the U-Pb isotopes analyses, i.e. on both pristine and LREE-Ca-Fe-rich domains (Fig. 3-5). Fifty-nine Lu-Hf isotopes analyses were carried out on zircon grains from the monazite-bearing PGD, thirty-six on zircon from the 13-TC-5072 allanite-bearing PGD and seventy-three on zircon from the 13-FS-1202 allanite-bearing PGD (Fig. 3-5).

Pristine domains from the monazite- and from the 13-TC-5072 and 13-FS-1202 allanite-bearing PGD have homogeneous initial $^{176}Hf/^{177}Hf$ comprised between 0.281945 and 0.282017, between 0.281811 and 0.281919, and between 0.281889 and 0.281974 (Table 3-1), respectively. They correspond to highly sub-chondritic $\varepsilon Hf_{(1003\ Ma)}$ ranging from -4.7 to -7.6 (Fig. 3-9, Table 3-1) for the monazite-bearing PGD, and from -8.2 to -11.8 and from -6.0 to -9.4 for the 13-TC-5072 and 13-FS-1202 allanite-bearing PGD (Fig. 3-9, Table 3-1), respectively, and to associated $T_{DM2\ (1003\ Ma)}$ Hf model ages comprised between 2.05 and 2.19 Ga (mean of 2.11 Ga), between 2.24 and 2.44 Ga (mean of 2.35 Ga) and between 2.13 and 2.29 Ga (mean of 2.21 Ga) (Fig. 3-9, Table 3-1), respectively (Fig. 3-10b).

LREE-Ca-Fe-rich domains display similar homogeneous initial $^{176}Hf/^{177}Hf$ between 0.281961 and 0.282002 for the 13-AM-13 monazite-bearing PGD, between 0.281832 and 0.281885 and between 0.281914 and 0.281964 for the 13-TC-5072 and 13-FS-1202 allanite-bearing PGD (Table 3-1), respectively. These ratios correspond to similar $\varepsilon Hf_{(1003\ Ma)}$ than those of pristine domains and range from -4.8 to -7.3 (Fig. 3-9, Table 3-1) for the monazite-bearing PGD, and from -9.0 to -11.8 and from -6.5 to -8.5 for the 13-TC-5072 and 13-FS-1202 allanite-bearing PGD (Fig. 3-9, Table 3-1), respectively, and to associated $T_{DM2\ (1003\ Ma)}$ Hf model ages

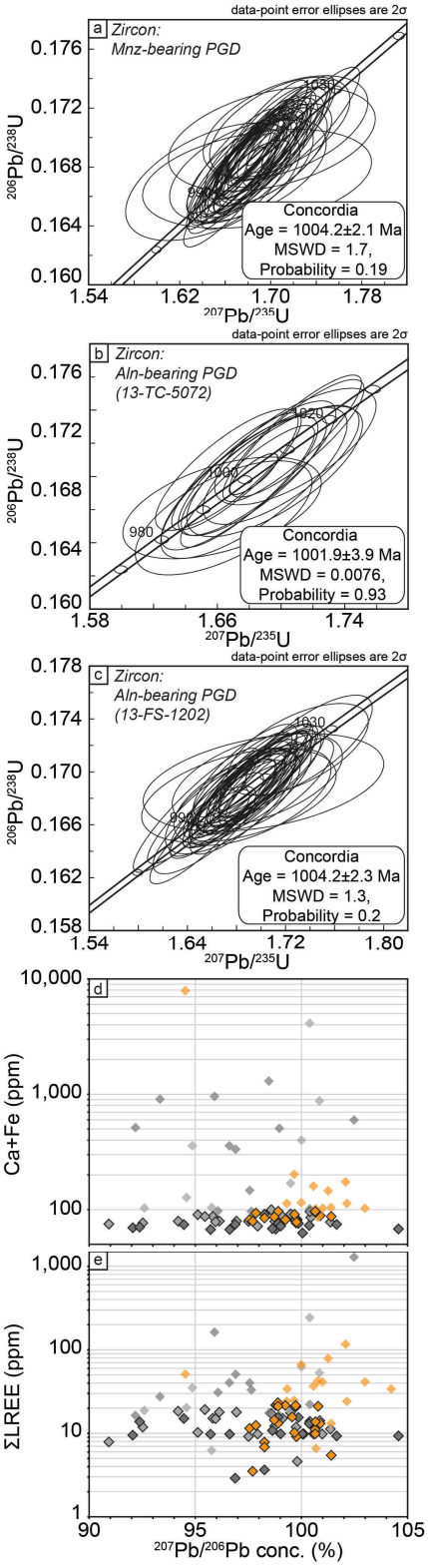

Figure 3-8: Concordia diagrams of U -Pb dating on magmatic zircon from the monazite- and the 13-TC-5072 and 13-FS-1202 allanite-bearing pegmatitic granite dykes investigated in this study. Legend is similar to Fig. 6. a: Concordia plots of U-Pb data obtained on zircon from the monazite-bearing dyke (sample 13-AM-13, n = 48, data-point error ellipses are 2σ); b: Concordia plots of U-Pb data obtained on zircon from the 13-TC-5072 allanite-bearing dyke (n = 14, data-point error ellipses are 2σ); c: Concordia plots of U-Pb data obtained on zircon from the 13-FS-1202 allanite-bearing dyke (n = 42, data-point error ellipses are 2σ); d and e: Ca+Fe (ppm) and ΣLREE (ppm) vs $^{207}Pb/^{206}Pb$ concordance for all three samples showing no correlations between non-pristine domains and the concordance of U-Pb dating analyses. Abbreviations: Aln-bearing PGD = allanite-bearing pegmatitic granite dyke; Mnz-bearing PGD = monazite-bearing pegmatitic granite dyke.

comprised between 2.08 and 2.17 Ga (mean of 2.11 Ga), between 2.30 and 2.41 Ga (mean of 2.35 Ga) and between 2.15 and 2.25 Ga (mean of 2.20 Ga) (Fig. 3-9, Table 3-1), respectively.

6. Discussion

6.1. Early-Rigolet timing of intrusion of Allochthonous Belt-hosted PGD

Turlin et al. (2017) described LREE-rich pegmatitic granite dykes (PGD) hosted in paragneisses (monazite-bearing) and metaplutonic complexes (allanite-bearing) of the Allochthonous Belt in the central Grenville Province (Figs. 3-2 and 3-3). They conclude to a post-tectonic emplacement of the dykes relative to their hosts and their derivation by partial melting of deeper-seated metasedimentary sequences (see section 2.3. for details). According to similarities in the structural position, textural, geochemical and petrological characteristics between Mnz- and Aln-bearing PGD, their emplacement was inferred to be coeval by Turlin et al. (2017).

Zircon from the 13-AM-13 monazite-bearing and the 13-TC-5072 and 13-FS-1202 allanite-bearing PGD are dominated by grains with a pristine character (Fig. 3-6a, see section 4.2. and 5.1. for details) (e.g. Geisler et al., 2007, 2001; Hanchar et al., 2001; Hoskin and Schaltegger, 2003) that lack textural evidence of inherited cores/domains, corrosion and rims dissolution/reprecipitation (Fig. 3-5). All these features argue in favor of an igneous origin of zircon grains associated with the pegmatitic dykes' magmas (e.g. Corfu et al., 2003; Crowley et al., 2008; Rubatto, 2017).

The chondrite normalized REE patterns of pristine zircon domains from the three investigated PGD are typical of igneous zircon from continental granitoids (Fig. 3-6f-h, e.g. Bea, 1996; Grimes et al., 2007). Non-pristine domains are associated with a flattening of the LREE in the chondrite normalized patterns (low Sm_N/La_N ratio down to 0.4, sample 13-FS-1202, Fig. 3-6c and h, Table 3-1) that is correlated in zircon from the monazite-bearing PGD with an increase of the Th (up to 820 ppm) and U (up to 1374 ppm) contents and of the Th/U (up to 1.43) ratio (Fig. 3-6b, Table 3-1). To the contrary only slight increase (sample 13-TC-5072) or stable (sample 13-FS-1202) Th and U contents are associated with stable Th/U ratios (Fig. 3-6b, Table 3-1) in non-pristine zircon domains from allanite-bearing PGD that are mostly characterized by an increase in ΣLREE, Ca and Fe contents (Fig. 3-6a-b, Table 3-1). Such zircon domains are usually attributed to large ionic radii/low ionic charge trace elements filling nanoscale pores or occurring as micrometric inclusions in fractures or porous or metamict domains (e.g. Geisler et al., 2007, 2001; Hanchar et al., 2001; Hoskin and Schaltegger, 2003).

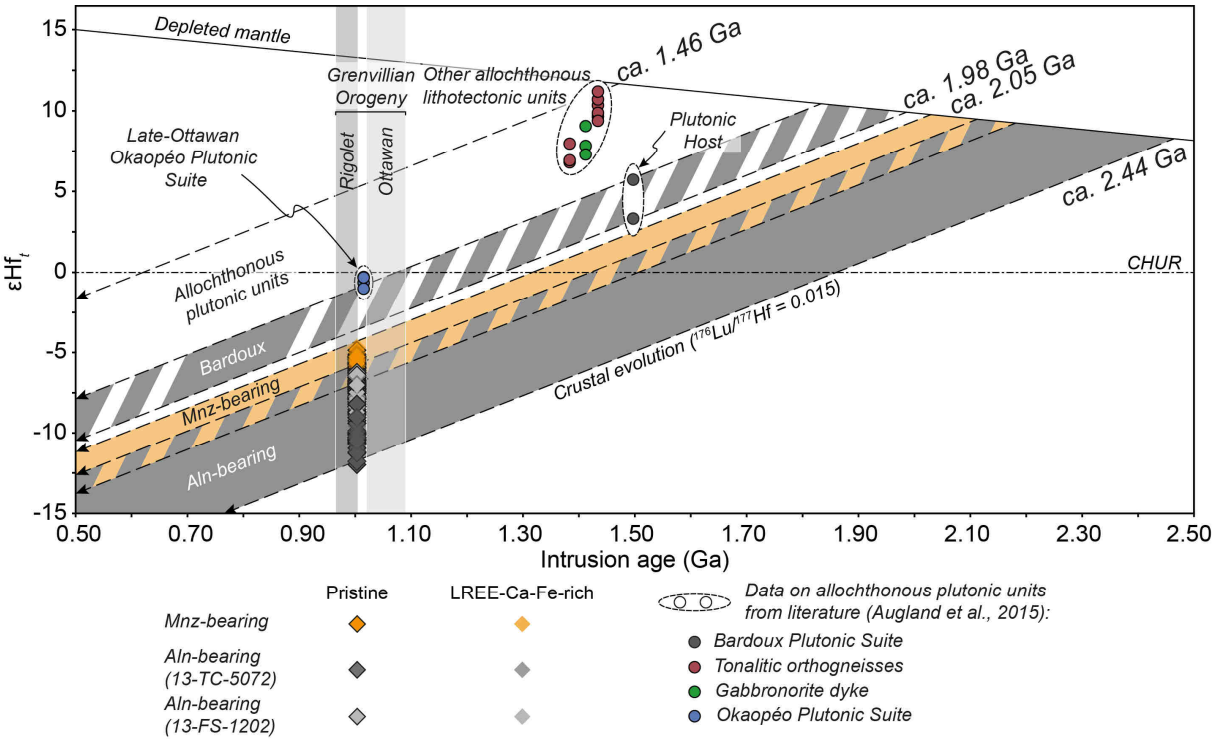

Figure 3-9: εHf_t signatures vs intrusion age of magmatic zircon from the monazite- and the 13-TC-5072 and 13-FS-1202 allanite-bearing pegmatitic granite dykes investigated in this study with reported values of allochthonous plutonic units from the Lac Okaopéo region (from Augland et al., 2015). Note that the zircon grains from the monazite- and allanite-bearing pegmatitic granite dykes plot in a distinct crustal evolution domain than surrounding allochthonous plutonic units yielding to older T_{DM2} Hf model ages. The εHf_t signatures of zircons from the monazite-bearing dyke shift towards the crustal evolution domain of allochthonous plutonic units, suggesting an assimilation of plutonic allochthonous material in the magma. Abbreviations: Aln-bearing = allanite-bearing pegmatitic granite dyke; Mnz-bearing = monazite-bearing pegmatitic granite dyke.

Systematic high resolution SEM images in the vicinity of LREE-Ca-Fe-rich domains investigated by laser spots did not allow to identify such fillings and/or inclusions. Fillings and/or inclusions may have been sampled in the laser spots and/or deeper than zircon surface during the course of a laser ablation analysis. The PGD hosts LREE either in monazite [$(Ce,La,Nd,Th)PO_4$] or allanite [$(Ce,Ca)_2(Al,Fe^{3+})_3(SiO_4)_3(OH)$], the former being (i) enriched in Th and U with higher Th/U ratio and (ii) depleted in Ca and Fe, compared to the latter (Bea, 1996; Gieré and Sorensen, 2004; Turlin et al., 2017). Accordingly, the enrichments associated with non-pristine domains mimic the mineralogy of the syn- to late-zircon growth LREE-bearing phases of the PGD. They are most likely related to small scale regions of local saturation trapped as nanoscale inclusions during zircon growth rather than dissolution/reprecipitation by late-magmatic fluids and alteration/metamictisation.

In the investigated zircon domains, the ΣLREE, Ca and Fe contents are not correlated with the degree of concordance of $^{207}Pb/^{206}Pb$ ages (Fig. 3-8d-e, Table 3-1), nor to any particular disturbance in $\delta^{18}O_{V\text{-}SMOW}$ (Fig. 3-7d) and εHf_t signatures (Fig. 3-9). On this basis, all

concordant U-Pb analyses were taken into account to constrain the crystallization ages of the dykes. They yield Concordia ages of 1004.2±2.1 Ma (Fig. 3-8a) for the 13-AM-13 monazite-bearing PGD, of 1001.9±3.9 Ma (Fig. 3-8b) and 1004.2±2.3 Ma (Fig. 3-8c) for the 13-TC-5072 and 13-FS-1202 allanite-bearing PGD, respectively, and are interpreted to reflect igneous crystallization ages of the PGD with no resetting of the U-Pb chronometer. They are similar within their uncertainties and with the ca. 1005-1000 Ma U-Pb ages obtained on syn- to late-zircon growth magmatic monazite from the 13-AM-13 and from another monazite-bearing PGD (sample 13-TC-5008, Turlin et al., 2017). These new zircon U-Pb ages confirm the emplacement of the 13-AM-13 monazite-bearing PGD at ca. 1005-1000 Ma as concluded by Turlin et al. (2017) and provide additional evidence for the coeval intrusion of steep-dipping monazite- and allanite-bearing PGD from the Lac Okaopéo region (central Grenville).

6.2. Partial melting of crustal components with a Paleoproterozoic-Archean affinity at the transition between the Ottawan and the Rigolet orogenic phases

The Grenvillian Orogeny is associated with the formation of an orogenic plateau structurally above a hot ductile crust during the Ottawan phase (ca. 1090-1020 Ma) (e.g. (Rivers, 2008, 2009; Rivers et al., 2012). In the aM*P* segment of the Allochthonous Belt of the central Grenville Province, the Ottawan peak of metamorphism is recorded between ca. 1070 and 1050 Ma and is characterized by a moderate-gradient *P-T* path reaching ca. 950 MPa and 850 °C in paragneisses from the Plus-Value Complex (aM-L*P*, Fig. 3-1b) (Lasalle et al., 2014; Lasalle and Indares, 2014). The ca. 1005-1000 Ma Concordia ages obtained in this study on zircon grains and those reported on associated magmatic monazite by Turlin et al. (2017) confirm the model of post-Ottawan peak of metamorphism timing of intrusion of the monazite- and allanite-bearing PGD, consistent with the proposition of Lentz (1991).

Late-Ottawan magmatism is marked in the study area by the intrusion of the ca. 1020-1015 Ma Sabot Mangerite and Okaopéo Plutonic Suite into the Allochthonous Belt (Augland et al., 2015; Gobeil et al., 2002; Moukhsil et al., 2014). This magmatism is coeval with the late-Ottawan crustal thinning/extension interpreted to represent orogenic collapse (Augland et al., 2015; Rivers, 2012). Augland et al. (2015) reported for a mangerite sample of the ca. 1015 Ma Okaopéo Plutonic Suite a slightly sub-chondritic signature with $\varepsilon Hf_{(1015\ Ma)}$ ranging from -1.73 and -1.01 (Fig. 3-9, Augland et al., 2015). Together with supra-chondritic $\varepsilon Hf_{(1383\text{-}1497\ Ma)}$ signatures of pre-Grenvillian allochthonous plutonic units that include tonalitic orthogneisses, gabbronorite dykes and granitic samples from the Bardoux Plutonic Suite, that host the 13-TC-

5072 allanite-bearing PGD, they define a crustal evolution domain (with $^{176}Lu/^{177}Hf = 0.015$) with a lower limit marked by the Bardoux's signature (Fig. 3-9, Augland et al., 2015). In contrast, zircon grains from the monazite- and allanite-bearing PGD of the study area yield significantly lower sub-chondritic $\varepsilon Hf_{(1003\ Ma)}$ signatures than the slightly older Okaopéo Plutonic Suite, between -4.7 and -11.8, that correspond to $T_{DM2\ (1003\ Ma)}$ Hf model ages ranging between ca. 2.05-2.44 Ga (Fig. 3-9, Table 3-1). Zircon grains have an igneous character with no inheritance, i.e. they reflect the chemical and isotopic compositions of the magma they grew in (e.g. Zeh et al., 2014) and the Lu-Hf isotope analyses carried out in these grains do not reveal any dependence on the pristine character of the investigated domains, i.e. Lu-Hf isotopes composition is not correlated to the ΣLREE, Ca and Fe contents (Fig. 3-9, Table 3-1). Accordingly, zircon from these PGD have $\varepsilon Hf_{(1003\ Ma)}$ signatures that plot in a distinct and older crustal evolution domain (with a $^{176}Lu/^{177}Hf$ of 0.015) than all Grenvillian and pre-Grenvillian plutonic units of the Allochthonous Belt from the Lac Okaopéo region reported by Augland et al. (2015). This is also consistent with the younger T_{DM2} Hf model ages of the latter than those obtained on zircon from the PGD (Fig. 3-9, Table 3-1), emphasizing their derivation from an older crustal component than the one of the host plutonic units of the Allochthonous Belt. There was, therefore, a major change in the isotopic signature of magmatism in this part of the Allochthonous Belt between ca. 1020 and 1005 Ma.

6.3. A contribution of the Allochthonous and/or Parautochthonous Belt in the formation of the PGD?

Zircon from the Allochthonous Belt-hosted PGD of the central Grenville yield Hf isotopes data that provide evidence for their derivation from the partial melting of older crustal components than the allochthonous plutonic units, i.e. compatible with Paleoproterozoic $T_{DM2\ (1003\ Ma)}$ Hf model ages. Older protoliths are represented in this area by (i) the Plus-Value Complex paragneisses in the Allochthonous Belt (Lasalle et al., 2013; Moukhsil et al., 2014), and by (ii) rocks of the Gagnon Terrane in the underlying Parautochthonous Belt that include the Knob Lake Group paragneisses and its tonalitic Archean basement (Jordan et al., 2006).

The Plus-Value Complex paragneisses, that host the 13-AM-13 monazite-bearing PGD (Fig. 3-3) represent the oldest protolith exposed in the study area according to the U-Pb ages of detrital zircon cores spreading from ca. 1.50 to 2.70 Ga, with a main mode of distribution between ca. 1.90 and 1.50 Ga (Lasalle et al., 2013; Moukhsil et al., 2014). Accordingly, the protolith of these paragneisses comprise a significant contribution from sediments from the

Laurentian margin, and thus similar in this respect to the Archean basement and Paleoproterozoic sequences of the Gagnon Terrane (Parautochthonous Belt) (Jordan et al., 2006; Lasalle et al., 2013; van Gool et al., 2008). Zircon grains from the Plus-Value Complex paragneisses also show three overgrowths, two are pre-Grenvillian and dated at ca. 1.40 Ga, 1.2 Ga, and one is syn-Ottawan and dated at ca. 1.08-1.04 Ga (Lasalle et al., 2013). No Hf isotopes data on these zircon grains are available in the literature but their partial melting up to complete dissolution of inherited zircons could generate magmas with εHf_t signatures and $T_{DM2\ (1003\ Ma)}$ Hf model ages compatible with that obtained in this study on zircon grains from the PGD. The intrusive contact of the PGD into the paragneisses of the Plus-Value Complex and the absence of textural continuity with concordant leucosomes (Fig. 3-4a), together with the ca. 1005-1000 Ma timing intrusion of the PGD (Fig. 3-8a-c, U-Pb on zircon, this study; and on monazite, Turlin et al., 2017) do not favour an origin of the pegmatites by syn-Ottawan partial melting of the Plus-Value paragneisses. However, data presented in this study cannot exclude the derivation of the PGD hosted in the Allochthonous Belt of the central Grenville Province from an early-Rigolet partial melting of the Plus-Value Complex paragneisses in a structurally lower crustal segment.

Dickin and Higgins (1992) and Thomson et al. (2011) reported Sm-Nd isotopic signatures from various terranes of the central Grenville Province that include the Southern Domains (Gabriel and Banded Complexes, Canyon and Island Domains), the MIZ, the Hart Jaune and Gagnon Terranes (Figs. 3-2 and 3-10a-b). The distribution of T_{DM} Nd model ages of granitoids orthogneisses (±minor paragneisses) in the Allochthonous Belt ranges from 1.70 to 2.20 Ga (mean of 2.01 Ga) in the MIZ and from 1.83 to 2.08 Ga (mean of 1.91 Ga) in the Hart Jaune Terrane (Thomson et al., 2011). The MIZ and the Hart Jaune Terrane outcrop ca. 100-150 kilometers north of the studied PGD (Fig. 3-2) and exhibit limited restricted subsurface continuity to the south (Hynes et al., 2000; Indares and Dunning, 2004). According to this large distance separating these two terranes and the PGD from the Lac Okaopéo region, the latter can be considered as genetically disconnected.

Crustal formation ages from lithotectonic units in the vicinity of the PGD intrusion area, i.e. the Southern Domains and the Manicouagan River, are mainly restricted to <1.97 Ga (mean of 1.86 Ga, one value up to 2.10 Ga for Canyon Domain paragneisses, Fig. 3-10b, Dickin and Higgins, 1992; Thomson et al., 2011) and are younger than $T_{DM2\ (1003\ Ma)}$ Hf model ages of zircon grains from the monazite- and the 13-TC-5072 and 13-FS-1202 allanite-bearing PGD (Fig. 3-10b-c, Table 3-1). To the contrary, the latter correspond to the range of T_{DM} Nd model ages

reported for the Gagnon Terrane, including paragneisses, and that falls between 2.30 and 2.89 Ga (mean of 2.70 Ga, Thomson et al., 2011).

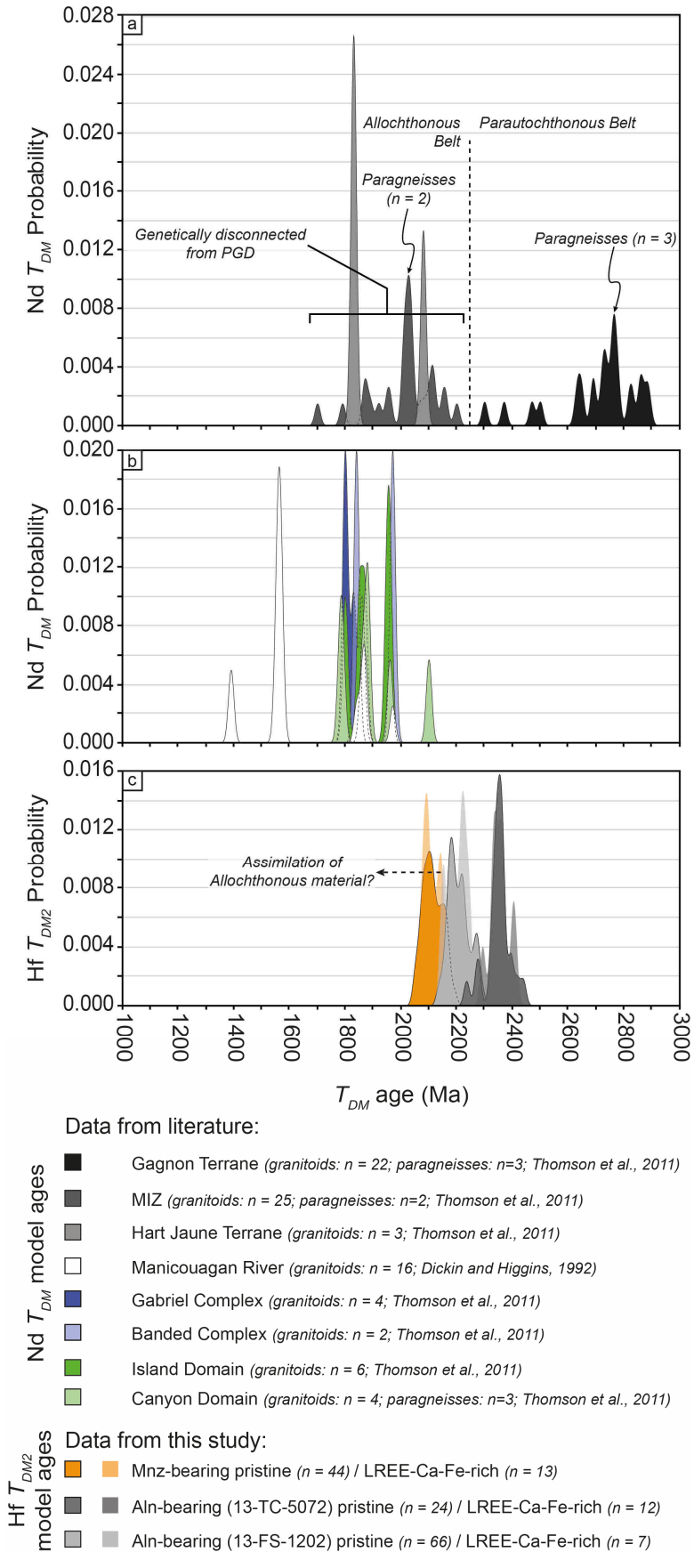

The Parautochthonous Belt recorded the short-lived Rigolet orogenic phase from ca. 1005 down to ca. 960 Ma, after a metamorphic and magmatic hiatus of ca. 10-20 Ma following the Ottawan phase, and is interpreted as the foreland-ward propagation of the Grenvillian high-grade deformation and metamorphism towards the northwestern front of the orogen ('Grenville Front', Figs. 3-1 and 3-2) (e.g. Krogh, 1994; Rivers, 2009, 2008, Rivers et al., 2012, 1989). It is recorded in the central Grenville Province in metapelites from the Knob Lake Group (Gagnon Terrane, pM*P*, Figs. 3-1b and 3-2) as a peak of metamorphism up to granulite facies conditions at ca. 1250-1500 MPa and ca. 815-850 °C from ca. 1002 and probably down to 960 Ma (Hynes et al., 2000; Jannin et al., accepted; Jordan et al., 2006; Rivers, 2009; Rivers et al., 2012; van Gool et al., 2008). Jannin et al. (accepted) demonstrated that it was associated with deformation phases in presence of melt as early as ca. 1002 Ma. The metamorphic peak temperatures are slightly higher than the calculated temperatures of the investigated zircon grains (using the Ti-in-zircon thermometer defined by Ferry and Watson, 2007) ranging from 640 to 721 °C (Fig. 3-6d, Table 3-1). However, the latter are compatible with the generation of magmas from partial melting at metamorphic peak *P-T* conditions, with their migration towards upper crustal levels and the slightly cooler crystallization of the PGD. Accordingly, favorable conditions for the partial melting of the Gagnon Terrane's lithotectonic units and for the generation of the Allochthonous Belt-hosted PGD were reached as early as ca. 1002 Ma.

The Hf isotopes signatures presented in this paper corroborate the proposition based on the structural position and U/Pb age of the PGD suggesting their origin by partial melting of rocks significantly different from the host plutonic rocks from the Allochthonous Belt of the Central Grenville Province, and points to a Paleoproterozoic-Archean affinity. These older components could belong to the Allochthonous and/or to the Parautochthonous Belt (Jordan et al., 2006; Lasalle et al., 2013; Moukhsil et al., 2014; van Gool et al., 2008). However, no Hf isotopes data are available on paragneisses from the former. To the contrary, the initiation at ca. 1002 Ma of the partial melting of the Parautochthonous Belt has been demonstrated south

Figure 3-10: Probability density plot of Nd T_{DM} model ages from parautochthonous and allochthonous domains from the central Grenville compiled from literature and of Hf T_{DM2} model ages of zircon from the monazite-bearing and the 13-TC-5072 and 13-FS-1202 allanite-bearing pegmatitic granite dykes investigated in this study. Probability density plots were realized using the AgeDisplay program of Sircombe (2004). a and b: T_{DM} Nd model ages of the Gagnon and Hart Jaune Terranes, Manicouagan Imbricate Zone, Gabriel and Banded Complexes, and Island and Canyon Domains from Thomson et al. (2011), and of the Manicouagan River from Dickin and Higgins (1992). Data were plotted using a 1s error of 10 Ma (Thomson et al., 2011); c: Hf T_{DM2} model ages of both pristine and LREE-Ca-Fe-rich domains of zircon grains from the pegmatitic granite dykes. The model ages of these dykes are older than those from the Manicouagan River, Gabriel and Banded Complexes, and Island and Canyon Domains, but correspond to those of the Gagnon Terrane. The dykes are considered as genetically disconnected from the Manicouagan Imbricate Zone and Hart Jaune Terrane (see text for details). Abbreviations: Aln-bearing = allanite-bearing pegmatitic granite dyke; Mnz-bearing = monazite-bearing pegmatitic granite dyke.

of the Manicouagan reservoir in the Knob Lake Group Paleoproterozoic metapelites of the Parautochthonous Belt (Jannin et al., accepted), i.e. north from the location of the investigated PGD intrusion into the Allochthonous Belt (Fig. 3-2). This timing is slightly younger than the crystallization ages of ca. 1005-1000 Ma of the PGD hosted in the Allochthonous Belt (U-Pb on zircon, this study, and U-Pb on monazite, Turlin et al., 2017). Accordingly, the derivation of the PGD by partial melting of Parautochthonous units would be consistent with (i) its partial melting in the early-Rigolet phase, and with (ii) the thinner crustal stack sequences composing the Allochthonous Belt in this area of the Grenville Province (Hynes et al., 2000; Indares and Dunning, 2004; Rivers, 2008; Rivers et al., 2012). Therefore, these results are pivotal to unravel the key geodynamic processes responsible for the transition between the Ottawan and the Rigolet crustal thickening phases.

6.4. Partial melting of Paleoproterozoic-Archean paragneisses as a source of Allochthonous Belt-hosted PGD in the central Grenville

Turlin et al. (2017) reported (i) a strong peraluminous character for all the PGD investigated in this study, (ii) high Nb/Ta ratios associated with low Nb and Ta contents, and (iii) a strong fractionation of the LREE over the HREE (ΣHREE contents below 128 ppm). On this basis they concluded to the derivation of the PGD by high-temperature partial melting of metasedimentary series associated with (i) the total consumption of biotite from the protolith, (ii) the formation of Nb-Ta-hosting Ti-oxides, and (iii) the crystallization of a HREE-bearing phase such as garnet in the residue following the common partial melting reaction in high-pressure granulite Bt + Pl ± Ky → Liq + Grt + Kfs + Qtz + Rt (Bea, 1996; Gervais and Crowley, 2017; Hönig et al., 2014; Stepanov et al., 2014). The Y, U, Yb contents of both pristine and LREE-Ca-Fe-rich domains of zircon from the monazite-bearing and from the 13-TC-5072 and 13-FS-1202 allanite-bearing PGD are typical of zircon grains from continental rocks as defined by Grimes et al. (2007) and confirm their derivation from crustal material (Fig. 3-6e).

Oxygen isotope investigations in zircon, especially carried out on rock materials from the Grenville and Superior Provinces, are commonly used to unravel the nature of the source of parental magmas including the involvement of supracrustal materials which reside in the near-surface allowing low temperature oxygen isotope fractionation and a shift of $\delta^{18}O_{V\text{-}SMOW}$ signatures towards a supra-mantellic domain (i.e. above the range 5.3±0.3 ‰, as defined by Valley et al., 2005) (e.g. Hawkesworth and Kemp, 2006; Valley, 2003; Valley et al., 2005, 1994). Magmatic zircon from the Grenville Province generally show higher and more variable

$\delta^{18}O_{V\text{-}SMOW}$ signatures (8.2±1.7 ‰) than igneous zircon from the Superior Province (5.7±0.6 ‰) in response to dramatic increase in the recycling of the Grenvillian crust through the subduction of supracrustal sequences (e.g. King et al., 1998; Valley, 2003; Valley et al., 2005; Van Kranendonk and Kirkland, 2013). The O isotopes analyses carried out in zircon from all samples do not show any correlation with ΣLREE, Ca and Fe contents, i.e. high or low $\delta^{18}O_{V\text{-}SMOW}$ signatures are not associated with pristine/non-pristine domains (Fig. 3-7b). Grains from the monazite- and the 13-TC-5072 allanite-bearing PGD are dominated by a multimodal distribution of supra-mantellic $\delta^{18}O_{V\text{-}SMOW}$ signatures between +5.91 and +9.52 ‰ (mean of +7.65 ‰) and between +5.92 and +7.80 ‰ (mean of +6.79 ‰) (Fig. 3-7a, Table 3-1), respectively. Such values are commonly attributed to a supracrustal source of the melt consistent with the peraluminous character of the PGD (Turlin et al., 2017; Valley, 2003; Valley et al., 2005). Zircon from these samples show variations of several units of $\delta^{18}O_{V\text{-}SMOW}$ values within a grain (Table 3-1) that might reflect the heterogeneity of the source. The lower supra-mantellic modes of distribution of $\delta^{18}O_{V\text{-}SMOW}$ signatures of the monazite-bearing and the 13-TC-5072 allanite-bearing PGD are atypical for Grenvillian igneous zircon grains but correspond to igneous grains of the Superior Province. Together with $\varepsilon Hf_{(1003\ Ma)}$ values and $T_{DM2\ (1003\ Ma)}$ Hf model ages they confirm the involvement of Paleoproterozoic-Archean sedimentary material from the Laurentian margin in the derivation of these two PGD.

Even if the $\delta^{18}O_{V\text{-}SMOW}$ values of zircon from the monazite-bearing PGD and the 13-TC-5072 allanite-bearing PGD present modes of distribution typical of igneous zircon from the Superior Province, a wider range towards typical Grenvillian igneous signatures is recorded (Fig. 3-7a, Table 3-1). It is associated with higher $\varepsilon Hf_{(1003\ Ma)}$ signatures, and consequently younger $T_{DM2\ (1003\ Ma)}$ Hf model ages, in the monazite-bearing PGD compared to allanite-bearing PGD (Figs. 3-9 and 3-10c). These features suggest a buffering of both Lu-Hf and O isotope signatures through the assimilation during magma ascent of younger, i.e. plutonic, crustal material from the Allochthonous Belt with higher εHf_t signatures (Augland et al., 2015), shifting towards heavier $^{18}O/^{16}O$ ratios and higher $\varepsilon Hf_{(1003\ Ma)}$ (e.g. Peck et al., 2000; Valley, 2003; Valley et al., 2005; Van Kranendonk and Kirkland, 2013). This effect would be more important in the case of the monazite-bearing PGD (Fig. 3-9).

Sub-mantellic $\delta^{18}O_{V\text{-}SMOW}$ signatures are ascribed to (i) a low temperature near-surface alteration of the protolith (Valley et al., 2005), or to (ii) a high temperature hydrothermal alteration by meteoric water (e.g. Hiess et al., 2011; see discussion in Valley et al., 2005). Even

if poorly represented, such low values are also recorded in the monazite-bearing PGD and the 13-TC-5072 allanite-bearing PGD, and range essentially from +2.83 to +5.33 ‰ (one value down to +0.69 ‰, Table 3-1) and from +5.04 to +5.31 ‰ (Fig. 3-7, Table 3-1) for the monazite-bearing and the 13-TC-5072 allanite-bearing PGD, respectively. According to the evidence for their derivation by partial melting of paragneisses, we interpret the few low $\delta^{18}O_{V\text{-}SMOW}$ signatures recorded in zircon from the monazite-bearing PGD and the 13-TC-5072 allanite-bearing PGD as a weathering of the protolith of the paragneisses by meteoritic water infiltration before burial and tectonic accretion in the Grenville orogenic belt.

Zircon grains from the 13-FS-1202 allanite-bearing PGD yield very variable $\delta^{18}O_{V\text{-}SMOW}$ signatures spreading from negative to supra-mantellic values (-1.65 to +10.26 ‰, Fig. 3-7c, Table 3-1). The 13-FS-1202 allanite-bearing PGD is located in the vicinity of the 13-TC-5072 allanite-bearing PGD (Fig. 3-3) and both share similarities in terms of textures, mineralogy, whole-rock geochemistry, timing of emplacement and Lu-Hf isotopes. Accordingly, a similar source is most probably involved in the genesis of both PGD. The only difference between these two allanite-bearing PGD is that the 13-FS-1202 is emplaced in the vicinity of a shear zone (Fig. 3-3), which might have allowed the penetration of meteoric fluids responsible for the spreading of the $\delta^{18}O_{V\text{-}SMOW}$ signatures.

In the central Grenville Province, Lasalle et al. (2014) proposed that the ca. 1010-990 Ma monazite rims in migmatitic aluminous gneisses from aM*P* segments were related to fluid circulations under greenschist facies conditions. Hence, they inferred that the Allochthonous Belt cooled down to subsolidus conditions before ca. 1010 Ma. The PGD investigated in this study are emplaced in the same aM*P* segment as the one studied by Lasalle et al. (2014). The (i) higher $\varepsilon Hf_{(1003\ Ma)}$ signatures of zircon from the monazite-bearing PGD suggesting assimilation of allochthonous crustal material (Fig. 3-9), (ii) the lack of contact metamorphism and evidence for thermal exchange between PGD and their respective hosts at the outcrop surface (Fig. 3-4a, d and g), and (iii) the textural continuity between PGD and 'pinch and swell' granitic veins (Fig. 3-4g) contrasts with the subsolidus conditions inferred for the Allochthonous Belt at the time of pegmatite intrusion. These features rather suggest intrusion of the pegmatites in a warm host rock, allowing material assimilation by the magma. Accordingly, further petrochronological investigations are required in mid-crustal levels of the Allochthonous Belt from the central Grenville Province to decipher the thermal record of this mid-pressure segment during the full duration of the Grenvillian Orogeny.

Lu-Hf-O isotopes analyses carried out on zircon grains from the monazite-bearing and the 13-TC-5072 and 13-FS-1202 allanite-bearing PGD provide evidence for their derivation (i) from partial melting of a deep-seated Paleoproterozoic-Archean metasedimentary source of the Allochthonous (Plus-Value Complex paragneisses) and/or Parautochthonous Belt (Knob Lake Group paragneisses), (ii) associated with more or less crustal assimilation during the magma ascent (sample 13-AM-13) and/or high-temperature hydrothermalism (sample 13-FS-1202).

6.5. Genetic implications

Two processes are generally proposed for the genesis of REE granitic pegmatites, namely (i) extreme fractionation from a magma, usually ascribed to a peralkaline composition, or (ii) partial melting of a crustal/sub-crustal component (e.g. Černý et al., 2012; Ercit, 2005; Lentz, 1991; London, 2016; Martin and De Vito, 2005). The latter is in particular inferred but still not demonstrated in the Grenville Province, since no coeval kilometric granitic plutons have been identified as their potential source (Ercit, 2005; Lentz, 1991). The U-Pb-Hf-O isotopic signatures of zircon from the LREE-enriched PGD from the Lac Okaopéo region presented in this contribution provide, to the authors' knowledge, the first evidence for the derivation of pegmatitic granite by partial melting of metasediments.

Peraluminous melts are usually enriched in inherited zircon grains that may present heterogeneous εHf_t signatures, as reported for instance for the Cape Granite Suite S-type granite (South Africa) (e.g. Farina et al., 2014; Villaros et al., 2012). These variations (up to ca. 12 εHf units) are attributed to heterogeneous isotopic signatures (i) directly transferred (Villaros et al., 2012) or (ii) through zircon dissolution/reprecipitation (Farina et al., 2014) from the metasedimentary protoliths to the magma. Even if zircon from these PGD show a multimodal distribution of (i) T_{DM2} Hf model ages (Fig. 3-10c, Table 3-1) and (ii) $\delta^{18}O_{V\text{-}SMOW}$ signatures, within a sample and within single grains (Fig. 3-7a-b, Table 3-1), the range of 2.0 to 3.6 εHf units recorded within a single sample (Figs. 3-9, 3-10c, Table 3-1) is much lower than the range observed in the Cape Suite S-type granite. These features could result from a rather homogeneous metasedimentary source and/or a transfer of the metasedimentary Hf isotopes heterogeneity to the magmas through complete dissolution and subsequent crystallization of zircon grains in the hosting PGD. The involved metasediments from the Allochthonous and/or Parautochthonous Belt in the genesis of the PGD are derived from a similar source, i.e. the Laurentian margin (Lasalle et al., 2013; van Gool et al., 2008), which erosion most probably led to a rather homogeneous metasedimentary sequence. The lack of isotopic inheritance of

zircon domains (see section 6.1. for details) indicates the derivation of PGD up to complete dissolution of zircon leading to isotopic homogenization of the resulting magma. Accordingly, the lower scattering of Hf isotopes signatures within zircon from PGD compared to peraluminous melt as those from the Cape Granite Suite (Farina et al., 2014; Villaros et al., 2012) could be the result of combined rather homogeneous metasedimentary source, which partial melting up to complete dissolution of zircon led to homogenization of the isotopic signatures in the resulting magmas.

Conclusions

Zircon grains from monazite- and allanite-bearing PGD hosted in the Allochthonous Belt of the central Grenville are dominated by a pristine continental granitoids igneous character and lack textural, chemical and isotopic evidence for inheritance. Therefore, they represent reliable witnesses of the magma compositions. Non-pristine zircon domains are not correlated to U-Pb discordance nor to a shift in $\delta^{18}O_{V\text{-}SMOW}$ and εHf_t signatures. The Th/U ratios are similar in LREE-Ca-Fe-rich domains of zircon from monazite- and allanite-bearing PGD. As these features mimic the mineralogy of the LREE-bearing phases of the dykes and as no inherited domains were identified in zircon grains, non-pristine domains might represent nanoscales inclusions trapped during zircon growth.

The U-Pb dating on zircon at ca. 1005-1000 Ma confirms a coeval intrusion of both monazite- and allanite-bearing pegmatitic granite dykes at the initiation of the Rigolet orogenic phase of the Grenvillian Orogeny. Together with (i) trace elements signatures typical of continental granitoids, (ii) lower sub-chondritic εHf_t values than plutonic rocks of the Allochthonous Belt, (iii) T_{DM2} Hf model ages between 2.05 and 2.44 Ga, (iv) supra-mantellic dominated $\delta^{18}O_{V\text{-}SMOW}$ values, and (v) no inherited domains in both zircon and monazite from these peraluminous pegmatitic granite, point to the derivation of the PGD by the partial melting of Paleoproterozoic-Archean metasedimentary rocks from the Allochthonous (Plus-Value Complex paragneisses) and/or the Parautochthonous Belt (Knob Lake Group paragneisses)t. The intrusion of the monazite-bearing and of the 13-FS-1202 allanite-bearing PGD is associated with crustal contamination and high-temperature hydrothermalism as shown by a shift towards higher $\varepsilon Hf_{(1003\ Ma)}$ signatures and a scattered multimodal distribution of $\delta^{18}O_{V\text{-}SMOW}$ values in both sub- and supra-mantellic domains.

Accordingly, this study brings the first evidence of molten Paleoproterozoic-Archean metasedimentary units at ca. 1005 Ma underneath the exhumed Allochthonous Belt at the transition between the Ottawan and the Rigolet orogenic phases.

Acknowledgements

The authors would like to thank the Ministère de l'Énergie et des Ressources naturelles (Québec, Canada) for providing technical and financial support for the field work and analyses. This contribution constitutes a Ministère de l'Energie et des Ressources naturelles du Québec (Canada) publication n° 8449 - 2017-2018 - 04. The authors are grateful to Pierre-Arthur Groulier (Memorial University, NL, Canada) for his help during field work, to Robert Joussemet, Frédéric Diot, Jean-Marie Fischbach, and to Christophe Gauthier (Steval, GeoRessources, Nancy) for their help in sample preparation and separation. This article benefited from constructive discussions with Sophie Jannin (École Polytechnique de Montréal, Canada) on the data and regional implications. This work was funded by the Labex Ressources 21 (supported by the French National Research Agency – France) through the national program "Investissements d'avenir", reference ANR-10-LABX-21–LABEX RESSOURCES 21 and the Région Grand-Est. It benefited from the framework of the DIVEX "Rare earth element" research program.

Table 3-1: Summary of the results obtained on zircon grains from the monazite-bearing (13-AM-13) and two allanite-bearing (13-FS-1202 and 13-TC-5072) pegmatitic granite dykes from the central Grenville Province. Abbreviations: Aln-bearing PGD = allanite-bearing pegmatitic granite dyke; Mnz-bearing PGD = monazite-bearing pegmatitic granite dyke; Temp. = temperature; Zrc = zircon.

Zone[a]	LREE-Ca-Fe content[b]	Ca (ppm)	Fe (ppm)	ΣLREE (ppm)	ΣHREE (ppm)	Ti (ppm)	Temp. (°C)[c]	Th (ppm)	U (ppm)	Th/U	Yb (ppm)	U/Yb	Y (ppm)	Ce/Ce*[d]	Pr/Pr*[d]	Sm/Sm*[d]	Eu/Eu*[d]	Sm_N[d]/La_N[d]	Yb_N[d]/Sm_N[d]	Yb_N[d]/Gd_N[d]	$\delta^{18}O$ (‰)	±2σ	$^{207}Pb/^{206}Pb$ age (Ma)	±2σ	Pb-Pb conc. (%)	$^{176}Hf/^{177}Hf$	±2σ	εHf_t[e]	±2σ	T_{DM2} (Ga)
Monazite-bearing PGD (sample 13-AM-13)																														
Grain 1-1																														
1	Low	80	1.7	11	511	4.2	670	136	378	0.36	208	1.82	777	26.36	0.12	7.12	0.06	1290	56	14			998	16	98	0.282013	36	-5.0	1.3	2.06
2	Low	83	b.d.	23	825	4.7	680	311	518	0.60	302	1.72	1324	29.02	0.11	7.87	0.06	2268	37	9.4			974	19	99	0.282006	35	-5.8	1.2	2.08
4	High	105	96	24	357	6.5	707	207	497	0.42	140	3.54	514	1.83	0.81	4.59	0.08	32	17	9.2			980	22	100	0.281983	35	-6.4	1.2	2.12
Grain 1-2																														
1	Low	84	2.7	14	652	4.7	680	179	464	0.39	260	1.79	1003	21.88	0.14	7.35	0.06	1348	49	13			1004	20	99	0.281995	36	-5.5	1.3	2.09
3	Low	91	2.7	12	551	5.0	685	166	442	0.38	213	2.07	848	27.02	0.12	7.94	0.06	1359	48	12			1009	20	98	0.281965	38	-6.4	1.4	2.15
4																							1013	18	97	0.281972	35	-6.1	1.2	2.13
6	Low	91	3.0	6.4	197	4.4	674	126	370	0.34	81	4.53	285	36.52	0.09	7.61	0.06	518	47	13										
Grain 1-3																														
1	Low	81	b.d.	21	787	5.1	686	278	530	0.52	297	1.78	1210	36.81	0.09	8.02	0.06	1823	44	11	6.74	0.12	1017	36	99	0.282008	38	-4.7	1.3	2.06
1																					7.00	0.12	989	15	101	0.281945	35	-7.6	1.2	2.19
1																					6.81	0.11								
2	Low	77	2.4	7.0	289	3.8	662	76	271	0.28	117	2.32	458	32.50	0.10	7.38	0.06	441	61	14	6.92	0.15								
2																					8.61	0.10								
3																					6.73	0.10								
3																					4.94	0.17								
3																					0.69	0.28								
4																					8.73	0.14								
4																					7.03	0.14								
5	Low	91	b.d.	6.8	547	5.5	693	87	445	0.19	217	2.05	785	20.52	0.13	8.71	0.05	1216	64	15			1012	25	98	0.281982	35	-5.7	1.2	2.11
5	Low	83	1.9	7.8	484	4.8	681	91	409	0.22	196	2.09	723	18.82	0.15	7.98	0.06	1025	60	15			1012	25	98	0.281982	35	-5.7	1.2	2.11
6																					8.18	0.12								
6																					8.06	0.14								
Grain 1-4																														
1	High	135	37	115	618	7.8	723	400	903	0.44	212	4.25	1018	1.19	1.06	3.32	0.08	18	7.0	5.7			975	66	102	0.281961	34	-7.3	1.2	2.17
2	High	131	13.1	78	589	8.0	725	373	821	0.45	207	3.97	900	1.25	1.02	3.42	0.08	18	10	6.7			991	15	101	0.281978	33	-6.4	1.2	2.13
3	High	102	4.3	7.9	472	7.3	717	172	609	0.28	169	3.59	720	14.93	0.17	10.02	0.04	861	42	10										
Grain 1-5																														
1																					6.39	0.14	990	15	102	0.281984	38	-6.2	1.3	2.12
2																					6.37	0.14	1012	21	98	0.281986	38	-5.6	1.4	2.10
2																					6.62	0.12								
2																					7.59	0.11								
3																					7.04	0.10	1009	24	100	0.282001	37	-5.1	1.3	2.08
3																					6.73	0.12								
3																					6.80	0.15								
3																					6.96	0.15								
Grain 1-6																														
1	High	81	78	36	1015	5.1	686	417	675	0.62	361	1.87	1608	8.12	0.27	6.70	0.08	125	23	7.6	6.91	0.12	1005	17	101	0.281991	37	-5.6	1.3	2.10
2																					6.71	0.14	1010	20	100	0.281980	39	-5.9	1.4	2.12
2																					6.61	0.14								
3	Low	83	5.8	5.1	208	4.5	676	84	302	0.28	85	3.55	304	37.49	0.08	7.62	0.06	856	55	14	9.52	0.14								
4	High	99	4.1	13	557	7.5	720	233	696	0.33	219	3.18	774	21.74	0.14	8.22	0.05	795	45	11	9.31	0.13	1002	50	101	0.281998	33	-5.4	1.2	2.09
4																					9.43	0.14								

4																					8.73	0.14								
5																					9.30	0.15	1006	23	99	0.281967	36	-6.4	1.3	2.14
Grain 1-7																														
1	High	99	1.9	41	1102	8.1	726	820	1374	0.60	369	3.72	1636	21.86	0.13	7.82	0.06	1558	23	6.4	8.55	0.15	1004	30	101	0.282000	37	-5.3	1.3	2.08
1																					8.58	0.14	994	48	103	0.281969	38	-6.6	1.4	2.14
1																					8.54	0.16								
2	Low	74	3.8	9.1	340	4.6	678	190	507	0.37	138	3.68	515	29.47	0.11	7.41	0.06	1008	47	12	9.11	0.17	1003	58	100	0.281986	38	-5.8	1.3	2.11
2																					8.80	0.14								
2	Low	94	3.1	11	380	6.4	706	255	707	0.36	145	4.88	553	29.46	0.11	7.83	0.06	872	39	10	8.35	0.10	995	20	101	0.281994	36	-5.7	1.3	2.10
2																					8.96	0.14								
2																					8.38	0.14								
2																					8.61	0.13								
Grain 1-8																														
1																					7.42	0.12	994	23	100	0.282017	36	-4.9	1.3	2.05
1																					7.07	0.13								
2																					6.92	0.14	989	18	103	0.281996	38	-5.8	1.4	2.09
2																					7.72	0.13								
4																					6.01	0.13	1003	20	100	0.281998	34	-5.4	1.2	2.08
5																					7.29	0.16								
Grain 1-9																														
1																					6.69	0.11	1029	21	99	0.281990	60	-5.1	2.1	2.09
1																					6.69	0.11	989	15	102	0.281982	38	-6.3	1.4	2.12
2																					6.47	0.12	989	25	98	0.282003	38	-5.5	1.4	2.08
2																					8.44	0.14								
3																					6.75	0.16	1004	21	100	0.281988	38	-5.7	1.3	2.10
3																					6.60	0.15								
Grain 1-10																														
2	High	7816	21	51	661	5.9	699	225	524	0.43	244	2.15	1040	1.47	0.87	3.21	0.13	4.7	20	8.9	7.77	0.15	1065	49	95	0.281974	34	-4.8	1.2	2.10
2																					7.86	0.14								
2																							1032	24	99	0.281981	34	-5.3	1.2	2.10
2	Low	90	b.d.	16	610	6.5	707	172	628	0.27	217	2.89	1009	3.39	0.56	5.20	0.08	59	34	10	9.17	0.15	1007	17	100	0.281990	36	-5.6	1.3	2.10
3	Low	76	b.d.	10	481	4.4	674	134	417	0.32	188	2.22	757	30.08	0.10	8.86	0.05	1272	53	13	8.58	0.15	1011	19	101	0.281959	34	-6.6	1.2	2.16
5																					9.20	0.17								
6	High	98	2.2	6.5	238	4.7	680	131	384	0.34	100	3.83	325	28.44	0.11	7.57	0.06	344	54	15	8.35	0.14	1001	23	101	0.282002	34	-5.3	1.2	2.08
Grain 1-11																														
1																					7.33	0.13	1003	16	103	0.281988	34	-5.7	1.2	2.10
1																					7.49	0.16								
2																					9.46	0.14	989	22	101	0.281965	34	-6.9	1.2	2.15
2																					9.48	0.13								
2																					7.20	0.13								
3																					9.20	0.15	1004	16	100	0.281973	37	-6.2	1.3	2.13
Grain 1-12																														
1																							1011	25	102	0.281952	46	-6.8	1.6	2.17
2																					7.26	0.18								
2																					7.42	0.13								
3																					6.28	0.14								
3																					8.31	0.13								
Grain 1-13																														
1	Low	79	2.5	22	743	4.6	678	290	496	0.58	277	1.79	1200	19.06	0.15	6.98	0.07	164	40	10	7.03	0.16	1012	41	99	0.282001	37	-5.1	1.3	2.07
1																					7.58	0.14	1006	18	100	0.281983	38	-5.9	1.4	2.11
2	Low	86	2.2	13	573	5.3	690	163	447	0.37	226	1.97	805	18.84	0.15	7.33	0.06	218	52	13	6.64	0.11	1007	61	101	0.281977	35	-6.0	1.2	2.12
3																					8.24	0.12								
4	Low	71	2.9	6.0	465	4.6	678	80	440	0.18	181	2.43	766	16.93	0.16	8.87	0.05	1228	62	14										

Grain 1-14																												
1	High	83	2.2	42	925	5.2	688	400	602	0.66	325	1.85	1487	3.99	0.50	5.85	0.08	72	19	7.1	6.60	0.11	1007	20	101	0.281993	37	-5.5	1.3	2.09
2	Low	74	b.d.	13	502	4.6	678	165	349	0.47	198	1.77	788	28.92	0.11	7.34	0.07	1394	45	12	7.59	0.15								
3																					6.53	0.11	1008	31	99	0.281976	37	-5.8	1.3	2.12
4	Low	77	2.6	3.5	215	3.9	665	40	246	0.16	86	2.86	332	13.37	0.21	7.96	0.05	336	63	15	7.65	0.11	1020	93	98	0.281965	38	-6.5	1.4	2.15
6	High	102	11	66	255	6.6	708	500	349	1.43	94	3.73	334	0.98	1.07	3.25	0.16	19	4.6	4.9	6.29	0.14	1007	27	100	0.281988	40	-5.6	1.4	2.10
6																					8.43	0.16								
Grain 1-15																														
1																							997	17	102					
2																							1017	19	100					
7																							1011	26	100					
10																							983	22	100					
Grain 1-16																														
1	High	99	14	24	294	6.7	710	128	428	0.30	105	4.10	469	1.26	1.01	2.72	0.17	16	16	8.1			1001	16	102					
1																							1005	14	99					
2																							998	19	100					
3	Low	90	6.3	13	425	6.2	703	222	564	0.39	169	3.33	566	14.93	0.19	7.00	0.07	220	39	11			1000	17	99					
4	Low	89	9.1	12	428	7.6	721	267	756	0.35	164	4.61	618	25.85	0.12	9.19	0.05	584	38	10										
5																							980	21	102					
6	Low	74	7.2	9	270	4.6	678	194	504	0.39	109	4.64	402	35.95	0.09	7.12	0.07	792	44	12										
Grain 1-17																														
1	High	84	b.d.	34	1194	6.6	708	402	819	0.49	414	1.98	1767	15.26	0.18	8.76	0.06	2127	26	7.5	3.77	0.15	1006	42	99	0.281965	36	-6.5	1.3	2.15
1																							977	14	104	0.281972	36	-6.9	1.3	2.15
2	Low	89	2.0	10	637	6.1	701	136	493	0.28	253	1.95	872	21.93	0.14	8.48	0.05	1358	62	14	5.33	0.17	1003	26	100	0.281956	40	-6.9	1.4	2.17
3	Low	92	2.9	14	530	6.2	703	238	729	0.33	197	3.69	766	26.01	0.12	9.31	0.05	938	38	10	6.74	0.15	995	18	101	0.281973	36	-6.5	1.3	2.14
4	Low	92	4.5	10	476	7.0	713	181	604	0.30	181	3.33	706	6.78	0.36	8.15	0.05	163	42	11	3.95	0.16	1001	22	101					
5	Low	76	11	5.5	369	5.6	694	114	466	0.25	143	3.27	581	16.78	0.15	9.73	0.04	946	52	12	2.83	0.19	995	13	101	0.281953	33	-7.2	1.2	2.17
Grain 1-18																														
1																					5.91	0.11	1028	23	97	0.281989	41	-5.1	1.5	2.09
2																					6.33	0.13	1012	22	99	0.282002	40	-5.1	1.4	2.07
2																					6.71	0.14								
3																					7.27	0.15								
3																					6.50	0.09								
4																					6.95	0.12	998	24	100	0.281970	39	-6.5	1.4	2.14
Grain 1-19																														
1																					8.09	0.11	1003	82	101	0.281959	35	-6.8	1.3	2.16
1																					8.78	0.11								
2																							1018	21	100	0.281950	36	-6.7	1.3	2.17
3																					7.91	0.15								
4																					9.37	0.17								
5																					8.29	0.13	994	19	101	0.281963	35	-6.9	1.2	2.16
5																					7.62	0.15								
Allanite-bearing PGD (sample 13-FS-1202)																														
Grain 2-1																														
1																							998	18	100	0.281949	34	-7.2	1.2	2.18
2																							998	16	102	0.281929	33	-7.9	1.2	2.22
Grain 2-2																														
1																					6.31	0.11	1012	24	100	0.281953	37	-6.8	1.3	2.17
1																					6.05	0.14								
2																							1006	21	99	0.281949	39	-7.0	1.4	2.18
4																					6.38	0.15	987	22	102	0.281903	35	-9.1	1.2	2.27
4																					2.40	0.18								

4																				5.08	0.10								
6																						1007	20	102	0.281915	39	-8.2	1.4	2.24
7																				4.63	0.13								
Grain 2-3																													
1																						1000	22	100	0.281951	33	-7.1	1.2	2.18
2																						1015	23	98	0.281945	33	-7.0	1.2	2.18
Grain 2-4																													
1	Low	79	12	18	1024	2.6	673	122	562	0.22	463	1.21	1325	4.60	0.44	5.15	0.06	10	115	26		1013	88	99	0.281943	34	-7.1	1.2	2.19
1	High	75	93	18	883	2.4	667	105	506	0.21	402	1.26	1235	2.85	0.56	4.10	0.08	3.8	122	27									
2																						1005	22	98	0.281933	34	-7.7	1.2	2.21
3																						1005	23	100	0.281937	34	-7.5	1.2	2.20
Grain 2-5																													
1																				6.62	0.11	996	23	100	0.281901	40	-9.0	1.4	2.27
2																				6.59	0.14	1007	25	99	0.281927	37	-7.8	1.3	2.22
2																				6.30	0.15	984	24	103	0.281906	39	-9.1	1.4	2.27
3																				6.04	0.16	1004	58	100	0.281919	38	-8.2	1.3	2.24
Grain 2-6																													
1																				2.37	0.23	999	13	101	0.281943	36	-7.4	1.3	2.19
1																				1.20	0.22								
2	High	92	777	52	801	2.9	682	100	385	0.26	360	1.07	1066	1.68	0.82	2.25	0.09	0.8	88	25		998	22	101	0.281914	38	-8.5	1.3	2.25
3	High	186	3897	240	851	4.5	720	155	556	0.28	374	1.49	1119	1.41	0.98	1.26	0.10	0.4	37	21		1006	15	100	0.281964	35	-6.5	1.3	2.15
3																				2.15	0.19								
Grain 2-7																													
1	Low	71	6.9	11	658	2.2	660	115	479	0.24	292	1.64	909	41.18	0.06	6.86	0.07	90	109	24	9.23	0.09	957	26	101	0.281947	41	-8.2	1.4	2.20
2	Low	72	17	11	935	2.3	663	122	547	0.22	422	1.29	1249	71.99	0.05	6.45	0.07	971	148	27	8.21	0.15							
3																						1003	20	101	0.281896	38	-9.0	1.3	2.28
4																				9.32	0.15	994	23	101	0.281931	37	-8.0	1.3	2.22
Grain 2-8																													
1	Low	87	b.d.	14	1492	3.0	685	170	668	0.25	672	0.99	1774	55.36	0.06	6.48	0.07	1100	154	27	8.17	0.14	1000	18	101	0.281945	34	-7.3	1.2	2.19
1																				9.05	0.11								
2																				8.40	0.11	1004	23	100	0.281960	33	-6.7	1.2	2.16
2																				8.96	0.08								
3																						1001	26	101	0.281952	33	-7.1	1.2	2.17
Grain 2-9																													
1	Low	74	22	14	886	2.6	673	112	489	0.23	390	1.25	1212	5.88	0.37	5.58	0.07	18	103	23	9.62	0.10	1008	21	100	0.281925	35	-7.9	1.2	2.22
1																				9.46	0.11								
1	High	84	60	21	815	2.7	676	98	445	0.22	366	1.21	1044	3.39	0.57	3.98	0.08	6.6	90	25									
2																				9.27	0.11	1024	33	100	0.281945	39	-6.8	1.4	2.18
3																						1029	26	98	0.281965	41	-6.0	1.4	2.14
4																				9.19	0.14								
4	Low	73	8.9	4.6	299	1.7	640	31	176	0.18	141	1.24	386	38.31	0.07	5.70	0.07	64	200	36		1001	38	100	0.281954	33	-7.0	1.2	2.17
Grain 2-10																													
1	Low	72	6.3	10	978	2.2	660	117	540	0.22	444	1.21	1304	56.74	0.06	6.51	0.07	878	158	28									
1	Low	74	b.d.	10	1001	2.3	663	118	537	0.22	455	1.18	1316	60.30	0.06	6.67	0.07	989	157	29	3.27	0.18	1001	70	100	0.281947	33	-7.2	1.2	2.18
1																				2.23	0.20	994	23	101	0.281928	39	-8.1	1.4	2.22
2	Low	73	11	21	1209	2.9	682	244	897	0.27	538	1.67	1593	58.90	0.06	6.60	0.07	845	109	23	6.99	0.18	1009	20	100	0.281937	34	-7.4	1.2	2.20
4	High	93	10	6.2	438	2.2	660	54	301	0.18	207	1.45	487	154.79	0.02	6.10	0.05	226	256	40	8.15	0.18	1021	27	96	0.281955	32	-6.5	1.1	2.16
Grain 2-11																													
1																				6.65	0.13	971	32	104	0.281961	34	-6.6	1.2	2.16
1																				6.57	0.11								
2																				4.90	0.13	1006	25	100	0.281937	33	-8.3	1.2	2.22
2																				7.24	0.13								
Grain 2-12																													

1																						1010	30	99	0.281931	34	-7.6	1.2	2.21
2																						1001	25	101	0.281931	35	-7.8	1.3	2.22
Grain 2-13																														
2																						997	19	101	0.281958	33	-6.9	1.2	2.16
3																				7.70	0.15									
4																				8.32	0.13	999	26	99	0.281952	33	-7.1	1.2	2.17
Grain 2-14																														
1																						972	22	103	0.281938	35	-8.2	1.2	2.21
3	Low	81	8.2	19	984	3.0	685	214	777	0.28	423	1.83	1314	47.64	0.07	6.92	0.07	442	87	20										
4	High	88	308	62	892	3.3	693	141	462	0.31	375	1.23	1248	1.68	0.83	2.98	0.10	1.8	43	16	7.30	0.11	1011	27	100	0.281926	33	-7.8	1.2	2.22
4																					6.88	0.13								
6	Low	82	18	17	791	2.7	676	147	547	0.27	349	1.57	1004	9.49	0.24	5.46	0.08	18	96	23			999	20	99	0.281954	34	-7.0	1.2	2.17
7																				6.69	0.10									
8																				6.62	0.11									
8	High	85	437	40	888	3.0	685	112	483	0.23	398	1.21	1154	1.89	0.77	3.04	0.08	1.6	79	24										
9																				6.96	0.15									
9																				5.87	0.11									
Grain 2-15																														
1																						1007	19	100	0.281947	34	-7.1	1.2	2.18
2	Low	66	20	13	944	2.4	667	107	514	0.21	431	1.19	1233	6.00	0.35	5.08	0.07	14	136	28	9.52	0.15	1017	44	100	0.281939	33	-7.1	1.2	2.19
3	Low	72	16	12	895	2.4	667	100	486	0.21	409	1.19	1158	7.88	0.28	5.27	0.07	18	149	29	10.26	0.12								
3																					10.17	0.08								
4																				8.59	0.17	962	18	104	0.281910	38	-9.4	1.3	2.27
Grain 2-16																														
1																						978	19	102	0.281953	36	-7.5	1.3	2.18
1																						1004	19	98	0.281926	50	-7.9	1.8	2.22
Grain 2-17																														
1	Low	73	14	15	1158	2.4	667	155	568	0.27	500	1.14	1584	38.68	0.08	6.90	0.07	325	98	20	6.53	0.13	1004	15	96	0.281957	36	-6.8	1.3	2.16
1																				6.78	0.13	976	15	99	0.281933	38	-8.3	1.3	2.22
1																				6.12	0.14									
3	Low	68	9.8	9.2	876	2.3	663	98	484	0.20	398	1.22	1195	55.59	0.06	6.81	0.07	875	150	28										
3	Low	71	8.1	12	728	2.4	667	104	382	0.27	323	1.18	986	10.89	0.21	5.69	0.07	22	113	24	7.03	0.11	1015	51	99	0.281953	39	-6.7	1.4	2.17
Grain 2-18																														
1																				3.53	0.15	994	17	92	0.281974	36	-6.4	1.3	2.13
2	Low	64	15	18	847	2.5	670	162	577	0.28	369	1.56	1193	11.72	0.20	5.73	0.08	22	94	21	5.95	0.17	1003	19	94	0.281889	37	-9.2	1.3	2.29
2																				5.06	0.13									
2																				3.50	0.14	980	16	98	0.281915	34	-8.9	1.2	2.26
3	High	71	37	21	765	3.3	693	150	561	0.27	335	1.67	1039	4.48	0.42	4.68	0.08	6.0	87	21	3.42	0.14								
Grain 2-19																														
2																				3.89	0.13	1012	16	100	0.281914	36	-8.2	1.3	2.24
2																				3.63	0.16									
Grain 2-20																														
1	Low	73	6.7	18	1220	2.2	660	189	550	0.34	504	1.09	1759	58.05	0.06	6.93	0.07	2410	89	17			973	17	96	0.281929	38	-8.5	1.4	2.23
1																						999	16	97	0.281900	37	-9.0	1.3	2.28
2	Low	64	11	7.9	766	2.3	663	76	414	0.18	356	1.16	1010	70.74	0.05	7.02	0.07	938	164	31			1006	23	91	0.281924	36	-7.9	1.3	2.23
2	Low	75	16	11	891	2.0	652	115	464	0.25	403	1.15	1138	59.25	0.05	6.66	0.07	297	149	28										
3	Low	69	9.9	9.1	759	2.3	663	89	345	0.26	342	1.01	1008	65.36	0.05	6.27	0.07	304	148	27			975	20	98	0.281954	41	-7.6	1.5	2.18
Grain 2-21																														
1	Low	77	13	10	950	2.5	670	106	498	0.21	436	1.14	1161	71.74	0.05	6.29	0.07	1072	162	30			980	20	95	0.281970	35	-6.9	1.3	2.15
2	Low	89	4.7	11	969	2.8	679	104	476	0.22	447	1.06	1091	28.67	0.09	6.10	0.07	80	172	31	2.29	0.18								
3	Low	67	5.6	9.2	864	2.1	656	96	489	0.20	393	1.24	1173	65.42	0.05	6.91	0.07	900	154	29	-0.92	0.21								
3																					0.69	0.19								
4	Low	60	12	10	939	2.2	660	111	545	0.20	426	1.28	1267	56.17	0.06	6.22	0.07	739	162	28	-1.63	0.20	980	17	98					

4																				9.20	0.24								
5	Low	75	12	19	643	2.3	663	96	378	0.25	287	1.32	838	2.28	0.65	3.72	0.07	2.0	106	25	0.41	0.18	989	20	95	0.281953	34	-7.3	1.2	2.18
Grain 2-22																													
1																							953	17	100	0.281923	35	-9.2	1.3	2.25
2																							967	16	99	0.281928	38	-8.7	1.3	2.23
3																							1006	24	94	0.281929	33	-7.8	1.2	2.22
Grain 2-23																													
1	High	75	51	20	1037	3.0	685	114	528	0.22	471	1.12	1324	4.17	0.47	3.27	0.13	7.3	119	27			999	19	95	0.281928	34	-8.0	1.2	2.22
1	Low	71	8.7	22	1463	2.4	667	235	705	0.33	604	1.17	2037	37.18	0.08	7.20	0.07	1526	71	16			969	17	99	0.281945	34	-8.0	1.2	2.20
2	High	65	37	19	672	2.5	670	82	311	0.26	299	1.04	932	3.33	0.56	3.38	0.11	4.0	102	24			985	18	93	0.281942	33	-7.8	1.2	2.20
2																							968	22	98	0.281950	33	-7.9	1.2	2.19
3	Low	80	8.8	7.0	550	2.2	660	60	280	0.21	257	1.09	624	101.12	0.03	5.88	0.07	531	189	33										
Grain 2-24																													
1	High	72	282	35	912	2.3	663	123	491	0.25	403	1.22	1287	1.73	0.81	3.28	0.07	1.6	86	22	0.58	0.19	1012	26	95	0.281918	34	-8.0	1.2	2.23
2																							972	15	97	0.281914	32	-9.1	1.1	2.26
2																					-0.57	0.16								
2																					-0.27	0.16								
2																					1.02	0.14								
3																					-0.88	0.19	1006	26	96	0.281939	33	-7.4	1.2	2.20
4																							1010	21	93	0.281940	33	-7.3	1.2	2.19
4	High	73	109	36	1424	2.8	679	230	676	0.34	585	1.16	2020	3.08	0.57	5.04	0.07	8.0	61	16	-1.49	0.15								
5	Low	72	4.1	6.8	509	1.9	648	58	255	0.23	232	1.10	659	103.46	0.03	6.81	0.06	1646	154	29	-1.65	0.21								
Grain 2-25																													
1	Low	66	10	12	1120	2.5	670	138	611	0.23	503	1.22	1498	52.72	0.06	6.36	0.07	500	149	27	4.53	0.13	1001	16	93	0.281905	35	-8.7	1.2	2.26
1																					6.12	0.14	997	20	100	0.281904	36	-8.8	1.3	2.27
1																					4.09	0.10								
4	Low	69	9.6	15	880	2.5	670	159	565	0.28	387	1.46	1250	45.67	0.07	6.51	0.07	364	109	23	6.21	0.11	1000	17	96	0.281952	34	-7.1	1.2	2.17
Allanite-bearing PGD (sample 13-TC-5072)																													
Grain 3-1																													
1	Low	58	4.2	10	550	3.3	693	75	322	0.23	227	1.42	825	21.56	0.14	7.18	0.06	1316	61	15	7.01	0.13	998	28	100	0.281897	35	-9.0	1.2	2.28
1																					7.24	0.11								
Grain 3-2																													
1	Low	68	5.0	13	690	3.7	702	105	392	0.27	281	1.40	1057	17.59	0.16	7.72	0.06	1210	53	14			1010	22	100	0.281811	37	-11.8	1.3	2.44
2	Low	68	8.7	12	598	3.9	705	90	332	0.27	244	1.36	898	21.34	0.14	7.75	0.06	1436	56	14	6.53	0.13								
2	Low	62	2.8	5.3	251	2.7	676	38	164	0.23	107	1.53	375	35.61	0.09	7.68	0.06	695	67	17	6.59	0.10								
4																							1016	37	99	0.281834	40	-10.9	1.4	2.40
5	Low	69	6.0	2.9	146	1.1	608	15	206	0.07	71	2.89	165	214.88	0.01	4.12	0.09	504	206	38	6.41	0.14	1006	29	97	0.281865	36	-10.0	1.3	2.34
5																					6.66	0.15								
Grain 3-3																													
1																					6.85	0.14	1006	20	101	0.281867	35	-10.0	1.2	2.34
1																					6.45	0.11								
3																							1008	36	99	0.281855	35	-10.3	1.2	2.36
Grain 3-4																													
1	High	80	251	50	892	5.0	729	236	741	0.32	349	2.12	1375	1.28	0.93	3.82	0.10	4.1	27	11	6.53	0.15	985	20	97	0.281857	34	-10.8	1.2	2.36
2	High	72	24	33	748	4.0	709	124	409	0.30	299	1.37	1134	0.88	1.13	3.87	0.08	3.0	35	13	7.47	0.11	1007	28	98	0.281855	33	-10.4	1.2	2.36
2																					7.02	0.17								
Grain 3-5																													
1	High	74	27	22	694	3.7	702	119	371	0.32	264	1.41	1081	2.92	0.51	6.22	0.07	15	31	10			1000	28	100	0.281851	40	-10.7	1.4	2.37
2	Low	69	5.0	9.3	527	3.5	698	70	305	0.23	220	1.38	774	22.03	0.14	7.65	0.06	1013	65	16	7.16	0.13	987	20	102	0.281866	34	-10.4	1.2	2.35
2																					6.15	0.14								
Grain 3-6																													
1	High	474	119	1274	877	4.1	711	167	469	0.36	331	1.42	1385	0.91	1.15	0.80	0.07	0.1	13	9.0	5.04	0.15	979	26	102	0.281872	33	-10.4	1.2	2.34

1																			6.36	0.13									
2																			7.22	0.12									
2																			6.49	0.14									
2	Low	72	4.3	15	594	3.7	702	79	331	0.24	246	1.34	857	2.20	0.58	5.83	0.06	3.9	62	16	7.26	0.12	1016	32	99	0.281858	39	-10.4	1.4	2.36
2																			6.75	0.16									
2																					1003	27	100	0.281919	43	-8.2	1.5	2.24
Grain 3-7																													
1	High	181	770	160	891	6.1	747	145	467	0.31	332	1.41	1363	0.95	1.27	3.38	0.10	4.5	8.8	7.0			1030	36	96	0.281862	34	-9.6	1.2	2.34
2	Low	63	8.6	10	517	3.4	695	68	291	0.23	215	1.35	762	8.91	0.20	6.27	0.07	26	65	16	6.85	0.16	1007	20	99	0.281869	43	-9.6	1.2	2.33
2																			6.70	0.14									
4																			6.18	0.13									
Grain 3-8																													
1	Low	67	7.6	15	702	3.8	705	106	398	0.27	282	1.41	1078	5.17	0.31	7.21	0.06	20	50	13	6.10	0.14	1019	13	94	0.281869	33	-9.6	1.2	2.33
1																			6.70	0.14									
3	High	73	436	16	479	3.5	698	65	267	0.24	198	1.34	697	1.63	0.76	4.70	0.07	3.8	48	15	7.06	0.14	1020	28	92	0.281885	32	-9.0	1.1	2.30
3																			7.25	0.13									
3																			6.37	0.19									
3																			6.12	0.14									
Grain 3-9																													
1	Low	65	5.7	14	759	3.9	707	119	432	0.27	309	1.40	1149	17.93	0.16	7.52	0.06	1031	56	14	7.40	0.13	1010	21	92	0.281860	37	-10.1	1.3	2.35
1																			7.25	0.15									
2																			6.97	0.19	1036	25	92	0.281817	35	-11.1	1.3	2.42
Grain 3-10																													
1	High	98	255	40	780	4.0	709	138	434	0.32	308	1.41	1217	1.23	1.05	3.46	0.11	3.8	33	12	6.88	0.11	1003	14	97	0.281861	32	-10.3	1.1	2.35
2																			6.33	0.13									
3																			5.92	0.17									
4	Low	83	8.4	3.6	174	2.4	667	23	148	0.16	79	1.86	217	57.13	0.05	4.75	0.08	129	124	25			1000	21	98	0.281850	34	-10.7	1.2	2.37
Grain 3-11																													
2																			7.07	0.11									
3																			7.11	0.16									
3																			6.76	0.11									
4																					984	16	95	0.281841	36	-11.4	1.3	2.40
5	High	78	18	31	719	3.9	707	115	396	0.29	287	1.38	1096	1.80	0.80	3.95	0.11	12	30	12			986	19	96	0.281856	34	-10.8	1.2	2.37
6	High	74	311	23	574	3.6	700	80	332	0.24	235	1.42	867	1.33	0.84	4.20	0.08	2.4	47	14	6.88	0.13								
6	High	75	1215	17	586	4.2	713	84	344	0.24	241	1.43	893	1.88	0.66	4.49	0.09	3.6	55	15	6.88	0.13	982	18	98	0.281849	38	-11.2	1.3	2.38
7	Low	62	11	11	398	3.2	690	87	334	0.26	160	2.08	604	18.12	0.16	6.76	0.06	283	48	13										
8																			6.20	0.11	998	82	90	0.281865	37	-10.2	1.3	2.34
Grain 3-12																													
1	Low	70	11.2	21	906	4.3	716	152	502	0.30	363	1.38	1347	3.76	0.41	6.56	0.06	17	45	13	12.57	0.14	1014	35	100	0.281851	37	-10.3	1.3	2.36
3																			13.06	0.16									
4																					999	20	91	0.281860	33	-10.4	1.2	2.35
4	High	83	62	39	713	3.9	707	108	398	0.27	289	1.38	1066	0.76	1.03	3.32	0.10	1.1	41	13	15.04	0.15	1012	43	98	0.281832	38	-11.1	1.3	2.40
Grain 3-13																													
1	Low	62	5.7	22	809	3.4	695	162	400	0.40	292	1.37	1305	15.03	0.18	8.24	0.06	1072	29	8.4	7.20	0.14	962	18	99	0.281861	32	-11.2	1.1	2.37
2	High	87	416	16	569	3.4	695	79	322	0.25	232	1.39	859	2.71	0.56	5.24	0.07	9.1	47	14	7.07	0.12	974	20	99	0.281835	38	-11.8	1.4	2.41
2	Low	63	6.9	9.5	461	3.0	685	88	315	0.28	192	1.64	689	19.60	0.14	7.25	0.06	194	62	16	7.80	0.13	1024	20	92	0.281895	33	-8.6	1.2	2.27
3	Low	64	4.4	9.3	447	3.2	690	73	235	0.31	180	1.30	690	35.62	0.09	8.14	0.06	1492	59	14	6.83	0.11	902	87	105	0.281886	35	-11.6	1.3	2.34
Grain 3-14																													
1	Low	64	4.7	11	480	3.5	698	76	248	0.31	194	1.28	727	31.02	0.10	7.61	0.06	1728	55	14	6.83	0.13	1004	54	99	0.281853	33	-10.5	1.2	2.36
1																			6.48	0.15									
2	Low	70	6.2	8.3	449	3.7	702	57	247	0.23	189	1.31	624	26.70	0.12	7.06	0.07	1229	68	17	5.31	0.16								
3	Low	63	4.2	10	451	3.4	695	72	241	0.30	181	1.33	679	33.38	0.10	7.57	0.06	1400	58	14			976	21	96	0.281859	34	-10.9	1.2	2.36
3																			7.69	0.15	996	22	97	0.281855	35	-10.6	1.3	2.36

3																				6.42	0.14										
4	High	97	803	27	185	2.7	676	26	104	0.25	80	1.31	252	1.30	1.66	0.16	29	16				1003	23	93	0.281871	32	-9.9	1.1	2.33		

[a] Zonation ordered from cores towards rims in each grain.
[b] Allowing to discriminate a pristine character of the investigated zircon domains. Blank lines correspond to undefined domains lacking trace elements analyses. See text for details.
[c] Calculations based on the Ti-in-zircon thermometer of Ferry and Watson (2007) using in all cases $a(SiO_2) = 1$ and $a(TiO_2) = 1$ for zircon grains from the monazite-bearing PGD and $a(TiO_2) = 0.6$ for zircon grains from the allanite-bearing PGD according to the lack of Ti-oxides. See text for details.
[d] Chondrite normalization after McDonough and Sun (1995).
[e] With *t* corresponding to the timing of intrusion determined by U-Pb dating.

Supplementary material: Analytical methods of U-Th-Pb-Lu-Hf isotopes and trace elements analyses of zircon grains using laser ablation-inductively coupled plasma-mass spectrometry (LA-ICP-MS)

1. U-Th-Pb isotope analyses

Uranium, thorium and lead isotopes were analyzed using a ThermoScientific Element 2 sector field ICP-MS coupled to a Resolution M-50 (Resonetics) 193 nm ArF excimer laser (ComPexPro 102F, Coherent) system at Goethe-University Frankfurt. Data were acquired in time resolved – peak jumping – pulse counting / analogue mode over 455 mass scans, with a 20 second background measurement followed by 21 second sample ablation. Laser spot-size was 20-42 µm for unknowns, 42 µm for the standard zircons GJ1 (primary standard) and Plešovice, and 64 µm for zircon 91500. The results of the standard zircon measurements are shown in Table S3-1. Sample surface was cleaned directly before each analysis by three pulses pre-ablation. Ablation were performed in a 0.6 l min^{-1} He stream, which was mixed directly after the ablation cell with 0.005 l min^{-1} N_2 and 0.71 l min^{-1} Ar prior to introduction into the Ar plasma of the SF-ICP-MS. All gases had a purity of >99.999% and no homogeniser was used while mixing the gases to prevent smoothing of the signal. Signal was tuned for maximum sensitivity for Pb and U while keeping oxide production, monitored as $^{254}UO/^{238}U$, below 1.9-0.7% during the analytical session. The sensitivity achieved was in the range of 9000-14000 cps/µg g^{-1} for ^{238}U with a 30 µm spot size, at 5.5 Hz and about 3 J cm^{-2} laser energy. The typical penetration depth was about 15 µm (spot size dependent). The two-volume ablation cell (Laurin Technic, Australia) of the M50 enables detection and sequential sampling of heterogeneous grains (e.g., growth zones) during time resolved data acquisition, due to its quick response time of <1s (time until maximum signal strength was achieved) and wash-out (< 99.9% of previous signal) time of about 2s. With a depth penetration of ~0.7 µms^{-1} and a 0.46s integration time (4 mass scans = 0.46 s = 1 integration) any significant variation of the $^{207}Pb/^{206}Pb$ and $^{238}U/^{206}Pb$ in the µm scale is detectable. Raw data were corrected offline for background signal, common Pb, laser induced elemental fractionation, instrumental mass discrimination, and time-dependent elemental fractionation of Pb/U using an in-house MS Excel© spreadsheet program (Gerdes and Zeh, 2009, 2006). A common-Pb correction based on the interference- and background-corrected ^{204}Pb signal and a model Pb composition (Stacey and Kramers, 1975) was carried out. The ^{204}Pb content for each ratio was estimated by subtracting the average mass 204 signal, obtained during the 20 second baseline acquisition, which mostly results from ^{204}Hg

in the carrier gas (c. 210-330 cps), from the mass 204 signal of the respective ratio. For the analyzed sample the calculated common ^{206}Pb contents was mostly <0.3% of the total ^{206}Pb but in very rare cases exceeded 1% (Table S3-1). Laser-induced elemental fractionation and instrumental mass discrimination were corrected by normalization to the reference zircon GJ-1 (Jackson et al., 2004). Prior to this normalization, the inter-elemental fractionation ($^{206}Pb^*/^{238}U$) during the 21s of sample ablation was corrected for each individual analysis. The correction was done by applying a linear regression through all measured, common Pb corrected ratios, excluding the outliers (± 2 standard deviation; 2SD), and using the intercept with the y-axis as the initial ratio. The total offset of the measured drift-corrected $^{206}Pb^*/^{238}U$ ratio from the "true" ID-TIMS value (0.0983 ± 0.0004; ID-TIMS GUF value) of the analyzed GJ-1 grain was between 15 and 22% (during the entire analytical session) and the drift over the day 7%.

Reported uncertainties (2σ) of the $^{206}Pb/^{238}U$ ratio were propagated by quadratic addition of the external reproducibility (2 SD) obtained from the standard zircon GJ-1 (see Table S3-1) and the within-run precision of each analysis (2 SE; standard error). In case of the $^{207}Pb/^{206}Pb$ we used a ^{207}Pb signal dependent uncertainty propagation (see Gerdes and Zeh, 2009). The $^{207}Pb/^{235}U$ ratio is derived from the normalized and error propagated $^{207}Pb/^{206}Pb^*$ and $^{206}Pb^*/^{238}U$ ratios assuming a $^{238}U/^{235}U$ natural abundance ratio of 137.88 and the uncertainty derived by quadratic addition of the propagated uncertainties of both ratios. The accuracy of the method was verified by multiple analyses of the reference zircon GJ1 (primary standard; quoted $^{207}Pb/^{206}Pb$ age = 608.5 ± 1.5 Ma, Jackson et al. 2004; $^{206}Pb/^{238}Pb$ age = 604.6 ± 2.9 Ma, Yuan et al., 2008), Plešovice (secondary standard 1: quoted $^{206}Pb/^{238}Pb$ age = 337.13 ± 0.37 Ma, Sláma et al., 2008), and 91500 (secondary standard 2:quoted $^{207}Pb/^{206}Pb$ age = 1065.4 ± 0.3 Ma, Wiedenbeck et al., 1995), which were measured together with the unknowns during the analytical session. Concordia ages obtained from all standards are within error identical to the quoted TIMS values. The results of measurements on reference materials are shown in Table S3-1. The data were plotted using the software ISOPLOT (Ludwig, 2001).

2. Lu-Hf isotope analyses

Hafnium isotope measurements were performed with a Thermo-Finnigan NEPTUNE multi collector ICP-MS at GUF coupled to the same laser as described in the U-Pb method (Resolution M-50 193 nm ArF excimer laser). Round spots with diameters of 64-100 µm were drilled with repetition rate of 6 Hz and an energy density of about 6-7 J/cm^2 during 45 s of data acquisition. All data were adjusted relative to the zircon standard GJ1 of $^{176}Hf/^{177}Hf$ ratio =

0.2820000. Quoted uncertainties are quadratic additions of the within run precision of each analysis and the reproducibility of the zircon standard GJ1 which was 0.0105% (2SD) during the analytical sessions (Table S3-2). Accuracy and external reproducibility of the method was verified by repeated analyses of reference zircons GJ-1, Plešovice, 91500, and Temora2, which yielded $^{176}Hf/^{177}Hf$ of 0.282000 ± 0.000029 (2SD, n=44), 0.282466 ± 0.000029 (n=11), 282294 ± 0.000028 (n = 6), and of 0.282657 ± 0.000028 (n=6), respectively (Table S3-2). These ratios are well within the range of solution mode data (Gerdes and Zeh, 2006; Woodhead and Hergt, 2005).

For calculation of the epsilon Hf $[\varepsilon Hf_t]$ the chondritic uniform reservoir (CHUR) was used as recommended by Bouvier et al. (2008; $^{176}Lu/^{177}Hf$ and $^{176}Hf/^{177}Hf$ of 0.0336 and 0.282785, respectively), and a decay constant of 1.867 $x10^{-11}$ (Scherer et al., 2001; Söderlund et al., 2004). Initial $^{176}Hf/^{177}Hf_t$ and εHf_t for all analysed zircon domains were calculated using the respective $^{207}Pb/^{206}Pb$ ages (Table S3-2). Depleted mantle hafnium model ages (T_{DM}) were calculated using values for the depleted mantle as suggested by Blichert-Toft and Puchtel (2010), with $^{176}Hf/^{177}Hf$ = 0.283294 and a $^{176}Lu/^{177}Hf$ of 0.03933, corresponding to a straight DM-evolution line with εHf_{today} = +18 and $\varepsilon Hf_{4.558Ga}$ = 0. T_{DM} ages for all data were calculated by using the measured $^{176}Lu/^{177}Hf$ of each spot for the time since zircon crystallization (Table S3-2), and a mean $^{176}Lu/^{177}Hf$ of 0.0113 for average continental crust (average of Taylor and McLennan, 1985; Wedepohl, 1995).

3. Trace element analyses

Trace elements were analyzed using a ThermoScientific Element 2 sector field ICP-MS coupled to a Resolution M-50 (Resonetics) 193 nm ArF excimer laser (ComPexPro 102F, Coherent) system at Goethe-University Frankfurt. Ablations were performed in a 0.6 l min^{-1} He stream, which was mixed directly after the ablation cell with 0.005 l min^{-1} N_2 and 0.85 l min^{-1} Ar prior introduction into the Ar plasma of the SF-ICP-MS. Zircon grains were ablated with 42 µm laser spot sizes, a repetition rate of at 6.0 Hz and 6-7 $J.cm^{-2}$ laser energy. The oxide production, monitored as $^{254}UO/^{238}U$ on the standard glass NIST 612 was below 0.5%, and measurements were carried out in low resolution mode, with 30s for background and 35s for data acquisition. During this study the following isotopes were analysed: ^{44}Ca, ^{49}Ti, ^{57}Fe, ^{89}Y, ^{93}Nb, ^{139}La, ^{140}Ce, ^{141}Pr, ^{146}Nd, ^{147}Sm, ^{151}Eu, ^{158}Gd, ^{159}Tb, ^{161}Dy, ^{165}Ho, ^{167}Er, ^{169}Tm, ^{172}Yb, ^{175}Lu, ^{178}Hf, ^{232}Th, and ^{238}U. To increase the background / peak ratio for Ti and Nd, the sampling time for these elements was enlarged from 0.01 ms (as used for all other elements per

scan) to 0.04 ms. For standardisation the glass standards NIST SRM 612 (primary standard), and the zircon standards GJ1 and 91500 (secondary standard) were used. Data processing was performed with GLITTER software, using Si as an internal standard, and SiO_2 =32.7 wt.% for all zircons (standard zircons and unknowns). Accuracy of the zircon measurements was checked by comparison between measured and recommended concentrations for the standard zircons 91500 and GJ1 (see summary in Liu et al., 2010). This check required an offset correction of about 5-11% for the trace elements Y, Ce, Nd, Gd, Tb, Dy, Ho, Er, Tm, Lu, Hf, Ta, U, and Th, and 30-50% for Pr and Nb. The same offset correction was applied to all unknown zircon analyses. For normalization of rare earth elements the concentrations of C1-chondrite of McDonough and Sun (1995) were used. The results are shown in Table S3-3.

Table S3-1: Results of LA-ICP-MS U-Pb dating of zircon grains from the monazite-bearing (13-AM-13) and two allanite-bearing (13-FS-1202 and 13-TC-5072) pegmatitic granite dykes from the central Grenville Province. Abbreviation: conc. = degree of concordance; PGD = pegmatitic granite dyke.

Analysis no.	^{207}Pb [a] (cps)	U [b] (ppm)	Pb [b] (ppm)	Th/U [b]	^{206}Pbc [c] (%)	$^{206}Pb/^{238}U$ [d]	± 2σ (%)	$^{207}Pb/^{235}U$ [d]	± 2σ (%)	$^{207}Pb/^{206}Pb$ [d]	± 2σ (%)	rho [e]	$^{206}Pb/^{238}U$	± 2σ (Ma)	$^{207}Pb/^{235}U$	± 2σ (Ma)	$^{207}Pb/^{206}Pb$	± 2σ (Ma)	conc. [f] (%)
Monazite-bearing PGD (13-AM-13)																			
8	338353	412	71	0.63	b.d.	0.16300	1.5	1.627	1.7	0.07241	0.8	0.89	973	14	981	11	998	16	98
9	240531	289	47	0.40	0.35	0.16120	1.7	1.591	1.9	0.07158	0.9	0.87	963	15	966	12	974	19	99
10	294000	348	56	0.29	b.d.	0.16360	1.6	1.620	1.9	0.07180	1.1	0.83	977	14	978	12	980	22	100
11	396605	479	79	0.39	b.d.	0.16440	1.6	1.654	1.8	0.07297	0.9	0.88	981	14	991	12	1013	18	97
12	193669	220	38	0.46	b.d.	0.16610	1.7	1.664	2.0	0.07263	1.0	0.87	991	16	995	13	1004	20	99
13	284371	346	58	0.39	0.28	0.16560	1.6	1.663	1.9	0.07283	1.0	0.84	988	14	994	12	1009	20	98
14	232503	282	46	0.22	0.21	0.16680	1.5	1.678	1.9	0.07294	1.2	0.77	995	14	1000	12	1012	25	98
15	401635	473	83	0.52	0.08	0.16890	1.6	1.703	2.4	0.07313	1.8	0.68	1006	15	1010	16	1017	36	99
16	405164	450	79	0.54	b.d.	0.16720	1.7	1.663	1.8	0.07211	0.7	0.92	997	16	994	12	989	15	101
17	275567	419	77	0.41	1.04	0.16700	2.0	1.649	3.8	0.07163	3.2	0.52	996	18	989	24	975	66	102
18	398534	487	80	0.24	b.d.	0.16850	1.5	1.677	1.7	0.07218	0.8	0.90	1004	14	1000	11	991	15	101
19	182932	223	37	0.40	b.d.	0.16570	1.6	1.666	1.9	0.07293	1.0	0.84	988	15	996	12	1012	21	98
20	370580	488	88	0.65	b.d.	0.16940	1.6	1.685	1.7	0.07213	0.7	0.90	1009	15	1003	11	990	15	102
21	203997	245	43	0.46	b.d.	0.17000	1.6	1.707	2.0	0.07284	1.2	0.81	1012	15	1011	13	1009	24	100
22	390772	454	83	0.71	b.d.	0.16970	1.6	1.701	1.9	0.07267	0.9	0.89	1011	15	1009	12	1005	17	101
23	238911	278	48	0.41	0.20	0.16880	1.7	1.695	1.9	0.07285	1.0	0.86	1005	16	1007	12	1010	20	100
24	371318	468	80	0.35	b.d.	0.17070	1.6	1.708	3.0	0.07257	2.5	0.55	1016	15	1011	19	1002	50	101
25	206408	241	41	0.37	b.d.	0.16800	1.7	1.684	2.0	0.07273	1.1	0.84	1001	16	1003	13	1006	23	99
26	644004	789	141	0.59	b.d.	0.17040	1.6	1.707	2.2	0.07266	1.5	0.74	1014	15	1011	14	1004	30	101
27	503013	818	142	0.36	0.07	0.17210	1.5	1.716	2.8	0.07229	2.4	0.54	1024	14	1014	18	994	48	103
28	296864	343	59	0.48	b.d.	0.16780	1.7	1.680	3.3	0.07259	2.9	0.51	1000	16	1001	22	1003	58	100
29	317279	388	66	0.39	0.33	0.16800	1.6	1.675	1.8	0.07232	1.0	0.85	1001	14	999	12	995	20	101
30	209872	255	44	0.45	0.05	0.16730	1.6	1.668	2.0	0.07229	1.1	0.81	997	15	996	12	994	23	100
31	346711	421	74	0.49	0.21	0.17040	1.7	1.693	1.9	0.07209	0.9	0.88	1014	16	1006	12	989	18	103
32	268401	323	55	0.42	b.d.	0.16830	1.6	1.684	1.9	0.07261	1.0	0.86	1002	15	1003	12	1003	20	100
38	236998	295	48	0.33	0.40	0.16190	1.6	1.610	2.0	0.07211	1.2	0.80	967	15	974	13	989	25	98
39	484658	571	104	0.54	0.34	0.17110	1.8	1.735	2.0	0.07353	1.0	0.86	1018	17	1021	13	1029	21	99
40	289438	341	57	0.27	b.d.	0.16900	1.5	1.681	1.7	0.07212	0.7	0.90	1007	14	1001	11	989	15	102
41	307604	339	57	0.31	0.23	0.16910	1.5	1.694	1.9	0.07266	1.0	0.83	1007	14	1006	12	1004	21	100
42	241423	287	47	0.23	b.d.	0.16830	1.7	1.689	1.9	0.07277	0.8	0.89	1003	16	1004	12	1007	17	100
43	240846	288	49	0.21	b.d.	0.17210	1.6	1.747	2.0	0.07364	1.2	0.81	1023	15	1026	13	1032	24	99
45	320931	376	64	0.36	0.19	0.16910	1.7	1.746	3.0	0.07488	2.4	0.57	1007	16	1026	19	1065	49	95
46	307162	375	63	0.29	b.d.	0.17090	1.6	1.717	1.8	0.07290	0.9	0.86	1017	15	1015	12	1011	19	101
47	215838	267	45	0.35	b.d.	0.16930	1.7	1.694	2.0	0.07255	1.1	0.83	1008	16	1006	13	1001	23	101
48	416128	504	92	0.53	b.d.	0.17450	1.6	1.747	1.8	0.07260	0.8	0.89	1037	15	1026	12	1003	16	103
49	202081	240	39	0.22	0.39	0.16760	1.6	1.667	2.0	0.07212	1.1	0.84	999	15	996	13	989	22	101
50	338228	406	70	0.46	b.d.	0.16920	1.6	1.695	1.8	0.07263	0.8	0.90	1008	15	1007	11	1004	16	100
52	181973	206	38	0.58	0.10	0.17300	1.8	1.739	2.2	0.07290	1.2	0.82	1028	17	1023	14	1011	25	102
53	337217	412	72	0.52	0.14	0.16870	1.6	1.696	2.6	0.07294	2.0	0.62	1005	15	1007	17	1012	41	99
54	300131	372	67	0.65	0.12	0.16840	1.7	1.689	1.9	0.07272	0.9	0.89	1003	16	1004	12	1006	18	100
55	239160	297	51	0.36	b.d.	0.17070	1.7	1.713	3.5	0.07276	3.0	0.48	1016	16	1013	22	1007	61	101
56	261956	353	58	0.20	0.24	0.17040	1.6	1.632	3.5	0.06945	3.1	0.47	1014	15	983	23	912	65	111

57	189624	233	41	0.57	0.43	0.16900	1.8	1.695	2.2	0.07274	1.3	0.80	1007	17	1007	14	1007	27	100
58	150507	188	30	0.13	b.d.	0.16720	1.6	1.688	4.9	0.07322	4.6	0.34	997	15	1004	32	1020	93	98
59	243187	306	53	0.53	0.32	0.16800	1.7	1.686	2.2	0.07280	1.5	0.74	1001	15	1003	14	1008	31	99
60	305233	364	67	0.95	0.16	0.17050	1.7	1.711	1.9	0.07276	1.0	0.86	1015	16	1013	12	1007	20	101
61	283981	354	65	0.73	b.d.	0.17010	1.6	1.698	1.8	0.07239	0.9	0.88	1013	15	1008	12	997	17	102
62	186787	236	40	0.37	b.d.	0.17020	1.7	1.716	1.9	0.07313	0.9	0.87	1013	16	1015	12	1017	19	100
63	199870	236	39	0.23	0.45	0.16930	1.7	1.702	2.1	0.07290	1.3	0.80	1008	16	1009	14	1011	26	100
64	282701	347	57	0.27	0.21	0.16530	1.7	1.639	2.0	0.07188	1.1	0.84	986	15	985	12	983	22	100
65	455421	655	113	0.39	0.19	0.17190	1.8	1.720	1.9	0.07255	0.8	0.91	1023	17	1016	13	1001	16	102
66	481307	600	103	0.47	b.d.	0.16750	1.6	1.679	1.7	0.07269	0.7	0.92	998	15	1000	11	1005	14	99
72	331616	428	72	0.42	b.d.	0.16590	1.6	1.658	1.8	0.07251	0.8	0.88	989	14	993	11	1000	17	99
73	257130	335	57	0.38	b.d.	0.16840	1.7	1.667	2.0	0.07179	1.0	0.86	1003	16	996	13	980	21	102
74	293298	371	62	0.36	0.17	0.16690	1.7	1.667	1.9	0.07244	0.9	0.87	995	15	996	12	998	19	100
75	370554	457	80	0.54	b.d.	0.16770	1.7	1.682	2.7	0.07273	2.1	0.63	1000	16	1002	17	1006	42	99
76	386535	502	89	0.55	0.12	0.17110	1.6	1.691	1.7	0.07168	0.7	0.92	1018	15	1005	11	977	14	104
77	250996	334	54	0.20	b.d.	0.16770	1.7	1.679	2.2	0.07261	1.3	0.80	1000	16	1001	14	1003	26	100
78	365650	464	78	0.37	0.00	0.16810	1.7	1.677	1.9	0.07233	0.9	0.88	1002	16	1000	12	995	18	101
79	300992	369	63	0.41	0.11	0.16920	1.6	1.692	1.9	0.07254	1.1	0.83	1007	15	1005	12	1001	22	101
80	311436	396	66	0.30	b.d.	0.16940	1.7	1.688	1.8	0.07231	0.6	0.93	1009	15	1004	11	995	13	101
81	190035	240	42	0.59	0.08	0.16670	1.7	1.690	2.1	0.07352	1.2	0.83	994	16	1005	13	1028	23	97
82	236504	302	52	0.49	0.55	0.16840	1.8	1.693	2.1	0.07292	1.1	0.85	1003	16	1006	13	1012	22	99
83	254148	327	57	0.57	b.d.	0.16770	1.7	1.675	2.1	0.07244	1.2	0.83	999	16	999	13	998	24	100
84	214688	264	44	0.25	0.14	0.17150	1.8	1.730	2.1	0.07315	1.1	0.87	1021	17	1020	14	1018	21	100
85	182390	239	39	0.22	b.d.	0.16990	1.7	1.701	4.4	0.07260	4.0	0.39	1012	16	1009	28	1003	82	101
86	289781	360	60	0.29	b.d.	0.16830	1.8	1.677	2.0	0.07227	0.9	0.89	1003	17	1000	13	994	19	101
Allanite-bearing PGD (13-FS-1202)																			
87	301878	410	67	0.24	b.d.	0.16760	1.6	1.674	1.8	0.07244	0.9	0.88	999	15	999	12	998	18	100
88	407816	506	87	0.38	b.d.	0.17050	1.6	1.703	1.8	0.07243	0.8	0.90	1015	15	1010	12	998	16	102
89	102893	132	22	0.20	b.d.	0.17000	1.7	1.709	2.0	0.07291	1.2	0.81	1012	16	1012	13	1012	24	100
90	200143	265	42	0.12	b.d.	0.16760	1.6	1.680	1.9	0.07270	1.1	0.83	999	15	1001	12	1006	21	99
91	320292	432	72	0.25	b.d.	0.16950	1.7	1.684	2.0	0.07205	1.1	0.84	1010	16	1003	13	987	22	102
92	341163	460	79	0.33	0.23	0.17310	1.5	1.736	1.8	0.07274	1.0	0.83	1029	14	1022	12	1007	20	102
93	269033	352	60	0.42	b.d.	0.16780	1.7	1.678	2.0	0.07250	1.1	0.85	1000	16	1000	13	1000	22	100
94	163357	239	39	0.22	b.d.	0.16720	1.7	1.684	2.0	0.07304	1.2	0.82	997	15	1002	13	1015	23	98
95	295149	399	64	0.23	0.25	0.16470	1.6	1.650	1.9	0.07267	1.1	0.83	983	14	989	12	1005	22	98
96	220681	298	49	0.21	b.d.	0.16950	1.7	1.698	2.1	0.07268	1.1	0.83	1009	16	1008	13	1005	23	100
97	217047	280	47	0.27	0.56	0.16920	1.8	1.702	4.7	0.07296	4.4	0.38	1008	17	1009	31	1013	88	99
98	189500	254	41	0.20	b.d.	0.16730	1.8	1.669	2.1	0.07236	1.2	0.84	997	17	997	14	996	23	100
99	198886	277	45	0.21	b.d.	0.16800	1.7	1.685	2.1	0.07275	1.2	0.80	1001	16	1003	13	1007	25	99
100	183244	247	41	0.21	0.10	0.17010	1.7	1.687	2.0	0.07192	1.2	0.82	1013	16	1004	13	984	24	103
101	230088	304	50	0.22	0.31	0.16940	1.7	1.697	3.3	0.07264	2.9	0.51	1009	16	1007	22	1004	58	100
107	279105	381	63	0.24	0.21	0.16950	1.6	1.693	1.8	0.07245	0.7	0.93	1009	15	1006	11	999	13	101
108	198191	285	47	0.28	0.26	0.16900	1.7	1.689	2.0	0.07244	1.1	0.84	1007	16	1004	13	998	22	101
109	352124	476	80	0.33	0.02	0.16950	1.7	1.699	1.9	0.07270	0.7	0.92	1009	16	1008	12	1006	15	100
110	251663	344	55	0.28	0.02	0.16240	1.6	1.589	2.0	0.07098	1.3	0.78	970	14	966	13	957	26	101
111	261221	358	60	0.24	0.16	0.17020	1.6	1.703	1.9	0.07260	1.0	0.86	1013	15	1010	12	1003	20	101
112	139807	189	31	0.20	b.d.	0.16880	1.7	1.682	2.0	0.07228	1.1	0.84	1006	16	1002	13	994	23	101
113	277487	362	60	0.23	b.d.	0.16930	1.5	1.692	1.8	0.07249	0.9	0.86	1008	14	1006	11	1000	18	101

114	137436	185	30	0.15	b.d.	0.16860	1.6	1.689	2.0	0.07264	1.1	0.82	1004	15	1004	13	1004	23	100
115	241036	323	54	0.23	b.d.	0.17010	1.7	1.702	2.1	0.07255	1.3	0.80	1013	16	1009	14	1001	26	101
116	204223	339	56	0.23	1.20	0.16770	1.9	1.677	2.7	0.07255	1.9	0.71	999	18	1000	17	1001	38	100
117	142199	195	33	0.25	b.d.	0.17200	1.8	1.739	2.4	0.07335	1.6	0.74	1023	17	1023	16	1024	33	100
118	225767	299	51	0.32	b.d.	0.16990	1.6	1.705	1.9	0.07278	1.0	0.84	1012	15	1010	12	1008	21	100
119	221902	297	49	0.24	0.59	0.16910	1.7	1.715	2.1	0.07355	1.3	0.79	1007	15	1014	14	1029	26	98
120	130697	182	29	0.17	0.29	0.16370	1.7	1.653	2.2	0.07324	1.3	0.79	977	16	991	14	1021	27	96
121	302635	463	76	0.22	b.d.	0.16820	1.7	1.682	3.9	0.07254	3.4	0.45	1002	16	1002	25	1001	70	100
122	285176	404	66	0.24	0.56	0.16840	1.7	1.678	2.0	0.07227	1.1	0.83	1003	15	1000	13	994	23	101
123	438726	662	111	0.30	b.d.	0.16900	1.6	1.697	1.9	0.07283	1.0	0.84	1007	15	1007	12	1009	20	100
124	165147	210	34	0.21	b.d.	0.16820	1.7	1.686	2.1	0.07272	1.2	0.81	1002	15	1003	13	1006	25	100
125	202792	274	45	0.22	0.28	0.16970	1.7	1.673	2.3	0.07149	1.6	0.73	1010	16	998	15	971	32	104
126	169908	237	40	0.28	0.12	0.16920	1.8	1.692	2.2	0.07255	1.2	0.82	1007	17	1006	14	1001	25	101
127	157914	218	36	0.25	0.61	0.16870	1.6	1.695	2.2	0.07287	1.5	0.74	1005	15	1007	14	1010	30	99
128	260856	375	63	0.38	b.d.	0.16560	1.6	1.654	2.1	0.07245	1.3	0.79	988	15	991	13	999	26	99
129	284756	374	62	0.27	b.d.	0.16840	1.7	1.681	1.9	0.07238	0.9	0.87	1004	15	1001	12	997	19	101
130	613739	863	144	0.35	0.28	0.16510	1.8	1.650	2.0	0.07247	1.0	0.88	985	16	989	13	999	20	99
131	247872	353	58	0.23	0.54	0.16970	1.6	1.705	2.1	0.07288	1.3	0.78	1011	15	1011	14	1011	27	100
132	238823	383	64	0.29	b.d.	0.16710	2.3	1.647	2.5	0.07149	1.1	0.91	996	21	988	16	972	22	103
133	163218	221	37	0.19	1.25	0.17170	1.7	1.730	2.7	0.07310	2.2	0.61	1021	16	1020	18	1017	44	100
134	274268	426	70	0.26	b.d.	0.16790	1.7	1.647	1.9	0.07115	0.9	0.89	1000	16	988	12	962	18	104
135	233375	325	53	0.21	0.20	0.16860	1.6	1.691	1.8	0.07274	0.9	0.86	1005	15	1005	12	1007	19	100
136	156062	226	37	0.32	b.d.	0.16670	1.8	1.648	2.0	0.07173	0.9	0.89	994	16	989	13	978	19	102
137	527218	367	59	0.25	0.22	0.16420	1.7	1.645	1.9	0.07265	1.0	0.87	980	15	987	12	1004	19	98
138	286575	202	34	0.31	0.31	0.16810	1.8	1.693	3.1	0.07302	2.5	0.57	1002	17	1006	20	1015	51	99
139	719060	541	88	0.37	0.01	0.16100	1.7	1.612	1.9	0.07264	0.7	0.92	962	15	975	12	1004	15	96
140	498816	347	55	0.23	b.d.	0.16200	1.6	1.600	1.8	0.07166	0.7	0.92	968	15	970	11	976	15	99
141	465129	355	53	0.25	0.00	0.15290	1.7	1.524	1.9	0.07227	0.8	0.90	917	15	940	12	994	17	92
142	533499	413	65	0.27	b.d.	0.16040	1.7	1.587	1.9	0.07177	0.8	0.90	959	15	965	12	980	16	98
143	632446	485	75	0.27	0.00	0.15780	1.7	1.580	1.9	0.07260	0.9	0.87	945	15	962	12	1003	19	94
144	393941	277	46	0.18	0.11	0.16940	1.6	1.704	1.8	0.07294	0.8	0.90	1009	15	1010	12	1012	16	100
145	648218	477	75	0.40	b.d.	0.15610	1.6	1.540	1.9	0.07154	0.8	0.89	935	14	946	11	973	17	96
151	494018	403	60	0.21	b.d.	0.15250	1.8	1.529	2.1	0.07273	1.1	0.84	915	15	942	13	1006	23	91
152	378485	288	46	0.33	0.13	0.15890	1.7	1.569	2.0	0.07162	1.0	0.87	951	15	958	12	975	20	98
153	631307	462	76	0.41	0.14	0.16210	1.6	1.620	1.8	0.07247	0.8	0.90	968	15	978	12	999	16	97
154	340598	264	40	0.20	0.06	0.15550	1.7	1.539	1.9	0.07177	1.0	0.86	932	14	946	12	980	20	95
155	585110	457	72	0.24	b.d.	0.16050	1.6	1.589	1.8	0.07179	0.8	0.88	960	14	966	11	980	17	98
156	365750	282	44	0.31	b.d.	0.15780	1.7	1.569	2.0	0.07212	1.0	0.87	944	15	958	12	989	20	95
157	715717	550	85	0.26	0.02	0.15840	1.7	1.547	1.9	0.07083	0.8	0.90	948	15	949	12	953	17	100
158	526413	399	63	0.29	0.03	0.15970	1.6	1.570	1.8	0.07133	0.8	0.90	955	14	959	11	967	16	99
159	228549	179	28	0.22	b.d.	0.15850	1.6	1.588	2.0	0.07270	1.2	0.81	948	14	966	12	1006	24	94
160	348679	275	41	0.33	b.d.	0.15200	1.6	1.508	1.9	0.07197	0.9	0.88	912	14	934	11	985	18	93
161	770649	586	95	0.39	b.d.	0.16030	1.7	1.579	1.9	0.07141	0.8	0.90	959	15	962	12	969	17	99
162	371285	293	46	0.33	b.d.	0.15810	1.7	1.556	2.0	0.07136	1.1	0.83	946	15	953	12	968	22	98
163	517454	402	62	0.23	0.19	0.15790	1.6	1.578	1.9	0.07247	0.9	0.86	945	14	962	12	999	19	95
164	248441	198	30	0.25	0.31	0.15640	1.7	1.572	2.0	0.07286	1.1	0.84	937	14	959	12	1010	21	93
165	767746	600	97	0.39	b.d.	0.16080	1.8	1.612	2.2	0.07272	1.3	0.81	961	16	975	14	1006	26	96
166	427455	362	57	0.21	0.63	0.16060	1.7	1.615	2.1	0.07293	1.3	0.79	960	15	976	13	1012	26	95
167	401456	318	50	0.30	b.d.	0.15770	1.6	1.555	1.8	0.07150	0.7	0.91	944	14	953	11	972	15	97

168	578908	469	71	0.25	0.13	0.15450	1.5	1.544	1.7	0.07252	0.8	0.89	926	13	948	11	1001	16	93
169	628126	483	79	0.25	b.d.	0.16670	1.6	1.664	1.9	0.07238	1.0	0.85	994	15	995	12	997	20	100
170	423325	322	51	0.28	b.d.	0.16050	1.6	1.605	1.8	0.07250	0.8	0.89	960	14	972	11	1000	17	96
Allanite-bearing PGD (13-TC-5072)																			
171	149226	248	41	0.24	b.d.	0.16760	2.0	1.674	2.4	0.07244	1.4	0.82	999	18	999	15	998	28	100
172	319379	478	83	0.39	0.06	0.17030	1.7	1.710	2.0	0.07285	1.1	0.84	1014	16	1012	13	1010	22	100
173	63920	103	17	0.22	b.d.	0.16830	1.9	1.696	2.7	0.07309	1.8	0.72	1003	18	1007	17	1016	37	99
174	104828	168	26	0.10	b.d.	0.16310	2.0	1.635	2.5	0.07270	1.5	0.82	974	18	984	16	1006	29	97
175	353477	581	98	0.27	b.d.	0.17030	1.8	1.707	2.1	0.07271	1.0	0.88	1014	17	1011	13	1006	20	101
176	83774	119	20	0.27	0.59	0.16760	2.2	1.683	2.8	0.07280	1.8	0.78	999	21	1002	18	1008	36	99
177	362125	597	97	0.35	0.08	0.15960	1.9	1.584	2.2	0.07198	1.0	0.89	955	17	964	14	985	20	97
178	155364	252	41	0.28	0.36	0.16480	1.7	1.654	2.2	0.07276	1.4	0.78	984	16	991	14	1007	28	98
179	166538	272	45	0.27	0.09	0.16830	1.7	1.672	2.0	0.07203	1.0	0.86	1003	16	998	13	987	20	102
180	191320	337	57	0.36	0.10	0.16850	2.0	1.685	2.4	0.07250	1.4	0.82	1004	18	1003	15	1000	28	100
181	207813	309	53	0.40	b.d.	0.16840	1.8	1.666	2.2	0.07176	1.3	0.81	1003	17	996	14	979	26	102
182	133744	208	34	0.26	b.d.	0.16810	1.8	1.683	2.2	0.07261	1.3	0.81	1002	17	1002	14	1003	27	100
183	138168	224	37	0.25	0.61	0.16870	1.7	1.700	2.4	0.07307	1.6	0.74	1005	16	1008	15	1016	32	99
184	180621	280	46	0.30	b.d.	0.16740	1.8	1.679	2.0	0.07277	1.0	0.88	998	17	1001	13	1007	20	99
185	332601	330	54	0.25	b.d.	0.16560	1.8	1.681	2.5	0.07359	1.8	0.71	988	17	1001	16	1030	36	96
186	504229	416	68	0.39	0.01	0.16100	1.6	1.625	1.8	0.07318	0.7	0.93	962	15	980	11	1019	13	94
187	250593	207	32	0.25	0.45	0.15710	1.7	1.586	2.2	0.07323	1.4	0.77	940	15	965	14	1020	28	92
188	375345	309	48	0.31	b.d.	0.15570	1.6	1.564	1.9	0.07285	1.0	0.85	933	14	956	12	1010	21	92
189	480805	386	63	0.41	0.63	0.15890	1.8	1.617	2.2	0.07380	1.2	0.82	951	16	977	14	1036	25	92
190	191906	149	24	0.27	0.00	0.16460	1.7	1.645	1.9	0.07248	1.0	0.85	982	15	987	12	1000	21	98
191	723661	601	100	0.48	0.06	0.16210	1.6	1.623	1.7	0.07259	0.7	0.92	969	14	979	11	1003	14	97
192	697492	587	95	0.47	b.d.	0.15830	1.6	1.572	1.9	0.07201	0.9	0.87	948	14	959	12	986	19	96
193	451881	382	62	0.38	0.12	0.16180	1.7	1.603	1.9	0.07185	0.9	0.90	967	16	971	12	982	18	98
199	633319	536	84	0.39	0.02	0.15680	1.6	1.555	1.8	0.07192	0.8	0.90	939	14	952	11	984	16	95
200	155755	129	19	0.16	0.78	0.14950	1.8	1.493	4.4	0.07244	4.1	0.40	898	15	928	27	998	82	90
201	592415	453	79	0.43	b.d.	0.16980	1.7	1.709	2.4	0.07301	1.7	0.70	1011	16	1012	16	1014	35	100
202	343887	288	43	0.28	b.d.	0.15110	1.8	1.510	2.1	0.07247	1.0	0.87	907	15	934	13	999	20	91
203	413063	350	58	0.33	b.d.	0.16550	1.7	1.664	2.7	0.07292	2.1	0.62	987	16	995	17	1012	43	98
204	220298	194	30	0.37	0.28	0.15750	1.9	1.501	4.6	0.06911	4.2	0.41	943	17	931	29	902	87	105
205	280841	230	36	0.27	b.d.	0.16140	1.8	1.593	2.1	0.07160	1.0	0.87	964	16	967	13	974	20	99
206	370838	309	50	0.48	b.d.	0.15880	1.7	1.558	1.9	0.07115	0.9	0.89	950	15	954	12	962	18	99
207	268856	233	36	0.26	b.d.	0.15750	1.9	1.593	2.1	0.07337	1.0	0.88	943	16	968	13	1024	20	92
208	216802	188	30	0.34	b.d.	0.16110	1.7	1.607	2.1	0.07237	1.1	0.85	963	16	973	13	996	22	97
209	336668	276	47	0.47	0.33	0.16610	1.5	1.663	3.1	0.07264	2.7	0.49	990	14	995	20	1004	54	99
210	221851	194	30	0.36	b.d.	0.15590	1.7	1.540	2.0	0.07164	1.0	0.85	934	15	947	12	976	21	96
211	163806	141	22	0.25	0.10	0.15630	1.7	1.564	2.1	0.07260	1.1	0.84	936	15	956	13	1003	23	93
Results of standard measurements																			
Standard zircon GJ1																			
GJ1-1	264716	295	27	0.03	0.07	0.09878	1.6	0.8225	1.8	0.06039	0.9	0.87	607	9	609	8	618	19	98
GJ1-2	263760	290	26	0.03	0.07	0.09751	1.6	0.7962	1.9	0.05922	1.0	0.84	600	9	595	9	575	22	104
GJ1-3	272703	289	26	0.03	0.06	0.09835	1.5	0.8067	1.7	0.05949	0.9	0.87	605	9	601	8	585	19	103
GJ1-4	245128	276	25	0.03	0.06	0.09827	1.5	0.8175	1.9	0.06034	1.0	0.83	604	9	607	9	616	23	98
GJ1-5	247455	275	25	0.03	0.06	0.09837	1.6	0.8197	2.0	0.06044	1.2	0.81	605	9	608	9	619	25	98

GJ1-6	224202	263	24	0.03	0.09	0.09714	1.6	0.8103	1.9	0.06050	1.0	0.86	598	9	603	9	621	21	96
GJ1-7	221924	266	24	0.03	0.06	0.09836	1.5	0.8154	1.9	0.06012	1.2	0.79	605	9	605	9	608	25	99
GJ1-8	217892	269	24	0.03	0.07	0.09823	1.6	0.8182	1.9	0.06041	1.1	0.82	604	9	607	9	618	23	98
GJ1-9	218421	270	25	0.03	0.10	0.09980	1.7	0.8249	1.9	0.05995	1.0	0.85	613	10	611	9	602	22	102
GJ1-10	206763	283	26	0.03	0.06	0.09775	1.6	0.8150	2.0	0.06047	1.2	0.81	601	9	605	9	620	25	97
GJ1-11	206063	282	25	0.03	0.08	0.09731	1.5	0.8004	1.9	0.05966	1.1	0.80	599	9	597	9	591	25	101
GJ1-12	186236	287	26	0.03	0.09	0.09845	1.7	0.8025	2.2	0.05912	1.3	0.79	605	10	598	10	572	29	106
GJ1-13	187697	288	26	0.03	0.08	0.09861	1.6	0.8283	2.0	0.06092	1.2	0.80	606	9	613	9	636	26	95
GJ1-14	172458	283	26	0.03	0.07	0.09882	1.7	0.8170	2.0	0.05996	1.1	0.83	607	10	606	9	602	24	101
GJ1-15	169647	287	26	0.03	0.08	0.09748	1.7	0.8154	2.1	0.06067	1.3	0.79	600	10	605	10	628	28	96
mean (n=15):						0.09822		0.81400		0.06011			604		605		607		
2SD(abs):						0.00138		0.01831		0.00107			8		10		38		
2SD(%)						1.41		2.25		1.78									
Standard zircon Plesovice																			
4	492793	957	49	0.20	0.06	0.05390	1.5	0.3954	2.5	0.05320	2.0	0.61	338	5	338	7	338	45	100
5	469358	912	47	0.20	0.17	0.05403	1.5	0.3979	3.0	0.05341	2.5	0.52	339	5	340	9	346	57	98
35	412497	801	42	0.20	b.d.	0.05427	1.6	0.3993	1.8	0.05336	0.7	0.92	341	5	341	5	344	16	99
36	423839	865	45	0.20	b.d.	0.05410	1.6	0.3997	1.8	0.05358	1.0	0.85	340	5	341	5	353	22	96
104	354650	821	42	0.20	b.d.	0.05404	1.6	0.3963	1.8	0.05319	0.7	0.91	339	5	339	5	337	17	101
105	365962	818	42	0.21	b.d.	0.05391	1.6	0.3957	1.8	0.05323	0.9	0.89	338	5	339	5	339	19	100
196	319778	857	44	0.22	0.16	0.05352	1.7	0.3926	2.1	0.05320	1.1	0.84	336	6	336	6	338	25	100
197	301840	864	44	0.20	0.22	0.05378	1.7	0.3968	2.0	0.05352	1.1	0.84	338	6	339	6	351	25	96
242	318292	996	51	0.20	b.d.	0.05369	1.7	0.3941	2.0	0.05324	1.1	0.84	337	6	337	6	339	25	99
243	289070	885	45	0.21	0.13	0.05386	1.8	0.3957	2.2	0.05328	1.3	0.82	338	6	339	6	341	28	99
mean (n=10):						0.05391		0.39635		0.05332			338		339		343		
2SD(abs):						0.00043		0.00439		0.00028			3		3		12		
2SD(%)						0.80		1.11		0.53									
Standard zircon 91500																			
69	237738	64	12	0.47	0.71	0.17940	1.9	1.853	2.6	0.07492	1.8	0.73	1064	19	1065	17	1066	35	100
70	240716	64	12	0.48	0.53	0.17850	1.6	1.847	2.1	0.07503	1.3	0.79	1059	16	1062	14	1069	25	99
148	213573	68	12	0.48	b.d.	0.17810	1.6	1.847	2.0	0.07520	1.2	0.80	1057	15	1062	13	1074	23	98
149	209152	68	12	0.47	0.08	0.17910	1.7	1.851	2.1	0.07495	1.3	0.80	1062	17	1064	14	1067	25	99
238	179394	71	13	0.48	0.54	0.17770	1.6	1.838	2.2	0.07503	1.5	0.73	1054	15	1059	14	1069	30	99
239	184923	70	13	0.50	0.01	0.17990	1.8	1.860	2.2	0.07497	1.3	0.80	1067	18	1067	15	1068	26	100
mean (n=8):						0.17878		1.84933		0.07502			1060		1063		1069		
2SD(abs):						0.00166		0.01468		0.00020			9		5		5		
2SD(%)						0.93		0.79		0.27									

[a] Within run background-corrected mean ^{207}Pb signal in cps (counts per second).
[b] U and Pb content and Th/U ratio were calculated relative to GJ-1 reference zircon.
[c] percentage of the common Pb on the ^{206}Pb. b.d. = below detection limit.
[d] corrected for background, within-run Pb/U fractionation (in case of $^{206}Pb/^{238}U$) and common Pb using Stacy and Kramers (1975) model Pb composition and subsequently normalized to GJ-1 (ID-TIMS value/measured value); $^{207}Pb/^{235}U$ calculated using $^{207}Pb/^{206}Pb/(^{238}U/^{206}Pb*1/137.88)$
[e] rho is the $^{206}Pb/^{238}U/^{207}Pb/^{235}U$ error correlation coefficient.
[f] degree of concordance = $^{206}Pb/^{238}U$ age / $^{207}Pb/^{206}Pb$ age x 100

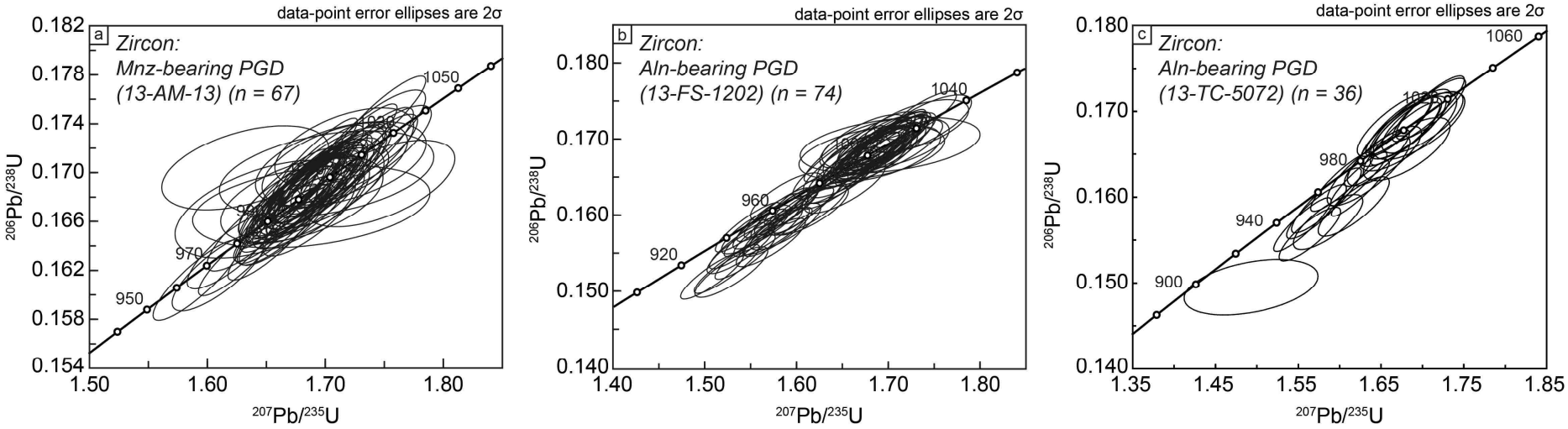

Figure S3-1: Concordia diagrams of all zircon U-Pb isotopes analyses performed on REE-rich PGD from the central Grenville. a: Concordia diagram for the zircon grains from the 13-AM-13 monazite-bearing pegmatitic granite dyke (n = 67; data-point error ellipses are 2σ); b: Concordia diagram for the zircon grains from the 13-FS-1202 allanite-bearing pegmatitic granite dyke (n = 74; data-point error ellipses are 2σ); c: Concordia diagram for the zircon grains from the 13-TC-5072 allanite-bearing pegmatitic granite dyke (n = 36; data-point error ellipses are 2σ).

Table S3-2: Results of LA-MC-ICPMS Lu-Hf isotope analyses of zircon grains from the monazite-bearing (13-AM-13) and two allanite-bearing (13-FS-1202 and 13-TC-5072) pegmatitic granite dykes from the central Grenville Province. Abbreviation: PGD = pegmatitic granite dyke.

Analysis no.	$^{176}Yb/^{177}Hf$ [a]	± 2σ	$^{176}Lu/^{177}Hf$ [a]	± 2σ	$^{178}Hf/^{177}Hf$	$^{180}Hf/^{177}Hf$	Sig_{Hf} [b] (V)	$^{176}Hf/^{177}Hf$	± 2σ [c]	$^{176}Hf/^{177}Hf_t$ [d]	εHf_t [d]	± 2σ [c]	T_{DM2} [e] (Ga)	Age [f] (Ma)	± 2σ [c]	Conc. (%)
Monazite-bearing PGD (13-AM-13)																
8	0.0164	1.7	0.00057	0.5	1.46723	1.88650	9	0.282109	36	0.282013	-5.0	1.3	2.06	998	16	98
9	0.0126	0.3	0.00045	0.1	1.46719	1.88642	9	0.282101	35	0.282006	-5.8	1.2	2.08	974	19	99
10	0.0118	1.8	0.00040	0.4	1.46720	1.88658	10	0.282078	35	0.281983	-6.4	1.2	2.12	980	22	100
11	0.0083	2.2	0.00030	0.8	1.46717	1.88650	9	0.282066	35	0.281972	-6.1	1.2	2.13	1013	18	97
12	0.0087	5.7	0.00031	2.0	1.46718	1.88661	8	0.282089	36	0.281995	-5.5	1.3	2.09	1004	20	99
13	0.0125	0.2	0.00043	0.1	1.46717	1.88671	9	0.282062	38	0.281965	-6.4	1.4	2.15	1009	20	98
14	0.0101	1.0	0.00036	0.3	1.46718	1.88652	10	0.282079	35	0.281982	-5.7	1.2	2.11	1012	25	98
15	0.0199	3.1	0.00068	1.1	1.46715	1.88637	8	0.282111	38	0.282008	-4.7	1.3	2.06	1017	36	99
16	0.0197	3.1	0.00066	1.1	1.46708	1.88637	9	0.282048	35	0.281945	-7.6	1.2	2.19	989	15	101
17	0.0125	9.2	0.00043	3.1	1.46718	1.88659	10	0.282060	34	0.281961	-7.3	1.2	2.17	975	66	102
18	0.0098	4.8	0.00032	1.6	1.46719	1.88660	10	0.282076	33	0.281978	-6.4	1.2	2.13	991	15	101
19	0.0070	0.8	0.00025	0.3	1.46718	1.88639	8	0.282084	38	0.281986	-5.6	1.4	2.10	1012	21	98
20	0.0199	4.0	0.00068	1.2	1.46718	1.88656	8	0.282090	38	0.281984	-6.2	1.3	2.12	990	15	102
21	0.0123	0.6	0.00043	0.3	1.46722	1.88645	9	0.282103	37	0.282001	-5.1	1.3	2.08	1009	24	100
22	0.0239	2.5	0.00082	0.8	1.46710	1.88644	8	0.282101	37	0.281991	-5.6	1.3	2.10	1005	17	101
23	0.0145	1.1	0.00051	0.5	1.46718	1.88658	9	0.282084	39	0.281980	-5.9	1.4	2.12	1010	20	100
24	0.0073	2.5	0.00025	0.7	1.46722	1.88668	10	0.282098	33	0.281998	-5.4	1.2	2.09	1002	50	101
25	0.0088	2.4	0.00030	1.0	1.46713	1.88663	10	0.282069	36	0.281967	-6.4	1.3	2.14	1006	23	99
26	0.0165	6.4	0.00056	2.2	1.46718	1.88651	8	0.282107	37	0.282000	-5.3	1.3	2.08	1004	30	101
27	0.0153	9.6	0.00051	3.3	1.46717	1.88643	9	0.282076	38	0.281969	-6.6	1.4	2.14	994	48	103
28	0.0082	0.3	0.00029	0.1	1.46721	1.88663	9	0.282090	38	0.281986	-5.8	1.3	2.11	1003	58	100
29	0.0079	0.4	0.00028	0.0	1.46722	1.88669	9	0.282098	36	0.281994	-5.7	1.3	2.10	995	20	101
30	0.0104	1.8	0.00037	0.6	1.46724	1.88665	9	0.282123	36	0.282017	-4.9	1.3	2.05	994	23	100
31	0.0167	4.5	0.00059	1.5	1.46719	1.88660	8	0.282107	38	0.281996	-5.8	1.4	2.09	989	18	103
32	0.0128	1.3	0.00044	0.4	1.46721	1.88662	9	0.282107	34	0.281998	-5.4	1.2	2.08	1003	20	100
38	0.0060	3.9	0.00021	1.4	1.46725	1.88677	9	0.282108	38	0.282003	-5.5	1.4	2.08	989	25	98
39	0.0252	6.9	0.00089	2.2	1.46710	1.88612	8	0.282109	60	0.281990	-5.1	2.1	2.09	1029	21	99
40	0.0233	7.4	0.00081	2.6	1.46720	1.88641	8	0.282099	38	0.281982	-6.3	1.4	2.12	989	15	102
41	0.0088	0.9	0.00029	0.2	1.46719	1.88655	10	0.282096	38	0.281988	-5.7	1.3	2.10	1004	21	100
42	0.0133	6.2	0.00045	2.1	1.46715	1.88653	9	0.282102	36	0.281990	-5.6	1.3	2.10	1007	17	100
43	0.0102	8.2	0.00034	2.6	1.46715	1.88649	9	0.282091	34	0.281981	-5.3	1.2	2.10	1032	24	99
45	0.0093	3.0	0.00031	0.9	1.46714	1.88652	10	0.282086	34	0.281974	-4.8	1.2	2.10	1065	49	95
46	0.0095	2.7	0.00032	1.0	1.46716	1.88663	10	0.282071	34	0.281959	-6.6	1.2	2.16	1011	19	101
47	0.0063	1.0	0.00022	0.4	1.46720	1.88652	10	0.282113	34	0.282002	-5.3	1.2	2.08	1001	23	101
48	0.0182	1.7	0.00060	0.4	1.46718	1.88657	9	0.282107	34	0.281988	-5.7	1.2	2.10	1003	16	103
49	0.0050	0.7	0.00016	0.1	1.46714	1.88654	10	0.282075	34	0.281965	-6.9	1.2	2.15	989	22	101
50	0.0070	0.3	0.00025	0.1	1.46715	1.88656	9	0.282086	37	0.281973	-6.2	1.3	2.13	1004	16	100
52	0.0179	6.8	0.00061	2.3	1.46716	1.88644	8	0.282082	46	0.281952	-6.8	1.6	2.17	1011	25	102
53	0.0168	2.8	0.00058	0.9	1.46716	1.88653	8	0.282131	37	0.282001	-5.1	1.3	2.07	1012	41	99
54	0.0202	2.2	0.00067	0.9	1.46717	1.88650	7	0.282194	38	0.281983	-5.9	1.4	2.11	1006	18	100
55	0.0117	0.9	0.00040	0.2	1.46722	1.88662	8	0.282105	35	0.281977	-6.0	1.2	2.12	1007	61	101
56	0.0122	1.2	0.00041	0.2	1.46717	1.88657	8	0.282165	36	0.281959	-8.8	1.3	2.20	912	65	111

57	0.0127	0.7	0.00044	0.2	1.46723	1.88650	8	0.282116	40	0.281988	-5.6	1.4	2.10	1007	61	101
58	0.0102	11.0	0.00035	4.1	1.46710	1.88649	9	0.282092	38	0.281965	-6.5	1.4	2.15	1007	27	100
59	0.0151	1.4	0.00052	0.4	1.46716	1.88652	8	0.282108	37	0.281976	-5.8	1.3	2.12	1020	93	98
60	0.0197	3.8	0.00065	1.6	1.46716	1.88655	8	0.282127	37	0.281993	-5.5	1.3	2.09	1007	20	101
75	0.0148	13.9	0.00050	4.5	1.46715	1.88623	8	0.282097	36	0.281965	-6.5	1.3	2.15	1006	42	99
76	0.0161	14.0	0.00052	4.4	1.46715	1.88642	8	0.282182	36	0.281972	-6.9	1.3	2.15	977	14	104
77	0.0102	0.4	0.00034	0.1	1.46719	1.88669	9	0.282085	40	0.281956	-6.9	1.4	2.17	1003	26	100
78	0.0090	1.5	0.00030	0.3	1.46717	1.88652	9	0.282102	36	0.281973	-6.5	1.3	2.14	995	18	101
80	0.0090	1.3	0.00030	0.4	1.46716	1.88659	19	0.282085	33	0.281953	-7.2	1.2	2.17	995	13	101
81	0.0128	0.7	0.00045	0.2	1.46718	1.88650	7	0.282199	41	0.281989	-5.1	1.5	2.09	1028	23	97
82	0.0179	0.9	0.00063	0.2	1.46719	1.88639	7	0.282215	40	0.282002	-5.1	1.4	2.07	1012	22	99
83	0.0138	1.7	0.00048	0.7	1.46709	1.88632	7	0.282181	39	0.281970	-6.5	1.4	2.14	998	24	100
84	0.0119	4.2	0.00040	1.6	1.46715	1.88643	8	0.282160	36	0.281950	-6.7	1.3	2.17	1018	21	100
85	0.0048	1.3	0.00016	0.4	1.46718	1.88656	8	0.282165	35	0.281959	-6.8	1.3	2.16	1003	82	101
86	0.0072	3.1	0.00025	1.1	1.46719	1.88636	8	0.282171	35	0.281963	-6.9	1.2	2.16	994	19	101
Allanite-bearing PGD (13-FS-1202)																
87	0.0247	5.2	0.00091	1.9	1.46718	1.88664	16	0.282093	34	0.281949	-7.2	1.2	2.18	998	18	100
88	0.0397	1.7	0.00142	0.5	1.46724	1.88678	16	0.282083	33	0.281929	-7.9	1.2	2.22	998	16	102
89	0.0109	13.9	0.00041	5.1	1.46717	1.88646	7	0.282165	37	0.281953	-6.8	1.3	2.17	1012	24	100
90	0.0131	15.5	0.00049	5.6	1.46715	1.88651	7	0.282163	39	0.281949	-7.0	1.4	2.18	1006	21	99
91	0.0276	3.6	0.00101	1.3	1.46716	1.88650	8	0.282128	35	0.281903	-9.1	1.2	2.27	987	22	102
92	0.0224	2.2	0.00081	0.8	1.46722	1.88658	8	0.282136	39	0.281915	-8.2	1.4	2.24	1007	20	102
93	0.0310	2.3	0.00109	0.8	1.46722	1.88667	16	0.282099	33	0.281951	-7.1	1.2	2.18	1000	22	100
94	0.0138	1.3	0.00051	0.4	1.46719	1.88666	17	0.282083	33	0.281945	-7.0	1.2	2.18	1015	23	98
95	0.0308	13.0	0.00113	4.7	1.46717	1.88665	16	0.282083	34	0.281933	-7.7	1.2	2.21	1005	22	98
96	0.0310	8.9	0.00111	3.3	1.46722	1.88669	17	0.282088	34	0.281937	-7.5	1.2	2.20	1005	23	100
97	0.0250	3.2	0.00091	1.3	1.46719	1.88670	16	0.282091	34	0.281943	-7.1	1.2	2.19	1013	88	99
98	0.0248	7.3	0.00092	2.6	1.46718	1.88647	7	0.282125	40	0.281901	-9.0	1.4	2.27	996	23	100
99	0.0270	7.9	0.00099	2.8	1.46718	1.88652	7	0.282153	37	0.281927	-7.8	1.3	2.22	1007	25	99
100	0.0215	2.5	0.00079	0.8	1.46717	1.88644	8	0.282128	39	0.281906	-9.1	1.4	2.27	984	24	103
101	0.0269	6.0	0.00098	2.2	1.46724	1.88637	8	0.282146	38	0.281919	-8.2	1.3	2.24	1004	58	100
107	0.0230	9.8	0.00085	3.5	1.46719	1.88670	16	0.282090	36	0.281943	-7.4	1.3	2.19	999	13	101
108	0.0210	4.8	0.00077	1.7	1.46725	1.88680	8	0.282140	38	0.281914	-8.5	1.3	2.25	998	22	101
109	0.0232	1.9	0.00084	0.6	1.46719	1.88681	17	0.282112	35	0.281964	-6.5	1.3	2.15	1006	15	100
110	0.0188	2.3	0.00068	0.8	1.46720	1.88652	7	0.282171	41	0.281947	-8.2	1.4	2.20	957	26	101
111	0.0270	1.1	0.00097	0.5	1.46718	1.88643	7	0.282127	38	0.281896	-9.0	1.3	2.28	1003	20	101
112	0.0136	3.8	0.00049	1.5	1.46723	1.88654	8	0.282153	37	0.281931	-8.0	1.3	2.22	994	23	101
113	0.0303	5.7	0.00111	2.1	1.46720	1.88670	17	0.282098	34	0.281945	-7.3	1.2	2.19	1000	18	101
114	0.0119	6.1	0.00045	2.2	1.46720	1.88666	19	0.282101	33	0.281960	-6.7	1.2	2.16	1004	23	100
115	0.0245	3.1	0.00088	1.1	1.46718	1.88661	19	0.282102	33	0.281952	-7.1	1.2	2.17	1001	26	101
116	0.0179	2.5	0.00066	0.9	1.46715	1.88681	16	0.282101	33	0.281954	-7.0	1.2	2.17	1001	38	100
117	0.0223	12.1	0.00082	4.3	1.46715	1.88653	7	0.282174	39	0.281945	-6.8	1.4	2.18	1024	33	100
118	0.0182	0.6	0.00065	0.3	1.46721	1.88677	16	0.282072	35	0.281925	-7.9	1.2	2.22	1008	21	100
119	0.0226	1.7	0.00082	0.8	1.46722	1.88643	8	0.282195	41	0.281965	-6.0	1.4	2.14	1029	26	98
120	0.0238	25.4	0.00087	9.3	1.46717	1.88655	17	0.282107	32	0.281955	-6.5	1.1	2.16	1021	27	96
121	0.0307	1.9	0.00111	0.7	1.46720	1.88663	17	0.282104	33	0.281947	-7.2	1.2	2.18	1001	70	100
122	0.0310	3.2	0.00112	1.3	1.46716	1.88646	7	0.282164	39	0.281928	-8.1	1.4	2.22	994	23	101
123	0.0272	4.3	0.00097	1.3	1.46721	1.88673	17	0.282092	34	0.281937	-7.4	1.2	2.20	1009	20	100

124	0.0230	2.2	0.00085	0.8	1.46718	1.88671	17	0.282114	33	0.281961	-6.6	1.2	2.16	1006	25	100
125	0.0271	7.4	0.00097	2.6	1.46720	1.88674	17	0.282093	34	0.281937	-8.3	1.2	2.22	971	32	104
126	0.0174	15.0	0.00064	5.4	1.46721	1.88683	16	0.282081	35	0.281931	-7.8	1.3	2.22	1001	25	101
127	0.0244	1.2	0.00087	0.4	1.46721	1.88675	16	0.282087	34	0.281931	-7.6	1.2	2.21	1010	30	99
128	0.0235	6.0	0.00084	2.1	1.46722	1.88665	16	0.282107	33	0.281952	-7.1	1.2	2.17	999	26	99
129	0.0164	2.5	0.00059	0.9	1.46722	1.88662	16	0.282109	33	0.281958	-6.9	1.2	2.16	997	19	101
130	0.0179	0.2	0.00064	0.1	1.46719	1.88667	17	0.282107	34	0.281954	-7.0	1.2	2.17	999	20	99
131	0.0295	1.1	0.00105	0.7	1.46717	1.88675	16	0.282087	33	0.281926	-7.8	1.2	2.22	1011	27	100
132	0.0273	5.3	0.00097	2.0	1.46722	1.88660	17	0.282098	35	0.281938	-8.2	1.2	2.21	972	22	103
133	0.0242	3.4	0.00090	1.2	1.46721	1.88685	16	0.282099	33	0.281939	-7.1	1.2	2.19	1017	44	100
134	0.0260	6.3	0.00093	2.2	1.46717	1.88640	7	0.282142	38	0.281910	-9.4	1.3	2.27	962	18	104
135	0.0211	9.1	0.00077	3.3	1.46722	1.88667	16	0.282105	34	0.281947	-7.1	1.2	2.18	1007	19	100
136	0.0231	3.4	0.00082	0.7	1.46726	1.88643	7	0.282116	36	0.281953	-7.5	1.3	2.18	978	19	102
137	0.0314	4.4	0.00112	1.7	1.46724	1.88635	7	0.282164	50	0.281926	-7.9	1.8	2.22	1004	19	98
138	0.0213	1.0	0.00074	0.2	1.46718	1.88646	7	0.282116	39	0.281953	-6.7	1.4	2.17	1015	51	99
139	0.0349	8.3	0.00120	3.4	1.46719	1.88647	7	0.282129	36	0.281957	-6.8	1.3	2.16	1004	15	96
140	0.0261	2.1	0.00091	0.1	1.46727	1.88649	8	0.282099	38	0.281933	-8.3	1.3	2.22	976	15	99
141	0.0202	5.6	0.00073	1.8	1.46714	1.88646	7	0.282138	36	0.281974	-6.4	1.3	2.13	994	17	92
142	0.0265	4.8	0.00092	1.3	1.46711	1.88633	8	0.282148	34	0.281915	-8.9	1.2	2.26	980	16	98
143	0.0287	2.1	0.00103	0.6	1.46717	1.88666	7	0.282060	37	0.281889	-9.2	1.3	2.29	1003	19	94
144	0.0318	23.9	0.00113	8.0	1.46713	1.88622	8	0.282087	36	0.281914	-8.2	1.3	2.24	1012	16	100
145	0.0343	7.5	0.00121	3.1	1.46708	1.88646	7	0.282103	38	0.281929	-8.5	1.4	2.23	973	17	96
151	0.0235	1.0	0.00086	0.2	1.46713	1.88649	8	0.282092	36	0.281924	-7.9	1.3	2.23	1006	23	91
152	0.0214	2.6	0.00077	0.7	1.46716	1.88633	8	0.282121	41	0.281954	-7.6	1.5	2.18	975	20	98
153	0.0331	2.0	0.00113	0.8	1.46714	1.88665	8	0.282075	37	0.281900	-9.0	1.3	2.28	999	16	97
154	0.0253	2.6	0.00091	0.9	1.46718	1.88643	7	0.282141	35	0.281970	-6.9	1.3	2.15	980	20	95
156	0.0192	2.8	0.00068	0.8	1.46723	1.88697	16	0.282121	34	0.281953	-7.3	1.2	2.18	989	20	95
157	0.0326	1.6	0.00120	0.6	1.46716	1.88668	16	0.282100	35	0.281923	-9.2	1.3	2.25	953	17	100
158	0.0222	0.4	0.00079	0.1	1.46711	1.88614	7	0.282160	38	0.281928	-8.7	1.3	2.23	967	16	99
159	0.0201	2.4	0.00075	0.8	1.46716	1.88660	16	0.282099	33	0.281929	-7.8	1.2	2.22	1006	24	94
160	0.0206	1.0	0.00075	0.4	1.46717	1.88662	16	0.282112	33	0.281942	-7.8	1.2	2.20	985	18	93
161	0.0355	0.4	0.00125	0.2	1.46715	1.88667	16	0.282125	34	0.281945	-8.0	1.2	2.20	969	17	99
162	0.0229	2.2	0.00081	0.9	1.46716	1.88676	16	0.282123	33	0.281950	-7.9	1.2	2.19	968	22	98
163	0.0166	15.5	0.00060	5.5	1.46716	1.88665	17	0.282098	34	0.281928	-8.0	1.2	2.22	999	19	95
164	0.0193	5.0	0.00070	1.9	1.46717	1.88674	16	0.282113	33	0.281940	-7.3	1.2	2.19	1010	21	93
165	0.0359	2.0	0.00127	0.6	1.46720	1.88661	16	0.282123	33	0.281939	-7.4	1.2	2.20	1006	26	96
166	0.0317	13.1	0.00114	4.8	1.46719	1.88672	16	0.282100	34	0.281918	-8.0	1.2	2.23	1012	26	95
167	0.0241	3.3	0.00088	1.3	1.46719	1.88659	16	0.282091	32	0.281914	-9.1	1.1	2.26	972	15	97
168	0.0295	3.9	0.00104	1.6	1.46715	1.88663	17	0.282087	35	0.281905	-8.7	1.2	2.26	1001	16	93
169	0.0301	5.3	0.00103	1.2	1.46715	1.88649	8	0.282142	36	0.281904	-8.8	1.3	2.27	997	20	100
170	0.0175	2.8	0.00062	0.7	1.46717	1.88662	17	0.282126	34	0.281952	-7.1	1.2	2.17	1000	17	96
Allanite-bearing PGD (13-TC-5072)																
171	0.0194	4.5	0.00069	1.61	1.46721	1.88659	14	0.282076	35	0.281897	-9.0	1.2	2.28	998	28	100
172	0.0246	7.8	0.00083	2.35	1.46709	1.88630	10	0.281993	37	0.281811	-11.8	1.3	2.44	1010	22	100
173	0.0076	5.2	0.00025	1.57	1.46709	1.88619	7	0.282059	40	0.281834	-10.9	1.4	2.40	1016	37	99
174	0.0059	1.0	0.00022	0.41	1.46718	1.88674	16	0.282035	36	0.281865	-10.0	1.3	2.34	1006	29	97
175	0.0233	3.2	0.00083	1.08	1.46714	1.88673	15	0.282050	35	0.281867	-10.0	1.2	2.34	1006	20	101
176	0.0156	7.5	0.00056	2.72	1.46714	1.88659	7	0.282088	35	0.281855	-10.3	1.2	2.36	1008	36	99

177	0.0242	4.9	0.00086	1.67	1.46717	1.88684	14	0.282040	34	0.281857	-10.8	1.2	2.36	985	20	97
178	0.0180	2.1	0.00064	0.85	1.46719	1.88677	15	0.282035	33	0.281855	-10.4	1.2	2.36	1007	28	98
179	0.0152	0.6	0.00053	0.32	1.46722	1.88681	15	0.282045	34	0.281866	-10.4	1.2	2.35	987	20	102
180	0.0187	1.9	0.00064	0.80	1.46709	1.88659	7	0.282085	40	0.281851	-10.7	1.4	2.37	1000	28	100
181	0.0157	4.4	0.00056	1.42	1.46718	1.88672	14	0.282052	33	0.281872	-10.4	1.2	2.34	979	26	102
182	0.0143	0.9	0.00048	0.28	1.46729	1.88650	8	0.282151	42	0.281919	-8.2	1.5	2.24	1003	27	100
183	0.0147	1.4	0.00051	0.68	1.46716	1.88659	7	0.282091	39	0.281858	-10.4	1.4	2.36	1003	3	0
184	0.0210	3.7	0.00074	1.50	1.46723	1.88659	7	0.282098	43	0.281860	-10.2	1.5	2.35	1007	20	99
185	0.0217	3.5	0.00077	1.35	1.46720	1.88665	14	0.282047	34	0.281862	-9.6	1.2	2.34	1030	36	96
186	0.0213	3.2	0.00075	1.11	1.46720	1.88664	14	0.282054	33	0.281869	-9.6	1.2	2.33	1019	13	94
187	0.0116	1.3	0.00042	0.50	1.46715	1.88679	15	0.282064	32	0.281885	-9.0	1.1	2.30	1020	28	92
188	0.0224	5.4	0.00080	1.91	1.46717	1.88676	14	0.282047	37	0.281860	-10.1	1.3	2.35	1010	21	92
189	0.0209	3.0	0.00073	0.91	1.46712	1.88647	7	0.282056	35	0.281817	-11.1	1.3	2.42	1036	25	92
190	0.0059	0.4	0.00022	0.15	1.46714	1.88675	15	0.282026	34	0.281850	-10.7	1.2	2.37	1000	21	98
191	0.0237	8.5	0.00083	2.76	1.46716	1.88663	14	0.282050	32	0.281861	-10.3	1.1	2.35	1003	14	97
192	0.0249	10.7	0.00087	3.57	1.46717	1.88677	14	0.282046	34	0.281856	-10.8	1.2	2.37	986	19	96
193	0.0212	1.5	0.00074	0.39	1.46721	1.88657	7	0.282088	38	0.281849	-11.2	1.3	2.38	982	18	98
199	0.0206	1.5	0.00070	0.23	1.46721	1.88659	7	0.282080	36	0.281841	-11.4	1.3	2.40	984	16	95
200	0.0188	4.7	0.00065	1.76	1.46718	1.88668	16	0.282051	37	0.281865	-10.2	1.3	2.34	998	82	90
201	0.0232	7.6	0.00082	2.57	1.46721	1.88651	7	0.282093	37	0.281851	-10.3	1.3	2.36	1014	35	100
202	0.0212	5.7	0.00076	1.92	1.46715	1.88674	17	0.282049	33	0.281860	-10.4	1.2	2.35	999	20	91
203	0.0221	2.1	0.00079	0.75	1.46719	1.88660	8	0.282074	38	0.281832	-11.1	1.3	2.40	1012	43	98
204	0.0121	0.1	0.00042	0.06	1.46722	1.88680	15	0.282069	35	0.281886	-11.6	1.3	2.34	902	87	105
205	0.0151	1.2	0.00054	0.50	1.46720	1.88645	7	0.282073	38	0.281835	-11.8	1.4	2.41	974	20	99
206	0.0195	1.0	0.00066	0.39	1.46717	1.88674	15	0.282049	32	0.281861	-11.2	1.1	2.37	962	18	99
207	0.0129	0.4	0.00046	0.18	1.46715	1.88662	16	0.282080	33	0.281895	-8.6	1.2	2.27	1024	20	92
208	0.0114	1.9	0.00038	0.45	1.46709	1.88640	8	0.282091	35	0.281855	-10.6	1.3	2.36	996	22	97
209	0.0135	4.9	0.00048	1.54	1.46719	1.88678	17	0.282040	33	0.281853	-10.5	1.2	2.36	1004	54	99
210	0.0115	0.6	0.00041	0.12	1.46718	1.88675	17	0.282044	34	0.281859	-10.9	1.2	2.36	976	21	96
211	0.0067	0.6	0.00025	0.21	1.46717	1.88672	18	0.282054	32	0.281871	-9.9	1.1	2.33	1003	23	93
Results of standard measurements																
Standard zircon GJ1																
GJ1-1	0.0065	0.2	0.00025	0.04	1.46717	1.88651	5	0.282007	42	0.282004	-14.1	1.5	2.25	604	1	100
GJ1-2	0.0065	0.1	0.00025	0.03	1.46721	1.88667	12	0.281994	35	0.281991	-14.6	1.3	2.27	604	1	100
GJ1-3	0.0066	0.1	0.00025	0.03	1.46718	1.88677	12	0.282005	34	0.282003	-14.2	1.2	2.25	604	1	100
GJ1-4	0.0066	0.1	0.00025	0.02	1.46718	1.88660	13	0.281995	35	0.281992	-14.6	1.2	2.27	604	1	100
GJ1-5	0.0066	0.1	0.00025	0.02	1.46716	1.88677	13	0.281994	33	0.281991	-14.6	1.2	2.27	604	1	100
GJ1-6	0.0066	0.1	0.00025	0.02	1.46710	1.88644	12	0.281991	35	0.281989	-14.7	1.2	2.28	604	1	100
GJ1-7	0.0066	0.1	0.00024	0.03	1.46724	1.88665	12	0.282000	35	0.281997	-14.4	1.2	2.26	604	1	100
GJ1-8	0.0069	0.6	0.00024	0.03	1.46723	1.88668	11	0.282004	34	0.282001	-14.3	1.2	2.25	604	1	100
GJ1-9	0.0065	0.2	0.00024	0.03	1.46721	1.88654	11	0.282013	34	0.282010	-13.9	1.2	2.23	604	1	100
GJ1-10	0.0067	0.3	0.00025	0.03	1.46718	1.88670	10	0.281992	34	0.281989	-14.7	1.2	2.28	604	1	100
GJ1-11	0.0065	0.2	0.00024	0.02	1.46719	1.88662	11	0.282027	36	0.282024	-13.4	1.3	2.21	604	1	100
GJ1-12	0.0066	0.1	0.00024	0.03	1.46714	1.88662	11	0.281979	34	0.281976	-15.1	1.2	2.30	604	1	100
GJ1-13	0.0066	0.1	0.00024	0.02	1.46719	1.88658	11	0.282009	34	0.282006	-14.1	1.2	2.24	604	1	100
GJ1-14	0.0065	0.3	0.00024	0.03	1.46716	1.88664	11	0.281988	37	0.281986	-14.8	1.3	2.28	604	1	100
GJ1-15	0.0066	0.2	0.00024	0.04	1.46714	1.88650	11	0.282003	36	0.282001	-14.3	1.3	2.25	604	1	100
GJ1-16	0.0066	0.1	0.00024	0.03	1.46726	1.88658	10	0.282022	37	0.282019	-13.6	1.3	2.22	604	1	100

GJ1t-18	0.0064	0.2	0.00024	0.03	1.46722	1.88659	10	0.281988	38	0.281985	-14.8	1.3	2.28	604	1	100
GJ1t-19	0.0064	0.1	0.00024	0.02	1.46719	1.88665	10	0.282000	34	0.281997	-14.4	1.2	2.26	604	1	100
GJ1t-20	0.0064	0.1	0.00024	0.02	1.46723	1.88654	9	0.282001	37	0.281998	-14.4	1.3	2.26	604	1	100
GJ1t-21	0.0065	0.3	0.00024	0.03	1.46715	1.88664	11	0.281992	35	0.281990	-14.7	1.2	2.27	604	1	100
GJ1t-22	0.0064	0.1	0.00024	0.03	1.46720	1.88669	9	0.282027	38	0.282024	-13.5	1.3	2.21	604	1	100
GJ1t-23	0.0066	0.1	0.00025	0.03	1.46711	1.88652	9	0.282041	36	0.282038	-13.0	1.3	2.18	604	1	100
GJ1t-24	0.0066	0.1	0.00025	0.03	1.46718	1.88660	9	0.282030	35	0.282028	-13.3	1.2	2.20	604	1	100
GJ1t-25	0.0066	0.1	0.00025	0.03	1.46718	1.88664	9	0.282000	37	0.281997	-14.4	1.3	2.26	604	1	100
GJ1t-26	0.0063	0.1	0.00024	0.03	1.46722	1.88667	9	0.282000	38	0.281998	-14.4	1.4	2.26	604	1	100
GJ1t-27	0.0064	0.1	0.00024	0.04	1.46718	1.88668	9	0.281987	38	0.281984	-14.9	1.3	2.28	604	1	100
GJ1t-28	0.0067	0.2	0.00025	0.03	1.46721	1.88678	9	0.281970	33	0.281967	-15.5	1.2	2.32	604	1	100
GJ1t-29	0.0067	0.1	0.00025	0.04	1.46719	1.88662	9	0.281990	35	0.281987	-14.8	1.2	2.28	604	1	100
GJ1t-30	0.0066	0.1	0.00025	0.03	1.46714	1.88673	9	0.281980	35	0.281977	-15.1	1.2	2.30	604	1	100
GJ1t-31	0.0066	0.1	0.00025	0.03	1.46714	1.88644	9	0.282005	35	0.282002	-14.2	1.3	2.25	604	1	100
GJ1t-32	0.0067	0.2	0.00025	0.03	1.46724	1.88668	9	0.281998	35	0.281995	-14.5	1.2	2.26	604	1	100
GJ1t-33	0.0066	0.1	0.00025	0.03	1.46721	1.88669	9	0.281986	35	0.281983	-14.9	1.2	2.29	604	1	100
GJ1t-34	0.0068	0.2	0.00025	0.02	1.46721	1.88676	10	0.282011	36	0.282008	-14.0	1.3	2.24	604	1	100
GJ1t-35	0.0068	0.2	0.00025	0.03	1.46714	1.88665	10	0.281982	35	0.281979	-15.1	1.3	2.30	604	1	100
GJ1t-36	0.0068	0.3	0.00025	0.03	1.46716	1.88669	10	0.281991	34	0.281988	-14.7	1.2	2.28	604	1	100
GJ1t-37	0.0066	0.1	0.00025	0.03	1.46716	1.88659	9	0.281999	38	0.281996	-14.4	1.4	2.26	604	1	100
GJ1t-38	0.0068	0.2	0.00025	0.03	1.46721	1.88663	9	0.281997	34	0.281994	-14.5	1.2	2.26	604	1	100
GJ1t-39	0.0063	0.1	0.00023	0.10	1.46714	1.88652	9	0.282000	35	0.281998	-14.4	1.2	2.26	604	1	100
GJ1t-40	0.0065	0.1	0.00024	0.03	1.46718	1.88652	9	0.281996	37	0.281993	-14.5	1.3	2.27	604	1	100
GJ1t-41	0.0064	0.1	0.00024	0.03	1.46720	1.88673	9	0.282017	37	0.282014	-13.8	1.3	2.23	604	1	100
GJ1t-42	0.0059	0.1	0.00023	0.03	1.46718	1.88642	8	0.282007	40	0.282005	-14.1	1.4	2.25	604	1	100
GJ1t-43	0.0062	0.1	0.00023	0.04	1.46721	1.88681	8	0.281977	35	0.281974	-15.2	1.2	2.30	604	1	100
GJ1t-44	0.0066	0.1	0.00025	0.04	1.46722	1.88666	9	0.282011	34	0.282008	-14.0	1.2	2.24	604	1	100
GJ1t-47	0.0068	0.2	0.00025	0.03	1.46718	1.88655	9	0.281992	34	0.281989	-14.7	1.2	2.28	604	1	100
mean (n=44):	0.0066		0.00024		1.46719	1.88663		0.282000		0.281997	-14.4		2.26			
2σ SD	0.0004		0.00001		0.00007	0.00019		0.000029		0.000029	1.0		0.06			
Standard zircon Plesovice																
Pleso1-1	0.0054	0.4	0.00014	0.10	1.46714	1.88650	8	0.282490	35	0.282489	-3.5	1.2	1.45	337	1	100
Pleso1-3	0.0058	0.3	0.00014	0.07	1.46719	1.88652	9	0.282472	35	0.282471	-4.1	1.2	1.49	337	1	100
Pleso1-4	0.0055	0.3	0.00013	0.09	1.46719	1.88658	14	0.282468	32	0.282468	-4.3	1.1	1.50	337	1	100
Pleso1-5	0.0057	0.4	0.00014	0.10	1.46715	1.88675	13	0.282477	34	0.282476	-4.0	1.2	1.48	337	1	100
Pleso1-6	0.0055	0.3	0.00013	0.09	1.46715	1.88661	14	0.282476	35	0.282475	-4.0	1.3	1.48	337	1	100
Pleso1-7	0.0050	0.4	0.00012	0.11	1.46720	1.88660	11	0.282463	36	0.282463	-4.4	1.3	1.51	337	1	100
Pleso1-8	0.0053	0.1	0.00013	0.02	1.46721	1.88665	12	0.282462	34	0.282461	-4.5	1.2	1.51	337	1	100
Pleso1-9	0.0056	0.1	0.00014	0.03	1.46719	1.88665	11	0.282466	37	0.282465	-4.3	1.3	1.50	337	1	100
Pleso1-10	0.0044	0.2	0.00011	0.05	1.46723	1.88679	12	0.282462	37	0.282462	-4.5	1.3	1.51	337	1	100
Pleso1-11	0.0047	1.0	0.00012	0.26	1.46723	1.88677	12	0.282450	35	0.282449	-4.9	1.2	1.53	337	1	100
Pleso1-12	0.0035	0.2	0.00009	0.04	1.46720	1.88685	13	0.282445	34	0.282445	-5.1	1.2	1.54	337	1	100
mean (n=11):	0.0051		0.00013		1.46719	1.88666		0.282466		0.282466	-4.3		1.50			
2s SD	0.0014		0.00003		0.00006	0.00023		0.000025		0.000025	0.9		0.05			
Standard zircon 91500																
91500-1	0.0088	0.4	0.00032	0.21	1.46718	1.88665	9	0.282300	37	0.282293	6.5	1.3	1.48	1065	1	100
91500-2	0.0086	0.3	0.00032	0.12	1.46717	1.88657	9	0.282269	37	0.282263	5.4	1.3	1.54	1065	1	100
91500-3	0.0084	1.1	0.00031	0.42	1.46720	1.88668	9	0.282290	37	0.282284	6.2	1.3	1.50	1065	1	100
91500-4	0.0080	1.1	0.00029	0.40	1.46716	1.88657	9	0.282296	37	0.282291	6.4	1.3	1.49	1065	1	100

91500-5	0.0078	0.8	0.00028	0.30	1.46721	1.88652	8	0.282301	37	0.282296	6.6	1.3	1.48	1065	1	100
91500-6	0.0078	0.2	0.00028	0.07	1.46718	1.88659	8	0.282309	38	0.282304	6.9	1.4	1.46	1065	1	100
mean (n=6):	0.0082		0.00030		1.46718	1.88660		0.282294		0.282288	6.3		1.49			
2σ SD	0.0008		0.00004		0.00003	0.00012		0.000028		0.000028	1.0		0.06			
Standard zircon Temora																
tem1-1	0.0192	6.4	0.00076	2.7	1.46713	1.88645	8	0.282654	36	0.282648	4.5	1.3	1.08	419	1	100
tem1-2	0.0270	1.8	0.00098	0.4	1.46723	1.88663	10	0.282669	39	0.282661	5.0	1.4	1.06	419	1	100
tem1-3	0.0304	3.5	0.00106	1.3	1.46728	1.88682	11	0.282653	33	0.282645	4.4	1.2	1.09	419	1	100
tem1-4	0.0228	6.0	0.00083	1.9	1.46720	1.88672	11	0.282636	32	0.282629	3.8	1.1	1.12	419	1	100
tem1-6	0.0320	1.5	0.00111	0.5	1.46724	1.88662	9	0.282655	34	0.282646	4.4	1.2	1.09	419	1	100
tem1-7	0.0273	1.0	0.00092	0.9	1.46724	1.88618	6	0.282676	42	0.282669	5.2	1.5	1.04	419	1	100
mean (n=6):	0.0265		0.00094		1.46722	1.88657		0.282657		0.282650	4.6		1.08			
2σ SD	0.0095		0.00027		0.00010	0.00045		0.000028		0.000028	1.0		0.05			

[a] $^{176}Yb/^{177}Hf = (^{176}Yb/^{173}Yb)_{true} \times (^{173}Yb/^{177}Hf)_{meas} \times (M_{173(Yb)}/M_{177(Hf)})^{\beta(Hf)}$, $\beta(Hf) = \ln(^{179}Hf/^{177}Hf_{true}/^{179}Hf/^{177}Hf_{measured})/\ln(M_{179(Hf)}/M_{177(Hf)})$, M=mass of respective isotope. The $^{176}Lu/^{177}Hf$ were calculated in a similar way by using the $^{175}Lu/^{177}Hf$ and β(Yb).
Quoted uncertainties (absolute) relate to the last quoted figure. The effect of the inter-element fractionation on the Lu/Hf was estimated to be about 6 % or less based on analyses of the GJ-1 and Plesoviče zircons.
[b] Mean Hf signal in volt.
[c] Uncertainties are quadratic additions of the within-run precision and the daily reproducibility of the zircon GJ-1. Uncertainties for GJ-1 is 2SD (2 standard deviation).
[d] Initial $^{176}Hf/^{177}Hf$ and εHf calculated using the apparent Pb-Pb age determined by LA-ICP-MS dating (see column f), and the CHUR parameters: $^{176}Lu/^{177}Hf = 0.0336$, and $^{176}Hf/^{177}Hf = 0.282785$ (Bouvier et al., 2008).
[e] Two stage model age in billion years using the measured $^{176}Lu/^{177}Lu$ and Pb-Pb age of each spot (first stage = age of zircon), a value of 0.02 for mafic crust (second stage), and a depleted mantle $^{176}Lu/^{177}Hf$ and $^{176}Hf/^{177}Hf$ of 0.03933 and 0.283294, see Blichert-Toft and Puchtel (2010).
[f] Apparent Pb-Pb age determined by LA-SF-ICP-MS

Table S3-3: Results of trace elements LA-ICP-MS measurements of zircon grains from the monazite-bearing (13-AM-13) and two allanite-bearing (13-FS-1202 and 13-TC-5072) pegmatitic granite dykes from the central Grenville Province. Abbreviation: PGD = pegmatitic granite dyke.

Analysis no.	Ca (ppm)	Fe (ppm)	Ti (ppm)	Y (ppm)	La (ppm)	Ce (ppm)	Pr (ppm)	Nd (ppm)	Sm (ppm)	Eu (ppm)	Gd (ppm)	Tb (ppm)	Dy (ppm)	Ho (ppm)	Er (ppm)	Tm (ppm)	Yb (ppm)	Lu (ppm)	Hf (ppm)	Th (ppm)	U (ppm)
Monazite-bearing PGD (sample 13-AM-13)																					
9	83	b.d.	4.73	1324	0.01	13	0.13	2.47	7.53	0.42	40	13	142	48	189	36	302	56	11634	311	518
10	80	1.71	4.19	777	0.00	6.69	0.08	1.31	3.41	0.20	18	6.35	74	27	113	24	208	40	11445	136	378
11	105	96	6.50	514	0.39	7.50	1.09	7.68	7.74	0.34	19	5.32	56	19	74	16	140	28	12964	207	497
12	91	3.03	4.44	285	0.00	4.16	0.03	0.60	1.60	0.09	7.68	2.53	28	9.86	41	8.87	81	16	12730	126	370
13	91	2.71	5.02	848	0.00	6.92	0.08	1.30	4.12	0.23	22	7.64	88	31	125	25	213	40	12080	166	442
14	84	2.71	4.70	1003	0.01	7.74	0.10	1.74	4.85	0.29	25	8.52	98	35	146	30	260	50	11437	179	464
15	135	37	7.78	1018	2.51	33	7.40	44	28	0.90	46	11	112	36	135	26	212	39	12543	400	903
16	131	13	7.95	900	1.77	22	4.75	29	19	0.71	38	10	105	34	130	25	207	39	13692	373	821
17	102	4.27	7.25	720	0.01	3.03	0.06	1.08	3.68	0.15	22	7.75	86	28	107	21	169	32	14364	172	609
18	77	2.42	3.81	458	0.01	4.54	0.04	0.67	1.76	0.10	10	3.59	42	15	64	13	117	23	12314	76	271
19	81	b.d.	5.1	1210	0.01	13	0.10	1.9	6.3	0.36	34	11	129	45	26	35	297	56	12007	278	530
20	83	1.90	4.75	723	0.00	3.73	0.06	1.01	3.02	0.16	17	6.12	72	26	108	22	196	38	12684	91	409
21	91	b.d.	5.48	785	0.00	2.79	0.04	0.91	3.09	0.16	18	7.12	85	30	123	25	217	42	13442	87	445
22	81	78	5.15	1608	0.18	15	0.49	6.25	14	0.86	59	17	180	58	227	44	361	68	11075	417	675
23	83	5.81	4.50	304	0.00	3.13	0.02	0.52	1.43	0.08	7.56	2.70	31	11	45	9.31	85	17	13015	84	302
24	99	4.11	7.53	774	0.01	6.83	0.09	1.53	4.50	0.23	24	7.95	87	30	120	25	219	44	15110	233	696
25	99	1.87	8.07	1636	0.02	20	0.28	5.02	15	0.84	72	21	214	66	245	46	369	68	15837	820	1374
26	74	3.75	4.64	515	0.00	5.39	0.05	0.96	2.70	0.16	14	4.55	51	18	72	15	138	27	12323	190	507
27	94	3.10	6.36	553	0.01	6.50	0.06	1.14	3.41	0.19	18	5.79	63	21	83	17	145	28	13038	255	707
28	90	b.d.	6.52	1009	0.16	5.67	0.45	3.57	5.83	0.41	28	9.85	110	37	141	27	217	39	12976	172	628
29	7816	21	5.91	1040	3.76	19	2.49	14	11	0.90	34	10	112	37	148	29	244	46	12246	225	524
30	98	2.20	4.68	325	0.01	4.09	0.04	0.66	1.69	0.09	8	2.86	33	12	50	11	100	20	13305	131	384
31	76	b.d.	4.40	757	0.00	5.51	0.05	1.01	3.28	0.16	18	6.67	76	26	108	22	188	36	11747	134	417
32	79	2.47	4.62	1200	0.06	13	0.18	2.23	6.32	0.41	33	11	124	43	170	33	277	52	11399	290	496
33	71	2.89	4.65	766	0.00	2.46	0.04	0.79	2.68	0.13	16	6.31	75	26	105	21	181	34	11906	80	440
34	86	2.23	5.30	805	0.03	7.44	0.11	1.51	4.02	0.23	21	7.55	88	31	129	26	226	43	13124	163	447
35	102	11	6.64	334	1.55	15	4.10	26	19	1.12	24	4.71	40	12	50	10	94	19	13571	500	349
36	77	2.58	3.88	332	0.01	1.76	0.04	0.44	1.26	0.07	7.00	2.68	32	12	48	9.93	86	17	12205	40	246
37	83	2.18	5.19	1487	0.34	16	1.06	9.21	15	0.87	56	16	167	53	206	39	325	60	11254	400	602
38	74	b.d.	4.57	788	0.00	7.74	0.08	1.39	4.05	0.25	20	6.78	77	27	112	23	198	38	11130	165	349
39	90	6.29	6.16	566	0.03	7.31	0.14	1.71	4.02	0.23	19	6.02	66	22	91	19	169	34	13248	222	564
40	99	14	6.74	469	0.59	6.96	1.44	8.89	5.93	0.56	16	5.02	54	17	65	13	105	19	13522	128	428
41	74	7.20	4.56	402	0.00	5.81	0.05	0.79	2.25	0.14	11	3.69	41	14	58	12	109	22	12159	194	504
42	89	9.14	7.58	618	0.01	6.89	0.08	1.11	3.96	0.19	20	6.52	70	23	93	19	164	32	14767	267	756
43	76	11	5.64	581	0.00	2.11	0.04	0.79	2.52	0.10	15	5.33	60	20	81	16	143	28	12178	114	466
44	92	4.54	6.95	706	0.04	4.13	0.17	1.54	3.96	0.18	20	7.16	79	27	106	21	181	34	15888	181	604
45	92	2.90	6.23	766	0.01	7.47	0.08	1.45	4.75	0.21	25	8.30	90	30	118	23	197	37	13658	238	729
46	89	1.96	6.10	872	0.00	5.20	0.07	1.17	3.73	0.19	23	8.27	98	35	144	29	253	48	14204	136	493
47	84	b.d.	6.65	1767	0.01	14	0.27	4.68	15	0.69	68	21	222	71	270	51	414	77	13770	402	819
Allanite-bearing PGD (sample 13-FS-1202)																					
48	79	12	2.61	1325	0.58	10	0.45	2.49	3.71	0.24	22	8.54	117	48	224	50	463	92	11971	122	562

49	75	93	2.42	1235	1.29	10	0.59	2.63	3.04	0.24	18	7.33	100	41	192	43	402	80	10930	105	506
50	186	3897	4.53	1119	39	136	14	41	9.26	0.49	23	7.94	103	41	187	41	374	74	11748	155	556
51	92	777	2.87	1066	7.47	30	2.55	8.12	3.78	0.28	18	7.05	93	38	175	39	360	72	11698	100	385
52	72	17	2.29	1249	0.00	7.68	0.03	0.68	2.62	0.22	19	7.84	107	44	205	46	422	85	11635	122	547
53	71	6.88	2.21	909	0.04	7.97	0.04	0.70	2.45	0.19	15	5.97	79	32	144	32	292	58	11577	115	479
54	87	b.d.	3.04	1774	0.01	9.15	0.05	0.95	4.02	0.36	31	13	174	71	330	74	672	128	15291	170	668
55	74	22	2.59	1212	0.31	7.97	0.29	1.81	3.47	0.25	21	8.20	108	43	195	43	390	78	11334	112	489
56	73	8.87	1.66	386	0.02	3.66	0.02	0.25	0.65	0.06	4.82	2.11	31	13	64	15	141	29	12149	31	176
57	84	60	2.73	1044	0.91	12	0.74	3.60	3.73	0.27	18	7.03	94	38	178	39	366	73	12086	98	445
66	73	11	2.94	1593	0.01	15	0.07	1.37	4.54	0.35	29	11	145	58	265	58	538	105	12223	244	897
67	72	6.29	2.18	1304	0.00	6.26	0.03	0.68	2.58	0.22	19	8.00	110	46	214	48	444	89	11278	117	540
68	74	b.d.	2.31	1316	0.00	6.46	0.03	0.69	2.65	0.22	20	8.22	112	46	220	49	455	91	11612	118	537
69	93	10	2.16	487	0.01	5.10	0.01	0.31	0.74	0.05	6.46	3.00	44	19	94	22	207	43	17295	54	301
70	88	308	3.27	1248	6.96	32	3.01	12	7.95	0.57	29	9.63	118	45	198	42	375	74	11583	141	462
71	81	8.16	3.00	1314	0.02	13	0.08	1.37	4.49	0.32	27	9.77	125	49	220	47	423	83	11992	214	777
72	82	18.12	2.72	1004	0.30	12	0.26	1.61	3.33	0.27	19	7.38	96	38	174	38	349	68	11939	147	547
73	85	437	2.99	1154	4.54	23	1.85	6.76	4.61	0.32	21	7.92	104	42	194	43	398	79	11983	112	483
74	66	20	2.41	1233	0.32	7.90	0.27	1.67	2.91	0.23	19	7.56	105	43	205	46	431	87	12244	107	514
75	72	16	2.37	1158	0.22	7.25	0.19	1.32	2.52	0.20	18	7.17	100	41	194	43	409	83	12149	100	486
76	73	14	2.36	1584	0.02	9.10	0.06	1.23	4.69	0.37	30	12	148	58	258	55	500	96	11834	155	568
77	68	9.83	2.25	1195	0.00	6.06	0.03	0.63	2.43	0.19	17	7.21	99	41	191	43	398	80	11262	98	484
78	71	8.10	2.37	986	0.19	8.05	0.15	1.19	2.63	0.21	17	6.69	88	35	160	35	323	63	11533	104	382
79	71	37	3.32	1039	0.94	13	0.52	2.57	3.55	0.26	19	7.34	95	37	168	37	335	65	11800	150	561
80	64	15	2.48	1193	0.26	13	0.23	1.54	3.62	0.29	22	8.28	105	42	188	41	369	73	11045	162	577
81	69	9.93	2.26	1008	0.01	6.37	0.03	0.59	2.13	0.19	16	6.47	88	36	166	37	342	68	11640	89	345
82	64	11	2.27	1010	0.00	5.39	0.02	0.47	1.99	0.16	14	5.82	83	35	164	38	356	71	11433	76	414
83	73	6.66	2.23	1759	0.00	11	0.06	1.19	5.20	0.42	36	14	171	64	278	58	504	96	11885	189	550
84	75	16	2.04	1138	0.01	7.76	0.03	0.66	2.48	0.20	18	7.43	101	41	195	43	403	81	12192	115	464
85	77	13	2.49	1161	0.00	7.07	0.03	0.67	2.47	0.22	18	7.54	105	44	206	47	436	88	12663	106	498
86	89	4.69	2.81	1091	0.05	7.69	0.06	0.76	2.39	0.20	18	7.43	105	44	209	47	447	91	14203	104	476
87	67	5.57	2.07	1173	0.00	6.24	0.03	0.55	2.34	0.19	17	7.02	97	40	188	42	393	78	11370	96	489
88	60	12	2.17	1267	0.01	6.72	0.03	0.62	2.42	0.22	19	7.80	107	44	205	46	426	85	11455	111	545
89	75	12	2.30	838	1.98	11	0.73	2.67	2.48	0.18	14	5.66	76	31	141	31	287	57	12360	96	378
90	65	37	2.52	932	1.07	12	0.63	2.61	2.69	0.28	15	5.95	81	32	146	33	299	60	11105	82	311
91	75	51	3.04	1324	0.79	12	0.57	2.86	3.63	0.49	21	8.68	119	48	225	50	471	94	12860	114	528
92	71	8.70	2.36	2037	0.01	12	0.09	1.97	7.78	0.58	46	17	204	77	330	68	604	117	11653	235	705
93	80	8.83	2.20	624	0.00	5.30	0.01	0.40	1.25	0.11	9.58	4.16	58	25	117	27	257	52	14176	60	280
94	72	4.12	1.94	659	0.00	5.05	0.01	0.39	1.38	0.11	9.95	4.13	57	23	111	25	232	47	12155	58	255
95	72	282	2.33	1287	4.19	19	1.62	5.89	4.29	0.27	22	8.36	111	44	199	44	403	79	10383	123	491
96	73	109	2.81	2020	1.77	19	1.13	5.84	8.84	0.61	46	16	200	75	322	67	585	113	11557	230	676
97	69	9.56	2.51	1250	0.01	11	0.06	0.97	3.28	0.26	21	8.25	107	43	196	42	387	75	11506	159	565
98	66	10.43	2.49	1498	0.01	7.83	0.04	0.87	3.10	0.26	23	9.51	129	53	247	55	503	101	12209	138	611
Allanite-bearing PGD (sample 13-TC-5072)																					
100	62	2.79	2.73	375	0.00	3.33	0.03	0.52	1.47	0.08	7.76	2.75	34	13	55	12	107	21	11170	38	164
101	68	8.74	3.88	898	0.00	6.07	0.08	1.47	4.04	0.22	21	7.20	85	31	133	28	244	48	11257	90	332
102	69	5.95	1.13	165	0.00	2.40	0.00	0.18	0.32	0.04	2.31	0.96	14	5.80	29	6.98	71	16	11702	15	206
103	68	5.00	3.65	1057	0.01	6.32	0.11	1.80	4.83	0.25	24	8.42	98	36	155	32	281	55	10745	105	392
104	80	251	4.99	1375	4.63	18	2.51	13	12	0.75	40	12	135	48	199	40	349	67	10485	236	741

104	80	251	4.99	1375	4.63	18	2.51	13	12	0.75	40	12	135	48	199	40	349	67	10485	236	741
105	72	24	4.02	1134	4.19	10	1.87	8.60	7.76	0.46	29	9.45	110	40	167	34	299	58	10943	124	409
106	74	27	3.67	1081	0.84	8.53	0.56	4.30	7.72	0.42	33	10	112	39	155	31	264	50	11382	119	371
107	69	4.95	3.47	774	0.00	5.05	0.07	1.06	3.10	0.18	17	6.01	73	27	117	24	220	43	11422	70	305
108	474	119	4.06	1385	349	644	77	179	24	0.82	45	13	140	49	196	39	331	63	10634	167	469
109	72	4.33	3.73	857	1.49	7.60	0.46	2.26	3.66	0.20	20	6.88	83	31	132	28	246	48	11952	79	331
110	63	8.60	3.37	762	0.18	5.16	0.10	1.38	3.02	0.20	17	5.97	72	27	114	24	215	42	11443	68	291
111	181	770	6.08	1363	12	51	11	51	35	1.51	59	15	144	48	191	38	332	63	10429	145	467
112	73	436	3.46	697	1.59	6.85	0.65	3.26	3.80	0.21	16	5.58	67	25	106	22	198	39	11644	65	267
113	67	7.58	3.77	1078	0.43	6.83	0.23	2.32	5.22	0.26	26	8.66	103	38	157	33	282	55	12349	106	398
114	98	255	4.01	1217	3.70	15	2.28	10	8.69	0.67	33	10	118	42	175	35	308	59	10315	138	434
115	83	8.36	2.45	217	0.01	2.73	0.01	0.31	0.59	0.06	3.95	1.51	20	8.13	37	8.18	79	16	12946	23	148
116	65	5.67	3.87	1149	0.01	6.77	0.11	1.78	5.09	0.30	27	9.14	109	40	169	35	309	60	11317	119	432
117	78	18	3.92	1096	1.19	11	1.34	8.42	8.89	0.67	30	9.31	106	38	159	33	287	55	10970	115	396
126	74	311	3.63	867	3.09	9.62	0.99	4.33	4.57	0.30	20	6.86	82	30	127	26	235	46	11407	80	332
127	75	1215	4.20	893	1.78	8.04	0.60	2.89	4.01	0.32	20	7.00	83	31	131	27	241	46	11203	84	344
128	62	11	3.16	604	0.02	6.00	0.09	1.42	3.06	0.17	15	4.93	58	21	88	18	160	32	10833	87	334
129	83	62	3.91	1066	9.27	14	1.89	7.81	6.49	0.53	27	8.74	102	38	159	33	289	56	11279	108	398
130	70	11	4.32	1347	0.70	8.69	0.42	3.64	7.40	0.41	35	11	133	48	202	42	363	71	11158	152	502
131	64	4.42	3.19	690	0.00	5.56	0.05	0.87	2.82	0.16	16	5.53	66	24	100	20	180	35	11213	73	235
132	87	416	3.40	859	0.81	7.07	0.47	3.11	4.57	0.28	20	6.87	81	30	127	26	232	45	11253	79	322
133	62	5.73	3.40	1305	0.01	9.04	0.18	3.15	9.31	0.47	43	13	141	47	183	35	292	54	11209	162	400
134	63	6.93	2.96	689	0.02	5.44	0.07	1.10	2.84	0.16	15	5.23	64	24	102	21	192	38	11604	88	315
135	63	4.20	3.35	679	0.00	5.87	0.05	0.97	2.85	0.17	16	5.60	66	24	102	21	181	35	11503	72	241
136	64	4.72	3.48	727	0.00	6.29	0.06	1.15	3.27	0.18	17	5.81	70	26	108	22	194	37	11844	76	248
137	70	6.17	3.72	624	0.00	4.73	0.05	0.94	2.57	0.16	14	5.00	61	23	99	21	189	37	12285	57	247
138	97	803	2.65	252	b.d.	15	2.44	7.65	2.54	0.22	6.19	2.00	24	8.89	39	8.72	80	16	11237	26	104

NIST612

	Ca	Fe	Ti	Y	La	Ce	Pr	Nd	Sm	Eu	Gd	Tb	Dy	Ho	Er	Tm	Yb	Lu	Hf	Th	U
mean (n=16)	85265	56	48	38	36	38	37	35	37	34	37	36	36	38	37	38	40	38	35	37	37
1 SD	359	1.32	0.23	0.31	0.25	0.27	0.29	0.37	0.34	0.30	0.36	0.34	0.36	0.39	0.41	0.27	0.33	0.27	0.28	0.29	0.31
1 SD %	0.4	2.3	0.5	0.8	0.7	0.7	0.8	1.1	0.9	0.9	1.0	0.9	1.0	1.0	1.1	0.7	0.8	0.7	0.8	0.8	0.8

Zircon standard GJ1

	Ca	Fe	Ti	Y	La	Ce	Pr	Nd	Sm	Eu	Gd	Tb	Dy	Ho	Er	Tm	Yb	Lu	Hf	Th	U
mean (n=6)	79		3.6	246	0.00	15.4	0.03	0.61	1.42	0.95	6.6	1.87	20	6.9	30	6.5	62	13	6,980	8.0	321
1 SD	3.5		0.06	3.0	0.00	0.11	0.00	0.03	0.02	0.01	0.1	0.03	0.2	0.1	0.4	0.1	1	0.2	87	0.1	3
1 SD %	4.5		1.4	1.2	14	0.80	6.3	4.2	1.7	0.86	1.7	1.7	0.89	1.7	1.3	1.1	1.6	1.3	1.3	1.6	0.76

Zircon standard 91500

	Ca	Fe	Ti	Y	La	Ce	Pr	Nd	Sm	Eu	Gd	Tb	Dy	Ho	Er	Tm	Yb	Lu	Hf	Th	U
mean (n=6)	79		5.1	139	0.00	2.90	0.02	0.33	0.50	0.24	2.3	0.84	11	4.8	25	6.3	65	13	5,556	30	76
1 SD	7		0.07	5	0.00	0.07	0.00	0.01	0.03	0.02	0.11	0.03	0.4	0.2	1	0.3	3	0.6	73	1	3
1 SD %	9.4		1.2	3.6	12	2.5	9.0	4.0	5.9	8.0	4.7	3.7	3.8	3.6	3.9	4.4	4.1	4.2	1.4	5.3	4.3

Table S3-4: Results of SIMS O isotope analyses of zircon grains from the monazite-bearing (13-AM-13) and two allanite-bearing (13-FS-1202 and 13-TC-5072) pegmatitic granite dykes from the central Grenville Province. Abbreviation: PGD = pegmatitic granite dyke.

Analysis no.	$\delta^{18}O$ (‰ V-SMOW)	±2σ
Monazite-bearing PGD (13-AM-13)		
1	7.03	0.16
2	7.58	0.14
3	6.64	0.11
4	8.24	0.12
5	6.60	0.11
6	6.53	0.11
7	7.65	0.11
8	6.29	0.14
9	8.43	0.16
10	7.59	0.15
17	3.77	0.15
18	5.33	0.17
19	6.74	0.15
20	3.95	0.16
21	2.83	0.19
22	6.47	0.12
23	6.75	0.16
24	6.69	0.11
25	8.44	0.14
26	6.60	0.15
27	7.42	0.12
28	7.07	0.13
29	6.92	0.14
30	6.01	0.13
31	7.29	0.16
32	7.72	0.13
33	7.04	0.10
34	6.73	0.12
35	6.39	0.14
36	6.80	0.15
37	6.96	0.15
38	6.37	0.14
39	6.62	0.12
40	7.59	0.11
41	9.37	0.17
42	8.29	0.13
43	7.91	0.15
44	8.09	0.11
45	7.62	0.15
46	8.78	0.11
47	6.71	0.14
48	6.50	0.09
49	6.33	0.13
50	5.91	0.11
51	7.27	0.15
52	6.95	0.12
53	8.18	0.12
54	8.06	0.14
55	6.92	0.15
56	6.81	0.11
57	8.61	0.10
58	7.00	0.12
59	6.74	0.12
60	6.73	0.10
61	8.73	0.14
62	7.03	0.14
63	4.94	0.17
64	0.69	0.28
65	8.38	0.14
66	8.61	0.13
67	8.55	0.15
68	8.58	0.14
69	8.54	0.16
70	9.11	0.17
71	8.80	0.14
72	8.35	0.10
73	8.96	0.14
74	9.46	0.14

75	9.20	0.15
76	9.48	0.13
77	7.33	0.13
78	7.49	0.16
79	7.20	0.13
80	7.26	0.18
81	7.42	0.13
82	6.28	0.14
83	8.31	0.13
84	9.17	0.15
85	7.77	0.15
86	8.58	0.15
87	9.20	0.17
88	8.35	0.14
89	7.86	0.14
91	6.71	0.14
92	6.91	0.12
93	6.61	0.14
94	9.31	0.13
95	9.30	0.15
96	9.52	0.14
97	9.43	0.14
98	8.73	0.14
Allanite-bearing PGD (13-FS-1202)		
99	8.17	0.14
100	9.05	0.11
101	8.40	0.11
102	8.96	0.08
103	9.23	0.09
104	8.21	0.15
105	9.32	0.15
106	9.27	0.11
107	9.62	0.10
108	9.19	0.14
109	9.46	0.11
110	3.27	0.18
111	2.23	0.20
112	6.99	0.18
113	8.15	0.18
114	2.37	0.23
115	2.15	0.19
116	1.20	0.22
118	7.70	0.15
119	8.32	0.13
121	9.52	0.15
122	10.26	0.12
123	10.17	0.08
124	8.59	0.17
125	6.31	0.11
126	6.38	0.15
127	2.40	0.18
128	4.63	0.13
129	5.08	0.10
130	6.05	0.14
131	6.62	0.11
132	6.04	0.16
133	6.59	0.14
134	6.30	0.15
135	7.30	0.11
136	6.96	0.15
137	5.87	0.11
138	6.69	0.10
139	6.88	0.13
140	6.62	0.11
141	6.78	0.13
142	6.53	0.13
143	7.03	0.11
144	6.12	0.14
145	5.95	0.17
146	3.53	0.15
147	3.42	0.14
148	3.50	0.14
149	5.06	0.13
152	2.29	0.18
153	-0.92	0.21
154	0.69	0.19

155	-1.63	0.20
156	0.41	0.18
157	9.20	0.24
158	-1.65	0.21
159	-1.49	0.15
160	0.58	0.19
161	-0.57	0.16
162	-0.27	0.16
163	1.02	0.14
164	-0.88	0.19
165	4.53	0.13
166	6.12	0.14
167	4.09	0.10
168	6.21	0.11
169	6.65	0.13
170	4.90	0.13
171	6.57	0.11
172	7.24	0.13
173	3.63	0.16
174	3.89	0.13
Allanite-bearing PGD (13-TC-5072)		
175	6.83	0.13
176	5.31	0.16
177	7.69	0.15
178	6.42	0.14
179	6.48	0.15
180	7.80	0.13
181	6.83	0.11
182	7.07	0.12
183	7.20	0.14
184	15.04	0.15
185	12.57	0.14
186	13.06	0.16
187	7.11	0.16
188	7.07	0.11
189	6.20	0.11
190	6.88	0.13
191	6.76	0.11
192	5.92	0.17
193	6.33	0.13
194	6.88	0.11
195	7.40	0.13
196	6.97	0.19
197	7.25	0.15
198	6.10	0.14
199	7.06	0.14
200	7.25	0.13
201	6.37	0.19
202	6.12	0.14
203	6.70	0.14
204	7.22	0.12
205	5.04	0.15
206	7.26	0.12
207	6.49	0.14
208	6.75	0.16
209	6.36	0.13
210	6.85	0.16
211	6.70	0.14
212	6.18	0.13
214	7.16	0.13
215	6.15	0.14
216	7.47	0.11
217	6.53	0.15
218	7.02	0.17
219	7.01	0.13
220	7.24	0.11
221	6.53	0.13
222	6.41	0.14
223	6.59	0.10
224	6.66	0.15
225	6.85	0.14
226	6.45	0.11

Results of standard measurements		
Standard zircon 91500		
91500-1	6.51	0.11
91500-2	6.57	0.12
91500-3	6.79	0.10
91500-4	6.65	0.10
91500-5	6.53	0.10
91500-6	6.80	0.10
91500-7	6.70	0.13
91500-8	6.71	0.11
91500-9	6.39	0.12
91500-10	6.90	0.12
91500-11	6.53	0.13
91500-12	7.00	0.12
91500-13	6.47	0.11
91500-14	7.06	0.13
91500-15	6.59	0.11
91500-16	7.09	0.12
91500-17	7.04	0.10
91500-18	6.70	0.13
91500-19	6.29	0.11
91500-20	6.69	0.15
91500-21	6.68	0.14
91500-22	6.63	0.12
91500-23	6.84	0.12
91500-24	6.24	0.11
91500-25	6.34	0.14
91500-26	6.53	0.15
91500-27	6.83	0.14
91500-28	6.63	0.11
91500-29	6.31	0.15
91500-30	6.69	0.15
91500-31	6.26	0.11
91500-32	6.51	0.12
91500-33	6.07	0.12
91500-34	6.49	0.13
91500-35	6.32	0.11
91500-36	6.07	0.15
91500-37	6.13	0.09
91500-38	6.39	0.13
91500-39	6.27	0.11
91500-40	6.60	0.13
91500-41	6.06	0.14
91500-42	6.36	0.12
91500-43	6.29	0.12
91500-44	6.72	0.15
91500-45	6.03	0.12
91500-47	5.92	0.13
91500-48	6.69	0.15
91500-49	6.35	0.18
91500-50	6.56	0.14
91500-51	6.22	0.16
91500-52	7.04	0.13
91500-53	7.08	0.10
91500-54	7.38	0.10
91500-55	7.12	0.14
91500-56	7.02	0.11
91500-57	6.71	0.11
91500-58	6.71	0.12
91500-59	6.92	0.09
91500-60	6.34	0.14
91500-61	6.39	0.11
91500-62	6.75	0.15
91500-63	6.52	0.15
91500-65	6.52	0.11
91500-66	6.52	0.12
91500-67	6.45	0.11
91500-68	6.29	0.12
91500-69	6.94	0.10
91500-70	6.60	0.08
91500-71	6.73	0.10
91500-72	6.33	0.10
91500-73	6.75	0.15
91500-74	6.66	0.11
91500-75	6.55	0.13
91500-76	6.88	0.11

91500-77	6.79	0.13
91500-78	6.52	0.14
91500-79	6.31	0.14
91500-80	6.47	0.11
91500-81	6.64	0.11
91500-83	6.84	0.11
91500-84	6.86	0.10
91500-85	6.75	0.09
91500-86	6.82	0.11
91500-87	6.56	0.11
mean (n=83)	6.60	
2σ SD	0.02	

References

Augland, L.E., Moukhsil, A., Solgadi, F., Indares, A., McFarlane, C., 2015. Pinwarian to Grenvillian magmatic evolution in the central Grenville Province: new constraints from ID-TIMS U-Pb ages and coupled Lu-Hf S-MC-ICP-MS data. Canadian Journal of Earth Sciences 52, 701–721. doi:10.1139/cjes-2014-0232

Ayres, L.D., Černý, P., 1982. Metallogeny of granitoid rocks in the Canadian Shield. Can. Mineral. 20, 439–536.

Barbarin, B., 1999. A review of the relationships between granitoid types, their origins and their geodynamic environments. Lithos 46, 605–626. doi:10.1016/S0024-4937(98)00085-1

Bea, F., 1996. Residence of REE, Y, Th and U in Granites and Crustal Protoliths; Implications for the Chemistry of Crustal Melts. J. Petrology 37, 521–552. doi:10.1093/petrology/37.3.521

Belousova, E.A., Kostitsyn, Y.A., Griffin, W.L., Begg, G.C., O'Reilly, S.Y., Pearson, N.J., 2010. The growth of the continental crust: Constraints from zircon Hf-isotope data. Lithos 119, 457–466. doi:10.1016/j.lithos.2010.07.024

Blichert-Toft, J., Puchtel, I.S., 2010. Depleted mantle sources through time: Evidence from Lu–Hf and Sm–Nd isotope systematics of Archean komatiites. Earth and Planetary Science Letters 297, 598–606. doi:10.1016/j.epsl.2010.07.012

Bouvier, A., Vervoort, J.D., Patchett, P.J., 2008. The Lu–Hf and Sm–Nd isotopic composition of CHUR: Constraints from unequilibrated chondrites and implications for the bulk composition of terrestrial planets. Earth and Planetary Science Letters 273, 48–57. doi:10.1016/j.epsl.2008.06.010

Busch, J.P., van der Pluijm, B.A., Hall, C.M., Essene, E.J., 1996. Listric normal faulting during postorogenic extension revealed by 40Ar/39Ar thermochronology near the Robertson Lake shear zone, Grenville orogen, Canada. Tectonics 15, 387–402. doi:10.1029/95TC03501

Carr, S.D., Easton, R.M., Jamieson, R.A., Culshaw, N.G., 2000. Geologic transect across the Grenville orogen of Ontario and New York. Can. J. Earth Sci. 37, 193–216. doi:10.1139/e99-074

Cawood, P.A., Hawkesworth, C.J., Dhuime, B., 2013. The continental record and the generation of continental crust. GSA Bulletin 125, 14–32. doi:10.1130/B30722.1

Černý, P., Ercit, T.S., 2005. The classification of granitic pegmatites revisited. Can. Mineral. 43, Part 6, 2005–2026.

Černý, P., London, D., Novák, M., 2012. Granitic Pegmatites as Reflections of Their Sources. Elements 8, 289–294. doi:10.2113/gselements.8.4.289

Chappell, B.W., White, A.J.R., 2001. Two contrasting granite types: 25 years later. Australian Journal of Earth Sciences 48.

Corfu, F., Hanchar, J.M., Hoskin, P.W.O., Kinny, P., 2003. Atlas of Zircon Textures. Reviews in Mineralogy and Geochemistry 53, 469–500. doi:10.2113/0530469

Corrigan, D., van Breemen, O., 1997. U – Pb age constraints for the lithotectonic evolution of the Grenville Province along the Mauricie transect, Quebec. Can. J. Earth Sci. 34, 299–316. doi:10.1139/e17-027

Crowley, J.L., Brown, R.L., Gervais, F., Gibson, H.D., 2008. Assessing Inheritance of Zircon and Monazite in Granitic Rocks from the Monashee Complex, Canadian Cordillera. J. Petrology 49, 1915–1929. doi:10.1093/petrology/egn047

Culshaw, N.G., Ketchum, J.W.F., Wodicka, N., Wallace, P., 1994. Deep crustal ductile extension following thrusting in the southwestern Grenville Province, Ontario. Can. J. Earth Sci. 31, 160–175. doi:10.1139/e94-013

David, J., 2006. Géochronologie d'échantillons provenant de Géologie Québec, année 2005-2006 - Rapport final. Ministère de l'Energie et des Ressources Naturelles, Québec GM 63236, 12 p.

David, J., Moukhsil, A., Clark, T., Hébert, C., Nantel, S., Dion, C., Sappin, A.-A., 2009. Datations U-Pb effectuées dans les provinces de Grenville et de Churchill en 2006-2007. Ministère des Ressources naturelles et de la Faune, Québec, RP2009-03, 32 p.

Dhuime, B., Hawkesworth, C.J., Cawood, P.A., Storey, C.D., 2012. A Change in the Geodynamics of Continental Growth 3 Billion Years Ago. Science 335, 1334–1336. doi:10.1126/science.1216066

Dickin, A.P., Higgins, M.D., 1992. Sm/Nd evidence for a major 1.5 Ga crust-forming event in the central Grenville province. Geology 20, 137–140. doi:10.1130/0091-7613(1992)020<0137:SNEFAM>2.3.CO;2

Dunning, G., Indares, A., 2010. New insights on the 1.7–1.0 Ga crustal evolution of the central Grenville Province from the Manicouagan – Baie Comeau transect. Precambrian Research 180, 204–226. doi:10.1016/j.precamres.2010.04.005

Ercit, T.S., 2005. REE-enriched granitic pegmatites. Short Course Notes - Geological Association of Canada 17, 175–199.

Farina, F., Stevens, G., Gerdes, A., Frei, D., 2014. Small-scale Hf isotopic variability in the Peninsula pluton (South Africa): the processes that control inheritance of source Hf/Hf diversity in S-type granites. Contrib. Mineral. Petrol. 168, 1–18. doi:10.1007/s00410-014-1065-8

Ferry, J.M., Watson, E.B., 2007. New thermodynamic models and revised calibrations for the Ti-in-zircon and Zr-in-rutile thermometers. Contrib. Mineral. Petrol. 154, 429–437. doi:10.1007/s00410-007-0201-0

Fowler, A.D., Doig, R., 1983. The age and origin of Grenville Province uraniferous granites and pegmatites. Can. J. Earth Sci. 20, 92–104. doi:10.1139/e83-009

Geisler, T., Schaltegger, U., Tomaschek, F., 2007. Re-equilibration of Zircon in Aqueous Fluids and Melts. Elements 3, 43–50. doi:10.2113/gselements.3.1.43

Geisler, T., Ulonska, M., Schleicher, H., Pidgeon, R.T., Bronswijk, W. van, 2001. Leaching and differential recrystallization of metamict zircon under experimental hydrothermal conditions. Contrib Mineral Petrol 141, 53–65. doi:10.1007/s004100000202

Gerdes, A., Zeh, A., 2009. Zircon formation versus zircon alteration — New insights from combined U–Pb and Lu–Hf in-situ LA-ICP-MS analyses, and consequences for the interpretation of Archean zircon from the Central Zone of the Limpopo Belt. Chemical Geology, Accessory minerals as tracers of crustal processes 261, 230–243. doi:10.1016/j.chemgeo.2008.03.005

Gerdes, A., Zeh, A., 2006. Combined U–Pb and Hf isotope LA-(MC-)ICP-MS analyses of detrital zircons: Comparison with SHRIMP and new constraints for the provenance and

age of an Armorican metasediment in Central Germany. Earth and Planetary Science Letters 249, 47–61. doi:10.1016/j.epsl.2006.06.039

Gervais, F., Crowley, J.L., 2017. Prograde and near-peak zircon growth in a migmatitic pelitic schist of the southeastern Canadian Cordillera. Lithos 282–283, 65–81. doi:10.1016/j.lithos.2017.02.016

Gieré, R., Sorensen, S.S., 2004. Allanite and other REE-rich epidote-group minerals. Reviews in Mineralogy and Geochemistry 56, 431–493. doi:10.2138/gsrmg.56.1.431

Gobeil, A., Hébert, C., Clark, T., Beaumier, M., Perreault, S., 2002. Géologie de la région du lac De la Blache (22K/03 et 22K/04). Ministère des Ressources Naturelles, Québec, RG 2002-01, 53 p.

Gower, C.F., Krogh, T.E., 2002. A U–Pb geochronological review of the Proterozoic history of the eastern Grenville Province. Can. J. Earth Sci. 39, 795–829.

Grimes, C.B., John, B.E., Kelemen, P.B., Mazdab, F.K., Wooden, J.L., Cheadle, M.J., Hanghøj, K., Schwartz, J.J., 2007. Trace element chemistry of zircons from oceanic crust: A method for distinguishing detrital zircon provenance. Geology 35, 643–646. doi:10.1130/G23603A.1

Hanchar, J.M., Finch, R.J., Hoskin, P.W.O., Watson, E.B., Cherniak, D.J., Mariano, A.N., 2001. Rare earth elements in synthetic zircon: Part 1. Synthesis, and rare earth element and phosphorus doping. American Mineralogist 86, 667–680. doi:10.2138/am-2001-5-607

Hawkesworth, C., Cawood, P., Kemp, T., Storey, C., Dhuime, B., 2009. A Matter of Preservation. Science 323, 49–50. doi:10.1126/science.1168549

Hawkesworth, C.J., Kemp, A.I.S., 2006. Using hafnium and oxygen isotopes in zircons to unravel the record of crustal evolution. Chemical Geology, Special Issue in Honour of R.K. O'Nions 226, 144–162. doi:10.1016/j.chemgeo.2005.09.018

Hayden, L.A., Watson, E.B., 2007. Rutile saturation in hydrous siliceous melts and its bearing on Ti-thermometry of quartz and zircon. Earth and Planetary Science Letters 258, 561–568. doi:10.1016/j.epsl.2007.04.020

Healy, B., Collins, W.J., Richards, S.W., 2004. A hybrid origin for Lachlan S-type granites: the Murrumbidgee Batholith example. Lithos, Selected Papers presented at the Symposium:

"Interaction between Mafic and Felsic Magmas in Orogenic Suites: Dynamics of Processes, Nature of End-Members, Effects" 78, 197–216. doi:10.1016/j.lithos.2004.04.047

Hiess, J., Bennett, V.C., Nutman, A.P., Williams, I.S., 2011. Archaean fluid-assisted crustal cannibalism recorded by low δ18O and negative εHf(T) isotopic signatures of West Greenland granite zircon. Contrib Mineral Petrol 161, 1027–1050. doi:10.1007/s00410-010-0578-z

Hoffman, P.F., 1991. Did the breakout of Laurentia turn Gondwanaland inside out? Science 252, 1409–1412.

Hoffman, P.F., 1989. Precambrian geology and tectonic history of North America The geology of North America. Geol. Soc. Am. : Boulder, CO, United States, United States, pp. 447–512.

Hönig, S., Čopjaková, R., Škoda, R., Novák, M., Dolejš, D., Leichmann, J., Galiová, M.V., 2014. Garnet as a major carrier of the Y and REE in the granitic rocks: An example from the layered anorogenic granite in the Brno Batholith, Czech Republic. American Mineralogist 99, 1922–1941. doi:10.2138/am-2014-4728

Hoskin, P.W.O., Schaltegger, U., 2003. The composition of zircon and igneous and metamorphic petrogenesis, in: Hanchar, J.M., Hoskin, P.W.O. (Eds.), Zircon, Reviews in Mineralogy and Geochemistry, Vol. 53. Mineralogical Society of America, pp. 27–62.

Hynes, A., Indares, A., Rivers, T., Gobeil, A., 2000. Lithoprobe line 55: integration of out-of-plane seismic results with surface structure, metamorphism, and geochronology, and the tectonic evolution of the eastern Grenville Province. Can. J. Earth Sci. 37, 341–358. doi:10.1139/e99-076

Hynes, A., Rivers, T., 2010. Protracted continental collision — evidence from the Grenville Orogen. Can. J. Earth Sci. 47, 591–620. doi:10.1139/E10-003

Indares, A., Dunning, G., 2004. Crustal architecture above the high-pressure belt of the Grenville Province in the Manicouagan area: new structural, petrologic and U–Pb age constraints. Precambrian Research 130, 199–228. doi:10.1016/j.precamres.2003.11.005

Indares, A., Dunning, G., 2001. Partial melting of high-P–T metapelites from the Tshenukutish Terrane (Grenville Province): Petrography and U–Pb geochronology. J. Petrology 42, 1547–1565. doi:10.1093/petrology/42.8.1547

Indares, A., Dunning, G., Cox, R., 2000. Tectono-thermal evolution of deep crust in a Mesoproterozoic continental collision setting: the Manicouagan example. Can. J. Earth Sci. 37, 325–340. doi:10.1139/e99-069

Indares, A., Dunning, G., Cox, R., Gale, D., Connelly, J., 1998. High-pressure, high-temperature rocks from the base of thick continental crust: Geology and age constraints from the Manicouagan Imbricate Zone, eastern Grenville Province. Tectonics 17, 426–440. doi:10.1029/98TC00373

Jackson, S.E., Pearson, N.J., Griffin, W.L., Belousova, E.A., 2004. The application of laser ablation-inductively coupled plasma-mass spectrometry to in situ U–Pb zircon geochronology. Chemical Geology 211, 47–69. doi:10.1016/j.chemgeo.2004.06.017

Jannin, S., Gervais, F., Moukhsil, A., Augland, L.E., Crowley, J.L., accepted. Déformations tardi-grenvilliennes dans la Ceinture parautochtone (Province de Grenville centrale) : contraintes géochronologiques par couplage de méthodes U/Pb de haute résolution spatiale et de haute précision. Canadian Journal of Earth Sciences.

Jordan, S.L., Indares, A., Dunning, G., 2006. Partial melting of metapelites in the Gagnon terrane below the high-pressure belt in the Manicouagan area (Grenville Province): pressure–temperature (P–T) and U–Pb age constraints and implications. Can. J. Earth Sci. 43, 1309–1329. doi:10.1139/E06-038

Ketchum, J.W.F., Heaman, L.M., Krogh, T.E., Culshaw, N.G., Jamieson, R.A., 1998. Timing and thermal influence of late orogenic extension in the lower crust: a U-Pb geochronological study from the southwest Grenville orogen, Canada. Precambrian Research 89, 25–45. doi:10.1016/S0301-9268(97)00079-X

Ketchum, J.W.F., Jamieson, R.A., Heaman, L.M., Culshaw, N.G., Krogh, T.E., 1994. 1.45 Ga granulites in the southwestern Grenville province: Geologic setting, P-T conditions, and U-Pb geochronology. Geology 22, 215–218. doi:10.1130/0091-7613(1994)022<0215:GGITSG>2.3.CO;2

King, E.M., Valley, J.W., Davis, D.W., Edwards, G.R., 1998. Oxygen isotope ratios of Archean plutonic zircons from granite–greenstone belts of the Superior Province: indicator of

magmatic source. Precambrian Research 92, 365–387. doi:10.1016/S0301-9268(98)00082-5

Krogh, T.E., 1994. Precise U-Pb ages for Grenvillian and pre-Grenvillian thrusting of Proterozoic and Archean metamorphic assemblages in the Grenville Front tectonic zone, Canada. Tectonics 13, 963–982. doi:10.1029/94TC00801

Lasalle, S., Dunning, G., Indares, A., 2014. In situ LA–ICP–MS dating of monazite from aluminous gneisses: insights on the tectono-metamorphic history of a granulite-facies domain in the central Grenville Province. Can. J. Earth Sci. 51, 558–572. doi:10.1139/cjes-2013-0170

Lasalle, S., Fisher, C.M., Indares, A., Dunning, G., 2013. Contrasting types of Grenvillian granulite facies aluminous gneisses: Insights on protoliths and metamorphic events from zircon morphologies and ages. Precambrian Research 228, 117–130. doi:10.1016/j.precamres.2013.01.014

Lasalle, S., Indares, A., 2014. Anatectic record and contrasting P-T paths of aluminous gneisses from the central Grenville Province. Journal of Metamorphic Geology 32, 627–646. doi:10.1111/jmg.12083

Lentz, D.R., 1991. Petrogenesis of uranium-, thorium-, molybdenum-, and rare earth element-bearing pegmatites, skarns, and veins in the central metasedimentary belt of the Grenville Province, Ontario and Quebec. (Unpublished Ph.D. thesis). University of Ottawa (Canada).

Li, Z.X., Bogdanova, S.V., Collins, A.S., Davidson, A., De Waele, B., Ernst, R.E., Fitzsimons, I.C.W., Fuck, R.A., Gladkochub, D.P., Jacobs, J., Karlstrom, K.E., Lu, S., Natapov, L.M., Pease, V., Pisarevsky, S.A., Thrane, K., Vernikovsky, V., 2008. Assembly, configuration, and break-up history of Rodinia: A synthesis. Precambrian Research, Testing the Rodinia hypothesis: Records in its building blocks 160, 179–210. doi:10.1016/j.precamres.2007.04.021

Liu, Y., Hu, Z., Zong, K., Gao, C., Gao, S., Xu, J., Chen, H., 2010. Reappraisement and refinement of zircon U-Pb isotope and trace element analyses by LA-ICP-MS. Chinese Science Bulletin 55, 1535–1546. doi:10.1007/s11434-010-3052-4

London, D., 2016. Rare-element granitic pegmatites. Reviews in Economic Geology 18, 165–193.

Ludwig, K.R., 2001. Isoplot/Ex, rev. 2.49. A geochronological toolkit for Microsoft Excel. Berkeley Geochronology Center, Special Publication No. 1a.

Martin, L.A.J., Duchêne, S., Deloule, E., Vanderhaeghe, O., 2008. Mobility of trace elements and oxygen in zircon during metamorphism: Consequences for geochemical tracing. Earth and Planetary Science Letters 267, 161–174. doi:10.1016/j.epsl.2007.11.029

Martin, R.F., De Vito, C., 2005. The patterns of enrichment in felsic pegmatites ultimately depend on tectonic setting. Can. Mineral. 43, 2027–2048. doi:10.2113/gscanmin.43.6.2027

Masson, S.L., Gordon, J.B., 1981. Radioactive mineral deposits of the Pembroke-Renfrew area (No. 23), Mineral Deposits Circ. Ont. Geol. Surv.

McDonough, W.F., Sun, S. -s., 1995. The composition of the Earth. Chemical Geology, Chemical Evolution of the Mantle 120, 223–253. doi:10.1016/0009-2541(94)00140-4

Moukhsil, A., Lacoste, P., Gobeil, A., David, J., 2009. Synthèse géologique de la région de Baie-Comeau. Ministère des Ressources naturelles et de la Faune, Québec, RG 2009-03, 30 p.

Moukhsil, A., Lacoste, P., Simard, M., Perreault, S., 2007. Géologie de la région septentrionale de Baie-Comeau (22F07, 22F08, 22F09, 22F15 et 22F16). Ministère des Ressources naturelles et de la Faune, Québec, RP 2007-04, 16 p.

Moukhsil, A., Solgadi, F., Belkacim, S., Elbasbas, A., Augland, L.E., 2014. Géologie de la région du lac Okaopéo, Côte-Nord. Ministère de l'Energie et des Ressources Naturelles, Québec, RG 2014-03, 34 p.

Moukhsil, A., Solgadi, F., Clark, T., Blouin, S., Indares, A., Davis, D.W., 2013a. Géologie du nord-ouest de la région du barrage Daniel-Johnson (Manic 5), Côte-Nord. Ministère des Ressources Naturelles, Québec, RG 2013-01, 46 p.

Moukhsil, A., Solgadi, F., Indares, A., Belkacim, S., 2013b. Géologie de la région septentrionale du réservoir aux Outardes 4, Côte-Nord. Ministère des Ressources Naturelles, Québec, RG 2013-03, 33 p.

Moukhsil, A., Solgadi, F., Lacoste, P., Gagnon, M., David, J., 2012. Géologie de la région du lac du Milieu (SNRC 22O03, 22O04, 22O06, 22J13 et 22J14). Ministère des Ressources Naturelles et de la Faune, Québec, RG 2012-01, 33 p.

Moyen, J.-F., Laurent, O., Chelle-Michou, C., Couzinié, S., Vanderhaeghe, O., Zeh, A., Villaros, A., Gardien, V., 2017. Collision vs. subduction-related magmatism: Two contrasting ways of granite formation and implications for crustal growth. Lithos, Eighth Hutton Symposium on Granites and Related Rocks 277, 154–177. doi:10.1016/j.lithos.2016.09.018

Peck, W., King, E., Valley, J., 2000. Oxygen isotope perspective on Precambrian crustal growth and maturation. GEOLOGY 28, 363–366.

Pidgeon, R.T., 1992. Recrystallisation of oscillatory zoned zircon: some geochronological and petrological implications. Contrib Mineral Petrol 110, 463–472. doi:10.1007/BF00344081

Rayner, N., Stern, R.A., Carr, S.D., 2005. Grain-scale variations in trace element composition of fluid-altered zircon, Acasta Gneiss Complex, northwestern Canada. Contrib Mineral Petrol 148, 721–734. doi:10.1007/s00410-004-0633-8

Rivers, T., 2012. Upper-crustal orogenic lid and mid-crustal core complexes: signature of a collapsed orogenic plateau in the hinterland of the Grenville Province. Can. J. Earth Sci. 49, 1–42. doi:10.1139/e11-014

Rivers, T., 2009. The Grenville Province as a large hot long-duration collisional orogen – insights from the spatial and thermal evolution of its orogenic fronts. Geological Society, London, Special Publications 327, 405–444. doi:10.1144/SP327.17

Rivers, T., 2008. Assembly and preservation of lower, mid, and upper orogenic crust in the Grenville Province—Implications for the evolution of large hot long-duration orogens. Precambrian Research 167, 237–259. doi:10.1016/j.precamres.2008.08.005

Rivers, T., 1997. Lithotectonic elements of the Grenville Province: review and tectonic implications. Precambrian Research 86, 117–154. doi:10.1016/S0301-9268(97)00038-7

Rivers, T., 1980. Revised stratigraphic nomenclature for Aphebian and other rock units, southern Labrador Trough, Grenville Province. Can. J. Earth Sci. 17, 668–670. doi:10.1139/e80-062

Rivers, T., Culshaw, N., Hynes, A., Indares, A., Jamieson, R., Martignole, J., 2012. The Grenville Orogen - A Post-LITHOPROBE Perspective, in: J.A. Percival, F.A. Cook,

and R.M. Clowes (eds) Tectonic Styles in Canada: The LITHOPROBE Perspective, Geological Association of Canada. Special Paper 49, pp. 97–236.

Rivers, T., Ketchum, J., Indares, A., Hynes, A., 2002. The High Pressure belt in the Grenville Province: architecture, timing, and exhumation. Can. J. Earth Sci. 39, 867–893.

Rivers, T., Martignole, J., Gower, C.F., Davidson, A., 1989. New tectonic divisions of the Grenville Province, Southeast Canadian Shield. Tectonics 8, 63–84. doi:10.1029/TC008i001p00063

Rivers, T., Schwerdtner, W., 2015. Post-peak evolution of the Muskoka domain, western Grenville Province: ductile detachment zone in a crustal-scale metamorphic core complex. Geoscience Canada 42, 403–436. doi:10.12789/geocanj.2015.42.080

Rubatto, D., 2017. Zircon: The metamorphic mineral. Reviews in Mineralogy & Geochemistry 83, 261–295. doi:10.2138/rmg.2017.83.09

Scherer, E., Münker, C., Mezger, K., 2001. Calibration of the Lutetium-Hafnium clock. Science 293, 683–687. doi:10.1126/science.1061372

Sircombe, K.N., 2004. AgeDisplay: an EXCEL workbook to evaluate and display univariate geochronological data using binned frequency histograms and probability density distributions. Computers & Geosciences 30, 21–31. doi:10.1016/j.cageo.2003.09.006

Sláma, J., Košler, J., Condon, D.J., Crowley, J.L., Gerdes, A., Hanchar, J.M., Horstwood, M.S.A., Morris, G.A., Nasdala, L., Norberg, N., Schaltegger, U., Schoene, B., Tubrett, M.N., Whitehouse, M.J., 2008. Plešovice zircon — A new natural reference material for U–Pb and Hf isotopic microanalysis. Chemical Geology 249, 1–35. doi:10.1016/j.chemgeo.2007.11.005

Smithies, R.H., Howard, H.M., Evins, P.M., Kirkland, C.L., Kelsey, D.E., Hand, M., Wingate, M.T.D., Collins, A.S., Belousova, E., 2011. High-temperature granite magmatism, crust–mantle interaction and the Mesoproterozoic intracontinental evolution of the Musgrave Province, Central Australia. J Petrology 52, 931–958. doi:10.1093/petrology/egr010

Söderlund, U., Patchett, P.J., Vervoort, J.D., Isachsen, C.E., 2004. The 176Lu decay constant determined by Lu–Hf and U–Pb isotope systematics of Precambrian mafic intrusions.

Earth and Planetary Science Letters 219, 311–324. doi:10.1016/S0012-821X(04)00012-3

Soucy La Roche, R., Gervais, F., Tremblay, A., Crowley, J.L., Ruffet, G., 2015. Tectono-metamorphic history of the eastern Taureau shear zone, Mauricie area, Québec: Implications for the exhumation of the mid-crust in the Grenville Province. Precambrian Research 257, 22–46. doi:10.1016/j.precamres.2014.11.012

Spencer, C.J., Cawood, P.A., Hawkesworth, C.J., Prave, A.R., Roberts, N.M.W., Horstwood, M.S.A., Whitehouse, M.J., 2015. Focus paper: Generation and preservation of continental crust in the Grenville Orogeny. Geoscience Frontiers 6, 357–372. doi:10.1016/j.gsf.2014.12.001

Stacey, J.S., Kramers, J.D., 1975. Approximation of terrestrial lead isotope evolution by a two-stage model. Earth and Planetary Science Letters 26, 207–221. doi:10.1016/0012-821X(75)90088-6

Stepanov, A., Mavrogenes, J.A., Meffre, S., Davidson, P., 2014. The key role of mica during igneous concentration of tantalum. Contrib. Mineral. Petrol. 167, 1–8. doi:10.1007/s00410-014-1009-3

Taylor, S.R., McLennan, S., 1985. The continental crust: Its composition and evolution, Blackwell, Oxford, 1985,.

Thomson, S.D., Dickin, A.P., Spray, J.G., 2011. Nd isotope mapping of Grenvillian crustal terranes in the vicinity of the Manicouagan Impact Structure. Precambrian Research 191, 184–193. doi:10.1016/j.precamres.2011.08.006

Toé, W., Vanderhaeghe, O., André-Mayer, A.-S., Feybesse, J.-L., Milési, J.-P., 2013. From migmatites to granites in the Pan-African Damara orogenic belt, Namibia. Journal of African Earth Sciences 85, 62–74. doi:10.1016/j.jafrearsci.2013.04.009

Tohver, E., Teixeira, W., Pluijm, B. van der, Geraldes, M.C., Bettencourt, J.S., Rizzotto, G., 2006. Restored transect across the exhumed Grenville orogen of Laurentia and Amazonia, with implications for crustal architecture. Geology 34, 669–672. doi:10.1130/G22534.1

Tucker, R.D., Gower, C.F., 1994. A U-Pb geochronological framework for the Pinware Terrane, Grenville Province, Southeast Labrador. Journal of Geology 102, 67.

Turlin, F., André-Mayer, A.-S., Moukhsil, A., Vanderhaeghe, O., Gervais, F., Solgadi, F., Groulier, P.-A., Poujol, M., 2017. Unusual LREE-rich, peraluminous, monazite- or allanite-bearing pegmatitic granite in the central Grenville Province, Québec. Ore Geology Reviews 89, 627–667. doi:10.1016/j.oregeorev.2017.04.019

Valley, J.W., 2003. Oxygen Isotopes in Zircon. Reviews in Mineralogy and Geochemistry 53, 343–385. doi:10.2113/0530343

Valley, J.W., Chiarenzelli, J.R., McLelland, J.M., 1994. Oxygen isotope geochemistry of zircon. Earth and Planetary Science Letters 126, 187–206. doi:10.1016/0012-821X(94)90106-6

Valley, J.W., Lackey, J.S., Cavosie, A.J., Clechenko, C.C., Spicuzza, M.J., Basei, M.A.S., Bindeman, I.N., Ferreira, V.P., Sial, A.N., King, E.M., Peck, W.H., Sinha, A.K., Wei, C.S., 2005. 4.4 billion years of crustal maturation: oxygen isotope ratios of magmatic zircon. Contrib. Mineral. Petrol. 150, 561–580. doi:10.1007/s00410-005-0025-8

van Gool, J.A.M., Rivers, T., Calon, T., 2008. Grenville Front zone, Gagnon terrane, southwestern Labrador: Configuration of a midcrustal foreland fold-thrust belt. Tectonics 27, TC1004. doi:10.1029/2006TC002095

Van Kranendonk, M.J.V., Kirkland, C.L., 2013. Orogenic climax of Earth: The 1.2–1.1 Ga Grenvillian superevent. Geology 41, 735–738. doi:10.1130/G34243.1

Villaros, A., Buick, I.S., Stevens, G., 2012. Isotopic variations in S-type granites: an inheritance from a heterogeneous source? Contrib Mineral Petrol 163, 243–257. doi:10.1007/s00410-011-0673-9

Wedepohl, K.H., 1995. The composition of the continental crust. Geochimica et Cosmochimica Acta 59, 1217–1232. doi:10.1016/0016-7037(95)00038-2

Wiedenbeck, M., Allé, P., Corfu, F., Griffin, W. l., Meier, M., Oberli, F., Quadt, A.V., Roddick, J. c., Spiegel, W., 1995. Three natural zircon standards for U-Th-Pb, Lu-Hf, trace element and REE analyses. Geostandards Newsletter 19, 1–23. doi:10.1111/j.1751-908X.1995.tb00147.x

Woodhead, J.D., Hergt, J.M., 2005. A preliminary appraisal of seven natural zircon reference materials for in situ Hf isotope determination. Geostandards and Geoanalytical Research 29, 183–195. doi:10.1111/j.1751-908X.2005.tb00891.x

Yuan, H.-L., Gao, S., Dai, M.-N., Zong, C.-L., Günther, D., Fontaine, G.H., Liu, X.-M., Diwu, C., 2008. Simultaneous determinations of U–Pb age, Hf isotopes and trace element compositions of zircon by excimer laser-ablation quadrupole and multiple-collector ICP-MS. Chemical Geology 247, 100–118. doi:10.1016/j.chemgeo.2007.10.003

Zeh, A., Gerdes, A., 2012. U–Pb and Hf isotope record of detrital zircons from gold-bearing sediments of the Pietersburg Greenstone Belt (South Africa)—Is there a common provenance with the Witwatersrand Basin? Precambrian Research 204, 46–56. doi:10.1016/j.precamres.2012.02.013

Zeh, A., Stern, R.A., Gerdes, A., 2014. The oldest zircons of Africa—Their U–Pb–Hf–O isotope and trace element systematics, and implications for Hadean to Archean crust–mantle evolution. Precambrian Research 241, 203–230. doi:10.1016/j.precamres.2013.11.006

PARTIE III : PÉTROGENÈSE DES GRANITES PEGMATITIQUES

Préambule

Les granites peralumineux enrichis en terres rares sont anomaliques, les forts enrichissements en terres rares étant plutôt associés aux granites alcalins (Kovalenko, 1978 ; Linnen et al., 2014 ; Linnen and Cuney, 2005 ; Pollard, 1989 ; Raimbault et al., 1995, 1991 ; Taylor, 1992). Le caractère peralumineux des granites pegmatitiques décrits en chapitre 1 (Turlin et al., 2017) questionne quant à leur pétrogenèse à partir d'une source que nous proposons métasédimentaire paléoprotérozoïque et/ou archéenne (chapitre 3).

Cette partie s'attachera donc à discuter de la pétrogenèses des dykes de granites pegmatitiques (« PGD ») à terres rares décrits par Turlin et al. (2017) qui ont été divisés en PGD à monazite et à allanite. Cette distinction est corrélée à leur encaissant respectif, les premiers intrudant des complexes métasédimentaires et les seconds des complexes métaplutoniques. De plus, Turlin et al. (2017) ont également distingués deux groupes de PGD, sur la base de caractéristiques structurales et géochimiques. Six d'entre eux présentent des contacts fortement pentés et un caractère fortement peralumineux. Le septième (PGD 13-AE-2149) présente quant à lui un dyke principal faiblement penté et un caractère moins peralumineux.

1. Processus magmatiques à l'origine des PGD à terres rares

L'âge de la mise en place des PGD fortement pentés à monazite et à allanite, et la nature et l'âge de leur source a été contrainte dans le chapitre 3 par une étude couplée d'isotopie U-Pb-Hf-O et éléments traces sur zircons magmatiques néoformés. Ces PGD se mettent en place dans la ceinture Allochtone du Grenville central à 1005-1000 Ma, à l'initiation de la phase orogénique du Rigolet qui est enregistrée dans la ceinture Parautochtone sous-jacente (par exemple Jannin et al., accepté ; Rivers, 2008 ; Rivers et al., 2012). Ils contiennent des zircons présentant des faibles teneurs en Ca, Fe et terres rares légères qui, couplées à l'absence d'héritage textural, chimique ou isotopique, démontrent leur caractère néoformé. Ainsi, les signatures isotopiques et chimiques de ces zircons reflètent la composition du magma, directement fonction de la source. Ils présentent des signatures $\varepsilon Hf_{(t)}$ fortement sub-chondritiques, des âges modèles T_{DM2} Hf paléoprotérozoïques, des signatures $\delta^{18}O_{V\text{-}SMOW}$ supra-mantelliques et des teneurs en U, Y et Yb typiques de zircons de granitoïdes continentaux, qui, couplés au caractère fortement peralumineux des PGD indiquent leur formation par fusion partielle de métapélites paléoprotérozoïques à archéennes. Celles-ci peuvent correspondre aux

paragneiss du Complexe de la Plus-Value de la ceinture Allochtone, intrudé par les PGD, ou aux métapélites du Groupe de Knob Lake de la ceinture Parautochtone.

Deux processus magmatiques ont pu conduire à la genèse de ces occurrences de terres rares associées à des PGD peralumineux, (i) la fusion partielle d'un protolithe fertile et/ou (ii) la cristallisation fractionnée d'un magma pré-enrichi. Pour contraindre le rôle respectif de chacun de ces processus dans la genèse de ces occurrences, les caractéristiques pétrogéochimiques de métapélites représentant une source potentielle des PGD seront comparées à celle d'un PGD. Les paragneiss du Complexe de la Plus-Value, déposés entre 1765 et 1497 Ma (Augland et al., 2015 ; Lasalle et al., 2013 ; Moukhsil et al., 2014, 2013b), ont enregistré des évènements métamorphiques pré-Grenvilliens de haute grade marqués par des couronnes de zircons à ~1,4 et ~1,2 Ga (Lasalle et al., 2013). Ainsi, même si ces paragneiss représentaient une source potentielle et fertile des PGD, ces évènements métamorphiques ont pu remobiliser et disperser les terres rares. Ils ne permettent donc pas d'évaluer la contribution de la marge de Laurentia dans la formation des occurrences de terres rares. Au contraire, les métapélites du Groupe de Knob Lake, déposées avant 1870 Ma, n'enregistrent qu'un seul évènement métamorphique pré-Grenvillien, à ~1740 Ma (Jordan et al., 2006), interprété comme n'ayant pas atteint les conditions de fusion partielle. Ainsi ces métapélites représentent un bon proxy de la contribution de la marge de Laurentia dans la genèse des PGD.

Le premier chapitre de cette partie (***chapitre 4***) compare les caractéristiques pétrogéochimiques du leucosome, mésosome et mélanosome d'un affleurement de métapélites migmatitiques du Groupe de Knob Lake et des différents faciès du PGD à monazite 13-AM-13, présentant la plus grande variabilité de faciès observée dans les PGD. Cette étude s'appuie sur (i) des données de géochimie roche totale, (ii) des observations pétrographiques, et (iii) des compositions en éléments traces de silicates du leucosome des métapélites et des différents faciès du PGD. Ces données permettent d'évaluer la fertilité des métapélites migmatitiques du Groupe de Knob Lake dans la genèse de ces occurrences de terres rares, d'évaluer le rôle de chaque processus magmatique dans leur concentration, et enfin de proposer un modèle pétrogénétique des PGD fortement peralumineux à terres rares de la Province de Grenville central.

2. Source, potentiel et implications métallogéniques du PGD faiblement penté 13-AE-2149

La source et les processus pétrogénétiques responsables de la formation des occurrences de terres associées à des PGD fortement pentés de la Province de Grenville central sont contraints via une approche multi-méthodes présentées dans les chapitres 3 et 4. Ces éléments restent à discuter pour le PGD 13-AE-2149 présentant un contact faiblement penté et des caractéristiques pétrogéochimiques différentes des autres PGD de la région telles qu'un caractère faiblement peralumineux, un plus faible fractionnement des terres rares légères par rapport aux lourdes, et des concentrations en Nb et Ta plus élevées. Toutes ces caractéristiques ont conduit Turlin et al. (2017) à proposer sa formation par une source et/ou des processus pétrogénétiques différents.

Le second chapitre de cette partie (***chapitre 5***) se focalise sur ce PGD faiblement penté dont les données de géochimie roche totale des faciès identifiés et les données isotopiques U-Pb-Hf-O et des éléments traces sur zircons permettent de discuter (i) de l'âge de mise en place du PGD, (ii) de sa source, et de (iii) mettre en évidence que la minéralisation en terres rares est très localisée. Ces données permettent de discuter de l'importance de la fertilité du protolithe dans la genèse des occurrences de terres rares associées à des PGD et d'en tirer des implications métallogéniques sur le cycle des terres rares dans la Province de Grenville central.

3. Facteurs contrôlant l'expression de la minéralisation sous la forme de monazite ou d'allanite

Turlin et al. (2017) ont mis en évidence une relation empirique entre l'expression de la minéralisation en terres rares légères dans les PGD et la nature de l'encaissant, les complexes métasédimentaires étant intrudés par des PGD à monazite et les complexes métaplutoniques par des PGD à allanite. L'expression de la monazite par rapport à l'allanite est en général attribuée aux activités de Na et Ca dans le magma (Berger et al., 2009 ; Budzyń et al., 2011). Cependant, aucune corrélation entre ces éléments et la nature de la minéralisation n'a pu être mis en évidence, au contraire, le contrôle de la minéralisation semble être lié à d'autres facteurs tels que les teneurs en Fe et Mg (Turlin et al., 2017).

Cette section complémentaire à la partie III a pour objectif de tester en première approche le rôle de l'encaissant sur l'expression de la monazite et de l'allanite, en regroupant les données de géochimie roche totale de l'ensemble des faciès de plusieurs PGD et de leurs encaissants respectifs, échantillonnés (i) au contact, ainsi (ii) qu'à quelques dizaines de

centimètres, et (iii) loin du contact avec le PGD. Cette approche permet d'apporter des perspectives de travail quant aux processus contrôlant l'expression de la minéralisation sous la forme d'allanite ou de monazite dans ces occurrences de terres rares.

Références

Augland, L.E., Moukhsil, A., Solgadi, F., Indares, A., McFarlane, C., 2015. Pinwarian to Grenvillian magmatic evolution in the central Grenville Province: new constraints from ID-TIMS U-Pb ages and coupled Lu-Hf S-MC-ICP-MS data. Canadian Journal of Earth Sciences 52, 701–721. doi:10.1139/cjes-2014-0232

Berger, A., Rosenberg, C., Schaltegger, U., 2009. Stability and isotopic dating of monazite and allanite in partially molten rocks: examples from the Central Alps. Swiss J. Geosci. 102, 15–29. doi:10.1007/s00015-009-1310-8

Budzyń, B., Harlov, D.E., Williams, M.L., Jercinovic, M.J., 2011. Experimental determination of stability relations between monazite, fluorapatite, allanite, and REE-epidote as a function of pressure, temperature, and fluid composition. American Mineralogist 96, 1547–1567. doi:10.2138/am.2011.3741

Jannin, S., Gervais, F., Moukhsil, A., Augland, L.E., Crowley, J.L., accepted. Déformations tardi-grenvilliennes dans la Ceinture parautochtone (Province de Grenville centrale) : contraintes géochronologiques par couplage de méthodes U/Pb de haute résolution spatiale et de haute précision. Canadian Journal of Earth Sciences.

Jordan, S.L., Indares, A., Dunning, G., 2006. Partial melting of metapelites in the Gagnon terrane below the high-pressure belt in the Manicouagan area (Grenville Province): pressure–temperature (P–T) and U–Pb age constraints and implications. Can. J. Earth Sci. 43, 1309–1329. doi:10.1139/E06-038

Kovalenko, V., 1978. The genesis of rare metal granitoids and related ore deposits, in: Štemprok, M., Burnol, and Tischendorf, G., Eds., Metallization associated with acid magmatism, Czech Geological Survey. pp. 235–258.

Lasalle, S., Fisher, C.M., Indares, A., Dunning, G., 2013. Contrasting types of Grenvillian granulite facies aluminous gneisses: Insights on protoliths and metamorphic events from zircon morphologies and ages. Precambrian Research 228, 117–130. doi:10.1016/j.precamres.2013.01.014

Linnen, R.L., Cuney, M., 2005. Granite-related rare-element deposits and experimental constraints on Ta-Nb-W-Sn-Zr-Hf mineralization. Short Course Notes - Geological Association of Canada 17, 45–68.

Linnen, R.L., Samson, I.M., Williams-Jones, A.E., Chakhmouradian, A.R., 2014. 13.21 - Geochemistry of the Rare-Earth Element, Nb, Ta, Hf, and Zr Deposits, in: Turekian, H.D.H.K. (Ed.), Treatise on Geochemistry (Second Edition). Elsevier, Oxford, pp. 543–568.

Moukhsil, A., Solgadi, F., Belkacim, S., Elbasbas, A., Augland, L.E., 2014. Géologie de la région du lac Okaopéo, Côte-Nord. Ministère de l'Energie et des Ressources Naturelles, Québec, RG 2014-03, 34 p.

Moukhsil, A., Solgadi, F., Indares, A., Belkacim, S., 2013. Géologie de la région septentrionale du réservoir aux Outardes 4, Côte-Nord. Ministère des Ressources Naturelles, Québec, RG 2013-03, 33 p.

Pollard, P.-J., 1989. Geochemistry of granites associated with tantalum and niobium mineralization, in: Lanthanides, Tantalum and Niobium. Springer Verlag, Berlin, pp. 27–29.

Raimbault, L., Charoy, B., Cuney, M., Pollard, P.-J., 1991. Comparative geochemistry of Ta-bearing granites, in: Pagel, M., and Leroy, J., Eds., Source, Transport and Deposition of Metals. Balkema, Rotterdam, pp. 793–796.

Raimbault, L., Cuney, M., Azencott, C., Duthou, J.-L., Joron, J.-L., 1995. Multistage magmatic genesis of a Ta–Sn–Li mineralized granite at Beauvoir, French Massif Central: a geochemical study. Economic Geology 90, 548–576.

Rivers, T., 2008. Assembly and preservation of lower, mid, and upper orogenic crust in the Grenville Province—Implications for the evolution of large hot long-duration orogens. Precambrian Research 167, 237–259. doi:10.1016/j.precamres.2008.08.005

Rivers, T., Culshaw, N., Hynes, A., Indares, A., Jamieson, R., Martignole, J., 2012. The Grenville Orogen - A Post-LITHOPROBE Perspective, in: J.A. Percival, F.A. Cook, and R.M. Clowes (eds) Tectonic Styles in Canada: The LITHOPROBE Perspective, Geological Association of Canada. Special Paper 49, pp. 97–236.

Taylor, R.P., 1992. Petrological and geochemical characteristics of the Pleasant Ridge zinnwaldite-topaz granite, southern New Brunswick, and comparisons with other topaz-bearing felsic rocks. Can Mineral 30, 895–921.

Turlin, F., André-Mayer, A.-S., Moukhsil, A., Vanderhaeghe, O., Gervais, F., Solgadi, F., Groulier, P.-A., Poujol, M., 2017. Unusual LREE-rich, peraluminous, monazite- or allanite-bearing pegmatitic granite in the central Grenville Province, Québec. Ore Geology Reviews 89, 627–667. doi:10.1016/j.oregeorev.2017.04.019

Chapitre 4 : Anatectic melt loss from metapelites and low magmatic fractionation: a prerequisite in the genesis of peraluminous high-grade LREE-rich peraluminous pegmatitic granite

François Turlin[a,*], Anne-Sylvie André-Mayer[a], Aurélien Eglinger[a], Olivier Vanderhaeghe[b], Clara Deruy[a], Marieke Van Lichtervelde[b], Félix Gervais[c], Abdelali Moukhsil[d], Fabien Solgadi[e]

Article en préparation pour *Journal of Petrology*

[a] *GeoRessources lab., Université de Lorraine, CNRS, CREGU, Campus Aiguillettes, Faculté des Sciences et Technologies, rue Jacques Callot, Vandœuvre-lès-Nancy, F-54506, France*

[b] *Géosciences Environnement Toulouse, UMR 5563, Université de Toulouse, France*

[c] *Département des génies civil, géologiques et des mines, Polytechnique Montréal, Canada*

[d] *Ministère de l'Énergie et des Ressources naturelle, Direction du Bureau de la connaissance géoscientifique du Québec, 5700, 4e Avenue Ouest, Québec (Québec), G1H 6R1*

[e] *Ministère de l'Énergie et des Ressources naturelles, Direction du Bureau de la connaissance géoscientifique du Québec, 400, boulevard Lamaque, Val-d'Or (Québec) J9P 3L4*

Abstract

Petro-geochemical comparison between a Paleoproterozoic metapelite partially molten during the Rigolet orogenic phase of the Grenvillian Orogeny, and a coeval LREE-rich peraluminous pegmatitic granite dyke from the central Grenville Province allow to discriminate the magmatic processes responsible for the genesis of such unusual LREE-enriched peraluminous granite magmatic occurrences.

The (i) poorly differentiated nature (low Rb contents and high K/Rb ratios of K-feldspar, plagioclase and biotite) of the leucosome of the migmatitic metapelites and of the various facies identified in the dyke attest to a genetic link. The (ii) ΣLREE content of 119 ppm of the mesosome of the metapelite that represents a minimal composition of the protolith, (iii) the total consumption of monazite, together with the formation of peritectic garnet in the melanosome, (iv) the cumulate and LREE-impoverished signature of the plagioclase+K-feldspar dominated leucosome, and (v) the low Nb/Ta ratios of the metapelite (11-19) are consistent with the derivation of the LREE-rich (up to 6,949 ppm), peraluminous (ASI between 1.12 and 1.36) pegmatitic granite dyke by high-temperature partial melting of the sampled paragneisses. It involves high-temperature partial melting of a fertile metapelitic protolith up to the total consumption of biotite allowing the complete dissolution of monazite and the subsequent LREE saturation of the produced anatectic melt.

The lack of variations attributable to the facies variability of the dyke of (i) Nb/Ta ratios, Nb and Ta contents of the whole-rock geochemistry and biotite, (ii) of K/Rb ratios, K and Rb contents of the K-feldspar and biotite, along with (iii) the corroded textures of biotite from the LREE-richest fine grained facies, (iv) the complex internal zoning of some monazite grains, and the (v) decrease of the LREE content towards pegmatitic facies (from 6,949 to 705 ppm), attest for the formation of high-grade LREE concentrations by early LREE saturated melt loss events from the source. Subsequent melt loss involve the migration of relatively LREE depleted melt that is responsible for the randomly organized zonation of the dyke and the LREE decrease towards pegmatitic facies.

Keywords: Pegmatitic granite; peraluminous; REE; partial melting; Grenville

1. Introduction

The "rare-elements" (also called rare-metals) are predominantly either large-ion-lithophile elements (LILE) or high-field-strength elements (HFSE), with low and high charge-to-ionic-radius ratios, and share several physical-chemical characteristics. They are lithophile, incompatible (Goldschmidt and Thomassen, 1923; Linnen et al., 2014; Linnen and Cuney, 2005; McDonough and Sun, 1995; Railsback, 2003), leading to enrichment in melts that result either from very low degrees of partial melting or from extreme fractionation. This includes carbonatites, peralkaline granites and silica-undersaturated rocks, and peraluminous granites and pegmatites (e.g. Linnen et al., 2014).

Various classifications of the rare-element granites have been proposed regarding to specific geochemical and mineralogical characteristics (Kovalenko, 1978; Linnen and Cuney, 2005; Pollard, 1989; Raimbault et al., 1991, 1995; Taylor, 1992) from peralkaline to peraluminous granites. This later granites are generally characterized by middle to under-chondritic REE content depending their P content (Linnen and Cuney, 2005). Unusual REE-rich peraluminous granitic pegmatites (7,563 ppm) have been recently described by Turlin et al. (2017). These light rare-earth elements (LREE) magmatic occurrences associated with peraluminous pegmatitic granite dykes (*further designated as 'PGD'*) are hosted either in paragneisses (monazite-bearing PGD) or metaplutonic complexes (allanite-bearing PGD) from the Allochthonous Belt of the central Grenville Province (Fig. 4-1). Intrusive dykes with ΣLREE content up to 7,435 ppm (Turlin et al., 2017) generally show discordant steep-dipping contacts with no interconnection with leucosomes, magmatic textures with no solid-state deformation and ca. 1005-1000 Ma timing of intrusion (U-Pb on monazite and zircon, Turlin et al., 2017, chapter 3) that postdate the Ottawan peak of metamorphism recorded in this part of the Allochthonous Belt (Lasalle et al., 2014; Lasalle and Indares, 2014; Turlin et al., submitted). On this basis, Turlin et al. (2017) concluded to their late-tectonic setting of emplacement relative to their hosts. In chapter 3 the authors reported for zircon from these PGD (i) sub-chondritic $\varepsilon Hf_{(1003\ Ma)}$ values and associated Paleoproterozoic $T_{DM2\ (1003\ Ma)}$ Hf model ages, and (ii) supra-mantellic $\delta^{18}O_{V\text{-}SMOW}$ signatures compatible with their derivation by partial melting of Paleoproterozoic-Archean metasedimentary units. These might belong to the Knob Lake Group metapelites (Gagnon Terrane, Parautochthonous Belt, Fig. 4-1) and/or to the Plus-Value Complex paragneisses that host monazite-bearing PGD defined by Turlin et al. (2017) (Allochthonous Belt, Fig. 4-1).

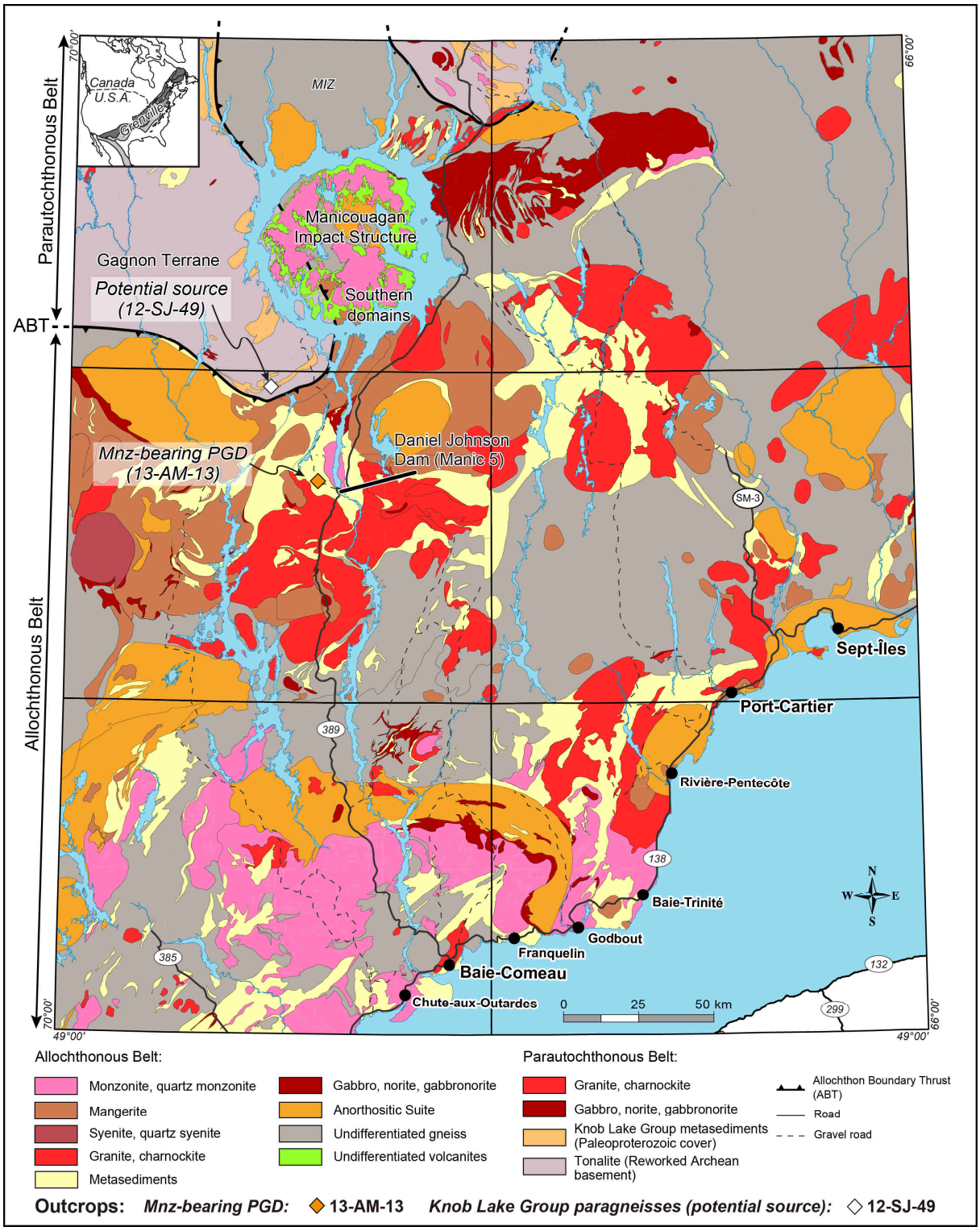

Figure 4-1: Geological map of the central Grenville Province (Quebec) showing the position of the 13-AM-13 monazite-bearing pegmatitic granite dyke (Allochthonous Belt) and of the sampled Knob Lake Group metapelites (Parautochthonous Belt) that represent its potential source (modified after Moukhsil et al., 2014; Turlin et al., 2017). Abbreviations: ABT = Allochthon Boundary Thrust; MIZ = Manicouagan Imbricate Zone; Mnz-bearing PGD = monazite-bearing pegmatitic granite dyke.

The magmatic processes that allowed these unusual LREE concentrations in the PGD might involve (i) silicate melt extraction from a fertile, partially molten source and/or (ii) fractional crystallization of this silicate melt. In order to test the Knob Lake Group metapelites as a potential partially molten source of the PGD and to document its specific role on their genesis we present petrography of the metapelites (outcrop 12-SJ-49, Fig. 4-1) and original whole-rock geochemical data of its leucosome, mesosome and melanosome that will be compared to the PGD (Table 4-1). Allanite-bearing and monazite-bearing steep-dipping PGD from the central Grenville Province share similar structural, textural, geochemical, mineralogical (exception is the LREE-bearing phase, Turlin et al., 2017), isotopic (Lu-Hf-O isotopes of zircon grains) signatures and crystallization ages (chapter 3). Accordingly, they are derived from similar sources/processes. Therefore, we will focus this study on one monazite-bearing PGD (outcrop 13-AM-13) that displays the widest facies variability (Figs. 4-4, 4-5, Table 4-1). From this PGD we report original trace element compositions from the major silicate phases and whole-rock geochemistry of every identified facies. These data, together with those of the potential source, allow to discuss the relative contribution of the partial melting and fractionated crystallization in the genesis of these LREE-occurrences.

2. Geological framework

The continent-continent collision designated as the Grenvillian Orogeny (1090-960 Ma) followed a protracted period of tectonomagmatic accretion to the southeastern margin of Laurentia from the late-Paleoproterozoic to the late-Mesoproterozoic (e.g. Carr et al., 2000; Dunning and Indares, 2010; Ketchum et al., 1994; Rivers, 1997; Rivers et al., 2012; Tucker and Gower, 1994).

Two tectonometamorphic domains compose the Grenville Province, namely the (i) Allochthonous Belt that consists of terranes that originated outboard of, and were accreted to the southeastern Laurentia margin during the Grenvillian Orogeny, and the (ii) Parautochthonous Belt that corresponds to the basement and cover of the Superior Province reworked during the Grenvillian Orogeny (Rivers et al., 1989, 2012). They are separated by the southeast-dipping orogen-scale high-grade shear zone designated as the Allochthon Boundary Thrust (ABT). Both domains are inferred to record the Grenvillian Orogeny as two spatially and temporally disconnected phases. The Allochthonous Belt, hosting the PGD investigated in this study and designated as aM-L*P*, south of the Manicouagan Reservoir (Fig. 4-1), reached a high-grade peak of metamorphism up to granulite-facies conditions (950 MPa and 850 °C) dated at ca. 1070-1050 Ma attributed to the Ottawan tectonic phase (Dunning and Indares, 2010;

Lasalle et al., 2014; Lasalle and Indares, 2014; Turlin et al., submitted). It is characterized by the development of a hot ductile crust above the ABT and underneath an orogenic plateau (e.g. Indares et al., 2000; Rivers, 1997, 2008; Rivers et al., 2012).

The late- to post-Ottawan (ca. 1050-1020 Ma) collapse of the plateau is inferred to have resulted in the reworking of the northwest-directed ABT as a top-to-the-southeast normal-sense shear zone (Allochthonous Boundary Detachment, ABD) (e.g. Busch et al., 1996; Carr et al., 2000; Corrigan and van Breemen, 1997; Rivers, 2012). This extensional setting would have resulted in the formation of a crustal-scale horsts and grabens architecture, the latter being occupied by the Orogenic Lid and the former by the aM-L*P* crustal segments, and by subhorizontal normal-sense flow of mid-crustal levels following the Ottawan peak of metamorphism (Culshaw et al., 1994; Ketchum et al., 1998; Rivers, 2008, 2012). In the central Grenville Province, protracted suprasolidus conditions were recorded down to the intrusion timing of the PGD at ca. 1005-1000 Ma (Turlin et al., submitted). Subsequent subsolidus cooling under the 450-500°C isotherm are recorded down to ca. 960 Ma (Turlin et al., submitted).

The Parautochthonous Belt, represented by the mid-pressure parautochthonous crustal segment of the central Grenville (pM*P*, Fig. 4-1), recorded a high-grade peak of metamorphism up to granulite-facies conditions (ca. 1250-1500 MPa and ca. 815-850 °C) dated at ca. 1005-960 Ma attributed to the Rigolet tectonic phase (Jannin et al., accepted; Jordan et al., 2006). Previous work by Jannin et al. (accepted) on the migmatitic paragneisses from the Knob Lake Group sampled for this study (Gagnon Terrane, Fig. 4-1) document syntectonic partial melting initiated at ca. 1002 Ma recorded in metamorphic zircon rims showing HREE-depletion and no negative Eu anomaly, suggesting they grew in presence of peritectic garnet and in the absence of plagioclase. This partial melting is attributed to dehydration melting of muscovite (Ms + Qtz + Pl → Kfs + Al_2SiO_5 + Liq.), and dehydration melting of biotite (Bt + Al_2SiO_5 + Qtz → Kfs + Grt + Liq.), both in the kyanite stability field. The retrograde *P-T* path is recorded in the sillimanite stability field most probably down to ca. 961 Ma (Jannin et al., accepted). This Rigolet phase is interpreted as the foreland-ward propagation of the Grenvillian high-grade metamorphism and thrusting towards the Grenville Front, a syn-Rigolet southeast-dipping orogen-scale high-grade shear zone (Krogh, 1994; Rivers et al., 1989; Rivers, 2008, 2009).

The LREE-rich PGD described by Turlin et al. (2017) intruded into the aM-L*P* segment of the central Grenville Province at ca. 1005-1000 Ma were derived by the partial melting of Paleoproterozoic-Archean metasedimentary units either belonging to the Knob Lake Group metapelites (Gagnon Terrane, Parautochthonous Belt, Fig. 4-1) and/or to the Plus-Value Complex paragneisses (Allochthonous Belt, Fig. 4-1). Pre-Grenvillian metamorphic events of the Plus-Value Complex paragneisses are recorded by zircon rims that yielded U-Pb dates at ca. 1.4 Ga and ca. 1.2 Ga (Lasalle et al., 2013). Accordingly, even if these paragneisses could represent a potential source of the LREE-rich PGD, the successive metamorphic events might have reworked inherited REE concentrations from the Laurentian margin. Therefore, these units do not allow to evaluate the potential contribution of the latter in the genesis of LREE-rich PGD. To the contrary, the metapelites from the Knob Lake Group have inherited U-Pb zircon ages older than ca. 1870 Ma (Moukhsil et al., 2013) and recorded a single pre-Grenvillian metamorphic event at ca. 1740 Ma (U-Pb on monazite, Jordan et al., 2006) that did not reach suprasolidus conditions (Jannin et al., accepted). They were metamorphosed up to partial melting conditions as early as ca. 1002 Ma (Jannin et al., accepted; Jordan et al., 2006). Accordingly, favorable conditions for the partial melting of the Knob Lake Group metapelites were reached by the time of PGD intrusion and they represent a suitable proxy to estimate the potential contribution of Laurentia to LREE-rich PGD.

3. Sampling and analytical methods

3.1. Sampling

The metapelites of the Knob Lake Group were sampled in 2016 on the 12-SJ-49 outcrop close to the ABT (Fig. 4-1). Its present coordinates are reported in Table 4-1. Representative hand-samples of the leucosome (sample 12-SJ-49-A) and melanosome (sample 12-SJ-49-D) were collected for petrography. Sampling was completed by a hand-sample of the mesosome (sample 12-SJ-49-C) for whole-rock geochemistry (Table 4-1).

The monazite-bearing PGD was sampled in 2014 and 2016 on the 13-AM-13 outcrop (Turlin et al., 2017). It is hosted in paragneisses from the Plus-Value Complex of the Allochthonous Belt (Fig. 4-1). Its present coordinates are reported in Table 4-1. Representative and large hand-samples of each facies were collected for petrography and whole-rock geochemistry, allowing to obtain reliable data of a pegmatitic granite dyke (Fig. 4-4, Table 4-1).

3.2. Electron microprobe (EMP)

Major and trace elements were carried out on EMP using a Cameca computer-controlled SX-100 at GeoRessources (Nancy, France) equipped with the wavelength spectrometer (WDS). Quantitative analyses of silicates (plagioclase, K-feldspar, dark micas, garnet) were performed using an accelerating voltage of 15 kV, a beam current of 12 nA and a peak counting time of 10s/per element (Si, Ti, Al, Cr, Fe, Mn, Mg, Ca, Na, K). Results are reported in Table 4-2 for plagioclase analyses, in Table 4-3 for K-feldspar analyses, in Table 4-4 for dark micas analyses, and in Table 4-5 for garnet analyses.

For quantitative analyses of monazite from the various facies of the monazite-bearing pegmatitic granite dyke, major and trace elements (Si, P, Ca, Y, La, Ce, Pr, Nd, Sm, Gd, Pb, Th, U) were measured using an accelerating voltage of 20 kV and a beam current of 100 nA. Peak counting time was set to 120 s for Pb, 100 s for U and 20 s for the others elements. Results are reported in Table 4-6.

3.3. Trace elements analyses of minerals using laser ablation-inductively coupled plasma-mass spectrometry (LA-ICP-MS)

Analyses were carried out at GeoRessources (Nancy, France) using a LA-ICP-MS (laser ablation inductively coupled plasma mass spectrometry) system composed of a GeoLas excimer laser (ArF, 193 nm, Microlas) coupled to a conventional transmitted and reflected light microscope (Olympus BX51) for sample observation and laser beam focusing onto the sample, and an Agilent 7500c quadrupole ICP-MS, with a fluence of 0.4 $J.cm^{-2}$ and a pulse rate of 5 Hz. The products of the ablation were conveyed by a mixing gas with He (541 mL/min) and Ar (0.93 mL/L) into the ICP-MS.

Rubidium content of K-feldspar and Rb, Nb and Ta of dark micas from the various facies of the monazite-bearing PGD and from the leucosome of the Knob Lake Group metapelites (Parautochthonous Belt) were performed as a profile of 180 µm long with a 120 µm laser spot size. External standard used was a NIST610 silicate glass and K (wt.%) obtained using EMP was used as internal standard. For each analysis, acquisition time was 0.01 s for ^{39}K and 0.02 s for others elements. Results of K-feldspar and dark micas analyses are reported in Tables 4-7 and 4-8 respectively.

Rare-earth elements, Y, Th and U contents of monazite from the various facies of the monazite-bearing PGD were performed as single spots with a spot size of 16 µm. The external

standard used was a NIST610 silicate glass and La (wt.%) obtained using EMP was used as internal standard. For each analysis, acquisition time was 0.02 s for all elements. Results of monazite analyses are reported in Table 4-9.

3.4. Whole-rock geochemistry

Migmatitic paragneisses from the Knob Lake Group were carefully split into leucosome, mesosome and melanosome (samples 12-SJ-49-A, -C and –D, respectively). They were crushed in a jaw and in a roller crusher. Powdered samples were prepared by Li-metaborate and acid solution. Major elements were analyzed by ICP-OES (inductively coupled plasma – optical emission spectrometry) and traces elements by ICP-MS (inductively coupled plasma – mass spectrometry) at the Service d'Analyses des Roches et des Minéraux (SARM, CRPG, Nancy). Results are reported in Table 4-10.

Whole-rock geochemistry of the various facies of the monazite-bearing PGD (samples 13-AM-13-E, -A5, -A4, -A6, -A1 and -F, respectively) was performed by Actlabs (Ancaster, Ontario). Powdered samples were prepared by Li-metaborate or -tetraborate. Major elements were analyzed by inductively coupled plasma - atomic emission spectroscopy (ICP‑AES), and trace elements by inductively coupled plasma - mass spectrometry (ICP‑MS). Results are reported in Table 4-10. In the present contribution, we report original geochemical data for samples 13-AM-13- A5, -A4, -A6, -A1 and -F and we include the 13-AM-13-E analysis from Turlin et al. (2017) (Tables 4-1 and 4-10).

4. Sample descriptions and petrography

4.1. Knob Lake Group metapelites (Parautochthonous Belt)

The metapelites of the Knob Lake Group correspond to a wide flat-lying outcrop of migmatitic paragneisses which foliation is underlined by centimetric leucosomes-mesosomes alternations locally associated with melanosomes (Fig. 4-2a-b). The leucosomes are dominated by a coarse-grained (up to 5 mm) quartz+plagioclase+K-feldspar (Fig. 4-2c) assemblage with minor biotite and garnet. They have a magmatic texture with no evidence for solid state deformation (Fig. 4-2b-c). The mesosomes are characterized by a finer grained (below 1.5 mm) quartz+plagioclase+K-feldspar+dark micas+garnet assemblage with a foliation delineated by the (001) dark micas cleavage planes (Fig. 4-2b and d). The melanosomes are dominated by a fine grained (in general below 1 mm) assemblage of dark micas+garnet with minor plagioclase, quartz (Fig. 4-2e) and Ti-oxides. The dark micas are found in two positions as marked by (001)

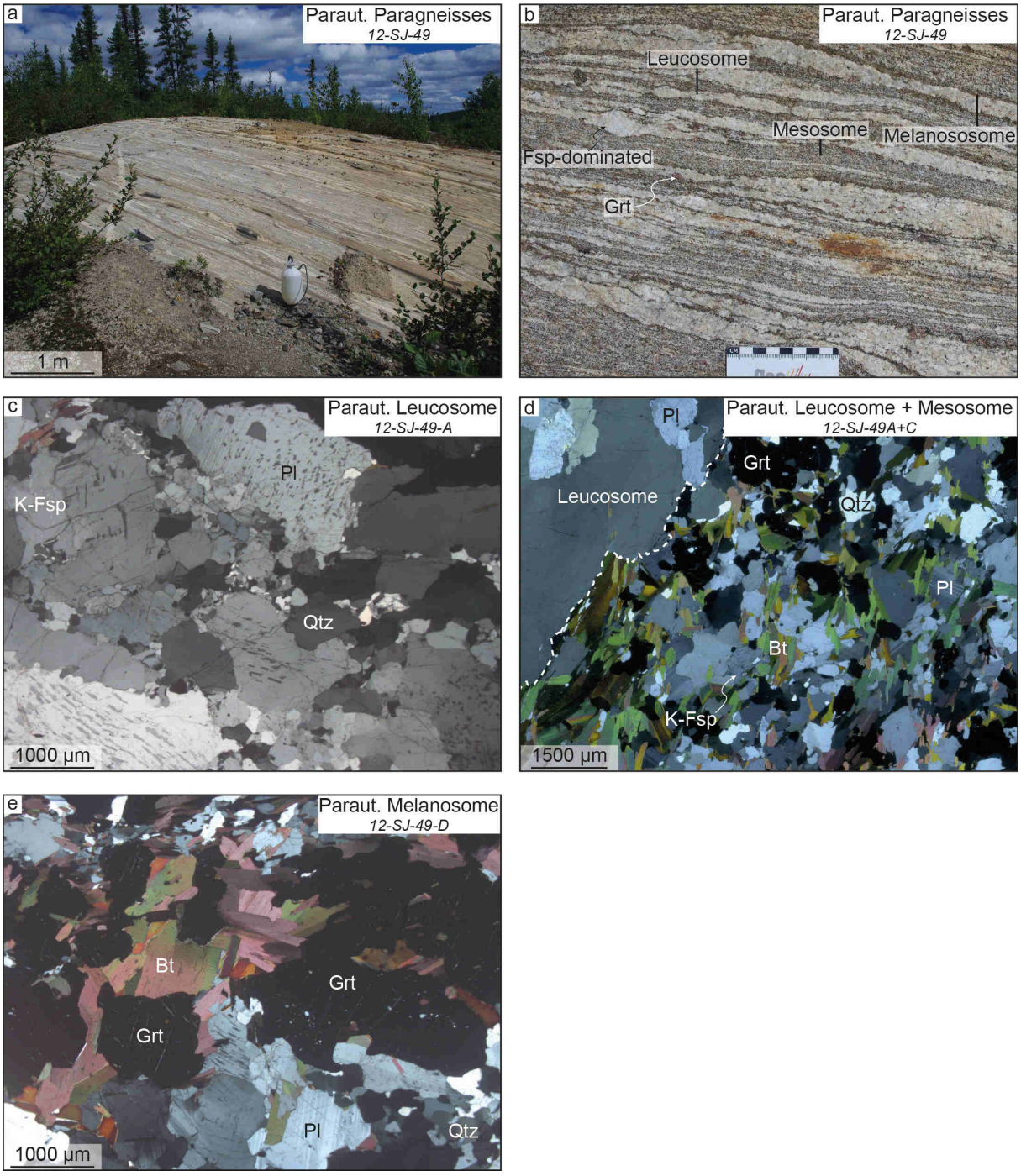

Figure 4-2: Photographs and photomicrographs of the outcrop of the Knob Lake Group migmatitic metapelites and of its typical petrography. a: general view of the outcrop; b: detailed view of the migmatitic metapelites. The foliation is underlined by centimetric leucosomes with a magmatic texture and by thin melanosomes; c: typical petrography of the leucosome of the migmatitic metapelites (polarized and analyzed light). Note the magmatic texture and the lack of solid state deformation that provide evidence for its formation during the last metamorphic event recorded in this part of the Parautochthonous Belt (polarized and analyzed light); d: typical petrography of the mesosome of the migmatitic metapelites and its relationships with the leucosome (polarized and analyzed light); e: typical petrography of the melanosome (polarized and analyzed light) leucosome of the migmatitic metapelites (polarized and analyzed light). Note the unwrapped garnet porphyroblasts. Abbreviations: Bt = biotite; Grt = garnet; K-Fsp = K-feldspar; Paraut. = Parautochthonous Belt; Pl = plagioclase; Qtz = quartz.

cleavage planes either underlining or oblique to the foliation (Fig. 4-2e). Garnet are commonly in equilibrium with K-feldspar and can reach a size up to 5 mm (Fig. 4-3c). They are not

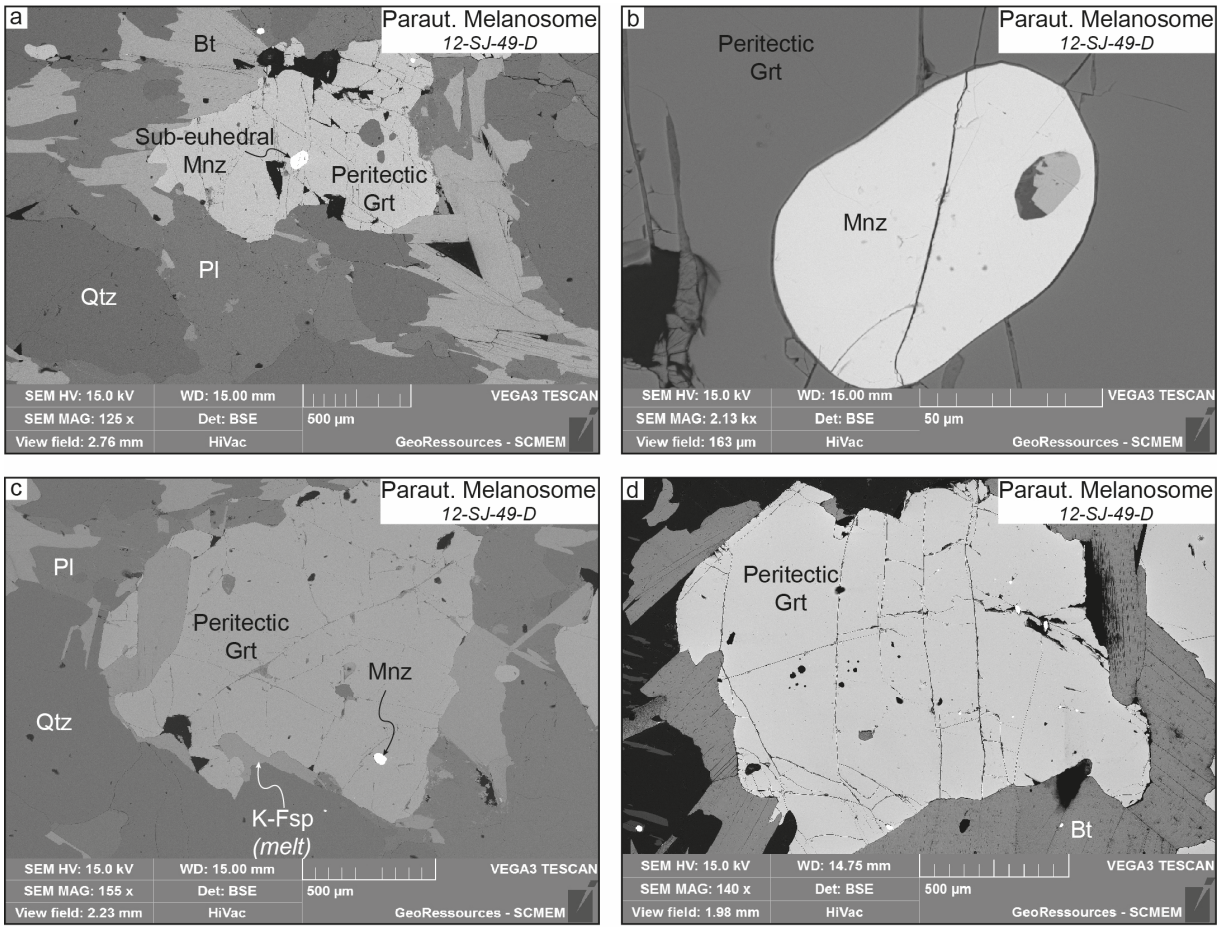

Figure 4-3: Petrographic characteristics of garnet from the melanosome of the Knob Lake Group metapelites and its relationships with monazite. a: inclusion of monazite in a peritectic garnet from the melanosome of the paragneisses (SEM); b: sub-euhedral monazite crystal enclosed within a peritectic garnet with no corrosion nor dissolution/reprecipitation textures (SEM); c: garnet unwrapped in the migmatitic foliation and in equilibrium with K-feldspar that indicates its peritectic origin in response to the biotite dehydration melting (SEM). Note the inclusion of monazite hosting the LREE of the melanosome (see text for details); d: unzoned peritectic garnet grain (SEM). Abbreviations: Bt = biotite; Grt = garnet; K-Fsp = K-feldspar; Mnz = monazite; Paraut. = Parautochthonous Belt; Pl = plagioclase; Qtz = quartz.

wrapped by the migmatitic foliation (Fig. 4-3a, c-d) and contain inclusions of dark micas, quartz, plagioclase, Fe-sulfides, zircon and sub-euhedral monazite, the size of latter can reach 200 µm (Fig. 4-3a-c).

All minerals of the leucosomes show homogeneous compositions (Tables 4-2 to 4-5). Plagioclase are albite-rich (X_{Ab} = 0.75, X_{An} = 0.23, X_{Or} = 0.02, Table 4-2), K-feldspar are microcline (X_{Or} = 0.87, X_{Ab} = 0.12, X_{An} = 0.01, Table 4-3), dark micas are typically biotite (X_{Mg} = 0.59, Table 4-4) and garnet are dominated by an almandine composition (X_{Alm} = 0.63, X_{Prp} = 0.22, X_{Grs} = 0.07, X_{Sps} = 0.02, Table 4-5). K-feldspar have K and Rb contents ranging between 124,250 and 128,150 ppm, and between 8.2 and 24.4 ppm, respectively, with associated K/Rb between 5,109 and 15,622 (Fig. 4-6b, Table 4-7). Biotite have K, Rb, Nb and Ta contents ranging between 80,600 and 84,150 ppm, 509 and 561 ppm, 65 and 80 ppm, and 4.47 and 6.69

ppm, respectively, with associated K/Rb and Nb/Ta ratios between 144 and 161 and 12 and 15, respectively (Fig. 4-6c-e, Table 4-8).

Dark micas from the melanosome in both textural positions have homogeneous biotite compositions (X_{Mg} = 0.59, Table 4-4). Garnet compositions are dominated by almandine end-member (X_{Alm} = 0.58, X_{Prp} = 0.21, X_{Grs} = 0.06, X_{Sps} = 0.02, Table 4-5). Plagioclase are albite-rich (X_{Ab} = 0.76, X_{An} = 0.22, X_{Or} = 0.02, Table 4-2).

4.2. Monazite-bearing PGD (Allochthonous Belt)

The monazite-bearing PGD is a flat lying outcrop composed of several showings of PGD dominated by a quartz+K-feldspar+plagioclase assemblage. Several facies were identified (Fig. 4-4, Turlin et al., 2017). They all have a magmatic textures with no evidence for solid state deformation (Fig. 4-5) and are dominated by a quartz+K-feldpsar+plagioclase assemblage completed with various amounts of dark micas and accessory minerals depending on the grain size.

The fine grained facies (1 mm to locally over 1 cm) are the ones showing the highest concentration of dark micas, monazite and zircon (sample 13-AM-13-E, Table 4-1) (Fig. 4-5g). Minor garnet may complete this petrographic assemblage (sample 13-AM-13-A5, Table 4-1). In fine grained facies, dark micas may present corroded textures (Fig. 4-5g). Other facies show increasing grain size and decreasing amounts of dark micas, monazite and zircon (Fig. 4-5b-f). They range from (i) an intermediate facies with more (sample 13-AM-13-A4) or less (sample 13-AM-13-A6) dark micas completed with disseminated monazite and zircon, to (ii) a coarse grained facies with minor dark micas, monazite and zircon (sample 13-AM-13-A1), and to (iii) a pegmatitic (some grains over 5 cm) facies with scarce biotite and even rarer monazite and zircon (sample 13-AM-13-F) (Fig. 4-5h).

In the whole PGD, plagioclase are albite-rich (X_{Ab} = 0.68-0.70, X_{An} = 0.28-0.31, X_{Or} = 0.01-0.02, Table 4-2) and K-feldspar are microcline (X_{Or} = 0.83-0.87, X_{Ab} = 0.13-0.16, X_{An} = 0.00-0.01, Table 4-3). Dark micas are biotite (X_{Mg} = 0.35-0.42, Table 4-4). K-feldspar have K and Rb contents ranging between 102,800 and 127,500 ppm, and between 6.9 and 109 ppm, with associated K/Rb ratios between 1,150 and 17,417 (Fig. 4-6b, Table 4-7). Biotite have K, Rb, Nb and Ta contents ranging between 60,800 and 82,600 ppm, 196 and 1,183 ppm, 20 and 138 ppm, and between 0.55 and 3.93 ppm, respectively, with associated K/Rb and Nb/Ta ratios

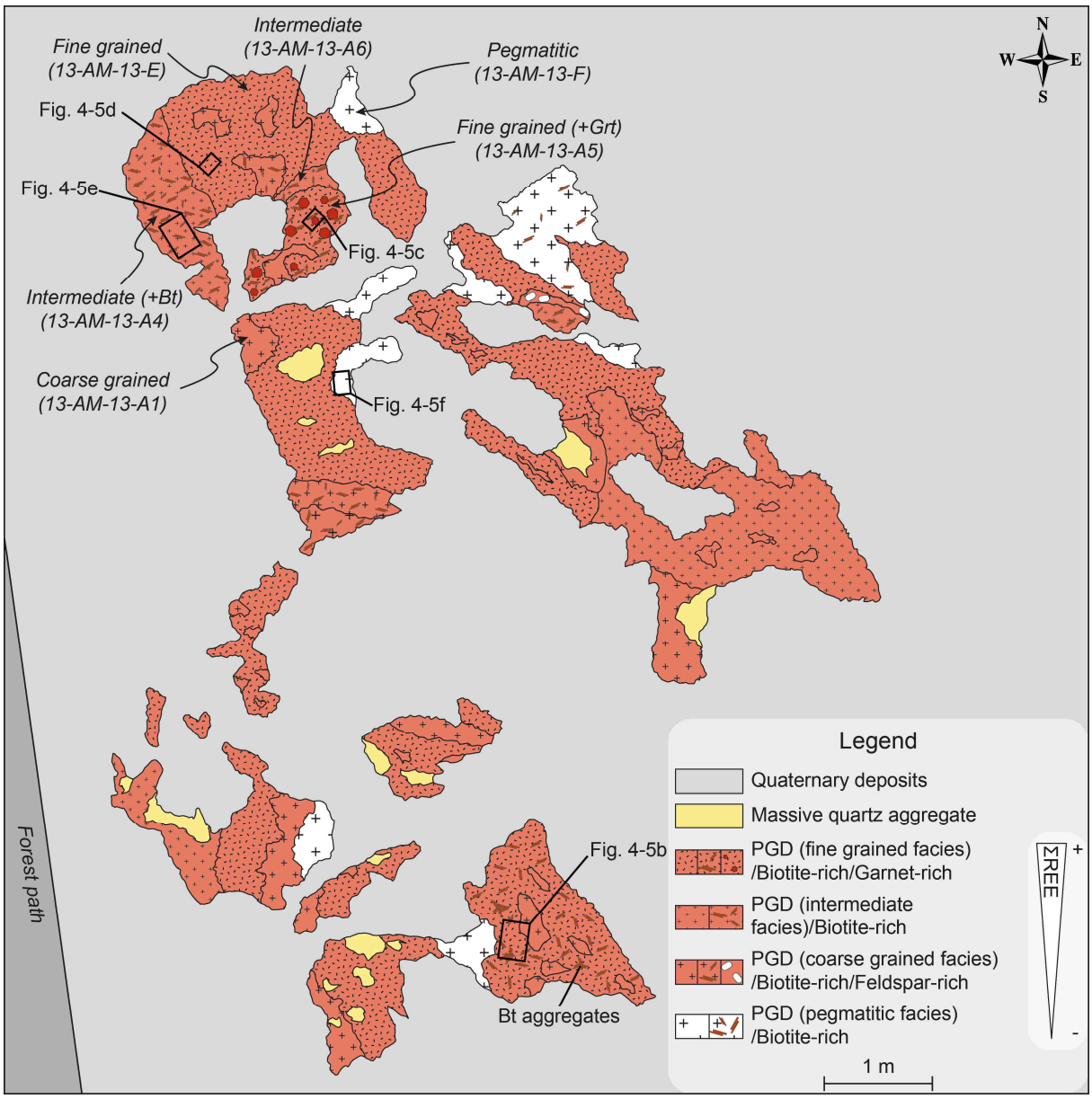

Figure 4-4: Detailed map of the 13-AM-13 outcrop made of a monazite-bearing pegmatitic granite dyke. Dark squares refer to the position of the photographs presented in Fig. 4-5. Abbreviations: Bt = biotite; Grt = garnet; PGD = pegmatitic granite dyke.

between 60 and 413 and between 30 and 53, respectively (Fig. 4-6c-e, Table 4-8). No major nor trace elements chemical variations of these silicates can be linked to the facies variability (Tables 4-2 to 4-4, 4-7 to 4-8).

Monazite from every facies of the PGD are associated with biotite and zircon (Fig. 4-5g). They are hundreds of micrometers to millimetric sub-euhedral grains that show a variety of inner zoning, from complex (Fig. 4-7a) to oscillatory (Fig. 4-7b), the former associated with several rim growths crosscutting previous ones. These textural variations cannot be linked to the facies variability. Monazite show variable compositions within a facies and within a grain as shown by the variable X_{Mnz} ranging between 0.79 and 0.88, X_{Brab} between 0.05 and 0.18,

X_{Hutt} between 0.03 and 0.14 (Table 4-6). These chemical variations are not correlated to a specific type of inner texture of the monazite nor to a particular facies of the dyke (Table 4-6). Chondrite-normalized REE patterns (normalization after McDonough and Sun, 1995) of several monazite inner zones from each facies of the pegmatitic granite are very similar with a strong fractionation of the LREE over the HREE (La_N/Yb_N between 926 and 5,201, mean of 2,351), a slight fractionation within the LREE (La_N/Sm_N between 5 and 12, mean of 8), a significant fractionation within the HREE (Gd_N/Yb_N between 42 and 198, mean of 111), and a strongly negative Eu anomaly (Eu/Eu* between 0.04 and 0.23, mean of 0.07) (Fig. 4-8, Table 4-9).

5. Whole-rock geochemistry

5.1. Knob Lake Group metapelites (Parautochthonous Belt)

The leucosome of the sampled Knob Lake Group metapelites has a granite composition with a high SiO_2 content (74.31 wt.%), and a high Al_2O_3 content (14.11 wt.%) pointing to a strongly peraluminous character marked by an (i) ASI (Fig. 4-9a), (ii) A/CNK, and (iii) A/NK of 1.23, 1.34 and 1.49, respectively (Table 4-10) (Aluminum Saturation Index, ASI = Al/(Ca – 1.67 x P + Na + K) (Frost et al., 2001; Shand, 1943); A/CNK = Al/(Na + K + Ca/2) (Shand, 1943); A/NK = Al/(Na + K) (Shand, 1943). It is associated with low $Fe_2O_{3\ (total)}$ (0.94 wt.%), MgO (0.39 wt.%), K_2O (2.80 wt.%) and P_2O_5 (0.11 wt.%) contents, and moderate CaO (2.36 wt.%) (Table 4-10). It has low contents of Nb (1.4 ppm), Ta (0.1 ppm), Th (0.2 ppm), U (0.3 ppm), Zr (35 ppm), Hf (1.0 ppm) and Y (4.6 ppm), and a low Nb/Ta ratio (11, Fig. 4-9b, Table 4-10).

The melanosome of the sampled Knob Lake Group metapelites has a low SiO_2 content (53.95 wt.%) and high Al_2O_3 (17.17 wt.%) (Fig. 4-9a), $Fe_2O_{3\ (total)}$ (11.34 wt.%), MgO (4.87 wt.%), K_2O (4.12 wt.%) and P_2O_5 (0.21 wt.%) contents (Table 4-10). It is associated with a low Na_2O (2.57 wt.%) content (Table 4-10). It has high contents of Nb (16 ppm), Th (15 ppm), Zr (217 ppm), Hf (5.8 ppm) and Y (41 ppm) and moderate contents of Ta (0.8 ppm), U (1.9 ppm), and a low Nb/Ta ratio (11, Fig. 4-9b, Table 4-10).

The mesosome of the sampled Knob Lake Group metapelites has a high Al_2O_3 content (14.81 wt.%) and intermediate SiO_2 (66.48 wt.%, Fig. 4-9a), $Fe_2O_{3\ (total)}$ (5.80 wt.%), MgO (2.47 wt.%), K_2O (1.60 wt.%), P_2O_5 (0.18 wt.%) and Na_2O (3.39 wt.%), Nb (9.0 ppm), Th (7.1 ppm), Zr (132 ppm), Hf (3.5 ppm), Y (20 ppm), Ta (0.7 ppm) and U (1.7 ppm) contents, associated with a low Nb/Ta ratio (12, Fig. 4-9b, Table 4-10).

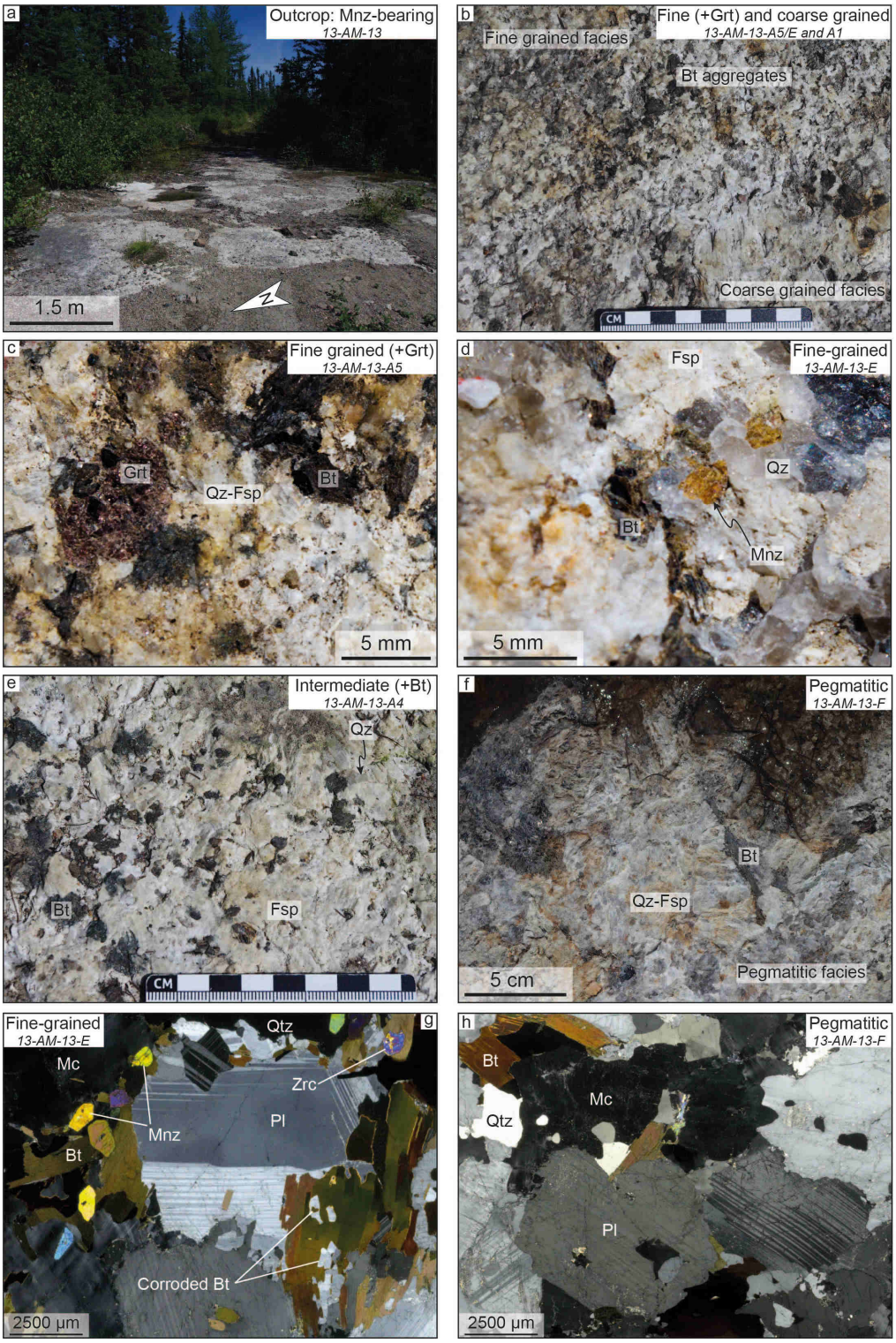

Figure 4-5: Photographs and photomicrographs of the outcrop of monazite-bearing pegmatitic granite dyke and of its petrographic variability. a: general view of the 13-AM-13 outcrop composed of a monazite-bearing pegmatitic granite; b: detail of the fine and coarse grained facies. Note that the abundance of biotite in the fine grained facies on this photograph is related to the vicinity of the coarse grained facies; c: detailed view of a garnet phenocryst in the fine grained facies; d: monazite crystals from the fine grained facies; e: typical intermediate facies composed of a quartz-feldspar-biotite assemblage; f: typical pegmatitic facies essentially composed of a quartz-feldspar-biotite assemblage in which feldspar and biotite crystals can reach over 5 cm; g: typical petrography of the fine grained facies of the pegmatitic granite (polarized and analyzed light). Note the abundance of millimetric monazite grains, the presence of zircon, and the local corroded texture of biotite; h: typical petrography of the pegmatitic facies of the pegmatitic granite (polarized and analyzed light). Note the general lack of accessory minerals. Abbreviations: Bt = biotite; Grt = garnet; K-Fsp = K-feldspar; Mnz = monazite; Paraut. = Parautochthonous Belt; Pl = plagioclase; Qtz = quartz.

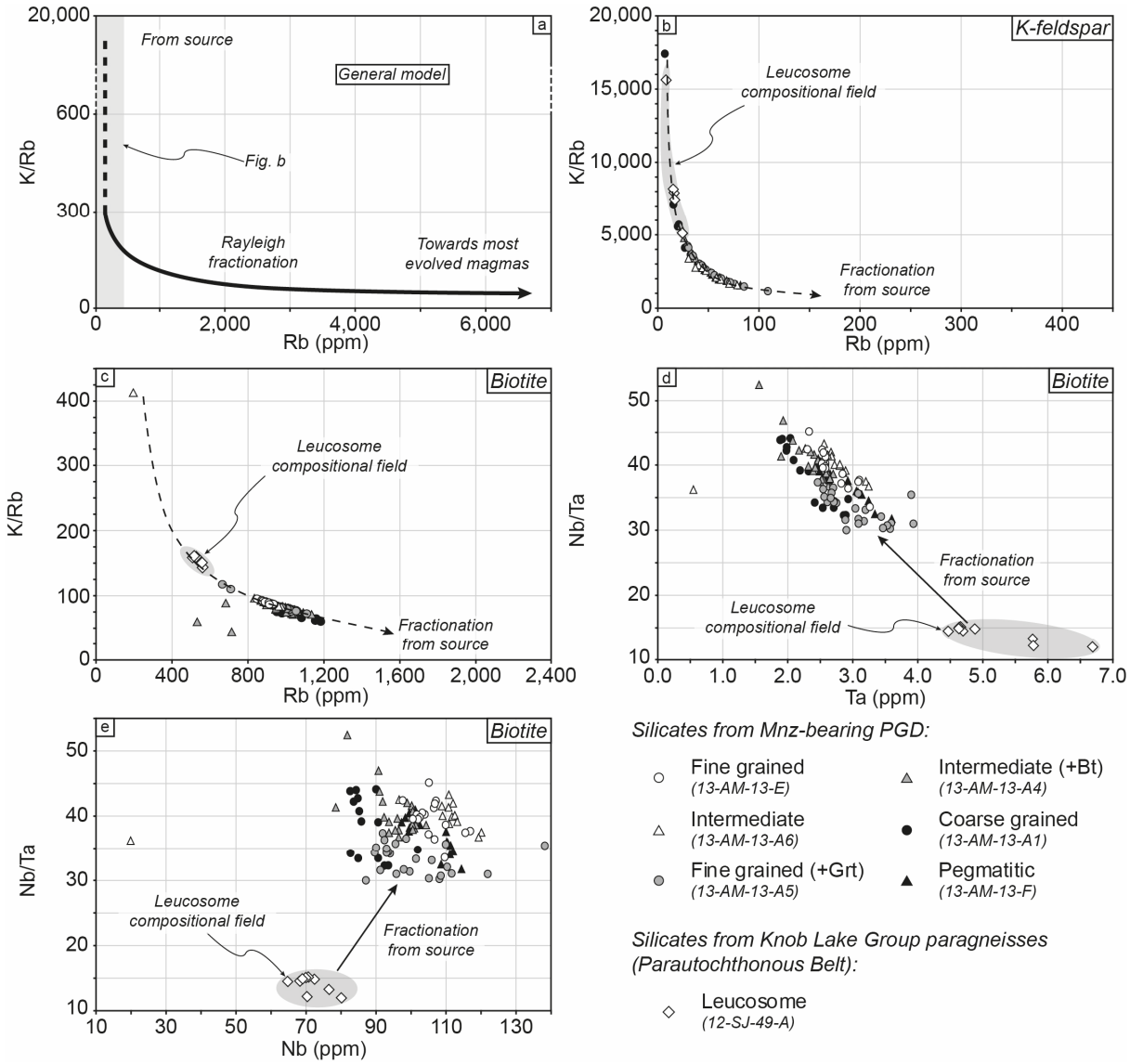

Figure 4-6: Trace element compositions of K-feldspar and biotite of the various facies of the monazite-bearing pegmatitic granite dyke and of the leucosome of the Knob Lake Group metapelites. a: general model of Rayleigh fractionation of alkali metals in K-feldspar through melt fractionation from a source towards most evolved pegmatitic magmas (adapted from Hulsbosch et al., 2014); b: K/Rb vs Rb (ppm) diagram of K-feldspar. Note the little fractionated character of all investigated K-feldspar compared to the model of Hulsbosch et al. (2014) and that K-feldspar from the leucosome show a slightly lower fractionation compared to those from the dyke. No correlation between these fractionations and a specific facies of the latter can be outlined; c: K/Rb vs Rb (ppm) diagram of biotite. Similar features to K-feldspar are observed; d-e: Nb/Ta vs Nb (ppm) and Nb/Ta vs Ta (ppm) diagrams of biotite. Biotite from the leucosomes show a lower Nb/Ta ratio than those from the dyke, that is associated with lower Nb and higher Ta contents, consistent with the magmatic fractionation of the dyke from the partial melting of a metapelitic source (see text for details). Abbreviation: Bt = biotite; Fsp = feldspar; Grt = garnet; Mnz-bearing PGD = monazite-bearing pegmatitic granite dyke.

The leucosome and the melanosome have contrasting REE contents. The leucosome is impoverished in REE with a ΣREE content of 39 ppm, and the melanosome is enriched with a ΣREE content of 232 ppm (Fig. 4-9c-d, f-h, Table 4-10). For both lithologies, the chondrite-normalized REE patterns are similarly fractionated in LREE over HREE (La_N/Yb_N of 3.4, Fig. 4-9e-f) with no fractionation within the LREE (La_N/Sm_N of 1.1, Fig. 4-9f-h) and a slight one within the HREE (Gd_N/Yb_N of 2.7) (Fig. 4-9f-h, Table 4-10). The leucosome pattern is

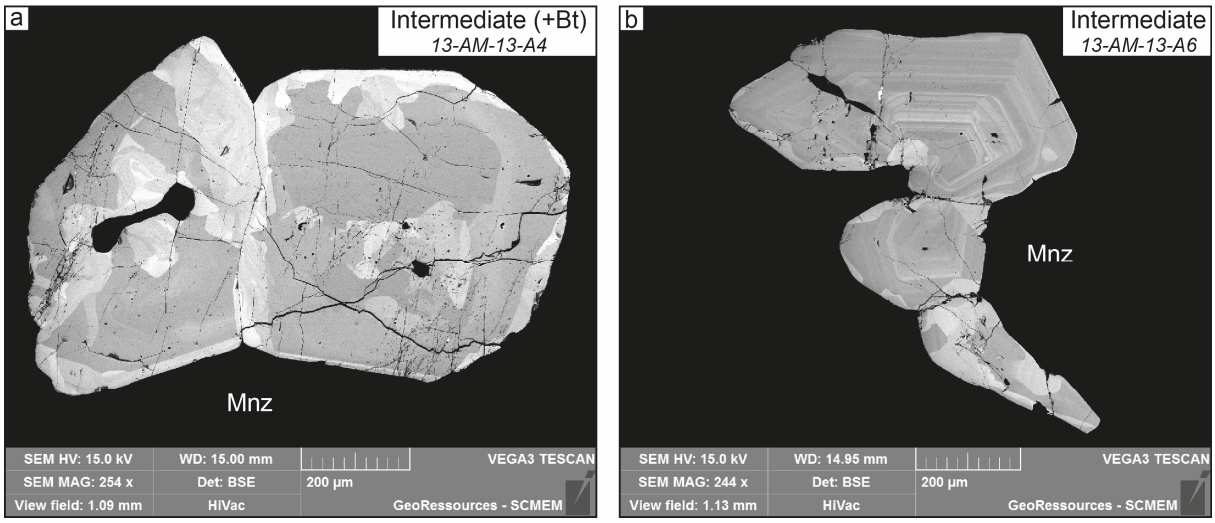

Figure 4-7: Variability of the inner textures of monazite grains from monazite-bearing pegmatitic granite dyke from the Lac Okaopéo region. a: monazite grains showing a complex zoning with several rims crosscutting the previous ones, suggesting a dynamic magmatic environment (SEM); b: oscillatory zoned monazite grains suggesting progressive and regular crystallization (SEM). Abbreviation: Mnz = monazite.

characterized by a strongly positive Eu anomaly (Eu/Eu* of 3.2) and the one of the melanosome by a negative Eu anomaly (Eu/Eu* of 0.5) (Fig. 4-9d-f, Table 4-10). The mesosome has a ΣREE content of 119 ppm and a chondrite-normalized REE pattern intermediate between the leucosome and the melanosome (Fig. 4-9f-h, Table 4-10).

5.2. Monazite-bearing PGD (Allochthonous Belt)

All facies of the monazite-bearing PGD from the Allochthonous Belt have granitic composition with high SiO_2 content (66.11-73.08 wt.%, Fig. 4-9a) to the exception of the fine grained facies showing a lower SiO_2 content (60.24 wt.%) (Table 4-10). They all are characterized by a peraluminous character as shown by their (i) ASI (Fig. 4-9c), (ii) A/CNK, and (iii) A/NK of 1.12-1.36, 1.12-1.46 and 1.16-1.64, respectively (Table 4-10). The peraluminous character tends to decrease from the fine grained towards the pegmatitic facies together with the $Fe_2O_{3\ (total)}$ (4.60-1.04 wt.%), CaO (3.10-0.86 wt.%) and Na_2O (3.10-0.86 wt.%) contents (Table 4-10). Its decrease is also positively correlated with Th (1,300-118 ppm), U (19-2.5 ppm), Y (53-12 ppm) and with the REE (ΣREE from 7,048-721 ppm, Fig. 4-9c) (Table 4-10). Variations in the K_2O (3.71-8.96 wt.%) and P_2O_5 (0.11-0.40 wt.%) along with high Zr (135-1,480 ppm) and Hf (3.6-60 ppm), and low Nb (4.6-21 ppm) and Ta (0.1-0.4 ppm, Fig. 4-6a) contents cannot be correlated to facies variability, even if high contents are generally recorded in the most enriched facies (Table 4-10). Similarly, all facies have a high Nb/Ta ratio between 40 and 53 (Fig. 4-9b, Table 4-10).

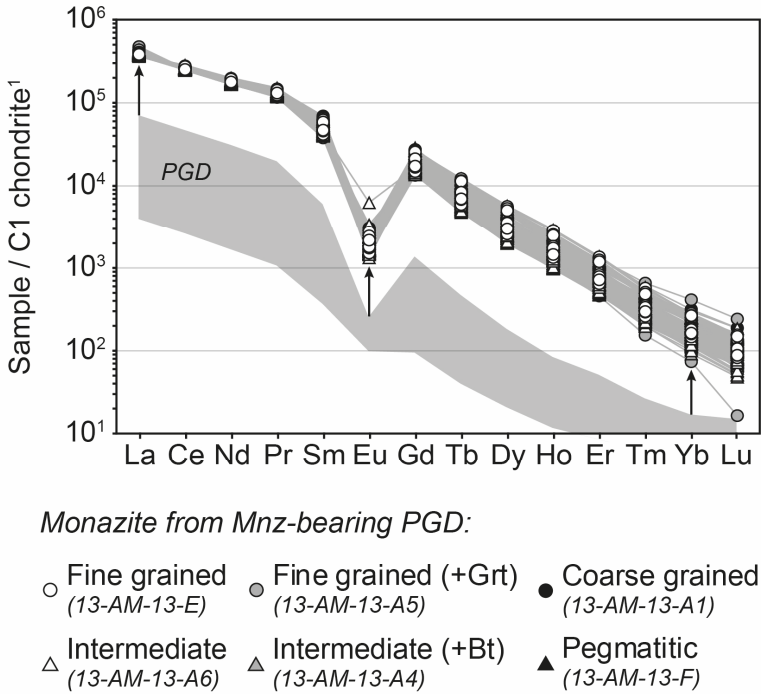

Figure 4-8: Chondrite-normalized REE patterns of monazite grains from the various facies of the monazite-bearing pegmatitic granite dyke from the Lac Okaopéo region. Note the homogeneity of the patterns within all investigated monazite grains and the similar shape compared to patterns of the pegmatitic granite, consistent with the presence of monazite as the sole LREE-bearing phase of the dyke. Abbreviations: [1]: normalization after McDonough and Sun (1995); Bt = biotite; Grt = garnet; Mnz-bearing = monazite-bearing pegmatitic granite dyke; PGD = pegmatitic granite dyke.

The chondrite-normalized and the REE-poorest pegmatitic facies-normalized patterns (Fig. 4-9f-h) show the increasing fractionation of the LREE over the HREE (La_N/Yb_N from 223 to 1,193) and Eu negative anomaly (Eu/Eu* from 0.6 to 0.1, Fig. 4-9d-f) with increasing ΣREE content (Table 4-10). No fractionation within the LREE is recorded with increasing ΣREE content (La_N/Sm_N between 6.8 and 7.2) (Fig. 4-9f-h, Table 4-10). A fractionation within the HREE is noticed (Gd_N/Yb_N between 11 and 54) but cannot be correlated to the facies variability (Fig. 4-9f-h, Table 4-10).

6. Discussion

6.1. The Knob Lake Group metapelites: a fertile protolith

The LREE content of an anatectic melt derived from the partial melting of metapelites is dependent on several factors including (i) the complete (and incomplete) dissolution of LREE-bearing phases (i.e. monazite, allanite; Spear, 2010) during partial melting and their entrainment in the produced melt, and (ii) the bulk-rock concentration of the protolith (e.g. Yakymchuk and Brown, 2014).

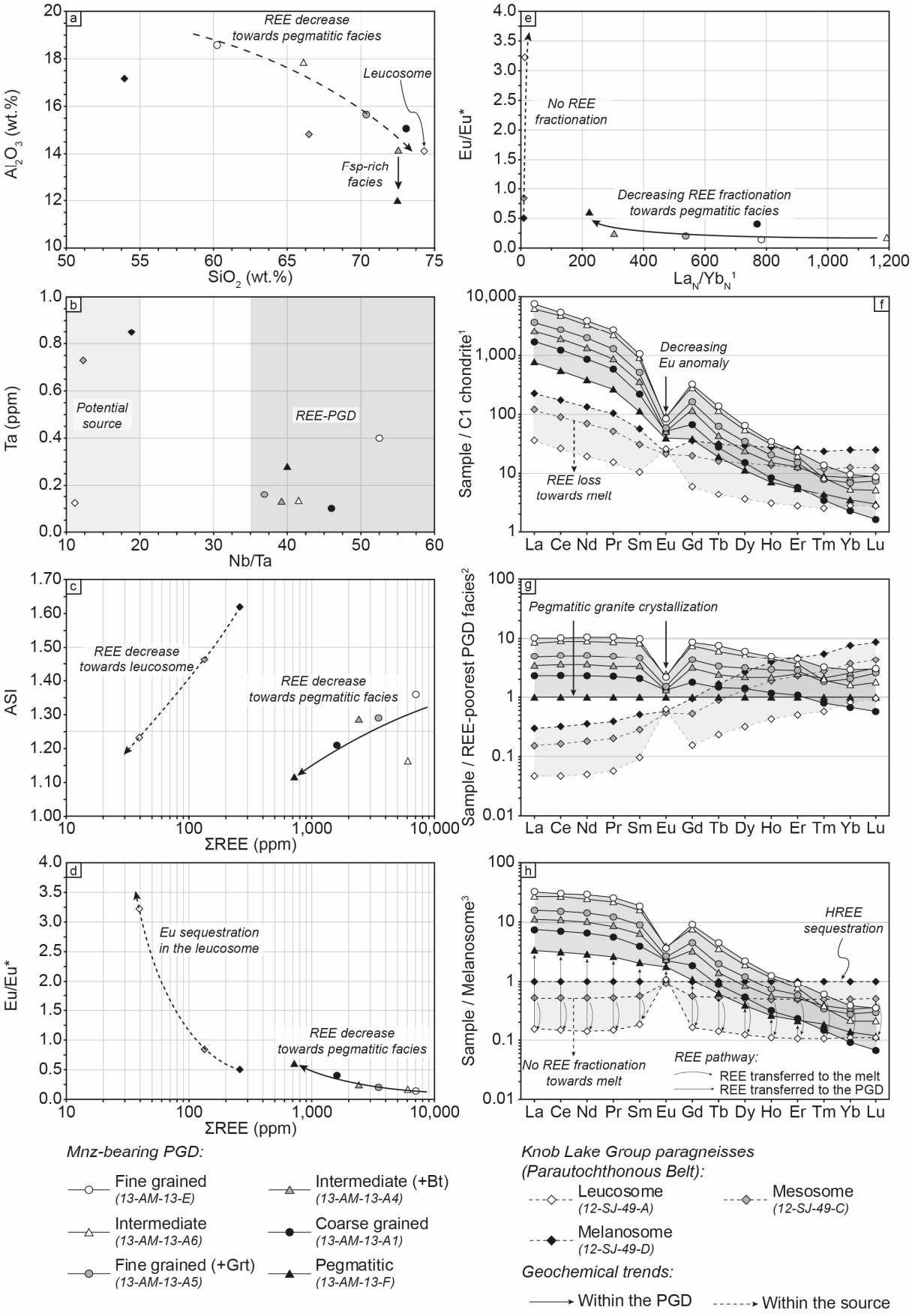
a
REE decrease towards pegmatitic facies
Leucosome
F-sp-rich facies
Al2O3 (wt.%)
SiO2 (wt.%)
b
Potential source
REE-PGD
Ta (ppm)
Nb/Ta
c
REE decrease towards leucosome
REE decrease towards pegmatitic facies
ASI
ΣREE (ppm)
d
Eu sequestration in the leucosome
REE decrease towards pegmatitic facies
Eu/Eu*
ΣREE (ppm)
e
No REE fractionation
Decreasing REE fractionation towards pegmatitic facies
Eu/Eu*
LaN/YbN1
f
Decreasing Eu anomaly
REE loss towards melt
Sample / C1 chondrite1
La Ce Nd Pr Sm Eu Gd Tb Dy Ho Er Tm Yb Lu
g
Pegmatitic granite crystallization
Sample / REE-poorest PGD facies2
La Ce Nd Pr Sm Eu Gd Tb Dy Ho Er Tm Yb Lu
h
HREE sequestration
No REE fractionation towards melt
REE pathway:
REE transferred to the melt
REE transferred to the PGD
Sample / Melanosome3
La Ce Nd Pr Sm Eu Gd Tb Dy Ho Er Tm Yb Lu
Mnz-bearing PGD:
Fine grained (13-AM-13-E)
Intermediate (+Bt) (13-AM-13-A4)
Intermediate (13-AM-13-A6)
Coarse grained (13-AM-13-A1)
Fine grained (+Grt) (13-AM-13-A5)
Pegmatitic (13-AM-13-F)
Knob Lake Group paragneisses (Parautochthonous Belt):
Leucosome (12-SJ-49-A)
Mesosome (12-SJ-49-C)
Melanosome (12-SJ-49-D)
Geochemical trends:
Within the PGD
Within the source

Rapp and Watson (1986) showed that for a typical hydrous melt (1-6 wt.% H_2O) at ca. 800-850 °C, complete dissolution of monazite grains (5-50 µm) is achieved within < 1 ka for water saturated melts and by > 1Ga for large monazite grains in water undersatured melts. Jordan et al. (2006) reported two monazite ages of 1738±5 Ma and 1719±30 Ma for the Knob Lake Group metapelites that they interpreted as inherited ages. However, these ages postdate the > 1870 Ma deposition of these metasediments constrained by the youngest ages obtained on zircon cores (Moukhsil et al., 2013). In the absence of metamorphic rims with ages younger than ca. 1870 Ma (ages of inherited zircon cores) and older than the oldest Grenvillian metamorphic rims, Jannin et al. (accepted) reinterpreted the monazite ages reported by Jordan et al. (2006) to reflect a subsolidus monazite growth. Accordingly, these metapelites did not record partial melting before the Rigolet phase of the Grenvillian Orogeny, suggesting that they potentially preserved a hydrous character prior to their subsequent partial melting. Jannin et al. (accepted) considered that these migmatites correspond to in-situ partial melting on the basis of the presence of melanosomes, of peritectic garnet and of the magmatic texture of the leucosomes. Protracted partial melting is characterized by dehydration melting of muscovite (Ms + Qtz + Pl → Kfs + Al_2SiO_5 + Liq.) at ca. 1250-1500 MPa and ca. 815-850 °C followed by subsequent dehydration melting of biotite (Bt + Al_2SiO_5 + Qtz → Kfs + Grt + Liq.), both in

Figure 4-9: Whole rock geochemistry of the various facies of the monazite-bearing pegmatitic granite dyke compared to signatures of the leucosome, mesosome and melanosome of the Knob Lake Group metapelites. a: Al_2O_3 (wt.%) vs SiO_2 (wt.%) diagram showing the chemical evolution of the various facies of the pegmatitic granite dyke. Note that the leucosome plot on the same trend, at the low Al_2O_3/high SiO_2 content extremity, suggesting the derivation of the dyke from this metasedimentary sequence; b: Ta (ppm) vs Nb/Ta diagram. The leucosome, mesosome and melanosome of the Knob Lake Group metapelites have similar Nb/Ta ratio and Ta contents. Similar features are observed within the pegmatitic granite dyke but with higher Nb/Ta ratios; c: ASI vs ΣREE (ppm) diagram. Note the concurrent decrease of the ΣREE content and the ASI within the pegmatitic granite showing the preferential concentration of the REE in Al-rich facies marked by the concentration of biotite. The ΣREE content and ASI are positively correlated within the metapelites that is consistent with the sequestration of monazite in peritectic garnet in the biotite-rich melanosome; d: Eu/Eu* vs ΣREE (ppm) showing the decrease of the ΣREE content within the pegmatitic granite towards feldspar-dominated pegmatitic facies. The highest REE content in the paragneisses is sequestrated in the melanosome which negative Eu anomaly is consistent with its mineralogy dominated by garnet and biotite; e: Eu/Eu* vs La_N/Yb_N diagram showing that the lower LREE over HREE fractionation towards pegmatitic facies of the pegmatitic granite dyke. No fractionation of REE is recorded within the metapelites; f: chondrite-normalized REE patterns. Note the strong LREE enrichment of all the facies of the pegmatitic granite dyke showing a strong fractionation of the LREE over the HREE in every facies and the more or less developed Eu negative anomaly that flattens towards relatively LREE-impoverished facies. The leucosome of the paragneisses is impoverished in REE compared to the mesosome and melanosome, and shows a positive Eu anomaly consistent with its feldspar-dominated mineralogy. These features suggest that the leucosome represent a cumulate; g: REE patterns normalized to the REE-poorest facies of the pegmatitic granite. Note the lack of fractionation in the LREE and the flattening Eu negative anomaly with decreasing ΣREE content; h: melanosome-normalized REE pattern showing the lack of fractionation of the REE from the melanosome towards the leucosome. The LREE over the HREE fractionation of the dyke is in every facies higher than in the melanosome and mesosome, suggesting the sequestration of the HREE in the paragneisses, consistent with the abundance of peritectic garnet. Abbreviations: [1]: normalization after McDonough and Sun (1995); [2]: normalization to the pegmatitic facies of the dyke (sample 13-AM-13-F, Table 4-2); [3]: normalization to the melanosome of the paragneisses (sample 12-SJ-49-D, Table 4-2); Bt = biotite; Fsp = feldspar; Grt = garnet; PGD = pegmatitic granite dyke.

the kyanite stability field (Jannin et al., accepted; Jordan et al., 2006). Partial melting was initiated as early as ca. 1002 Ma as recorded by U-Pb dating of metamorphic zircon rims with HREE-depletion and no negative Eu anomaly showing their growth in presence of peritectic garnet with no plagioclase (Jannin et al., accepted). The subsequent retrograde *P-T* path is recorded in the sillimanite stability field at least until ca. 972 Ma and most probably until ca. 961 Ma (Jannin et al., accepted), consistent with the slightly younger ages of 961±3 and 956±4 Ma reported by Jordan et al. (2006) on titanite which closure temperatures of ca. 550-650°C (Schoene and Bowring, 2007 and references therein) suggest the cooling of this metasedimentary sequence down to subsolidus conditions. Accordingly, suprasolidus conditions were reached for the first time in the Knob Lake Group metapelites during the Rigolet phase and for at least ca. 30 Ma. They were associated with complete dehydration melting of muscovite and biotite, the latter being a likely host of monazite in high-grade metamorphic rocks (e.g. Yakymchuk and Brown, 2014), i.e. favorable conditions for (i) the complete liberation of monazite of the protolith and for (ii) its total consumption during partial melting were reached coevally with the intrusion of the LREE-rich PGD.

Kelsey et al. (2008) modeled that for an average metapelite composition, the LREE content of the protolith has a strong control on the preservation of inherited monazite. For the *P-T* conditions recorded during the Rigolet partial melting of the Knob Lake Group metapelites, i.e. ca. 815-850 °C and above ca. 1200 MPa, they estimated that the total consumption of monazite from a metapelite can occur if the initial LREE content of the protolith is greater than 500 ppm. These results were later confirmed by Yakymchuk and Brown (2014). Accordingly, under thermal conditions of ca. 800 °C, the total consumption of monazite can be achieved with an initial LREE content in the protolith around 500 ppm. The mesosome of the Knob Lake Group paragneisses sampled for this study is the thickest facies of the migmatitic metapelites that contrasts with the thin melanosome restricted to the vicinity of the leucosome (Fig. 4-2b). It has a ΣLREE content of 119 ppm that is intermediate between the leucosome (35 ppm) and the melanosome (232 ppm) (Fig. 4-9c-d, f, Table 4-10). The melanosome contains garnet that are not wrapped by the migmatitic foliation (Figs. 4-2e, 4-3a, c-d) and have homogeneous compositions from core to rim (Table 4-5). Together with their intergrowths with K-feldspar (Fig. 4-3c), these features are consistent with a peritectic origin as proposed by Jannin et al. (accepted), following the metamorphic reactions of dehydration melting of muscovite and biotite. The melanosome has a chondrite-normalized REE pattern showing only a slight fractionation of the LREE over the HREE (La_N/Yb_N of 3.4, Fig. 4-9e, Table 4-10), consistent

with the coexistence of monazite and garnet (e.g. Bea, 1996). Monazite grains are not found in the matrix of the melanosome but as up to 200 µm sub-euhedral inclusions in peritectic garnet, and lack evidence for corrosion and dissolution/re-precipitation textures (Fig. 4-3a-c). Accordingly, monazite from the melanosome are unlikely to represent inherited grains and such features suggest the prograde monazite growth following its total consumption from the protolith undergoing protracted partial melting, and entrapment of prograde grains within peritectic garnet, as shown by Dumond et al. (2015) and Lasalle et al. (2014). These conclusions are consistent with the common observation in granulite-facies migmatites that peritectic garnet may be entrained in the melt or concentrated within the restite (e.g. Stevens et al., 2007; Taylor and Stevens, 2010). In contrast, the leucosome of the Knob Lake Group metapelites is essentially composed of plagioclase and K-feldspar (Fig. 4-2c), and is depleted in LREE compared to the melanosome (35 ppm vs 232 ppm, Fig. 4-9c-d, Table 4-10), and its chondrite-normalized REE pattern shows a strongly positive Eu anomaly (Eu/Eu* of 3.2, Fig. 4-9f, Table 4-2). These features are indicative of its cumulate character after migration of the melt out of the source region towards upper crustal levels (e.g. Carrington and Watt, 1995; Vanderhaeghe, 2009; White and Powell, 2002). Accordingly, the mesosome represents the paleosome of the Knob Lake Group metapelites that differentiated into (i) a LREE-depleted leucosome that acquired its cumulate character after LREE-saturated melt extraction, and (ii) a LREE-enriched melanosome that represents the residual phase of the partially molten metapelites (e.g. Sawyer, 2001) and that sequestrated LREE as prograde monazite grains shielded in trapped peritectic garnet. Hence, the ΣLREE content of the mesosome of 119 ppm (Table 4-10) represents the minimal composition of the protolith of the metapelites that is expected to be higher and below ca. 500 ppm based on the total consumption of monazite under these *P-T* conditions (Kelsey et al., 2008). These contents are lower, by less than an order of magnitude, to the one of the least enriched facies of the investigated monazite-bearing PGD that contains 705 ppm of LREE (sample 13-AM-13-F, Table 4-10). Accordingly, we conclude that the Knob Lake Group metapelites from the Gagnon Terrane of the Parautochthonous Belt represent a fertile protolith relative to the genesis of the LREE-rich PGD of the central Grenville Province.

6.2. Genetic link between the PGD and metapelitic sequences from the Knob Lake Group

The differentiation of granitic pegmatites from their respective source can be estimated on the basis of alkali metal contents and ratios (e.g. K, Rb, K/Rb) in K-feldspar and micas, for which variations are commonly interpreted to be related to differentiation processes (e.g. Černý et al., 1985; London, 2008). A first attempt at the quantification of such processes and of the fractionation between granitic pegmatites with increasing fractionated character was proposed by Hulsbosch et al. (2014). They investigated and quantified the Rayleigh fractionation in particular through the K, and Rb contents, and K/Rb ratio of K-feldspar and muscovite within a pegmatitic suite from the Gatumba field (Rwanda), from their granitic source towards highly fractionated end-members. Their general model is represented in Fig. 4-6a, showing that the highest K/Rb ratios (and lowest Rb contents) represent the least fractionated objects (Hulsbosch et al., 2014). Plotted on a K/Rb vs Rb (ppm) diagram, K-feldspar from all the facies of the PGD and of the leucosome of the Knob Lake Group metapelites define a single curve (Fig. 4-6b). Data from K-feldspar of the leucosome show distinctively higher K/Rb ratios and lower Rb contents (Fig. 4-6b) consistent with its cumulative nature, whereas no distinction between K-feldspar of the various facies of the PGD can be outlined. Similar trends are noticeable in biotite from the leucosome and the PGD (Fig. 4-6c). The close association of K/Rb ratios and Rb contents between K-feldspar and biotite from the leucosome and the PGD imply the only slight fractionation of the PGD relative to its source (Černý et al., 1985; Hulsbosch et al., 2014; London, 2008). This is consistent with the presence of biotite in the PGD and the lack of muscovite, tourmaline, and other rare-metals-containing minerals that characterize highly fractionated pegmatitic granite suites (e.g. Ercit, 2005; Hulsbosch et al., 2014; London, 2016, 2008). It is strengthened by the low Ta values (below 1 ppm) and Nb/Ta ratios above 10 of both the metapelites and the various facies of the PGD that are typical of the upper continental crust, and that indicate the lack of fractionation towards peralkaline or peraluminous values (Ballouard et al., 2016; Stepanov et al., 2014). It confirms the hypothesis of Turlin et al. (2017) who argued that the LREE-rich PGD from the Lac Okaopéo region represent slightly fractionated magmas from their source. Accordingly, the close association of K/Rb ratios and Rb contents from K-feldspar and biotite of the leucosome of the Knob Lake Group metapelites and of the various facies of the PGD provide evidence for (i) the derivation of the PGD from equivalents of these metapelitic sequences, consistent with the sub-chondritic $\varepsilon Hf_{(1003\ Ma)}$

signatures of magmatic zircon grains from the PGD and associated Paleoproterozoic T_{DM2} Hf model ages (chapter 3), and for (ii) the slight fractionation of the dyke from its source.

The genetic link established between the Knob Lake Group metapelites, sampled in the outcropping area of the Parautochthonous Belt of the central Grenville Province, i.e. in the Gagnon Terrane, north of the ABT, and the Allochthonous Belt-hosted PGD may seem odd considering their geographic disconnection (Fig. 4-1). However, in chapter 3 the authors argued that the remobilization of the Paleoproterozoic-Mesoproterozoic sequences for the genesis of the LREE-rich PGD from the central Grenville required the partial melting of deep-seated metasedimentary sequences below the thickened allochthonous orogenic crust before the timing of crystallization of these PGD, recorded at ca. 1005-1000 Ma using U-Pb dating on monazite (Turlin et al., 2017) and zircon (chapter 3). This timing is slightly older than the initiation of partial melting recorded in the sampled metapelites that was dated at ca. 1002 Ma by Jannin et al. (accepted). Nevertheless, this age was obtained on the outcropping sequences from the Parautochthonous Belt, i.e. not at depth below the PGD intrusion area. Accordingly, these sequences are inferred to have been partially molten earlier below the intrusion area of the PGD, compatible with the derivation of the PGD from their partial melting.

6.3. Respective roles of partial melting and fractional crystallization in the genesis of the LREE-rich PGD

The genesis of mineralized peraluminous granitic intrusions requires partial melting of a fertile protolith and the extraction and migration of the melt from its source. Melt extraction controls the composition of the residual solid and also of residual melt trapped in the restite, which directly impact the solubility of accessory phases in the restite (Kelsey et al., 2008; White and Powell, 2002). In the case of monazite, calculations of Kelsey et al. (2008) showed that melt loss events enhance the dissolution of monazite from the protolith. These conclusions were completed by Yakymchuk and Brown (2014) who demonstrated that each melt extraction enriches the melt in LREE compared to the initial protolith, leading to progressive depletion of the source. The Knob Lake Group metapelites sampled for this study represent a fertile protolith for the genesis of the LREE-PGD from the central Grenville. The leucosome of these metapelites is LREE-depleted (35 ppm, Fig. 4-9c-d, Table 4-10) that contrasts with the LREE-enriched melanosome (232 ppm, Fig. 4-9c-d, Table 4-10) containing prograde monazite. The chondrite-normalized REE pattern of the melanosome and of the leucosome are both marked by a slight fractionation of the LREE over the HREE and the latter show a strong positive Eu

anomaly (Fig. 4-9f), reflecting the plagioclase+K-feldspar dominant assemblage, and provide evidence for its cumulative character. These contrasting features between the melanosome and the leucosome point to the incompatible behavior of the REE during the partial melting that allowed the generation of LREE-rich peraluminous granitic melt during the Rigolet tectonic phase of the Grenvillian Orogeny.

The LREE-PGD sampled for this study displays a strong facies variability randomly organized (Fig. 4-4) and that range from a LREE(monazite)-rich fine grained facies (sample 13-AM-13-E, Fig. 4-5g) with corroded biotite (Fig. 4-5g) and complexly zoned monazite (Fig. 4-7a), to a LREE-poor pegmatitic facies (sample 13-AM-13-F, Fig. 4-5h) (Table 4-1). In pegmatitic granite (LCT family, Černý et al., 2012), the crystallization sequence usually evolves from the formation of aplitic facies towards pegmatitic ones (e.g. London, 2016, 2014, 2008). However, the variations of the fractionation indicators that are K/Rb ratios and Rb contents of K-feldspar and biotite (Fig. 4-6b-c), and the Nb/Ta ratios and Nb and Ta contents of both the whole-rock (Fig. 4-9b) and biotite (Fig. 4-6d-e) are not linked to the facies variations of the sampled PGD (Tables 4-7 to 4-10). This suggests that this facies variability is not linked to fractional crystallization of the magma. To the contrary, the corroded textures of biotite from the fine grained facies (Fig. 4-5g) and the complex zoning of monazite grains (Fig. 4-7a) witness a dynamic magmatic activity with successive pulses probably reflecting dynamic processes at the source with no fractionation of the K/Rb and Nb/Ta ratios.

The evolution from the fine grained to the pegmatitic facies is associated with (i) decreasing ASI (1.36 to 1.12) and (ii) decreasing ΣREE content (7,048 to 705 ppm) (Fig. 4-9c, Table 4-10), with (iii) the flattening of the negative Eu anomaly in the chondrite-normalized REE pattern (Fig. 4-9f), (iv) no change in the fractionation within the LREE as marked by the La_N/Sm_N ratio ranging between 6.8 and 7.7 (Fig. 4-9g, Table 4-10), and (v) a strong decrease of the fractionation of the LREE over the HREE as marked by La_N/Yb_N ratio ranging from 1193 to 223 that however remains higher than in the metapelites (Fig. 4-9g, Table 4-10). The latter is consistent with the sequestration of the HREE within the source in peritectic garnet, a typical HREE-bearing phase (Bea, 1996; Hönig et al., 2014), as proposed by Turlin et al. (2017). The fine grained facies of the PGD has the same chondrite-normalized REE patterns as monazite (Figs. 4-8 and 4-9f), consistent with monazite being the dominant host of REE within the PGD. The highest ΣLREE content and the highest ASI recorded in the fine grained facies reflects the close association of monazite and biotite (compare Fig. 4-5g and h, Table 4-10). The decreasing ASI of the anatectic melt with protracted partial melting (Jeanneret, 2016) and the decreasing

solubility of monazite with increasing ASI (Montel, 1986) argue in favor of the derivation of the LREE-richest fine grained facies of the PGD by a first melt loss from the partially molten metapelites. Furthermore, as the HREE are sequestrated within the metapelites, the decrease in the fractionation of the LREE over the HREE within the PGD that is recorded from the fine grained to the pegmatitic facies is essentially controlled by a ΣLREE content diminution. This feature suggests a diminution of the LREE saturation of the anatectic melt with protracted partial melting. Taken together these features point to successive melt loss events during partial melting of the metapelites associated with a decreasing content of the LREE content in the anatectic melt. Along with the incompatible behavior of the REE during the partial melting of the metapelites discussed above, this suggests that the first melt loss events are responsible for the highest LREE enrichment of the PGD, and that they are associated with the fine grained facies and that the subsequent formation of the pegmatitic facies, relatively impoverished in LREE, is associated with a lower LREE saturation of the anatectic melt (Table 4-10).

Two processes can lead to the genesis of pegmatitic textures within a rock, namely (i) a liquidus undercooling coupled to a nucleation delay, or (ii) slow cooling and crystallization close to the liquidus temperature (e.g. London, 2016, 2014, 2008). The latter is especially encountered in pegmatitic granite emplaced at depths where the thermal contrast with their host is low (London, 2016). In chapter 3 the authors reported crystallization temperatures of this PGD between 662 and 721°C (Ti-in-zircon thermometry using the thermometer defined by Ferry and Watson, 2007) and Turlin et al. (submitted) proposed, based on the lobate contacts of a PGD intruding allochthonous paragneisses and on the absence of contact metamorphism, that at the time of intrusion of the PGD from the central Grenville Province, i.e. at ca. 1005-1000 Ma, the intruded allochthonous mid-crustal level was under close to wet-solidus thermal conditions followed by slow cooling at a rate of 2 to 6 °C/Ma. In this model, the pegmatitic texture of this PGD might be the result of slow cooling of the magma.

From discussion above, (i) the LREE content of the mesosome, that we consider to represent the minimum content of the protolith, (ii) the modeling of the behavior of the LREE during partial melting from literature, (iii) the peritectic growth of garnet that sequestrates and control the HREE and to a minor extent the LREE content of the melt, (iv) the cumulate signature of the leucosome, (v) the lack of evidence for fractional crystallization within the PGD marked by Nb/Ta ratios from the whole-rock geochemistry and by K/Rb ratios of the K-feldspar and biotite, and (vii) the structural position of the Knob Lake Group metapelitic sequence and its wide lateral continuity (e.g. van Gool et al., 2008) are consistent with the

derivation of the investigated PGD from protracted high-temperature partial melting of the Knob Lake Group Paleoproterozoic-Archean metapelites associated with LREE saturated melt loss events. Partial melting of this metapelitic sequence up to complete dissolution of monazite controls the bulk LREE concentration within the PGD.

Conclusion

Data from this study, along with field relationships, geochronological and isotopic constraints previously obtained on this PGD (chapter 3) and already published on the Knob Lake Group metapelites (Jannin et al., accepted; Jordan et al., 2006) allow to propose a petrogenetic model for the genesis of LREE-rich peraluminous pegmatitic granite dykes intruding the Allochthonous Belt of the central Grenville during the early-Rigolet tectonic phase. These dykes were derived from the remobilization of hydrated Paleoproterozoic-Archean metapelitic sequences through protracted high-temperature partial melting that allowed (i) the total consumption of biotite and the subsequent total liberation of monazite, (ii) the saturation of the anatectic melt in LREE, (iii) the sequestration of the HREE within peritectic garnet in the residue, (iv) successive melt loss events responsible for the cumulate signatures of the leucosomes and the migration of anatectic products towards upper crustal levels. The high-grade LREE concentrations within the PGD are associated with the first LREE saturated melt loss events from the partially molten source. Subsequent melt loss events are marked by a decreasing LREE saturation of the anatectic melt and are responsible for the successive liquid inputs within the PGD responsible for its randomly organized zonation.

Acknowledgements

The authors would like to thank the Ministère de l'Énergie et des Ressources naturelles (Québec, Canada) for providing technical and financial support for the field work and analyses. The authors are grateful to Pierre-Arthur Groulier (Memorial University, NL, Canada) and Alexandre Crépon (GeoRessources, Nancy) for their help during field work, to Sophie Jannin (École Polytechnique de Montréal, Canada) for her advice in the choice of the paragneiss outcrop, to Andreï Lecomte (SEM) and Olivier Rouer (EMP) (GeoRessources, Nancy) for technical support in providing analytical data on SEM and EMP, and to Chantal Peiffert (GeoRessources, Nancy) for her help in the acquisition of LA-ICP-MS data. This work was funded by the Labex Ressources 21 (supported by the French National Research Agency – France) through the national program "Investissements d'avenir", reference ANR-10-LABX-21–LABEX RESSOURCES 21 and the Région Grand-Est. It benefited from the framework of the DIVEX "Rare earth element" research program.

Table 4-1: Representative hand-samples of a LREE-rich monazite-bearing pegmatitic granite dyke (Allochthonous Belt; 13-AM-13) and of the Knob Lake Group paragneisses (Parautochthonous Belt, potential source of the pegmatitic granite dykes) sampled for this study. Facies are first ordered by outcrops then from LREE-richest to LREE-poorest. Abbreviations: Bt = biotite; Mnz-bearing PGD = monazite-bearing pegmatitic granite dyke; NTS = National Topographic System.

Tectono-metamorphic domain	Type of outcrop	Purpose	Facies	LREE content (ppm)[3]	Sample no.	Results presented in this study		
						Whole-rock geochemistry	Mineral compositions	Trace elements on minerals
Allochthonous Belt	*Mnz-bearing PGD (13-AM-13)*[1]	Processes responsible for LREE enrichment within the PGD	Fine-grained	6,949	13-AM-13-E	Fig. 4-9, Table 4-10[4]	Tables 4-2 to 4-4, 4-6	Figs. 4-6 and 4-8, Tables 4-7 to 4-9
			Intermediate	5,979	13-AM-13-A6	Fig. 4-9, Table 4-10	Tables 4-2 to 4-4, 4-6	Figs. 4-6 and 4-8, Tables 4-7 to 4-9
			Fine-grained (+Grt)	3,446	13-AM-13-A5	Fig. 4-9, Table 4-10	Tables 4-2 to 4-4, 4-6	Figs. 4-6 and 4-8, Tables 4-7 to 4-9
			Intermediate (+Bt)	2,380	13-AM-13-A4	Fig. 4-9, Table 4-10	Tables 4-2 to 4-4, 4-6	Figs. 4-6 and 4-8, Tables 4-7 to 4-9
			Coarse-grained	1,580	13-AM-13-A1	Fig. 4-9, Table 4-10	Tables 4-2 to 4-4, 4-6	Figs. 4-6 and 4-8, Tables 4-7 to 4-9
			Pegmatitic	705	13-AM-13-F	Fig. 4-9, Table 4-10	Tables 4-2 to 4-4, 4-6	Figs. 4-6 and 4-8, Tables 4-7 to 4-9
Parautochthonous Belt	*Knob Lake Group paragneisses*[2]	Test of a potential source of LREE-rich PGD	Melanosome	232	12-SJ-49-C	Fig. 4-9, Table 4-10	Tables 4-2 to 4-5	-
			Mesosome	119	12-SJ-49-B	Fig. 4-9, Table 4-10	Tables 4-2 to 4-5	-
			Leucosome	35	12-SJ-49-A	Fig. 4-9, Table 4-10	Tables 4-2 to 4-5	Fig. 4-6, Tables 4-7, 4-8

[1] Coordinates: NTS sheet = 22K10; Universal Transverse Mercator (UTM) zone = U19; Easting = 512052; Northing = 5614036.
[2] Coordinates: NTS sheet = 22K14; UTM zone = U19; Easting = 497222; Northing = 5644910.
[3] Reported in Table 4-10.
[4] Geochemical data are from Turlin et al. (2017).

Table 4-2: Analyses of plagioclase grains of the various facies of the 13-AM-13 monazite-bearing pegmatitic granite dyke (Allochthonous Belt), and of the leucosome and melanosome from the Knob Lake Group paragneisses (Parautochthonous Belt). Data were obtained using EMP. They are reported with confidence interval of 95% in brackets (n = number of analyses). Abbreviations: Ab = albite; An = anorthite; Bt = biotite; Grt = garnet; Or = orthose.

Type	***Monazite-bearing PGD***						***Parautochthonous Paragneisses***	
Outcrop	**13-AM-13**						**12-SJ-49**	
Sample no.	**-13-E**	**-13-A6**	**-13-A5**	**-13-A4**	**-13-A1**	**-13-F**	**12-SJ-49-A**	**12-SJ-49-D**
Facies	**Fine grained**	**Intermediate**	**Fine grained (+Grt)**	**Intermediate (+Bt)**	**Coarse grained**	**Pegmatitic**	**Leucosome**	**Melanosome**
SiO_2	59.36	61.08	59.79	59.05	59.55	60.42	63.31	63.29
	(0.49)	(0.23)	(0.25)	(1.27)	(0.38)	(0.43)	(0.77)	(1.18)
TiO_2	0.01	0.01	0.01	0.01	0.02	0.01	0.01	0.00
	(0.01)	(0.01)	(0.01)	(0.01)	(0.04)	(0.01)	(0.01)	(0.01)
Al_2O_3	25.01	25.08	25.27	24.92	24.83	24.73	24.42	24.07
	(0.28)	(0.23)	(0.52)	(0.63)	(0.34)	(0.21)	(0.27)	(0.81)
FeO	0.07	0.02	0.01	0.04	0.05	0.02	0.03	0.01
	(0.05)	(0.02)	(0.02)	(0.07)	(0.09)	(0.03)	(0.04)	(0.02)
MnO	0.02	0.01	0.03	0.02	0.01	0.03	0.02	0.03
	(0.03)	(0.02)	(0.06)	(0.03)	(0.01)	(0.04)	(0.02)	(0.03)
MgO	0.01	0.01	0.01	0.01	0.00	0.01	0.01	0.03
	(0.01)	(0.01)	(0.02)	(0.02)	(0.01)	(0.01)	(0.02)	(0.09)
CaO	6.45	6.30	6.16	5.91	6.24	6.37	4.67	4.29
	(0.20)	(0.20)	(0.16)	(0.61)	(0.26)	(0.23)	(0.27)	(1.12)
Na_2O	8.38	7.67	7.69	7.63	8.53	7.89	8.31	8.36
	(0.20)	(0.13)	(0.12)	(0.35)	(0.32)	(0.17)	(0.18)	(0.53)
K_2O	0.27	0.31	0.27	0.36	0.26	0.33	0.39	0.39
	(0.08)	(0.04)	(0.04)	(0.38)	(0.08)	(0.06)	(0.11)	(0.08)
Total	99.57	100.47	99.24	97.94	99.49	99.80	101.16	100.49
	(0.69)	(0.31)	(0.77)	(1.79)	(0.29)	(0.51)	(0.89)	(0.73)
Oxygens	8	8	8	8	8	8	8	8
Si	2.640	2.710	2.682	2.682	2.648	2.693	2.783	2.799
	(0.014)	(0.015)	(0.015)	(0.024)	(0.012)	(0.014)	(0.015)	(0.046)
Ti	0.000	0.000	0.000	0.000	0.001	0.000	0.000	0.000
	(0.000)	(0.000)	(0.000)	(0.000)	(0.001)	(0.000)	(0.000)	(0.000)
Al	1.311	1.311	1.336	1.334	1.301	1.299	1.265	1.255
	(0.010)	(0.009)	(0.019)	(0.032)	(0.020)	(0.010)	(0.015)	(0.043)
Fe_{tot}	0.002	0.001	0.001	0.002	0.002	0.001	0.001	0.001
	(0.002)	(0.001)	(0.001)	(0.003)	(0.003)	(0.001)	(0.001)	(0.001)
Mn	0.001	0.000	0.001	0.001	0.000	0.001	0.001	0.001
	(0.001)	(0.001)	(0.002)	(0.001)	(0.000)	(0.002)	(0.001)	(0.001)
Mg	0.000	0.001	0.001	0.001	0.000	0.000	0.001	0.002
	(0.001)	(0.001)	(0.001)	(0.001)	(0.001)	(0.000)	(0.001)	(0.006)
Ca	0.307	0.300	0.296	0.287	0.298	0.304	0.220	0.203
	(0.009)	(0.009)	(0.006)	(0.028)	(0.013)	(0.011)	(0.013)	(0.053)
Na	0.723	0.660	0.669	0.672	0.735	0.682	0.708	0.717
	(0.017)	(0.010)	(0.012)	(0.027)	(0.025)	(0.013)	(0.014)	(0.045)
K	0.015	0.017	0.015	0.021	0.015	0.019	0.022	0.022
	(0.004)	(0.002)	(0.002)	(0.023)	(0.005)	(0.003)	(0.006)	(0.004)
% An	29.39	30.68	30.18	29.27	28.41	30.26	23.14	21.54
	(0.87)	(0.88)	(0.66)	(2.58)	(1.42)	(1.10)	(1.35)	(5.57)
% Ab	69.14	67.55	68.24	68.56	70.16	67.89	74.53	76.11
	(1.08)	(0.80)	(0.77)	(2.01)	(1.81)	(1.09)	(1.22)	(5.54)
% Or	1.48	1.77	1.58	2.17	1.43	1.85	2.33	2.35
	(0.41)	(0.22)	(0.23)	(2.63)	(0.45)	(0.32)	(0.62)	(0.47)
n	22	11	8	28	9	18	23	11

Table 4-3: Analyses of K-feldspar grains of the various facies of the 13-AM-13 monazite-bearing pegmatitic granite dyke (Allochthonous Belt), and of the leucosome from the Knob Lake Group paragneisses (Parautochthonous Belt). Data were obtained using EMP. They are reported with confidence interval of 95% in brackets (n = number of analyses). Abbreviations: Ab = albite; An = anorthite; Bt = biotite; Grt = garnet; Or = orthose.

Type	***Monazite-bearing PGD***					***Parautochthonous Paragneisses***
Outcrop	**13-AM-13**					**12-SJ-49**
Sample no.	**-13-A6**	**-13-A5**	**-13-A4**	**-13-A1**	**-13-F**	**12-SJ-49-A**
Facies	**Intermediate**	**Fine grained (+Grt)**	**Intermediate (+Bt)**	**Coarse grained**	**Pegmatitic**	**Leucosome**
SiO_2	65.24	63.86	63.55	63.70	63.90	64.48
	(0.45)	(0.48)	(0.34)	(0.40)	(0.34)	(1.16)
TiO_2	0.01	0.00	0.01	0.04	0.00	0.01
	(0.01)	(0.00)	(0.01)	(0.05)	(0.01)	(0.01)
Al_2O_3	18.91	19.00	19.01	18.91	18.56	18.88
	(0.23)	(0.50)	(0.27)	(0.14)	(0.22)	(0.41)
FeO	0.02	0.06	0.03	0.02	0.04	0.04
	(0.03)	(0.06)	(0.02)	(0.03)	(0.04)	(0.04)
MnO	0.02	0.02	0.01	0.04	0.03	0.01
	(0.04)	(0.02)	(0.02)	(0.04)	(0.04)	(0.02)
MgO	0.01	0.00	0.01	0.01	0.01	0.01
	(0.01)	(0.01)	(0.01)	(0.01)	(0.01)	(0.01)
CaO	0.07	0.04	0.04	0.03	0.09	0.03
	(0.08)	(0.06)	(0.02)	(0.05)	(0.12)	(0.04)
Na_2O	1.85	1.49	1.54	1.39	1.71	1.41
	(0.76)	(0.23)	(0.27)	(0.29)	(0.67)	(0.46)
K_2O	14.36	15.10	15.13	14.56	14.64	15.01
	(1.16)	(0.32)	(0.45)	(0.48)	(1.14)	(0.61)
Total	100.49	99.56	99.33	98.70	98.97	99.88
	(0.48)	(0.81)	(0.42)	(0.58)	(0.45)	(1.47)
Oxygens	8	8	8	8	8	8
Si	2.977	2.943	2.933	2.966	2.960	2.965
	(0.011)	(0.019)	(0.010)	(0.010)	(0.011)	(0.014)
Ti	0.000	0.000	0.000	0.001	0.000	0.000
	(0.000)	(0.000)	(0.000)	(0.002)	(0.000)	(0.000)
Al	1.017	1.032	1.034	1.038	1.013	1.023
	(0.008)	(0.022)	(0.014)	(0.008)	(0.010)	(0.012)
Fe_{tot}	0.001	0.002	0.001	0.001	0.001	0.001
	(0.001)	(0.002)	(0.001)	(0.001)	(0.002)	(0.002)
Mn	0.001	0.001	0.000	0.001	0.001	0.000
	(0.002)	(0.001)	(0.001)	(0.002)	(0.002)	(0.001)
Mg	0.001	0.000	0.000	0.001	0.001	0.000
	(0.001)	(0.001)	(0.001)	(0.001)	(0.001)	(0.001)
Ca	0.003	0.002	0.002	0.002	0.004	0.002
	(0.004)	(0.003)	(0.001)	(0.002)	(0.006)	(0.002)
Na	0.163	0.133	0.138	0.125	0.154	0.126
	(0.066)	(0.021)	(0.024)	(0.026)	(0.060)	(0.039)
K	0.837	0.888	0.891	0.865	0.865	0.881
	(0.071)	(0.015)	(0.027)	(0.029)	(0.068)	(0.043)
% An	0.32	0.17	0.17	0.16	0.41	0.16
	(0.39)	(0.28)	(0.11)	(0.25)	(0.59)	(0.18)
% Ab	16.30	13.01	13.39	12.62	15.05	12.48
	(6.56)	(1.97)	(2.32)	(2.52)	(6.11)	(3.92)
% Or	83.37	86.82	86.44	87.21	84.54	87.35
	(6.90)	(2.04)	(2.37)	(2.74)	(6.24)	(3.98)
n	26	6	9	13	21	23

Table 4-4: Analyses of dark micas grains of the various facies of the 13-AM-13 monazite-bearing pegmatitic granite dyke (Allochthonous Belt), and of the leucosome and melanosome from the Knob Lake Group paragneisses (Parautochthonous Belt). Data were obtained using EMP. They are reported with confidence interval of 95% in brackets (n = number of analyses). Abbreviations: Bt = biotite; Grt = garnet.

Type	*Monazite-bearing PGD*						*Parautochthonous Paragneisses*		
Outcrop	**13-AM-13**						**12-SJ-49**		
Sample no.	**-13-E**	**-13-A6**	**-13-A5**	**-13-A4**	**-13-A1**	**-13-F**	**12-SJ-49-A**	**12-SJ-49-D**	
Facies	**Fine grained**	**Intermediate**	**Fine grained (+Grt)**	**Intermediate (+Bt)**	**Coarse grained**	**Pegmatitic**	**Leucosome**	**Melanosome (parallel to foliation)**	**Melanosome (oblique to foliation)**
SiO_2	34.32	34.50	34.45	34.67	33.85	34.51	36.32	36.86	36.86
	(0.34)	(1.47)	(0.48)	(0.79)	(0.78)	(0.32)	(1.07)	(0.69)	(0.68)
TiO_2	4.65	4.56	4.38	5.18	4.47	4.66	4.45	4.25	4.11
	(0.39)	(0.79)	(0.34)	(0.43)	(0.51)	(0.37)	(0.23)	(0.15)	(0.59)
Al_2O_3	16.51	17.41	17.54	16.69	17.18	17.09	15.85	16.25	16.23
	(0.15)	(0.31)	(0.37)	(0.30)	(0.61)	(0.26)	(0.54)	(0.36)	(0.48)
FeO	20.24	22.98	23.08	22.54	21.38	21.67	16.06	16.00	15.91
	(0.58)	(1.66)	(0.63)	(0.82)	(0.64)	(0.51)	(0.65)	(0.84)	(0.89)
MnO	0.07	0.08	0.10	0.03	0.05	0.08	0.02	0.02	0.04
	(0.04)	(0.06)	(0.05)	(0.05)	(0.04)	(0.06)	(0.03)	(0.03)	(0.08)
MgO	8.24	7.81	7.82	7.28	7.95	7.39	12.91	13.15	12.96
	(0.18)	(0.59)	(0.31)	(0.28)	(0.41)	(0.25)	(0.58)	(0.59)	(0.63)
CaO	0.01	0.08	0.01	0.00	0.04	0.01	0.01	0.00	0.01
	(0.02)	(0.31)	(0.01)	(0.02)	(0.06)	(0.01)	(0.05)	(0.01)	(0.02)
Na_2O	0.10	0.10	0.07	0.09	0.10	0.18	0.09	0.08	0.07
	(0.04)	(0.05)	(0.03)	(0.04)	(0.01)	(0.07)	(0.05)	(0.04)	(0.04)
K_2O	9.66	8.97	9.60	10.10	9.17	9.70	9.85	10.08	10.07
	(0.16)	(1.97)	(0.56)	(0.65)	(0.50)	(0.11)	(0.75)	(0.29)	(0.20)
Total	97.62	100.40	100.96	100.47	98.01	99.13	95.56	96.68	96.26
	(0.74)	(1.57)	(0.83)	(1.38)	(2.14)	(0.77)	(2.17)	(1.06)	(1.11)
Oxygens	22	22	22	22	22	22	22	22	22
Si	5.380	5.289	5.272	5.338	5.298	5.354	5.464	5.509	5.496
	(0.038)	(0.146)	(0.047)	(0.070)	(0.019)	(0.034)	(0.082)	(0.062)	(0.056)
Al^{IV}	2.620	2.711	2.728	2.662	2.702	2.646	2.525	2.491	2.503
	(0.038)	(0.146)	(0.047)	(0.070)	(0.019)	(0.034)	(0.014)	(0.009)	(0.033)
Al^{VI}	0.430	0.436	0.436	0.366	0.467	0.479	0.284	0.369	0.349
	(0.048)	(0.071)	(0.061)	(0.040)	(0.060)	(0.055)	(0.063)	(0.062)	(0.055)
Ti	0.548	0.525	0.504	0.600	0.525	0.543	0.503	0.477	0.461
	(0.046)	(0.087)	(0.036)	(0.047)	(0.056)	(0.043)	(0.073)	(0.060)	(0.068)
Fe	2.653	2.951	2.955	2.902	2.800	2.811	2.021	1.999	1.985
	(0.070)	(0.270)	(0.094)	(0.113)	(0.098)	(0.060)	(0.042)	(0.056)	(0.060)
Mn	0.009	0.011	0.013	0.004	0.007	0.010	0.003	0.003	0.006
	(0.005)	(0.008)	(0.007)	(0.006)	(0.005)	(0.008)	(0.002)	(0.002)	(0.005)
Mg	1.926	1.787	1.784	1.671	1.854	1.709	2.897	2.929	2.882
	(0.046)	(0.167)	(0.077	(0.068)	(0.079)	(0.058)	(0.073)	(0.077)	(0.079)
Ca	0.001	0.014	0.002)	0.000	0.006	0.001	0.002	0.001	0.001
	(0.003)	(0.053)	(0.002	(0.003)	(0.010)	(0.002)	(0.004)	(0.001)	(0.001)
Na	0.029	0.028	0.021	0.027	0.030	0.053	0.026	0.023	0.019
	(0.013)	(0.014)	(0.008)	(0.011)	(0.004)	(0.021)	(0.008)	(0.006)	(0.006)
K	1.932	1.749	1.873	1.983	1.832	1.919	1.889	1.921	1.917
	(0.029)	(0.372)	(0.100)	(0.118)	(0.091)	(0.018)	(0.071)	(0.028)	(0.023)
X_{Mg}	0.42	0.35	0.38	0.37	0.40	0.38	0.59	0.59	0.59
	(0.01)	(0.01)	(0.01)	(0.01)	(0.01)	(0.01)	(0.02)	(0.02)	(0.02)
n	20	20	14	16	12	31	28	51	30

Table 4-5: Analyses of garnet grains of the leucosome and melanosome from the Knob Lake Group paragneisses (Parautochthonous Belt). Data were obtained using EMP. They are reported with confidence interval of 95% in brackets (n = number of analyses). Abbreviations: Alm = almandine; And = andradite; Grs = grossular; Prp = pyrope; Sps = spessartine; Uvt = uvarovite.

Type	***Parautochthonous Paragneisses***	
Outcrop	**12-SJ-49**	
Sample no.	**12-SJ-49-A**	**12-SJ-49-D**
Facies	**Leucosome**	**Melanosome**
SiO_2	38.51	38.34
	(0.38)	(0.56)
TiO_2	0.04	0.02
	(0.03)	(0.02)
Al_2O_3	21.63	21.40
	(0.34)	(0.63)
Cr_2O_3	0.00	0.00
	(0.00)	(0.00)
FeO	32.70	33.26
	(2.22)	(1.45)
MnO	0.75	0.73
	(0.14)	(0.09)
MgO	5.57	5.32
	(1.32)	(1.00)
CaO	2.87	2.43
	(0.29)	(0.18)
Total	102.07	101.50
	(0.98)	(0.96)
Oxygens	12	12
Si	2.960	2.946
	(0.029)	(0.043)
Ti	0.002	0.001
	(0.002)	(0.001)
Al	1.959	1.939
	(0.031)	(0.057)
Cr	0.000	0.000
	(0.000)	(0.000)
Fe(III)	0.227	0.421
	(0.183)	(0.275)
Fe(II)	1.875	1.716
	(0.185)	(0.245)
Mn	0.049	0.048
	(0.009)	(0.006)
Mg	0.638	0.609
	(0.151)	(0.114)
Ca	0.236	0.200
	(0.024)	(0.015)
% Alm.	63.33	58.18
	(6.19)	(7.78)
% Prp.	21.54	20.66
	(4.95)	(3.75)
% Grs.	7.17	5.65
	(0.95)	(0.80)
% Sps.	1.66	1.61
	(0.31)	(0.22)
% Uvt.	0.00	0.00
	(0.00)	(0.00)
% Adr.	0.79	1.15
	(0.61)	(0.70)
n	12	37

Table 4-6: Analyses of monazite grains of the various facies of the 13-AM-13 monazite-bearing pegmatitic granite dyke (Allochthonous Belt). Data were obtained using EMP. They are reported with confidence interval of 95% in brackets (n = number of analyses). Abbreviations: Brab. = brabantite; Bt = biotite; Grt = garnet; Hutt. = huttonite; Mnz. = monazite; Xen. = xenotime.

Type	***Monazite-bearing PGD***					
Outcrop	**13-AM-13**					
Sample no.	**-13-E**	**-13-A6**	**-13-A5**	**-13-A4**	**-13-A1**	**-13-F**
Facies	**Fine grained**	**Intermediate**	**Fine grained (+Grt)**	**Intermediate (+Bt)**	**Coarse grained**	**Pegmatitic**
P_2O_5	27.54	26.18	26.90	27.30	27.15	27.22
	(1.67)	(1.12)	(1.72)	(1.42)	(1.92)	(1.76)
SiO_2	1.81	2.21	1.75	1.68	2.13	2.14
	(1.02)	(0.78)	(1.06)	(0.86)	(1.20)	(1.14)
CaO	0.88	0.93	1.01	0.88	1.36	1.15
	(0.27)	(0.36)	(0.46)	(0.27)	(0.53)	(0.56)
Y_2O_3	0.20	0.19	0.25	0.25	0.24	0.19
	(0.13)	(0.10)	(0.14)	(0.15)	(0.15)	(0.12)
La_2O_3	14.78	14.39	14.56	14.82	14.00	14.49
	(0.96)	(0.63)	(1.00)	(0.67)	(0.68)	(0.87)
Ce_2O_3	28.33	27.67	28.38	28.84	27.00	27.83
	(2.29)	(1.27)	(2.02)	(1.36)	(1.99)	(2.16)
Pr_2O_3	3.26	3.22	3.30	3.35	3.09	3.17
	(0.19)	(0.36)	(0.29)	(0.35)	(0.26)	(0.24)
Nd_2O_3	10.24	9.55	9.79	10.14	9.81	9.90
	(0.60)	(0.71)	(1.03)	(0.75)	(1.03)	(0.96)
Sm_2O_3	1.28	0.91	0.95	0.93	1.24	1.19
	(0.19)	(0.33)	(0.35)	(0.36)	(0.28)	(0.23)
Gd_2O_3	0.60	0.54	0.56	0.52	0.59	0.53
	(0.15)	(0.29)	(0.29)	(0.29)	(0.18)	(0.14)
PbO	0.54	0.00	0.00	0.00	0.86	0.50
	(0.36)	(0.00)	(0.00)	(0.00)	(0.64)	(0.51)
ThO_2	10.86	13.26	11.75	11.03	13.71	12.72
	(3.96)	(2.80)	(4.77)	(3.34)	(4.81)	(4.77)
UO_2	0.10	0.20	0.19	0.18	0.11	0.11
	(0.03)	(0.15)	(0.16)	(0.15)	(0.04)	(0.04)
Total	100.79	99.26	99.38	99.93	101.29	101.14
	(0.76)	(1.34)	(1.15)	(0.88)	(0.65)	(0.72)
Oxygens	4	4	4	4	4	4
P	0.931	0.906	0.923	0.929	0.916	0.917
	(0.046)	(0.029)	(0.045)	(0.037)	(0.050)	(0.047)
Si	0.073	0.090	0.072	0.068	0.086	0.086
	(0.042)	(0.033)	(0.044)	(0.036)	(0.050)	(0.047)
ΣT-site	1.004	0.996	0.995	0.997	1.001	1.003
	(0.012)	(0.012)	(0.006)	(0.005)	(0.003)	(0.005)
Ca	0.038	0.041	0.044	0.038	0.058	0.049
	(0.011)	(0.016)	(0.020)	(0.012)	(0.023)	(0.024)
Y	0.004	0.004	0.005	0.005	0.005	0.004
	(0.003)	(0.002)	(0.003)	(0.003)	(0.003)	(0.003)
La	0.218	0.217	0.218	0.220	0.206	0.213
	(0.013)	(0.009)	(0.013)	(0.010)	(0.008)	(0.012)
Ce	0.414	0.414	0.421	0.425	0.394	0.406
	(0.030)	(0.017)	(0.026)	(0.017)	(0.025)	(0.029)
Pr	0.047	0.048	0.049	0.049	0.045	0.046
	(0.002)	(0.005)	(0.004)	(0.005)	(0.003)	(0.003)
Nd	0.146	0.139	0.142	0.146	0.140	0.141
	(0.007)	(0.010)	(0.013)	(0.010)	(0.013)	(0.013)
Sm	0.018	0.013	0.013	0.013	0.017	0.016
	(0.002)	(0.005)	(0.005)	(0.005)	(0.004)	(0.003)
Gd	0.008	0.007	0.008	0.007	0.008	0.007
	(0.002)	(0.004)	(0.004)	(0.004)	(0.002)	(0.002)
Pb	0.006	0.000	0.000	0.000	0.009	0.005
	(0.004)	(0.000)	(0.000)	(0.000)	(0.007)	(0.006)
Th	0.099	0.124	0.109	0.101	0.125	0.116
	(0.037)	(0.027)	(0.046)	(0.032)	(0.045)	(0.045)
U	0.001	0.002	0.002	0.002	0.001	0.001
	(0.000)	(0.001)	(0.001)	(0.001)	(0.000)	(0.000)
Σa-site	0.999	1.008	1.010	1.005	1.007	1.003
	(0.021)	(0.012)	(0.010)	(0.008)	(0.007)	(0.008)
% Hutt.	7.22	9.05	7.18	6.81	8.56	8.57
	(4.14)	(3.25)	(4.44)	(3.56)	(4.98)	(4.73)
% Brab.	8.82	8.49	9.08	7.92	13.66	11.04
	(2.36)	(3.14)	(4.06)	(2.33)	(4.45)	(4.92)

% Mnz.	83.72	83.10	84.27	85.21	80.10	82.13
	(4.03)	(3.27)	(5.15)	(3.10)	(5.02)	(5.73)
% Xen.	1.20	1.15	1.28	1.23	1.27	1.11
	(0.39)	(0.48)	(0.56)	(0.56)	(0.52)	(0.41)
n	203	268	32	80	22	42

Table 4-7: Rubidium analyses of K-feldspar of the various facies of the 13-AM-13 monazite-bearing pegmatitic granite dyke (Allochthonous Belt), and of the leucosome from the Knob Lake Group paragneisses (Parautochthonous Belt). Data were obtained using LA-ICP-MS. Abbreviations: Bt = biotite; Grt = garnet.

K-feldspar																							
Sample	**13-AM-13-A61**										**13-AM-13-A5**												
Facies	**Intermediate**										**Fine grained (+Grt)**												
Analysis no.	**A6-3**	**A6-4**	**A6-7**	**A6-8**	**A6-13**	**A6-14**	**A6-20**	**A6-21**	**A6-27**	**A6-28**	**A5-1**	**A5-2**	**A5-7**	**A5-8**	**A5-13**	**A5-14**	**A5-15**	**A5-23**	**A5-24**	**A5-25**	**A5-26**	**A5-42**
K (ppm)[1]	118000	118000	123500	127000	121000	121000	102800	102800	122000	122000	124100	124100	124100	124100	124100	124100	124100	126600	126600	126600	126600	125100
Rb	71	40	79	46	58	44	30	37	62	48	47.5	34.8	44.9	54.6	41.2	69.5	75.7	43.5	53.1	53.1	62.8	29.54
K/Rb	1674	2943	1573	2785	2090	2744	3392	2771	1958	2563	2613	3566	2764	2273	3012	1786	1639	2910	2384	2384	2016	4235

Sample						**13-AM-13-A4**												**13-AM-13-A1**				
Facies						**Intermediate (+Bt)**												**Coarse grained**				
Analysis no.	**A5-43**	**A5-44**	**A5-45**	**A5-59**	**A5-60**	**A4-1**	**A4-2**	**A4-20**	**A4-21**	**A4-22**	**A4-31**	**A4-34**	**A4-35**	**A4-41**	**A4-43**	**A4-48**	**A4-49**	**A1-11**	**A1-12**	**A1-13**	**A1-14**	**A1-15**
K (ppm) [1]	125100	125100	125100	125100	125100	126900	126900	126500	126500	126500	125600	124000	124000	124400	124400	127500	127500	118000	118000	118000	118000	118000
Rb	108.8	30.33	56	85.3	71.5	52.2	61	32.8	60.8	64.5	22.29	42.5	25.88	41.3	34.8	37.5	62.1	40.1	60.7	39.6	20.7	32.4
K/Rb	1150	4125	2234	1467	1750	2431	2080	3857	2081	1961	5635	2918	4791	3012	3575	3400	2053	2943	1944	2980	5700	3642

Sample							**13-AM-13-F**										**12-SJ-49-A**				
Facies							**Pegmatitic**										**Leucosome**				
Analysis no.	**A1-16**	**A1-17**	**A1-18**	**A1-25**	**A1-26**	**A1-27**	**F-3**	**F-4**	**F-12**	**F-13**	**F-16**	**F-17**	**F-22**	**F-23**	**F-26**	**F-29**	**49-A1**	**49-A 2**	**49-A 22**	**49-A 23**	**49-A 24**
K (ppm)[1]	120700	120700	120700	109800	109800	109800	127100	118300	125800	127400	119500	127400	127100	123800	123000	120700	128150	125000	124400	124650	124250
Rb	6.93	28.9	14.8	15.4	26.7	19.7	34.7	60.2	73.1	81.7	57	68	68.1	57.6	53.6	46.2	16.2	15.3	16.7	24.4	24.3
K/Rb	17417	4176	8155	7130	4112	5574	3663	1965	1721	1559	2096	1874	1866	2149	2295	2613	7910	8170	7449	5109	5113

Sample	
Facies	
Analysis no.	**49-A 25**
K (ppm) [1]	128100
Rb	8.2
K/Rb	15622

[1]: Internal standard value obtained using EMP.

Table 4-8: Rubidium, Nb and Ta analyses of biotite of the various facies of the 13-AM-13 monazite-bearing pegmatitic granite dyke (Allochthonous Belt), and of the leucosome from the Knob Lake Group paragneisses (Parautochthonous Belt). Data were obtained using LA-ICP-MS. Abbreviations: Bt = biotite; Grt = garnet.

Biotite																	
Sample	**13-AM-13-E**																**13-AM-13-A6**
Facies	**Fine grained**																**Intermediate**
Analysis no.	**E-1**	**E-2**	**E-5**	**E-6**	**E-12**	**E-13**	**E-14**	**E-15**	**E-16**	**E-17**	**E-18**	**E-23**	**E-24**	**E-27**	**E-28**	**E-29**	**E-33**	**A6-1**
K (ppm) [1]	80800	80800	81300	81300	81300	81300	81300	81300	81300	81300	81300	80600	80600	81600	81600	81600	79200	77300
Rb	856	847	908	895	927	937	893	873	891	922	893	878	890	910	927	934	912	949
Nb	117	116	98	110	104	103	102	103	102	105	107	107	107	101	105	107	110	112
Ta	3.10	3.09	2.30	2.84	2.58	2.55	2.53	2.58	2.58	2.33	2.53	2.58	2.55	2.54	2.82	2.93	3.26	2.67
Nb/Ta	37.7	37.4	42.4	38.7	40.3	40.5	40.2	39.8	39.5	45.1	42.3	41.3	41.9	39.6	37.2	36.4	33.6	42.0
K/Rb	94.4	95.4	89.5	90.8	87.7	86.8	91.1	93.1	91.3	88.2	91.0	91.8	90.6	89.7	88.0	87.4	86.8	81.5

Sample						**13-AM-13-A5**																
Facies						**Fine grained (+Grt)**																
Analysis no.	**A6-19**	**A6-22**	**A6-25**	**A6-26**	**A6-29**	**A5-3**	**A5-4**	**A5-5**	**A5-6**	**A5-16**	**A5-17**	**A5-18**	**A5-19**	**A5-20**	**A5-21**	**A5-31**	**A5-32**	**A5-33**	**A5-34**	**A5-35**	**A5-36**	**A5-37**
K (ppm) [1]	81600	81600	80500	80500	80900	82000	82000	82000	82000	78200	78200	78200	78200	78200	78200	80600	80600	80600	80600	80600	80600	80600
Rb	946	976	940	931	962	1038	1008	1020	1053	1029	946	946	665	947	709	945	997	968	1021	972	981	1019
Nb	113	113	111	109	111	110	112	108	109	106	110	138	122	105	87	90	92	91	92	94	90	94
Ta	2.80	2.89	2.68	2.62	2.56	3.44	3.59	3.58	3.53	3.20	3.08	3.90	3.93	3.47	2.90	2.61	2.46	2.89	2.55	2.75	2.56	2.71
Nb/Ta	40.1	39.2	41.4	41.6	43.3	32.1	31.1	30.2	30.7	33.1	35.6	35.4	31.0	30.3	30.0	34.3	37.3	31.6	36.3	34.2	35.1	34.5
K/Rb	86.3	83.6	85.7	86.5	84.1	79.0	81.4	80.4	77.9	76.0	82.7	82.7	117.6	82.6	110.3	85.3	80.8	83.2	78.9	82.9	82.1	79.1

Sample									**13-AM-13-A4**													
Facies									**Intermediate (+Bt)**													
Analysis no.	**A5-38**	**A5-39**	**A5-40**	**A5-41**	**A5-46**	**A5-47**	**A5-48**	**A5-49**	**A4-10**	**A4-11**	**A4-12**	**A4-13**	**A4-14**	**A4-15**	**A4-25**	**A4-26**	**A4-27**	**A4-28**	**A4-29**	**A4-30**	**A4-39**	**A4-40**
K (ppm) [1]	80600	80600	80600	80600	80600	80600	80600	80600	80500	81300	81300	74500	74500	81300	75300	75300	75300	75300	75300	75300	81700	60800
Rb	1109	986	1053	999	1006	983	978	953	834	975	1061	1038	1042	1135	951	1031	1030	1004	949	946	939	683
Nb	99	93	100	98	96	96	101	93	94	97	94	92	91	82	101	100	100	96	104	101	101	99
Ta	2.70	2.71	3.17	3.09	2.67	3.09	3.04	2.66	2.50	2.62	2.39	2.17	2.08	1.56	2.64	2.59	2.41	2.42	2.70	2.62	2.47	2.35
Nb/Ta	36.5	34.3	31.4	31.7	35.7	31.0	33.3	34.9	37.5	36.8	39.1	42.3	43.8	52.5	38.2	38.8	41.6	39.7	38.6	38.6	40.8	42.0
K/Rb	72.7	81.7	76.5	80.7	80.2	82.0	82.4	84.6	96.5	83.4	76.6	71.8	71.5	71.6	79.2	73.0	73.1	75.0	79.4	79.6	87.0	89.0

Sample						**13-AM-13-A1**												
Facies						**Coarse grained**												
Analysis no.	**A5-38**	**A4-45**	**A4-46**	**A4-51**	**A4-52**	**A1-1**	**A1-2**	**A1-3**	**A1-4**	**A1-5**	**A1-6**	**A1-7**	**A1-8**	**A1-22**	**A1-23**	**A1-24**	**A1-36**	**A1-37**	**A1-38**
K (ppm) [1]	80600	82600	82600	82600	82600	71600	71600	79700	79700	78400	78400	78400	78400	75600	75600	75600	71500	71500	71500
Rb	1109	983	1046	997	1013	979	952	993	991	1036	1019	1048	1088	1080	1159	996	1155	1183	1082
Nb	99	97	100	92	96	90	84	85	83	84	85	91	86	83	94	85	91	102	92
Ta	2.70	2.55	2.59	2.32	2.52	2.04	1.98	1.98	1.88	1.92	2.09	2.32	2.19	2.42	2.89	2.54	2.71	2.93	2.86
Nb/Ta	36.5	37.9	38.7	39.8	37.9	44.1	42.2	42.7	43.8	44.0	40.8	39.1	39.2	34.2	32.3	33.4	33.5	34.8	32.3
K/Rb	72.7	84.0	79.0	82.8	81.5	73.1	75.2	80.3	80.4	75.7	76.9	74.8	72.1	70.0	65.2	75.9	61.9	60.4	66.1

Sample	13-AM-13-F																12-SJ-49-A					
Facies	Pegmatitic																Leucosome					
Analysis no.	F-1	F-2	F-5	F-6	F-7	F-8	F-18	F-19	F-28	F-30	F-31	F-32	F-33	F-34	F-35	F-36	49-A3	49-A4	49-A8	49-A9	49-A10	49-A11
K (ppm) [1]	80900	81800	81300	77400	80900	80600	80400	79400	80800	80300	79000	79900	80000	80600	81200	80600	80900	82900	83450	83850	83850	84150
Rb	1008	1014	1091	1024	1006	1074	1055	1065	898	884	968	970	906	959	897	902	509	541	546	548	542	527
Nb	110	110	109	114	111	112	111	111	101	97	100	102	99	100	103	98	65	80	77	72	71	70
Ta	2.93	3.06	3.34	3.60	3.14	3.24	3.26	3.08	2.47	2.49	2.46	2.50	2.64	2.60	2.65	2.47	4.47	6.69	5.77	4.88	4.66	4.64
Nb/Ta	37.6	36.0	32.5	31.8	35.5	34.5	34.1	35.9	41.0	39.1	40.5	40.5	37.7	38.2	38.7	39.8	14.5	12.0	13.3	14.8	15.2	15.1
K/Rb	80.2	80.7	74.5	75.6	80.4	75.1	76.2	74.6	90.0	90.8	81.6	82.4	88.3	84.0	90.5	89.4	158.9	153.3	152.7	153.0	154.8	159.8

Sample			
Facies			
Analysis no.	49-A12	49-A16	49-A17
K (ppm) [1]	83100	80600	84050
Rb	516	561	558
Nb	70	68	69
Ta	5.78	4.69	4.63
Nb/Ta	12.2	14.5	14.9
K/Rb	161.0	143.6	150.7

[1]: Internal standard value obtained using EMP.

Table 4-9: Y, REE, Th and U analyses of monazite from the various facies of the 13-AM-13 monazite-bearing pegmatitic granite dyke from the Lac Okaopéo region. Data were obtained using LA-ICP-MS. Abbreviations: Bt = biotite; Grt = garnet.

Sample	13-AM-13-E												13-AM-13-A6											
Facies	Fine grained												Intermediate											
Analysis no.	E-1	E-2	E-3	E-4	E-5	E-6	E-7	E-8	E-9	E-10	E-11	E-12	A6-1	A6-2	A6-3	A6-4	A6-5	A6-6	A6-7	A6-8	A6-9	A6-10	A6-11	A6-12
Y (ppm)	4950	2153	2609	2854	2783	2818	2647	4305	4260	2910	2969	2335	2700	3448	2370	1787	2080	1935	1836	3550	1623	1671	2510	2230
La	129200	134200	114400	119900	120400	122700	119700	126300	124900	115500	120000	118400	126600	122500	116000	120800	128400	126900	128500	115300	126200	125600	132200	117100
Ce	217500	203500	210400	206900	208000	208900	211100	215000	215300	213800	220100	203400	208200	216500	205000	202600	215600	214000	203400	229400	201700	206600	211300	205900
Pr	22670	21380	21800	22110	21100	22900	22480	22790	22780	22620	23500	21700	21720	23330	21110	20800	21350	22310	21190	24330	20870	20760	21150	21030
Nd	79500	74600	77700	78500	74500	81700	80000	82200	83800	79500	85000	78700	77200	84000	74500	73500	74000	78800	74700	90800	72600	73100	74500	73300
Sm	11780	8140	9870	10490	8910	10720	10060	12220	12120	10590	11430	9140	9930	12250	8730	8420	8980	9280	8470	12720	7890	8380	8500	8200
Eu	183	115	122	124	203	123	111	176	180	128	133	160	127	120	174	124	114	200	122	118	128	126	123	163
Gd	6810	3860	4780	5170	4340	5140	4910	6870	6640	5370	5500	4480	7470	6980	4860	4430	4940	5080	4430	7050	4110	4230	4720	4250
Tb	582	283	337	378	325	375	353	550	540	398	398	331	453	479	320	267	309	315	273	477	248	245	315	273
Dy	1822	835	982	1124	1010	1066	1056	1720	1620	1182	1147	973	1220	1370	949	692	816	803	731	1378	639	676	922	796
Ho	207	96	111	124	118	117	119	184	179	132	125	105	137	144	97	76	89	83	79	149	72	70	104	91
Er	286	136	158	171	173	158	168	263	250	175	165	151	192	201	134	110	131	111	113	206	106	99	150	135
Tm	19	8	10	11	12	9	11	17	16	11	11	10	14	13	8	8	9	8	7	16	7	7	10	9
Yb	59	31	36	40	41	33	37	56	56	39	38	34	48	49	28	28	31	28	26	52	26	23	34	38
Lu	5	3	3	3	3	3	3	4	5	3	3	3	5	5	3	3	3	3	2	5	2	2	3	3
Th	55600	43700	125400	110500	133300	91300	128000	68100	69700	135000	114600	147000	86800	87100	144000	113300	86700	91800	124900	108500	111400	110200	40400	148300
U	975	382	1221	1065	1252	846	1233	920	956	1370	1092	1120	1216	1013	1283	1073	887	797	1117	1216	1025	982	523	1679
Th/U	57	114	103	104	106	108	104	74	73	99	105	131	71	86	112	106	98	115	112	89	109	112	77	88
ΣLREE	454850	436820	453970	432400	432410	444620	446340	451910	460300	451410	455530	432940	443650	458580	425340	426120	448330	451290	436260	472550	429260	434440	447650	425530
ΣHREE	9973	5366	6540	7146	6225	7024	6769	9840	9485	7439	7520	6246	9667	9362	6573	5736	6442	6631	5784	9451	5338	5478	6380	5759
ΣREE	464823	442186	460510	439546	438635	451644	453109	461750	469785	458849	463050	439186	453317	467942	431913	431856	454772	457921	442044	482001	434598	439918	454030	431289
La_N/Yb_N[1]	1418	2868	2525	1962	2006	2456	2229	1452	1546	2164	2081	2391	1777	1685	2845	2984	2860	3057	3332	1503	3285	3694	2665	2088
La_N/Sm_N[1]	6.5	9.9	8.5	6.8	8.4	7.0	7.6	6.1	6.5	7.4	6.3	8.2	8.0	6.2	8.3	9.0	8.9	8.5	9.5	5.7	10	9.4	9.7	8.9
Gd_N/Yb_N[1]	93	102	107	106	86	125	106	99	97	111	118	106	125	114	142	130	131	146	137	109	127	148	113	90
Eu/Eu*[1]	0.06	0.06	0.05	0.05	0.10	0.05	0.05	0.06	0.06	0.05	0.05	0.08	0.05	0.04	0.08	0.06	0.05	0.09	0.06	0.04	0.07	0.06	0.06	0.08

Sample																									
Facies																									
Analysis no.	A6-13	A6-14	A6-15	A6-16	A6-17	A6-18	A6-19	A6-20	A6-21	A6-22	A6-23	A6-24	A6-25	A6-26	A6-27	A6-28	A6-29	A6-30	A6-31	A6-32	A6-33	A6-34	A6-35	A6-36	A6-37
Y (ppm)	3506	2376	3165	2270	1649	2603	1926	1832	2034	3919	1685	2735	2790	2802	2260	2684	4120	2547	1948	2569	2916	3047	2667	1693	2537
La	127200	118900	121800	116500	121200	129800	122700	119000	120500	128700	117000	121300	115100	125100	125600	120600	127000	121800	127900	122900	122900	119600	117600	123400	116000
Ce	214400	212000	219800	216600	204200	207700	203400	205600	201700	216700	204100	214500	214500	214800	211300	216600	215800	208800	206800	212400	214100	217200	211400	201300	208700
Pr	23040	22440	23270	22690	20470	21630	21200	21130	20400	22330	20880	22310	22150	22200	21780	22490	22340	21770	20990	22030	22240	22870	22380	20560	21890
Nd	84400	80000	84100	81100	72100	75300	73500	72400	72800	79400	72400	82400	80100	82300	77300	81400	78600	79100	75100	77800	82200	82200	79600	73000	79600
Sm	11850	9990	11800	10240	7860	9870	8600	7990	8200	10840	7980	10530	10260	10500	9340	10400	10450	9870	8470	9970	10650	11180	10100	8040	9270
Eu	120	121	122	125	123	116	463	172	163	180	127	106	110	121	115	118	172	111	115	115	123	122	124	120	174
Gd	6500	5270	6370	5270	3850	5090	4290	3960	4070	6160	3880	5570	5220	5310	4820	5280	6120	5030	4110	4990	5540	5740	5190	3750	4540
Tb	456	335	425	329	237	347	267	259	257	483	235	376	358	357	320	361	483	342	272	337	377	409	349	241	306
Dy	1320	917	1211	899	644	1000	749	746	743	1460	658	1069	1037	1043	881	1042	1539	967	751	979	1121	1194	1048	672	916
Ho	151	101	133	93	72	111	82	79	79	166	73	119	116	121	97	118	172	107	82	108	123	132	117	72	106
Er	215	143	182	129	101	159	119	101	112	223	103	172	164	168	134	166	232	153	114	157	185	187	161	107	170
Tm	15	10	13	9	7	11	9	6	8	15	7	12	11	12	9	11	17	11	8	11	12	13	12	7	15
Yb	51	32	48	31	24	40	29	21	25	49	25	40	40	41	32	42	52	36	30	35	43	46	41	26	63
Lu	5	3	4	3	2	4	3	2	2	4	2	4	4	4	3	4	5	3	3	4	4	4	4	2	6
Th	102100	103500	91400	98100	157800	81000	134500	148900	143000	50500	161000	124700	124500	97000	103800	107100	52700	103300	134300	93900	112600	108900	120500	146700	135900
U	1261	1071	1047	1013	1334	953	1193	1197	1273	908	1297	1263	1317	1042	1013	1126	961	1090	1144	1002	1200	1217	1315	1170	2110
Th/U	81	97	87	97	118	85	113	124	112	56	124	99	95	93	102	95	55	95	117	94	94	89	92	125	64
ΣLREE	460890	443330	460770	447130	425830	444300	429400	426120	423600	457970	422360	451040	442110	454900	445320	451490	454190	441340	439260	445100	452090	453050	441080	426300	435460
ΣHREE	8832	6931	8508	6887	5061	6879	6010	5346	5458	8740	5110	7469	7060	7176	6411	7142	8791	6760	5485	6734	7528	7847	7045	4996	6296
ΣREE	469722	450261	469278	454017	430891	451179	435410	431466	429058	466710	427470	458509	449170	462076	451731	458632	462981	448100	444745	451834	459618	460897	448125	431296	441756
La_N/Yb_N[1]	1681	2564	1720	2578	3474	2188	2874	3868	3223	1784	3231	2065	1980	2058	2683	1955	1672	2298	2945	2420	1955	1751	1958	3287	1261
La_N/Sm_N[1]	6.7	7.4	6.4	7.1	9.6	8.2	8.9	9.3	9.2	7.4	9.2	7.2	7.0	7.4	8.4	7.2	7.6	7.7	9.4	7.7	7.2	6.7	7.3	9.6	7.8
Gd_N/Yb_N[1]	102	135	107	139	131	102	120	153	130	102	128	113	107	104	123	102	96	113	113	117	105	100	103	119	59
Eu/Eu*[1]	0.04	0.05	0.04	0.05	0.07	0.05	0.23	0.09	0.09	0.07	0.07	0.04	0.05	0.05	0.05	0.05	0.07	0.05	0.06	0.05	0.05	0.05	0.05	0.07	0.08

Sample									13-AM-13-A5													
Facies									Fine grained (+Grt)													
Analysis no.	A6-38	A6-39	A6-40	A6-41	A6-42	A6-43	A6-44	A6-45	A5-1	A5-2	A5-3	A5-4	A5-5	A5-6	A5-7	A5-8	A5-9	A5-10	A5-11	A5-12	A5-13	A5-14
Y (ppm)	2366	1704	3465	2168	2508	2114	2129	2440	4765	2847	3348	1901	3229	3487	1833	1766	2020	4123	2817	2227	1981	2256
La	125800	119800	117600	120100	124000	114500	115400	121300	127100	126400	111400	120200	121900	124800	117900	114600	113900	122000	130800	140700	112800	114000
Ce	209000	204200	220200	204600	209100	203600	205800	211000	217900	202700	210400	208300	214400	217500	203800	202500	203500	214900	216900	207300	202200	200400
Pr	22180	20780	22890	21040	21870	21050	21020	21620	22430	21790	21430	20880	22620	23210	21290	20960	20960	22750	22520	21600	20970	20230
Nd	78300	72900	84100	73400	77600	73900	72500	75600	80300	76400	76900	74700	80800	84000	73100	73500	73700	83200	81600	73500	75200	71300
Sm	9990	7930	11850	8980	10090	8030	8130	9720	11340	8910	9930	8220	11270	12520	8360	8220	8100	12100	10140	8010	8490	7800
Eu	112	125	123	98	110	250	137	107	169	198	218	162	164	173	197	125	139	169	162	117	131	182
Gd	4900	3740	6320	4340	5040	3940	4070	4680	6560	4330	5260	3810	5790	6730	3770	3690	3770	6760	5070	4020	4010	3740
Tb	326	238	454	289	342	274	281	324	565	320	396	264	438	522	266	241	251	524	369	289	276	279
Dy	953	674	1342	836	1015	790	806	928	1777	1005	1252	751	1283	1491	754	686	742	1650	1099	881	793	828
Ho	107	74	156	94	113	87	92	104	205	117	140	83	135	146	76	78	86	180	124	101	90	91
Er	146	109	218	135	161	123	131	149	280	171	205	112	176	181	96	110	134	239	167	148	126	123
Tm	10	7	15	9	11	8	9	10	18	12	15	7	11	10	5	8	10	15	11	10	9	8
Yb	35	25	52	33	39	29	33	36	59	39	51	25	36	30	15	26	34	52	35	32	27	24
Lu	3	2	5	3	4	3	3	3	5	3	4	2	3	2	1	3	3	4	3	3	3	2
Th	94300	141800	99500	107700	88000	137800	146500	92000	58200	147400	102600	151000	100600	62700	143000	172000	165000	62000	52000	35400	149000	145000
U	974	1257	1174	1115	968	1220	1244	951	1057	1530	1562	1188	1033	976	1390	1300	1520	960	641	402	1196	1468
Th/U	97	113	85	97	91	113	118	97	55	96	66	127	97	64	103	132	109	65	81	88	125	99
ΣLREE	445270	425610	456640	428120	442660	421080	422850	439240	459070	436200	430060	432300	450990	462030	424450	419780	420160	454950	461960	451110	419660	413730
ΣHREE	6592	4994	8684	5836	6834	5504	5562	6341	9638	6194	7541	5215	8037	9285	5180	4967	5169	9593	7040	5600	5465	5275
ΣREE	451862	430604	465324	433956	449494	426584	428412	445581	468708	442394	437601	437515	459027	471315	429630	424747	425329	464543	469000	456710	425125	419005
La_N/Yb_N[1]	2442	3282	1530	2450	2171	2673	2397	2264	1476	2207	1496	3333	2281	2855	5201	2960	2269	1603	2539	2978	2817	3281
La_N/Sm_N[1]	7.9	9.4	6.2	8.4	7.7	8.9	8.9	7.8	7.0	8.9	7.0	9.1	6.8	6.2	8.8	8.7	8.8	6.3	8.1	11	8.3	9.1
Gd_N/Yb_N[1]	113	122	98	105	105	110	101	104	91	90	84	126	129	183	198	114	89	106	117	101	119	128
Eu/Eu^*[1]	0.05	0.07	0.04	0.05	0.05	0.14	0.07	0.05	0.06	0.10	0.09	0.09	0.06	0.06	0.11	0.07	0.08	0.06	0.07	0.06	0.07	0.10

Sample									13-AM-13-A4															
Facies									Intermediate (+Bt)															
Analysis no.	A5-15	A5-16	A5-17	A5-18	A5-19	A5-20	A5-21	A5-22	A4-1	A4-2	A4-3	A4-4	A4-5	A4-6	A4-7	A4-8	A4-9	A4-10	A4-11	A4-12	A4-13	A4-14	A4-15	A4-16
Y (ppm)	2990	2354	4130	3907	3668	4122	3018	1924	2692	2508	4361	4391	2009	1751	2008	4381	2914	3158	2169	2571	1667	3470	3987	4840
La	120900	119000	123200	117800	127400	131100	122200	146900	117500	122000	123000	132100	123000	127200	118700	129900	119500	135100	127800	128300	122300	117100	123800	123700
Ce	213300	207600	215500	206400	216900	213600	216100	207600	214900	213000	212800	210200	198200	201300	204500	218000	215300	213300	209200	209700	200600	214200	216500	214800
Pr	21900	21500	23300	21560	23240	22530	22560	20530	23150	22470	22880	21710	20350	20530	20970	23310	22910	22390	22040	22210	20280	23130	23140	23050
Nd	78500	73100	84400	75900	83100	81600	81700	69700	82600	80300	84500	76900	71900	72500	74700	83200	83400	79000	77200	80800	70900	84000	82900	83300
Sm	10390	8690	12770	8980	11490	11780	10990	7380	10590	10470	12500	10560	8250	7880	8340	12510	11370	10170	9590	10370	7750	12450	11840	11980
Eu	132	149	173	175	146	165	128	107	122	110	172	181	157	232	144	180	130	147	121	110	120	177	160	205
Gd	5310	4210	6940	4470	6100	6650	5560	3477	5230	5040	6870	5970	3830	3634	3982	7030	5540	5130	4711	4981	3541	6910	6490	6860
Tb	405	301	551	359	476	529	409	246	370	351	562	503	267	250	273	567	403	395	320	345	227	525	518	583
Dy	1196	890	1660	1267	1448	1583	1194	744	1108	1035	1707	1629	767	704	784	1708	1185	1235	900	998	658	1505	1572	1857
Ho	128	98	182	162	162	175	128	86	118	114	186	184	87	75	89	186	130	141	95	110	73	151	176	212
Er	172	138	251	271	226	232	174	124	161	153	258	260	124	102	123	253	176	193	136	160	107	179	234	291
Tm	12	10	16	21	15	15	11	8	11	10	16	16	8	6	8	16	12	13	8	10	7	10	16	19
Yb	34	32	51	86	49	48	37	28	35	33	54	53	28	19	25	51	39	42	30	36	26	31	49	58
Lu	3	3	4	8	4	4	3	3	3	3	5	5	2	2	2	5	3	4	3	3	2	3	4	5
Th	86000	131000	68400	133000	63300	64000	87600	33000	97600	103800	71900	52600	123900	121000	118300	62600	96900	50170	84700	84400	131400	68800	63400	52400
U	862	1124	987	1760	753	917	894	362	981	1061	938	959	1091	906	1069	965	938	591	853	897	1034	970	813	1002
Th/U	100	117	69	76	84	70	98	91	99	98	77	55	114	134	111	65	103	85	99	94	127	71	78	52
ΣLREE	444990	429890	459170	430640	462130	460610	453550	452110	448740	448240	455680	451470	421700	429410	427210	466920	452480	459960	445830	451380	421830	450880	458180	456830
ΣHREE	7391	5830	9829	6819	8626	9400	7645	4823	7158	6850	9831	8800	5269	5023	5429	9995	7618	7298	6323	6753	4760	9490	9218	10089
ΣREE	452381	435720	468999	437459	470756	470010	461195	456933	455898	455090	465511	460270	426969	434433	432639	476915	460098	467258	452153	458133	426590	460370	467398	466919
La_N/Yb_N[1]	2401	2558	1635	926	1755	1875	2244	3629	2268	2481	1547	1690	3027	4501	3265	1717	2098	2165	2875	2401	3220	2591	1727	1459
La_N/Sm_N[1]	7.3	8.6	6.0	8.2	6.9	6.9	6.9	12	6.9	7.3	6.1	7.8	9.3	10	8.9	6.5	6.6	8.3	8.3	7.7	9.9	5.9	6.5	6.4
Gd_N/Yb_N[1]	126	108	110	42	100	113	122	102	120	122	103	91	112	153	130	111	116	98	126	111	111	182	108	96
Eu/Eu*[1]	0.05	0.08	0.06	0.08	0.05	0.06	0.05	0.06	0.05	0.05	0.06	0.07	0.08	0.13	0.08	0.06	0.05	0.06	0.05	0.05	0.07	0.06	0.06	0.07

Sample										13-AM-13-A1										13-AM-13-F			
Facies										Coarse grained										Pegmatitic			
Analysis no.	A4-17	A4-18	A4-19	A4-20	A4-21	A4-22	A4-23	A4-24	A4-25	A1-1	A1-2	A1-3	A1-4	A1-5	A1-6	A1-7	A1-8	A1-9	A1-10	F-1	F-2	F-3	F-4
Y (ppm)	2580	2066	1807	4312	2504	4360	4190	2717	2740	3364	4733	3120	2256	4194	3200	4425	3105	4309	2445	2608	2121	3050	1787
La	122400	126000	119200	124400	129200	127700	132300	123200	123400	115300	128500	117300	112800	116600	115200	129400	115100	131700	123400	116800	115500	118000	112100
Ce	204500	204300	209600	210200	210000	212600	206300	215600	213100	206200	217400	202900	205800	224400	214900	218100	203500	213900	208700	216300	210900	215200	218000
Pr	21550	20980	22270	21810	21250	23000	21370	23350	23050	21240	23110	20660	21470	24080	22610	23040	21010	22350	21850	22130	20620	21150	21130
Nd	75600	73400	79300	77100	75700	82600	77500	85600	84100	75000	83700	72800	75700	88200	81200	83700	73500	79700	77800	78600	74500	76300	75600
Sm	9060	8270	9550	10340	9190	11880	10570	11590	10920	9090	13130	8650	8640	13530	11080	12200	8700	11110	9500	8860	8410	8360	8440
Eu	134	139	148	176	125	164	178	130	152	217	158	228	151	159	161	164	216	178	140	220	157	203	142
Gd	4540	3740	4340	5720	4430	6380	5820	5700	5400	4510	7060	4463	4167	7090	5780	6790	4369	6260	4597	4290	3930	4210	3800
Tb	323	268	295	489	310	512	482	401	395	375	559	367	294	553	423	553	358	523	330	325	259	321	250
Dy	946	783	780	1532	915	1597	1542	1143	1127	1220	1775	1146	866	1644	1265	1716	1161	1672	966	968	813	1069	703
Ho	109	90	82	180	107	179	168	113	126	134	206	131	99	180	142	192	131	187	107	110	89	124	78
Er	160	128	108	249	164	246	238	149	162	188	277	171	139	248	191	259	174	252	149	144	136	184	109
Tm	12	8	7	17	13	16	16	9	10	13	19	11	9	17	13	17	11	16	10	9	10	15	8
Yb	51	31	24	52	54	59	53	33	33	38	66	34	33	55	41	55	33	51	35	30	31	45	27
Lu	5	3	2	5	5	5	4	3	3	3	6	3	3	5	4	5	2	4	3	2	3	4	3
Th	96700	124700	78900	52000	92000	67400	55100	97700	97800	144200	46910	147000	191400	107400	130200	57000	147600	55700	133700	149000	161000	144300	178000
U	1140	1025	725	897	1149	914	873	968	928	1385	1298	1345	1525	1220	1197	1000	1338	915	1154	1380	1378	1390	1410
Th/U	85	122	109	58	80	74	63	101	105	104	36	109	126	88	109	57	110	61	116	108	117	104	126
ΣLREE	433110	432950	439920	443850	445340	457780	448040	459340	454570	426830	465840	422310	424410	466810	444990	466440	421810	458760	441250	442690	429930	439010	435270
ΣHREE	6281	5189	5787	8420	6122	9158	8502	7681	7409	6698	10127	6553	5760	9952	8020	9750	6456	9144	6336	6096	5427	6175	5118
ΣREE	439391	438139	445707	452270	451462	466938	456542	467021	461979	433528	475967	428863	430170	476762	453010	476190	428266	467904	447586	448786	435357	445185	440388
La_N/Yb_N[1]	1624	2788	3388	1613	1641	1475	1702	2544	2564	2056	1327	2351	2358	1430	1904	1601	2398	1741	2430	2681	2556	1781	2820
La_N/Sm_N[1]	8.4	9.5	7.8	7.5	8.8	6.7	7.8	6.6	7.1	7.9	6.1	8.5	8.2	5.4	6.5	6.6	8.3	7.4	8.1	8.2	8.6	8.8	8.3
Gd_N/Yb_N[1]	72	99	147	88	67	88	89	140	134	96	87	107	104	104	114	100	108	99	108	117	104	76	114
Eu/Eu*[1]	0.06	0.08	0.07	0.07	0.06	0.06	0.07	0.05	0.06	0.10	0.05	0.11	0.08	0.05	0.06	0.05	0.11	0.07	0.06	0.11	0.08	0.10	0.08

Sample											
Facies											
Analysis no.	F-5	F-6	F-7	F-8	F-9	F-10	F-11	F-12	F-13	F-14	F-15
Y (ppm)	1839	2260	3010	3350	3340	4130	3124	2343	3220	2489	2127
La	120300	133400	115500	117700	124700	124200	131200	137500	132900	117200	115100
Ce	206500	214200	219700	213900	216600	219700	213100	205500	207900	201600	204200
Pr	20550	21500	23400	21400	22000	23300	21800	21000	22700	20900	20900
Nd	74300	78500	82300	74700	80300	82800	79900	75800	82900	72000	76300
Sm	8320	8840	11010	8920	9990	11850	10100	8830	10600	7870	8270
Eu	164	150	129	202	201	147	148	122	157	197	217
Gd	3830	4360	5440	4520	5040	6410	5330	4340	5540	3730	4030
Tb	248	292	408	351	395	469	398	312	399	299	300
Dy	744	839	1254	1163	1238	1483	1255	906	1184	862	848
Ho	82	94	132	134	139	172	143	103	130	101	89
Er	113	144	181	191	196	242	193	148	189	129	115
Tm	8	10	13	14	13	17	13	10	12	8	7
Yb	29	40	42	53	45	54	42	36	42	25	22
Lu	3	3	4	4	4	5	3	3	3	2	2
Th	141000	98700	66500	130000	132100	69100	54500	61100	55900	146000	167000
U	1143	1330	671	1710	1410	838	695	492	645	1298	1320
Th/U	123	74	99	76	94	82	78	124	87	112	127
ΣLREE	429970	456440	451910	436620	453590	461850	456100	448630	457000	419570	424770
ΣHREE	5220	5933	7603	6633	7272	8999	7525	5980	7656	5353	5629
ΣREE	435190	462373	459513	443253	460862	470849	463625	454610	464656	424923	430399
La_N/Yb_N[1]	2808	2271	1868	1509	1870	1577	2148	2587	2150	3223	3554
La_N/Sm_N[1]	9.0	9.4	6.6	8.2	7.8	6.5	8.1	9.7	7.8	9.3	8.7
Gd_N/Yb_N[1]	106	88	105	69	90	97	104	97	107	122	148
Eu/Eu^*[1]	0.09	0.07	0.05	0.10	0.09	0.05	0.06	0.06	0.06	0.11	0.11

[1]: Normalization to the chondrite after McDonough and Sun (1995).

Table 4-10: Whole rock geochemistry of the various facies of the 13-AM-13 monazite-bearing pegmatitic granite dyke (Allochthonous Belt) and of the melanosome, mesosome and leucosome of the Knob Lake Group paragneisses that represent its potential source. Abbreviations: A/CNK = Al/ (Na + K + Ca/2) (Shand, 1943); Allanite-bearing = allanite-bearing pegmatitic granite dyke; A/NK = Al/(Na + K) (Shand, 1943); ASI = Aluminum Saturation Index given by the expression ASI = Al/(Ca – 1.67 x P + Na + K) (Frost et al., 2001; Shand, 1943); Bt = biotite; Grt = garnet; L.D. = limit of detection; Monazite-bearing = monazite-bearing pegmatitic granite dyke.

Type	*Monazite-bearing PGD*						*Parautochthonous Paragneisses*		
Outcrop	**13-AM-13**						**12-SJ-49**		
Sample no.	**-13-E[1]**	**-13-A6**	**-13-A5**	**-13-A4**	**-13-A1**	**-13-F**	**-49-A**	**-49-C**	**-49-D**
Facies	**Fine grained**	**Intermediate**	**Fine grained (+Grt)**	**Intermediate (+Bt)**	**Coarse grained**	**Pegmatitic**	**Leucosome**	**Mesosome**	**Melanosome**
SiO_2 ***(wt.%)***	60.24	66.11	70.37	72.55	73.08	72.50	74.31	66.48	53.95
Al_2O_3	18.58	17.82	15.66	14.14	15.06	12.00	14.11	14.81	17.17
Fe_2O_3 ***(total)***	4.60	1.71	1.96	1.94	1.04	2.52	0.94	5.80	11.34
MgO	1.16	0.41	0.43	0.47	0.21	0.58	0.39	2.47	4.87
MnO	0.03	0.01	0.01	0.01	0.01	0.01	0.00	0.07	0.12
CaO	3.10	1.23	2.17	2.16	1.80	0.86	2.36	3.34	2.38
Na_2O	4.02	3.00	3.42	3.15	2.97	1.70	3.90	3.39	2.57
K_2O	4.36	8.96	4.43	3.71	5.58	6.96	2.80	1.60	4.12
TiO_2	0.89	0.30	0.32	0.33	0.18	0.42	0.09	0.65	1.18
P_2O_5	0.40	0.36	0.21	0.14	0.11	0.30	0.11	0.18	0.21
Cr_2O_3	< L.D.	< L.D.	< L.D.	< L.D.	< L.D.	< L.D.	-	-	-
LOI	0.82	0.53	0.57	0.69	0.55	0.60	0.5	0.68	1.04
Total	98.19	100.40	99.55	99.29	100.60	98.44	99.51	99.46	98.94
ASI	1.36	1.16	1.29	1.29	1.21	1.12	1.23	-	-
A/CNK	1.46	1.17	1.37	1.39	1.28	1.12	1.34	-	-
A/NK	1.64	1.22	1.50	1.54	1.38	1.16	1.49	-	-
Sr ***(ppm)***	550	639	507	462	702	421	372	341	272
Ba	899	1981	915	857	1384	1458	976	481	1232
Nb	21	5.4	5.9	5.1	4.6	11	1.4	9.0	16
V	27	11	10	12	7	13	15	97	186
Co	6	2	2	2	1	3	2.2	13	26
Ga	60	42	34	29	26	21	14	19	25
Ge	6.9	3.7	2.5	2	2.6	2.1	0.9	1.5	2.2
In	< L.D.	< L.D.	< L.D.	< L.D.	< L.D.	< L.D.	< L.D.	0.0	0.1
Sn	< L.D.	< L.D.	< L.D.	< L.D.	< L.D.	< L.D.	0.6	1.3	1.7
Cs	1.5	0.9	0.7	0.5	0.6	1.2	0.6	2.2	4.0
Pb	34	58	37	31	34	35	19	10	15
Be	3	2	3	3	2	1	1.6	1.5	1.1
Hf	42	22	41	60	3.6	3.8	1.0	3.5	5.8
Ta	0.4	0.1	0.2	0.1	0.1	0.3	0.1	0.7	0.8
W	1.1	< L.D.	< L.D.	< L.D.	0.7	0.7	< L.D.	< L.D.	< L.D.
Tl	1.4	1.5	0.8	0.7	1.2	1.6	-	-	-
Bi	< L.D.	< L.D.	< L.D.	< L.D.	< L.D.	< L.D.	< L.D.	< L.D.	< L.D.
Th	1300	1210	560	420	340	118	0.2	7.1	15
U	19	17	10	8.3	4.8	2.5	0.3	1.7	1.9
Rb	214	317	173	156	172	259	47	72	153
Y	53	46	30	23	13	12	4.6	20	41
Zr	1480	715	1440	2130	135	142	35	132	217
Nb/Ta	53	42	37	39	46	40	11	12	19
Zr/Hf	36	32	35	36	38	37	36	37	38
Th/U	68	70	56	50	71	48	1	4	8
La	1800	1510	886	613	419	184	8.5	28	55
Ce	3370	2980	1710	1180	776	344	16	55	109
Pr	370	313	182	126	82	36	1.8	6.4	13
Nd	1250	1040	592	407	270	124	6.9	25	47
Sm	159	136	76	54	34	17	1.5	4.6	8.4
Eu	4.7	4.9	3.3	2.9	2.9	2.3	1.4	1.2	1.3
Gd	65	57	33	24	14	7.7	1.2	4.0	7.2
Tb	5.0	4.1	2.3	1.6	1.0	0.7	0.2	0.6	1.1
Dy	16.3	13.8	8.6	6.0	3.8	2.8	0.9	3.6	7.2
Ho	1.9	1.7	1.1	0.8	0.5	0.4	0.2	0.8	1.5
Er	3.8	3.2	2.4	2.1	0.9	0.9	0.4	2.0	4.1
Tm	0.3	0.2	0.2	0.2	0.1	0.1	0.1	0.3	0.6
Yb	1.6	0.9	1.1	1.4	0.4	0.6	0.4	2.0	4.1
Lu	0.2	0.1	0.2	0.2	0.0	0.1	0.1	0.3	0.6
ΣLREE	6949	5979	3446	2380	1580	705	35	119	232
ΣHREE	99	86	52	39	23	15	4.8	15	28
ΣREE	7048	6065	3498	2419	1603	721	39	134	259
Eu/Eu*[2]	0.1	0.2	0.2	0.2	0.4	0.6	3.2	0.8	0.5
La_N/Sm_N[2]	7.1	6.9	7.2	7.1	7.7	6.8	1.1	1.1	1.1
La_N/Yb_N[2]	784	1193	537	304	769	223	3.4	3.4	3.4
Gd_N/Yb_N[2]	34	54	24	14	30	11	2.7	2.7	2.7

B	-	3	< 2	4	-	-	2.7	2.7	2.7
F	-	< L.D.	< L.D.	< L.D.	-	-	11	12	19
Li	-	< L.D.	< L.D.	< L.D.	-	-	36	37	38
Cd	< L.D.	< L.D.	< L.D.	< L.D.	< L.D.	< L.D.	0.6	4.3	7.8
Cu	20	5	5	6	3	2	-	-	-
Ag	< L.D.	< L.D.	< L.D.	< L.D.	< L.D.	< L.D.	-	-	-
Ni	3	1	2	1	2	6	-	-	-
Mo	4	3	2	3	< L.D.	< L.D.	< L.D.	< L.D.	< L.D.
Zn	110	45	77	57	24	68	< L.D.	41	12
S	1100	100	< L.D.	< L.D.	300	500	-	-	-
Au *(ppb)*	< L.D.	< L.D.	< L.D.	< L.D.	< L.D.	< L.D.	6.3	32	66
As	< L.D.	< L.D.	< L.D.	< L.D.	< L.D.	< L.D.	< L.D.	< L.D.	0.5
Br	< L.D.	< L.D.	< L.D.	< L.D.	< L.D.	< L.D.	15	77	176
Ir	< L.D.	< L.D.	< L.D.	< L.D.	< L.D.	< L.D.	-	-	-
Sc	3.5	0.9	1.4	1.6	0.6	1.5	-	-	-
Sb	< L.D.	< L.D.	< L.D.	< L.D.	< L.D.	< L.D.	< L.D.	< L.D.	< L.D.
Se	< L.D.	< L.D.	< L.D.	< L.D.	< L.D.	< L.D.	-	-	-

[1]: Data from Turlin et al. (2017).

[2]: Normalization to the chondrite after McDonough and Sun (1995).

References

Ballouard, C., Poujol, M., Boulvais, P., Branquet, Y., Tartèse, R., Vigneresse, J.-L., 2016. Nb-Ta fractionation in peraluminous granites: A marker of the magmatic-hydrothermal transition. Geology G37475.1. doi:10.1130/G37475.1

Bea, F., 1996. Residence of REE, Y, Th and U in granites and crustal protoliths; Implications for the chemistry of crustal melts. J. Petrology 37, 521–552. doi:10.1093/petrology/37.3.521

Busch, J.P., van der Pluijm, B.A., Hall, C.M., Essene, E.J., 1996. Listric normal faulting during postorogenic extension revealed by 40Ar/39Ar thermochronology near the Robertson Lake shear zone, Grenville orogen, Canada. Tectonics 15, 387–402. doi:10.1029/95TC03501

Carr, S.D., Easton, R.M., Jamieson, R.A., Culshaw, N.G., 2000. Geologic transect across the Grenville orogen of Ontario and New York. Can. J. Earth Sci. 37, 193–216. doi:10.1139/e99-074

Carrington, D.P., Watt, G.R., 1995. A geochemical and experimental study of the role of K-feldspar during water-undersaturated melting of metapelites. Chemical Geology 122, 59–76. doi:10.1016/0009-2541(95)00046-O

Černý, P., London, D., Novák, M., 2012. Granitic pegmatites as reflections of their sources. Elements 8, 289–294. doi:10.2113/gselements.8.4.289

Černý, P., Meintzer, R.E., Anderson, A.J., 1985. Extreme fractionation in rare-element granitic pegmatites; selected examples of data and mechanisms. Can. Mineral. 23, 381–421.

Chappell, B.W., White, A.J.R., 2001. Two contrasting granite types: 25 years later. Australian Journal of Earth Sciences 48.

Corrigan, D., van Breemen, O., 1997. U – Pb age constraints for the lithotectonic evolution of the Grenville Province along the Mauricie transect, Quebec. Can. J. Earth Sci. 34, 299–316. doi:10.1139/e17-027

Culshaw, N.G., Ketchum, J.W.F., Wodicka, N., Wallace, P., 1994. Deep crustal ductile extension following thrusting in the southwestern Grenville Province, Ontario. Can. J. Earth Sci. 31, 160–175. doi:10.1139/e94-013

Dumond, G., Goncalves, P., Williams, M.L., Jercinovic, M.J., 2015. Monazite as a monitor of melting, garnet growth and feldspar recrystallization in continental lower crust. J. Metamorph. Geol. 33, 735–762. doi:10.1111/jmg.12150

Dunning, G., Indares, A., 2010. New insights on the 1.7–1.0 Ga crustal evolution of the central Grenville Province from the Manicouagan – Baie Comeau transect. Precambrian Research 180, 204–226. doi:10.1016/j.precamres.2010.04.005

Ercit, T.S., 2005. REE-enriched granitic pegmatites. Short Course Notes - Geological Association of Canada 17, 175–199.

Ferry, J.M., Watson, E.B., 2007. New thermodynamic models and revised calibrations for the Ti-in-zircon and Zr-in-rutile thermometers. Contrib. Mineral. Petrol. 154, 429–437. doi:10.1007/s00410-007-0201-0

Frost, B.R., Barnes, C.G., Collins, W.J., Arculus, R.J., Ellis, D.J., Frost, C.D., 2001. A geochemical classification for granitic rocks. J. Petrology 42, 2033–2048.

Goldschmidt, V., Thomassen, L., 1923. Videnskapsselskapets Skrifter I, Mat. Naturv. Klasse 3, 1–17.

Hönig, S., Čopjaková, R., Škoda, R., Novák, M., Dolejš, D., Leichmann, J., Galiová, M.V., 2014. Garnet as a major carrier of the Y and REE in the granitic rocks: An example from the layered anorogenic granite in the Brno Batholith, Czech Republic. American Mineralogist 99, 1922–1941. doi:10.2138/am-2014-4728

Hulsbosch, N., Hertogen, J., Dewaele, S., André, L., Muchez, P., 2014. Alkali metal and rare earth element evolution of rock-forming minerals from the Gatumba area pegmatites (Rwanda): Quantitative assessment of crystal-melt fractionation in the regional zonation of pegmatite groups. Geochimica et Cosmochimica Acta 132, 349–374. doi:10.1016/j.gca.2014.02.006

Indares, A., Dunning, G., Cox, R., 2000. Tectono-thermal evolution of deep crust in a Mesoproterozoic continental collision setting: the Manicouagan example. Can. J. Earth Sci. 37, 325–340. doi:10.1139/e99-069

Jannin, S., Gervais, F., Moukhsil, A., Augland, L.E., Crowley, J.L., accepted. Déformations tardi-grenvilliennes dans la Ceinture parautochtone (Province de Grenville centrale) :

contraintes géochronologiques par couplage de méthodes U/Pb de haute résolution spatiale et de haute précision. Canadian Journal of Earth Sciences.

Jeanneret, P., 2016. Rôle du métamorphisme et de la déformation dans la redistribution et la pré-concentration d'Uranium dans la croûte continentale : Exemple de la zone de transition Wollaston-Mudjatik (Saskatchewan, Canada) (Unpublished Ph.D. thesis). Université Bourgogne Franche-Comté.

Johnson, T.E., Clark, C., Taylor, R.J.M., Santosh, M., Collins, A.S., 2015. Prograde and retrograde growth of monazite in migmatites: An example from the Nagercoil Block, southern India. Geoscience Frontiers 6, 373–387. doi:10.1016/j.gsf.2014.12.003

Jordan, S.L., Indares, A., Dunning, G., 2006. Partial melting of metapelites in the Gagnon terrane below the high-pressure belt in the Manicouagan area (Grenville Province): pressure–temperature (P–T) and U–Pb age constraints and implications. Can. J. Earth Sci. 43, 1309–1329. doi:10.1139/E06-038

Kelsey, D.E., Clark, C., Hand, M., 2008. Thermobarometric modelling of zircon and monazite growth in melt-bearing systems: examples using model metapelitic and metapsammitic granulites. Journal of Metamorphic Geology 26, 199–212. doi:10.1111/j.1525-1314.2007.00757.x

Ketchum, J.W.F., Heaman, L.M., Krogh, T.E., Culshaw, N.G., Jamieson, R.A., 1998. Timing and thermal influence of late orogenic extension in the lower crust: a U-Pb geochronological study from the southwest Grenville orogen, Canada. Precambrian Research 89, 25–45. doi:10.1016/S0301-9268(97)00079-X

Ketchum, J.W.F., Jamieson, R.A., Heaman, L.M., Culshaw, N.G., Krogh, T.E., 1994. 1.45 Ga granulites in the southwestern Grenville province: Geologic setting, P-T conditions, and U-Pb geochronology. Geology 22, 215–218. doi:10.1130/0091-7613(1994)022<0215:GGITSG>2.3.CO;2

Kovalenko, V., 1978. The genesis of rare metal granitoids and related ore deposits, in: Štemprok, M., Burnol, and Tischendorf, G., Eds., Metallization associated with acid magmatism, Czech Geological Survey. pp. 235–258.

Krogh, T.E., 1994. Precise U-Pb ages for Grenvillian and pre-Grenvillian thrusting of Proterozoic and Archean metamorphic assemblages in the Grenville Front tectonic zone, Canada. Tectonics 13, 963–982. doi:10.1029/94TC00801

Lasalle, S., Dunning, G., Indares, A., 2014. In situ LA–ICP–MS dating of monazite from aluminous gneisses: insights on the tectono-metamorphic history of a granulite-facies domain in the central Grenville Province. Can. J. Earth Sci. 51, 558–572. doi:10.1139/cjes-2013-0170

Lasalle, S., Fisher, C.M., Indares, A., Dunning, G., 2013. Contrasting types of Grenvillian granulite facies aluminous gneisses: Insights on protoliths and metamorphic events from zircon morphologies and ages. Precambrian Research 228, 117–130. doi:10.1016/j.precamres.2013.01.014

Lasalle, S., Indares, A., 2014. Anatectic record and contrasting P-T paths of aluminous gneisses from the central Grenville Province. Journal of Metamorphic Geology 32, 627–646. doi:10.1111/jmg.12083

Linnen, R.L., Cuney, M., 2005. Granite-related rare-element deposits and experimental constraints on Ta-Nb-W-Sn-Zr-Hf mineralization. Short Course Notes - Geological Association of Canada 17, 45–68.

Linnen, R.L., Samson, I.M., Williams-Jones, A.E., Chakhmouradian, A.R., 2014. 13.21 - Geochemistry of the Rare-Earth Element, Nb, Ta, Hf, and Zr Deposits, in: Turekian, H.D.H.K. (Ed.), Treatise on Geochemistry (Second Edition). Elsevier, Oxford, pp. 543–568.

London, D., 2016. Rare-element granitic pegmatites. Reviews in Economic Geology 18, 165–193.

London, D., 2014. A petrologic assessment of internal zonation in granitic pegmatites. Lithos 184–187, 74–104. doi:10.1016/j.lithos.2013.10.025

London, D., 2008. Pegmatites, Mineralogical Association of Canada.

McDonough, W.F., Sun, S. -s., 1995. The composition of the Earth. Chemical Geology, Chemical Evolution of the Mantle 120, 223–253. doi:10.1016/0009-2541(94)00140-4

Montel, J.-M., 1986. Experimental determination of the solubility of Ce-monazite in SiO2-Al2O3-K2O-Na2O melts at 800 °C, 2 kbar, under H2O-saturated conditions. Geology 14, 659–662. doi:10.1130/0091-7613(1986)14<659:EDOTSO>2.0.CO;2

Moukhsil, A., Solgadi, F., Belkacim, S., Elbasbas, A., Augland, L.E., 2014. Géologie de la région du lac Okaopéo, Côte-Nord. Ministère de l'Energie et des Ressources Naturelles, Québec, RG 2014-03, 34 p.

Moukhsil, A., Solgadi, F., Clark, T., Blouin, S., Indares, A., Davis, D.W., 2013. Géologie du nord-ouest de la région du barrage Daniel-Johnson (Manic 5), Côte-Nord. Ministère des Ressources Naturelles, Québec, RG 2013-01, 46 p.

Pollard, P.-J., 1989. Geochemistry of granites associated with tantalum and niobium mineralization, in: Lanthanides, Tantalum and Niobium. Springer Verlag, Berlin, pp. 27–29.

Railsback, L.B., 2003. An earth scientist's periodic table of the elements and their ions. Geology 31, 737–740. doi:10.1130/G19542.1

Raimbault, L., Charoy, B., Cuney, M., Pollard, P.-J., 1991. Comparative geochemistry of Ta-bearing granites, in: Pagel, M., and Leroy, J., Eds., Source, Transport and Deposition of Metals. Balkema, Rotterdam, pp. 793–796.

Raimbault, L., Cuney, M., Azencott, C., Duthou, J.-L., Joron, J.-L., 1995. Multistage magmatic genesis of a Ta–Sn–Li mineralized granite at Beauvoir, French Massif Central: a geochemical study. Economic Geology 90, 548–576.

Rapp, R.P., Watson, E.B., 1986. Monazite solubility and dissolution kinetics: implications for the thorium and light rare earth chemistry of felsic magmas. Contr. Mineral. and Petrol. 94, 304–316. doi:10.1007/BF00371439

Rivers, T., 2012. Upper-crustal orogenic lid and mid-crustal core complexes: signature of a collapsed orogenic plateau in the hinterland of the Grenville Province. Can. J. Earth Sci. 49, 1–42. doi:10.1139/e11-014

Rivers, T., 2009. The Grenville Province as a large hot long-duration collisional orogen – insights from the spatial and thermal evolution of its orogenic fronts. Geological Society, London, Special Publications 327, 405–444. doi:10.1144/SP327.17

Rivers, T., 2008. Assembly and preservation of lower, mid, and upper orogenic crust in the Grenville Province—Implications for the evolution of large hot long-duration orogens. Precambrian Research 167, 237–259. doi:10.1016/j.precamres.2008.08.005

Rivers, T., 1997. Lithotectonic elements of the Grenville Province: review and tectonic implications. Precambrian Research 86, 117–154. doi:10.1016/S0301-9268(97)00038-7

Rivers, T., Culshaw, N., Hynes, A., Indares, A., Jamieson, R., Martignole, J., 2012. The Grenville Orogen - A Post-LITHOPROBE Perspective, in: J.A. Percival, F.A. Cook, and R.M. Clowes (eds) Tectonic Styles in Canada: The LITHOPROBE Perspective, Geological Association of Canada. Special Paper 49, pp. 97–236.

Rivers, T., Martignole, J., Gower, C.F., Davidson, A., 1989. New tectonic divisions of the Grenville Province, Southeast Canadian Shield. Tectonics 8, 63–84. doi:10.1029/TC008i001p00063

Sawyer, E.W., 2001. Melt segregation in the continental crust: distribution and movement of melt in anatectic rocks. Journal of Metamorphic Geology 19, 291–309. doi:10.1046/j.0263-4929.2000.00312.x

Schoene, B., Bowring, S.A., 2007. Determining accurate temperature–time paths from U–Pb thermochronology: An example from the Kaapvaal craton, southern Africa. Geochimica et Cosmochimica Acta 71, 165–185. doi:10.1016/j.gca.2006.08.029

Shand, S.J., 1943. The Eruptive Rocks, 2nd edition. ed. New York: John Wiley.

Spear, F.S., 2010. Monazite–allanite phase relations in metapelites. Chemical Geology 279, 55–62. doi:10.1016/j.chemgeo.2010.10.004

Stepanov, A., Mavrogenes, J.A., Meffre, S., Davidson, P., 2014. The key role of mica during igneous concentration of tantalum. Contrib. Mineral. Petrol. 167, 1–8. doi:10.1007/s00410-014-1009-3

Stevens, G., Villaros, A., Moyen, J.-F., 2007. Selective peritectic garnet entrainment as the origin of geochemical diversity in S-type granites. Geology 35, 9–12. doi:10.1130/G22959A.1

Taylor, J., Stevens, G., 2010. Selective entrainment of peritectic garnet into S-type granitic magmas: Evidence from Archaean mid-crustal anatectites. Lithos 120, 277–292. doi:10.1016/j.lithos.2010.08.015

Taylor, R.P., 1992. Petrological and geochemical characteristics of the Pleasant Ridge zinnwaldite-topaz granite, southern New Brunswick, and comparisons with other topaz-bearing felsic rocks. Can Mineral 30, 895–921.

Tucker, R.D., Gower, C.F., 1994. A U-Pb geochronological framework for the Pinware Terrane, Grenville Province, Southeast Labrador. Journal of Geology 102, 67.

Turlin, F., André-Mayer, A.-S., Moukhsil, A., Vanderhaeghe, O., Gervais, F., Solgadi, F., Groulier, P.-A., Poujol, M., 2017. Unusual LREE-rich, peraluminous, monazite- or allanite-bearing pegmatitic granite in the central Grenville Province, Québec. Ore Geology Reviews 89, 627–667. doi:10.1016/j.oregeorev.2017.04.019

Turlin, F., Deruy, C., Eglinger, A., Vanderhaeghe, O., André-Mayer, A.-S., Poujol, M., Moukhsil, A., Solgadi, F., submitted. A record of 70 Ma suprasolidus conditions in the Grenville large, hot and long-duration orogen. Terra Nova.

van Gool, J.A.M., Rivers, T., Calon, T., 2008. Grenville Front zone, Gagnon terrane, southwestern Labrador: Configuration of a midcrustal foreland fold-thrust belt. Tectonics 27, TC1004. doi:10.1029/2006TC002095

Vanderhaeghe, O., 2009. Migmatites, granites and orogeny: Flow modes of partially-molten rocks and magmas associated with melt/solid segregation in orogenic belts. Tectonophysics, Hot orogens 477, 119–134. doi:10.1016/j.tecto.2009.06.021

White, R.W., Powell, R., 2002. Melt loss and the preservation of granulite facies mineral assemblages. Journal of Metamorphic Geology 20, 621–632. doi:10.1046/j.1525-1314.2002.00206_20_7.x

Yakymchuk, C., Brown, M., 2014. Behaviour of zircon and monazite during crustal melting. Journal of the Geological Society 171, 465–479. doi:10.1144/jgs2013-115

Yakymchuk, C., Clark, C., White, R.W., 2017. Phase Relations, Reaction Sequences and Petrochronology. Reviews in Mineralogy & Geochemistry 83, 13–53. doi:10.2138/rmg.2017.83.2

Chapitre 5 : Pegmatitic granite dyke from the central Grenville derived from partial melting of plutonic rocks from the Allochthonous Belt

François Turlin[a], Anne-Sylvie André-Mayer[a], Olivier Vanderhaeghe[b], Félix Gervais[c], Abdelali Moukhsil[d], Armin Zeh[e,f], Fabien Solgadi[g], I.P.T.N.[h]

Article en préparation pour *Canadian Journal of Earth Sciences*

[a] *GeoRessources lab., Université de Lorraine, CNRS, CREGU, Campus Aiguillettes, Faculté des Sciences et Technologies, rue Jacques Callot, Vandœuvre-lès-Nancy, F-54506, France*

[b] *Géosciences Environnement Toulouse, UMR 5563, Université de Toulouse, France*

[c] *Département des génies civil, géologiques et des mines, Polytechnique Montréal, Canada*

[d] *Ministère de l'Énergie et des Ressources naturelle, Direction du Bureau de la connaissance géoscientifique du Québec, 5700, 4e Avenue Ouest, Québec (Québec)*

[e] *Institut für Geowissenschaften, Frankfurt, Germany*

[f] *Now at KIT-Karlsruhe Institute of Technology, Campus South, Institute for Applied Geosciences, Mineralogy and Petrology*

[g] *Ministère de l'Énergie et des Ressources naturelles, Direction du Bureau de la connaissance géoscientifique du Québec, 400, boulevard Lamaque, Val-d'Or (Québec)*

[h] *Ion Probe Team Nancy, CRPG, UMR 7358, CNRS, Université de Lorraine, Vandœuvre-lès-Nancy, F-54501, France*

Abstract

Petrogeochemical characteristics and U-Pb-Hf-O isotopic and trace elements data of zircon grains from a shallow-dipping pegmatitic granite dyke hosted in a layered metamangerite from the mid- to low-pressure Allochthonous Belt allow to discuss the petrogenetic processes involved in its generation, and the nature and age of its source.

This pegmatitic granite presents a layered fine grained barren core with a cumulate signature and Zr/Hf ratios of 20-25 differentiated into fine grained discordant veins to the foliation of its host with Zr/Hf ratios of 14-20, and to a pegmatitic facies at the contacts with Zr/Hf ratios of 19-37. The latter locally show very diffuse contacts with the host metamangerite and scarce LREE mineralization from 55 to 8757 ppm associated with disseminated allanite phenocrysts.

Prismatic zircon grains from the fine grained core of the pegmatitic granite show complex internal zoning marked by porous or altered zones. They have high Ca, Fe and LREE contents up to 21,999, 10,961 and 915 ppm, respectively and associated flat LREE chondrite normalized patterns. Along with the very variable $\delta^{18}O_{V\text{-}SMOW}$ signatures from supra-mantellic values of +9.16 ‰ down to sub-mantellic values of +2.58 ‰, these features suggest the zircon growth took place at the magmatic-hydrothermal transition.

The zircon grains lack textural, chemical and isotopic evidence for inherited domains. Their U-Pb dating yield an upper intercept age at 1006.2±5.9 Ma that is similar to other pegmatitic granite dykes from the same area. The chondritic to slightly sub-chondritic $\varepsilon Hf_{(1005\ Ma)}$ between -6.2 and 1.0 and associated $T_{DM2\ (1005\ Ma)}$ Hf model ages between 1.74 and 1.90 Ga are similar to the plutonic units of the same area. Accordingly, these features provide evidence for the derivation of the pegmatitic granite dyke from partial melting of plutonic rocks from the Allochthonous Belt, consistent with the suprasolidus conditions recorded until ca. 1005 Ma in this mid- to low-pressure allochthonous crustal segment.

Keywords: Pegmatitic granite; Zircon; U-Pb dating; Hf-O isotopes; Trace elements; Grenville Province

1. Introduction

The magmatic REE mineralization are usually associated with alkaline magmas, in particular peralkaline granites and their pegmatitic end-members usually of alkaline affinity (e.g. Chakhmouradian and Zaitsev, 2012). Recent investigations demonstrated that the genesis of LREE-rich pegmatitic granite dykes (*further designated as 'PGD'*) were associated with strongly peraluminous magmas derived from the partial melting of metapelites (chapters 3 and 4).

The Grenville Province contains numerous REE magmatic occurrences associated with a wide spectrum of magma compositions including carbonatite (Bergeron, 1980; Groulier, 2013), nepheline syenite (Bergeron, 1980; Gauthier and Chartrand, 2005; Groulier, 2013; Sangster et al., 1992), and numerous granitic pegmatites (Ayres and Černý, 1982; Černý, 1990; Ercit, 2005; Lentz, 1996; Masson and Gordon, 1981; Turlin et al., 2017). In particular, the central Grenville Province is particularly enriched in the latter (Turlin et al., 2017) and therefore represents a perfect natural laboratory to investigate the magmatic processes and sources involved in the genesis of REE-mineralization associated with PGD.

Turlin et al. (2017) described seven LREE occurrences associated with PGD in the central Grenville Province, intruding metasedimentary and metaplutonic complexes of a mid- to low-pressure crustal segment of the Allochthonous Belt. Among them, six were attributed as being derived from the high temperature protracted partial melting of Paleoproterozoic-Archean metapelites of the underlying Parautochthonous Belt composed of rocks of the Superior Province and of its metasedimentary cover, all of them reworked during the Grenvillian Orogeny (Rivers et al., 2012; Turlin et al., 2017; chapters 3-4). These conclusions were based on (i) the steep-dipping contacts of the PGD with their hosts, (ii) their strong peraluminous character associated with a strong fractionation of the LREE over the HREE, (iii) the strongly sub-chondritic $\varepsilon Hf_{(1003\ Ma)}$ signatures and associated Paleoproterozoic $T_{DM2\ (1003\ Ma)}$ Hf model ages of pristine zircon grains, (iv) the supra-mantellic $\delta^{18}O_{V\text{-}SMOW}$ signatures of zircon, and (v) the comparison of petrogeochemical characteristics of one PGD with metapelites from the Knob Lake Group. To the contrary, the seventh PGD described in the region has a shallow-dipping contact, distinct petrogeochemical characteristics with a lower peraluminous character and a lower fractionation of the LREE over the HREE, that Turlin et al. (2017) attributed to its derivation from a distinct source and/or magmatic processes.

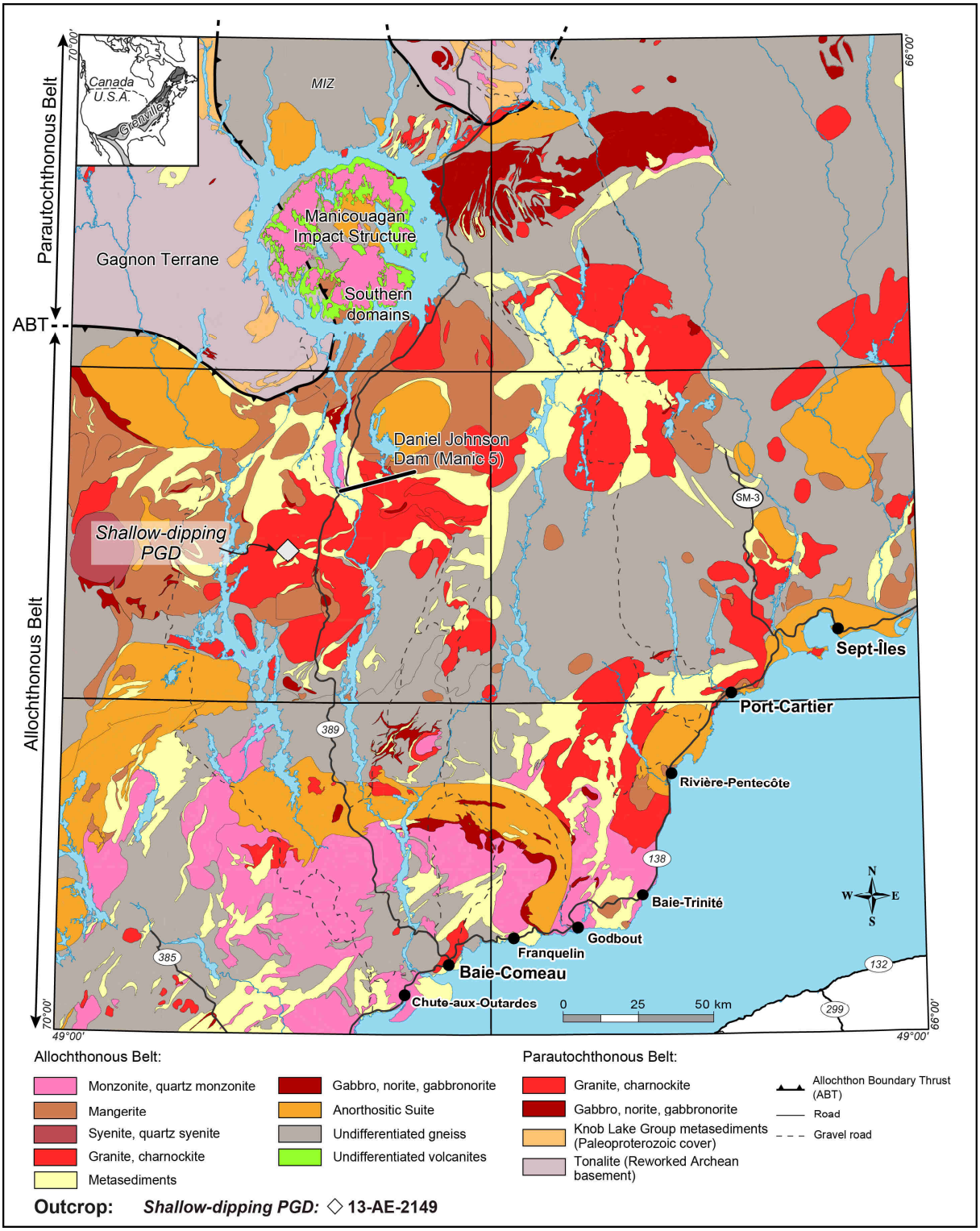

Figure 5-1: Geological map of the central Grenville (Quebec) showing the position of the shallow-dipping 13-AE-2149 allanite-bearing pegmatitic granite dyke investigated in this study (modified after Moukhsil et al., 2014; Turlin et al., 2017). Abbreviations: ABT = Allochthon Boundary Thrust; PGD = pegmatitic granite dyke; MIZ = Manicouagan Imbricate Zone.

Zircon is one of the best tools to investigate the nature and age of its source by coupling Hf-O isotopic and trace element data (e.g. Belousova et al., 2010; Cawood et al., 2013; Dhuime et al., 2012; Eglinger et al., 2017; Hawkesworth and Kemp, 2006; Ibanez-Mejia et al., 2015). This study presents original petrogeochemical characteristics of various facies identified in a shallow-dipping PGD from the central Grenville Province and coupled to zircon U-Pb-Hf-O isotopic and trace element data allow to discuss the source, its nature and age, and the petrogenetic processes responsible for the genesis of this dyke. These results will be compared to similar data of other LREE-rich PGD from the same area to discuss metallogenic implications.

2. Geological setting

2.1. Grenvillian Orogeny

Successive orogenies took place at the southeastern margin of Laurentia, namely Labradorian (ca. 1.71-1.60 Ga), Pinwarian (ca. 1.47-1.45 Ga), Elzevirian (ca. 1.25-1.23 Ma) and Shawinigan (ca. 1.19-1.14 Ga), the metamorphic effects of the two latter being restricted to the western Grenville Province (Ketchum et al., 1994; Rivers, 1997; Rivers et al., 2012; Tucker and Gower, 1994). This tectonic-magmatic accretion ended with the the Grenvillian Orogeny, a continent-continent collision (e.g. Carr et al., 2000; Dunning and Indares, 2010; Gower and Krogh, 2002; Rivers et al., 2012; Tucker and Gower, 1994). Two tectonometamorphic domains compose the Grenville Province and are distinguished on the basis of their origin and metamorphic signatures (Rivers et al., 2012). The Allochthonous Belt consists of terranes that originated outboard of, and were accreted to the Laurentian margin, whereas the Parautochthonous Belt is composed of rocks from the Superior Province and its cover sequence or accreted arcs that all were reworked during the Grenvillian Orogeny (Rivers et al., 2012). They are separated by the Allochthon Boundary Thrust (ABT, Fig. 5-1), a southeast-dipping orogenic-scale high-grade shear zone (Rivers, 2008; Rivers et al., 2012, 1989).

The study area, i.e. south of the Manicouagan area in the central Grenville, is part of a medium to low pressure segment of this belt (aM-L*P*, Rivers, 2008). In this crustal segment, the Grenvillian Orogeny is recorded as the Ottawan phase (ca. 1090-1020 Ma) that is characterized by a peak of metamorphism at ca. 1080-1050 Ma up to sillimanite-grade conditions at ca. 950 MPa and 850°C with a moderate-gradient *P-T* path (Dunning and Indares, 2010; Lasalle et al., 2014; Lasalle and Indares, 2014; Turlin et al., submitted). Following this

peak of metamorphism, Turlin et al. (submitted) proposed that this crustal segment recorded slow cooling under suprasolidus conditions at constant cooling rates of ca. 2 to 6°C/Ma until the ca. 1005 Ma intrusion of a pegmatitic granite dyke in paragneisses from the aM-L*P* segment under close to wet-solidus conditions.

In the Parautochthonous Belt, structurally below the ABT, the Grenvillian Orogeny is recorded after a ca. 10-20 Ma metamorphic and magmatic hiatus as the Rigolet crustal thickening phase (ca. 1005-960 Ma) characterized by an up to granulite-facies peak of metamorphism in a medium pressure crustal segment (pM*P*) at ca. 1250-1500 MPa and ca. 815-850 °C between ca. 1005 and 960 Ma (Hynes et al., 2000; Jannin et al., accepted; Jordan et al., 2006; Rivers, 2009; Rivers et al., 2012; van Gool et al., 2008). This peak of metamorphism is recorded on the southern shore of the Manicouagan Reservoir in the Knob Lake Group metapelites that unconformably overlie the Laurentian basement (Fig. 5-1). This orogenic phase is attributed to the foreland-ward propagation of the Grenvillian high-grade metamorphism and thrusting towards the Grenville Front, a syn-Rigolet orogen-scale southeast-dipping shear zone (Krogh, 1994; Rivers, 2009, 2008; Rivers et al., 1989).

2.2. Lithotectonic units of the aM-L*P* of the central Grenville and isotopic signatures

The study focuses on a pegmatitic granite dyke (*further designated as 'PGD'*) from the Lac Okaopéo region, part of the aM-L*P* segment of the central Grenville Province, south of the Manicouagan Reservoir (Figs. 5-1 and 5-2). Numerous pre-Grenvillian units compose this crustal segment, the oldest protolith being the Plus-Value Complex paragneisses with deposition ages comprised between 1765 and 1497 Ma (Augland et al., 2015; Lasalle et al., 2013; Moukhsil et al., 2013a, 2014). Detrital zircon grains from this paragneisses have U-Pb ages of inherited core ranging between ca. 2.70 and 1.50 Ga (mainly between 1.90 and 1.50 Ga). These are assumed to reflect their correlation to other Paleoproterozoic sequences and Archean basement of the Gagnon Terrane (Parautochthonous Belt) and their source from the Laurentian margin (Lasalle et al., 2013).

Pre-Grenvillian plutonic units intruded this area between ca. 1450 Ma and 1100 Ma, and comprise granitic, tonalitic to dioritic orthogneisses, metamangerite, metagranite and gabbronorite dykes (Augland et al., 2015; David et al., 2009; Gobeil et al., 2002; Moukhsil et al., 2014, 2013a, 2013b, 2012, 2007). The pre-Pinwarian I-type to minor peraluminous S-type metagranitoids from the Bardoux Plutonic Suite have supra-chondritic $\varepsilon Hf_{1497\ Ma}$ values between +2.30 and +4.70 (Fig. 5-10, Augland et al., 2015; Moukhsil et al., 2014, 2012). Late-

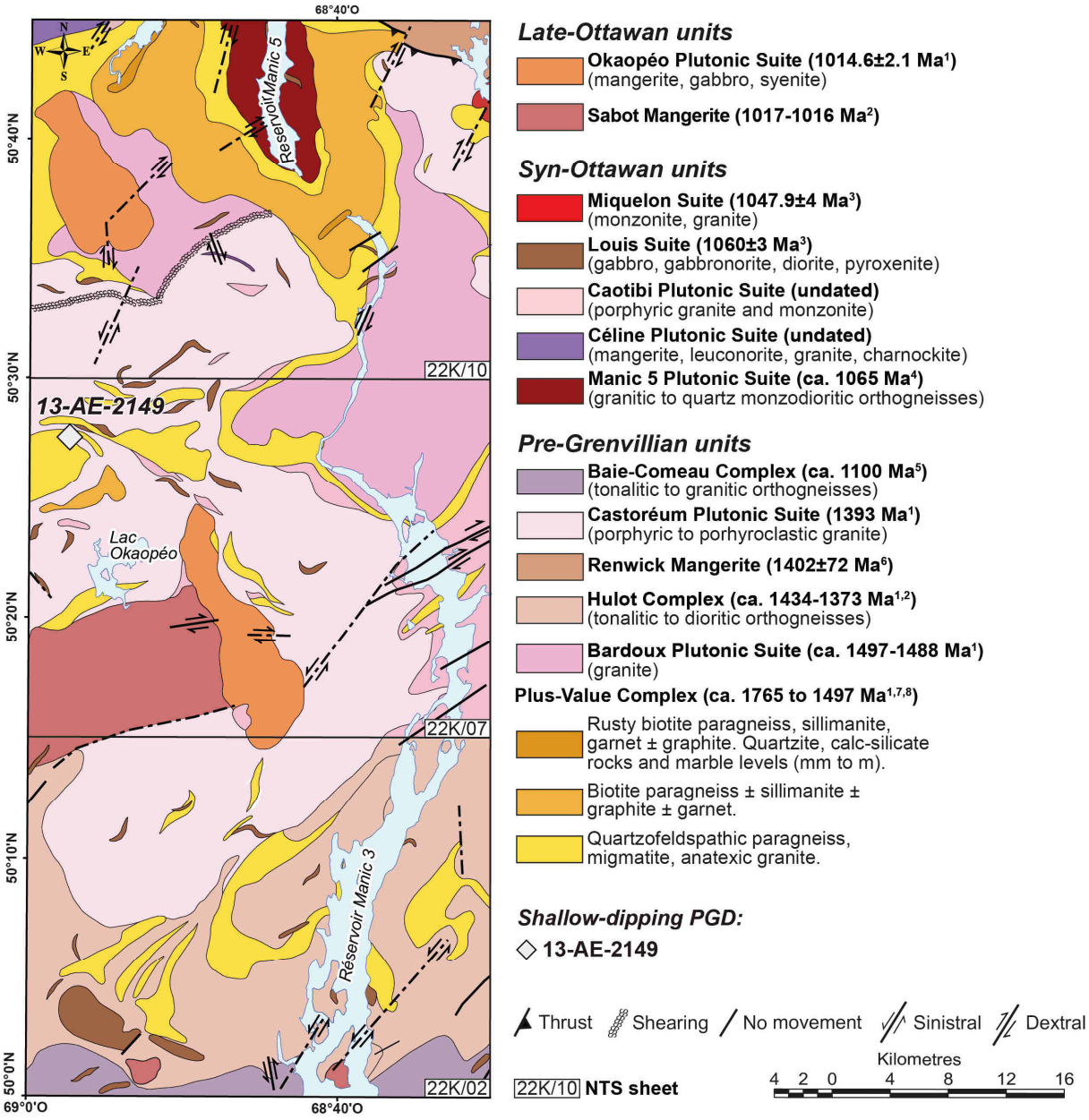

Figure 5-2: Simplified geological map of the environment of the investigated pegmatitic granite dyke in the Lac Okaopéo region (modified after Moukhsil et al., 2014; Turlin et al., 2017). [1]: Augland et al. (2015); [2]: Gobeil et al. (2002); [3]: David (2006); [4]: Dunning and Indares (2010); [5]: David et al. (2009); [6]: Moukhsil et al. (2013a); [7]: Moukhsil et al. (2012); [8]: Lasalle et al. (2013). Abbreviation: PGD = pegmatitic granite dyke.

Pinwarian tonalitic orthogneisses and gabbronorite have supra-chondritic $\varepsilon Hf_{1434\text{-}1383.4\ Ma}$ values between +6.04 and +10.17 that point to their mixed crustal and mantle sources (Augland et al., 2015). The ca. 1383 Ma metagabbronorite dykes intrusive into the tonalitic dioritic orthogneisses of the ca. 1434-1413 Ma Hulot Complex have $\varepsilon Hf_{1434\text{-}1383.4\ Ma}$ values between +5.78 and +6.95 that similarly indicate its mixed source (Fig. 5-10, Augland et al., 2015).

Grenvillian plutonic units coeval with the Ottawan peak of metamorphism include (i) granitic to quartz-monzodioritic orthogneisses, (ii) slightly deformed monzonitic to granitic plutonic bodies, and (iii) undeformed mafic rocks (David, 2006; Dunning and Indares, 2010;

Moukhsil et al., 2014, 2013b, 2009, 2007). The late-Ottawan units are represented by anorthosite, mangerite and charnockite±leuconorite±granite of the Sabot Mangerite (ca. 1016-1017 Ma) and the high-alkalic mangerite±gabbro±syenite from the Okaopéo Plutonic Suite (1014.6±2.1 Ma) (Augland et al., 2015; Gobeil et al., 2002; Moukhsil et al., 2014, 2013a, 2013b, 2009, 2007). The latter has near-chondritic $\varepsilon Hf_{1015\ Ma}$ values between -1.73 and -1.01 (Augland et al., 2015).

Altogether, the plutonic units from the Lac Okaopéo region define a crustal evolution domain (with $^{176}Lu/^{177}Hf = 0.015$), of which the lower limit is marked by the Bardoux Plutonic Suite (Fig. 5-10, Augland et al., 2015).

2.3. Pegmatitic granite dykes (PGD) of the Lac Okaopéo region

Turlin et al. (2017) described LREE-enriched PGD from the Lac Okaopéo region hosted by paragneisses from the Plus-Value Complex and by metaplutons from the Bardoux and the Castoréum Plutonic Suites. These field relationships are correlated to the nature of the LREE-bearing phase within the PGD: monazite in paragneisses-hosted PGD and allanite in metaplutons-hosted PGD (Turlin et al., 2017). The authors identified two contrasting types of PGD. A first type is represented by steep-dipping PGD that show a strongly peraluminous, low Nb and Ta contents and present an extreme fractionation of the LREE over the HREE (Turlin et al., 2017). These dykes were emplaced at ca. 1005-1000 Ma (U-Pb on monazite, Turlin et al., 2017; on zircon, chapter 3) and their pristine zircon grains show strongly sub-chondritic $\varepsilon Hf_{(1003\ Ma)}$, Paleoproterozoic $T_{DM2\ (1003\ Ma)}$ Hf model ages, and $\delta^{18}O_{V\text{-}SMOW}$ signatures dominated by supra-mantellic values, compatible with their derivation by partial melting of Paleoproterozoic-Archean metapelites (chapter 3), attributed to the Knob Lake Group metapelites of the Parautochthonous Belt (chapter 4).

To the contrary, a second type of PGD, represented by the 13-AE-2149 PGD investigated in this study, is composed of a main shallow-dipping dyke discordant to locally sub-concordant to the foliation of its hosts layered metamangerite of the Castoréum Plutonic Suite (Fig. 5-2). The main dyke is in textural continuity with concordant/discordant granitic veins (Fig. 5-3) and whole-rock geochemistry of its REE-richest facies (LREE up to 8,757 ppm) reported by Turlin et al. (2017) shows a weaker peraluminous character, higher Nb and Ta contents, and a lower fractionation of the LREE over the HREE that the authors interpreted as the reflection of its derivation from another source than the steep-dipping PGD.

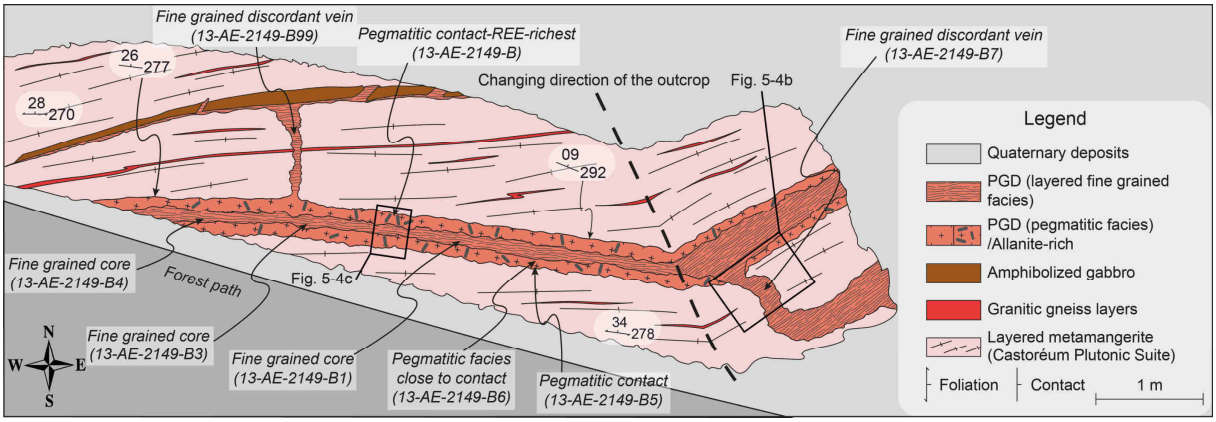

Figure 5-3: Detailed map of the 13-AE-2149 outcrop made of a layered metamangerite from the Castoréum Plutonic Suite intruded by a discordant shallow-dipping REE-rich pegmatitic granite dyke. The position of the samples investigated in this study is reported. The squares refer to the position of the photographs presented in Fig. 5-4. Abbreviation: PGD = pegmatitic granite dyke.

3. Sampling and analytical methods

3.1. Sampling

The PGD was sampled in 2014 and 2016 on the 13-AE-2149 outcrop (Turlin et al., 2017). It is hosted in a layered metamangerite from the Castoréum Plutonic Suite of the Allochthonous Belt (Fig. 5-2) and is exposed as a large and steep-dipping outcrop (Fig. 5-4a). It is composed of main PGD connected to a network of textural continuous veins concordant and discordant to the foliation of its hosts (Figs. 5-3 and 5-4a-b). The main PGD shows a shallow-dipping, discordant to sub-concordant contact, that may be very diffuse (Fig. 5-4c-d, Turlin et al., 2017). The PGD is dominated by a quartz+K-feldspar+plagioclase assemblage completed with allanite. Several facies were identified from pegmatitic contacts containing the LREE-mineralization to a fine grained layered core composed of quartz-K-feldspar-rich and quartz-plagioclase-rich lenses generally shorter than 30 cm (Fig. 5-4c). Several representative large hand-samples of (i) the layered core, (ii) pegmatitic contacts and of (iii) the fine-grained granitic discordant veins were collected for petrography and whole-rock geochemistry (Fig. 5-3, Table 5-1).

3.2. Whole-rock geochemistry

Whole-rock geochemistry of the various facies of the 13-AE-2149 PGD (samples 13-AE-2149-B, -B1, -B4, -B3, -B5, -B6, -B7 and -B99, respectively) was performed by Actlabs (Ancaster, Ontario). Powdered samples were prepared by Li-metaborate or -tetraborate. Major elements were analyzed by inductively coupled plasma - atomic emission spectroscopy (ICP-AES), and trace elements by inductively coupled plasma - mass spectrometry (ICP-MS). Results are reported in Table 5-1. In the present contribution, we report original geochemical

data of samples 13-AE-2149-B1, -B4, -B3, -B5, -B6, -B7 and -B99 and we include the 13-AE-2149-B analysis from Turlin et al. (2017).

3.3. U-Pb dating and Lu-Hf isotope analyses of zircon

In-situ U-Pb and Lu-Hf isotopes analyses of seventeen zircon grains from the 13-AE-2149 PGD (fine-grained core, sample 13-AE-2149-B1, Fig. 5-3) were carried out by laser ablation-inductively coupled plasma-sector field-mass spectrometry (LA-ICP-SF-MS) at Goethe University Frankfurt (Germany), using similar methods and instruments as described by Gerdes and Zeh (2006, 2009), with modifications explained in Zeh and Gerdes (2012). Laser spots of Lu-Hf analyses (round spots with a size of 64-100 µm) were placed on-top of U-Pb laser spots (round spots with a size of 20-42 µm). Detailed analytical methods of U-Pb dating and Lu-Hf isotopes analyses and results are provided in Supplementary material and in Tables S5-1 and S5-2, respectively.

3.4. Trace elements analyses of zircon

In-situ trace elements analyses were carried out on thirteen zircon grains from the 13-AE-2149 PGD by using LA-SF-ICP-MS at Goethe University Frankfurt (Germany). Laser spots (round spots with a size of 42 µm) were placed on representative domains of the investigated grains, as close as possible to the U-Pb and Lu-Hf laser spots. The following isotopes were analyzed: ^{44}Ca, ^{49}Ti, ^{57}Fe, ^{89}Y, ^{139}La, ^{140}Ce, ^{141}Pr, ^{146}Nd, ^{147}Sm, ^{151}Eu, ^{158}Gd, ^{159}Tb, ^{161}Dy, ^{165}Ho, ^{167}Er, ^{169}Tm, ^{172}Yb, ^{175}Lu, ^{232}Th, and ^{238}U. Detailed analytical methods of trace elements analyses and the results are provided in Supplementary material and in Table S5-3, respectively.

3.5. O isotopes analyses of zircon

In-situ ion probe oxygen isotopes analyses were carried out on nine zircon grains from the 13-AE-2149 PGD with the Cameca IMS 1280 HR2 ion microprobe, following Martin et al. (2008). The Cs^+ primary ion beam of 5 to7 nA was focused on a 20 µm diameter area and the electron gun used for the charge compensation. The negative secondary ions were measured with a mass resolution of 3000 (M/ΔM) with an energy slit of 35 eV. Pre-sputtering for 60 s with a beam rastering on 10 µm was carried out to clean up the sample surface before each measurement. The secondary beam was then automatically centered in the field aperture and contrast aperture. The measurements are made on FC in multicollection mode with counting

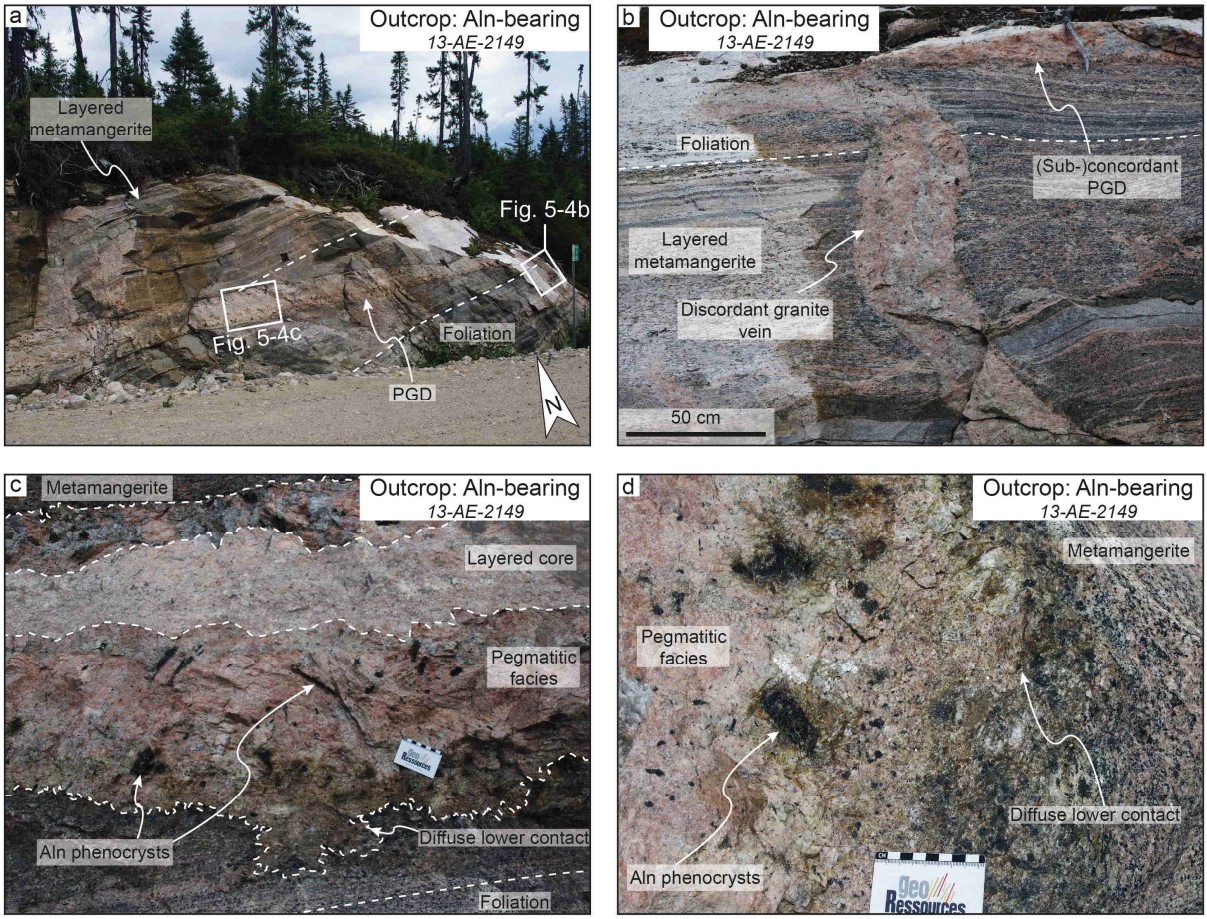

Figure 5-4: Photographs of the 13-AE-2149 outcrop from the Allochthonous Belt of the central Grenville Province. a: general view of the outcrop composed of a pegmatitic granite dyke intruding a layered metamangerite from the Castoréum Plutonic Suite; b: detailed view of a discordant granite vein to the foliation of its host rock in textural continuity with the main pegmatitic granite dyke, here with a sub-concordant contact with the layered metamangerite; c: dyke zonation from its upper to its lower contact, both marked by a pegmatitic facies with allanite phenocrysts, through a layered fine grained facies making the core of the dyke. Note the diffuse lower contact suggesting that the intruded metamangerite was under suprasolidus to close to wet-solidus conditions at the time of dyke intrusion; d: detailed view of the diffuse contact between the main dyke and its host. Abbreviations: Aln = allanite; Aln-bearing = allanite-bearing pegmatitic granite; PGD = pegmatitic granite dyke.

time of 120 s. The instrumental mass fractionation was determined on the reference zircon 91500. The results are shown in Table S5-4.

4. Petrogeochemical characteristics

4.1. Petrography

The core of the PGD is composed of an assemblage of plagioclase+microcline+quartz+biotite showing a magmatic texture with no mineral orientation (Fig. 5-5a). The assemblage is characterized by a finer grain size than the pegmatitic contacts, with grain size ranging from several hundred microns to <5 mm, the latter essentially for plagioclase and microcline (Fig. 5-5a).

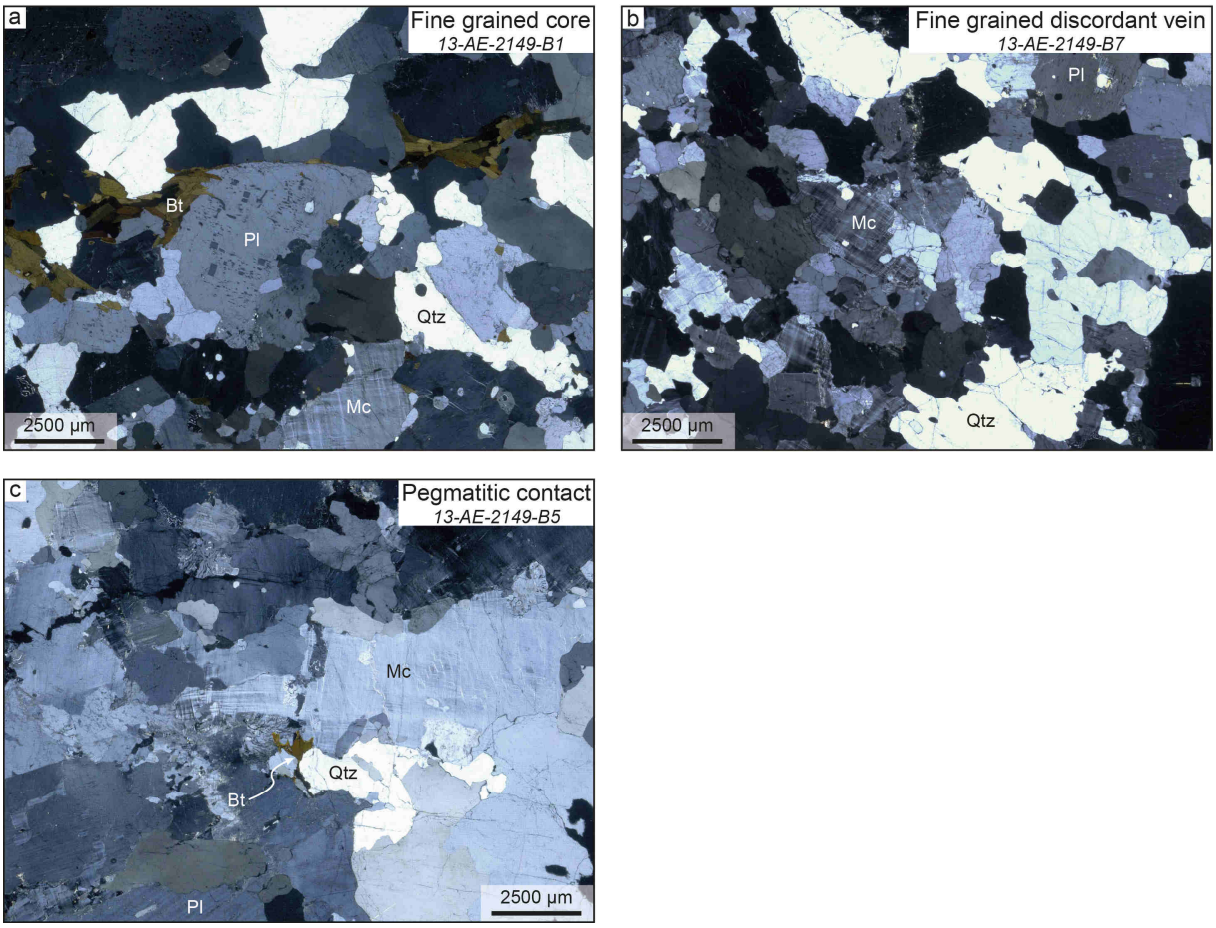

Figure 5-5: Photomicrographs of the petrographic assemblage composing the facies identified in the 13-AE-2149 PGD. All facies show a magmatic texture with no mineral orientation. a: fine grained assemblage of plagioclase+microcline+quartz+biotite (polarized and analyzed light); b: fine grained discordant veins composed of an assemblage of microcline+quartz±plagioclase (polarized and analyzed light); c: pegmatitic facies made of a coarse grained assemblage of microcline+plagioclase+quartz+biotite (polarized and analyzed light). Abbreviation: Bt = biotite; Mc = microcline; Pl = plagioclase; Qtz = quartz.

The fine grained discordant veins are marked by a finer assemblage dominated by microcline+quartz and minor plagioclase showing a magmatic texture with no mineral orientation (Fig. 5b). Rare biotite grains can be observed. Grains generally range in size from several hundred microns to <3 mm, the latter essentially reported for quartz (Fig. 5-5b).

The pegmatitic facies expressed at the contacts of the main dyke composing the PGD (Fig. 5-3) is marked by a coarse grained assemblage dominated by microcline+plagioclase+quartz+biotite showing a magmatic texture with no mineral orientation (Fig. 5-5c). The assemblage is characterized by a grain size ranging from several hundred microns for biotite to several centimeters for microcline and plagioclase (Fig. 5-5c).

4.2. Whole-rock geochemistry

All facies of the PGD and of the connected veins have typical granitic compositions with SiO_2 contents between 71.26 and 75.50 wt.% (Table 5-1) to the exception of one sample from the upper pegmatitic contact that shows the highest REE content (sample 13-AE-2149-B, Table 5-1). No strong Al_2O_3 and Na_2O content variations are noticeable between all samples and range between 13.02 and 15.25 wt.%, and between 2.68 and 4.30 wt.%, respectively (Table 5-1). The $Fe_2O_{3\ (total)}$ and K_2O contents are strongly variable between the various identified facies. The $Fe_2O_{3\ (total)}$ content is of 1.24 and 1.38 wt.% in fine grained discordant veins, below 0.89 wt.% in the fine grained core and ranges from 2.34 to 12.42 wt.% (Table 5-1). The K_2O content is of 5.05 and 5.70 wt.% in fine grained discordant veins, between 3.60 and 7.47 wt.% in the fine grained core and ranges between 1.93 to 7.13 in pegmatitic contacts (Table 5-1). The CaO content is quite stable from the fine grained core (0.59 to 1.56 wt.%) towards fine grained discordant veins (0.70 to 1.35 wt.%), but ranges between 1.15 to 5.54 in pegmatitic contacts (Table 5-1). These differences do not significantly affect the ASI (Aluminum Saturation Index, ASI = Al/(Ca – 1.67 x P + Na + K), Frost et al., 2001; Shand, 1943), for which variations cannot be linked to any facies, as it ranges between 1.07 and 1.12 in the fine grained discordant veins, between 1.08 and 1.21 in the fine grained core and between 1.04 and 1.12 in pegmatitic contacts (Fig. 5-6a, Table 5-1).

The different identified facies also show differences in Zr and Hf contents. The Zr and Hf contents of the fine grained discordant veins are of 24 and 54, and of 1.7 and 2.7, respectively, leading to Zr/Hf ratios of 14 and 20 (Fig. 5-6b-c, Table 5-1). The Zr and Hf contents of the fine grained core range from 12 to 139, and from 0.6 to 5.6, respectively, leading to Zr/Hf ratios between 20 and 25 (Fig. 5-6b-c, Table 5-1). The Zr and Hf contents of the pegmatitic contacts range from 19 to 6,340, and from 1.0 to 171, respectively, leading to Zr/Hf ratios between 19 and 37 (Fig. 5-6b-c, Table 5-1). Accordingly, the Zr/Hf ratios decrease from the pegmatitic contacts towards finer grained cores and towards discordant veins, and with the ΣREE content (Fig. 5-6c, Table 5-1). It also shows a negative correlation with the K_2O content (Fig. 5-6b, Table 5-1).

Extreme variability within the REE are recorded between the identified facies. The fine grained discordant veins have ΣLREE contents of 27 and 34 ppm and ΣHREE contents of 24 and 8.8 ppm (Table 5-1). These two samples have contrasting chondrite normalized REE patterns, one with a positive Eu anomaly (Eu/Eu* of 2.7), a slight fractionation within the LREE

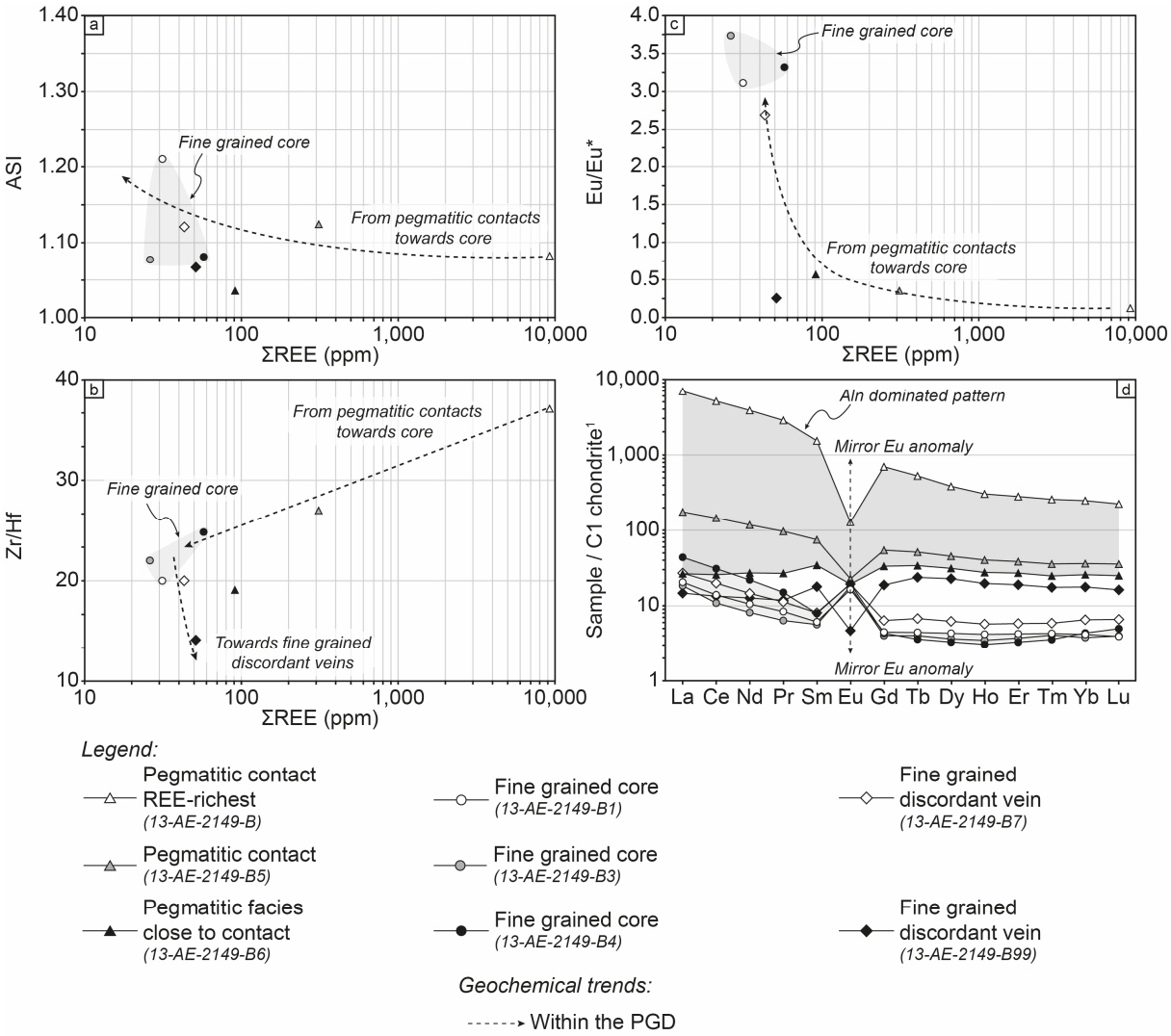

Figure 5-6: Whole rock geochemistry of the various facies of the 13-AE-2149 pegmatitic granite dyke hosted in the Allochthonous Belt of the central Grenville Province. a: ASI vs ΣREE (ppm) diagram. Note the slight ASI increase towards the fine grained core; b: Zr/Hf vs ΣREE (ppm) diagram. Note the ΣREE decrease with the fractional crystallization from the pegmatitic facies towards the fine grained core and discordant veins; c: Eu/Eu* vs ΣREE (ppm) diagram showing the contrasting characteristics of the fine grained core and of the pegmatitic facies (see text for details); d: chondrite-normalized REE patterns of the various facies of the dyke. Cores systematically have a cumulate signatures characterized by flat and low patterns with a positive Eu anomaly. A sample of fine-grained discordant vein in textural continuity with the main dyke shows a similar pattern. To the contrary, the other fine-grained discordant vein shows a mirror pattern. Similarly, all pegmatitic contacts have a higher REE content with a slight to strong negative Eu anomaly and fractionation of the LREE over the HREE. These three features increase from pegmatitic facies sampled close to contact towards pegmatitic contacts. Abbreviations: Aln = allanite; PGD = pegmatitic granite dyke.

(La_N/Sm_N of 3.3), and of the LREE over the HREE (La_N/Yb_N of 4.2) (Fig. 5-6e, Table 5-1). The second sample shows a negative Eu anomaly (Eu/Eu* of 0.3), and almost no fractionation within the LREE (La_N/Sm_N of 0.8), and of the LREE over the HREE (La_N/Yb_N of 0.8) (Fig. 5-6e, Table 5-1). The fine grained core has ΣLREE contents ranging from 20 to 52 ppm and ΣHREE contents ranging from 5.8 to 6.3 ppm (Table 5-1). These three samples have similar chondrite normalized REE patterns with a positive Eu anomaly (Eu/Eu* from 3.1 to 3.7), a slight fractionation within the LREE (La_N/Sm_N from 3.2 to 5.5), and of the LREE over the

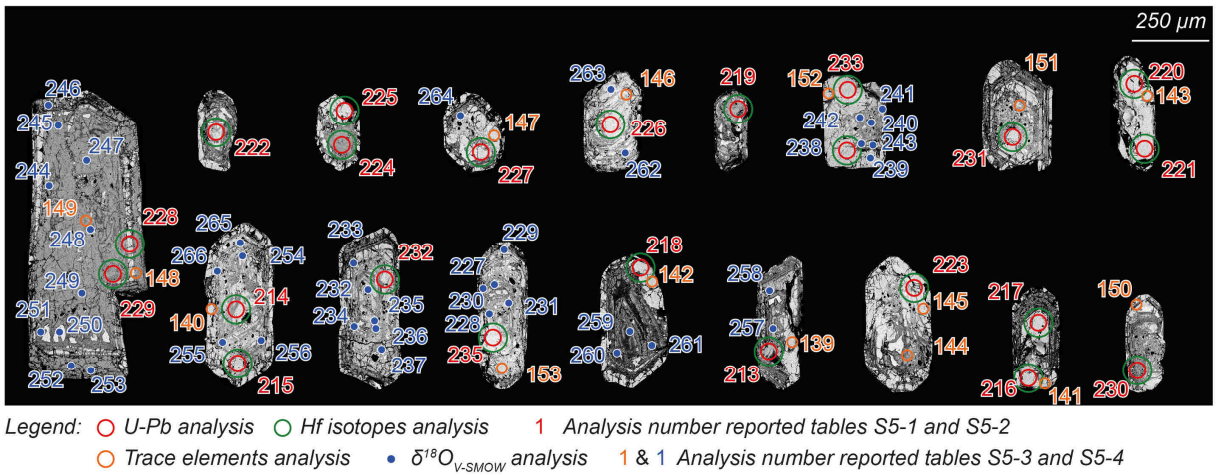

Figure 5-7: Back scattered electron (BSE) images of zircon grains from the 13-AE-2149 allanite-bearing pegmatitic granite dyke of the central Grenville. The circles mark the positions of the laser ablation analyses of trace elements (orange), U-Pb dating (red) and Lu-Hf isotopes (green), and of the SIMS spots for $\delta^{18}O$analyses (blue). Note the complex internal zoning marked by porous or altered zones.

HREE (La_N/Yb_N from 4.9 to 10) (Fig. 5-6e, Table 5-1). The pegmatitic contacts show contrasting ΣLREE contents ranging from 55 and 8,757 ppm and ΣHREE contents ranging from 36 and 485 ppm (Table 5-1). They are associated with chondrite normalized REE patterns marked by negative Eu anomaly (Eu/Eu* from 0.1 to 0.6), a slight fractionation within the LREE (La_N/Sm_N from 0.8 to 4.5), and of the LREE over the HREE (La_N/Yb_N from 1.0 to 28) (Fig. 5-6e, Table 5-1). In all samples almost no fractionation within the HREE is recorded as marked by the Gd_N/Yb_N ratio ranging from 1.0 to 1.5 (Fig. 5-6e, Table 5-1), to the exception of the upper pegmatitic contact that shows the highest REE content (sample 13-AE-2149-B, Table 5-1) and a slight fractionation within the HREE marked by Gd_N/Yb_N of 2.8 (Fig. 5-6e, Table 5-1).

5. Trace elements and U-Pb-Hf-O isotopes of zircon grains

5.1. Zircon textures

Zircon grains from the fine-grained core of the PGD (sample 13-AE-2149-B1, Fig. 5-3) range in length from 275 to 1,000 µm and widths from 125 and 400 µm with elongated sub-moderate aspect ratio ranging from 1:1.5 to 1:3 (Fig. 5-7). They display prismatic shapes with dominant {100} crystal faces and subrounded terminations. SEM images reveal complex oscillatory zoning with porous or altered zones (Fig. 5-7).

5.2. Trace elements

Fourteen trace element analyses were carried out on twelve zircon grains. They all show high Ca, Fe and ΣLREE contents from 476 to 21,999 ppm, from 810 to 10,961 ppm and from

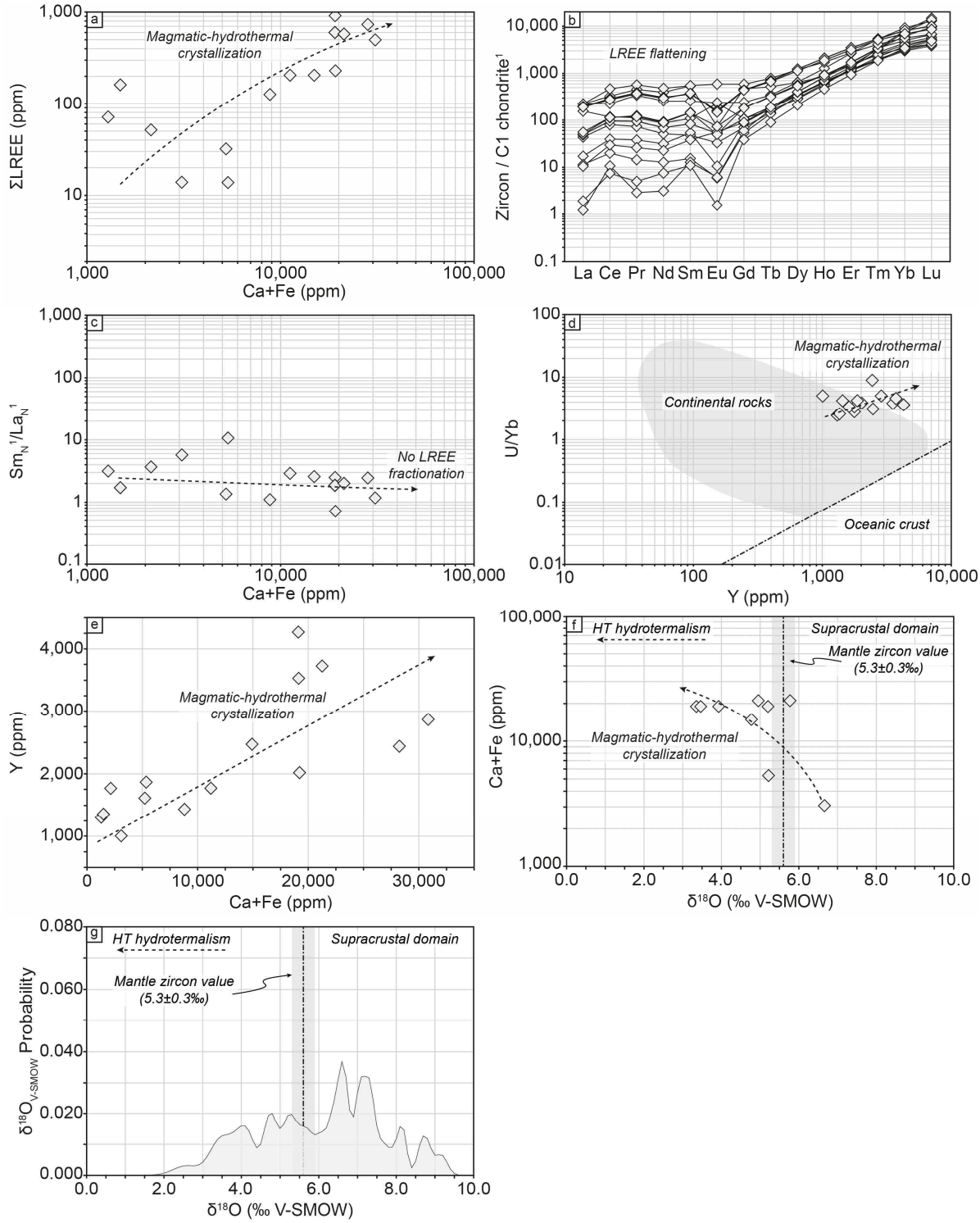

14 to 915 ppm respectively (Fig. 5-8a, Table 5-2). Th/U ratios and ΣHREE contents are low, ranging from 0.04 to 0.28 and from 1239 to 3630 ppm (Table 5-2). Chondrite normalized REE patterns are rather homogeneous within the HREE with Yb_N/Gd_N ranging from 9.5 to 88 (Fig. 5-8b, Table 5-2), but are very variable within the LREE with a general flattening of the pattern marked by Ce/Ce* and Sm/Sm* as low as 0.80 and 0.70, respectively and Pr/Pr* and Eu/Eu* up to 1.41 and 2.10, respectively (Fig. 5-8b, Table 5-2). This flattening, marked by Sm_N/La_N between 0.7 and 10.7, is not correlated to the Ca and Fe contents (Fig. 5-8c, Table 5-2). The

Th, U, Y and Yb contents of these zircon grains range from 106 to 7,059 ppm, from 1,537 to 14,069 ppm, from 1,006 to 4,269 ppm and from 626 to 1,919 ppm (Table 5-1), respectively. Plotted in the U/Yb vs Y (ppm) diagrams of Grimes et al. (2007), data are clustered to a domain both in and outside the continental rocks domains (Fig. 5-8d). The Ca+Fe and Y contents are positively correlated (Fig. 5-8e).

5.3. Oxygen isotopes

Forty O isotope analyses were carried out on nine zircon grains (Fig. 5-7). Zircon grains have heterogeneous sub- to supra-mantellic (as defined by Valley et al. (2005) at 5.3±0.3 ‰) $\delta^{18}O_{V\text{-}SMOW}$ signatures ranging from +9.16 to +2.58 ‰ (2σ error below 0.33 ‰, Fig. 5-8f-g, Table 5-2) with a main mode of distribution around ca. +6.5 to +7.5 ‰ (Fig. 5-8g). The $\delta^{18}O_{V\text{-}SMOW}$ signatures are negatively correlated with Ca and Fe contents of zircon grains (Fig. 5-8f).

5.4. U-Pb dating and Lu-Hf isotopes

Twenty-three U-Pb isotopes analyses were carried out on seventeen zircon grains from the 13-AE-2149 PGD (Fig. 5-7, Table S5-1). Most analyses yielded a discordant character with data spreading along a Discordia curve. They define an upper intercept at 1006.2±5.9 Ma (Fig. 5-9).

Twenty-two Lu-Hf isotopes analyses were performed on top of U-Pb dating analyses (Fig. 5-7). Zircon grains have homogeneous $^{176}Hf/^{177}Hf$ comprised between 0.282311 and 0.282402 (Table 5-2) that correspond to chondritic to slightly sub-chondritic $\varepsilon Hf_{(1005\ Ma)}$ comprised between -6.2 and 1.0 (Fig. 5-10, Table 5-2), and to associated $T_{DM2\ (1005\ Ma)}$ Hf model ages comprised between 1.74 and 1.90 Ga (mean of 1.81 Ga) (Figs. 5-10 and 5-11c, Table 5-2), respectively.

Figure 5-8: Trace elements and $\delta^{18}O_{V\text{-}SMOW}$ signatures of zircon grains from the 13-AE-2149 pegmatitic granite dyke from the central Grenville Province. a: ΣLREE vs Ca+Fe (ppm) diagram. The high LREE, Ca and Fe contents provide evidence for the non-pristine character of all the investigated domains. The increasing contents of these elements are most probably related to crystallization of the zircon grains at the magmatic-hydrothermal transition; b: chondrite-normalized REE patterns showing flat LREE patterns with complete to incomplete loss of Ce, Pr, Sm and Eu anomalies associated with high ΣLREE contents. These features are consistent with the non-pristine character of the investigated domains; c: Sm_N/La_N vs Ca+Fe (ppm) diagram. Note the lack of fractionation within the LREE with increasing Ca and Fe contents; d: U/Yb vs Y (ppm) diagram of Grimes et al. (2007). Note that some investigated zircon domains plot outside of the continental granitoids field. This is consistent with the high Y content that is correlated with the high Ca and Fe contents; e: Y (ppm) vs Ca+Fe (ppm) diagram showing the positive correlation between the Y and Ca+Fe contents; f: Ca+Fe (ppm) vs $\delta^{18}O_{V\text{-}SMOW}$ diagram of the investigated zircon domains. Note that the only supra-mantellic signature is associated with the lowest Ca and Fe contents recorded in zircon grains. The decrease in the $\delta^{18}O_{V\text{-}SMOW}$ signatures is correlated with increasing Ca and Fe contents; g: probability density plot of $\delta^{18}O_{V\text{-}SMOW}$ signatures of zircon grains showing the multimodal widespread distribution of $\delta^{18}O_{V\text{-}SMOW}$ signatures.

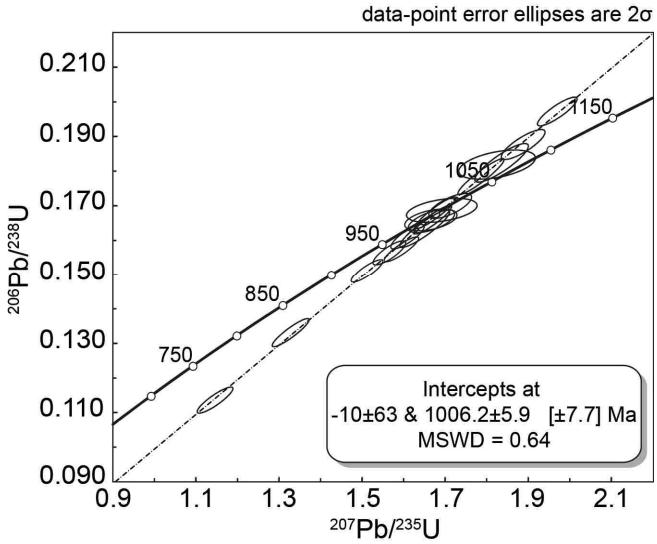

Figure 5-9: Concordia diagrams of U -Pb dating on zircon from the 13-AE-2149 pegmatitic granite dyke from the central Grenville Province.

6. Discussion

6.1. Early-Rigolet intrusion of the PGD

Turlin et al. (2017) and the study presented in chapter 3 reported U-Pb ages of ca. 1005-1000 Ma on magmatic monazite and zircon from PGD of the aM-L*P* segment of the central Grenville that are coeval with the initiation of the Rigolet orogenic phase in the underlying Parautochthonous Belt as early as ca. 1002 Ma in this area (Jannin et al., accepted; Rivers, 2008). Zircon grains from the 13-AE-2149 allanite-bearing PGD show complex oscillatory zoning with porous to altered zones and prismatic shapes (Fig. 5-7). They lack textural and isotopic evidence of inherited cores/domains (Figs. 5-7, 5-9 and 5-10). All trace element analyses report very high Ca, Fe and LREE contents up to 21,999 ppm, 10,961 ppm and 915 ppm, respectively (Fig. 5-8a, Table 5-2). These contents are not compatible with a pristine character of the zircon and are attributed to elements with large ionic radii/low ionic charge fillings nanoscale pores or occurring as micrometric inclusions in cracks, metamict or porous domains (Geisler et al., 2007, 2001; Hanchar et al., 2001; Hoskin and Schaltegger, 2003). However, the lack of any pristine domains in these zircon grains does not favor small inclusions filling cracks, porous or metamict domains but to a widespread change in the zircon composition. They suggest either (i) a widespread post-zircon growth alteration or (ii) its crystallization at the magmatic-hydrothermal transition assisted by magmatic fluids. The lack of petrographic evidence for alteration associated with subsolidus fluid circulations (Fig. 5-5) are in favor of the second hypotheses but no data from this study allow to constrain it. Such characteristics are consistent with the discordance of the U-Pb isotopic system that yield an

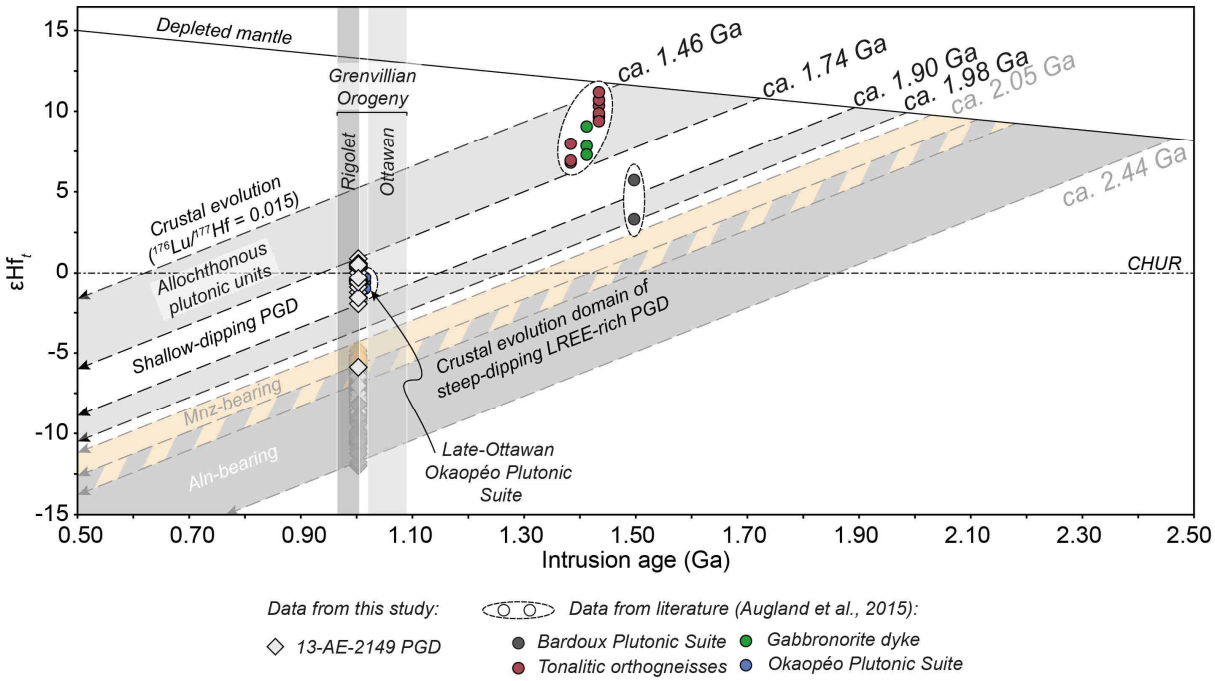

Figure 5-10: εHf_t signatures vs intrusion age of magmatic zircon from the 13-AE-2149 pegmatitic granite dyke from the central Grenville Province with reported values of paragneisses-derived pegmatitic granite dykes from the same area (chapter 3), and of allochthonous units from the Lac Okaopéo region (Augland et al., 2015). Note that the zircon grains from the 13-AE-2149 pegmatitic granite dyke plot in a similar crustal evolution domain than surrounding plutonic allochthonous units yielding to similar T_{DM2} Hf model ages. To the contrary, zircon from this dyke plot in a distinct crustal evolution than those from other pegmatitic granite dykes. These emphasize the distinct sources of these two types of pegmatitic granite dykes, the one investigated in this study being derived from the partial melting of allochthonous metaplutonic suites. Abbreviations: Aln-bearing = allanite-bearing pegmatitic granite dyke; Mnz-bearing = monazite-bearing pegmatitic granite dyke; PGD = pegmatitic granite dyke.

upper intercept at 1006.2±5.9 Ma (Fig. 5-9) (Geisler et al., 2007; Pidgeon, 1992; Rayner et al., 2005). This new U-Pb age confirms the model of Turlin et al. (2017) and of chapter 3 of coeval intrusion of monazite- and allanite-bearing PGD in the central Grenville at the initiation of the Rigolet orogenic phase at ca. 1005-1000 Ma.

6.2. PGD derived from the reworking of allochthonous plutonic units

Zircon is capable of keeping its isotopic integrity (relative to Hf and O) through magmatic and alteration processes, i.e. once integrated into the zircon lattice during growth, the $^{176}Hf/^{177}Hf$ and $^{18}O/^{16}O$ ratios remain unaffected by subsequent hydrothermal, magmatic or metamorphic process (Gerdes and Zeh, 2009; Hawkesworth et al., 2010; Lenting et al., 2015; Martin et al., 2008; Valley, 2003; Xia et al., 2009). Accordingly, even if zircon grains from the 13-AE-2149 PGD show non-pristine domains with high Ca, Fe and LREE contents, associated with a discordance of the U-Pb isotopic system, both Hf and O isotopic systems are reliable and offer insights on the source and processes involved in the genesis of the PGD.

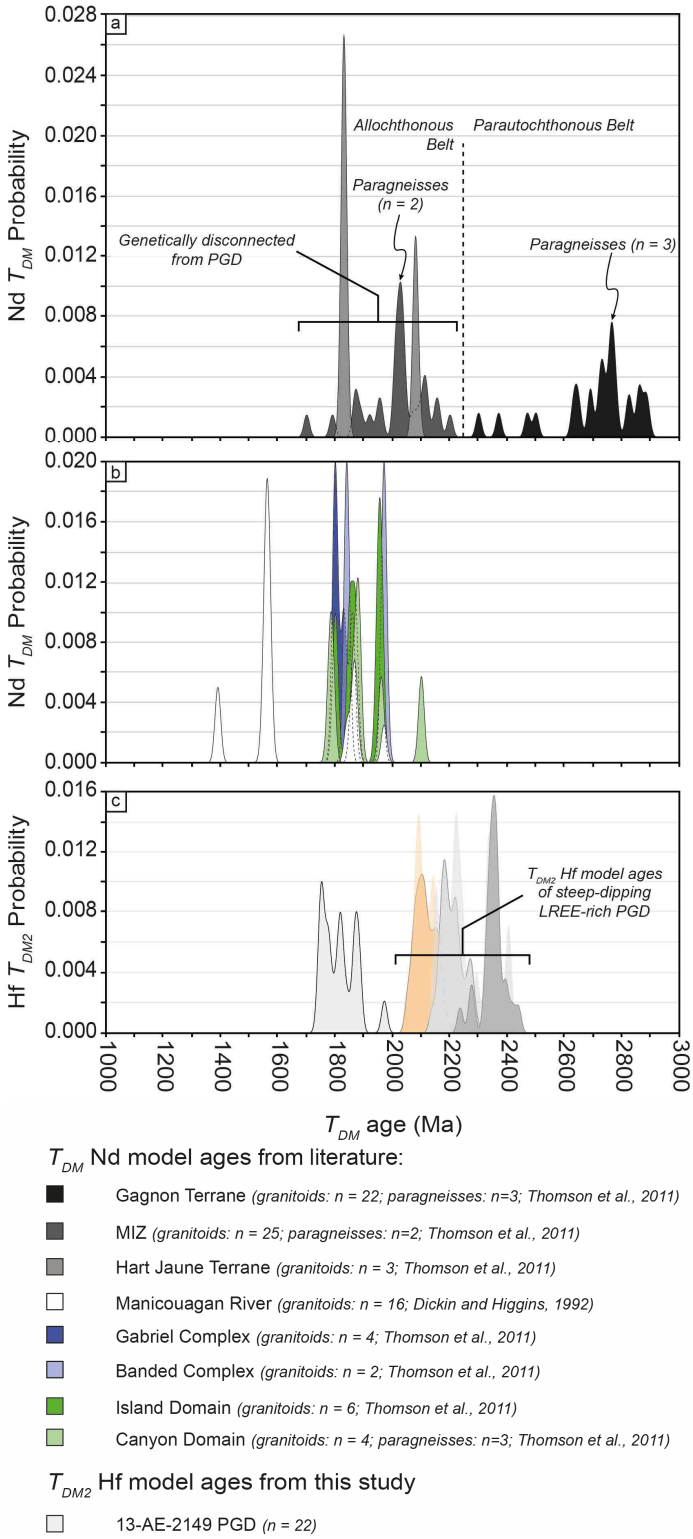

Figure 5-11: Probability density plot of Nd T_{DM} model ages from parautochthonous and allochthonous domains from the central Grenville compiled from literature and of Hf T_{DM2} model ages of zircon from the 13-AE-2149 pegmatitic granite dyke investigated in this study. Probability density plots were realized using the AgeDisplay program of (Sircombe, 2004). a and b: T_{DM} Nd model ages of the Gagnon and Hart Jaune Terranes, Manicouagan Imbricate Zone, Gabriel and Banded Complexes, and Island and Canyon Domains from (Thomson et al., 2011), and of the Manicouagan River from (Dickin and Higgins, 1992). Data were plotted using a 1s error of 10 Ma (Thomson et al., 2011); c: Hf T_{DM2} model ages of zircon grains from the 13-AE-2149 pegmatitic granite dykes. Note that these model ages are older than those of the steep-dipping LREE-rich pegmatitic granite dyke reported in chapter 3 but are similar to those of the Manicouagan River, Gabriel and Banded Complexes, and Island and Canyon Domains from the Allochthonous Belt. The dyke is considered as genetically disconnected from the Manicouagan Imbricate Zone and Hart Jaune Terrane (see text for details). Abbreviations: PGD = pegmatitic granite dyke.

Turlin et al. (2017) divided the PGD from the Lac Okaopéo region (central Grenville Province, Fig. 5-2) into two groups on the basis of the contrasting dips of the contacts of the dykes with their respective hosts, of textures of the dykes and of geochemical signatures. They also proposed that their genesis was linked to distinct sources and/or processes. The steep-dipping PGD were derived from the partial melting of Paleoproterozoic-Archean metapelites from the Knob Lake Group (Gagnon Terrane, Parautochthonous Belt, Fig. 5-1) as indicated by their strongly sub-chondritic zircon $\varepsilon Hf_{(t)}$ signatures, associated Paleoproterozoic T_{DM2} Hf model ages, their zircon supra-mantellic $\delta^{18}O_{V\text{-}SMOW}$ signatures and U, Yb, Y trace element contents, and petrogeochemical comparisons with these metapelites (Figs. 5-10 and 5-11c, chapters 3 and 4). The source and petrogenetic processes of the shallow-dipping PGD, represented by the 13-AE-2149 PGD, remained unconstrained.

Oxygen isotope analyses of zircon grains have been widely used to decipher the nature of the source involved in the genesis of the rock hosting the considered zircon grains (Hawkesworth and Kemp, 2006; Valley et al., 2005, 2005; Zeh et al., 2014). The mantle $\delta^{18}O_{V\text{-}SMOW}$ value (5.3±0.3 ‰ as defined by Valley et al., 2005) is used as a reference from which (i) fractionation towards supra-mantellic values up to 8.2±1.7 ‰ are typical of Grenvillian igneous zircons (Peck et al., 2000) and linked to the strong involvement of supracrustal material that underwent low temperature oxygen isotope fractionation in igneous sources (e.g. Van Kranendonk and Kirkland, 2013); and (ii) fractionation towards sub-mantellic values to the involvement of *HT* hydrothermalism (e.g. Valley, 2003; Valley et al., 2005). The $\delta^{18}O_{V\text{-}SMOW}$ signatures of zircon grains from the 13-AE-2149 PGD range from +9.16 to +2.58 ‰ (Fig. 5-8e-f, Table 5-2) and show a main mode of distribution around ca. +6.5 to +7.5 ‰ (Fig. 5-8f). Their negative correlation with Ca and Fe contents (Fig. 5-8f) indicates that the +9.16±0.15 ‰ is the closest to the initial signature of the magma, the lower values being related to variable degrees of interaction with magmatic-hydrothermal fluids. This highest $\delta^{18}O_{V\text{-}SMOW}$ value (+9.16±0.15 ‰) is typical of Grenvillian igneous zircons (Peck et al., 2000; Valley et al., 2005) and therefore suggest the derivation of the PGD from allochthonous plutonic units.

The U, Yb and Y contents of zircon grains are commonly used to unravel a continental vs oceanic crustal contribution in the genesis of magmas (Grimes et al., 2007). Zircon from the 13-AE-2149 PGD show U/Yb ratios and Y contents that plot both in and outside the continental rocks domain (Fig. 5-8d) (Grimes et al., 2007). The shift of composition outside the continental domain is essentially linked to increasing Y content that is positively correlated to Ca and Fe contents (Fig. 5-8e), which increase marks the non-pristine character of zircon domains.

Accordingly, the lowest Ca, Fe and therefore Y contents are the most reliable proxies for the magma composition and the latter plot in the continental rocks domains defined by Grimes et al. (2007). The 13-AE-2149 PGD is therefore derived from the reworking of continental rocks and the shift towards higher Y contents outside this compositional fields is not relevant of the initial magma composition.

Augland et al. (2015) reported $\varepsilon Hf_{(t)}$ signatures of pre-Grenvillian and late-Ottawan allochthonous plutonic units from the Lac Okaopéo region (Figs. 5-3 and 5-10). The (i) pre-Pinwarian Bardoux Plutonic Suite has supra-chondritic $\varepsilon Hf_{1497\ Ma}$ values between +2.30 and +4.70, (ii) late-Pinwarian tonalitic orthogneisses and gabbronorite have supra-chondritic $\varepsilon Hf_{1434\text{-}1383.4\ Ma}$ values between +6.04 and +10.17, and (iii) the ca. 1383 Ma metagabbronorite dykes have $\varepsilon Hf_{1434\text{-}1383.4\ Ma}$ values between +5.78 and +6.95 (Fig. 5-10, Augland et al., 2015). Together with the late-Ottawan Okaopéo Plutonic Suite that yielded near-chondritic $\varepsilon Hf_{1015\ Ma}$ values between -1.73 and -1.01, they define a crustal evolution domain (with $^{176}Lu/^{177}Hf$ = 0.015), of which the lower limit is marked by the Bardoux Plutonic Suite (Fig. 5-10, Augland et al., 2015). Zircon grains from the shallow-dipping 13-AE-2149 PGD have chondritic to slightly sub-chondritic $\varepsilon Hf_{(1005\ Ma)}$ ranging from -6.2 (extreme and single value) to 1.0 (Fig. 5-10, Table 5-2), and associated Paleoproterozoic $T_{DM2\ (1005\ Ma)}$ Hf model ages ranging from 1.74 to 1.90 Ga (mean of 1.81 Ga) (Figs. 5-10 and 5-11c, Table 5-2), respectively. Even if no Hf isotopic data are available for the paragneisses from the Plus-Value Complex, the U-Pb ages of their detrital zircon cores spread from ca. 1.50 to 2.70 Ga (Lasalle et al., 2013; Moukhsil et al., 2014) and would most probably lead to higher $\varepsilon Hf_{(1005\ Ma)}$ values and older $T_{DM2\ (1005\ Ma)}$ Hf model ages. Accordingly, zircon grains from the 13-AE-2149 PGD plot in a distinct crustal evolution domain as zircon from steep-dipping LREE-rich PGD from the same area (Fig. 5-10, chapter 3) and together with their coeval emplacement provide evidence for their derivation from distinct sources. This is consistent with the shallow-dipping contact of the 13-AE-2149 PGD that contrast with the steep-dipping contacts of the LREE-rich ones, and with the lower fractionation of the LREE over the HREE compared to steep-dipping PGD, indicating a distinct source (Turlin et al., 2017; chapter 4). In addition, zircon grains from this PGD plot in the same crustal evolution domain as allochthonous plutonic units that indicate the derivation of this PGD from the exclusive reworking of the Allochthonous Belt. This is consistent with the results of Turlin et al. (submitted) who demonstrated that this aM-L*P* crustal segment hosting the PGD, and extensively the underlying aH*P* crustal segments, were still under suprasolidus conditions

at ca. 1005 Ma following a slow and constant cooling from the ca. 1070-1050 Ma Ottawan high-grade peak of metamorphism.

In summary, U-Pb-Lu-Hf-O isotopic data obtained on zircon grains from the shallow-dipping 13-AE-2149 PGD provide evidence for the coeval emplacement of shallow- and steep-dipping PGD of the Lac Okaopéo region (central Grenville Province) and their derivation from contrasting sources, the steep-dipping PGD being derived from the partial melting of metapelites from the underlying Parautochthonous Belt while the shallow-dipping PGD exclusively reworks allochthonous plutonic units.

6.3. Petrogenesis of the shallow-dipping 13-AE-2149 PGD

In metaluminous to peraluminous magmas, the fractionation of zircon with the fractional crystallization strongly decreases the Zr/Hf ratios, whereas in depolymerized alkaline melts, all minerals prefer Hf over Zr leading to an increase of the Zr/Hf ratios with fractional crystallization (e.g. Linnen and Keppler, 2002; Zaraisky et al., 2009). The fine grained core of the PGD show the highest ASI (1.08 to 1.21, Fig. 5-6a) and among the lowest Zr/Hf ratios (20 to 25, Fig. 5-6b-c). In contrast, the pegmatitic contacts have lower ASI (1.04 to 1.12, Fig. 5-6a) and higher Zr/Hf ratios (19 to 37, Fig. 5-6b-c) (Table 5-1). In addition, the fine grained core of the PGD shows a flat chondrite normalized REE pattern marked by positive Eu anomalies (Eu/Eu* between 3.1 and 3.7, Fig. 5-6e) and low REE contents (Fig. 5-6e) (Table 5-1), consistent with the petrographic assemblage dominated by K-feldspar (microcline) and plagioclase (e.g. Bea, 1996) suggestive of its cumulative nature. It contrasts with the fractionated chondrite normalized REE patterns in favor of LREE of the pegmatitic contacts, marked by negative Eu anomalies (Eu/Eu* between 0.1 and 0.6, Fig. 5-6e) and up to high grade LREE mineralization (ΣLREE up to 8,757 ppm, Fig. 5-6e) (Table 5-1). Together with the general evolution of crystallization of granitic pegmatite from fine grained facies towards pegmatitic ones (e.g. London, 2016, 2008), the increasing Zr/Hf ratios suggest an alkaline, and therefore depolymerized, character of the magma. This interpretation is consistent with the lower fractionation of the LREE over the HREE of this PGD compared to other PGD reported from the same area as marked by La_N/Yb_N between 0.8 to 28 for the former (Fig. 5-6d, Table 5-1) and between 261 and 937 for the latter (Chakhmouradian and Zaitsev, 2012; Turlin et al., 2017), and the expression of the LREE mineralization as allanite (e.g. Bea, 1996). Therefore, the slight peraluminous character of the magma would have been acquired at the end of the crystallization through any process involving the cumulative concentration of Al-rich silicate

such as biotite and/or loss of H_2O etc. In this frame, the fine grained discordant veins showing slightly lower ASI (1.07 to 1.12, Fig. 5-6a) and Zr/Hf ratios (14 to 20, Fig. 5-6b) than the core could reflect magma extraction at different stages of fractional crystallization of the PGD (Figs. 5-3 and 5-4b).

The genesis of pegmatitic textures of a granitic pegmatite emplaced at depth in crustal segment where the temperatures between the magma and its host is low may be the result of slow cooling of the magma and crystallization at temperatures close to the liquidus, whereas for granitic pegmatites emplaced at higher structural levels it is in general the result of a liquidus undercooling coupled to a nucleation delay (London, 2016, 2014, 2008). In the aM-L*P* crustal segment where the 13-AE-2149 PGD emplaced, Turlin et al. (submitted) argued that suprasolidus conditions were recorded as late as ca. 1005 Ma, i.e. when the 13-AE-2149 PGD investigated in this study emplaced, as indicated by the lobate contact of a PGD with its metasedimentary host with no evidence for thermal exchange nor contact metamorphism. Accordingly, the pegmatitic facies of the shallow-dipping 13-AE-2149 PGD are interpreted as the result of slow cooling of the magma and a close to liquidus temperature crystallization.

Conclusions

Petrogeochemical investigations of a shallow-dipping pegmatitic granite dyke in the Allochthonous Belt of the central Grenville Province provide evidence for its alkaline affinity marked by an increase of Zr/Hf ratios and a decrease of ASI from cores towards pegmatitic contacts. Scarce LREE mineralization developed at the pegmatitic contacts in response to interactions with the hosts layered metamangerite.

The U-Pb dating of zircon grains from this dyke of the central Grenville Province indicates the coeval emplacement of this dyke and of the LREE-rich steep-dipping pegmatitic granite dykes from the same area at ca. 1005-1000 Ma. The zircon Hf-O isotopic and trace element signatures provide evidence that this shallow-dipping dyke was derived from a distinct source corresponding to allochthonous plutonic units as indicated by its chondritic to slightly sub-chondritic $\varepsilon Hf_{(1005\ Ma)}$ signatures and late-Paleoproterozoic $T_{DM2\ (1005\ Ma)}$ Hf model ages. Accordingly, this study demonstrates that allochthonous plutonic units do not represent fertile protoliths in regards to REE mineralization, and provides constraints on the exploration targeting of REE mineralization in the central Grenville Province.

Acknowledgements

The authors are grateful to the Ministère de l'Énergie et des Ressources naturelles (Québec, Canada) for providing technical and financial support for the field work and analyses, to Pierre-Arthur Groulier (Memorial University, NL, Canada) for his help during field work, to Robert Joussemet, Frédéric Diot, Jean-Marie Fischbach, and to Christophe Gauthier (Steval, GeoRessources, Nancy) for their help in sample preparation and separation. This work was funded by the Labex Ressources 21 (supported by the French National Research Agency – France) through the national program "Investissements d'avenir", reference ANR-10-LABX-21–LABEX RESSOURCES 21 and the Région Grand-Est. It benefited from the framework of the DIVEX "Rare earth element" research program.

Table 5-1: Whole rock geochemistry of the various facies of the 13-AE-2149 allanite-bearing pegmatitic granite dyke from the Allochthonous Belt of the central Grenville Province. Abbreviations: A/CNK = Al/ (Na + K + Ca/2) (Shand, 1943); Allanite-bearing PGD = allanite-bearing pegmatitic granite dyke; A/NK = Al/(Na + K) (Shand, 1943); ASI = Aluminum Saturation Index given by the expression ASI = Al/(Ca – 1.67 x P + Na + K) (Frost et al., 2001; Shand, 1943); L.D. = limit of detection.

Type	***Allanite-bearing PGD***							
Outcrop	**13-AE-2149**							
Sample no.	**13-AE-2149 B1**	**13-AE-2149-B4**	**13-AE-2149 B3**	**13-AE-2149 B[1]**	**13-AE-2149-B5**	**13-AE-2149-B6**	**13-AE-2149-B7**	**13-AE-2149-B99**
Facies	**Fine grained core**	**Fine grained core**	**Fine grained core**	**Pegmatitic contact (REE-richest)**	**Pegmatitic contact**	**Pegmatitic facies close to contact**	**Fine grained discordant vein**	**Fine grained discordant vein**
SiO_2 *(wt. %)*	75.07	74.15	72.49	55.84	71.63	71.26	74.25	75.50
Al_2O_3	13.72	14.02	14.04	15.05	14.66	14.26	13.92	13.02
$Fe_2O_{3\ total}$	0.77	0.89	0.69	12.42	2.99	2.34	1.38	1.24
MgO	0.10	0.07	0.05	0.85	0.17	0.14	0.10	0.07
MnO	0.01	0.01	0.01	0.22	0.04	0.04	0.02	0.03
CaO	1.56	0.86	0.59	5.54	2.57	1.15	1.35	0.70
Na_2O	3.66	3.07	2.68	4.28	4.30	3.04	3.48	3.28
K_2O	3.60	6.59	7.47	1.93	3.44	7.13	5.05	5.70
TiO_2	0.05	0.05	0.04	0.63	0.13	0.09	0.12	0.01
P_2O_5	0.00	0.00	0.00	0.22	0.08	0.00	0.00	0.00
Cr_2O_3	0.01	< L.D.	< L.D.	< L.D.	< L.D.	< L.D.	< L.D.	< L.D.
LOI	0.38	0.60	0.35	0.83	0.36	0.44	0.39	0.45
Total	98.94	100.30	98.40	97.80	100.40	99.90	100.10	100.00
ASI	1.21	1.08	1.08	1.08	1.12	1.04	1.12	1.07
A/CNK	1.29	1.11	1.10	1.29	1.23	1.08	1.18	1.10
A/NK	1.38	1.15	1.12	1.65	1.36	1.12	1.24	1.13
Sr *(ppm)*	107	133	118	147	105	102	131	13
Ba	289	560	603	181	270	528	503	38
Nb	10	7.8	8.5	132	25	20	15	41
V	5	< L.D.	< L.D.	38	< L.D.	< L.D.	< L.D.	< L.D.
Co	< L.D.	< L.D.	< L.D.	6	1	1	< L.D.	< L.D.
Ga	26	26	23	79	28	25	27	33
Ge	1.9	1.3	2.2	9.7	1.7	1.7	1.7	2.2
In	< L.D.	< L.D.	< L.D.	0.2	0.2	0.1	< L.D.	< L.D.
Sn	< L.D.	< L.D.	< L.D.	4	< L.D.	< L.D.	< L.D.	< L.D.
Cs	0.4	0.5	0.8	0.7	0.3	0.6	0.5	1.9
Pb	25	40	36	41	29	41	32	93
Be	5.0	3.0	2.0	9.0	5.0	3.0	4.0	10
Hf	0.6	5.6	2.0	171	3.0	1.0	2.7	1.7
Ta	0.3	0.4	0.3	3.2	0.6	0.6	0.6	2.2
W	1.3	< 0.5	0.8	3	< L.D.	< L.D.	< L.D.	< L.D.
Tl	1.0	0.8	1.4	0.3	0.4	1.0	0.6	1.7
Bi	< L.D.	< L.D.	< L.D.	< L.D.	< L.D.	< L.D.	< L.D.	< L.D.
Th	1.9	6.38	2	766	20	2	3	15
U	0.7	2.2	1.1	30	0.9	0.5	1.7	6.3
Rb	98	197	196	42	96	221	147	403
Y	7.9	5.7	7	544	82	55	11	35
Zr	12	139	44	6340	81	19	54	24
Zr/Hf	20	25	22	37	27	19	20	14

La	6.3	14	5.7	2150	54	8.2	8.3	4.5
Ce	11	25	8.8	4130	117	21	16	11
Pr	1.3	2.7	1.0	470	14	3.3	1.8	1.5
Nd	5.0	9.0	3.8	1710	58	16	6.7	7.1
Sm	1.2	1.5	1.1	297	15	6.7	1.6	3.5
Eu	1.2	1.4	1.3	9.4	1.7	1.4	1.4	0.3
Gd	1.2	1.1	1.0	180	14	8.6	1.7	4.9
Tb	0.2	0.2	0.2	25	2.4	1.6	0.3	1.1
Dy	1.4	1.1	1.2	123	15	10	2.0	7.3
Ho	0.3	0.2	0.3	22	2.9	2.0	0.4	1.4
Er	0.9	0.7	0.8	59	8.0	5.7	1.2	4.0
Tm	0.1	0.1	0.1	8.3	1.2	0.8	0.2	0.6
Yb	0.9	0.9	0.8	52	7.5	5.4	1.4	3.7
Lu	0.1	0.2	0.1	7.2	1.1	0.8	0.2	0.5
ΣLREE	25	52	20	8757	258	55	34	27
ΣHREE	6.3	5.9	5.8	485	53	36	8.8	24
ΣREE	31	57	26	9242	311	91	43	51
Eu/Eu*[2]	3.1	3.3	3.7	0.1	0.4	0.6	2.7	0.3
La_N/Sm_N[2]	3.3	5.5	3.2	4.5	2.3	0.8	3.3	0.8
La_N/Yb_N[2]	4.9	10	4.9	28	4.9	1.0	4.2	0.8
Gd_N/Yb_N[2]	1.1	1.0	1.1	2.8	1.5	1.3	1.0	1.1
B	-	4	-	-	4	2	< L.D.	4
F	-	< L.D.	-	-	< L.D.	< L.D.	< L.D.	< L.D.
Li	-	< L.D.	-	-	< L.D.	< L.D.	< L.D.	< L.D.
Cd	< L.D.	< L.D.	< L.D.	< L.D.	< L.D.	< L.D.	< L.D.	< L.D.
Cu	3	5	2	16	8	3	16	10
Ag	< L.D.	0.4	< L.D.		< L.D.	< L.D.	< L.D.	< L.D.
Ni	2	2	< L.D.	3	2	2	2	2
Mo	< L.D.	< L.D.	< L.D.	6	1	< L.D.	< L.D.	1
Zn	20	24	15	288	78	45	30	58
S	100	< L.D.	< L.D.	600	< L.D.	< L.D.	< L.D.	500
Au *(ppb)*	< L.D.	< L.D.	< L.D.	< L.D.	< L.D.	< L.D.	< L.D.	< L.D.
As	< L.D.	< L.D.	2.2	< L.D.	< L.D.	1.3	< L.D.	< L.D.
Br	< L.D.	< L.D.	< L.D.	< L.D.	< L.D.	< L.D.	< L.D.	< L.D.
Ir	< L.D.	< L.D.	< L.D.	< L.D.	< L.D.	< L.D.	< L.D.	< L.D.
Sc	0.9	0.2	1.1	32	16	8.5	1.2	2.5
Sb	0.2	< L.D.	< L.D.	< L.D.	< L.D.	< L.D.	< L.D.	< L.D.
Se	< L.D.	< L.D.	< L.D.	< L.D.	< L.D.	< L.D.	< L.D.	< L.D.

[1]: Data from Turlin et al. (2017).

[2]: Normalization to the chondrite after McDonough and Sun (1995).

Table 5-2: Summary of the results obtained on zircon grains from the 13-AE-2149 allanite-bearing pegmatitic granite dyke from the Allochthonous Belt of the central Grenville Province. Abbreviations: Aln-bearing PGD = allanite-bearing pegmatitic granite dyke; Temp. = temperature; Zrc = zircon.

Zone[a]	LREE-Ca-Fe content[b]	Ca (ppm)	Fe (ppm)	ΣLREE (ppm)	ΣHREE (ppm)	Th (ppm)	U (ppm)	Th/U	Yb (ppm)	U/Yb	Y (ppm)	Ce/Ce*[c]	Pr/Pr*[c]	Sm/Sm*[c]	Eu/Eu*[c]	Sm_N[c]/La_N[c]	Yb_N[c]/Sm_N[c]	Yb_N[c]/Gd_N[c]	$\delta^{18}O$ (‰)	±2σ	$^{207}Pb/^{206}Pb$ age (Ma)	±2σ	Pb-Pb conc. (%)	$^{176}Hf/^{177}Hf$	±2σ	$\varepsilon Hf_{(t)}$[d]	±2σ	T_{DM} (Ga)
13-AE-2149 Allanite-bearing PGD																												
Grain 1																												
2																			5,61	0,17								
3																			4,21	0,19	974	75	111	0.282138	38	-1.1	1.4	1.82
5	High	4,810	6,388	206	1,582	364	2,404	0.15	725	3.32	1,772	1.29	1.21	2.06	0.30	2.9	23	19			909	31	93					
Grain 2																												
2																					1017	29	68	0.282163	33	0.8	1.2	1.76
3																			6,30	0,17								
4																			6,35	0,12								
4																			5,41	0,16								
5																			4,66	0,14	877	97	83	0.282138	32	-3.3	1.1	1.87
6	High	10,930	3,992	206	2,352	243	3,949	0.06	1,271	3.11	2,471	1.31	1.16	1.76	0.45	2.6	42	34	4,78	0,17								
Grain 3																												
1																					1022	25	96	0.282129	32	-0.3	1.1	1.82
3	High	476	810	71	1,239	106	1,537	0.07	626	2.45	1,304	1.44	1.07	2.56	0.15	3.2	55	35			934	87	117	0.282117	37	-2.7	1.3	1.88
Grain 4																												
1																			8,18	0,10								
2																			7,37	0,13								
4																			7,59	0,15								
5	High	11,417	7,718	915	2,842	689	4,465	0.15	1,169	3.82	3,529	1.19	1.20	1.03	1.03	2.5	10	9.5			1014	29	106	0.282134	42	-0.3	1.5	1.82
Grain 5																												
2																					807	58	97	0.282101	33	-6.2	1.2	1.97
Grain 6																												
2	High	579	907	162	1,316	111	1,719	0.06	665	2.58	1,357	1.34	1.15	1.38	0.55	1.7	38	30			1006	76	100	0.282106	36	-1.5	1.3	1.87
2																												
2																					1003	18	105	0.282158	35	0.3	1.2	1.77
Grain 7																												
1	High	21,999	8,845	499	3,466	2,071	9,683	0.21	1,919	5.05	2,866	0.80	1.41	1.05	0.95	1.2	35	38										
4	High	4,048	1,179	32	1,663	188	3,091	0.06	919	3.36	1,614	1.55	0.88	1.64	0.18	1.4	282	83			1013	26	109	0.282167	34	0.8	1.2	1.75
Grain 8																												
2																					996	23	81	0.282175	36	0.7	1.3	1.74
Grain 9																												
1																					1014	19	98	0.282166	33	0.8	1.2	1.75
3	High	4,500	851	14	1,938	258	4,397	0.06	1,037	4.24	1,869	5.22	0.42	2.77	0.17	10.7	381	83	5,22	0,14								
3																			4,84	0,15								
Grain 10																												
2	High	18,605	9,634	734	2,844	7,059	14,069	0.50	1,569	8.97	2,439	0.97	1.26	2.32	0.14	2.4	14	16			1034	35	55	0.282149	39	0.7	1.4	1.78
3																			6,63	0,16								
Grain 11																												
1																					935	23	77	0.282126	34	-2.4	1.2	1.87
4																					1007	75	107	0.282136	39	-0.4	1.4	1.81
Grain 12																												
1	High	8,952	10,150	600	3,630	600	6,124	0.10	1,689	3.63	4,269	0.99	1.30	1.57	0.39	1.9	22	18	5,20	0,16	908	22	93	0.282167	35	-1.5	1.2	1.80
1																			3,35	0,26								
1																			3,47	0,25								
1																			3,93	0,32								
2	High	10,398	10,861	578	3,205	289	6,629	0.04	1,443	4.59	3,726	0.98	1.30	1.71	0.36	2.0	18	16	5,77	0,28	938	29	87	0.282138	35	-1.9	1.2	1.84
2																			4,95	0,31						-1.9	1.2	1.84
3																			3,95	0,25								

3																		2,58	0,33									
3																		3,58	0,30									
Grain 13																												
3																				934	19	97	0.282162	35	-0.3	1.3	1.78
7	High	6,636	2,175	127	1,435	203	3,307	0.06	784	4.22	1,436	1.38	1.11	1.14	0.56	1.1	77	53										
Grain 14																												
1	High	14,161	5,053	230	2,738	1,548	6,567	0.24	1,692	3.88	2,020	0.89	1.09	0.70	2.10	0.7	73	75										
3																				1028	30	98	0.282163	33	1.0	1.2	1.75
Grain 15																												
2																		7,27	0,12									
2																		6,07	0,13									
3																		6,63	0,12									
3																		7,06	0,12									
4																		6,53	0,14	980	18	97	0.282106	36	-2.1	1.3	1.88
4																		6,64	0,14									
Grain 16																												
1																		8,65	0,12									
1																		7,08	0,16									
2																		9,16	0,15									
2																		7,02	0,19									
2																		8,07	0,13									
3	High	953	1,188	52	1,645	220	2,368	0.09	849	2.79	1,770	1.63	0.99	0.98	0.88	3.7	104	45										
3																			7,33	0,11	997	19	100	0.282141	33	-0.5	1.2	1.81
Grain 17																												
2																		5,78	0,17									
4																		7,79	0,18									
4																		8,82	0,13									
7																		7,08	0,13									
9	High	2,208	883	14	1,247	1,000	3,612	0.28	717	5.04	1,006	2.14	0.67	2.43	0.06	5.7	307	88	6,66	0,12	984	15	83					

[a] Zonation ordered from cores towards rims in each grain.

[b] Allowing to discriminate a pristine character of the investigated zircon domains. Blank lines correspond to undefined domains lacking trace elements analyses. See text for details.

[c] Chondrite normalization after McDonough and Sun (1995).

[d] With *t* corresponding to the timing of intrusion determined by U-Pb dating.

Supplementary material: Analytical methods of U-Th-Pb-Lu-Hf isotopes and trace elements analyses of zircon grains using laser ablation-inductively coupled plasma-mass spectrometry (LA-ICP-MS)

1. U-Th-Pb isotope analyses

Uranium, thorium and lead isotopes were analyzed using a ThermoScientific Element 2 sector field ICP-MS coupled to a Resolution M-50 (Resonetics) 193 nm ArF excimer laser (ComPexPro 102F, Coherent) system at Goethe-University Frankfurt. Data were acquired in time resolved – peak jumping – pulse counting / analogue mode over 455 mass scans, with a 20 second background measurement followed by 21 second sample ablation. Laser spot-size was 20-42 µm for unknowns, 42 µm for the standard zircons GJ1 (primary standard) and Plešovice, and 64 µm for zircon 91500. The results of the standard zircon measurements are shown in Table S1. Sample surface was cleaned directly before each analysis by three pulses pre-ablation. Ablation were performed in a 0.6 l min^{-1} He stream, which was mixed directly after the ablation cell with 0.005 l min^{-1} N_2 and 0.71 l min^{-1} Ar prior to introduction into the Ar plasma of the SF-ICP-MS. All gases had a purity of >99.999% and no homogeniser was used while mixing the gases to prevent smoothing of the signal. Signal was tuned for maximum sensitivity for Pb and U while keeping oxide production, monitored as $^{254}UO/^{238}U$, below 1.9-0.7% during the analytical session. The sensitivity achieved was in the range of 9000-14000 cps/µg g^{-1} for ^{238}U with a 30 µm spot size, at 5.5 Hz and about 3 J cm^{-2} laser energy. The typical penetration depth was about 15 µm (spot size dependent). The two-volume ablation cell (Laurin Technic, Australia) of the M50 enables detection and sequential sampling of heterogeneous grains (e.g., growth zones) during time resolved data acquisition, due to its quick response time of <1s (time until maximum signal strength was achieved) and wash-out (< 99.9% of previous signal) time of about 2s. With a depth penetration of ~0.7 µms^{-1} and a 0.46s integration time (4 mass scans = 0.46 s = 1 integration) any significant variation of the $^{207}Pb/^{206}Pb$ and $^{238}U/^{206}Pb$ in the µm scale is detectable. Raw data were corrected offline for background signal, common Pb, laser induced elemental fractionation, instrumental mass discrimination, and time-dependent elemental fractionation of Pb/U using an in-house MS Excel© spreadsheet program (Gerdes and Zeh, 2009, 2006). A common-Pb correction based on the interference- and background-corrected ^{204}Pb signal and a model Pb composition (Stacey and Kramers, 1975) was carried out. The ^{204}Pb content for each ratio was estimated by subtracting the average mass 204 signal, obtained during the 20 second baseline acquisition, which mostly results from ^{204}Hg in the carrier gas (c. 210-330 cps), from the mass 204 signal of the respective ratio. For the

analyzed sample the calculated common ^{206}Pb contents were mostly <0.3% of the total ^{206}Pb but in very rare cases exceeded 1% (Table S1). Laser-induced elemental fractionation and instrumental mass discrimination were corrected by normalization to the reference zircon GJ-1 (Jackson et al., 2004). Prior to this normalization, the inter-elemental fractionation ($^{206}Pb^*/^{238}U$) during the 21s of sample ablation was corrected for each individual analysis. The correction was done by applying a linear regression through all measured, common Pb corrected ratios, excluding the outliers (± 2 standard deviation; 2SD), and using the intercept with the y-axis as the initial ratio. The total offset of the measured drift-corrected $^{206}Pb^*/^{238}U$ ratio from the "true" ID-TIMS value (0.0983 ± 0.0004; ID-TIMS GUF value) of the analyzed GJ-1 grain was between 15 and 22% (during the entire analytical session) and the drift over the day was 7%.

Reported uncertainties (2σ) of the $^{206}Pb/^{238}U$ ratio were propagated by quadratic addition of the external reproducibility (2 SD) obtained from the standard zircon GJ-1 (see Table S1) and the within-run precision of each analysis (2 SE; standard error). In case of the $^{207}Pb/^{206}Pb$ we used a ^{207}Pb signal dependent uncertainty propagation (see Gerdes and Zeh, 2009). The $^{207}Pb/^{235}U$ ratio is derived from the normalized and error propagated $^{207}Pb/^{206}Pb^*$ and $^{206}Pb^*/^{238}U$ ratios assuming a $^{238}U/^{235}U$ natural abundance ratio of 137.88 and the uncertainty derived by quadratic addition of the propagated uncertainties of both ratios. The accuracy of the method was verified by multiple analyses of the reference zircon GJ1 (primary standard; quoted $^{207}Pb/^{206}Pb$ age = 608.5 ± 1.5 Ma, Jackson et al. 2004; $^{206}Pb/^{238}Pb$ age = 604.6 ± 2.9 Ma, Yuan et al., 2008), Plešovice (secondary standard 1: quoted $^{206}Pb/^{238}Pb$ age = 337.13 ± 0.37 Ma, Sláma et al., 2008), and 91500 (secondary standard 2:quoted $^{207}Pb/^{206}Pb$ age = 1065.4 ± 0.3 Ma, Wiedenbeck et al., 1995), which were measured together with the unknowns during the analytical session. Concordia ages obtained from all standards are within error identical to the quoted TIMS values. The results of measurements on reference materials are shown in Table S1. The data were plotted using the software ISOPLOT (Ludwig, 2001).

2. Lu-Hf isotope analyses

Hafnium isotope measurements were performed with a Thermo-Finnigan NEPTUNE multi collector ICP-MS at GUF coupled to the same laser as described in the U-Pb method (Resolution M-50 193 nm ArF excimer laser). Round spots with diameters of 64-100 µm were drilled with repetition rate of 6 Hz and an energy density of about 6-7 J/cm^2 during 45 s of data acquisition. All data were adjusted relative to the zircon standard GJ1 of $^{176}Hf/^{177}Hf$ ratio = 0.2820000. Quoted uncertainties are quadratic additions of the within run precision of each

analysis and the reproducibility of the zircon standard GJ1 which was 0.0105% (2SD) during the analytical sessions (Table S2). Accuracy and external reproducibility of the method was verified by repeated analyses of reference zircons GJ-1, Plešovice, 91500, and Temora2, which yielded $^{176}Hf/^{177}Hf$ of 0.282000 ± 0.000029 (2SD, n=44), 0.282466 ± 0.000029 (n=11), 282294 ± 0.000028 (n = 6), and of 0.282657 ± 0.000028 (n=6), respectively (Table S2). These ratios are well within the range of solution mode data (Gerdes and Zeh, 2006; Woodhead and Hergt, 2005).

For calculation of the epsilon Hf *[εHf_t]* the chondritic uniform reservoir (CHUR) was used as recommended by Bouvier et al. (2008; $^{176}Lu/^{177}Hf$ and $^{176}Hf/^{177}Hf$ of 0.0336 and 0.282785, respectively), and a decay constant of 1.867 x10^{-11} (Scherer et al., 2001; Söderlund et al., 2004). Initial $^{176}Hf/^{177}Hf_t$ and εHf_t for all analysed zircon domains were calculated using the respective $^{207}Pb/^{206}Pb$ ages (Table S2). Depleted mantle hafnium model ages (T_{DM}) were calculated using values for the depleted mantle as suggested by Blichert-Toft and Puchtel (2010), with $^{176}Hf/^{177}Hf$ = 0.283294 and a $^{176}Lu/^{177}Hf$ of 0.03933, corresponding to a straight DM-evolution line with εHf_{today} = +18 and $\varepsilon Hf_{4.558Ga}$ = 0. T_{DM} ages for all data were calculated by using the measured $^{176}Lu/^{177}Hf$ of each spot for the time since zircon crystallization (Table S2), and a mean $^{176}Lu/^{177}Hf$ of 0.0113 for average continental crust (average of Taylor and McLennan, 1985; Wedepohl, 1995).

3. Trace element analyses

Trace elements were analyzed using a ThermoScientific Element 2 sector field ICP-MS coupled to a Resolution M-50 (Resonetics) 193 nm ArF excimer laser (ComPexPro 102F, Coherent) system at Goethe-University Frankfurt. Ablation were performed in a 0.6 l min^{-1} He stream, which was mixed directly after the ablation cell with 0.005 l min^{-1} N_2 and 0.85 l min^{-1} Ar prior introduction into the Ar plasma of the SF-ICP-MS. Zircon grains were ablated with 42 µm laser spot sizes, a repetition rate of at 6.0 Hz and 6-7 J.cm^{-2} laser energy. The oxide production, monitored as $^{254}UO/^{238}U$ on the standard glass NIST 612 was below 0.5%, and measurements were carried out in low resolution mode, with 30s for background and 35s for data acquisition. During this study the following isotopes were analysed: ^{44}Ca, ^{49}Ti, ^{57}Fe, ^{89}Y, ^{93}Nb, ^{139}La, ^{140}Ce, ^{141}Pr, ^{146}Nd, ^{147}Sm, ^{151}Eu, ^{158}Gd, ^{159}Tb, ^{161}Dy, ^{165}Ho, ^{167}Er, ^{169}Tm, ^{172}Yb, ^{175}Lu, ^{178}Hf, ^{232}Th, and ^{238}U. To increase the background / peak ratio for Ti and Nd, the sampling time for these elements was enlarged from 0.01 ms (as used for all other elements per scan) to 0.04 ms. For standardisation the glass standards NIST SRM 612 (primary standard),

and the zircon standards GJ1 and 91500 (secondary standard) were used. Data processing was performed with GLITTER software, using Si as an internal standard, and SiO_2 =32.7 wt.% for all zircons (standard zircons and unknowns). Accuracy of the zircon measurements was checked by comparison between measured and recommended concentrations for the standard zircons 91500 and GJ1 (see summary in Liu et al., 2010). This check required an offset correction of about 5-11% for the trace elements Y, Ce, Nd, Gd, Tb, Dy, Ho, Er, Tm, Lu, Hf, Ta, U, and Th, and 30-50% for Pr and Nb. The same offset correction has been applied to all unknown zircon analyses. For normalization of rare earth elements the concentrations of C1-chondrite of McDonough and Sun (1995) have been used. The results are shown in Table S3.

Table S5-1: Results of LA-ICP-MS U-Pb dating of zircon grains from the 13-AE-2149 allanite-bearing pegmatitic granite dyke from the Allochthonous Belt of the central Grenville Province. Abbreviation: conc. = degree of concordance; PGD = pegmatitic granite dyke.

Analysis no.	^{207}Pb[a] (cps)	U[b] (ppm)	Pb[b] (ppm)	Th/U[b]	^{206}Pbc[c] (%)	$^{206}Pb/^{238}U$[d]	± 2σ (%)	$^{207}Pb/^{235}U$[d]	± 2σ (%)	$^{207}Pb/^{206}Pb$[d]	± 2σ (%)	rho[e]	$^{206}Pb/^{238}U$	± 2σ (Ma)	$^{207}Pb/^{235}U$	± 2σ (Ma)	$^{207}Pb/^{206}Pb$	± 2σ (Ma)	conc.[f] (%)
13-AE-2149 Allanite-bearing PGD																			
213	376542	1127	195	0.05	0.51	0.18340	3.0	1.810	4.7	0.07159	3.7	0.62	1085	30	1049	31	974	75	111
214	341405	1344	144	0.03	0.64	0.11360	2.7	1.146	3.1	0.07311	1.4	0.88	694	18	775	17	1017	29	68
215	281032	826	94	0.08	0.83	0.11910	3.0	1.121	5.5	0.06829	4.7	0.54	725	21	764	30	877	97	83
216	233765	419	73	0.06	b.d.	0.18450	1.6	1.786	4.5	0.07018	4.2	0.36	1092	17	1040	30	934	87	117
217	274533	520	80	0.05	0.12	0.16340	2.7	1.651	3.0	0.07328	1.3	0.91	976	24	990	19	1022	25	96
218	236660	379	65	0.05	b.d.	0.18240	2.5	1.836	2.9	0.07301	1.4	0.87	1080	25	1059	19	1014	29	106
219	838692	2319	290	0.14	1.17	0.12890	2.9	1.173	4.0	0.06601	2.8	0.72	782	21	788	22	807	58	97
220	286078	770	122	0.03	b.d.	0.16870	1.7	1.692	4.1	0.07272	3.7	0.41	1005	16	1005	27	1006	76	100
221	231395	458	77	0.04	0.40	0.17840	2.4	1.786	2.5	0.07262	0.9	0.93	1058	23	1041	17	1003	18	105
222	515540	1261	159	0.05	0.32	0.13310	2.5	1.328	2.7	0.07235	1.1	0.91	805	19	858	16	996	23	81
223	347204	754	134	0.05	0.51	0.18770	1.9	1.888	2.3	0.07296	1.3	0.82	1109	19	1077	15	1013	26	109
224	504092	2135	237	0.03	0.06	0.11860	3.7	1.148	3.9	0.07023	1.1	0.96	722	25	776	21	935	23	77
225	302469	573	99	0.08	0.05	0.18190	1.9	1.825	4.1	0.07276	3.7	0.46	1077	19	1054	27	1007	75	107
226	250109	327	51	0.05	b.d.	0.16600	2.0	1.670	2.2	0.07300	0.9	0.91	990	19	997	14	1014	19	98
227	282099	1008	89	0.04	1.23	0.09251	4.4	0.941	4.7	0.07374	1.7	0.93	570	24	673	23	1034	35	55
228	864008	2358	298	0.04	0.37	0.13450	2.4	1.304	2.8	0.07032	1.4	0.86	814	18	848	16	938	29	87
229	685344	2244	296	0.05	0.13	0.14060	3.5	1.344	3.6	0.06932	1.0	0.96	848	28	865	21	908	22	93
230	349610	1038	149	0.04	b.d.	0.15310	2.9	1.508	3.1	0.07144	1.0	0.94	918	25	934	19	970	21	95
231	192787	265	43	0.08	b.d.	0.17000	1.9	1.724	2.4	0.07353	1.5	0.79	1012	18	1017	16	1028	30	98
232	351464	578	87	0.06	0.09	0.15890	2.0	1.573	2.2	0.07180	0.9	0.91	950	18	960	14	980	18	97
233	314823	568	105	0.05	b.d.	0.19720	1.7	1.970	2.0	0.07244	1.0	0.87	1160	18	1105	13	998	20	116
234	413783	992	157	0.05	0.23	0.16800	2.2	1.677	2.4	0.07238	0.9	0.92	1001	21	1000	15	997	19	100
235	680929	633	82	0.09	b.d.	0.13450	3.2	1.334	3.3	0.07193	0.7	0.98	814	25	861	19	984	15	83
Results of standard measurements																			
Standard zircon GJ1																			
GJ1-1	264716	295	27	0.03	0.07	0.09878	1.6	0.8225	1.8	0.06039	0.9	0.87	607	9	609	8	618	19	98
GJ1-2	263760	290	26	0.03	0.07	0.09751	1.6	0.7962	1.9	0.05922	1.0	0.84	600	9	595	9	575	22	104
GJ1-3	272703	289	26	0.03	0.06	0.09835	1.5	0.8067	1.7	0.05949	0.9	0.87	605	9	601	8	585	19	103
GJ1-4	245128	276	25	0.03	0.06	0.09827	1.5	0.8175	1.9	0.06034	1.0	0.83	604	9	607	9	616	23	98
GJ1-5	247455	275	25	0.03	0.06	0.09837	1.6	0.8197	2.0	0.06044	1.2	0.81	605	9	608	9	619	25	98
GJ1-6	224202	263	24	0.03	0.09	0.09714	1.6	0.8103	1.9	0.06050	1.0	0.86	598	9	603	9	621	21	96
GJ1-7	221924	266	24	0.03	0.06	0.09836	1.5	0.8154	1.9	0.06012	1.2	0.79	605	9	605	9	608	25	99
GJ1-8	217892	269	24	0.03	0.07	0.09823	1.6	0.8182	1.9	0.06041	1.1	0.82	604	9	607	9	618	23	98
GJ1-9	218421	270	25	0.03	0.10	0.09980	1.7	0.8249	1.9	0.05995	1.0	0.85	613	10	611	9	602	22	102
GJ1-10	206763	283	26	0.03	0.06	0.09775	1.6	0.8150	2.0	0.06047	1.2	0.81	601	9	605	9	620	25	97
GJ1-11	206063	282	25	0.03	0.08	0.09731	1.5	0.8004	1.9	0.05966	1.1	0.80	599	9	597	9	591	25	101
GJ1-12	186236	287	26	0.03	0.09	0.09845	1.7	0.8025	2.2	0.05912	1.3	0.79	605	10	598	10	572	29	106
GJ1-13	187697	288	26	0.03	0.08	0.09861	1.6	0.8283	2.0	0.06092	1.2	0.80	606	9	613	9	636	26	95
GJ1-14	172458	283	26	0.03	0.07	0.09882	1.7	0.8170	2.0	0.05996	1.1	0.83	607	10	606	9	602	24	101
GJ1-15	169647	287	26	0.03	0.08	0.09748	1.7	0.8154	2.1	0.06067	1.3	0.79	600	10	605	10	628	28	96
mean (n=15):						0.09822		0.81400		0.06011			604		605		607		

2SD(abs):						0.00138		0.01831		0.00107			8		10		38		
2SD(%)						1.41		2.25		1.78									
Standard zircon Plesovice																			
4	492793	957	49	0.20	0.06	0.05390	1.5	0.3954	2.5	0.05320	2.0	0.61	338	5	338	7	338	45	100
5	469358	912	47	0.20	0.17	0.05403	1.5	0.3979	3.0	0.05341	2.5	0.52	339	5	340	9	346	57	98
35	412497	801	42	0.20	b.d.	0.05427	1.6	0.3993	1.8	0.05336	0.7	0.92	341	5	341	5	344	16	99
36	423839	865	45	0.20	b.d.	0.05410	1.6	0.3997	1.8	0.05358	1.0	0.85	340	5	341	5	353	22	96
104	354650	821	42	0.20	b.d.	0.05404	1.6	0.3963	1.8	0.05319	0.7	0.91	339	5	339	5	337	17	101
105	365962	818	42	0.21	b.d.	0.05391	1.6	0.3957	1.8	0.05323	0.9	0.89	338	5	339	5	339	19	100
196	319778	857	44	0.22	0.16	0.05352	1.7	0.3926	2.1	0.05320	1.1	0.84	336	6	336	6	338	25	100
197	301840	864	44	0.20	0.22	0.05378	1.7	0.3968	2.0	0.05352	1.1	0.84	338	6	339	6	351	25	96
242	318292	996	51	0.20	b.d.	0.05369	1.7	0.3941	2.0	0.05324	1.1	0.84	337	6	337	6	339	25	99
243	289070	885	45	0.21	0.13	0.05386	1.8	0.3957	2.2	0.05328	1.3	0.82	338	6	339	6	341	28	99
mean (n=10):						0.05391		0.39635		0.05332			338		339		343		
2SD(abs):						0.00043		0.00439		0.00028			3		3		12		
2SD(%)						0.80		1.11		0.53									
Standard zircon 91500																			
69	237738	64	12	0.47	0.71	0.17940	1.9	1.853	2.6	0.07492	1.8	0.73	1064	19	1065	17	1066	35	100
70	240716	64	12	0.48	0.53	0.17850	1.6	1.847	2.1	0.07503	1.3	0.79	1059	16	1062	14	1069	25	99
148	213573	68	12	0.48	b.d.	0.17810	1.6	1.847	2.0	0.07520	1.2	0.80	1057	15	1062	13	1074	23	98
149	209152	68	12	0.47	0.08	0.17910	1.7	1.851	2.1	0.07495	1.3	0.80	1062	17	1064	14	1067	25	99
238	179394	71	13	0.48	0.54	0.17770	1.6	1.838	2.2	0.07503	1.5	0.73	1054	15	1059	14	1069	30	99
239	184923	70	13	0.50	0.01	0.17990	1.8	1.860	2.2	0.07497	1.3	0.80	1067	18	1067	15	1068	26	100
mean (n=8):						0.17878		1.84933		0.07502			1060		1063		1069		
2SD(abs):						0.00166		0.01468		0.00020			9		5		5		
2SD(%)						0.93		0.79		0.27									

[a] Within run background-corrected mean ^{207}Pb signal in cps (counts per second).
[b] U and Pb content and Th/U ratio were calculated relative to GJ-1 reference zircon.
[c] percentage of the common Pb on the ^{206}Pb. b.d. = below detection limit.
[d] corrected for background. within-run Pb/U fractionation (in case of $^{206}Pb/^{238}U$) and common Pb using Stacy and Kramers (1975) model Pb composition and subsequently normalized to GJ-1 (ID-TIMS value/measured value); $^{207}Pb/^{235}U$ calculated using $^{207}Pb/^{206}Pb/(^{238}U/^{206}Pb*1/137.88)$
[e] rho is the $^{206}Pb/^{238}U/^{207}Pb/^{235}U$ error correlation coefficient.
[f] degree of concordance = $^{206}Pb/^{238}U$ age / $^{207}Pb/^{206}Pb$ age x 100

Table S5-2: Results of LA-MC-ICPMS Lu-Hf isotope analyses of zircon grains from 13-AE-2149 allanite-bearing pegmatitic granite dyke from the Allochthonous Belt of the central Grenville Province. Abbreviation: PGD = pegmatitic granite dyke.

Analysis no.	$^{176}Yb/^{177}Hf$ [a]	± 2σ	$^{176}Lu/^{177}Hf$ [a]	± 2σ	$^{178}Hf/^{177}Hf$	$^{180}Hf/^{177}Hf$	Sig_{Hf} [b] (V)	$^{176}Hf/^{177}Hf$	± 2σ [c]	$^{176}Hf/^{177}Hf_t$ [d]	εHf_t [d]	± 2σ [c]	T_{DM2} [e] (Ga)	Age [f] (Ma)	± 2σ [c]	Conc. (%)
13-AE-2149 Allanite-bearing PGD																
213	0.0249	10	0.00088	3	1.46717	1.88658	11	0.282347	38	0.282138	-1.1	1.4	1.82	974	75	111
214	0.0411	4	0.00160	1	1.46717	1.88682	26	0.282375	33	0.282163	0.8	1.2	1.76	1017	29	68
215	0.0442	3	0.00173	2	1.46719	1.88693	28	0.282348	32	0.282138	-3.3	1.1	1.87	877	97	83
216	0.0462	8	0.00168	3	1.46714	1.88656	18	0.282329	37	0.282117	-2.7	1.3	1.88	934	87	117
217	0.0679	5	0.00253	2	1.46715	1.88672	20	0.282361	32	0.282129	-0.3	1.1	1.82	1022	25	96
218	0.0909	34	0.00291	11	1.46727	1.88690	22	0.282373	42	0.282134	-0.3	1.5	1.82	1014	29	106
219	0.0474	41	0.00168	13	1.46719	1.88662	22	0.282311	33	0.282101	-6.2	1.2	1.97	807	58	97
220	0.0313	3	0.00120	2	1.46716	1.88641	8	0.282322	36	0.282106	-1.5	1.3	1.87	1006	76	100
221	0.0282	3	0.00109	1	1.46721	1.88685	19	0.282363	35	0.282158	0.3	1.2	1.77	1003	18	105
222	0.0377	5	0.00137	2	1.46715	1.88654	12	0.282395	36	0.282175	0.7	1.3	1.74	996	23	81
223	0.0372	4	0.00157	1	1.46715	1.88669	21	0.282382	34	0.282167	0.8	1.2	1.75	1013	26	109
224	0.0442	8	0.00156	3	1.46713	1.88673	25	0.282340	34	0.282126	-2.4	1.2	1.87	935	23	77
225	0.0321	9	0.00118	3	1.46717	1.88643	8	0.282388	39	0.282136	-0.4	1.4	1.81	1007	75	107
226	0.0357	2	0.00141	1	1.46719	1.88683	28	0.282379	33	0.282166	0.8	1.2	1.75	1014	19	98
227	0.0382	6	0.00180	5	1.46716	1.88649	17	0.282379	39	0.282149	0.7	1.4	1.78	1034	35	55
228	0.0525	7	0.00189	2	1.46718	1.88667	23	0.282359	35	0.282138	-1.9	1.2	1.84	938	29	87
229	0.0692	15	0.00232	5	1.46722	1.88679	12	0.282402	35	0.282167	-1.5	1.2	1.80	908	22	93
230	0.0583	17	0.00221	5	1.46715	1.88656	11	0.282398	35	0.282162	-0.3	1.3	1.78	970	21	95
231	0.0426	3	0.00207	3	1.46718	1.88703	34	0.282391	33	0.282163	1.0	1.2	1.75	1028	30	98
232	0.0444	8	0.00164	3	1.46718	1.88683	22	0.282325	36	0.282106	-2.1	1.3	1.88	980	18	97
233	0.0392	12	0.00152	5	1.46721	1.88688	20	0.282351	33	0.282133	-0.7	1.2	1.82	998	20	116
234	0.0367	6	0.00140	3	1.46722	1.88676	20	0.282357	33	0.282141	-0.5	1.2	1.81	997	19	100
Results of standard measurements																
Standard zircon GJ1																
GJ1-1	0.0065	0.2	0.00025	0.04	1.46717	1.88651	5	0.282007	42	0.282004	-14.1	1.5	2.25	604	1	100
GJ1-2	0.0065	0.1	0.00025	0.03	1.46721	1.88667	12	0.281994	35	0.281991	-14.6	1.3	2.27	604	1	100
GJ1-3	0.0066	0.1	0.00025	0.03	1.46718	1.88677	12	0.282005	34	0.282003	-14.2	1.2	2.25	604	1	100
GJ1-4	0.0066	0.1	0.00025	0.02	1.46718	1.88660	13	0.281995	35	0.281992	-14.6	1.2	2.27	604	1	100
GJ1-5	0.0066	0.1	0.00025	0.02	1.46716	1.88677	13	0.281994	33	0.281991	-14.6	1.2	2.27	604	1	100
GJ1-6	0.0066	0.1	0.00025	0.02	1.46710	1.88644	12	0.281991	35	0.281989	-14.7	1.2	2.28	604	1	100
GJ1-7	0.0066	0.1	0.00024	0.03	1.46724	1.88665	12	0.282000	35	0.281997	-14.4	1.2	2.26	604	1	100
GJ1-8	0.0069	0.6	0.00024	0.03	1.46723	1.88668	11	0.282004	34	0.282001	-14.3	1.2	2.25	604	1	100
GJ1-9	0.0065	0.2	0.00024	0.03	1.46721	1.88654	11	0.282013	34	0.282010	-13.9	1.2	2.23	604	1	100
GJ1-10	0.0067	0.3	0.00025	0.03	1.46718	1.88670	10	0.281992	34	0.281989	-14.7	1.2	2.28	604	1	100
GJ1-11	0.0065	0.2	0.00024	0.02	1.46719	1.88662	11	0.282027	36	0.282024	-13.4	1.3	2.21	604	1	100
GJ1-12	0.0066	0.1	0.00024	0.03	1.46714	1.88662	11	0.281979	34	0.281976	-15.1	1.2	2.30	604	1	100
GJ1-13	0.0066	0.1	0.00024	0.02	1.46719	1.88658	11	0.282009	34	0.282006	-14.1	1.2	2.24	604	1	100
GJ1-14	0.0065	0.3	0.00024	0.03	1.46716	1.88664	11	0.281988	37	0.281986	-14.8	1.3	2.28	604	1	100
GJ1-15	0.0066	0.2	0.00024	0.04	1.46714	1.88650	11	0.282003	36	0.282001	-14.3	1.3	2.25	604	1	100
GJ1-16	0.0066	0.1	0.00024	0.03	1.46726	1.88658	10	0.282022	37	0.282019	-13.6	1.3	2.22	604	1	100
GJ1t-18	0.0064	0.2	0.00024	0.03	1.46722	1.88659	10	0.281988	38	0.281985	-14.8	1.3	2.28	604	1	100

GJ1t-19	0.0064	0.1	0.00024	0.02	1.46719	1.88665	10	0.282000	34	0.281997	-14.4	1.2	2.26	604	1	100
GJ1t-20	0.0064	0.1	0.00024	0.02	1.46723	1.88654	9	0.282001	37	0.281998	-14.4	1.3	2.26	604	1	100
GJ1t-21	0.0065	0.3	0.00024	0.03	1.46715	1.88664	11	0.281992	35	0.281990	-14.7	1.2	2.27	604	1	100
GJ1t-22	0.0064	0.1	0.00024	0.03	1.46720	1.88669	9	0.282027	38	0.282024	-13.5	1.3	2.21	604	1	100
GJ1t-23	0.0066	0.1	0.00025	0.03	1.46711	1.88652	9	0.282041	36	0.282038	-13.0	1.3	2.18	604	1	100
GJ1t-24	0.0066	0.1	0.00025	0.03	1.46718	1.88660	9	0.282030	35	0.282028	-13.3	1.2	2.20	604	1	100
GJ1t-25	0.0066	0.1	0.00025	0.03	1.46718	1.88664	9	0.282000	37	0.281997	-14.4	1.3	2.26	604	1	100
GJ1t-26	0.0063	0.1	0.00024	0.03	1.46722	1.88667	9	0.282000	38	0.281998	-14.4	1.4	2.26	604	1	100
GJ1t-27	0.0064	0.1	0.00024	0.04	1.46718	1.88668	9	0.281987	38	0.281984	-14.9	1.3	2.28	604	1	100
GJ1t-28	0.0067	0.2	0.00025	0.03	1.46721	1.88678	9	0.281970	33	0.281967	-15.5	1.2	2.32	604	1	100
GJ1t-29	0.0067	0.1	0.00025	0.04	1.46719	1.88662	9	0.281990	35	0.281987	-14.8	1.2	2.28	604	1	100
GJ1t-30	0.0066	0.1	0.00025	0.03	1.46714	1.88673	9	0.281980	35	0.281977	-15.1	1.2	2.30	604	1	100
GJ1t-31	0.0066	0.1	0.00025	0.03	1.46714	1.88644	9	0.282005	35	0.282002	-14.2	1.3	2.25	604	1	100
GJ1t-32	0.0067	0.2	0.00025	0.03	1.46724	1.88668	9	0.281998	35	0.281995	-14.5	1.2	2.26	604	1	100
GJ1t-33	0.0066	0.1	0.00025	0.03	1.46721	1.88669	9	0.281986	35	0.281983	-14.9	1.2	2.29	604	1	100
GJ1t-34	0.0068	0.2	0.00025	0.02	1.46721	1.88676	10	0.282011	36	0.282008	-14.0	1.3	2.24	604	1	100
GJ1t-35	0.0068	0.2	0.00025	0.03	1.46714	1.88665	10	0.281982	35	0.281979	-15.1	1.3	2.30	604	1	100
GJ1t-36	0.0068	0.3	0.00025	0.03	1.46716	1.88669	10	0.281991	34	0.281988	-14.7	1.2	2.28	604	1	100
GJ1t-37	0.0066	0.1	0.00025	0.03	1.46716	1.88659	9	0.281999	38	0.281996	-14.4	1.4	2.26	604	1	100
GJ1t-38	0.0068	0.2	0.00025	0.03	1.46721	1.88663	9	0.281997	34	0.281994	-14.5	1.2	2.26	604	1	100
GJ1t-39	0.0063	0.1	0.00023	0.10	1.46714	1.88652	9	0.282000	35	0.281998	-14.4	1.2	2.26	604	1	100
GJ1t-40	0.0065	0.1	0.00024	0.03	1.46718	1.88652	9	0.281996	37	0.281993	-14.5	1.3	2.27	604	1	100
GJ1t-41	0.0064	0.1	0.00024	0.03	1.46720	1.88673	9	0.282017	37	0.282014	-13.8	1.3	2.23	604	1	100
GJ1t-42	0.0059	0.1	0.00023	0.03	1.46718	1.88642	8	0.282007	40	0.282005	-14.1	1.4	2.25	604	1	100
GJ1t-43	0.0062	0.1	0.00023	0.04	1.46721	1.88681	8	0.281977	35	0.281974	-15.2	1.2	2.30	604	1	100
GJ1t-44	0.0066	0.1	0.00025	0.04	1.46722	1.88666	9	0.282011	34	0.282008	-14.0	1.2	2.24	604	1	100
GJ1t-47	0.0068	0.2	0.00025	0.03	1.46718	1.88655	9	0.281992	34	0.281989	-14.7	1.2	2.28	604	1	100
mean (n=44):	0.0066		0.00024		1.46719	1.88663		0.282000		0.281997	-14.4		2.26			
2σ SD	0.0004		0.00001		0.00007	0.00019		0.000029		0.000029	1.0		0.06			
Standard zircon Plesovice																
Pleso1-1	0.0054	0.4	0.00014	0.10	1.46714	1.88650	8	0.282490	35	0.282489	-3.5	1.2	1.45	337	1	100
Pleso1-3	0.0058	0.3	0.00014	0.07	1.46719	1.88652	9	0.282472	35	0.282471	-4.1	1.2	1.49	337	1	100
Pleso1-4	0.0055	0.3	0.00013	0.09	1.46719	1.88658	14	0.282468	32	0.282468	-4.3	1.1	1.50	337	1	100
Pleso1-5	0.0057	0.4	0.00014	0.10	1.46715	1.88675	13	0.282477	34	0.282476	-4.0	1.2	1.48	337	1	100
Pleso1-6	0.0055	0.3	0.00013	0.09	1.46715	1.88661	14	0.282476	35	0.282475	-4.0	1.3	1.48	337	1	100
Pleso1-7	0.0050	0.4	0.00012	0.11	1.46720	1.88660	11	0.282463	36	0.282463	-4.4	1.3	1.51	337	1	100
Pleso1-8	0.0053	0.1	0.00013	0.02	1.46721	1.88665	12	0.282462	34	0.282461	-4.5	1.2	1.51	337	1	100
Pleso1-9	0.0056	0.1	0.00014	0.03	1.46719	1.88665	11	0.282466	37	0.282465	-4.3	1.3	1.50	337	1	100
Pleso1-10	0.0044	0.2	0.00011	0.05	1.46723	1.88679	12	0.282462	37	0.282462	-4.5	1.3	1.51	337	1	100
Pleso1-11	0.0047	1.0	0.00012	0.26	1.46723	1.88677	12	0.282450	35	0.282449	-4.9	1.2	1.53	337	1	100
Pleso1-12	0.0035	0.2	0.00009	0.04	1.46720	1.88685	13	0.282445	34	0.282445	-5.1	1.2	1.54	337	1	100
mean (n=11):	0.0051		0.00013		1.46719	1.88666		0.282466		0.282466	-4.3		1.50			
2s SD	0.0014		0.00003		0.00006	0.00023		0.000025		0.000025	0.9		0.05			
Standard zircon 91500																
91500-1	0.0088	0.4	0.00032	0.21	1.46718	1.88665	9	0.282300	37	0.282293	6.5	1.3	1.48	1065	1	100
91500-2	0.0086	0.3	0.00032	0.12	1.46717	1.88657	9	0.282269	37	0.282263	5.4	1.3	1.54	1065	1	100
91500-3	0.0084	1.1	0.00031	0.42	1.46720	1.88668	9	0.282290	37	0.282284	6.2	1.3	1.50	1065	1	100
91500-4	0.0080	1.1	0.00029	0.40	1.46716	1.88657	9	0.282296	37	0.282291	6.4	1.3	1.49	1065	1	100
91500-5	0.0078	0.8	0.00028	0.30	1.46721	1.88652	8	0.282301	37	0.282296	6.6	1.3	1.48	1065	1	100

91500-6	0.0078	0.2	0.00028	0.07	1.46718	1.88659	8	0.282309	38	0.282304	6.9	1.4	1.46	1065	1	100
mean (n=6):	0.0082		0.00030		1.46718	1.88660		0.282294		0.282288	6.3		1.49			
2σ SD	0.0008		0.00004		0.00003	0.00012		0.000028		0.000028	1.0		0.06			
Standard zircon Temora																
tem1-1	0.0192	6.4	0.00076	2.7	1.46713	1.88645	8	0.282654	36	0.282648	4.5	1.3	1.08	419	1	100
tem1-2	0.0270	1.8	0.00098	0.4	1.46723	1.88663	10	0.282669	39	0.282661	5.0	1.4	1.06	419	1	100
tem1-3	0.0304	3.5	0.00106	1.3	1.46728	1.88682	11	0.282653	33	0.282645	4.4	1.2	1.09	419	1	100
tem1-4	0.0228	6.0	0.00083	1.9	1.46720	1.88672	11	0.282636	32	0.282629	3.8	1.1	1.12	419	1	100
tem1-6	0.0320	1.5	0.00111	0.5	1.46724	1.88662	9	0.282655	34	0.282646	4.4	1.2	1.09	419	1	100
tem1-7	0.0273	1.0	0.00092	0.9	1.46724	1.88618	6	0.282676	42	0.282669	5.2	1.5	1.04	419	1	100
mean (n=6):	0.0265		0.00094		1.46722	1.88657		0.282657		0.282650	4.6		1.08			
2σ SD	0.0095		0.00027		0.00010	0.00045		0.000028		0.000028	1.0		0.05			

[a] $^{176}Yb/^{177}Hf = (^{176}Yb/^{173}Yb)_{true} \times (^{173}Yb/^{177}Hf)_{meas} \times (M_{173(Yb)}/M_{177(Hf)})^{\beta(Hf)}$. $\beta(Hf) = \ln(^{179}Hf/^{177}Hf_{true}/^{179}Hf/^{177}Hf_{measured})/\ln(M_{179(Hf)}/M_{177(Hf)})$, M=mass of respective isotope. The $^{176}Lu/^{177}Hf$ were calculated in a similar way by using the $^{175}Lu/^{177}Hf$ and β(Yb).
Quoted uncertainties (absolute) relate to the last quoted figure. The effect of the inter-element fractionation on the Lu/Hf was estimated to be about 6 % or less based on analyses of the GJ-1 and Plesoviče zircons.
[b] Mean Hf signal in volt.
[c] Uncertainties are quadratic additions of the within-run precision and the daily reproducibility of the zircon GJ-1. Uncertainties for GJ-1 is 2SD (2 standard deviation).
[d] Initial $^{176}Hf/^{177}Hf$ and εHf calculated using the apparent Pb-Pb age determined by LA-ICP-MS dating (see column f), and the CHUR parameters: $^{176}Lu/^{177}Hf = 0.0336$, and $^{176}Hf/^{177}Hf = 0.282785$ (Bouvier et al.. 2008).
[e] Two stage model age in billion years using the measured $^{176}Lu/^{177}Lu$ and Pb-Pb age of each spot (first stage = age of zircon), a value of 0.02 for mafic crust (second stage), and a depleted mantle $^{176}Lu/^{177}Hf$ and $^{176}Hf/^{177}Hf$ of 0.03933 and 0.283294, see Blichert-Toft and Puchtel (2010).
[f] Apparent Pb-Pb age determined by LA-SF-ICP-MS

Table S5-3: Results of trace elements LA-ICP-MS measurements of zircon grains from the 13-AE-2149 allanite-bearing pegmatitic granite dyke from the Allochthonous Belt of the central Grenville Province. Abbreviation: PGD = pegmatitic granite dyke.

Analysis no.	Ca (ppm)	Fe (ppm)	Ti (ppm)	Y (ppm)	La (ppm)	Ce (ppm)	Pr (ppm)	Nd (ppm)	Sm (ppm)	Eu (ppm)	Gd (ppm)	Tb (ppm)	Dy (ppm)	Ho (ppm)	Er (ppm)	Tm (ppm)	Yb (ppm)	Lu (ppm)	Hf (ppm)	Th (ppm)	U (ppm)
13-AE-2149 Allanite-bearing PGD																					
139	4,810	6,388	24	1,772	16	91	15	56	28	3.7	48	15	184	67	325	80	725	134	15,653	364	2,404
140	10,930	3,992	44	2,471	17	92	14	54	28	5.4	47	15	175	66	355	109	1,271	309	30,355	243	3,949
141	476	810	10	1,304	5.3	32	4.6	19	11	0.8	22	8.3	110	46	240	61	626	123	13,673	106	1,537
142	11,417	7,718	925	3,529	69	379	70	290	107	43	153	37	387	124	577	134	1,169	217	15,228	689	4,465
143	579	907	23	1,357	15	77	12	41	16	3.8	28	9.0	115	48	250	65	665	133	14,929	111	1,719
144	21,999	8,845	175	2,866	69	182	42	155	50	17	62	16	210	92	562	172	1,919	415	18,812	2,071	9,683
145	4,048	1,179	5.8	1,614	3.5	16	1.8	7.7	3.0	0.4	14	6.5	107	50	291	90	919	185	17,979	188	3,091
146	4,500	851	6.3	1,869	0.4	8.7	0.4	1.9	2.5	0.5	16	8.0	129	61	361	111	1,037	213	19,915	258	4,397
147	18,605	9,634	32	2,439	69	265	56	238	106	5.4	122	25	207	62	313	104	1,569	439	26,840	7,059	14,069
148	10,398	10,861	95	3,726	59	222	45	178	74	11	114	32	365	136	665	164	1,443	275	17,663	289	6,629
149	8,952	10,150	137	4,269	61	234	47	186	71	12	115	33	399	151	734	174	1,689	323	18,296	600	6,124
150	6,636	2,175	14	1,436	14	65	8.9	31	9.3	2.4	18	6.8	97	44	247	72	784	165	19,103	203	3,307
151	14,161	5,053	19	2,020	48	95	14	52	21	17	28	7.6	92	41	273	110	1,692	477	34,229	1,548	6,567
152	953	1,188	4.1	1,770	3.3	24	3.2	14	7.5	4.1	23	8.9	131	60	318	82	849	168	12,445	220	2,368
153	2,208	883	7.0	1,006	0.6	6.0	0.6	4.5	2.1	0.1	10	4.3	68	33	198	61	717	156	18,064	1000	3,612
NIST612																					
	Ca	**Fe**	**Ti**	**Y**	**La**	**Ce**	**Pr**	**Nd**	**Sm**	**Eu**	**Gd**	**Tb**	**Dy**	**Ho**	**Er**	**Tm**	**Yb**	**Lu**	**Hf**	**Th**	**U**
mean (n=16)	85265	56	48	38	36	38	37	35	37	34	37	36	36	38	37	38	40	38	35	37	37
1 SD	359	1.32	0.23	0.31	0.25	0.27	0.29	0.37	0.34	0.30	0.36	0.34	0.36	0.39	0.41	0.27	0.33	0.27	0.28	0.29	0.31
1 SD %	0.4	2.3	0.5	0.8	0.7	0.7	0.8	1.1	0.9	0.9	1.0	0.9	1.0	1.0	1.1	0.7	0.8	0.7	0.8	0.8	0.8
Zircon standard GJ1																					
	Ca	**Fe**	**Ti**	**Y**	**La**	**Ce**	**Pr**	**Nd**	**Sm**	**Eu**	**Gd**	**Tb**	**Dy**	**Ho**	**Er**	**Tm**	**Yb**	**Lu**	**Hf**	**Th**	**U**
mean (n=6)	79		3.6	246	0.00	15.4	0.03	0.61	1.42	0.95	6.6	1.87	20	6.9	30	6.5	62	13	6,980	8.0	321
1 SD	3.5		0.06	3.0	0.00	0.11	0.00	0.03	0.02	0.01	0.1	0.03	0.2	0.1	0.4	0.1	1	0.2	87	0.1	3
1 SD %	4.5		1.4	1.2	14	0.80	6.3	4.2	1.7	0.86	1.7	1.7	0.89	1.7	1.3	1.1	1.6	1.3	1.3	1.6	0.76
Zircon standard 91500																					
	Ca	**Fe**	**Ti**	**Y**	**La**	**Ce**	**Pr**	**Nd**	**Sm**	**Eu**	**Gd**	**Tb**	**Dy**	**Ho**	**Er**	**Tm**	**Yb**	**Lu**	**Hf**	**Th**	**U**
mean (n=6)	79		5.1	139	0.00	2.90	0.02	0.33	0.50	0.24	2.3	0.84	11	4.8	25	6.3	65	13	5,556	30	76
1 SD	7		0.07	5	0.00	0.07	0.00	0.01	0.03	0.02	0.11	0.03	0.4	0.2	1	0.3	3	0.6	73	1	3
1 SD %	9.4		1.2	3.6	12	2.5	9.0	4.0	5.9	8.0	4.7	3.7	3.8	3.6	3.9	4.4	4.1	4.2	1.4	5.3	4.3

Table S5-4: Results of SIMS O isotope analyses of zircon grains from the 13-AE-2149 allanite-bearing pegmatitic granite dyke from the Allochthonous Belt of the central Grenville Province. Abbreviation: PGD = pegmatitic granite dyke.

Analysis no.	$\delta^{18}O$ (‰ V-SMOW)	±2σ
13-AE-2149 Allanite-bearing PGD		
227	7.79	0.18
228	6.66	0.12
229	7.08	0.13
230	8.82	0.13
231	5.78	0.17
232	7.27	0.12
233	6.64	0.14
234	7.06	0.12
235	6.07	0.13
236	6.63	0.12
237	6.53	0.14
238	7.02	0.19
239	7.33	0.11
240	8.65	0.12
241	9.16	0.15
242	7.08	0.16
243	8.07	0.13
244	5.20	0.16
245	4.07	0.22
246	3.95	0.25
247	3.35	0.26
248	3.47	0.25
249	3.93	0.32
250	5.77	0.28
251	4.95	0.31
252	2.58	0.33
253	3.58	0.30
254	5.41	0.16
255	6.30	0.17
256	6.35	0.12
257	5.61	0.17
258	4.21	0.19
259	8.18	0.10
260	7.37	0.13
261	7.59	0.15
262	4.84	0.15
263	5.22	0.14
264	6.63	0.16
265	4.66	0.14
266	4.78	0.17
Results of standard measurements		
Standard zircon 91500		
91500-83	6.84	0.11
91500-84	6.86	0.10
91500-85	6.75	0.09
91500-86	6.82	0.11
91500-87	6.56	0.11
91500-88	6.59	0.14
91500-89	6.33	0.13
91500-90	6.27	0.14
91500-91	6.58	0.13
91500-92	6.76	0.14
91500-93	6.55	0.13
91500-94	5.47	0.16
91500-95	6.25	0.13
91500-96	6.63	0.16
91500-97	5.87	0.16
91500-98	6.09	0.14
91500-99	6.04	0.14
91500-100	6.52	0.15
91500-101	6.37	0.15
91500-102	6.17	0.11
mean (n=20)	6.28	
2σ SD	0.02	

References

Augland, L.E., Moukhsil, A., Solgadi, F., Indares, A., McFarlane, C., 2015. Pinwarian to Grenvillian magmatic evolution in the central Grenville Province: new constraints from ID-TIMS U-Pb ages and coupled Lu-Hf S-MC-ICP-MS data. Canadian Journal of Earth Sciences 52, 701–721. doi:10.1139/cjes-2014-0232

Ayres, L.D., Černý, P., 1982. Metallogeny of granitoid rocks in the Canadian Shield. Can. Mineral. 20, 439–536.

Bea, F., 1996. Residence of REE, Y, Th and U in granites and crustal protoliths; Implications for the chemistry of crustal melts. J. Petrology 37, 521–552. doi:10.1093/petrology/37.3.521

Belousova, E.A., Kostitsyn, Y.A., Griffin, W.L., Begg, G.C., O'Reilly, S.Y., Pearson, N.J., 2010. The growth of the continental crust: Constraints from zircon Hf-isotope data. Lithos 119, 457–466. doi:10.1016/j.lithos.2010.07.024

Bergeron, A., 1980. Pétrographie et géochimie du complexe igné alcalin de Crevier et de son encaissant métasomatisé (Unpublished MSc thesis). Université du Québec à Chicoutimi, Chicoutimi.

Blichert-Toft, J., Puchtel, I.S., 2010. Depleted mantle sources through time: Evidence from Lu–Hf and Sm–Nd isotope systematics of Archean komatiites. Earth and Planetary Science Letters 297, 598–606. doi:10.1016/j.epsl.2010.07.012

Bouvier, A., Vervoort, J.D., Patchett, P.J., 2008. The Lu–Hf and Sm–Nd isotopic composition of CHUR: Constraints from unequilibrated chondrites and implications for the bulk composition of terrestrial planets. Earth and Planetary Science Letters 273, 48–57. doi:10.1016/j.epsl.2008.06.010

Carr, S.D., Easton, R.M., Jamieson, R.A., Culshaw, N.G., 2000. Geologic transect across the Grenville orogen of Ontario and New York. Can. J. Earth Sci. 37, 193–216. doi:10.1139/e99-074

Cawood, P.A., Hawkesworth, C.J., Dhuime, B., 2013. The continental record and the generation of continental crust. GSA Bulletin 125, 14–32. doi:10.1130/B30722.1

Černý, P., 1990. Distribution, affiliation and derivation of rare-element granitic pegmatites in the Canadian Shield. Geol. Rundsch. 79, 183–226. doi:10.1007/BF01830621

Chakhmouradian, A.R., Zaitsev, A.N., 2012. Rare earth mineralization in igneous rocks: Sources and processes. Elements 8, 347–353. doi:10.2113/gselements.8.5.347

David, J., 2006. Géochronologie d'échantillons provenant de Géologie Québec, année 2005-2006 - Rapport final. Ministère de l'Energie et des Ressources Naturelles, Québec GM 63236, 12 p.

David, J., Moukhsil, A., Clark, T., Hébert, C., Nantel, S., Dion, C., Sappin, A.-A., 2009. Datations U-Pb effectuées dans les provinces de Grenville et de Churchill en 2006-2007. Ministère des Ressources naturelles et de la Faune, Québec, RP2009-03, 32 p.

Dhuime, B., Hawkesworth, C.J., Cawood, P.A., Storey, C.D., 2012. A change in the geodynamics of continental growth 3 billion years ago. Science 335, 1334–1336. doi:10.1126/science.1216066

Dickin, A.P., Higgins, M.D., 1992. Sm/Nd evidence for a major 1.5 Ga crust-forming event in the central Grenville province. Geology 20, 137–140. doi:10.1130/0091-7613(1992)020<0137:SNEFAM>2.3.CO;2

Dunning, G., Indares, A., 2010. New insights on the 1.7–1.0 Ga crustal evolution of the central Grenville Province from the Manicouagan – Baie Comeau transect. Precambrian Research 180, 204–226. doi:10.1016/j.precamres.2010.04.005

Eglinger, A., Thébaud, N., Zeh, A., Davis, J., Miller, J., Parra-Avila, L.A., Loucks, R., McCuaig, C., Belousova, E., 2017. New insights into the crustal growth of the Paleoproterozoic margin of the Archean Kéména-Man domain, West African craton (Guinea): Implications for gold mineral system. Precambrian Research 292, 258–289. doi:10.1016/j.precamres.2016.11.012

Ercit, T.S., 2005. REE-enriched granitic pegmatites. Short Course Notes - Geological Association of Canada 17, 175–199.

Frost, B.R., Barnes, C.G., Collins, W.J., Arculus, R.J., Ellis, D.J., Frost, C.D., 2001. A geochemical classification for granitic rocks. J. Petrology 42, 2033–2048.

Gauthier, M., Chartrand, F., 2005. Metallogeny of the Grenville Province revisited. Can. J. Earth Sci. 42, 1719–1734. doi:10.1139/E05-051

Geisler, T., Schaltegger, U., Tomaschek, F., 2007. Re-equilibration of Zircon in Aqueous Fluids and Melts. Elements 3, 43–50. doi:10.2113/gselements.3.1.43

Geisler, T., Ulonska, M., Schleicher, H., Pidgeon, R.T., Bronswijk, W. van, 2001. Leaching and differential recrystallization of metamict zircon under experimental hydrothermal conditions. Contrib Mineral Petrol 141, 53–65. doi:10.1007/s004100000202

Gerdes, A., Zeh, A., 2009. Zircon formation versus zircon alteration — New insights from combined U–Pb and Lu–Hf in-situ LA-ICP-MS analyses, and consequences for the interpretation of Archean zircon from the Central Zone of the Limpopo Belt. Chemical Geology, Accessory minerals as tracers of crustal processes 261, 230–243. doi:10.1016/j.chemgeo.2008.03.005

Gerdes, A., Zeh, A., 2006. Combined U–Pb and Hf isotope LA-(MC-)ICP-MS analyses of detrital zircons: Comparison with SHRIMP and new constraints for the provenance and age of an Armorican metasediment in Central Germany. Earth and Planetary Science Letters 249, 47–61. doi:10.1016/j.epsl.2006.06.039

Gobeil, A., Hébert, C., Clark, T., Beaumier, M., Perreault, S., 2002. Géologie de la région du lac De la Blache (22K/03 et 22K/04). Ministère des Ressources Naturelles, Québec, RG 2002-01, 53 p.

Gower, C.F., Krogh, T.E., 2002. A U–Pb geochronological review of the Proterozoic history of the eastern Grenville Province. Can. J. Earth Sci. 39, 795–829.

Grimes, C.B., John, B.E., Kelemen, P.B., Mazdab, F.K., Wooden, J.L., Cheadle, M.J., Hanghøj, K., Schwartz, J.J., 2007. Trace element chemistry of zircons from oceanic crust: A method for distinguishing detrital zircon provenance. Geology 35, 643–646. doi:10.1130/G23603A.1

Groulier, P.-A., 2013. Étude des minéralisations en Nb-Ta du complexe igné alcalin de Crevier (Québec) (Rapport de Master). Université de Lorraine.

Hanchar, J.M., Finch, R.J., Hoskin, P.W.O., Watson, E.B., Cherniak, D.J., Mariano, A.N., 2001. Rare earth elements in synthetic zircon: Part 1. Synthesis, and rare earth element and phosphorus doping. American Mineralogist 86, 667–680. doi:10.2138/am-2001-5-607

Hawkesworth, C.J., Dhuime, B., Pietranik, A.B., Cawood, P.A., Kemp, A.I.S., Storey, C.D., 2010. The generation and evolution of the continental crust. Journal of the Geological Society 167, 229–248. doi:10.1144/0016-76492009-072

Hawkesworth, C.J., Kemp, A.I.S., 2006. Using hafnium and oxygen isotopes in zircons to unravel the record of crustal evolution. Chemical Geology, Special Issue in Honour of R.K. O'Nions 226, 144–162. doi:10.1016/j.chemgeo.2005.09.018

Hoskin, P.W.O., Schaltegger, U., 2003. The composition of zircon and igneous and metamorphic petrogenesis, in: Hanchar, J.M., Hoskin, P.W.O. (Eds.), Zircon, Reviews in Mineralogy and Geochemistry, Vol. 53. Mineralogical Society of America, pp. 27–62.

Hynes, A., Indares, A., Rivers, T., Gobeil, A., 2000. Lithoprobe line 55: integration of out-of-plane seismic results with surface structure, metamorphism, and geochronology, and the tectonic evolution of the eastern Grenville Province. Can. J. Earth Sci. 37, 341–358. doi:10.1139/e99-076

Ibanez-Mejia, M., Pullen, A., Arenstein, J., Gehrels, G.E., Valley, J., Ducea, M.N., Mora, A.R., Pecha, M., Ruiz, J., 2015. Unraveling crustal growth and reworking processes in complex zircons from orogenic lower-crust: The Proterozoic Putumayo Orogen of Amazonia. Precambrian Research 267, 285–310. doi:10.1016/j.precamres.2015.06.014

Jackson, S.E., Pearson, N.J., Griffin, W.L., Belousova, E.A., 2004. The application of laser ablation-inductively coupled plasma-mass spectrometry to in situ U–Pb zircon geochronology. Chemical Geology 211, 47–69. doi:10.1016/j.chemgeo.2004.06.017

Jannin, S., Gervais, F., Moukhsil, A., Augland, L.E., Crowley, J.L., accepted. Déformations tardi-grenvilliennes dans la Ceinture parautochtone (Province de Grenville centrale) : contraintes géochronologiques par couplage de méthodes U/Pb de haute résolution spatiale et de haute précision. Canadian Journal of Earth Sciences.

Jordan, S.L., Indares, A., Dunning, G., 2006. Partial melting of metapelites in the Gagnon terrane below the high-pressure belt in the Manicouagan area (Grenville Province): pressure–temperature (P–T) and U–Pb age constraints and implications. Can. J. Earth Sci. 43, 1309–1329. doi:10.1139/E06-038

Ketchum, J.W.F., Jamieson, R.A., Heaman, L.M., Culshaw, N.G., Krogh, T.E., 1994. 1.45 Ga granulites in the southwestern Grenville province: Geologic setting, P-T conditions, and U-Pb geochronology. Geology 22, 215–218. doi:10.1130/0091-7613(1994)022<0215:GGITSG>2.3.CO;2

Krogh, T.E., 1994. Precise U-Pb ages for Grenvillian and pre-Grenvillian thrusting of Proterozoic and Archean metamorphic assemblages in the Grenville Front tectonic zone, Canada. Tectonics 13, 963–982. doi:10.1029/94TC00801

Lasalle, S., Dunning, G., Indares, A., 2014. In situ LA–ICP–MS dating of monazite from aluminous gneisses: insights on the tectono-metamorphic history of a granulite-facies domain in the central Grenville Province. Can. J. Earth Sci. 51, 558–572. doi:10.1139/cjes-2013-0170

Lasalle, S., Fisher, C.M., Indares, A., Dunning, G., 2013. Contrasting types of Grenvillian granulite facies aluminous gneisses: Insights on protoliths and metamorphic events from zircon morphologies and ages. Precambrian Research 228, 117–130. doi:10.1016/j.precamres.2013.01.014

Lasalle, S., Indares, A., 2014. Anatectic record and contrasting P-T paths of aluminous gneisses from the central Grenville Province. Journal of Metamorphic Geology 32, 627–646. doi:10.1111/jmg.12083

Lenting, C., Geisler, T., Gerdes, A., Kooijman, E., Scherer, E.E., Zeh, A., 2015. The behavior of the Hf isotope system in radiation-damaged zircon during experimental hydrothermal alteration. American Mineralogist 95, 1343–1348. doi:10.2138/am.2010.3521

Lentz, D., 1996. U, Mo, and REE mineralization in late-tectonic granitic pegmatites, southwestern Grenville Province, Canada. Ore Geology Reviews 11, 197–227. doi:10.1016/0169-1368(95)00034-8

Linnen, R.L., Keppler, H., 2002. Melt composition control of Zr/Hf fractionation in magmatic processes. Geochimica et Cosmochimica Acta 66, 3293–3301. doi:10.1016/S0016-7037(02)00924-9

Liu, Y., Hu, Z., Zong, K., Gao, C., Gao, S., Xu, J., Chen, H., 2010. Reappraisement and refinement of zircon U-Pb isotope and trace element analyses by LA-ICP-MS. Chinese Science Bulletin 55, 1535–1546. doi:10.1007/s11434-010-3052-4

London, D., 2016. Rare-element granitic pegmatites. Reviews in Economic Geology 18, 165–193.

London, D., 2014. A petrologic assessment of internal zonation in granitic pegmatites. Lithos 184–187, 74–104. doi:10.1016/j.lithos.2013.10.025

London, D., 2008. Pegmatites, Mineralogical Association of Canada.

Ludwig, K.R., 2001. Isoplot/Ex, rev. 2.49. A geochronological toolkit for Microsoft Excel. Berkeley Geochronology Center, Special Publication No. 1a.

Martin, L.A.J., Duchêne, S., Deloule, E., Vanderhaeghe, O., 2008. Mobility of trace elements and oxygen in zircon during metamorphism: Consequences for geochemical tracing. Earth and Planetary Science Letters 267, 161–174. doi:10.1016/j.epsl.2007.11.029

Masson, S.L., Gordon, J.B., 1981. Radioactive mineral deposits of the Pembroke-Renfrew area (No. 23), Mineral Deposits Circ. Ont. Geol. Surv.

McDonough, W.F., Sun, S. -s., 1995. The composition of the Earth. Chemical Geology, Chemical Evolution of the Mantle 120, 223–253. doi:10.1016/0009-2541(94)00140-4

Moukhsil, A., Lacoste, P., Gobeil, A., David, J., 2009. Synthèse géologique de la région de Baie-Comeau. Ministère des Ressources naturelles et de la Faune, Québec, RG 2009-03, 30 p.

Moukhsil, A., Lacoste, P., Simard, M., Perreault, S., 2007. Géologie de la région septentrionale de Baie-Comeau (22F07, 22F08, 22F09, 22F15 et 22F16). Ministère des Ressources naturelles et de la Faune, Québec, RP 2007-04, 16 p.

Moukhsil, A., Solgadi, F., Belkacim, S., Elbasbas, A., Augland, L.E., 2014. Géologie de la région du lac Okaopéo, Côte-Nord. Ministère de l'Energie et des Ressources Naturelles, Québec, RG 2014-03, 34 p.

Moukhsil, A., Solgadi, F., Clark, T., Blouin, S., Indares, A., Davis, D.W., 2013a. Géologie du nord-ouest de la région du barrage Daniel-Johnson (Manic 5), Côte-Nord. Ministère des Ressources Naturelles, Québec, RG 2013-01, 46 p.

Moukhsil, A., Solgadi, F., Indares, A., Belkacim, S., 2013b. Géologie de la région septentrionale du réservoir aux Outardes 4, Côte-Nord. Ministère des Ressources Naturelles, Québec, RG 2013-03, 33 p.

Moukhsil, A., Solgadi, F., Lacoste, P., Gagnon, M., David, J., 2012. Géologie de la région du lac du Milieu (SNRC 22O03, 22O04, 22O06, 22J13 et 22J14). Ministère des Ressources Naturelles et de la Faune, Québec, RG 2012-01, 33 p.

Peck, W., King, E., Valley, J., 2000. Oxygen isotope perspective on Precambrian crustal growth and maturation. Geology 28, 363–366.

Pidgeon, R.T., 1992. Recrystallisation of oscillatory zoned zircon: some geochronological and petrological implications. Contrib Mineral Petrol 110, 463–472. doi:10.1007/BF00344081

Rayner, N., Stern, R.A., Carr, S.D., 2005. Grain-scale variations in trace element composition of fluid-altered zircon, Acasta Gneiss Complex, northwestern Canada. Contrib Mineral Petrol 148, 721–734. doi:10.1007/s00410-004-0633-8

Rivers, T., 2009. The Grenville Province as a large hot long-duration collisional orogen – insights from the spatial and thermal evolution of its orogenic fronts. Geological Society, London, Special Publications 327, 405–444. doi:10.1144/SP327.17

Rivers, T., 2008. Assembly and preservation of lower, mid, and upper orogenic crust in the Grenville Province—Implications for the evolution of large hot long-duration orogens. Precambrian Research 167, 237–259. doi:10.1016/j.precamres.2008.08.005

Rivers, T., 1997. Lithotectonic elements of the Grenville Province: review and tectonic implications. Precambrian Research 86, 117–154. doi:10.1016/S0301-9268(97)00038-7

Rivers, T., Culshaw, N., Hynes, A., Indares, A., Jamieson, R., Martignole, J., 2012. The Grenville Orogen - A Post-LITHOPROBE Perspective, in: J.A. Percival, F.A. Cook, and R.M. Clowes (eds) Tectonic Styles in Canada: The LITHOPROBE Perspective, Geological Association of Canada. Special Paper 49, pp. 97–236.

Rivers, T., Martignole, J., Gower, C.F., Davidson, A., 1989. New tectonic divisions of the Grenville Province, Southeast Canadian Shield. Tectonics 8, 63–84. doi:10.1029/TC008i001p00063

Sangster, A.L., Gauthier, M., Gower, C.F., 1992. Metallogeny of structural zones, Grenville Province, northeastern North America. Precambrian Research, Precambrian Metallogeny Related to Plate Tectonics 58, 401–426. doi:10.1016/0301-9268(92)90127-A

Scherer, E., Münker, C., Mezger, K., 2001. Calibration of the Lutetium-Hafnium clock. Science 293, 683–687. doi:10.1126/science.1061372

Shand, S.J., 1943. The eruptive rocks, 2nd edition. ed. New York: John Wiley.

Sircombe, K.N., 2004. AgeDisplay: an EXCEL workbook to evaluate and display univariate geochronological data using binned frequency histograms and probability density distributions. Computers & Geosciences 30, 21–31. doi:10.1016/j.cageo.2003.09.006

Sláma, J., Košler, J., Condon, D.J., Crowley, J.L., Gerdes, A., Hanchar, J.M., Horstwood, M.S.A., Morris, G.A., Nasdala, L., Norberg, N., Schaltegger, U., Schoene, B., Tubrett, M.N., Whitehouse, M.J., 2008. Plešovice zircon — A new natural reference material for U–Pb and Hf isotopic microanalysis. Chemical Geology 249, 1–35. doi:10.1016/j.chemgeo.2007.11.005

Söderlund, U., Patchett, P.J., Vervoort, J.D., Isachsen, C.E., 2004. The 176Lu decay constant determined by Lu–Hf and U–Pb isotope systematics of Precambrian mafic intrusions. Earth and Planetary Science Letters 219, 311–324. doi:10.1016/S0012-821X(04)00012-3

Stacey, J.S., Kramers, J.D., 1975. Approximation of terrestrial lead isotope evolution by a two-stage model. Earth and Planetary Science Letters 26, 207–221. doi:10.1016/0012-821X(75)90088-6

Taylor, S.R., McLennan, S., 1985. The continental crust: Its composition and evolution, Blackwell, Oxford, 1985,.

Thomson, S.D., Dickin, A.P., Spray, J.G., 2011. Nd isotope mapping of Grenvillian crustal terranes in the vicinity of the Manicouagan Impact Structure. Precambrian Research 191, 184–193. doi:10.1016/j.precamres.2011.08.006

Tucker, R.D., Gower, C.F., 1994. A U-Pb geochronological framework for the Pinware Terrane, Grenville Province, Southeast Labrador. Journal of Geology 102, 67.

Turlin, F., André-Mayer, A.-S., Moukhsil, A., Vanderhaeghe, O., Gervais, F., Solgadi, F., Groulier, P.-A., Poujol, M., 2017. Unusual LREE-rich, peraluminous, monazite- or allanite-bearing pegmatitic granite in the central Grenville Province, Québec. Ore Geology Reviews 89, 627–667. doi:10.1016/j.oregeorev.2017.04.019

Turlin, F., Deruy, C., Eglinger, A., Vanderhaeghe, O., André-Mayer, A.-S., Poujol, M., Moukhsil, A., Solgadi, F., submitted. A record of 70 Ma suprasolidus conditions in the Grenville large, hot and long-duration orogen. Terra Nova.

Valley, J.W., 2003. Oxygen isotopes in zircon. Reviews in Mineralogy and Geochemistry 53, 343–385. doi:10.2113/0530343

Valley, J.W., Lackey, J.S., Cavosie, A.J., Clechenko, C.C., Spicuzza, M.J., Basei, M.A.S., Bindeman, I.N., Ferreira, V.P., Sial, A.N., King, E.M., Peck, W.H., Sinha, A.K., Wei, C.S., 2005. 4.4 billion years of crustal maturation: oxygen isotope ratios of magmatic zircon. Contrib. Mineral. Petrol. 150, 561–580. doi:10.1007/s00410-005-0025-8

van Gool, J.A.M., Rivers, T., Calon, T., 2008. Grenville Front zone, Gagnon terrane, southwestern Labrador: Configuration of a midcrustal foreland fold-thrust belt. Tectonics 27, TC1004. doi:10.1029/2006TC002095

Van Kranendonk, M.J.V., Kirkland, C.L., 2013. Orogenic climax of Earth: The 1.2–1.1 Ga Grenvillian superevent. Geology 41, 735–738. doi:10.1130/G34243.1

Wedepohl, K.H., 1995. The composition of the continental crust. Geochimica et Cosmochimica Acta 59, 1217–1232. doi:10.1016/0016-7037(95)00038-2

Wiedenbeck, M., Allé, P., Corfu, F., Griffin, W. l., Meier, M., Oberli, F., Quadt, A.V., Roddick, J. c., Spiegel, W., 1995. Three natural zircon standards for U-Th-Pb, Lu-Hf, trace element and REE analyses. Geostandards Newsletter 19, 1–23. doi:10.1111/j.1751-908X.1995.tb00147.x

Woodhead, J.D., Hergt, J.M., 2005. A Preliminary Appraisal of Seven Natural Zircon Reference Materials for In Situ Hf Isotope Determination. Geostandards and Geoanalytical Research 29, 183–195. doi:10.1111/j.1751-908X.2005.tb00891.x

Xia, Q.-X., Zheng, Y.-F., Yuan, H., Wu, F.-Y., 2009. Contrasting Lu–Hf and U–Th–Pb isotope systematics between metamorphic growth and recrystallization of zircon from eclogite-facies metagranites in the Dabie orogen, China. Lithos, The genesis and significance of adakitic, high-Mg andesites, and other refractory magmas in intra-oceanic forearc settings 112, 477–496. doi:10.1016/j.lithos.2009.04.015

Yuan, H.-L., Gao, S., Dai, M.-N., Zong, C.-L., Günther, D., Fontaine, G.H., Liu, X.-M., Diwu, C., 2008. Simultaneous determinations of U–Pb age, Hf isotopes and trace element compositions of zircon by excimer laser-ablation quadrupole and multiple-collector ICP-MS. Chemical Geology 247, 100–118. doi:10.1016/j.chemgeo.2007.10.003

Zaraisky, G.P., Aksyuk, A.M., Devyatova, V.N., Udoratina, O.V., Chevychelov, V.Y., 2009. The Zr/Hf ratio as a fractionation indicator of rare-metal granites. Petrology 17, 25. doi:10.1134/S0869591109010020

Zeh, A., Gerdes, A., 2012. U–Pb and Hf isotope record of detrital zircons from gold-bearing sediments of the Pietersburg Greenstone Belt (South Africa)—Is there a common provenance with the Witwatersrand Basin? Precambrian Research 204, 46–56. doi:10.1016/j.precamres.2012.02.013

Zeh, A., Stern, R.A., Gerdes, A., 2014. The oldest zircons of Africa—Their U–Pb–Hf–O isotope and trace element systematics, and implications for Hadean to Archean crust–mantle evolution. Precambrian Research 241, 203–230. doi:10.1016/j.precamres.2013.11.006

Compléments : Preliminary study: Controlling factors on the mineralization of allanite vs monazite in the pegmatitic granite dykes from the central Grenville Province

1. Introduction

Allanite and monazite are two of the main LREE carriers in granitoids, the former usually ascribed to granitoids with an ASI (Aluminum Saturation Index, ASI = Al/(Ca – 1.67 x P + Na + K), Frost et al., 2001; Shand, 1943) below 1.2, and the latter in peraluminous granite (e.g. Bea, 1996; Linnen and Cuney, 2005; Montel, 1986; Rapp and Watson, 1986). Even though both minerals may be observed in a same sample, they are not coeval, one being linked to the destabilization of the other (e.g. Broska et al., 2000). These minerals and their growth within a rock might witness distinct (i) *P-T* conditions of metamorphic path (Finger et al., 1998; Janots et al., 2007; Krenn and Finger, 2007; Wang et al., 2017), and/or (ii) f_{H2} or f_{O2} (Gieré and Sorensen, 2004; Schmidt and Thompson, 1996), but are in general ultimately attributed to (iii) distinct Na, Ca and/or Al activities (Berger et al., 2009; Budzyń et al., 2011; Wing et al., 2003).

The central Grenville Province contains seven coeval LREE-rich pegmatitic granite dykes (*further designated as 'PGD'*) emplaced at ca. 1005-1000 Ma in close to wet-solidus thermal conditions (Turlin et al., 2017, submitted, chapters 3 to 5), i.e. in favorable conditions for interactions between the PGD and their hosts, as suggested in chapter 5 for a shallow-dipping PGD. Six of them are proposed to have been derived from the partial melting of similar metapelitic sequences to the Knob Lake Group (chapters 3 and 4), and one from allochthonous plutonic units (chapter 5). An empirical relationship shows that monazite-bearing PGD are hosted in metasedimentary complexes and allanite-bearing PGD in metaplutonic ones (Turlin et al., 2017).

In this preliminary study, we present whole-rock geochemistry from every identified facies of several allanite- and monazite-bearing PGD from the same area and of their respective hosts sampled (i) at the contact with the PGD, (ii) in the vicinity of the contact (few tens of centimeters away) and (iii) far from the contact. These data allow to evaluate the hypothesis of a control of the LREE mineralization in these PGD as allanite and monazite by their respective hosts.

2. Analytical methods: whole-rock geochemistry

Whole-rock geochemistry of the various facies of the PGD and of their respective hosts was performed by Actlabs (Ancaster, Ontario). Powdered samples were prepared by Li-metaborate or -tetraborate. Major elements were analyzed by inductively coupled plasma - atomic emission spectroscopy (ICP–AES), and trace elements by inductively coupled plasma - mass spectrometry (ICP–MS). Results are reported in Table 6-1. In the present contribution, we

report original geochemical data except for samples 13-AM-13- A5, -A4, -A6, -A1, - E and -F, 13-AM-07-A1, 13-TC-5072-B1,13-FS-1202-B1, 13-AE-2149-B, -B1, -B4, -B3, -B5, -B6, -B7, -B99 from Turlin et al. (2017), chapters 4 and 5. Results are reported in Table 6-1.

3. Results

3.1. Whole-rock geochemistry of monazite-bearing PGD and their hosts

The aluminous migmatitic paragneisses of the Plus-Value Complex of the central Grenville Province (Moukhsil et al., 2014; Turlin et al., 2017) in which the 13-AM-07 monazite-bearing PGD is intruded has a Na_2O content ranging between 2.29 and 4.14 wt.%, CaO between 1.49 and 9.99 wt.%, P_2O_5 between 0.04 and 0.31 wt.%, $Fe_2O_{3\ (total)}$ between 5.27 and 7.21 wt.%, and MgO between 1.19 and 2.26 wt.% (Table 6-1). They lead to Na/Ca and Fe/Mg ratios ranging between 0.41 and 5.03, and between 1.54 and 2.24, respectively (Table 6-1). The intruding 13-AM-07 PGD has a Na_2O content ranging between 2.59 and 3.68 wt.%, CaO between 1.39 and 2.31 wt.%, P_2O_5 between 0.03 and 0.29 wt.%, $Fe_2O_{3\ (total)}$ between 1.23 and 1.94 wt.%, and MgO between 0.36 and 0.70 wt.% (Table 6-1). They lead to Na/Ca and Fe/Mg ratios ranging between 2.79 and 3.43, and between 1.25 and 2.03, respectively (Table 6-1).

The 13-AM-13 monazite-bearing PGD intrudes the same metasedimentary unit as the 13-AM-07 PGD (Moukhsil et al., 2014; Turlin et al., 2017) and has a Na_2O content ranging between 1.70 and 4.02 wt.%, CaO between 0.86 and 3.10 wt.%, P_2O_5 between 0.11 and 0.40 wt.%, $Fe_2O_{3\ (total)}$ between 1.04 and 4.60 wt.%, and MgO between 0.21 and 1.16 wt.% (Table 6-1). They lead to Na/Ca and Fe/Mg ratios ranging between 2.35 and 4.41, and between 2.00 and 2.50, respectively (Table 6-1).

3.2. Whole-rock geochemistry of allanite-bearing PGD and their hosts

The 13-TC-5072 allanite-bearing PGD intrudes a metamonzogranite of the Bardoux Plutonic Suite of the central Grenville Province (Moukhsil et al., 2014; Turlin et al., 2017). This metamonzogranite has a Na_2O content ranging between 2.72 and 3.75 wt.%, CaO between 2.39 and 3.54 wt.%, P_2O_5 between 0.18 and 0.31 wt.%, $Fe_2O_{3\ (total)}$ between 4.68 and 6.97 wt.%, and MgO between 0.64 and 0.89 wt.% (Table 6-1). They lead to Na/Ca and Fe/Mg ratios ranging between 1.43 and 2.07, and between 3.69 and 4.07, respectively (Table 6-1). The intruding 13-TC-5072 PGD has a Na_2O content ranging between 2.16 and 2.74 wt.%, CaO between 0.76 and

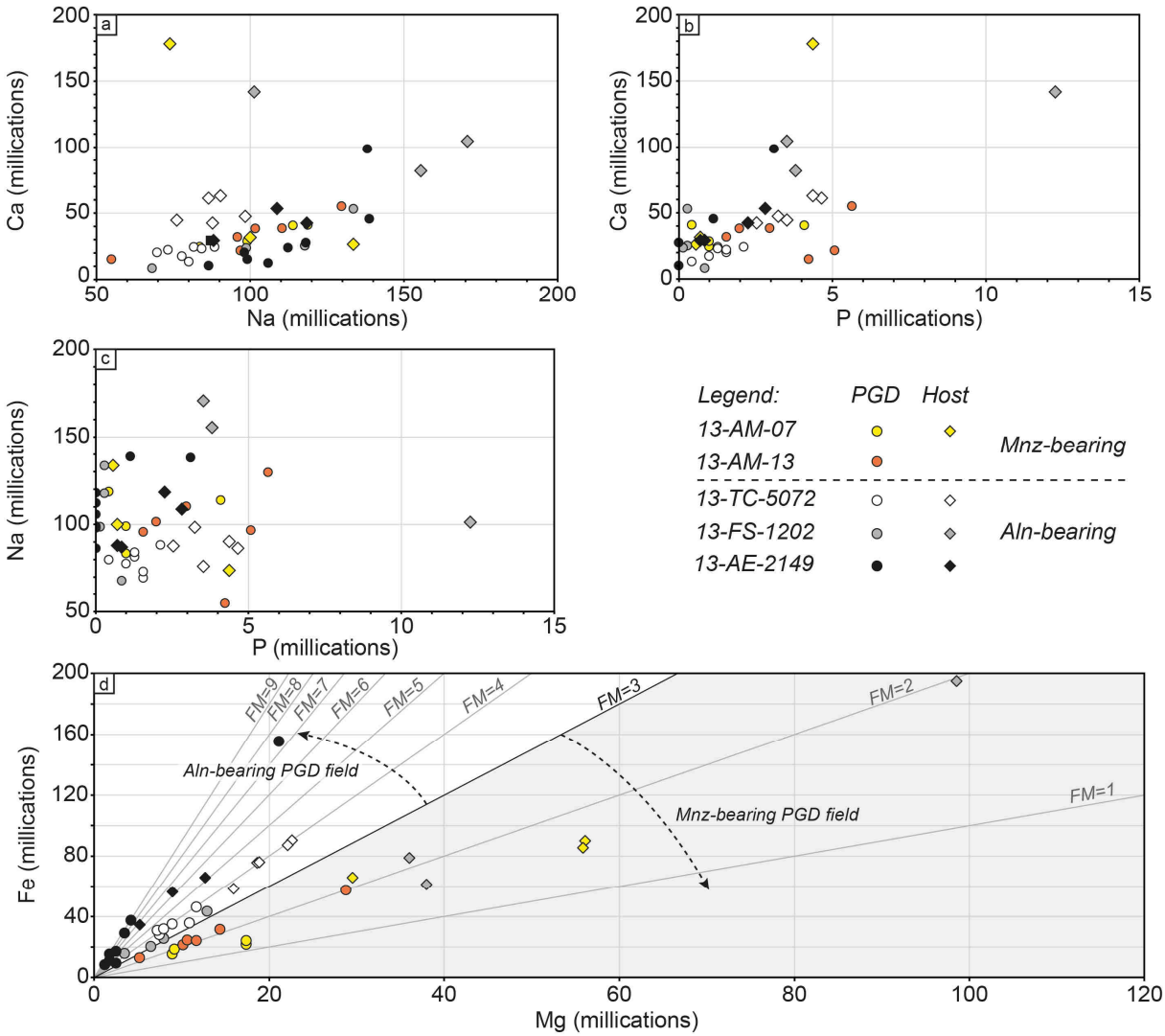

Figure 6-1: Whole-rock geochemistry of the allanite- and monazite-bearing pegmatitic granite dykes from the central Grenville and of their respective hosts. a, b and c: Ca vs Na, Ca vs P and Na vs P (millications) diagrams showing a common behavior between allanite and monazite-bearing pegmatitic granite; d: Fe vs Mg (millications) diagram. Note the distinct and linear trend defined by samples from a single pegmatitic granite dyke and its host. Two compositional fields can be outlined on the basis of Fe/Mg ratio. Allanite-bearing pegmatitic granite dykes and their hosts show Fe/Mg above three, whereas monazite-bearing dykes and their hosts show Fe/Mg below three. Abbreviations: Aln-bearing = allanite-bearing pegmatitic granite dyke; FM = Fe/Mg ratio; Mnz-bearing = monazite-bearing pegmatitic granite dyke; PGD = pegmatitic granite dyke.

1.38 wt.%, P_2O_5 between 0.03 and 0.15 wt.%, $Fe_2O_{3\ (total)}$ between 2.24 and 3.69 wt.%, and MgO between 0.29 and 0.47 wt.% (Table 6-1). They lead to Na/Ca and Fe/Mg ratios ranging between 3.26 and 5.91, and between 3.27 and 4.32, respectively (Table 6-1).

The 13-FS-1202 allanite-bearing PGD intrudes a quartz metamonzodiorite of the Castoréum Plutonic Suite of the central Grenville Province (Moukhsil et al., 2014; Turlin et al., 2017). This quartz metamonzodiorite has a Na_2O content ranging between 3.14 and 5.29 wt.%, CaO between 4.60 and 7.96 wt.%, P_2O_5 between 0.25 and 0.87 wt.%, $Fe_2O_{3\ (total)}$ between 4.91 and 15.59 wt.%, and MgO between 1.45 and 3.97 wt.% (Table 6-1). They lead to Na/Ca and Fe/Mg ratios ranging between 0.71 and 1.90, and between 1.62 and 2.19, respectively (Table

6-1). The intruding 13-FS-1202 PGD has a Na_2O content ranging between 2.11 and 4.14 wt.%, CaO between 0.48 and 2.99 wt.%, P_2O_5 between 0.01 and 0.06 wt.%, $Fe_2O_{3\ (total)}$ between 1.26 and 3.48 wt.%, and MgO between 0.14 and 0.52 wt.% (Table 6-1). They lead to Na/Ca and Fe/Mg ratios ranging between 2.51 and 7.96, and between 3.19 and 4.55, respectively (Table 6-1).

The 13-AE-2149 allanite-bearing PGD intrudes a metamangerite of the Castoréum Plutonic Suite of the central Grenville Province (Moukhsil et al., 2014; Turlin et al., 2017). This metamangerite has a Na_2O content ranging between 2.70 and 3.67 wt.%, CaO between 1.65 and 3.00 wt.%, P_2O_5 between 0.05 and 0.20 wt.%, $Fe_2O_{3\ (total)}$ between 2.76 and 5.26 wt.%, and MgO between 0.21 and 0.51 wt.% (Table 6-1). They lead to Na/Ca and Fe/Mg ratios ranging between 2.03 and 2.99, and between 5.21 and 6.66, respectively (Table 6-1). The intruding 13-AE-2149 PGD has a Na_2O content ranging between 2.68 and 4.30 wt.%, CaO between 0.59 and 5.54 wt.%, P_2O_5 between 0.00 and 0.22 wt.%, $Fe_2O_{3\ (total)}$ between 0.69 and 12.42 wt.%, and MgO between 0.05 and 0.85 wt.% (Table 6-1). They lead to Na/Ca and Fe/Mg ratios ranging between 1.40 and 8.48, and between 3.89 and 8.95, respectively (Table 6-1).

The 13-FS-1202 allanite-bearing PGD intrudes a quartz metamonzodiorite of the Castoréum Plutonic Suite of the central Grenville Province (Moukhsil et al., 2014; Turlin et al., 2017) that has a Na_2O content ranging between 3.14 and 5.29 wt.%, CaO between 4.60 and 7.96 wt.%, P_2O_5 between 0.25 and 0.87 wt.%, $Fe_2O_{3\ (total)}$ between 4.91 and 15.59 wt.%, and MgO between 1.45 and 3.97 wt.% (Table 6-1). They lead to Na/Ca and Fe/Mg ratios ranging between 0.71 and 1.90, and between 1.62 and 2.19, respectively (Table 6-1). The intruding 13-FS-1202 PGD has a Na_2O content ranging between 2.11 and 4.14 wt.%, CaO between 0.48 and 2.99 wt.%, P_2O_5 between 0.01 and 0.06 wt.%, $Fe_2O_{3\ (total)}$ between 1.26 and 3.48 wt.%, and MgO between 0.14 and 0.52 wt.% (Table 6-1). They lead to Na/Ca and Fe/Mg ratios ranging between 2.51 and 7.96, and between 3.19 and 4.55, respectively (Table 6-1).

The 13-AE-2149 allanite-bearing PGD intrudes a metamangerite of the Castoréum Plutonic Suite of the central Grenville Province (Moukhsil et al., 2014; Turlin et al., 2017) that has a Na_2O content ranging between 2.70 and 3.67 wt.%, CaO between 1.65 and 3.00 wt.%, P_2O_5 between 0.05 and 0.20 wt.%, $Fe_2O_{3\ (total)}$ between 2.76 and 5.26 wt.%, and MgO between 0.21 and 0.51 wt.% (Table 6-1). They lead to Na/Ca and Fe/Mg ratios ranging between 2.03 and 2.99, and between 5.21 and 6.66, respectively (Table 6-1). The intruding 13-AE-2149 PGD has a Na_2O content ranging between 2.68 and 4.30 wt.%, CaO between 0.59 and 5.54 wt.%, P_2O_5 between 0.00 and 0.22 wt.%, $Fe_2O_{3\ (total)}$ between 0.69 and 12.42 wt.%, and MgO between

0.05 and 0.85 wt.% (Table 6-1). They lead to Na/Ca and Fe/Mg ratios ranging between 1.40 and 8.48, and between 3.89 and 8.95, respectively (Table 6-1).

3.3. Geochemical trends

Plotted in a Ca vs Na and Ca vs P diagrams (Fig. 6-1a and b), data of PGD and their host show a positive correlation but no link between allanite-bearing PGD and their host can be outlined and conversely for monazite-bearing PGD. No correlation between Na and P contents is noticeable (Fig. 6-1c). In the same way, no compositional field favorable for the expression of monazite or allanite is visible (Fig. 6-1a-c).

Plotted in a Fe vs Mg diagram (Fig. 6-1d), Fe and Mg contents of a PGD are systematically lower than that of their respective host. Each monazite-bearing and allanite-bearing PGD and their respective host spread along a similar line corresponding to distinct Fe/Mg ratios. Moreover, allanite-bearing PGD and their hosts spread along Fe/Mg ratios over 3 and monazite-bearing PGD and their hosts spread along Fe/Mg ratios below 3 (Fig. 6-1d).

4. Discussion

It is accepted that the growth of monazite over allanite is ultimately controlled by the activities of Na and Ca in the rock (e.g. Berger et al., 2009; Budzyń et al., 2011) that can be induced by a modification of the *P-T* conditions of metamorphic rocks (Finger et al., 1998; Janots et al., 2007; Krenn and Finger, 2007; Wang et al., 2017), and/or of f_{H2} or f_{O2} (Gieré and Sorensen, 2004; Schmidt and Thompson, 1996).

The investigated PGD from the central Grenville Province are all coeval at ca. 1005-1000 Ma (U-Pb on monazite, Turlin et al., 2017, zircon, chapters 3 and 5) and emplaced in mid- to low-pressure allochthonous crustal segment under close to wet-solidus thermal conditions (Turlin et al., submitted). Accordingly, no changes in the *P-T* conditions can account for the control of monazite over allanite and conversely.

Most PGD are proposed to be derived from a similar metapelitic sequence belonging to the Knob Lake Group from the Parautochthonous Belt (chapters 3 and 4), to the exception of the 13-AE-2149 PGD derived from the reworking of allochthonous plutonic units (chapter 5). Accordingly, the control of the LREE-mineralization in the PGD is unlikely to be related to an initial melt composition inherited from distinct sources.

The empirical relationships between monazite-bearing PGD and a metasedimentary host, and between allanite-bearing PGD and a metaplutonic host (Turlin et al., 2017) raise the

question of the role of the host in the expression of both LREE phases. Monazite [$(Ce,La,Nd,Th)PO_4$] and allanite [$(Ce,Ca)_2(Al,Fe^{3+})_3(SiO_4)_3(OH)$] differ in their chemical compositions especially in the incorporation in the structure of the latter of Fe^{3+} and to a lesser extent of Mg^{2+} (e.g. Gieré and Sorensen, 2004; Turlin et al., 2017). The Fe and Mg contents of the hosts are higher than of the PGD and are variable according to the distance to the PGD but their associated Fe/Mg ratios remain quite stable (within a range below 1.45), whereas the Na/Ca ratios are more variable (up to 4.62 difference) (Fig. 6-1d, Table 6-1). In the same way, the Fe and Mg contents of the PGD show variations within a dyke between the various sampled facies but they show rather homogeneous Fe/Mg ratios, in general within a range of 1.36 to the exception of an extreme variation up to a difference of 5.06 for the 13-AE-2149 PGD (Fig. 6-1d, Table 6-1). The Na/Ca ratios within a PGD are more variable, within a range up to 7.08 (Fig. 6-1d, Table 6-1). These geochemical features lead to the spreading of the PGD and of their respective hosts on quite similar Fe/Mg ratios (Fig. 6-1d, Table 6-1). In addition, these data allow the distinction of an allanite-bearing and of a monazite-bearing PGD compositional fields on the basis of a Fe/Mg ratio around 3.

Accordingly, these data suggest a control of the Fe/Mg ratio of the PGD by their respective host that ultimately control the expression of monazite and allanite, strengthened by the decrease of Fe and Mg contents of the hosts towards the PGD (Fig. 6-1d, Table 6-1). This control implies that the PGD interacted with their host, either at their outcropping structural levels and/or at depth during magma ascent. Such interactions have already been proposed by Lentz (1996, 1991) who described a skarnification of the host in response to the emplacement of pegmatites in the southwestern Grenville Province. Such features have not been observed for the PGD of the central Grenville Province and therefore do not argue in favor of an interaction at the outcropping level but rather at depth during magma ascent (Turlin et al., 2017). However, no contacts are associated with fracturation of the hosts minerals and are slightly to locally diffuse and/or lobate as on the 13-TC-5008 outcrop where they were attributed to the intrusion of the PGD under close to wet-solidus conditions, therefore favoring interactions between the magma and a partially molten host (Turlin et al., 2017, submitted). Such interactions are also proposed for the generation of the LREE mineralization as allanite in the shallow-dipping 13-AE-2149 PGD which locally very diffuse contacts with its hosts suggest significant interactions between the two lithologies (chapter 5). Accordingly, some PGD provide evidence for interactions with their hosts at the outcropping level whereas others suggest interactions to be produced at depth.

Even if this interpretation of the control of the Fe/Mg ratios of the PGD and of the expression of allanite over monazite by their host is compatible with geochemical trends, empirical field relationships and the thermal evolution of the allochthonous mid- to low-pressure crustal segments intruded by the PGD, no data from this preliminary study allow to distinguish the process responsible for such interactions. Whether the host lithologies transferred Fe and Mg to the PGD or controlled (i) the redox conditions, (ii) f_{O2} and/or (iii) f_{H2} of the intruding magma responsible for the availability of Fe^{3+} and the subsequent growth of allanite remain unconstrained.

Conclusion

Field relationships and whole-rock geochemistry of monazite-bearing and allanite-bearing PGD and of their respective hosts argue in favor of a control of the Fe/Mg ratios of the PGD by their respective hosts, consistent with the intrusion of the PGD under close to wet-solidus thermal conditions and the observation of locally diffuse contacts suggesting interactions between the PGD and their hosts at the site of emplacement and therefore most probably also at depth during magma ascent. Moreover, these preliminary results show that monazite-bearing and allanite-bearing PGD define two compositional fields, the latter corresponding to Fe/Mg ratios above 3 and the former below.

However, no data from this study allow to constrain the process responsible for this control, whether the interactions of the PGD with their hosts and crosscutting lithologies at depth are responsible for (i) the transfer of contrasting proportions of Fe and Mg to the PGD, or for the control of redox conditions and/or of f_{O2} and f_{H2}. Accordingly, further work is required to constrain these processes.

Table 6-1: Whole rock geochemistry of the various facies of the monazite- and allanite-bearing pegmatitic granite dykes from the Lac Okaopéo region and of their respective hosts sampled at the contact, close to the contact and far from the contact (labelled 'unaffected'). Abbreviations: A/CNK = Al/ (Na + K + Ca/2) (Shand, 1943); Allanite-bearing PGD = allanite-bearing pegmatitic granite dyke; A/NK = Al/(Na + K) (Shand, 1943); ASI = Aluminum Saturation Index given by the expression ASI = Al/(Ca – 1.67 x P + Na + K) (Frost et al., 2001; Shand, 1943); Bt = biotite; Grt = garnet; L.D. = limit of detection; Monazite-bearing PGD = monazite-bearing pegmatitic granite dyke.

Type	*Monazite-bearing PGD*				*Host*			*Monazite-bearing PGD*					
Outcrop	**13-AM-07**							**13-AM-13**					
Sample no.	**13-AM-07-A1[1]**	**13-AM-07-A31**	**13-AM-07-A4**	**13-AM-07-A32**	**13-AM-07-B31**	**13-AM-07-B33**	**13-AM-07-B4**	**13-AM-13-E[1]**	**13-AM-13-A6[2]**	**13-AM-13-A5[2]**	**13-AM-13-A4[2]**	**13-AM-13-A1[2]**	**13-AM-13-F[2]**
Facies	**Coarse grained**	**Fine grained**	**Fine grained**	**Contact**	**Contact**	**Close to contact**	**Unaffected**	**Fine grained**	**Intermediate**	**Fine grained (+Grt)**	**Intermediate (+Bt)**	**Coarse grained**	**Pegmatitic**
SiO_2 *(wt. %)*	71.03	72.03	69.61	70.75	61.92	60.77	64.30	60.24	66.11	70.37	72.55	73.08	72.50
Al_2O_3	15.93	14.28	16.37	14.47	15.80	13.86	14.47	18.58	17.82	15.66	14.14	15.06	12.00
$Fe_2O_{3\ total}$	1.23	1.73	1.49	1.94	7.21	5.27	6.85	4.60	1.71	1.96	1.94	1.04	2.52
MgO	0.36	0.70	0.37	0.70	2.26	1.19	2.25	1.16	0.41	0.43	0.47	0.21	0.58
MnO	0.01	0.01	0.01	0.02	0.07	0.28	0.05	0.03	0.01	0.01	0.01	0.01	0.01
CaO	2.29	1.39	2.31	1.62	1.78	9.99	1.49	3.10	1.23	2.17	2.16	1.80	0.86
Na_2O	3.53	2.59	3.68	3.07	3.10	2.29	4.14	4.02	3.00	3.42	3.15	2.97	1.70
K_2O	4.32	5.82	4.76	4.98	4.96	1.14	1.82	4.36	8.96	4.43	3.71	5.58	6.96
TiO_2	0.241	0.31	0.24	0.40	0.72	0.46	0.61	0.89	0.30	0.32	0.33	0.18	0.42
P_2O_5	0.29	0.07	0.03	0.07	0.05	0.31	0.04	0.40	0.36	0.21	0.14	0.11	0.30
Cr_2O_3	< L.D.	< L.D.	< L.D.	< L.D.	0.01	0.01	0.01	< L.D.	< L.D.	< L.D.	< L.D.	< L.D.	< L.D.
LOI	0.63	0.94	0.67	0.83	2.04	4.58	4.00	0.82	0.53	0.57	0.69	0.55	0.60
Total	99.87	99.87	99.54	98.85	99.92	100.10	100.00	98.19	100.40	99.55	99.29	100.60	98.44
Na/Ca	2.79	3.37	2.88	3.43	3.15	0.41	5.03	2.35	4.41	2.85	2.64	2.99	3.58
Fe/Mg	1.73	1.25	2.03	1.40	1.61	2.24	1.54	2.00	2.11	2.30	2.08	2.50	2.19
ASI	1.30	1.22	1.23	1.22	1.31	1.01	1.43	1.36	1.16	1.29	1.29	1.21	1.12
A/CNK	1.38	1.28	1.34	1.29	1.40	1.45	1.53	1.46	1.17	1.37	1.39	1.28	1.12
A/NK	1.52	1.35	1.46	1.39	1.51	2.77	1.65	1.64	1.22	1.50	1.54	1.38	1.16
Sr *(ppm)*	448	758	478	516	292	208	301	550	639	507	462	702	421
Ba	1191	1975	1307	1174	1038	145	401	899	1981	915	857	1384	1458
Nb	5.6	5.2	3.8	6.2	11.4	16	7.9	21	5.4	5.9	5.1	4.6	11
V	16	20	14	19	119	73	121	27	11	10	12	7	13
Co	2.0	2.0	3.0	2.0	14	9.0	24	6	2	2	2	1	3
Ga	39	22	22	23	19	23	20	60	42	34	29	26	21
Ge	4.7	1.4	1.2	1.4	1.5	2.3	0.9	6.9	3.7	2.5	2	2.6	2.1
In	< L.D.	< L.D.	< L.D.	< L.D.	< L.D.	< L.D.	< L.D.	< L.D.	< L.D.	< L.D.	< L.D.	< L.D.	< L.D.
Sn	< L.D.	< L.D.	< L.D.	< L.D.	< L.D.	< L.D.	< L.D.	< L.D.	< L.D.	< L.D.	< L.D.	< L.D.	< L.D.
Cs	0.5	0.4	0.5	0.5	0.8	0.3	0.2	1.5	0.9	0.7	0.5	0.6	1.2
Pb	35	30	39	32	21	6.0	42	34	58	37	31	34	35
Be	2.0	2.0	3.0	2.0	2.0	6.0	3.0	3	2	3	3	2	1
Hf	23	29	5.8	20	6.6	4.2	8.0	42	22	41	60	3.6	3.8
Ta	0.1	0.1	0.1	0.2	0.5	0.8	0.3	0.4	0.1	0.2	0.1	0.1	0.3
W	0.9	< L.D.	< L.D.	< L.D.	< L.D.	< L.D.	< L.D.	1.1	< L.D.	< L.D.	< L.D.	0.7	0.7
Tl	1.0	0.6	0.5	0.5	0.6	0.2	0.3	1.4	1.5	0.8	0.7	1.2	1.6
Bi	< L.D.	< L.D.	< L.D.	< L.D.	< L.D.	< L.D.	< L.D.	< L.D.	< L.D.	< L.D.	< L.D.	< L.D.	< L.D.
Th	561	91	37	94	6.6	7.5	4.9	1300	1210	560	420	340	118
U	11	3.8	1.3	3.3	1.1	3.1	1.3	19	17	10	8.3	4.8	2.5
Rb	98	141	116	128	136	54	51	214	317	173	156	172	259
Y	30	12	3.3	13	68	25	31	53	46	30	23	13.2	12
Zr	860	1060	201	750	229	141	277	1480	715	1440	2130	135	142
Nb/Ta	56	11	12	41	24	19	32	53	42	37	39	46	40

Zr/Hf	37	174	281	38	35	34	35	36	32	35	36	38	37
Th/U	51	4.3	7.0	28	5.8	2.5	3.7	68	70	56	50	71	48
La	1560	307	116	315	36	31	29	1800	1510	886	613	419	184
Ce	2720	548	201	572	66	65	58	3370	2980	1710	1180	776	344
Pr	271	54	19	56	7.1	7.6	6.6	370	313	182	126	82	36
Nd	843	307	116	167	25	28	24	1250	1040	592	407	270	124
Sm	85	548	201	18	4.7	5.4	4.2	159	136	76	54	34	17
Eu	3.47	54	19.2	2.37	1.6	1.0	1.0	4.7	4.9	3.3	2.9	2.9	2.3
Gd	28.6	163	57.2	6.85	4.9	4.3	3.3	65	57	33	24	14	7.7
Tb	2.07	17.4	6.16	0.59	1.1	0.7	0.6	5.0	4.1	2.3	1.6	1.0	0.7
Dy	8.41	2.81	2.62	2.61	9.2	4.0	4.5	16.3	13.8	8.6	6.0	3.8	2.8
Ho	1.12	6.31	2.42	0.44	2.2	0.8	1.0	1.9	1.7	1.1	0.8	0.5	0.4
Er	2.42	0.56	0.2	1.31	7.3	2.3	3.3	3.8	3.2	2.4	2.1	0.9	0.9
Tm	0.226	2.34	0.93	0.164	1.1	0.3	0.5	0.3	0.2	0.2	0.2	0.1	0.1
Yb	1.13	0.41	0.14	0.96	8.1	2.4	3.4	1.6	0.9	1.1	1.4	0.4	0.6
Lu	0.174	1.24	0.36	0.155	1.3	0.4	0.5	0.2	0.1	0.2	0.2	0.0	0.1
ΣLREE	5479	1089	400	1128	139	137	122	6949	5979	3446	2380	1580	705
ΣHREE	48	15	7.0	15	37	16	18	99	86	52	39	23	15
ΣREE	5526	1105	407	1144	176	153	141	7048	6065	3498	2419	1603	721
Eu/Eu*[4]	0.2	0.8	2.1	0.6	1.0	0.6	0.8	0.1	0.2	0.2	0.2	0.4	0.6
La_N/Sm_N[4]	12	11	12	11	4.8	3.6	4.3	7.1	6.9	7.2	7.1	7.7	6.8
La_N/Yb_N[4]	938	174	281	223	3.0	8.9	5.8	784	1193	537	304	769	223
Gd_N/Yb_N[4]	20	4.3	7.0	5.8	0.5	1.4	0.8	34	54	24	14	30	11
B	**-**	< L.D.	< L.D.	< L.D.	**-**	**-**	**-**	-	3	< 2	4	-	-
F	**-**	< L.D.	< L.D.	< L.D.	**-**	**-**	**-**	-	< L.D.	< L.D.	< L.D.	-	-
Li	**-**	< L.D.	< L.D.	< L.D.	**-**	**-**	**-**	-	< L.D.	< L.D.	< L.D.	-	-
Cd	< L.D.	< L.D.	< L.D.	< L.D.	< L.D.	< L.D.	< L.D.	< L.D.	< L.D.	< L.D.	< L.D.	< L.D.	< L.D.
Cu	5	3	20	5	70	44	132	20	5	5	6	3	2
Ag	< L.D.	1.8	0.4	0.4	0.4	< L.D.	0.6	< L.D.	< L.D.	< L.D.	< L.D.	< L.D.	< L.D.
Ni	< L.D.	3	4	2	41	32	76	3	1	2	1	2	6
Mo	2	1	3	< L.D.	5	3	9	4	3	2	3	< L.D.	< L.D.
Zn	27	45	27	47	117	120	59	110	45	77	57	24	68
S	300	< L.D.	1500	< L.D.	10900	6700	8300	1100	100	< L.D.	< L.D.	300	500
Au *(ppb)*	< L.D.	< L.D.	< L.D.	< L.D.	< L.D.	< L.D.	< L.D.	< L.D.	< L.D.	< L.D.	< L.D.	< L.D.	< L.D.
As	< L.D.	< L.D.	< L.D.	< L.D.	< L.D.	< L.D.	< L.D.	< L.D.	< L.D.	< L.D.	< L.D.	< L.D.	< L.D.
Br	< L.D.	< L.D.	< L.D.	< L.D.	< L.D.	5.2	< L.D.	< L.D.	< L.D.	< L.D.	< L.D.	< L.D.	< L.D.
Ir	< L.D.	< L.D.	< L.D.	< L.D.	< L.D.	< L.D.	< L.D.	< L.D.	< L.D.	< L.D.	< L.D.	< L.D.	< L.D.
Sc	1.1	1.7	1	1.9	19	6.5	10.1	3.5	0.9	1.4	1.6	0.6	1.5
Sb	< L.D.	< L.D.	< L.D.	< L.D.	< L.D.	< L.D.	< L.D.	< L.D.	< L.D.	< L.D.	< L.D.	< L.D.	< L.D.
Se	< L.D.	< L.D.	< L.D.	< L.D.	< L.D.	< L.D.	< L.D.	< L.D.	< L.D.	< L.D.	< L.D.	< L.D.	< L.D.

Type	*Allanite-bearing PGD*							*Host*		
Outcrop	**13-TC-5072**									
Sample no.	**13-TC-5072-B1[1]**	**13-TC-5072-B91**	**13-TC-5072-B101**	**13-TC-5072-B111**	**13-TC-5072-B121**	**13-TC-5072-B81**	**13-TC-5072-B83**	**13-TC-5072-A101**	**13-TC-5072-A112**	**13-TC-5072-A7**
Facies	**Undifferentiated**	**Fine grained**	**Fine grained**	**Pegmatitic**	**Fine grained**	**Contact**	**Contact**	**Contact**	**Close to contact**	**Unaffected**
SiO_2 ***(wt. %)***	70.27	71.17	71.94	70.36	72.43	73.29	72.65	67.83	69.25	66.67
Al_2O_3	14.18	13.73	13.82	14.65	13.81	12.90	12.78	14.65	14.25	13.97
$Fe_2O_{3\ total}$	2.38	2.85	2.24	3.69	2.48	2.82	2.55	6.05	4.68	6.97
MgO	0.30	0.44	0.30	0.47	0.29	0.36	0.32	0.75	0.64	0.89
MnO	0.02	0.02	0.02	0.03	0.02	0.02	0.02	0.08	0.06	0.09
CaO	1.38	1.38	0.99	0.76	1.31	1.15	1.26	2.67	2.39	3.54
Na_2O	2.74	2.53	2.41	2.48	2.61	2.16	2.27	3.05	2.72	2.80
K_2O	5.90	6.06	6.74	7.26	5.93	6.26	5.97	3.42	4.91	3.55
TiO_2	0.34	0.42	0.34	0.56	0.38	0.43	0.41	0.75	0.59	0.88
P_2O_5	0.15	0.09	0.07	0.03	0.09	0.11	0.11	0.23	0.18	0.31
Cr_2O_3	< L.D.	< L.D.	< L.D.	< L.D.	< L.D.	< L.D.	< L.D.	< L.D.	< L.D.	< L.D.
LOI	0.73	1.08	0.78	0.53	0.92	0.84	0.93	0.62	0.47	0.37
Total	98.39	99.77	99.66	100.80	100.30	100.30	99.28	100.10	100.10	100.00
Na/Ca	3.59	3.32	4.41	5.91	3.61	3.40	3.26	2.07	2.06	1.43
Fe/Mg	4.01	3.27	3.77	3.96	4.32	3.96	4.02	4.07	3.69	3.95
ASI	1.18	1.16	1.14	1.16	1.17	1.15	1.14	1.35	1.21	1.24
A/CNK	1.23	1.21	1.18	1.19	1.22	1.19	1.19	1.47	1.31	1.39
A/NK	1.30	1.28	1.23	1.23	1.29	1.25	1.25	1.68	1.46	1.65
Sr ***(ppm)***	164	152	139	142	142	153	141	198	210	198
Ba	661	691	706	770	667	720	679	1201	1509	1275
Nb	7.5	6.7	5.7	11	5.9	5.6	6.7	12	13	13
V	7	< L.D.	< L.D.	7	< L.D.	6	7	35	32	45
Co	2	2	2	3	2	2	2	7	7	9
Ga	29	24	21	22	23	27	24	24	24	22
Ge	2.9	1.6	1.4	1.1	1.4	2	1.7	1.5	1.5	1.6
In	< L.D.	< L.D.	< L.D.	< L.D.	< L.D.	< L.D.	< L.D.	< L.D.	< L.D.	< L.D.
Sn	< L.D.	< L.D.	< L.D.	< L.D.	< L.D.	< L.D.	< L.D.	< L.D.	< L.D.	< L.D.
Cs	0.3	0.3	0.7	0.9	0.4	0.3	0.4	0.4	0.9	0.2
Pb	31	34	39	40	35	34	33	20	27	17
Be	< L.D.	1	1	1	1	< L.D.	< L.D.	2	4	2
Hf	7.4	16.5	3.5	0.5	1.6	4.3	2.3	11	9	11
Ta	0.1	0.2	0.2	0.5	0.2	0.2	0.2	0.7	1.0	1.1
W	1.4	< L.D.	< L.D.	< L.D.	< L.D.	< L.D.	< L.D.	< L.D.	< L.D.	< L.D.
Tl	1.0	0.7	0.8	0.9	0.7	0.6	0.6	0.5	0.7	0.4
Bi	< L.D.	< L.D.	< L.D.	< L.D.	< L.D.	< L.D.	< L.D.	< L.D.	< L.D.	< L.D.
Th	71	44	24	4.6	31	68	44	7.7	6.3	2.8
U	1.1	1.3	0.7	0.4	0.6	1.11	0.7	0.6	1.1	0.6
Rb	122	139	160	186	135	141	139	106	153	84
Y	16	14	11	5.3	11	17	13	54	50	55
Zr	290	616	134	13	60	174	91	422	330	434
Nb/Ta	68	45	25	23	39	37	45	16	13	12
Zr/Hf	39	37	38	26	38	40	40	38	37	39
Th/U	64	34	33	11	52	62	59	13	5.9	4.7
La	674	446	219	49	313	730	451	66	42	44
Ce	1160	811	407	84	572	1330	828	122	83	94
Pr	120	82	40	8.4	58	134	82	15	10	12
Nd	377	252	125	27	178	417	257	55	39	49
Sm	38	26	14	3.1	18.8	42.7	26.5	10	8.1	11

Eu	2.6	2.5	2.1	2.1	2.4	2.7	2.5	2.1	2.1	2.2
Gd	13	9.2	5.2	1.4	6.8	14	9.3	8.8	7.9	11
Tb	1.1	0.9	0.5	0.2	0.6	1.1	0.8	1.5	1.3	1.6
Dy	4.3	3.3	2.3	1.0	2.6	4.7	3.3	9.1	8.1	9.5
Ho	0.7	0.5	0.4	0.2	0.4	0.7	0.5	1.8	1.6	1.9
Er	1.5	1.4	0.9	0.5	1.0	1.8	1.1	5.2	4.9	5.4
Tm	0.2	0.2	0.1	0.1	0.1	0.2	0.1	0.8	0.7	0.8
Yb	0.7	1.1	0.7	0.5	0.6	0.9	0.6	5.3	4.9	5.4
Lu	0.1	0.2	0.1	0.1	0.1	0.1	0.1	0.8	0.8	0.9
ΣLREE	2369	1618	805	171	1139	2654	1645	268	181	210
ΣHREE	24	19	12	6.1	15	27	18	35	32	38
ΣREE	2393	1637	818	177	1154	2680	1663	303	213	249
Eu/Eu*[4]	0.4	0.5	0.8	3.0	0.6	0.3	0.5	0.7	0.8	0.6
La_N/Sm_N[4]	11	11	9.9	9.9	10	11	11	4.1	3.2	2.5
La_N/Yb_N[4]	619	278	207	71	373	533	511	8.4	5.9	5.5
Gd_N/Yb_N[4]	14	6.8	5.9	2.5	9.7	13	13	1.3	1.3	1.6
B	-	6	3	7	3	7	7	-	-	-
F	-	0.01	< L.D.	0.01	< L.D.	0.01	0.01	-	-	-
Li	-	< L.D.	< L.D.	< L.D.	< L.D.	< L.D.	< L.D.	-	-	-
Cd	< L.D.	< L.D.	< L.D.	< L.D.	< L.D.	< L.D.	< L.D.	< L.D.	< L.D.	< L.D.
Cu	2	12	6	8	10	8	41	20	11	16
Ag	< L.D.	1	< L.D.	< L.D.	< L.D.	< L.D.	< L.D.	< L.D.	< L.D.	< L.D.
Ni	< L.D.	3	2	3	2	2	2	6	7	8
Mo	5	5	3	< L.D.	< L.D.	11	5	< L.D.	1	1
Zn	46	39	39	82	36	44	40	107	95	109
S	< L.D.	< 100	< 100	< 100	< 100	< 100	100	600	400	600
Au *(ppb)*	< L.D.	< L.D.	< L.D.	< L.D.	< L.D.	< L.D.	< L.D.	< L.D.	< L.D.	< L.D.
As	3.3	< L.D.	< L.D.	< L.D.	< L.D.	< L.D.	< L.D.	< L.D.	1	< L.D.
Br	< L.D.	< L.D.	< L.D.	< L.D.	< L.D.	< L.D.	< L.D.	< L.D.	< L.D.	< L.D.
Ir	< L.D.	< L.D.	< L.D.	< L.D.	< L.D.	< L.D.	< L.D.	< L.D.	< L.D.	< L.D.
Sc	2.6	3	2.1	3.5	2.6	3.2	2.7	10.6	8.7	12.9
Sb	< L.D.	< L.D.	< L.D.	< L.D.	< L.D.	< L.D.	< L.D.	< L.D.	< L.D.	< L.D.
Se	< L.D.	< L.D.	< L.D.	< L.D.	< L.D.	< L.D.	< L.D.	< L.D.	< L.D.	< L.D.

Type	*Allanite-bearing PGD*				*Host*		
Outcrop	**13-FS-1202**						
Sample no.	**13-FS-1202 C1**[1]	**13-FS-1202-C7**	**13-FS-1202-C8**	**13-FS-1202-C91**	**13-FS-1202-A4**	**13-FS-1202-A6**	**13-FS-1202-A7**
Facies	**Intermediate**	**Coarse grained**	**Fine grained**	**Pegmatitic**	**Contact**	**Close to contact**	**Unaffected**
SiO_2 ***(wt. %)***	70.85	70.68	73.50	74.60	62.27	59.72	48.04
Al_2O_3	14.83	15.91	13.59	13.36	17.68	18.58	15.23
$Fe_2O_{3\ total}$	3.48	1.64	1.26	2.06	6.30	4.91	15.59
MgO	0.52	0.26	0.14	0.32	1.45	1.53	3.97
MnO	0.05	0.02	0.02	0.03	0.10	0.10	0.22
CaO	2.99	1.43	0.48	1.34	4.60	5.87	7.96
Na_2O	4.14	3.65	2.11	3.06	4.82	5.29	3.14
K_2O	1.33	5.86	7.90	4.60	1.84	1.25	2.12
TiO_2	0.43	0.15	0.09	0.21	0.75	0.77	2.85
P_2O_5	0.02	0.02	0.06	0.01	0.27	0.25	0.87
Cr_2O_3	< L.D.	< L.D.	< L.D.	< L.D.	0.01	0.01	< L.D.
LOI	1.01	0.61	0.42	0.57	0.71	0.69	0.41
Total	99.64	100.20	99.57	100.20	100.80	98.96	100.40
Na/Ca	2.51	4.62	7.96	4.13	1.90	1.63	0.71
Fe/Mg	3.38	3.19	4.55	3.25	2.19	1.62	1.98
ASI	1.35	1.17	1.10	1.19	1.28	1.23	1.12
A/CNK	1.54	1.22	1.11	1.26	1.47	1.46	1.37
A/NK	1.80	1.29	1.13	1.33	1.78	1.85	2.04
Sr ***(ppm)***	275	268	149	161	381	645	475
Ba	147	716	658	461	347	212	754
Nb	17	4.1	7.6	7.9	18	17	21
V	15	< L.D.	5	6	58	54	324
Co	3.0	1	1	2	7	7	36
Ga	53	23	19	23	27	23	25
Ge	7.4	1.1	1.4	1.6	1.4	1.3	1.6
In	< L.D.	< L.D.	< L.D.	< L.D.	0.1	0.1	0.2
Sn	2.0	< L.D.	< L.D.	< L.D.	2	2	2
Cs	1.0	1	0.7	0.9	2.1	0.5	0.3
Pb	17	43	49	35	18	15	9
Be	4.0	3	2	3	4	3	2
Hf	51	1.4	27.1	0.3	4.1	3.1	8.8
Ta	0.3	0.2	0.4	0.4	0.7	0.9	1.17
W	0.8	< L.D.	< L.D.	< L.D.	4.7	< L.D.	< L.D.
Tl	0.8	0.8	1.1	0.8	0.7	0.2	0.2
Bi	< L.D.	< L.D.	< L.D.	< L.D.	< L.D.	< L.D.	< L.D.
Th	392	3.2	23	58	4.9	1.23	1.67
U	6.9	0.2	1.9	1.2	0.4	0.5	0.8
Rb	58	170	219	147	121	34	35
Y	84	3	11	22	29	49	60
Zr	1760	41	849	9	131	104	343
Nb/Ta	58	20	17	20	27	19	18
Zr/Hf	35	29	31	30	32	34	39
Th/U	57	16	12	49	11	2.6	2.1
La	1870	18	97	294	47	30	41
Ce	3580	33	215	624	90	69	98
Pr	406	3.5	22	64	11	10	13
Nd	1400	12	72	208	40	42.3	57
Sm	179	1.8	11	29	7.7	10.0	13

Eu	4.7	1.2	1.3	1.6	1.4	2.4	3.1
Gd	73	1.0	4.8	13	6.0	9.2	12
Tb	6.8	0.1	0.5	1.2	0.9	1.5	1.8
Dy	25.7	0.6	2.2	5.3	5.0	8.6	11
Ho	3.6	0.1	0.4	0.8	0.9	1.6	2.1
Er	7.7	0.3	1.1	2.2	2.7	4.6	5.6
Tm	0.9	0.0	0.2	0.3	0.4	0.6	0.8
Yb	4.9	0.4	1.4	1.5	2.5	4.2	5.1
Lu	0.7	0.1	0.3	0.2	0.4	0.7	0.8
ΣLREE	7435	68	417	1218	196	161	223
ΣHREE	128	3.7	12	26	20	33	42
ΣREE	7563	72	429	1244	216	194	265
Eu/Eu*[4]	0.1	2.6	0.5	0.3	0.6	0.8	0.8
La_N/Sm_N[4]	6.5	6.2	5.8	6.4	3.8	1.9	2.0
La_N/Yb_N[4]	261	35	47	133	13	4.8	5.5
Gd_N/Yb_N[4]	12	2.4	2.8	6.8	1.9	1.8	1.9
B	-	8	5	11	-	-	-
F	-	< L.D.	< L.D.	< L.D.	-	-	-
Li	-	< L.D.	< L.D.	< L.D.	-	-	-
Cd	< L.D.	< L.D.	< L.D.	< L.D.	< L.D.	< L.D.	< L.D.
Cu	6	9	8	5	3	14	25
Ag	3.6	< L.D.	1.3	< L.D.	< L.D.	< L.D.	< L.D.
Ni	< L.D.	3	2	2	6	9	12
Mo	< L.D.	< L.D.	< L.D.	< L.D.	< L.D.	2	< L.D.
Zn	56	24	22	31	146	118	145
S	300	< L.D.	< L.D.	< L.D.	100	300	1600
Au *(ppb)*	< L.D.	< L.D.	< L.D.	< L.D.	< L.D.	< L.D.	< L.D.
As	< L.D.	< L.D.	< L.D.	< L.D.	< L.D.	< L.D.	< L.D.
Br	< L.D.	< L.D.	< L.D.	< L.D.	< L.D.	< L.D.	< L.D.
Ir	< L.D.	< L.D.	< L.D.	< L.D.	< L.D.	< L.D.	< L.D.
Sc	6.7	1.3	1.5	3	10	11.2	30.5
Sb	< L.D.	< L.D.	< L.D.	< L.D.	< L.D.	< L.D.	< L.D.
Se	< L.D.	< L.D.	< L.D.	< L.D.	< L.D.	< L.D.	< L.D.

Type	*Allanite-bearing PGD*								*Host*			
Outcrop	**13-AE-2149**											
Sample no.	**13-AE-2149 B[1]**	**13-AE-2149 B1[3]**	**13-AE-2149-B4[3]**	**13-AE-2149 B3[3]**	**13-AE-2149-B5[3]**	**13-AE-2149-B6[3]**	**13-AE-2149-B7[3]**	**13-AE-2149-B99[3]**	**13-AE-2149-A7**	**13-AE-2149-A41**	**13-AE-2149-A42**	**13-AE-2149-A5**
Facies	**REE-richest**	**Fine grained core**	**Fine grained core**	**Pegmatitic contact**	**Pegmatitic contact**	**Pegmatitic facies close to contact**	**Fine grained discordant vein**	**Fine grained discordant vein**	**Contact**	**Host with fine leucosome - Grt-rich**	**Host with fine leucosome - no Grt**	**Unaffected**
SiO_2 ***(wt. %)***	55.84	75.07	74.15	72.49	71.63	71.26	74.25	75.50	68.68	70.84	71.09	68.26
Al_2O_3	15.05	13.72	14.02	14.04	14.66	14.26	13.92	13.02	14.78	13.59	13.68	14.53
$Fe_2O_{3\ total}$	12.42	0.77	0.89	0.69	2.99	2.34	1.38	1.24	4.52	2.76	2.77	5.26
MgO	0.85	0.10	0.07	0.05	0.17	0.14	0.10	0.07	0.36	0.21	0.21	0.51
MnO	0.22	0.01	0.01	0.01	0.04	0.04	0.02	0.03	0.06	0.04	0.04	0.07
CaO	5.54	1.56	0.86	0.59	2.57	1.15	1.35	0.70	2.39	1.65	1.65	3.00
Na_2O	4.28	3.66	3.07	2.68	4.30	3.04	3.48	3.28	3.67	2.70	2.73	3.37
K_2O	1.93	3.60	6.59	7.47	3.44	7.13	5.05	5.70	4.56	5.80	5.85	4.21
TiO_2	0.63	0.05	0.05	0.04	0.13	0.09	0.12	0.01	0.44	0.24	0.24	0.60
P_2O_5	0.22	0.00	0.00	0.00	0.08	0.00	0.00	0.00	0.16	0.06	0.05	0.20
Cr_2O_3	< L.D.	0.01	< L.D.	< L.D.	< L.D.	< L.D.	< L.D.	< L.D.	< L.D.	< L.D.	< L.D.	< L.D.
LOI	0.83	0.38	0.60	0.35	0.36	0.44	0.39	0.45	0.40	0.66	0.65	0.29
Total	97.80	98.94	100.30	98.40	100.40	99.90	100.10	100.00	100.00	98.55	98.97	100.30
Na/Ca	1.40	4.25	6.46	8.22	3.03	4.78	4.66	8.48	2.78	2.96	2.99	2.03
Fe/Mg	7.38	3.89	6.42	6.97	8.88	8.44	6.97	8.95	6.34	6.64	6.66	5.21
ASI	1.08	1.21	1.08	1.08	1.12	1.04	1.12	1.07	1.14	1.12	1.12	1.15
A/CNK	1.29	1.29	1.11	1.10	1.23	1.08	1.18	1.10	1.23	1.18	1.18	1.27
A/NK	1.65	1.38	1.15	1.12	1.36	1.12	1.24	1.13	1.35	1.27	1.26	1.44
Sr ***(ppm)***	147	107	133	118	105	102	131	13	130	141	143	174
Ba	181	289	560	603	270	528	503	38	933	972	977	1214
Nb	132	10	7.8	8.5	25	20	15	41	31	46	45	14
V	38	5	< L.D.	< L.D.	< L.D.	< L.D.	< L.D.	< L.D.	17	6	7	24
Co	6	< L.D.	< L.D.	< L.D.	1	1	< L.D.	< L.D.	3	2	2	5
Ga	79	26	26	23	28	25	27	33	24	25	24	22
Ge	9.7	1.9	1.3	2.2	1.7	1.7	1.7	2.2	1.5	1.6	1.6	1.5
In	0.2	< L.D.	< L.D.	< L.D.	0.2	0.1	< L.D.	< L.D.	0.2	0.2	0.2	< 0.1
Sn	4	< L.D.	< L.D.	< L.D.	< L.D.	< L.D.	< L.D.	< L.D.	< 1	< 1	< 1	< 1
Cs	0.7	0.4	0.5	0.8	0.3	0.6	0.5	1.9	0.7	0.4	0.4	0.5
Pb	41	25	40	36	29	41	32	93	30	29	28	22
Be	9.0	5.0	3.0	2.0	5.0	3.0	4.0	10	5	3	3	3
Hf	171	0.6	5.6	2.0	3.0	1.0	2.7	1.7	7.7	13	13	12
Ta	3.2	0.3	0.4	0.3	0.6	0.6	0.6	2.2	1.6	1.8	1.9	0.8
W	3	1.3	< 0.5	0.8	< L.D.	< L.D.	< L.D.	< L.D.	< L.D.	< L.D.	< L.D.	< L.D.
Tl	0.3	1.0	0.8	1.4	0.4	1.0	0.6	1.7	0.7	0.7	0.7	0.5
Bi	< L.D.	< L.D.	< L.D.	< L.D.	< L.D.	< L.D.	< L.D.	< L.D.	< L.D.	< L.D.	< L.D.	< L.D.
Th	766	1.9	6.38	2	20	2	3	15	2.5	23	23	6.2
U	30	0.7	2.2	1.1	0.9	0.5	1.7	6.3	0.8	2.7	2.6	1.4
Rb	42	98	197	196	96	221	147	403	149	145	141	103
Y	544	7.9	5.7	7	82	55	11	35	67	94	93	50
Zr	6340	12	139	44	81	19	54	24	287	373	369	455
Nb/Ta	41	36	22	31	42	35	24	18	20	26	24	17
Zr/Hf	37	20	25	22	27	19	20	14	37	30	29	38
Th/U	25	2.8	2.8	1.7	22	2.9	2.0	2.4	3.1	8.5	8.6	4.6
La	2150	6.3	14	5.7	54	8.2	8.3	4.5	27	113	116	48
Ce	4130	11	25	8.8	117	21	16	11	61	229	234	99
Pr	470	1.3	2.7	1.0	14	3.3	1.8	1.5	8.2	26	26.7	12
Nd	1710	5.0	9.0	3.8	58	16	6.7	7.1	35	94	96.2	47
Sm	297	1.2	1.5	1.1	15	6.7	1.6	3.5	9.6	18	19.4	10.0
Eu	9.4	1.2	1.4	1.3	1.7	1.4	1.4	0.3	1.7	2.6	2.55	2.1
Gd	180	1.2	1.1	1.0	14	8.6	1.7	4.9	10	16	16.4	8.7

Tb	25	0.2	0.2	0.2	2.4	1.6	0.3	1.1	1.8	2.7	2.73	1.4
Dy	123	1.4	1.1	1.2	15	10	2.0	7.3	11.3	17	16.8	8.5
Ho	22	0.3	0.2	0.3	2.9	2.0	0.4	1.4	2.2	3.3	3.36	1.7
Er	59	0.9	0.7	0.8	8.0	5.7	1.2	4.0	6.4	10.0	10.1	4.9
Tm	8.3	0.1	0.1	0.1	1.2	0.8	0.2	0.6	0.9	1.5	1.5	0.7
Yb	52	0.9	0.9	0.8	7.5	5.4	1.4	3.7	6.0	10	10.7	4.9
Lu	7.2	0.1	0.2	0.1	1.1	0.8	0.2	0.5	0.9	1.7	1.71	0.8
ΣLREE	8757	25	52	20	258	55	34	27	140	481	492	217
ΣHREE	485	6.3	5.9	5.8	53	36	8.8	24	42	65	66	33
ΣREE	9242	31	57	26	311	91	43	51	182	545	558	250
Eu/Eu*[4]	0.1	3.1	3.3	3.7	0.4	0.6	2.7	0.3	0.5	0.5	0.4	0.7
La_N/Sm_N[4]	4.5	3.3	5.5	3.2	2.3	0.8	3.3	0.8	1.8	3.8	3.7	3.0
La_N/Yb_N[4]	28	4.9	10	4.9	4.9	1.0	4.2	0.8	3.1	7.4	7.4	6.8
Gd_N/Yb_N[4]	2.8	1.1	1.0	1.1	1.5	1.3	1.0	1.1	1.4	1.2	1.2	1.4
B	-	-	4	-	4	2	< L.D.	4	-	-	-	-
F	-	-	< L.D.	-	< L.D.	< L.D.	< L.D.	< L.D.	-	-	-	-
Li	-	-	< L.D.	-	< L.D.	< L.D.	< L.D.	< L.D.	-	-	-	-
Cd	< L.D.	< L.D.	< L.D.	< L.D.	< L.D.	< L.D.	< L.D.	< L.D.	< L.D.	< L.D.	< L.D.	0.6
Cu	16	3	5	2	8	3	16	10	31	11	11	18
Ag		< L.D.	0.4	< L.D.	< L.D.	< L.D.	< L.D.	< L.D.	0.4	0.8	0.8	< L.D.
Ni	3	2	2	< L.D.	2	2	2	2	3	3	3	3
Mo	6	< L.D.	< L.D.	< L.D.	1	< L.D.	< L.D.	1	2	4	5	3
Zn	288	20	24	15	78	45	30	58	124	104	106	111
S	600	100	< L.D.	< L.D.	< L.D.	< L.D.	< L.D.	500	300	400	400	300
Au *(ppb)*	< L.D.	< L.D.	< L.D.	< L.D.	< L.D.	< L.D.	< L.D.	< L.D.	< L.D.	< L.D.	< L.D.	< L.D.
As	< L.D.	< L.D.	< L.D.	2.2	< L.D.	1.3	< L.D.	< L.D.	< L.D.	< L.D.	< L.D.	< L.D.
Br	< L.D.	< L.D.	< L.D.	< L.D.	< L.D.	< L.D.	< L.D.	< L.D.	< L.D.	< L.D.	< L.D.	< L.D.
Ir	< L.D.	< L.D.	< L.D.	< L.D.	< L.D.	< L.D.	< L.D.	< L.D.	< L.D.	< L.D.	< L.D.	< L.D.
Sc	32	0.9	0.2	1.1	16	8.5	1.2	2.5	7.4	4.3	4.4	8.5
Sb	< L.D.	0.2	< L.D.	< L.D.	< L.D.	< L.D.	< L.D.	< L.D.	< L.D.	< L.D.	0.1	< L.D.
Se	< L.D.	< L.D.	< L.D.	< L.D.	< L.D.	< L.D.	< L.D.	< L.D.	< L.D.	< L.D.	< L.D.	< L.D.

[1]: Data from Turlin et al. (2017).

[2]: Data from chapter 4.

[3]: Data from chapter 5.

[4]: Normalization to the chondrite after McDonough and Sun (1995)

References

Bea, F., 1996. Residence of REE, Y, Th and U in granites and crustal protoliths; Implications for the chemistry of crustal melts. J. Petrology 37, 521–552. doi:10.1093/petrology/37.3.521

Berger, A., Rosenberg, C., Schaltegger, U., 2009. Stability and isotopic dating of monazite and allanite in partially molten rocks: examples from the Central Alps. Swiss J. Geosci. 102, 15–29. doi:10.1007/s00015-009-1310-8

Broska, I., Petrík, I., Williams, C.T., 2000. Coexisting monazite and allanite in peraluminous granitoids of the Tribeč Mountains, Western Carpathians. American Mineralogist 85, 22–32. doi:10.2138/am-2000-0104

Budzyń, B., Harlov, D.E., Williams, M.L., Jercinovic, M.J., 2011. Experimental determination of stability relations between monazite, fluorapatite, allanite, and REE-epidote as a function of pressure, temperature, and fluid composition. American Mineralogist 96, 1547–1567. doi:10.2138/am.2011.3741

Finger, F., Broska, I., Roberts, M.P., Schermaier, A., 1998. Replacement of primary monazite by apatite-allanite-epidote coronas in an amphibolite facies granite gneiss from the eastern Alps. American Mineralogist 83, 248–258. doi:10.2138/am-1998-3-408

Frost, B.R., Barnes, C.G., Collins, W.J., Arculus, R.J., Ellis, D.J., Frost, C.D., 2001. A geochemical classification for granitic rocks. J. Petrology 42, 2033–2048.

Gieré, R., Sorensen, S.S., 2004. Allanite and other REE-rich epidote-group minerals. Reviews in Mineralogy and Geochemistry 56, 431–493. doi:10.2138/gsrmg.56.1.431

Janots, E., Brunet, F., Goffé, B., Poinssot, C., Burchard, M., Cemič, L., 2007. Thermochemistry of monazite-(La) and dissakisite-(La): implications for monazite and allanite stability in metapelites. Contrib Mineral Petrol 154, 1–14. doi:10.1007/s00410-006-0176-2

Krenn, E., Finger, F., 2007. Formation of monazite and rhabdophane at the expense of allanite during Alpine low temperature retrogression of metapelitic basement rocks from Crete, Greece: Microprobe data and geochronological implications. Lithos, The Role of Accessory Minerals in Rocks: Petrogenetic Indicators of Metamorphic and Igneous Processes 95, 130–147. doi:10.1016/j.lithos.2006.07.007

Lentz, D., 1996. U, Mo, and REE mineralization in late-tectonic granitic pegmatites, southwestern Grenville Province, Canada. Ore Geology Reviews 11, 197–227. doi:10.1016/0169-1368(95)00034-8

Lentz, D.R., 1991. Petrogenesis of uranium-, thorium-, molybdenum-, and rare earth element-bearing pegmatites, skarns, and veins in the central metasedimentary belt of the Grenville Province, Ontario and Quebec. (Unpublished Ph.D. thesis). University of Ottawa (Canada).

Linnen, R.L., Cuney, M., 2005. Granite-related rare-element deposits and experimental constraints on Ta-Nb-W-Sn-Zr-Hf mineralization. Short Course Notes - Geological Association of Canada 17, 45–68.

McDonough, W.F., Sun, S. -s., 1995. The composition of the Earth. Chemical Geology, Chemical Evolution of the Mantle 120, 223–253. doi:10.1016/0009-2541(94)00140-4

Montel, J.-M., 1986. Experimental determination of the solubility of Ce-monazite in SiO2-Al2O3-K2O-Na2O melts at 800 °C, 2 kbar, under H2O-saturated conditions. Geology 14, 659–662. doi:10.1130/0091-7613(1986)14<659:EDOTSO>2.0.CO;2

Moukhsil, A., Solgadi, F., Belkacim, S., Elbasbas, A., Augland, L.E., 2014. Géologie de la région du lac Okaopéo, Côte-Nord. Ministère de l'Energie et des Ressources Naturelles, Québec, RG 2014-03, 34 p.

Rapp, R.P., Watson, E.B., 1986. Monazite solubility and dissolution kinetics: implications for the thorium and light rare earth chemistry of felsic magmas. Contr. Mineral. and Petrol. 94, 304–316. doi:10.1007/BF00371439

Schmidt, M.W., Thompson, A.B., 1996. Epidote in calc-alkaline magmas: An experimental study of stability, phase relationships, and the role of epidote in magmatic evolution. American Mineralogist 81, 462–474. doi:10.2138/am-1996-3-420

Shand, S.J., 1943. The eruptive rocks, 2nd edition. ed. New York: John Wiley.

Turlin, F., André-Mayer, A.-S., Moukhsil, A., Vanderhaeghe, O., Gervais, F., Solgadi, F., Groulier, P.-A., Poujol, M., 2017. Unusual LREE-rich, peraluminous, monazite- or allanite-bearing pegmatitic granite in the central Grenville Province, Québec. Ore Geology Reviews 89, 627–667. doi:10.1016/j.oregeorev.2017.04.019

Turlin, F., Deruy, C., Eglinger, A., Vanderhaeghe, O., André-Mayer, A.-S., Poujol, M., Moukhsil, A., Solgadi, F., submitted. A record of 70 Ma suprasolidus conditions in the Grenville large, hot and long-duration orogen. Terra Nova.

Wang, J.-M., Wu, F.-Y., Rubatto, D., Liu, S.-R., Zhang, J.-J., Liu, X.-C., Yang, L., 2017. Monazite behaviour during isothermal decompression in pelitic granulites: a case study from Dinggye, Tibetan Himalaya. Contrib Mineral Petrol 172, 81. doi:10.1007/s00410-017-1400-y

Wing, B.A., Ferry, J.M., Harrison, T.M., 2003. Prograde destruction and formation of monazite and allanite during contact and regional metamorphism of pelites: petrology and geochronology. Contrib Mineral Petrol 145, 228–250. doi:10.1007/s00410-003-0446-1

GENERAL CONCLUSIONS

This thesis focused on REE-rich pegmatitic granite dykes ("PGD") hosted in the Allochthonous Belt of the central Grenville Province (Figs. 7-1 and 7-2). This work coupled field work (Turlin et al., 2017, submitted, chapters 3 to 5), geochronology of REE-rich pegmatitic granite dykes ("PGD") (Turlin et al., 2017, chapters 3 and 5) and of their metasedimentary hosts (Turlin et al., submitted), isotopy of zircon from the PGD (chapters 3 and 5), and petrogeochemisty of the PGD (chapters 4-5) and of their potential metasedimentary source (chapter 4). These results allow (i) to integrate these new REE occurrences in the framework of the Grenvillian Orogeny and more specifically to constrain the favorable geodynamic context of their genesis, (ii) to decipher the crustal residence of the REE prior to their high-grade concentration within the PGD, (iii) to constrain the respective roles of partial melting and fractional crystallization on the genesis of these occurrences, and (iv) to discuss their metallogenic cycle within a model of the Grenvillian crustal evolution.

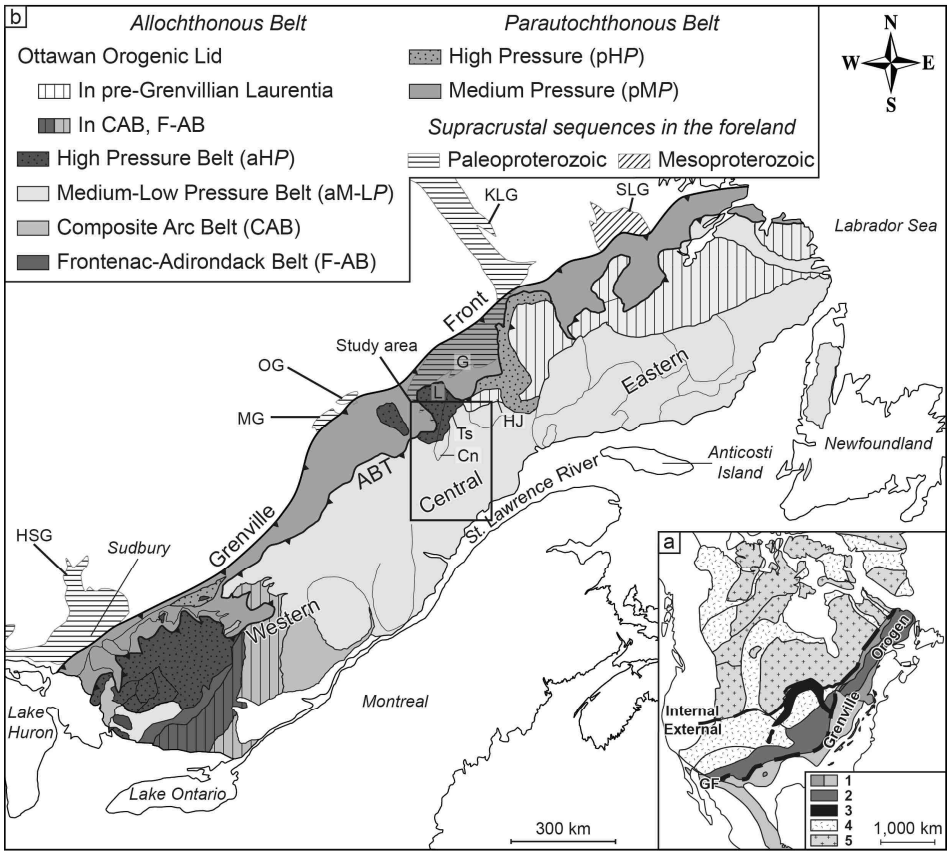

Figure 7-1: a: Map of Proterozoic Laurentia showing the different north-American orogens with Paleozoic and younger cover omitted (modified from Hoffman, 1989; Rivers et al., 2012). The northern dashed line represents the boundary between Internal and External Paleoproterozoic Laurentia and the southern dashed line represents the Grenville Front (GF); b: Simplified geological map of the Grenville Province. Extension of supracrustal sequences in the foreland after Rivers (2008). Abbreviations: 1 = exposed Grenville Province, light grey represents the inferred extension of subsurface allochthonous Grenville Province; 2 = Granite-Rhyolite Igneous Province, ca. 1.50-1.34 Ga and reworked equivalents in the Grenville Province; 3 = Mid-Continental Rift system; 4 = Paleoproterozoic orogens, ca. 1.9-1.8 Ga, ca. 1.65 Ga and reworked equivalents in the Grenville Province; 5 = cratons; Cn = Canyon domain; G = Gagnon Terrane; GF = Grenville Front; HJ = Hart-Jaune terrane; HSG = Huron Supergroup; KLG = Knob Lake Group; L = Lelukuau terrane; MG = Mistassini Group; OG = Otish Group; SLG = Seal Lake Group; Ts = Tshenukutish terrane.

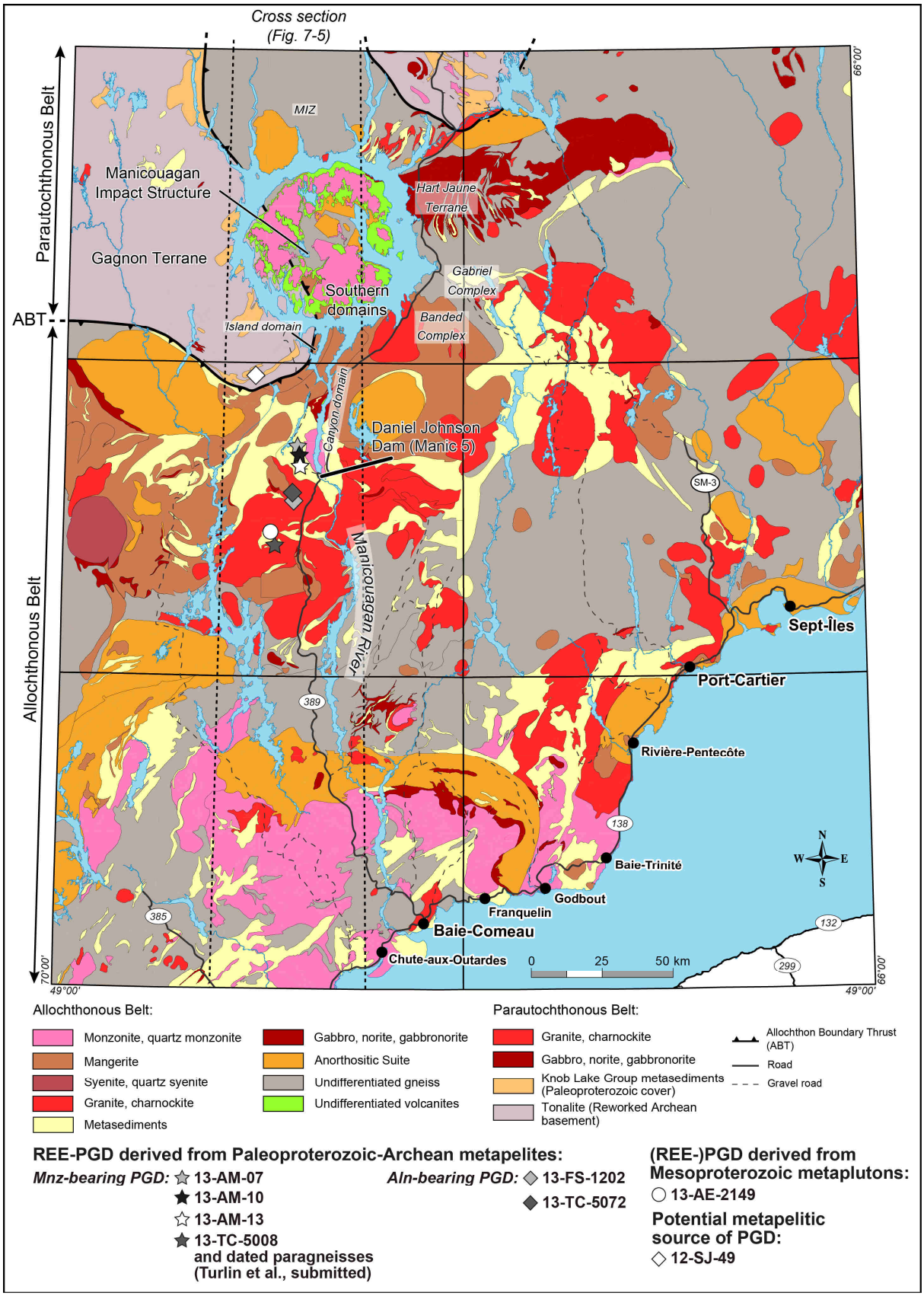

Figure 7-2: Geological map of the central Grenville (Quebec) showing the position of the outcrops investigated during this thesis: pegmatitic granite dykes, dated allochthonous migmatitic paragneisses, and potential Paleoproterozoic metapelitic source (modified after Moukhsil et al., 2014; Turlin et al., 2017). Abbreviations: ABT = Allochthon Boundary Thrust; Aln-bearing PGD = allanite-bearing pegmatitic granite dyke; MIZ = Manicouagan Imbricate Zone; Mnz-bearing PGD = monazite-bearing pegmatitic granite dyke.

1. Evolution of the orogenic crust

1.1. Geodynamic framework

The Grenvillian Orogeny is commonly referred to the succession of two tectonic phases (Fig. 7-3). The earlier Ottawan orogenic phase (ca. 1090-1020 Ma, Fig. 7-3a-b) of the Grenvillian Orogeny corresponds to crustal thickening in the Allochthonous Belt associated with the development of an orogenic plateau overlying ductile mid-crustal allochthonous crust above the ABT (Rivers, 2008; Rivers et al., 2012). In the central Grenville Province, it is recorded as contrasting peaks of metamorphism at ca. 1070-1050 Ma according to the distance from the ABT. Paleoproterozoic and Mesoproterozoic rocks of the Manicouagan Imbricate Zone (MIZ) of the high pressure Allochthonous Belt (aH*P*, Figs. 7-1b and 7-3), close to the ABT, record kyanite-grade conditions as a steep *P-T* path and a peak of metamorphism at ca. 1450-1600 MPa and 860-900 °C (Indares et al., 1998; Indares and Dunning, 2001; Lasalle and Indares, 2014; Rivers et al., 2002). The medium to low pressure Allochthonous Belt (aM-L*P*, Figs. 7-1b and 7-3) south of the Manicouagan Reservoir records sillimanite-grade conditions with a moderate-gradient *P-T* path and a peak of metamorphism at ca. 950 MPa and 850 °C (Dunning and Indares, 2010; Lasalle et al., 2014; Lasalle and Indares, 2014). These contrasting *P-T* paths recorded in the Allochthonous Belt have been attributed to syn-Ottawan channel flow of the ductile crust underneath an orogenic plateau that was active until ca. 1050 Ma (Fig. 7-3a, e.g. Rivers, 2008). The subsequent late- to post-Ottawan (ca. 1050-1020 Ma) collapse of the plateau (Fig. 7-3b) resulted in the reworking of the northwest-directed ABT as a top-to-the-southeast normal-sense shear zone (Allochthon Boundary Detachment, ABD) and in a material extrusion recorded in the central Grenville by the Tshenukutish shear zone that was active until ca. 1020 Ma (Hynes et al., 2000; Indares et al., 2000; Rivers et al., 2002). This extensional setting led to the formation of a crustal-scale horst and graben architecture, the latter being occupied by the Orogenic Lid and the former by the aM-L*P* crustal segments (Fig. 7-3b).

The younger Rigolet orogenic phase (ca. 1005-960 Ma) of the Grenvillian Orogeny corresponds to a crustal thickening in the Parautochthonous Belt (Fig. 7-3c, e.g. Rivers et al., 2012). It is recorded in the central Grenville by an up to granulite-facies high-grade peak of metamorphism recorded in metapelites from the Knob Lake Group of the medium pressure segment (pM*P*, Figs. 7-1b and 7-3c) at ca. 1250-1500 MPa and ca. 815-850 °C (Hynes et al., 2000; Jannin et al., accepted; Jordan et al., 2006; Rivers, 2009; Rivers et al., 2012; van Gool et al., 2008). The partial melting of these Paleoproterozoic metapelites was initiated as early as ca. 1002 Ma and was associated with the dehydration melting of muscovite (Ms + Qtz + Pl →

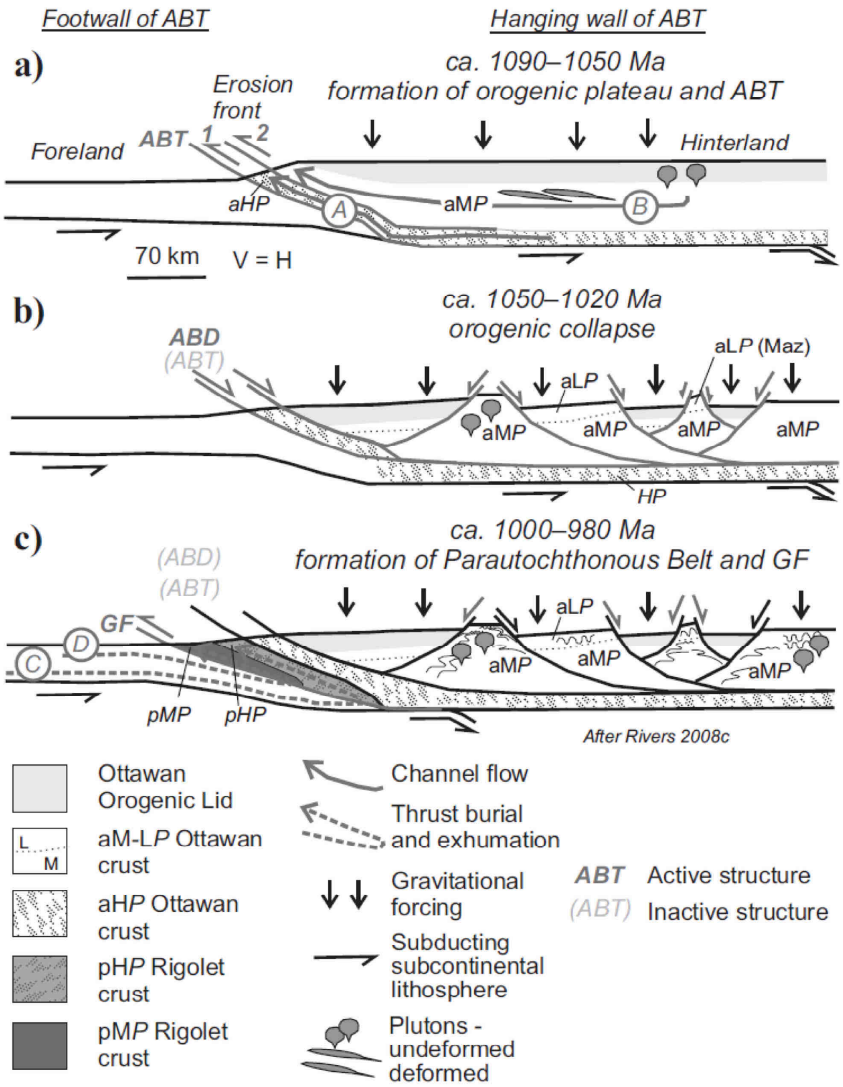

Figure 7-3: Schematic cross-sections across the Grenville Province illustrating its tectonic evolution during the Grenvillian Orogeny (from Rivers et al., 2012). a: formation and exhumation of the allochthonous high-pressure as a hot nappe (path A) and medium- to low-pressure segments by some form of channel flow (path B), both above the ABT and below an orogenic plateau between ca. 1090-1050 Ma; b: ABT reworked as a detachment (ABD) ending the channel flow in response to the ca. 1050-1020 Ma orogenic collapse; c: formation of the Grenville Front and high-grade metamorphism in the lower- (path C) and mid-crust (path D) Parautochthonous Belt. Abbreviations: ABT/ABD = Allochthonous Boundary Thrust/Detachment; aH*P* = allochthonous high-pressure segments; aM-L*P* = allochthonous mid- to low-pressure segments; GF = Grenville Front; pH*P* = parautochthonous high-pressure segments; pM*P* = parautochthonous mid-pressure segments.

Kfs + Al_2SiO_5 + Liq.), and followed by the subsequent dehydration melting of biotite (Bt + Al_2SiO_5 + Qtz → Kfs + Grt + Liq.), both in the kyanite stability field (Jannin et al., accepted). The subsequent retrograde *P-T* path is recorded in the sillimanite stability field and most probably lasted until ca. 961 Ma (Jannin et al., accepted; Jordan et al., 2006). Accordingly, the Rigolet orogenic phase is attributed to the foreland-ward propagation of Grenvillian high-grade metamorphism and thrusting towards the Grenville Front (Figs. 7-1 and 7-3c), a syn-Rigolet orogen-scale southeast-dipping shear zone (Krogh, 1994; Rivers et al., 1989; Rivers, 2008, 2009).

1.2. A continuity between the Ottawan and Rigolet orogenic phases?

The PGD investigated in this thesis (Fig. 7-2) intruded their metasedimentary or metaplutonic hosts in the aM-L*P* segment of the central Grenville Province coeval with the initiation of the Rigolet tectonic phase at ca. 1005-1000 Ma (U-Pb on monazite and zircon, Turlin et al., 2017, chapter 3) under close to wet-solidus thermal conditions, i.e. ca. 650-700 °C (Turlin et al., submitted). The PGD contain zircon grains with no textural/chemical/isotopic inheritance that point to their formation in equilibrium with the magmas at temperatures ranging between 640 and 721 °C (Ti-in-zircon thermometry, chapter 3) consistent with the lack of evidence for contact metamorphism and thermal exchange between the 13-TC-5008 PGD and its metasedimentary host. The U-Pb dating of monazite and apatite from a leucosome of migmatitic paragneisses from the Plus-Value Complex, that host the 13-TC-5008 PGD, was coupled with (i) calculated apatite isotopic closure temperatures, (ii) geochronological data from literature reported for similar series of the same area, and (iii) with field relationships between the paragneisses and the PGD. These data allowed to reappraise the thermal evolution of the aM-L*P* crustal segment of the central Grenville Province (Fig. 7-4, Turlin et al., submitted). The first episode of prograde monazite growth in the leucosomes of the Plus-Value Complex migmatitic paragneisses between ca. 1080-1070 Ma under suprasolidus conditions is constrained from ca. 700 °C up to the peak temperature of the Ottawan metamorphism at ca. 850 °C (Fig. 7-4, Lasalle et al., 2014; Turlin et al., submitted). The subsequent retrograde *P-T* path is recorded under suprasolidus conditions down to the intrusion of the 13-TC-5008 PGD at ca. 1005 Ma and ca. 700-650 °C, and under subsolidus conditions down to ca. 970-950 Ma and ca. 500-450 °C (Fig. 7-4, Turlin et al., submitted). This interpretation is strengthened by the ca. 1005 Ma emplacement age of the 13-AE-2149 shallow-dipping PGD that was derived by partial melting of surrounding allochthonous plutonic units, as indicated by chondritic to sub-chondritic zircon $\varepsilon Hf_{(1005\ Ma)}$ signatures ranging between -6.2 (single value) and 1.0 and associated $T_{DM2\ (1005\ Ma)}$ Hf model ages ranging between ca. 1.75 and 1.97 Ga (chapter 5). The retrograde *P-T* path is associated with constant and slow cooling of this crustal segment at a rate of 2 to 6 °C/Ma (Fig. 7-4, Turlin et al., submitted). Accordingly, the aM-L*P* segment of the central Grenville Province recorded at least ca. 70 Ma of suprasolidus conditions and at least ca. 110 Ma of up to 450-500 °C thermal conditions. Such protracted suprasolidus conditions with constant cooling rates from the Ottawan peak of metamorphism at ca. 1070-1050 Ma down to ca. 960 Ma might represent a longer duration of the Ottawan channel flow in the central Grenville Province, inferred to have stopped at ca. 1050 Ma (Figs. 7-3a-b, e.g. Rivers, 2008).

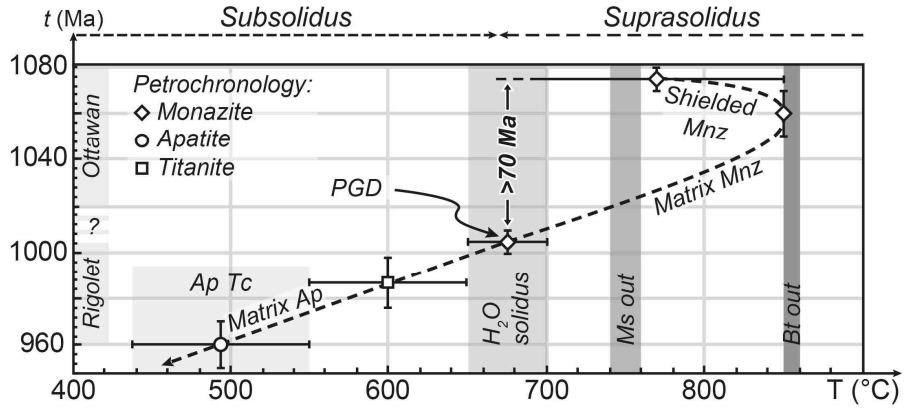

Figure 7-4: Time vs temperature diagram of aluminous gneisses from mid-pressure crustal segment of the central Grenville considered in this study. It was constructed using the geochronological data and thermometric constraints from this study and those reported by Dunning and Indares (2010), Indares and Dunning (2004), Lasalle and Indares (2014) and Lasalle et al. (2014). Temperatures of partial melting reactions are from Lasalle and Indares (2014). The suprasolidus prograde *T-t* path is recorded by shielded monazite in peritectic garnet and K-feldspar up to a temperature of ca. 850°C characterized by the biotite breakdown and indicated by the biotite-K-feldspar symplectite. The suprasolidus retrograde *T-t* path is recorded by monazite from the matrix and down to ca. 1005 Ma as indicated by the intrusion of a pegmatitic granite dyke into paragneisses which lobate contact with no evidence of contact metamorphism nor thermal exchange with the host provide evidence for the close to wet-solidus temperature of the host. The retrograde *T-t* path is recorded by titanite from the same segment and dated between ca. 1000 and 975 Ma, and by apatite from the matrix of the investigated leucosome dated at ca. 960±10 Ma with isotopic closure temperatures of ca. 440-550°C. Abbreviations: Ap = apatite; Bt = biotite; Mnz = monazite; Ms = muscovite; PGD = pegmatitic granite dyke; Tc = isotopic closure temperature.

All PGD have magmatic textures with no solid-state deformation and a peraluminous character (Turlin et al., 2017, chapters 3-4). The PGD that show steep-dipping discordant contacts lack evidence of in-situ collect of melt from their hosts (Turlin et al., 2017). Their pristine zircon grains yield supra-mantellic $\delta^{18}O_{V\text{-}SMOW}$ signatures, sub-chondritic $\varepsilon Hf_{(1003\ Ma)}$ signatures between -4.7 and -11.8, corresponding to $T_{DM2\ (1003\ Ma)}$ Hf model ages ranging between ca. 2.05 and 2.44 Ga (chapter 3). These features provide evidence that these PGD derived from partial melting of a Paleoproterozoic-Archean metapelitic source. The source is attributed to represent an extension of the Knob Lake Group metapelites of the Parautochthonous Belt (Figs. 7-1b and 7-2) below the Allochthonous Belt intruded by the PGD (chapter 3) on the basis of (i) their fertile character, the (ii) protracted high temperature partial melting coeval with the crystallization of the PGD, and (iii) the K and Rb signatures of feldspar and biotite from their leucosomes that spread on a similar fractionation trend as those from the PGD (chapter 4). Accordingly, results from this thesis provide evidence for partial melting of the Parautochthonous Belt below the Allochthonous Belt (Fig. 7-5) initiated before ca. 1005 Ma to allow for the rise of the magma and the crystallization of pegmatitic granite dykes within their allochthonous hosts at that time. These conclusions are consistent with the protracted and high-temperature partial melting of the Knob Lake Group metapelites demonstrated by Jannin et al. (accepted) that was initiated as early as ca. 1002 Ma in the outcropping areas of the Parautochthonous Belt further north (Fig. 7-2).

Results presented in this thesis provide evidence for long-lived partially molten mid to lower crustal segments during the whole continent-continent collision that is the Grenvillian Orogeny. This partial melting developed from the early-Ottawan crustal thickening of the Allochthonous Belt within the aM-L*P* and aH*P* crustal segments between the ABT and an orogenic plateau. Material extrusion was associated with some form of channel flow inferred to have stopped by ca. 1050 Ma (e.g. Rivers, 2008). Even though no data from this thesis allow the documentation of younger material extrusion, they demonstrate the partially molten character of the crustal segments potentially involved in the Ottawan channel flow as late as ca. 1005 Ma, i.e. until the initiation of the Rigolet orogenic phase (Fig. 7-5). The latter is associated with the partial melting of the Parautochthonous Belt below the ABT (Fig. 7-5). The constant and slow cooling of the aM-L*P* segment of the central Grenville Province that followed the Ottawan peak of metamorphism under suprasolidus conditions until ca. 1005 Ma (Fig. 7-4) and the partial melting of the underlying Parautochthonous Belt as early as ca. 1005 Ma (Fig. 7-5) are consistent with the conclusions of Rivers (2008) who proposed that the Ottawan and Rigolet orogenic phases represent a single prolonged collision.

1.3. REE-rich PGD as tracers of crustal growth and differentiation processes

By focusing on REE-rich PGD from the Grenville Province, this thesis allowed: (i) to reappraise the thermal evolution of the crustal segment they intrude, (ii) to demonstrate the partially molten character of deeper crustal levels, (iii) to give insights on the geodynamic processes responsible for the transition between the Ottawan and Rigolet orogenic phases, and (iv) to contribute to the proposition of Rivers (2008) that the Grenvillian Orogeny corresponds to a single prolonged continental collision. Accordingly, taken together, the results of this thesis provide evidence that the magmas responsible for the genesis of the REE-rich PGD are associated with the syn-collisional widespread partial melting of mid to low crustal segments.

Figure 7-5: Schematic cross section of the central Grenville Province at ca. 1005-1000 Ma that corresponds to the timing of intrusion of the REE-rich pegmatitic granite dykes into the Allochthonous Belt. The partially molten crustal levels involved in their genesis is reported and encompasses variable proportions of the Allochthonous and Parautochthonous Belts. Abbreviations: A.B.T. = Allochthonous Boundary Thrust; PGD = pegmatitic granite dyke.

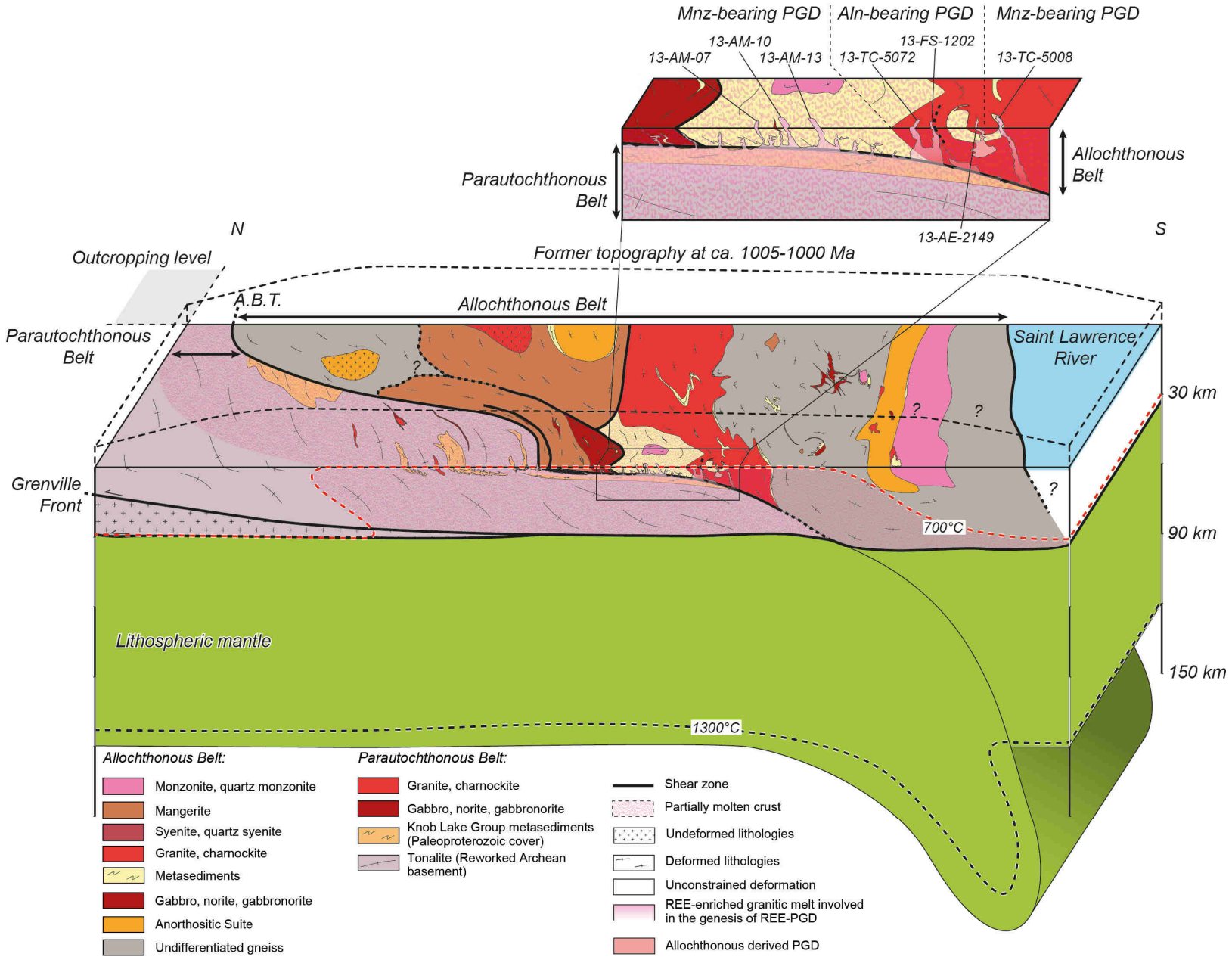
Mnz-bearing PGD
Aln-bearing PGD
Mnz-bearing PGD
13-AM-07
13-AM-10
13-AM-13
13-TC-5072
13-FS-1202
13-TC-5008
Allochthonous Belt
Parautochthonous Belt
13-AE-2149
N
S
Outcropping level
Former topography at ca. 1005-1000 Ma
A.B.T.
Allochthonous Belt
Parautochthonous Belt
Saint Lawrence River
30 km
Grenville Front
700°C
90 km
Lithospheric mantle
150 km
1300°C
Allochthonous Belt:
Monzonite, quartz monzonite
Mangerite
Syenite, quartz syenite
Granite, charnockite
Metasediments
Gabbro, norite, gabbronorite
Anorthositic Suite
Undifferentiated gneiss
Parautochthonous Belt:
Granite, charnockite
Gabbro, norite, gabbronorite
Knob Lake Group metasediments (Paleoproterozoic cover)
Tonalite (Reworked Archean basement)
Shear zone
Partially molten crust
Undeformed lithologies
Deformed lithologies
Unconstrained deformation
REE-enriched granitic melt involved in the genesis of REE-PGD
Allochthonous derived PGD

2. REE cycle and metallogenic implications

The REE-rich PGD investigated in this thesis show strong LREE enrichments up to 8757 ppm (13-AE-2149 PGD) either hosted in allanite or monazite for PGD hosted in metaplutonic and in metasedimentary complexes, respectively (Turlin et al., 2017).

2.1. PGD derived from the partial melting of allochthonous plutonic units

The shallow-dipping 13-AE-2149 allanite-bearing PGD presents LREE enrichments limited to its pegmatitic facies, which exhibits local diffuse contacts with the layered metamangerite it intrudes suggesting their formation from interactions between the granitic magma and its host (complements on part III, chapter 5). The fine-grained layered core of the PGD, essentially has a flat chondrite-normalized REE pattern with a strong positive Eu anomaly (Eu/Eu* up to 3.7) and low ΣLREE contents (below 52 ppm) (chapter 5). Zircon grains from this PGD yield chondritic to sub-chondritic zircon $\varepsilon Hf_{(1005\ Ma)}$ signatures ranging between -6.2 and 1.0 and associated $T_{DM2\ (1005\ Ma)}$ Hf model ages ranging between ca. 1.75 and 1.97 Ga. These data provide evidence for its derivation from the partial melting of allochthonous metaplutonic units (chapter 5), the protolith of which formed in an arc setting from the pre-Grenvillian (ca. 1500 Ma) to syn-Ottawan times, and in an extensional setting during late-Ottawan phase (ca. 1015 Ma) (Augland et al., 2015; Gobeil et al., 2002; Moukhsil et al., 2007, 2009, 2013a, 2013b, 2014). Accordingly, PGD derived from the partial melting of allochthonous plutonic units might be expected to present LREE mineralization where the magma interacted with the hosts, but these would be localized and not disseminated within the PGD.

2.2. PGD derived from the partial melting of Paleoproterozoic-Archean metapelites

The six other monazite- and allanite-bearing PGD are strongly peraluminous, they present LREE enrichments up to 7435 ppm (13-FS-1202 PGD, Turlin et al., 2017) with a strong fractionation of LREE over HREE (La_N/Yb_N up to 1193, chapter 4), low ΣHREE contents (below 128 ppm, Turlin et al., 2017, chapter 4), and a more or less developed negative Eu anomaly (Eu/Eu* down to 0.1, chapter 4). Along with the subchondritic $\varepsilon Hf_{(1003\ Ma)}$ of pristine zircon grains from a monazite-bearing and two allanite-bearing PGD, and associated Paleoproterozoic $T_{DM2\ (1003\ Ma)}$ Hf model ages (chapter 3), these features point to their derivation from the protracted high temperature partial melting of the Paleoproterozoic-Archean Knob Lake Group metapelites from the underlying Parautochthonous Belt that was initiated as early as ca. 1002 Ma under *P-T* conditions of ca. 1250-1500 MPa and ca. 815-850 °C (chapter 4,

Jannin et al., accepted; Jordan et al., 2006). The partial melting of the metapelites involved (i) the dehydration melting of muscovite, (ii) of biotite (Jannin et al., accepted), (iii) the total consumption of monazite, (iv) the LREE saturation of the anatectic melt that migrated towards higher crustal levels through melt loss event(s), and (v) the coeval prograde monazite growth shielded within unentrained peritectic garnet that were concentrated within the residual melanosome (chapter 4). Accordingly, the LREE had an incompatible behavior during this partial melting.

The comparison of the K and Rb contents, and associated K/Rb ratios of feldspar and micas from both the leucosome of the Knob Lake Group migmatitic metapelites and the various facies of the 13-AM-13 monazite-bearing PGD allowed discussion of the fractionation of the latter from the metapelites as proposed by e.g. Černý et al. (1985) and Hulsbosch et al. (2014) (chapter 4). In K/Rb vs Rb (ppm) diagrams, K-feldspar, plagioclase and biotite from the leucosome and the PGD plot on a same trend, the former with higher K/Rb ratios and lower Rb contents (chapter 4). The K/Rb ratios and Rb contents obtained on the silicates from the PGD are very high and very low, respectively. These features (i) confirm the derivation of the PGD from the partial melting of the Knob Lake Group metapelites, and (ii) show that the PGD is only slightly fractionated from its source (chapter 4). This slight fractionation is consistent with the presence of biotite with no muscovite in the PGD and with the lack of other rare-elements-containing minerals such as Li, B, Be, Rb, Sn, Nb-Ta (Turlin et al., 2017, chapter 4). Such granitic pegmatites represent the closest bodies to their source as argued in other pegmatites fields such as Cap de Creus (Spain, Alfonso and Melgarejo, 2008; Druguet et al., 2014; Van Lichtervelde et al., 2016) and Gatumba (Rwanda, Hulsbosch et al., 2014; London, 2016, 2008).

When considered together, data presented in this thesis for the steep-dipping REE-rich monazite- and allanite-bearing PGD from the central Grenville Province provide evidence for their genesis through (i) protracted high-temperature partial melting of Paleoproterozoic-Archean metapelites from the Knob Lake Group metapelites and (ii) migration of LREE saturated anatectic melts towards allochthonous mid- to low-pressure crustal segments through melt loss event(s). High-grade LREE mineralizations are achieved through the first LREE-saturated melt loss events and slight fractionation from the anatectic source. Accordingly, the key factor in the genesis of such peraluminous LREE-rich PGD is the partial melting up to complete dissolution of the LREE-bearing phase in a fertile protolith.

2.3. Control of the LREE-bearing phase

The LREE in the PGD from the central Grenville Province are hosted within monazite in paragneisses-hosted PGD and in allanite in metaplutons-hosted PGD (Turlin et al., 2017, complements on part III). Monazite is a common LREE-bearing phase in peraluminous granitic magmas and abyssal granitic pegmatites (e.g. Bea, 1996; Ercit, 2005; Linnen and Cuney, 2005; Montel, 1993; Rapp and Watson, 1986), therefore its occurrence in the strongly peraluminous PGD investigated in this thesis is not surprising. To the contrary, allanite is inferred to be restricted to granitoids with an ASI below 1.2 and to metaluminous to subaluminous abyssal pegmatites (e.g. Bea, 1996; Ercit, 2005; Ford, 1982). In addition, the control of the growth of monazite or allanite is usually ascribed to be related to the activities of Na and Ca (Berger et al., 2009; Budzyń et al., 2011). On the basis of the whole-rock geochemistry of the REE-richest facies of the PGD, Turlin et al. (2017) already suggested that in the case of the PGD from the central Grenville Province, the growth of monazite or allanite might not be only related to the activities of these elements, but also to other elements such as P, Fe and Mg. When comparing the whole-rock geochemistry of the various facies of several PGD investigated in this thesis to their respective hosts sampled at the contact and away from the contact, it appears that no link between the nature of the LREE-bearing phase in the PGD and the Ca, Na and P contents of the hosts could be outlined (Fig. 7-6a-c, complements on part III). In contrast, plotted in a Fe vs Mg diagram, PGD and their respective hosts spread along a similar Fe/Mg ratio (Fig. 7-6d). Furthermore, all monazite-bearing PGD and their metasedimentary hosts show Fe/Mg ratios below 3, whereas allanite-bearing PGD and their metaplutonic hosts show Fe/Mg over 3 (complements on part III). Turlin et al. (submitted) provided evidence supporting the intrusion of the PGD into their respective hosts under close to wet-solidus conditions (Fig. 7-4). Together, these features point to the control of the LREE mineralization as allanite or monazite in the PGD by interactions with metaplutons or metasediments from the Allochthonous Belt, at depth during magma ascent and/or at the outcropping level (Fig. 7-5). In addition, these results strengthen the conclusions of Turlin et al. (submitted) who proposed that the allochthonous mid- to low-pressure crustal segments were under suprasolidus conditions at the time of the PGD intrusion.

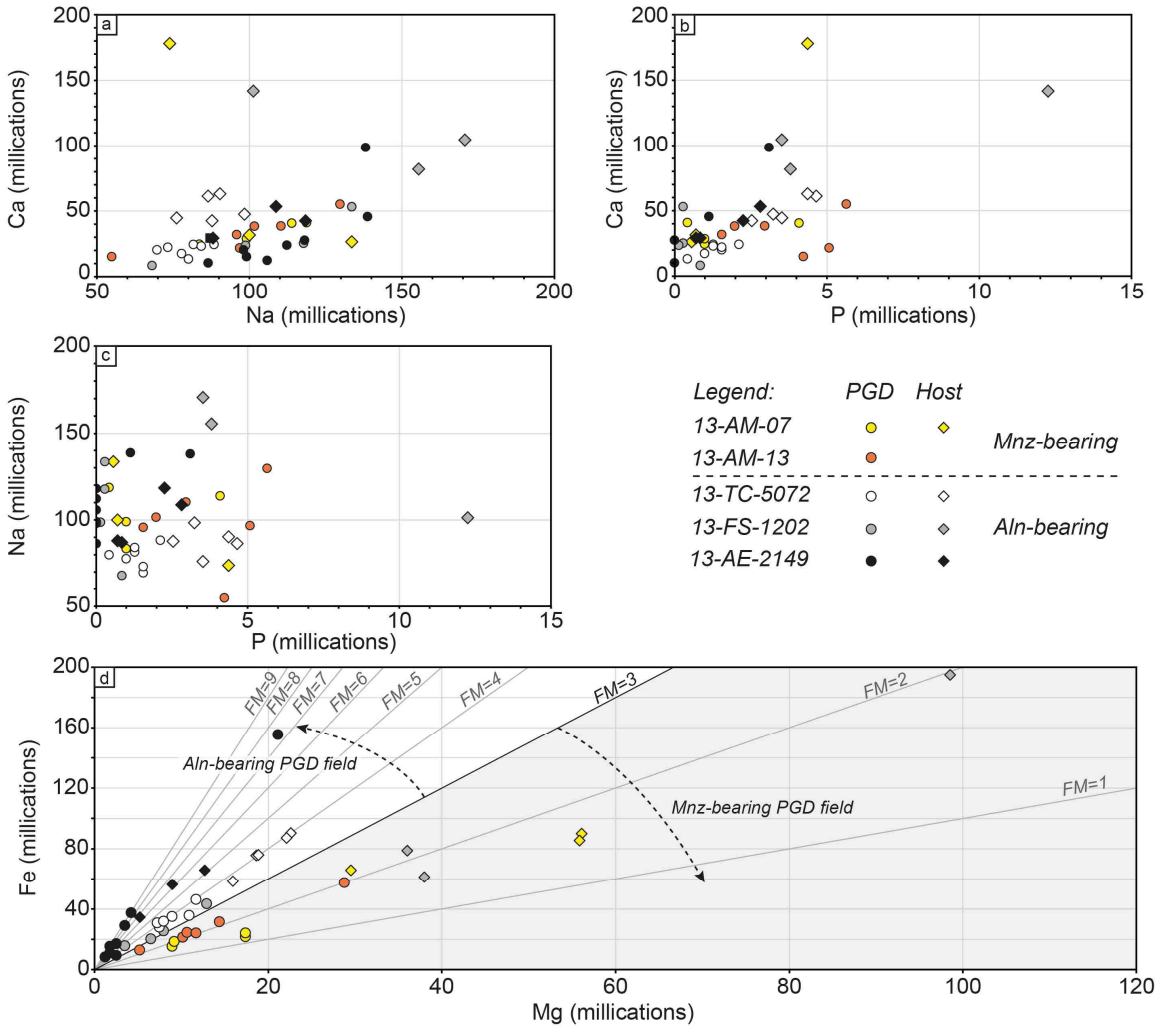

Figure 7-6: Whole-rock geochemistry of the allanite- and monazite-bearing pegmatitic granite dykes from the central Grenville and of their respective hosts. a, b and c: Ca vs Na, Ca vs P and Na vs P (millications) diagrams that do not allow to distinct allanite from monazite-bearing pegmatitic granite and from their respective host; d: Fe vs Mg (millications) diagram. Note the distinct and linear trend defined by samples from a single pegmatitic granite dyke and its host. Two compositional fields can be outlined on the basis of Fe/Mg ratio. Allanite-bearing pegmatitic granite dykes and their hosts show Fe/Mg above three, whereas monazite-bearing dykes and their hosts show Fe/Mg below three. Abbreviations: Aln-bearing = allanite-bearing pegmatitic granite dyke; FM = Fe/Mg ratio; Mnz-bearing = monazite-bearing pegmatitic granite dyke; PGD = pegmatitic granite dyke.

2.4. Source, transport and mineralization

Results presented in this thesis provide evidence that the key factor in the first order enrichment of the magma responsible for the genesis of REE-rich PGD from the central Grenville Province lies in the partial melting of a fertile protolith (chapter 4) represented by the Knob Lake Group metapelites from the Parautochthonous Belt. It corresponds to a Paleoproterozoic sequence that also occurs in the New Québec Orogen of the Churchill Province and was deposited on the Archean margin of Laurentia (Jordan et al., 2006; Rivers, 1980; van Gool et al., 2008). Accordingly, the REE were likely derived from the Superior Province and were therefore extracted from the mantle prior to the Grenvillian Orogeny.

Whether they were reworked and reconcentrated prior to their deposition within the Knob Lake Group sequences, or eroded from a fertile plutonic protolith remain unconstrained.

The REE were saturated within anatectic melt through protracted (at least 20 Ma, Jannin et al., accepted) high temperature (ca. 815-850 °C, Jannin et al., accepted; Jordan et al., 2006) partial melting that allowed complete dissolution of matrix monazite from the protolith and the release of LREE into the melt. Subsequent upward migration of the LREE-enriched anatectic melt towards the allochthonous mid- to low-pressure crustal segments was achieved through melt loss event(s).

The high-grade concentrations of the LREE within the PGD were achieved through the first LREE-saturated melt loss events and slight fractionation from the anatectic source. Further melt loss events led to the LREE depletion of the anatectic melt and to the formation of relatively depleted coarser grained facies, up to pegmatitic, within the PGD. The subsequent growth of monazite or allanite during melt crystallization was controlled by interactions with a metasedimentary or a metaplutonic host, respectively.

3. Perspectives

Complementary investigations would be required to confirm the model presented in this thesis. First, a comparison of Hf-O isotopes of zircon grains from the Knob Lake Group and of the Plus-Value Complex metapelites with the signatures of the PGD presented in this manuscript would allow to test the conclusion that the PGD were derived from the former and to assess whether there was in addition a minor contribution from the latter. Furthermore, this might give insights on the nature and age of the protoliths of the metapelites which dismantling led *in fine* to the genesis of the LREE-rich PGD. In addition, experimental studies on the LREE behavior during fractional crystallization of a LREE-saturated peraluminous magma would bring pivotal information with respect to the comprehension of petrogenetic processes of such intrusions.

Pegmatitic granite dykes are widespread in the Grenville Province (e.g. Ayres and Černý, 1982; Černý, 1990; Fowler and Doig, 1983; Jannin et al., accepted; Lentz, 1991; Masson and Gordon, 1981; Moukhsil et al., 2014; Turlin et al., 2017), but although widely reported, they are poorly studied. One of the findings of this work is that studying such PGD through several approaches that mix detailed mapping of field relationships, geochronology, isotopy and petrogeochemistry has the potential to yield new insights on the geodynamic evolution of an orogenic belt, in our case the Grenville Province.

The Grenvillian Orogeny has equivalents on the margins of Baltica with the Sveconorwegian orogenic belt formed during the assembly of the Rodinia supercontinent and exposed in south Norway (e.g. Li et al., 2008). This belt contains numerous granitic pegmatites with local REE enrichment hosted especially in allanite and monazite (Goodenough et al., 2016; Müller et al., 2008; Romer and Smeds, 1996). Accordingly, the results presented in this thesis and the implications for (i) the REE metallogenic cycle in high-grade metamorphic environments and for (ii) the geodynamic evolution of the Proterozoic Grenvillian orogenic belt may offer new clues to decipher the processes responsible for the genesis of Sveconorwegian REE-rich pegmatitic granite.

The Grenvillian Orogeny is a Proterozoic equivalent of the Himalaya-Tibet Orogen (e.g. Rivers, 2008). Pegmatitic granite dykes in the latter orogen occur in association with leucogranite from the top of which they emanate (Searle et al., 2016). These intrusions are found within the channel flow system that is developed in the Greater Himalaya Sequence, structurally above the Indian Shield Archean granulites, with the Main Central Thrust (MCT) representing the base of the channel and the South Tibetan Detachment (STD) representing its top (e.g. Beaumont et al., 2001; Cottle et al., 2015; Searle et al., 2016, 2009, 2006). These melts are derived from kyanite±sillimanite metamorphism of the Greater Himalayan Sequence in response to crustal thickening (e.g. Searle et al., 2016, 2006) and originate from kyanite-bearing metapelitic protoliths (e.g. Harris and Massey, 1994). This Greater Himalayan Sequence contains, among others, Proterozoic pelites and augen gneisses (e.g. Searle et al., 2006) that, together with the genesis of leucogranite and pegmatites in response to crustal thickening, suggests a similar configuration to that proposed for the PGD in the central Grenville investigated in this thesis. However, the granitic pegmatites in the Greater Himalaya Sequence only show LILE, Sn and U mineralization, whereas those investigated in this thesis from the central Grenville Province show REE mineralization. These contrasting signatures suggest the derivation of these two types of pegmatitic granites from more (Himalaya-Tibet Belt) or less (Grenville Province) evolved protoliths, consistent with the exposure of the orogenic root of the latter. Further identification of similar protoliths to those involved in the genesis of the REE-rich PGD from the central Grenville Province and exploration research in the vicinity of the source, i.e. where granitic melts are only slightly fractionated from their source, might allow the identification of REE-rich PGD similar to those of the central Grenville Province.

References

Alfonso, P., Melgarejo, J.C., 2008. Fluid Evolution in the Zoned Rare-Element Pegmatite Field at Cap De Creus, Catalonia, Spain. Can. Mineral. 46, 597–617. doi:10.3749/canmin.46.3.597

Augland, L.E., Moukhsil, A., Solgadi, F., Indares, A., McFarlane, C., 2015. Pinwarian to Grenvillian magmatic evolution in the central Grenville Province: new constraints from ID-TIMS U-Pb ages and coupled Lu-Hf S-MC-ICP-MS data. Canadian Journal of Earth Sciences 52, 701–721. doi:10.1139/cjes-2014-0232

Ayres, L.D., Černý, P., 1982. Metallogeny of granitoid rocks in the Canadian Shield. Can. Mineral. 20, 439–536.

Bea, F., 1996. Residence of REE, Y, Th and U in granites and crustal protoliths; Implications for the chemistry of crustal melts. J. Petrology 37, 521–552. doi:10.1093/petrology/37.3.521

Beaumont, C., Jamieson, R.A., Nguyen, M.H., Lee, B., 2001. Himalayan tectonics explained by extrusion of a low-viscosity crustal channel coupled to focused surface denudation. Nature 414, 738–742.

Berger, A., Rosenberg, C., Schaltegger, U., 2009. Stability and isotopic dating of monazite and allanite in partially molten rocks: examples from the Central Alps. Swiss J. Geosci. 102, 15–29. doi:10.1007/s00015-009-1310-8

Budzyń, B., Harlov, D.E., Williams, M.L., Jercinovic, M.J., 2011. Experimental determination of stability relations between monazite, fluorapatite, allanite, and REE-epidote as a function of pressure, temperature, and fluid composition. American Mineralogist 96, 1547–1567. doi:10.2138/am.2011.3741

Černý, P., 1990. Distribution, affiliation and derivation of rare-element granitic pegmatites in the Canadian Shield. Geol. Rundsch. 79, 183–226. doi:10.1007/BF01830621

Černý, P., Meintzer, R.E., Anderson, A.J., 1985. Extreme fractionation in rare-element granitic pegmatites; selected examples of data and mechanisms. Can. Mineral. 23, 381–421.

Cottle, J.M., Larson, K.P., Kellett, D.A., 2015. How does the mid-crust accommodate deformation in large, hot collisional orogens? A review of recent research in the

Himalayan orogen. Journal of Structural Geology 78, 119–133. doi:10.1016/j.jsg.2015.06.008

Druguet, E., Castro, A., Chichorro, M., Pereira, M.F., Fernández, C., 2014. Zircon geochronology of intrusive rocks from Cap de Creus, Eastern Pyrenees. Geological Magazine 151, 1095–1114. doi:10.1017/S0016756814000041

Dunning, G., Indares, A., 2010. New insights on the 1.7–1.0 Ga crustal evolution of the central Grenville Province from the Manicouagan – Baie Comeau transect. Precambrian Research 180, 204–226. doi:10.1016/j.precamres.2010.04.005

Ercit, T.S., 2005. REE-enriched granitic pegmatites. Short Course Notes - Geological Association of Canada 17, 175–199.

Ford, K.L., 1982. Uraniferous pegmatites of the Sharbot Lake area, Ontario, Uranium in Granites. Geological Survey Canada, Paper 81-23.

Fowler, A.D., Doig, R., 1983. The significance of europium anomalies in the REE spectra of granites and pegmatites, Mont Laurier, Quebec. Geochimica et Cosmochimica Acta 47, 1131–1137. doi:10.1016/0016-7037(83)90243-0

Gobeil, A., Hébert, C., Clark, T., Beaumier, M., Perreault, S., 2002. Géologie de la région du lac De la Blache (22K/03 et 22K/04). Ministère des Ressources Naturelles, Québec, RG 2002-01, 53 p.

Goodenough, K.M., Schilling, J., Jonsson, E., Kalvig, P., Charles, N., Tuduri, J., Deady, E.A., Sadeghi, M., Schiellerup, H., Müller, A., Bertrand, G., Arvanitidis, N., Eliopoulos, D.G., Shaw, R.A., Thrane, K., Keulen, N., 2016. Europe's rare earth element resource potential: An overview of REE metallogenetic provinces and their geodynamic setting. Ore Geology Reviews 72, Part 1, 838–856. doi:10.1016/j.oregeorev.2015.09.019

Harris, N., Massey, J., 1994. Decompression and anatexis of Himalayan metapelites. Tectonics 13, 1537–1546. doi:10.1029/94TC01611

Hoffman, P.F., 1989. Precambrian geology and tectonic history of North America The geology of North America. Geol. Soc. Am. : Boulder, CO, United States, United States, pp. 447–512.

Hulsbosch, N., Hertogen, J., Dewaele, S., André, L., Muchez, P., 2014. Alkali metal and rare earth element evolution of rock-forming minerals from the Gatumba area pegmatites

(Rwanda): Quantitative assessment of crystal-melt fractionation in the regional zonation of pegmatite groups. Geochimica et Cosmochimica Acta 132, 349–374. doi:10.1016/j.gca.2014.02.006

Hynes, A., Indares, A., Rivers, T., Gobeil, A., 2000. Lithoprobe line 55: integration of out-of-plane seismic results with surface structure, metamorphism, and geochronology, and the tectonic evolution of the eastern Grenville Province. Can. J. Earth Sci. 37, 341–358. doi:10.1139/e99-076

Indares, A., Dunning, G., 2004. Crustal architecture above the high-pressure belt of the Grenville Province in the Manicouagan area: new structural, petrologic and U–Pb age constraints. Precambrian Research 130, 199–228. doi:10.1016/j.precamres.2003.11.005

Indares, A., Dunning, G., 2001. Partial melting of high-P–T metapelites from the Tshenukutish Terrane (Grenville Province): Petrography and U–Pb geochronology. J. Petrology 42, 1547–1565. doi:10.1093/petrology/42.8.1547

Indares, A., Dunning, G., Cox, R., 2000. Tectono-thermal evolution of deep crust in a Mesoproterozoic continental collision setting: the Manicouagan example. Can. J. Earth Sci. 37, 325–340. doi:10.1139/e99-069

Indares, A., Dunning, G., Cox, R., Gale, D., Connelly, J., 1998. High-pressure, high-temperature rocks from the base of thick continental crust: Geology and age constraints from the Manicouagan Imbricate Zone, eastern Grenville Province. Tectonics 17, 426–440. doi:10.1029/98TC00373

Jannin, S., Gervais, F., Moukhsil, A., Augland, L.E., Crowley, J.L., accepted. Déformations tardi-grenvilliennes dans la Ceinture parautochtone (Province de Grenville centrale) : contraintes géochronologiques par couplage de méthodes U/Pb de haute résolution spatiale et de haute précision. Canadian Journal of Earth Sciences.

Jordan, S.L., Indares, A., Dunning, G., 2006. Partial melting of metapelites in the Gagnon terrane below the high-pressure belt in the Manicouagan area (Grenville Province): pressure–temperature (P–T) and U–Pb age constraints and implications. Can. J. Earth Sci. 43, 1309–1329. doi:10.1139/E06-038

Krogh, T.E., 1994. Precise U-Pb ages for Grenvillian and pre-Grenvillian thrusting of Proterozoic and Archean metamorphic assemblages in the Grenville Front tectonic zone, Canada. Tectonics 13, 963–982. doi:10.1029/94TC00801

Lasalle, S., Dunning, G., Indares, A., 2014. In situ LA–ICP–MS dating of monazite from aluminous gneisses: insights on the tectono-metamorphic history of a granulite-facies domain in the central Grenville Province. Can. J. Earth Sci. 51, 558–572. doi:10.1139/cjes-2013-0170

Lasalle, S., Indares, A., 2014. Anatectic record and contrasting P-T paths of aluminous gneisses from the central Grenville Province. Journal of Metamorphic Geology 32, 627–646. doi:10.1111/jmg.12083

Lentz, D.R., 1991. Petrogenesis of uranium-, thorium-, molybdenum-, and rare earth element-bearing pegmatites, skarns, and veins in the central metasedimentary belt of the Grenville Province, Ontario and Quebec. (Unpublished Ph.D. thesis). University of Ottawa (Canada).

Li, Z.X., Bogdanova, S.V., Collins, A.S., Davidson, A., De Waele, B., Ernst, R.E., Fitzsimons, I.C.W., Fuck, R.A., Gladkochub, D.P., Jacobs, J., Karlstrom, K.E., Lu, S., Natapov, L.M., Pease, V., Pisarevsky, S.A., Thrane, K., Vernikovsky, V., 2008. Assembly, configuration, and break-up history of Rodinia: A synthesis. Precambrian Research, Testing the Rodinia hypothesis: Records in its building blocks 160, 179–210. doi:10.1016/j.precamres.2007.04.021

Linnen, R.L., Cuney, M., 2005. Granite-related rare-element deposits and experimental constraints on Ta-Nb-W-Sn-Zr-Hf mineralization. Short Course Notes - Geological Association of Canada 17, 45–68.

London, D., 2016. Rare-element granitic pegmatites. Reviews in Economic Geology 18, 165–193.

London, D., 2008. Pegmatites, Mineralogical Association of Canada.

Masson, S.L., Gordon, J.B., 1981. Radioactive mineral deposits of the Pembroke-Renfrew area (No. 23), Mineral Deposits Circ. Ont. Geol. Surv.

Montel, J.-M., 1993. A model for monazite/melt equilibrium and application to the generation of granitic magmas. Chemical Geology, Geochemistry of Accessory Minerals 110, 127–146. doi:10.1016/0009-2541(93)90250-M

Moukhsil, A., Lacoste, P., Gobeil, A., David, J., 2009. Synthèse géologique de la région de Baie-Comeau. Ministère des Ressources naturelles et de la Faune, Québec, RG 2009-03, 30 p.

Moukhsil, A., Lacoste, P., Simard, M., Perreault, S., 2007. Géologie de la région septentrionale de Baie-Comeau (22F07, 22F08, 22F09, 22F15 et 22F16). Ministère des Ressources naturelles et de la Faune, Québec, RP 2007-04, 16 p.

Moukhsil, A., Solgadi, F., Belkacim, S., Elbasbas, A., Augland, L.E., 2014. Géologie de la région du lac Okaopéo, Côte-Nord. Ministère de l'Energie et des Ressources Naturelles, Québec, RG 2014-03, 34 p.

Moukhsil, A., Solgadi, F., Clark, T., Blouin, S., Indares, A., Davis, D.W., 2013a. Géologie du nord-ouest de la région du barrage Daniel-Johnson (Manic 5), Côte-Nord. Ministère des Ressources Naturelles, Québec, RG 2013-01, 46 p.

Moukhsil, A., Solgadi, F., Indares, A., Belkacim, S., 2013b. Géologie de la région septentrionale du réservoir aux Outardes 4, Côte-Nord. Ministère des Ressources Naturelles, Québec, RG 2013-03, 33 p.

Müller, A., Ihlen, P.M., Kronz, A., 2008. Quartz chemistry in polygeneration Sveconorwegian pegmatites, Froland, Norway. European Journal of Mineralogy 20, 447–463. doi:10.1127/0935-1221/2008/0020-1822

Rapp, R.P., Watson, E.B., 1986. Monazite solubility and dissolution kinetics: implications for the thorium and light rare earth chemistry of felsic magmas. Contr. Mineral. and Petrol. 94, 304–316. doi:10.1007/BF00371439

Rivers, T., 2009. The Grenville Province as a large hot long-duration collisional orogen – insights from the spatial and thermal evolution of its orogenic fronts. Geological Society, London, Special Publications 327, 405–444. doi:10.1144/SP327.17

Rivers, T., 2008. Assembly and preservation of lower, mid, and upper orogenic crust in the Grenville Province—Implications for the evolution of large hot long-duration orogens. Precambrian Research 167, 237–259. doi:10.1016/j.precamres.2008.08.005

Rivers, T., 1980. Revised stratigraphic nomenclature for Aphebian and other rock units, southern Labrador Trough, Grenville Province. Can. J. Earth Sci. 17, 668–670. doi:10.1139/e80-062

Rivers, T., Culshaw, N., Hynes, A., Indares, A., Jamieson, R., Martignole, J., 2012. The Grenville Orogen - A Post-LITHOPROBE Perspective, in: J.A. Percival, F.A. Cook, and R.M. Clowes (eds) Tectonic Styles in Canada: The LITHOPROBE Perspective, Geological Association of Canada. Special Paper 49, pp. 97–236.

Rivers, T., Ketchum, J., Indares, A., Hynes, A., 2002. The High Pressure belt in the Grenville Province: architecture, timing, and exhumation. Can. J. Earth Sci. 39, 867–893.

Rivers, T., Martignole, J., Gower, C.F., Davidson, A., 1989. New tectonic divisions of the Grenville Province, Southeast Canadian Shield. Tectonics 8, 63–84. doi:10.1029/TC008i001p00063

Romer, R.L., Smeds, S.-A., 1996. U-Pb columbite ages of pegmatites from Sveconorwegian terranes in southwestern Sweden. Precambrian Research 76, 15–30. doi:10.1016/0301-9268(95)00023-2

Searle, M.P., Cottle, J.M., Streule, M.J., Waters, D.J., 2009. Crustal melt granites and migmatites along the Himalaya: melt source, segregation, transport and granite emplacement mechanisms. Earth and Environmental Science Transactions of The Royal Society of Edinburgh 219–233. doi:10.1017/S175569100901617X

Searle, M.P., Law, R.D., Jessup, M.J., 2006. Crustal structure, restoration and evolution of the Greater Himalaya in Nepal-South Tibet; implications for channel flow and ductile extrusion of the middle crust, in: Law, R. D., Searle, M. P. & Godin, L. (Eds) Channel flow, ductile extrusion and exhumation in continental collision zones. Geological Society, London, Special Publications 268. pp. 355–378.

Searle, M.P., Robb, L.J., Gardiner, N.J., 2016. Tectonic processes and metallogeny along the Tethyan Mountain Ranges of the Middle East and South Asia (Oman, Himalaya, Karakoram, Tibet, Myanmar, Thailand, Malaysia). Special Publication 19 Chapter 12, 301–327.

Turlin, F., André-Mayer, A.-S., Moukhsil, A., Vanderhaeghe, O., Gervais, F., Solgadi, F., Groulier, P.-A., Poujol, M., 2017. Unusual LREE-rich, peraluminous, monazite- or allanite-bearing pegmatitic granite in the central Grenville Province, Québec. Ore Geology Reviews 89, 627–667. doi:10.1016/j.oregeorev.2017.04.019

Turlin, F., Deruy, C., Eglinger, A., Vanderhaeghe, O., André-Mayer, A.-S., Poujol, M., Moukhsil, A., Solgadi, F., submitted. A record of 70 Ma suprasolidus conditions in the Grenville large, hot and long-duration orogen. Terra Nova.

van Gool, J.A.M., Rivers, T., Calon, T., 2008. Grenville Front zone, Gagnon terrane, southwestern Labrador: Configuration of a midcrustal foreland fold-thrust belt. Tectonics 27, TC1004. doi:10.1029/2006TC002095

Van Lichtervelde, M., Grand'Homme, A., Saint-Blanquat, M. de, Olivier, P., Gerdes, A., Paquette, J.-L., Melgarejo, J.C., Druguet, E., Alfonso, P., 2016. U-Pb geochronology on zircon and columbite-group minerals of the Cap de Creus pegmatites, NE Spain. Miner Petrol 1–21. doi:10.1007/s00710-016-0455-1

LISTE DES ILLUSTRATIONS

Introduction

Partie I : Granites pegmatitiques à REE du Grenville central

Préambule

Chapitre 1 : Unusual LREE-rich, peraluminous, monazite- or allanite-bearing pegmatitic granite in the central Grenville Province, Québec

Partie II : Contexte géodynamique et traçage de la source

Chapitre 2 : A record of 70 Ma suprasolidus conditions in the Grenville large, hot and long-duration orogen

Partie III : Pétrogenèse des granites pegmatitiques

Chapitre 4 : Anatectic melt loss from metapelites and low magmatic fractionation: a prerequisite in the genesis of peraluminous high-grade LREE-rich peraluminous pegmatitic granite

REE in Al-rich facies marked by the concentration of biotite. The ΣREE content and ASI are positively correlated within the metapelites that is consistent with the sequestration of monazite in peritectic garnet in the biotite-rich melanosome; d: Eu/Eu* vs ΣREE (ppm) showing the decrease of the ΣREE content within the pegmatitic granite towards feldspar-dominated pegmatitic facies. The highest REE content in the paragneisses is sequestrated in the melanosome which negative Eu anomaly is consistent with its mineralogy dominated by garnet and biotite; e: Eu/Eu* vs La_N/Yb_N diagram showing that the lower LREE over HREE fractionation towards pegmatitic facies of the pegmatitic granite dyke. No fractionation of REE is recorded within the metapelites; f: chondrite-normalized REE patterns. Note the strong LREE enrichment of all the facies of the pegmatitic granite dyke showing a strong fractionation of the LREE over the HREE in every facies and the more or less developed Eu negative anomaly that flattens towards relatively LREE-impoverished facies. The leucosome of the paragneisses is impoverished in REE compared to the mesosome and melanosome, and shows a positive Eu anomaly consistent with its feldspar-dominated mineralogy. These features suggest that the leucosome represent a cumulate; g: REE patterns normalized to the REE-poorest facies of the pegmatitic granite. Note the lack of fractionation in the LREE and the flattening Eu negative anomaly with decreasing ΣREE content; h: melanosome-normalized REE pattern showing the lack of fractionation of the REE from the melanosome towards the leucosome. The LREE over the HREE fractionation of the dyke is in every facies higher than in the melanosome and mesosome, suggesting the sequestration of the HREE in the paragneisses, consistent with the abundance of peritectic garnet. Abbreviations: [1]: normalization after McDonough and Sun (1995); [2]: normalization to the pegmatitic facies of the dyke (sample 13-AM-13-F, Table 4-2); [3]: normalization to the melanosome of the paragneisses (sample 12-SJ-49-D, Table 4-2); Bt = biotite; Fsp = feldspar; Grt = garnet; PGD = pegmatitic granite dyke. 279

Chapitre 5 : Pegmatitic granite dyke from the central Grenville derived from partial melting of plutonic rocks from the Allochthonous Belt

Compléments : Preliminary study: Controlling factors on the mineralization of allanite vs monazite in the pegmatitic granite dykes from the central Grenville Province

General conclusions

LISTE DES TABLEAUX

Partie I : Granites pegmatitiques à REE du Grenville central

Chapitre 1 : Unusual LREE-rich, peraluminous, monazite- or allanite-bearing pegmatitic granite in the central Grenville Province, Québec

Partie II : Contexte géodynamique et traçage de la source

Chapitre 2 : A record of 70 Ma suprasolidus conditions in the Grenville large, hot and long-duration orogen

Chapitre 3 : Pegmatitic granite dykes in the central Grenville Belt a result of partial melting of Paleoproterozoic-Archean metasedimentary rocks: evidence from zircon U-Pb-Hf-O isotope and trace element analyses

Partie III : Pétrogenèse des granites pegmatitiques

Chapitre 4 : Anatectic melt loss from metapelites and low magmatic fractionation: a prerequisite in the genesis of peraluminous high-grade LREE-rich peraluminous pegmatitic granite

Chapitre 5 : Pegmatitic granite dyke from the central Grenville derived from partial melting of plutonic rocks from the Allochthonous Belt

Résumé : Les éléments de terres rares (ÉTR) sont des métaux de grand intérêt économique et des traceurs géologiques de premier ordre mais leur cycle métallogénique reste encore méconnu. La Province de Grenville expose sa racine orogénique et présente une grande concentration d'occurrences d'ÉTR, notamment associées à des granites pegmatitiques (« PGD ») dans le Grenville central. Deux mécanismes peuvent être à l'origine de ces PGD, (i) la fusion partielle d'une croûte continentale archéenne et/ou paléoprotérozoïque de la racine orogénique, ou (ii) l'extrême différenciation de magmas mantelliques produits en contexte d'extension post-orogénique. Une approche multi-méthodes (terrain, pétrogéochimie, géochronologie et isotopie) permet de caractériser ces PGD à ÉTR et de discuter leur pétrogénèse dans le cadre de l'évolution géodynamique de la province. Ils ont intrudé à ~1005-1000 Ma (U-Pb monazite et zircon) des métaplutons (minéralisation en allanite) ou des séries métasédimentaires (minéralisation en monazite) du segment de moyenne pression de la ceinture Allochtone. La datation U-Pb sur monazite et apatite d'un leucosome de ces paragneiss migmatitiques met en évidence un pic de métamorphisme au faciès granulite à 1080-1050 Ma suivi d'un refroidissement lent à un taux de 2 à 6°C/Ma, d'abord dans les conditions suprasolidus jusqu'à l'intrusion des PGD dans des conditions proches du solidus hydraté, puis dans des conditions subsolidus jusqu'à l'isotherme 450-500°C enregistré à 970-950 Ma. L'intrusion des PGD est synchrone de l'initiation dès ~1005 Ma de la fusion partielle prolongée (> 20 Ma) des métasédiments parautochtones sous-jacents. Le caractère peralumineux des PGD, l'étude de zircons néoformés des PGD (isotopes U-Pb-Hf-O et éléments traces), et l'étude pétrogéochimique des PGD et des métapélites paléoprotérozoïques à archéennes de la ceinture Parautochtone, issues de l'érosion de la marge de Laurentia, traduisent la formation des PGD par leur fusion partielle. Au contraire, un PGD issu de la remobilisation de plutons allochtones est peu minéralisé en ÉTR, confirmant que l'extraction des ÉTR de ces occurrences du Grenville central est associée à des roches d'affinité crustale du Craton du Supérieur.

Abstract: The Rare Earth Elements (REE) are of great economic interest and first order geological tracers. However, their metallogenic cycle remains poorly defined. The Grenville Province exposes its orogenic root and shows numerous REE occurrences that are especially associated with pegmatitic granite dykes ("PGD") in the central Grenville. Two hypotheses can account for the genesis of these PGD, whether (i) the partial melting of the orogenic root composed of reworked Archean and/or Proterozoic pre-existing continental crust, or (ii) the extreme differentiation of mantle melts produced during post-orogenic extension. A multi-method approach (field geology, petrogeochemistry, geochronology and isotopy) allow to characterize the PGD and discuss their petrogenesis during the geodynamic evolution of the province. They intruded at ca. 1005-1000 Ma (U-Pb on monazite and zircon) metaplutons (mineralization hosted in allanite) or metasedimentary sequences (mineralization hosted in monazite) from the mid-pressure allochthonous crustal segment. U-Pb dating on monazite and apatite from a single leucosome of these migmatitic paragneisses evidence for a peak of metamorphism at ca. 1080-1050 Ma that was followed by a slow cooling at a rate of 2 to 6°C/Ma, first under suprasolidus conditions until the close to wet-solidus intrusion of PGD, and then under subsolidus conditions down to the 450-500°C isotherm dated at ca. 970-950 Ma. The intrusion of the PGD is coeval with the initiation as early as ca. 1005 Ma of the protracted (> 20 Ma) partial melting of underlying parautochthonous paragneisses. The peraluminous character of the PGD, the investigation of pristine magmatic zircon of the PGD (U-Pb-Hf-O isotopes and trace elements), and the petrogeochemical investigations of parautochthonous Paleoproterozoic-Archean metapelites that derive from the Laurentian margin's erosion, points to the derivation of the PGD from their partial melting. To the contrary, one PGD derived from the reworking of allochthonous plutonic units is poorly mineralized in REE, and confirms that REE from the central Grenville occurrences are issued from crustal rocks of the Superior Craton.